

# frontiers

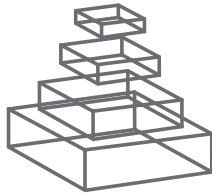
## RESEARCH TOPICS



## ACTIVE TOUCH SENSING

### Topic Editors

Robyn Grant, Pavel M. Itskov, Blythe Towal  
and Tony J. Prescott



# frontiers

## **FRONTIERS COPYRIGHT STATEMENT**

© Copyright 2007-2014  
Frontiers Media SA.  
All rights reserved.

All content included on this site, such as text, graphics, logos, button icons, images, video/audio clips, downloads, data compilations and software, is the property of or is licensed to Frontiers Media SA ("Frontiers") or its licensees and/or subcontractors. The copyright in the text of individual articles is the property of their respective authors, subject to a license granted to Frontiers.

The compilation of articles constituting this e-book, wherever published, as well as the compilation of all other content on this site, is the exclusive property of Frontiers. For the conditions for downloading and copying of e-books from Frontiers' website, please see the Terms for Website Use. If purchasing Frontiers e-books from other websites or sources, the conditions of the website concerned apply.

Images and graphics not forming part of user-contributed materials may not be downloaded or copied without permission.

Individual articles may be downloaded and reproduced in accordance with the principles of the CC-BY licence subject to any copyright or other notices. They may not be re-sold as an e-book.

As author or other contributor you grant a CC-BY licence to others to reproduce your articles, including any graphics and third-party materials supplied by you, in accordance with the Conditions for Website Use and subject to any copyright notices which you include in connection with your articles and materials.

All copyright, and all rights therein, are protected by national and international copyright laws.

The above represents a summary only. For the full conditions see the Conditions for Authors and the Conditions for Website Use.

ISSN 1664-8714

ISBN 978-2-88919-248-9

DOI 10.3389/978-2-88919-248-9

## **ABOUT FRONTIERS**

Frontiers is more than just an open-access publisher of scholarly articles: it is a pioneering approach to the world of academia, radically improving the way scholarly research is managed. The grand vision of Frontiers is a world where all people have an equal opportunity to seek, share and generate knowledge. Frontiers provides immediate and permanent online open access to all its publications, but this alone is not enough to realize our grand goals.

## **FRONTIERS JOURNAL SERIES**

The Frontiers Journal Series is a multi-tier and interdisciplinary set of open-access, online journals, promising a paradigm shift from the current review, selection and dissemination processes in academic publishing.

All Frontiers journals are driven by researchers for researchers; therefore, they constitute a service to the scholarly community. At the same time, the Frontiers Journal Series operates on a revolutionary invention, the tiered publishing system, initially addressing specific communities of scholars, and gradually climbing up to broader public understanding, thus serving the interests of the lay society, too.

## **DEDICATION TO QUALITY**

Each Frontiers article is a landmark of the highest quality, thanks to genuinely collaborative interactions between authors and review editors, who include some of the world's best academicians. Research must be certified by peers before entering a stream of knowledge that may eventually reach the public - and shape society; therefore, Frontiers only applies the most rigorous and unbiased reviews.

Frontiers revolutionizes research publishing by freely delivering the most outstanding research, evaluated with no bias from both the academic and social point of view.

By applying the most advanced information technologies, Frontiers is catapulting scholarly publishing into a new generation.

## **WHAT ARE FRONTIERS RESEARCH TOPICS?**

Frontiers Research Topics are very popular trademarks of the Frontiers Journals Series: they are collections of at least ten articles, all centered on a particular subject. With their unique mix of varied contributions from Original Research to Review Articles, Frontiers Research Topics unify the most influential researchers, the latest key findings and historical advances in a hot research area!

Find out more on how to host your own Frontiers Research Topic or contribute to one as an author by contacting the Frontiers Editorial Office: [researchtopics@frontiersin.org](mailto:researchtopics@frontiersin.org)

# ACTIVE TOUCH SENSING

Topic Editors:

**Robyn Grant**, Manchester Metropolitan University, United Kingdom

**Pavel M. Itskov**, Champalimaud Foundation, Portugal

**Blythe Towal**, California Institute of Technology, USA

**Tony J. Prescott**, University of Sheffield, United Kingdom



Left: finger tips exploring a textured surface using active touch strategies; middle: rats use their whiskers for active touch; right: tactile robot hoover using its robot whiskers to discriminate between different floor textures.

in articles on the behavioral, physiological and neuronal underpinnings of active touch in a range of species (including humans) for submission to *Frontiers in Behavioral Neuroscience*. We also welcomed articles describing robotic systems with biomimetic or bio-inspired tactile sensing systems for publication in *Frontiers in Neurorobotics*.

Active touch can be described as the control of the position and movement of tactile sensing systems to facilitate information gain. In other words, it is finding out about the world by reaching out and exploring—sensing by ‘touching’ as opposed to ‘being touched’. In this Research Topic (with cross-posting in both *Behavioral Neuroscience* and *Neurorobotics*) we welcomed articles from junior researchers on any aspect of active touch. We were especially interested

# Table of Contents

- 04** ***Active Touch Sensing: Finger Tips, Whiskers, and Antennae***  
Robyn A. Grant, Pavel M. Itskov, Blythe Towal and Tony J. Prescott
- 06** ***An fMRI Study on Cortical Responses During Active Self-Touch and Passive Touch From Others***  
Rochelle Ackerley, Eusra Hassan, Andrew Curran, Johan Wessberg, Håkan Olausson and Francis McGlone
- 15** ***Bayesian Exploration for Intelligent Identification of Textures***  
Jeremy A. Fishel and Gerald E. Loeb
- 35** ***Learning Tactile Skills Through Curious Exploration***  
Leo Pape, Calogero M. Oddo, Marco Controzzi, Christian Cipriani, Alexander Förster, Maria C. Carrozza and Jürgen Schmidhuber
- 51** ***Use of Tactile Feedback to Control Exploratory Movements to Characterize Object Compliance***  
Zhe Su, Jeremy A. Fishel, Tomonori Yamamoto and Gerald E. Loeb
- 60** ***Texture-Induced Vibrations in the Forearm During Tactile Exploration***  
Benoit Delhayé, Vincent Hayward, Philippe Lefèvre and Jean-Louis Thonnard
- 70** ***Rasch-Built Measure of Pleasant Touch Through Active Fingertip Exploration***  
Anne Klöcker, Carlyne Arnould, Massimo Penta and Jean-Louis Thonnard
- 79** ***Whisker Encoding of Mechanical Events During Active Tactile Exploration***  
Yves Boubenec, Daniel E. Shulz and Georges Debrégeas
- 95** ***Sensory Prediction on a Whiskered Robot: A Tactile Analogy to “Optical Flow”***  
Christopher L. Schroeder and Mitra J. Z. Hartmann
- 106** ***The Effect of Whisker Movement on Radial Distance Estimation: A Case Study in Comparative Robotics***  
Mathew H. Evans, Charles W. Fox, Nathan F. Lepora, Martin J. Pearson, J. Charles Sullivan and Tony J. Prescott
- 119** ***The Role of Orienting in Vibrissal Touch Sensing***  
Robyn A. Grant, Anna L. Sperber and Tony J. Prescott
- 131** ***Tactile Experience Shapes Prey-Capture Behavior in Etruscan Shrews***  
Farzana Anjum and Michael Brecht
- 139** ***An Insect-Inspired Bionic Sensor for Tactile Localization and Material Classification with State-Dependent Modulation***  
Luca Patanè, Sven Hellbach, André F. Krause, Paolo Arena and Volker Dürri
- 157** ***Active Tactile Sampling by an Insect in a Step-Climbing Paradigm***  
André F. Krause and Volker Dürri



# Active touch sensing: finger tips, whiskers, and antennae

Robyn A. Grant<sup>1\*</sup>, Pavel M. Itskov<sup>2</sup>, R. Blythe Towal<sup>3</sup> and Tony J. Prescott<sup>4</sup>

<sup>1</sup> Division of Biology and Conservation Ecology, Manchester Metropolitan University, Manchester, UK

<sup>2</sup> Champalimaud Foundation, Lisbon, Portugal

<sup>3</sup> Qualcomm, La Jolla, San Diego, CA, USA

<sup>4</sup> Department of Psychology, University of Sheffield, Sheffield, UK

\*Correspondence: robyn.grant@mmu.ac.uk

## Edited and reviewed by:

Nuno Sousa, University of Minho, Portugal

**Keywords:** sensorimotor, animal models, sensation, active sensing, touch

Active touch can be described as the control of the position and movement of tactile sensing systems by reaching out and exploring—sensing by “touching” as opposed to being touched. The active nature of these movements entails precise control of the sensory apparatus, which is task-specific and maximizes sensory information from the environment. This collection brings together a group of articles from progressive, early career scientists who are researching active touch sensing from a variety of different perspectives including behavioral, physiological, neuronal, computational, and robotic. There are a host of different model systems that are used to investigate active touch sensing and this collection sees the three main systems represented; that of the human hand, mammalian whiskers, and insect antennae. In this collection we have grouped the studies together into sections by their system and each section contains a collection of articles from both *Frontiers in Behavioral Neuroscience* and *Frontiers in Neurorobotics*. We feel that this indicates the truly multidisciplinary nature of studying active touch.

The first section of articles covers various aspects of human touch. As with all active touch systems, humans move their fingertips through a sequence of exploratory movements that yields the most information from the task. These movements depend on both the task in hand and prior experience. Ackerley et al. (2012), demonstrated using fMRI that different brain areas are functional in active touch tasks compared to passive touch ones. Articles within this section of the collection demonstrate that biomimetic robots can exploit the information generated by different movements to select the most “useful” movements that maximize information to successfully discriminate between different textures (Fishel and Loeb, 2012; Pape et al., 2012) and are able to judge surface compliance (Su et al., 2012). Texture tasks can be achieved by processing sensor information from fingertips, but also the movements of the wrists and fingertips in relation to the surface, which can code for surface properties (Delhaye et al., 2012). Klöcker et al. (2012) show that as well as movement, force and vibration data, touch can also be related to feelings of pleasantness, with fingertip moisture levels as a good correlate of unpleasantness.

The whisker, or vibrissal, system of small mammals is an important model of active touch sensing. The majority of the work in this area is aimed at understanding the neural substrates that are involved in this complex sensorimotor system. In order to obtain reliable tactile information about their environment most of the whiskered mammals move their vibrissae

rhythmically, a motion known as whisking. Unlike in human touch, the whiskers are ultimately made up of dead cells, with sensory information obtained at the base of the whisker, in the follicle. Boubenec et al. (2012) propose that the contact and detachment of a whisker with a surface is likely to give rise to the most significant neural responses. Changes in the bending moment of the whisker can then be used to calculate the position of contact with an object along the whisker, and used to predict the object curvature and translation (Schroeder and Hartmann, 2012). However, predicting the position of object contact from bending moments is complex, and changes with whisker velocity (Evans et al., 2013). As with humans, movements of the sensory apparatus, the whiskers, are dependent on prior experience. Small mammals have functional whiskers from birth. Grant et al. (2012) show that rats orient to whisker contacts from conspecifics from a young age to maintain aggregations, indicating the crucial role the whiskers play in development. Anjum and Brecht (2012) show that young shrews can use their whiskers to locate and hunt crickets in an adult manner, and can moderate their attack strategy to novel prey items. This demonstrates that hunting behavior is both innate, subject to modification from experience and reliant on active touch.

In our final section we look for inspiration in the insect antennal system. Insects have a pair of antennae on their head that are involved in a range of sensory-guided behaviors. Just like with the mammalian whiskers, these antennae can be used to locate the position of an object contact along the antennae, discriminate between surfaces and their sensory information is also affected by velocity (Pape et al., 2012). However, as well as object discrimination and orienting to prey and conspecifics, tactile information can also be used to guide locomotion. Krause and Dürr (2012) show that antennal touches guide the positions and speeds of joint movements as stick insects step over objects.

We believe that this collection of papers on humans, small mammals, and insects represents the current state of research in active touch sensing. As biologists, neuroscientists, roboticists, and computational modelers continue to work together, we predict that this field will continue to expand and hope to see more active touch behaviors defined and characterized in the future; with an emphasis on their function in the behaving animals. We hope that you enjoy reading this collection of papers as much as we have enjoyed putting them together.

## REFERENCES

- Ackerley, R., Hassan, E., Curran, A., Wessberg, J., Olausson, H., and McGlone, F. (2012). An fMRI study on cortical responses during active self-touch and passive touch from others. *Front. Behav. Neurosci.* 6:51. doi: 10.3389/fnbeh.2012.00051
- Anjum, F., and Brecht, M. (2012). Tactile experience shapes prey-capture behavior in Etruscan shrews. *Front. Behav. Neurosci.* 6:28. doi: 10.3389/fnbeh.2012.00028
- Boubenec, Y., Shulz, D. E., and Debrégeas, G. (2012). Whisker encoding of mechanical events during active tactile exploration. *Front. Behav. Neurosci.* 6:74. doi: 10.3389/fnbeh.2012.00074
- Delhaye, B., Hayward, V., Lefèvre, P., and Thonnard, J.-L. (2012). Texture-induced vibrations in the forearm during tactile exploration. *Front. Behav. Neurosci.* 6:37. doi: 10.3389/fnbeh.2012.00037
- Evans, M. H., Fox, C. W., Lepora, N. F., Pearson, M. J., Sullivan, J. C., and Prescott, T. J. (2013). The effect of whisker movement on radial distance estimation: a case study in comparative robotics. *Front. Neurobot.* 6:12. doi: 10.3389/fnbot.2012.00012
- Fishel, J. A., and Loeb, G. E. (2012). Bayesian exploration for intelligent identification of textures. *Front. Neurobot.* 6:4. doi: 10.3389/fnbot.2012.00004
- Grant, R. A., Sperber, A. L., and Prescott, T. J. (2012). The role of orienting in vibrissal touch sensing. *Front. Behav. Neurosci.* 6:39. doi: 10.3389/fnbeh.2012.00039
- Klöcker, A., Arnould, C., Penta, M., and Thonnard, J.-L. (2012). Rasch-built measure of pleasant touch through active fingertip exploration. *Front. Neurobot.* 6:5. doi: 10.3389/fnbot.2012.00005
- Krause, A. F., and Dürr, V. (2012). Active tactile sampling by an insect in a step-climbing paradigm. *Front. Behav. Neurosci.* 6:30. doi: 10.3389/fnbeh.2012.00030
- Pape, L., Oddo, C. M., Controzzini, M., Cipriani, C., Förster, A., Carrozza, M. C., et al. (2012). Learning tactile skills through curious exploration. *Front. Neurobot.* 6:6. doi: 10.3389/fnbot.2012.00006
- Patanè, L., Hellbach, S., Krause, A. F., Arena, P., and Dürr, V. (2012). An insect-inspired bionic sensor for tactile localization and material classification with state-dependent modulation. *Front. Neurobot.* 6:8. doi: 10.3389/fnbot.2012.00008
- Schroeder, C. L., and Hartmann, M. J. Z. (2012). Sensory prediction on a whiskered robot: a tactile analogy to optical flow. *Front. Neurobot.* 6:9. doi: 10.3389/fnbot.2012.00009
- Su, Z., Fishel, J. A., Yamamoto, T., and Loeb, G. E. (2012). Use of tactile feedback to control exploratory movements to characterize object compliance. *Front. Neurobot.* 6:7. doi: 10.3389/fnbot.2012.00007

Received: 26 January 2014; accepted: 01 February 2014; published online: 20 February 2014.

Citation: Grant RA, Itskov PM, Towal RB and Prescott TJ (2014) Active touch sensing: finger tips, whiskers, and antennae. *Front. Behav. Neurosci.* 8:50. doi: 10.3389/fnbeh.2014.00050

This article was submitted to the journal *Frontiers in Behavioral Neuroscience*.

Copyright © 2014 Grant, Itskov, Towal and Prescott. This is an open-access article distributed under the terms of the Creative Commons Attribution License (CC BY). The use, distribution or reproduction in other forums is permitted, provided the original author(s) or licensor are credited and that the original publication in this journal is cited, in accordance with accepted academic practice. No use, distribution or reproduction is permitted which does not comply with these terms.



# An fMRI study on cortical responses during active self-touch and passive touch from others

Rochelle Ackerley<sup>1\*</sup>, Eusra Hassan<sup>2</sup>, Andrew Curran<sup>3</sup>, Johan Wessberg<sup>1</sup>, Håkan Olausson<sup>1</sup> and Francis McGlone<sup>4</sup>

<sup>1</sup> Department of Physiology, University of Gothenburg, Gothenburg, Sweden

<sup>2</sup> Magnetic Resonance and Image Analysis Research Centre, University of Liverpool, Liverpool, UK

<sup>3</sup> Alder Hey Children's NHS Foundation Trust, Liverpool, UK

<sup>4</sup> School of Natural Sciences and Psychology, Liverpool John Moores University, Liverpool, UK

## Edited by:

Robyn Grant, University of Sheffield, UK

## Reviewed by:

Francoise Schenk, Université de Lausanne, Switzerland

Jonathan Cole, Poole Hospital, UK

Luke Boorman, University of Sheffield, UK

## \*Correspondence:

Rochelle Ackerley, Department of Physiology, University of Gothenburg, Box 432, Göteborg, 405 30, Sweden.  
e-mail: rochelle@physiol.gu.se

Active, self-touch and the passive touch from an external source engage comparable afferent mechanoreceptors on the touched skin site. However, touch directed to glabrous skin compared to hairy skin will activate different types of afferent mechanoreceptors. Despite perceptual similarities between touch to different body sites, it is likely that the touch information is processed differently. In the present study, we used functional magnetic resonance imaging (fMRI) to elucidate the cortical differences in the neural signal of touch representations during active, self-touch and passive touch from another, to both glabrous (palm) and hairy (arm) skin, where a soft brush was used as the stimulus. There were two active touch conditions, where the participant used the brush in their right hand to stroke either their left palm or arm. There were two similar passive, touch conditions where the experimenter used an identical brush to stroke the same palm and arm areas on the participant. Touch on the left palm elicited a large, significant, positive blood-oxygenation level dependence (BOLD) signal in right sensorimotor areas. Less extensive activity was found for touch to the arm. Separate somatotopical palm and arm representations were found in Brodmann area (BA) 3 of the right primary somatosensory cortex (SI) and in both these areas, active stroking gave significantly higher signals than passive stroking. Active, self-touch elicited a positive BOLD signal in a network of sensorimotor cortical areas in the left hemisphere, compared to the resting baseline. In contrast, during passive touch, a significant negative BOLD signal was found in the left SI. Thus, each of the four conditions had a unique cortical signature despite similarities in afferent signaling or evoked perception. It is hypothesized that attentional mechanisms play a role in the modulation of the touch signal in the right SI, accounting for the differences found between active and passive touch.

**Keywords:** glabrous, hairy, motor, sensorimotor, skin, somatosensory, stroking

## INTRODUCTION

The brain receives afferent information from the activation of mechanoreceptors in the skin during interactions with the environment. The present study focuses on the cortical representations from active, self-touch and passive (other) touch to the palm and arm. There are differences in the types of low-threshold mechanoreceptors found in the glabrous skin of the palm compared to the hairy skin on the arm (for an overview, see Macefield, 2005). The mechanoreceptors on the glabrous skin allow high discriminatory abilities for touch, whereas the input from hairy skin does not give such discrimination. Despite these differences, glabrous and hairy skin are both sensitive to touch; a recent study has shown that psychophysical ratings of the intensity and the pleasantness of touch were not different between the skin of the palm and the arm (McGlone et al., 2012). However, the study also found that using a Touch Perception Task (from Guest et al., 2011), subjects used more sensory descriptors when evaluating touch to the palm, whereas they used more emotional descriptors

for touch to the arm, indicating that touch is processed over many cognitive levels.

The high discriminatory ability from human glabrous skin (e.g., the ventral surfaces of the hands and feet) is based on inputs from four main classes of low-threshold mechanoreceptors, namely: rapidly-adapting types I (RAI; Meissner's corpuscles) and II (RAII; Pacinian corpuscles), and slowly-adapting types I (SAI; Merkel's disks) and II (SAII; Ruffini's endings). These afferents are in the A $\beta$  conduction range of myelinated mechanoreceptors and send information to the brain very quickly (conducting at 36–73 m/s; Kakuda, 1992) at a high temporal resolution (Perge et al., 2012). This type of mechanoreceptive input provides an excellent source of information during discriminative touch; the incoming, high-quality tactile information can be compared in areas of the brain such as SI. This capacity can be demonstrated in ways such as using two-point discrimination tests, where the fingertip skin has high discriminatory ability (2–4 mm; Bickley and Szilagyi, 2007).

Hairy skin is defined as the non-glabrous and non-mucocutaneous skin that covers the majority of the body surface. Hairy skin does not contain RAI mechanoreceptors but instead, includes hair, field and C-tactile (CT) afferents. These afferents have myelinated axons (e.g., A $\beta$  terminal hair and field units; Vallbo et al., 1995), or are unmyelinated (CT; Vallbo et al., 1993). The density of myelinated afferents in hairy skin is much less than in glabrous skin (Provitera et al., 2007). In contrast to glabrous skin, hairy skin has a much lower discriminatory ability (e.g., 30–40 mm in the two-point discrimination test; Bickley and Szilagyi, 2007), but is nevertheless sensitive to touch; in fact, CT afferents respond to <250 mg force (Vallbo et al., 1993; Wessberg et al., 2003; Cole et al., 2006). The touch information relayed to the brain from CT afferents is comparatively lower in temporal resolution due to the slower conduction velocity and more variable firing discharge (Vallbo et al., 1993, 1999; Wessberg et al., 2003).

Touch information is described classically as having a somatotopical representation in the contralateral SI (Penfield and Rasmussen, 1950), where discriminative and integrative aspects of touch are processed, such as form, texture, shape, and size (Hsiao, 2008). Tactile input is also processed in other cortical areas and the information flow can be split into dorsal and ventral streams (Romo et al., 2002). The dorsal stream sends information to Brodmann areas (BA) 5 and 7 and has been associated with processing during active touch, such as during voluntary movements (Shanks et al., 1985; Cavada and Goldman-Rakic, 1989; Romo et al., 2002). The ventral stream has been more associated with discrimination, feature and pattern recognition, and flows through lateral somatosensory areas, such as the secondary somatosensory cortex (SII), but also includes activation of premotor and prefrontal areas (Pons et al., 1987; Carmichael and Price, 1995; Romo et al., 2002). Both of these streams include reciprocal connections with motor areas and there are within- and between-hemispheric somatosensory connections (Goldring et al., 1970; Fabri et al., 1999; Tommerdahl et al., 2006; Eickhoff et al., 2008; Ragert et al., 2011; Schäfer et al., 2012). In active touch, the motor system must communicate with the somatosensory system during behavior, such as in the fine-detail exploration of a surface. Here, there must be an exchange of sensory and motor information and the primary motor cortex (MI) also receives direct input from SI (Huerta and Pons, 1990). It is likely that combinations of these areas work together to integrate and process touch information and shape how we act on it.

The present study aims to investigate the differences between the cortical representations from active and passive forms of touch. The mode of touch relates to the skin site: active touch is typically carried out by the hands whereas the rest of the body is more involved in passive touch, for example, from another person. Active, self-touch and the passive touch from another will engage similar afferent mechanoreceptors on the same skin site but may be processed differently. Active touch is self-governed, where there is a motivation and an expectation of upcoming sensory input. A feed-forward efference copy signal predicting the expected outcome of movements is sent to somatosensory areas, such as SI and the cerebellum, for movement-related gating of the incoming sensory input (Chapin and Woodward, 1981;

Blakemore et al., 1998). This has been hypothesized to be for sensory cancellation e.g., how you cannot tickle yourself because an internal forward model captures the relationship between the motor efference copy and the predicted sensory consequences of the action (Weiskrantz et al., 1971; Blakemore et al., 1998, 2000). Sensory cancellation allows you to attend to any unexpected parts of the input, while ignoring the expected sensory feedback. Conversely, during passive touch, an expectation of touch may be present, but there is no motor efference copy to nullify or cancel the subsequent, sensory input.

Previous neuroimaging studies have found that active touch produces sensations that are less intense, compared to that from passive touch, in part due to sensory cancellation (Blakemore et al., 1998, 1999). In these studies, the BOLD signal in SI contralateral to the touched surface was found to be significantly lower for active touch. It is reasoned that incoming signals are attended to less if they match the expected parameters, so can be ignored, thus a decrease in the signal is observed. The finding of decreased activity in SI for active compared to passive touch is controversial. Some studies have found a decreased SI signal, for example, in animal *in vivo* recordings (Chapin and Woodward, 1981; Jiang et al., 1991), electroencephalography (EEG; Abbruzzese et al., 1981; Tapia et al., 1987), magnetoencephalography (Hesse et al., 2010), and fMRI (Blakemore et al., 1998). However, other animal *in vivo* electrophysiological experiments (Chapman and Ageranioti-Bélanger, 1991; Ageranioti-Bélanger and Chapman, 1992) and a recent fMRI experiment (Simões-Franklin et al., 2011) have found different results: an increased contralateral SI signal during active touch.

Information gained from active touch and dynamic passive touch has been shown to be perceptually similar (Lederman, 1981; Verrillo et al., 1999). It is therefore likely that the motor component in active touch can be countermanded to the extent that movement-related gating has virtually no effect. Similar effects have been seen in other sensory-motor tasks, such as the interaction of vision with head movement, where a cancellation signal occurs but has little effect on the response (Ackerley and Barnes, 2011). It is to be expected that all available sensory and motor information is used together in processing the information from touch. The present study uses fMRI to detect significant modulations in the BOLD signal to active (self-touch) and passive stroking (touch via the experimenter) of the glabrous skin (palm) and hairy skin (arm), using a soft, cosmetic brush for stimulation. This was specifically used to activate low-threshold mechanoreceptors and investigate the cortical differences within and between the touch conditions. Therefore, despite similarities in perception, we hypothesize that each condition (active, passive, hairy, or glabrous) has a unique cortical representation.

## MATERIALS AND METHODS

The study was carried out using a Siemens 3T MRI scanner with an eight channel head coil, at the University of Liverpool, UK. All participants were screened prior to taking part for safety and were supplied with information about the study, which conformed to local ethical approval and was performed in accordance with the Declaration of Helsinki. Written, informed consent was obtained for a total of 12 healthy, male volunteers (aged 18–35).

The study compared intra-personal touch where the person actively stroked themselves (self-touch) using a soft cosmetic brush (width = 4 cm), with inter-personal touch where the participant was stroked using an identical brush, by the experimenter (other-touch). The body sites stroked were the palm (glabrous skin in the middle of the left palm) and the arm (dorsal hairy surface of the left mid-arm). Each stroked area was approximately 10 cm long and the stroking velocity was between 6 and 8 cm/s. The participant could not see the experimenter during the session, although, they were instructed about the type of stroking via a viewing screen.

The paradigm consisted of four different randomized touch conditions that were repeated eight times each. Each block consisted of 9 s of stroking, then 6 s of rest. During the stroking, the participant saw a continuous visual instruction (e.g., “Stroke your palm” and “Your arm will be stroked”), which was projected onto a screen in front of the participant, viewed via a mirror on the head coil. The participants were made aware of the timings and task beforehand, and they practiced the conditions before going into the scanner, and also in the scanner before the experiment started. This aided in gaining consistency in stroking within and between participants and also allowed for similar forces to be applied (~0.8 N). To minimize motion artifacts that would produce head movement in the scanner, the participants were instructed to make only small arm movements during brushing.

The parameters used for the functional gradient echo-planar imaging sequence were: in-plane resolution =  $64 \times 64$  matrix, field of view = 192 mm, flip angle =  $90^\circ$ , TR = 3000 ms, TE = 30 ms, and inter-slice interval = 71 ms over 160 volumes (42 slices for whole-brain coverage at a resolution of  $3 \times 3 \times 2.5$  mm with slice gap = 0.5 mm). A  $T_1$ -weighted, high resolution anatomical scan (176 slices at  $224 \times 256$  mm coverage, 1 mm isotropic voxels) was conducted either before or after the paradigm. Brain Voyager (v2.4, Brain Innovation, Maastricht, Netherlands) was used for the analysis of the fMRI data and Statistical Package for the Social Sciences (SPSS) (IBM, Armonk, NY) was used for further statistical investigations in region-of-interest (ROI) analyses. The raw fMRI data were imported and preprocessed with the following standard parameters: slice scan time correction, 3D motion correction, spatial smoothing (with a Gaussian filter of full width half maximum = 3 mm in the space domain), and temporal filtering. All of the subjects had  $<3$  mm motion and  $<3^\circ$  translation. Anatomical data were imported and corrected for image intensity inhomogeneity (a step that included brain extraction from surrounding skull and tissue, and the segregation of gray and white matter), before conversion to Talairach space. The preprocessed functional data were coregistered with the original anatomical data to make a volume time course file. Data were saved in neurological convention (where left-is-left and vice versa) at a resolution of  $3 \times 3 \times 3$  mm.

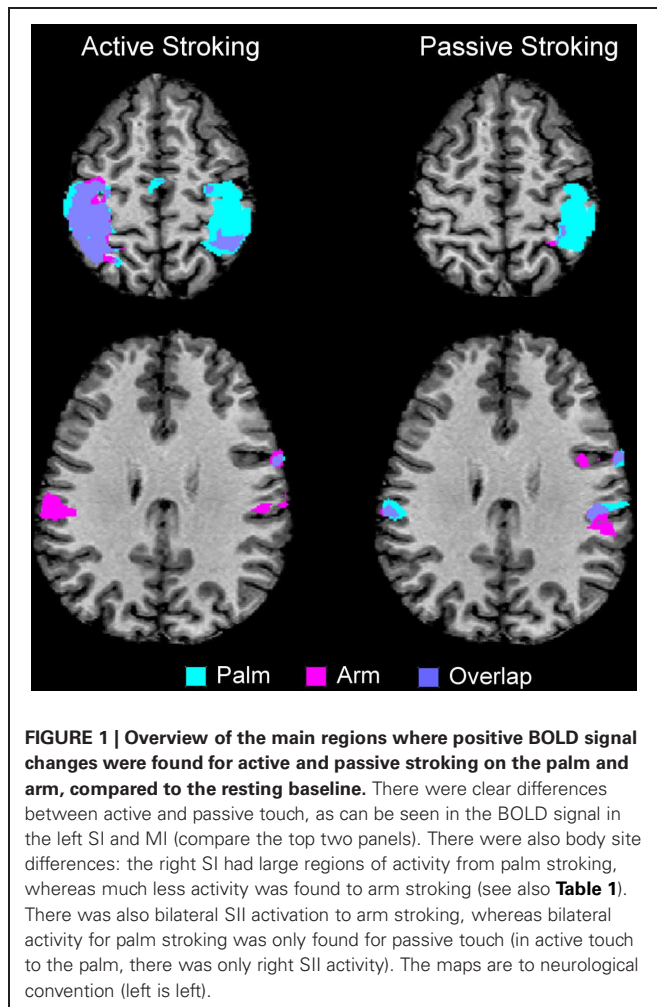
The processed functional data were linked to the Talairach brain (Talairach and Tournoux, 1988) and a single-subject general linear model (GLM) was carried out with four predictors (the stroking conditions) using Z-scores as a change from the signal baseline (rest), with a hemodynamic response function applied. Each participant's data was inspected for significant BOLD activity changes from the resting baseline between the

conditions. A multi-subject group-level GLM was then carried out, for random effects significant differences in the BOLD signal. The different stroking conditions were contrasted against the baseline rest period and significantly activated voxels were sought at a false discovery rate (FDR) of  $q < 0.05$ , which corrected for multiple comparisons (see Genovesi et al. (2002), Goebel et al. (2006), and Gordon et al. (2011) for use of FDR correction to increase statistical power over Bonferroni correction). ROIs were identified based on the results of the contrasts, although, the main targets for analysis were sensory and motor cortical areas in the brain (e.g., SI, SII and MI). The Talairach co-ordinates for regions showing significant changes in the BOLD signal were entered into Talairach Client (Talairach.org; Lancaster et al., 1997, 2000) to determine the exact brain area modulated. Beta-weights (relating to the BOLD z-score amplitude) were computed for each participant in each condition in ROIs. SPSS (IBM, Armonk, NY) was used to calculate significant differences between touch conditions using analysis of variance [ANOVA;  $2 \times 2$  design: mode of stimulation (active or passive) and the body site touched (palm or arm)], with *post-hoc* multiple comparisons where the factors were contrasted separately (sought at  $p < 0.05$ ).

## RESULTS

The results from comparing the different touch conditions showed striking differences in sensorimotor areas. From inspection of each participant's data, and as found previously (Olausson et al., 2002; Björnsdotter et al., 2009), the data from some participants ( $n = 4$ ) showed less BOLD activation, due to increased head movement and also drowsiness may have played a factor. Although, these participants' data followed similar trends, they were not used in calculations. Overall in the data, there were more extensive areas showing positive BOLD signal changes for palm compared to arm stroking in the right sensorimotor cortex, irrespective of whether the stroking was active or passive (**Figure 1**). A somatotopical representation was found in the right SI (BA03): the palm representation was in the middle of the post-central gyrus and covered a large area (see **Figure 1**), whereas the arm representation was further lateral (not shown in **Figure 1** due to the slice orientation; see **Table 1** for details). In both of these specific body site regions in BA03, active touch gave significantly higher beta values than passive touch to the same area, respectively ( $p < 0.05$ ; **Figure 2**). Other areas in the left sensorimotor cortex showed significant positive BOLD modulations compared to the resting baseline for touch to the palm and arm (see **Table 1**), however, none of these regions showed significant differences between the active and passive touch beta values.

Comparing touch to the palm and arm, there were other region-specific differences. For touch to the arm, there were significant BOLD signals found bilaterally in SII during both active and passive touch, compared to the resting baseline. For touch to the palm, there was a bilateral activation of SII during passive touch compared to rest, however, during active stroking of the palm there was only significant BOLD signal changes in the right SII (see **Figure 1** and **Table 1**). During touch to the palm, the right MI showed significant positive BOLD signals compared to the resting baseline. There were also significant positive BOLD signals in the right premotor cortex during active touch to the palm and



arm; however, there were no right-sided motor area activations for passive stroking of the arm (see **Table 1**).

Differences between active and passive touch were mainly seen in the left sensorimotor cortex, as would be expected for the right, contralateral, and limb movement. During active stroking of the palm and arm, a network of left cortical areas showed significant positive BOLD signals including: SI, MI, premotor cortex, and somatosensory association areas (BA05 and BA07; see **Table 1**). These activations likely reflect the interaction of motor and sensory components during active, self-touch including movement planning, co-ordination and sensory feedback from the skin of the right palm. Furthermore, in contrast to the positive BOLD signals during active touch compared to the resting baseline (see **Figure 1**, top left panel and **Figure 3** top panel), a significant negative BOLD signal was found in the left SI during passive touch to both the palm and arm (**Figure 3**). This covered an extensive part of SI and also spread into the left MI. A further difference was seen in the insula cortices: there were significant bilateral positive BOLD signals during passive touch to both the palm and arm, compared to the resting baseline. In contrast, during active touch, only the right insula showed a significant BOLD signal in self-palm stroking, compared to the resting baseline.

## DISCUSSION

The present study used light brush stroking to elicit cortical responses from glabrous and hairy skin. The BOLD signal was modulated by the skin site (palm or arm) and by the type of stroking (active or passive), and an interaction was seen in the right SI (contralateral to the touch) in BA03 between active and passive stroking of the palm and the arm. Here, a clear somatotopical difference was observed between the representations of each body site, the palm being a much larger representation and the arm was represented more laterally, and in both respective areas, active stroking gave an increased BOLD signal over passive stroking. Previous studies have also found that the arm is represented more laterally than from the Penfield and Rasmussen (1950) cortical homunculus, e.g., Olausson et al. (2002) and Gordon et al. (2011). The larger representation of the glabrous skin of the hand would be expected in SI, due to both the increased peripheral receptor density and differences in the type of receptors present (i.e., the glabrous skin also sends RAI afferents to the cortex), however, the finding of active touch, in general, producing significantly higher BOLD signals was more controversial. The present study adds to the evidence that the signal in contralateral SI is indeed modulated, for both glabrous and hairy skin sites, although it is likely that the afferent signal to SI touch may be modulated in a context-dependent manner (Chapman and Ageranioti-Bélanger, 1991; Ageranioti-Bélanger and Chapman, 1992; Chapman, 1994; Jackson et al., 2011). If there is behavioral relevance for the tactile information gained from active touch, the cancellation effect from the sensory prediction of the consequences of the motor efference may be countermanded by an internal mechanism to attend to the touch afference. This attentional or cognitive internal drive may determine whether the signal to contralateral SI is attenuated or amplified. It is therefore likely that the input to SI is nevertheless subject to movement-related gating, which would decrease the incoming signal during active touch; however, the efference copy of the movement and/or the prediction of its sensory consequence may be countermanded by the demands of the task.

The extent to which the signal is attenuated or amplified may be modulated by factors such as attention and motor strategy, depending on the situation (Chapman, 1994). Previous studies have shown that there is not necessarily a direct relationship between activity in afferent touch systems and changes in the BOLD signal and the relationship can vary with attention (Johansen-Berg and Lloyd, 2000; Arthurs et al., 2004). During active touch, interactions between motor and sensory cortices may also regulate context-dependent information processing in SI (Lee et al., 2008). Evidence from humans for the modulation of this movement-related gating comes from Master and Tremblay (2009, 2010), who found that active tactile exploration increases corticomotor excitability when tactile information is sought, rather than ignored. In present study, the participants may have paid more attention to the active stroking as they did not have visual feedback from their touch, thus giving the higher signal in SI. Furthermore, the current study provides evidence that this signal was only modulated in BA03; no significant modulations in the level of the positive BOLD signal were seen between

**Table 1 | Overview of all the cortical regions showing significant differences from the resting baseline for each touch conditions.**

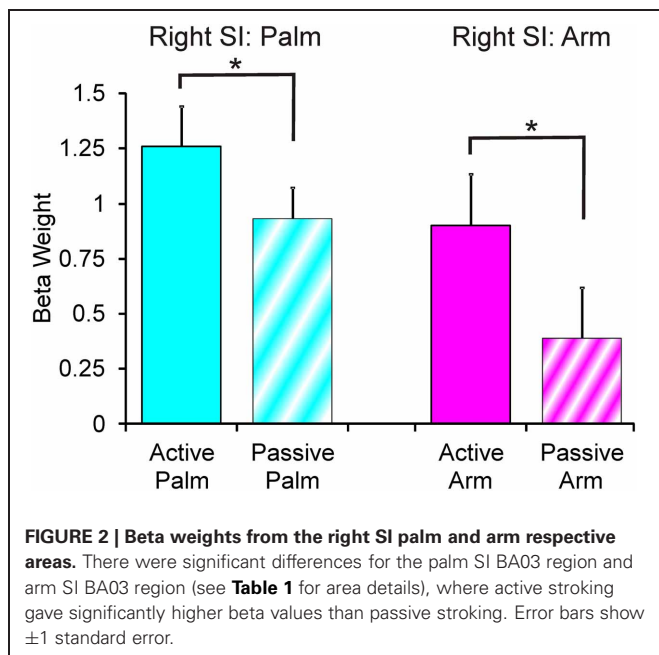
	Brodmann area	Peak Talairach co-ordinates			Maximum t-score	Number of voxels
		x	y	z		
<b>ACTIVE PALM VS. REST</b>						
Left premotor cortex	6	-4	-15	53	8.96	203
	6	-58	2	39	9.56	710
Left precentral gyrus (MI)	4	-29	-23	67	11.93	912
Left postcentral gyrus (SI)	3	-35	-30	57	12.66	956
	2	-54	-28	50	11.49	491
	2	-60	-22	35	9.70	918
	40	-40	-44	53	12.80	497
Left somatosensory association cortex	5	-34	-40	59	12.46	964
	7	-21	-54	61	4.81	483
	7	-35	-54	54	7.02	650
Right premotor cortex	6	7	-19	72	5.42	586
	6	57	1	39	7.16	601
Right precentral gyrus (MI)	4	31	-20	63	13.28	792
Right postcentral gyrus (SI)	3	37	-31	58	13.15	955
	40	35	-44	52	14.31	845
	2	56	-22	41	10.04	900
Right operculum (SII)	40	58	-18	24	7.61	523
Right insula	13	49	-18	17	3.30	151
Right inferior frontal gyrus	44	54	7	14	3.67	87
<b>ACTIVE ARM VS. REST</b>						
Left premotor cortex	6	-4	-12	54	7.11	708
	6	-58	0	39	6.57	324
Left precentral gyrus (MI)	4	-30	-21	66	11.66	992
Left postcentral gyrus (SI)	3	-35	-29	59	11.66	1000
	2	-52	-26	50	9.41	939
	2	-59	-22	36	11.09	989
	40	-36	-42	53	9.67	998
Left somatosensory association cortex	5	-34	-38	59	10.75	945
	7	-26	-65	53	3.14	148
	7	-35	-54	54	6.57	380
Left operculum (SII)	40	-59	-23	23	6.11	452
Right premotor cortex	6	7	-10	62	5.47	47
	6	58	0	37	8.72	503
Right postcentral gyrus (SI)	3	57	-21	41	9.63	755
	40	36	-42	54	7.83	438
Right operculum (SII)	40	53	-22	27	5.28	127
Right inferior frontal gyrus	44	54	4	14	6.70	191
<b>PASSIVE PALM VS. REST</b>						
Left premotor cortex	6	60	0	35	6.42	394
Left postcentral gyrus (SI)	2	-60	-23	34	8.93	939
<i>Left postcentral gyrus (SI)</i>	3	-36	-31	59	-11.87	632
Left operculum (SII)	40	-59	-23	24	6.24	616
Left insula	13	-49	-38	23	3.41	142
	13	-40	-5	11	4.10	150
Right precentral gyrus (MI)	4	40	-18	58	9.57	900
Right postcentral gyrus (SI)	3	40	-31	59	8.66	984
	2	56	-22	35	7.98	772
	40	36	-40	56	8.72	991
Right operculum (SII)	40	52	-22	21	6.03	784
	40	57	-31	24	4.91	553

Continued

Table 1 | Continued

	Brodmann area	Peak Talairach co-ordinates			Maximum <i>t</i> -score	Number of voxels
		<i>x</i>	<i>y</i>	<i>z</i>		
Right insula	13	43	-19	20	5.07	450
	13	40	-14	11	4.75	217
Right inferior frontal gyrus	44	54	3	17	3.37	71
<b>PASSIVE ARM VS. REST</b>						
<i>Left postcentral gyrus (SI)</i>	3	-35	-31	59	-12.98	570
Left operculum (SII)	40	-61	-24	32	5.78	485
Left insula	13	-50	-37	23	3.87	73
Right postcentral gyrus (SI)	3	58	-21	37	5.91	346
	40	27	-43	56	3.64	17
Right operculum (SII)	40	52	-22	21	4.73	637
	40	58	-34	26	6.59	840
Right insula	13	42	-31	21	5.54	557
	13	39	-15	12	3.64	89
Right inferior frontal gyrus	44	54	1	17	4.18	211
Right superior temporal gyrus	22	67	-37	16	4.04	217
Right angular gyrus	39	47	-55	8	3.88	189

The table details the Brodmann area, Talairach co-ordinates (*x*, *y*, *z*) of the peak of the BOLD signal, the maximum *t*-score and the number of voxels in each region. The italicized numbers denote a significant negative BOLD signal; all other regions show significant positive BOLD signals compared to the baseline.

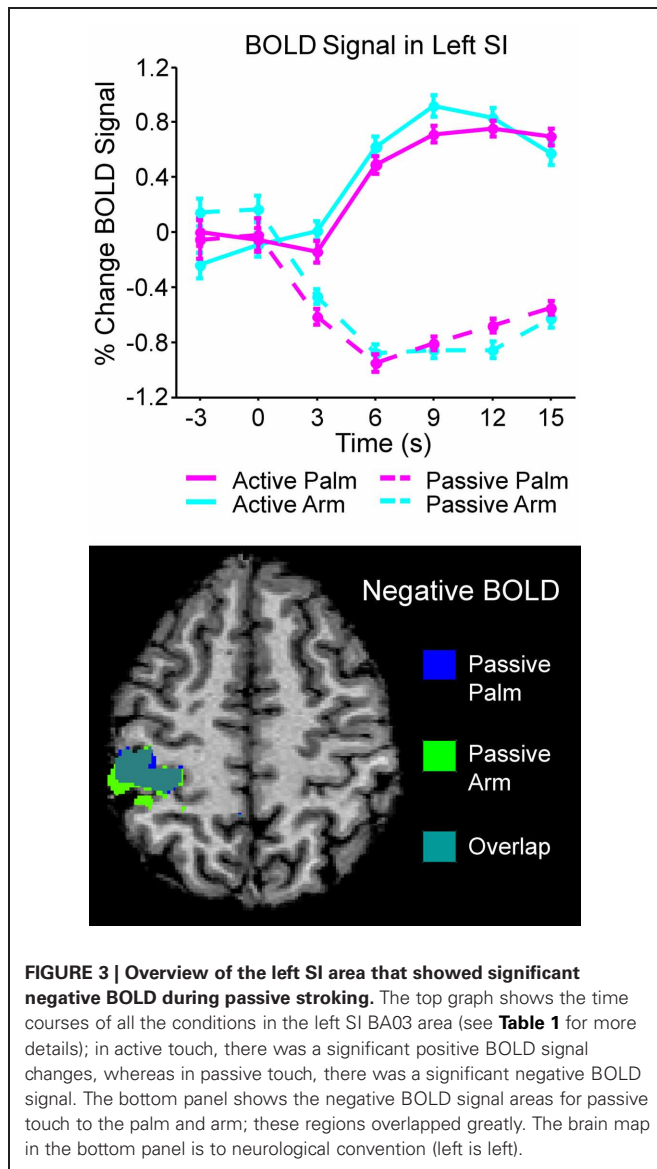


active and passive touch for other areas during stroking of the palm or arm. There was an interaction between the touch conditions in SII: all the conditions apart from active touch to the palm elicited significant positive BOLD signals bilaterally in SII. Active touch to the palm, however, only showed significant positive BOLD signal changes in the right SII. The present results suggest that somatosensory signals arriving in SII from both palms may culminate in a gating effect to focus on the most relevant input

for the current task. Different patterns of activity in SII may aid in attention to a certain body area, especially during bilateral body interactions with input from the same body area on both sides.

We investigated self-touch with an instrument, rather than the direct skin-to-skin contact. It was deemed that a brush was a better, more controlled stimulus for factors such as temperature and social interactions. Furthermore, the participants were able to train in stroking with the brush, which also allowed a constant force to be applied between the conditions. A potential confound of the finding of the active/passive touch modulation in BA03 may have been small differences in the applied force of the brushing. An increased signal in SI for both the palm and arm active brushing may have been due to the participant stroking themselves with more force. However, the force from the brush would not have been too different as the hairs on the brush provided only light forces (typically <1 N) and it was difficult to achieve a heavy force with the brush, unless it was pushed into the skin. As the participant was able to practice stroking with the brush beforehand, the experimenter was able to make sure that the brushing was consistent within and between participants. Although, the task was repetitive, the participants were required to pay attention to the task at hand and no overall decrease in the modulation of the BOLD signal was seen over the experiments. Also, as the effect was only found in BA03, this points to an attentional mechanism for gating of the initial processing of incoming touch information. It is likely that self-touch using skin-to-skin contact would produce a somewhat different signal. With this reasoning, the left sensorimotor touch network found during active touch in the present study may be different when touch is directed to another object that is not the self.

During active touch, a network of sensorimotor areas was recruited in the left cortex, contralateral to the moving limb.



Strong, positive BOLD signals were observed particularly in left SI and MI, with other sensory (somatosensory association cortex) and motor (premotor cortex) areas also following the same pattern of modulation during active touch. A similar network of connectivity between motor, premotor, sensory, and sensory association areas has been demonstrated in the monkey (Morecraft et al., 2004, 2012). In the present study, a negative BOLD signal was found in the left sensorimotor cortex during passive touch. There are a number of potential explanations for this including “vascular blood stealing” from surrounding areas. This entails that an area showing a positive BOLD signal can produce a nearby negative BOLD signal due to blood being diverted from a nearby inactive area. In the present study, this is unlikely as there was no positive BOLD signal in close proximity to the negative BOLD signal during the passive stroking. Another potential explanation may be that the negative BOLD signal may have been due to a “memory” of previous active touch modulations, such as,

residual neuronal inhibition or a compensatory decrease in blood flow after the large BOLD signal from active touch. However, the BOLD signals returned to the resting baseline level after each touch stimulus had ceased and the stimuli were randomized, making this explanation less likely. Negative BOLD signals have been shown to correlate with decreases in neuronal activity (Shmuel et al., 2006), which could manifest as a change in ongoing brain rhythms. We believe that the negative BOLD signal in the ipsilateral, left SI during passive touch was due to a change in the neuronal activity as a result of unilateral touch to the left side of the body. Recent papers have shown that somatosensory stimulation of one hand elicits positive BOLD signals in the contralateral cortex with accompanying negative BOLD signal modulations in the ipsilateral cortex (Hlushchuk and Hari, 2006; Kastrup et al., 2008; Klingner et al., 2010, 2011; Schäfer et al., 2012).

EEG studies have shown that a unilateral somatosensory stimulus to one hand will elicit an event-related potential in the contralateral SI, which is accompanied by a concurrent event-related desynchronization of the ongoing mu rhythm over both somatosensory cortices, although, more strongly on the contralateral side to the somatosensory event (Korvenoja et al., 1995; Nikouline et al., 2000). The evidence shows, that a somatosensory event to one side of the body only, will elicit a response in the contralateral SI, which has an effect on the ipsilateral SI, via transcallosal connections between the sensorimotor cortices (Fabri et al., 1999; Ragert et al., 2011). We postulate that crosstalk between sensorimotor cortices will facilitate attention and differentiation of somatosensory information from each side of the body. Specifically, the inhibitory signal that is sent from the activated SI to the opposite SI may aid in bimanual processing and the interpretation of tactile localizations and interactions (Kastrup et al., 2008). The differences in the BOLD signals may play a role in distinguishing between active, self-touch (with the internally-generated efferent copy feedback) from passive, external touch (with no predictions of the consequences). It is possible that the shift between significant positive and negative BOLD signals to active and passive stroking, respectively, do also reflect the timing and expectancy of previous and subsequent touch stimuli during the paradigm. Also, only during passive touch was bilateral insula activity seen. This again may be part of a network of sensory areas that help distinguish both between self- and other touch.

In conclusion, the present study found a distinct cortical pattern associated with each of the four touch conditions. Differences between touch to the palm and arm were found: the glabrous skin of the palm showed a significant representation in the contralateral, right SI, whereas this signal was less extensive for touch to the arm, which relates to the mechanoreceptive input and usage for discriminative touch. The significant, positive BOLD signal was modulated in the respective body site areas in BA03, where active touch gave an increased signal over passive touch. Active touch using the right hand/arm elicited a network of positive BOLD signal changes in left sensorimotor areas; conversely, a negative BOLD signal for passive touch in the left SI. The present study has implications for understanding how touch information is processed and gated according to the behavioral situation and

could be used to refine touch interactions with everyday objects in rehabilitation studies. Furthermore, touch processing appears to be heavily influenced by the reasons and attentional demand of the task at hand, where both motor and sensory information

is relevant. Future studies will explore factors, such as, attentional modulations to touch, including bilateral touch and touch at other body sites, and how active movement influences touch both to the self and other objects.

## REFERENCES

- Abbruzzese, G., Ratto, S., Favale, E., and Abbruzzese, M. (1981). Proprioceptive modulation of somatosensory evoked potentials during active or passive finger movements in man. *J. Neurol. Neurosurg. Psychiatry* 44, 942–949.
- Ackerley, R., and Barnes, G. R. (2011). The interaction of visual, vestibular and extra-retinal mechanisms in the control of head and gaze during head-free pursuit. *J. Physiol.* 589, 1627–1642.
- Ageranioti-Bélanger, S. A., and Chapman, C. E. (1992). Discharge properties of neurones in the hand area of primary somatosensory cortex in monkeys in relation to the performance of an active tactile discrimination task. II. Area 2 as compared to areas 3b and 1. *Exp. Brain Res.* 91, 207–228.
- Arthurs, O. J., Johansen-Berg, H., Matthews, P. M., and Boniface, S. J. (2004). Attention differentially modulates the coupling of fMRI BOLD and evoked potential signal amplitudes in the human somatosensory cortex. *Exp. Brain Res.* 157, 269–274.
- Bickley, L., and Szilagyi, P. (2007). *Bates' Guide to Physical Examination and History Taking*, 9th Edn. Philadelphia, PA: Lippincott Williams and Wilkins.
- Björnsdotter, M., Löken, L., Olsson, H., Vallbo, A., and Wessberg, J. (2009). Somatotopic organization of gentle touch processing in the posterior insular cortex. *J. Neurosci.* 29, 9314–9320.
- Blakemore, S. J., Wolpert, D., and Frith, C. (2000). Why can't you tickle yourself? *Neuroreport* 11, R11–R16.
- Blakemore, S. J., Wolpert, D. M., and Frith, C. D. (1998). Central cancellation of self-produced tickle sensation. *Nat. Neurosci.* 1, 635–640.
- Blakemore, S. J., Wolpert, D. M., and Frith, C. D. (1999). The cerebellum contributes to somatosensory cortical activity during self-produced tactile stimulation. *Neuroimage* 10, 448–459.
- Carmichael, S. T., and Price, J. L. (1995). Sensory and premotor connections of orbital and medial prefrontal cortex of macaque monkeys. *J. Comp. Neurol.* 363, 642–664.
- Cavada, C., and Goldman-Rakic, P. S. (1989). Posterior parietal cortex in rhesus monkey: I. Parcellation of areas based on distinctive limbic and sensory corticocortical connections. *J. Comp. Neurol.* 287, 393–421.
- Chapin, J. K., and Woodward, D. J. (1981). Modulation of sensory responsiveness of single somatosensory cortical cells during movement and arousal behaviors. *Exp. Neurol.* 72, 164–178.
- Chapman, C. E. (1994). Active versus passive touch: factors influencing the transmission of somatosensory signals to primary somatosensory cortex. *Can. J. Physiol. Pharmacol.* 72, 558–570.
- Chapman, C. E., and Ageranioti-Bélanger, S. A. (1991). Discharge properties of neurones in the hand area of primary somatosensory cortex in monkeys in relation to the performance of an active tactile discrimination task. I. Areas 3b and 1. *Exp. Brain Res.* 87, 319–339.
- Cole, J., Bushnell, M. C., McGlone, F., Elam, M., Lamarre, Y., Vallbo, A., and Olsson, H. (2006). Unmyelinated tactile afferents underpin detection of low-force monofilaments. *Muscle Nerve* 34, 105–107.
- Eickhoff, S. B., Grefkes, C., Fink, G. R., and Zilles, K. (2008). Functional lateralization of face, hand, and trunk representation in anatomically defined human somatosensory areas. *Cereb. Cortex* 18, 2820–2830.
- Fabri, M., Polonara, G., Quattrini, A., Salvolini, U., Del Pesce, M., and Manzoni, T. (1999). Role of the corpus callosum in the somatosensory activation of the ipsilateral cerebral cortex: an fMRI study of callosotomized patients. *Eur. J. Neurosci.* 11, 3983–3994.
- Genovese, C. R., Lazar, N. A., and Nichols, T. (2002). Thresholding of statistical maps in functional neuroimaging using the false discovery rate. *Neuroimage* 15, 870–878.
- Goebel, R., Esposito, F., and Formisano, E. (2006). Analysis of functional image analysis contest (FIAC) data with brainvoyager QX: from single-subject to cortically aligned group general linear model analysis and self-organizing group independent component analysis. *Hum. Brain Mapp.* 27, 392–401.
- Goldring, S., Aras, E., and Weber, P. C. (1970). Comparative study of sensory input to motor cortex in animals and man. *Electroencephalogr. Clin. Neurophysiol.* 29, 537–550.
- Gordon, I., Voos, A. C., Bennett, R. H., Bolling, D. Z., Pelphrey, K. A., and Kaiser, M. D. (2011). Brain mechanisms for processing affective touch. *Hum. Brain Mapp.* doi: 10.1002/hbm.21480. [Epub ahead of print].
- Guest, S., Dessirier, J., Mehrabyan, A., McGlone, F., Essick, G., Gescheider, G., Fontana, A., Xiong, R., Ackerley, R., and Blot, K. (2011). The development and validation of sensory and emotional scales of touch perception. *Atten. Percept. Psychophys.* 73, 531–550.
- Hesse, M. D., Nishitani, N., Fink, G. R., Jousmäki, V., and Hari, R. (2010). Attenuation of somatosensory responses to self-produced tactile stimulation. *Cereb. Cortex* 20, 425–432.
- Hlushchuk, Y., and Hari, R. (2006). Transient suppression of ipsilateral primary somatosensory cortex during tactile finger stimulation. *J. Neurosci.* 26, 5819–5824.
- Hsiao, S. (2008). Central mechanisms of tactile shape perception. *Curr. Opin. Neurobiol.* 18, 418–424.
- Huerta, M. F., and Pons, T. P. (1990). Primary motor cortex receives input from area 3a in macaques. *Brain Res.* 537, 367–371.
- Jackson, S. R., Parkinson, A., Pears, S. L., and Nam, S. H. (2011). Effects of motor intention on the perception of somatosensory events: a behavioural and functional magnetic resonance imaging study. *Q. J. Exp. Psychol.* 64, 839–854.
- Jiang, W., Chapman, C. E., and Lamarre, Y. (1991). Modulation of the cutaneous responsiveness of neurones in the primary somatosensory cortex during conditioned arm movements in the monkey. *Exp. Brain Res.* 84, 342–354.
- Johansen-Berg, H., and Lloyd, D. M. (2000). The physiology and psychology of selective attention to touch. *Front. Biosci.* 5:D894–D904.
- Kakuda, N. (1992). Conduction velocity of low-threshold mechanoreceptive afferent fibers in the glabrous and hairy skin of human hands measured with microneurography and spike-triggered averaging. *Neurosci. Res.* 15, 179–188.
- Kastrup, A., Baudewig, J., Schnaudigel, S., Huonker, R., Becker, L., Sohns, J. M., Dechent, P., Klingner, C., and Witte, O. W. (2008). Behavioral correlates of negative BOLD signal changes in the primary somatosensory cortex. *Neuroimage* 41, 1364–1371.
- Klingner, C. M., Hasler, C., Brodoehl, S., and Witte, O. W. (2010). Dependence of the negative BOLD response on somatosensory stimulus intensity. *Neuroimage* 53, 189–195.
- Klingner, C. M., Huonker, R., Flemming, S., Hasler, C., Brodoehl, S., Preul, C., Burmeister, H., Kastrup, A., and Witte, O. W. (2011). Functional deactivations: multiple ipsilateral brain areas engaged in the processing of somatosensory information. *Hum. Brain Mapp.* 32, 127–140.
- Korvenoja, A., Wikstrom, H., Huttunen, J., Virtanen, J., Laine, P., Aronen, H. J., Seppäläinen, A. M., and Ilmoniemi, R. J. (1995). Source activation of ipsilateral primary sensorimotor cortex by median nerve stimulation. *Neuroreport* 6, 2589–2593.
- Lancaster, J. L., Rainey, L. H., Summerlin, J. L., Freitas, C. S., Fox, P. T., Evans, A. C., Toga, A. W., and Mazziotta, J. C. (1997). Automated labeling of the human brain: a preliminary report on the development and evaluation of a forward-transform method. *Hum. Brain Mapp.* 5, 238–242.
- Lancaster, J. L., Woldorff, M. G., Parsons, L. M., Liotti, M., Freitas, C. S., Rainey, L., Kochunov, P. V., Nickerson, D., Mikiten, S. A., and Fox, P. T. (2000). Automated Talairach atlas labels for functional brain mapping. *Hum. Brain Mapp.* 10, 120–131.
- Lederman, S. J. (1981). The perception of surface roughness by active and passive touch. *Bull. Psychon. Soc.* 18, 253–255.
- Lee, S., Carvell, G. E., and Simons, D. J. (2008). Motor modulation of afferent somatosensory circuits. *Nat. Neurosci.* 11, 1430–1438.
- Macefield, V. G. (2005). Physiological characteristics of low-threshold mechanoreceptors in joints, muscle

- and skin in human subjects. *Clin. Exp. Pharmacol. Physiol.* 32, 135–144.
- Master, S., and Tremblay, F. (2009). Task-specific increase in corticomotor excitability during tactile discrimination. *Exp. Brain Res.* 194, 163–172.
- Master, S., and Tremblay, F. (2010). Selective increase in motor excitability with intraactive (self) versus interactive touch. *Neuroreport* 21, 206–209.
- McGlone, F., Olausson, H., Boyle, J., Jonesgotman, M., Dancer, C., Guest, S., and Essick, G. (2012). Touching and feeling: differences in pleasant touch processing between glabrous and hairy skin in humans. *Eur. J. Neurosci.* 35, 1782–1788.
- Morecraft, R. J., Cipolloni, P. B., Stilwell-Morecraft, K. S., Gedney, M. T., and Pandya, D. N. (2004). Cytoarchitecture and cortical connections of the posterior cingulate and adjacent somatosensory fields in the rhesus monkey. *J. Comp. Neurol.* 469, 37–69.
- Morecraft, R. J., Stilwell-Morecraft, K. S., Cipolloni, P. B., Ge, J., McNeal, D. W., and Pandya, D. N. (2012). Cytoarchitecture and cortical connections of the anterior cingulate and adjacent somatomotor fields in the rhesus monkey. *Brain Res. Bull.* 87, 457–497.
- Nikouline, V. V., Linkenkaer-Hansen, K., Wikström, H., Kesäniemi, M., Antonova, E. V., Ilmoniemi, R. J., and Huttunen, J. (2000). Dynamics of mu-rhythm suppression caused by median nerve stimulation: a magnetoencephalographic study in human subjects. *Neurosci. Lett.* 294, 163–166.
- Olausson, H., Lamarre, Y., Backlund, H., Morin, C., Wallin, B. G., Starck, G., Ekholm, S., Strigo, I., Worsley, K., Vallbo, A. B., and Bushnell, M. C. (2002). Unmyelinated tactile afferents signal touch and project to insular cortex. *Nat. Neurosci.* 5, 900–904.
- Penfield, W., and Rasmussen, T. (1950). *The Cerebral Cortex of Man: A Clinical Study of Localization and Function*. New York, NY: Macmillan.
- Perge, J. A., Niven, J. E., Mugnaini, E., Balasubramanian, V., and Sterling, P. (2012). Why do axons differ in caliber? *J. Neurosci.* 32, 626–638.
- Pons, T. P., Garraghty, P. E., Friedman, D. P., and Mishkin, M. (1987). Physiological evidence for serial processing in somatosensory cortex. *Science* 237, 417–420.
- Provitiera, V., Nolano, M., Pagano, A., Caporaso, G., Stancanelli, A., and Santoro, L. (2007). Myelinated nerve endings in human skin. *Muscle Nerve* 35, 767–775.
- Ragert, P., Nierhaus, T., Cohen, L. G., and Villringer, A. (2011). Interhemispheric interactions between the human primary somatosensory cortices. *PLoS ONE* 6:e16150. doi: 10.1371/journal.pone.0016150
- Romo, R., Hernandez, A., Salinas, E., Brody, C. D., Zainos, A., Lemus, L., de Lafuente, V., and Luna, R. (2002). From sensation to action. *Behav. Brain Res.* 135, 105–118.
- Schäfer, K., Blankenburg, F., Kupers, R., Grüner, J. M., Law, I., Lauritzen, M., and Larsson, H. B. (2012). Negative BOLD signal changes in ipsilateral primary somatosensory cortex are associated with perfusion decreases and behavioral evidence for functional inhibition. *Neuroimage* 59, 3119–3127.
- Shanks, M. F., Pearson, R. C., and Powell, T. P. (1985). The ipsilateral cortico-cortical connexions between the cytoarchitectonic subdivisions of the primary somatic sensory cortex in the monkey. *Brain Res.* 356, 67–88.
- Shmuel, A., Augath, M., Oeltermann, A., and Logothetis, N. K. (2006). Negative functional MRI response correlates with decreases in neuronal activity in monkey visual area V1. *Nat. Neurosci.* 9, 569–577.
- Simões-Franklin, C., Whitaker, T. A., and Newell, F. N. (2011). Active and passive touch differentially activate somatosensory cortex in texture perception. *Hum. Brain Mapp.* 32, 1067–1080.
- Talairach, J., and Tournoux, P. (1988). *Co-planar Stereotaxic Atlas of the Human Brain*. New York, NY: Thieme.
- Tapia, M. C., Cohen, L. G., and Starr, A. (1987). Selectivity of attenuation (i.e., gating) of somatosensory potentials during voluntary movement in humans. *Electroencephalogr. Clin. Neurophysiol.* 68, 226–230.
- Tommerdahl, M., Simons, S. B., Chiu, J. S., Favorov, O., and Whitsel, B. (2006). Ipsilateral input modifies the primary somatosensory cortex response to contralateral skin flutter. *J. Neurosci.* 26, 5970–5977.
- Vallbo, A., Olausson, H., Wessberg, J., and Norrsell, U. (1993). A system of unmyelinated afferents for innocuous mechanoreception in the human skin. *Brain Res.* 628, 301–304.
- Vallbo, A. B., Olausson, H., and Wessberg, J. (1999). Unmyelinated afferents constitute a second system coding tactile stimuli of the human hairy skin. *J. Neurophysiol.* 81, 2753–2763.
- Vallbo, A. B., Olausson, H., Wessberg, J., and Kakuda, N. (1995). Receptive field characteristics of tactile units with myelinated afferents in hairy skin of human subjects. *J. Physiol.* 483, 783–795.
- Verrillo, R. T., Bolanowski, S. J., and McGlone, F. P. (1999). Subjective magnitude of tactile roughness. *Somatosens. Mot. Res.* 16, 352–360.
- Weiskrantz, L., Elliott, J., and Darlington, C. (1971). Preliminary observations on tickling oneself. *Nature* 230, 598–599.
- Wessberg, J., Olausson, H., Fernström, K. W., and Vallbo, A. B. (2003). Receptive field properties of unmyelinated tactile afferents in the human skin. *J. Neurophysiol.* 89, 1567–1575.

**Conflict of Interest Statement:** The authors declare that the research was conducted in the absence of any commercial or financial relationships that could be construed as a potential conflict of interest.

Received: 19 March 2012; paper pending published: 19 April 2012; accepted: 20 July 2012; published online: 07 August 2012.

Citation: Ackerley R, Hassan E, Curran A, Wessberg J, Olausson H and McGlone F (2012) An fMRI study on cortical responses during active self-touch and passive touch from others. *Front. Behav. Neurosci.* 6:51. doi: 10.3389/fnbeh.2012.00051

Copyright © 2012 Ackerley, Hassan, Curran, Wessberg, Olausson and McGlone. This is an open-access article distributed under the terms of the Creative Commons Attribution License, which permits use, distribution and reproduction in other forums, provided the original authors and source are credited and subject to any copyright notices concerning any third-party graphics etc.



# Bayesian exploration for intelligent identification of textures

Jeremy A. Fishel<sup>1,2</sup>\* and Gerald E. Loeb<sup>1,2</sup>

<sup>1</sup> Department of Biomedical Engineering, University of Southern California, Los Angeles, CA, USA

<sup>2</sup> SynTouch LLC, Los Angeles, CA, USA

## Edited by:

Blythe Towal, California Institute of Technology, USA

## Reviewed by:

Juan Pablo Carbajal, University of Zürich, Switzerland

Michael Wiertelowski, Université Pierre et Marie Curie, France

Jivko Sinapov, Iowa State University, USA

## \*Correspondence:

Jeremy A. Fishel, Department of Biomedical Engineering, University of Southern California, 1042 Downey Way, Denny Research Center (DRB 140), Los Angeles, CA 90089-1111, USA.

e-mail: jeremy.fishel@syntouchllc.com

In order to endow robots with human-like abilities to characterize and identify objects, they must be provided with tactile sensors and intelligent algorithms to select, control, and interpret data from useful exploratory movements. Humans make informed decisions on the sequence of exploratory movements that would yield the most information for the task, depending on what the object may be and prior knowledge of what to expect from possible exploratory movements. This study is focused on texture discrimination, a subset of a much larger group of exploratory movements and percepts that humans use to discriminate, characterize, and identify objects. Using a testbed equipped with a biologically inspired tactile sensor (the BioTac), we produced sliding movements similar to those that humans make when exploring textures. Measurement of tactile vibrations and reaction forces when exploring textures were used to extract measures of textural properties inspired from psychophysical literature (traction, roughness, and fineness). Different combinations of normal force and velocity were identified to be useful for each of these three properties. A total of 117 textures were explored with these three movements to create a database of *prior experience* to use for identifying these same textures in future encounters. When exploring a texture, the discrimination algorithm adaptively selects the optimal movement to make and property to measure based on previous experience to differentiate the texture from a set of plausible candidates, a process we call Bayesian exploration. Performance of 99.6% in correctly discriminating pairs of similar textures was found to exceed human capabilities. Absolute classification from the entire set of 117 textures generally required a small number of well-chosen exploratory movements (median = 5) and yielded a 95.4% success rate. The method of *Bayesian exploration* developed and tested in this paper may generalize well to other cognitive problems.

**Keywords:** texture discrimination, tactile sensor, vibration, fingerprints, exploratory movements, roughness, classification, Bayesian exploration

## INTRODUCTION

*The tactual properties of our surroundings do not chatter at us like their colors; they remain mute until we make them speak. . . Eye movements do not create color the way finger movements create touch.* Katz (1925)

Touch, by necessity, is an interactive sense, unique from the senses of vision and hearing. While we are able to observe the sights and sounds of our environment without any physical interaction, the tactual properties of an object can only be sensed by physical contact. When interacting with an object, humans not only need to interpret the tactile information they sense, they also need to decide which types of movements to make in order to produce these tactual percepts. Artificial systems will require similar strategies (Loeb et al., 2011). Experimental psychologists have identified six general types of exploratory movements that humans make when tactually exploring objects to determine their properties: enclosure to determine global shape and volume, hefting to determine weight, pressure to determine hardness, static contact to determine thermal properties, contour following to determine

exact shape, and lateral sliding movements to determine surface texture (Lederman and Klatzky, 1987). Performing all of these movements and their many variants when identifying objects by touch may not be practical or useful. Instead, prior knowledge can be used to intelligently guide the selection of which exploratory movements to make. In this work we present a novel methodology for selecting these optimal exploratory movements called *Bayesian exploration*. The process works by using prior experience to determine which of the many possible exploratory movements is expected to produce the greatest distinction between the most plausible candidate objects. To simplify the analysis, we reduced the scope of the discrimination task to only texture discrimination, a modality for which human strategies and capabilities have been well-described in the literature.

Early work from David Katz provided some of the first insights into the psychophysics of texture discrimination. In his studies he observed that while coarse textures could be discriminated based on their static contours by simply pressing down on an object, fine textures instead required sliding motion in order to generate vibrations for their discrimination (Katz, 1925). More recent studies

have supported that lateral movements and vibrations do, in fact, play a critical role in the perception of fine textures (Hollins and Risner, 2000), for which discrimination is impaired after vibrotactile adaptation (Hollins et al., 2001). The human hand has a wealth of sensory receptors responding to mechanical and thermal stimuli (Jones and Lederman, 2006). Pacinian corpuscles with frequency responses of 60–700 Hz (Mountcastle et al., 1972) are capable of sensing vibrations associated with slip and texture that can be less than a micrometer in amplitude at their characteristic frequency of 200 Hz (Johansson et al., 1982; Brisben et al., 1999), suggesting that highly sensitive transducers will be required if this capability is to be reproduced artificially.

A great body of research has focused on the physical stimuli and perceptual properties that permit the identification and discrimination of textures. The perception of roughness has been one of the most studied of these properties. Early psychophysical experiments attributed this to the friction coefficient between the skin and object for fine textures (Katz, 1925). Other studies using coarser textures (spatial periods greater than 0.5 mm) have proposed that spatial period and contact force, and not friction, are correlated with perceived roughness (Lederman et al., 1982). Smith et al. (2002a) contested these findings, providing additional support for the role of friction and shear force in the perception of these coarse textures. Further studies involving fine textures have indicated that the power of vibrations as sensed by the Pacinian corpuscles could play an integral role in the perception of roughness (Bensmaïa and Hollins, 2005). Early studies into the perceptive dimensionality of surfaces have suggested that sticky/slippery, hard/soft, and rough/smooth represent three independent dimensions of a surface (Hollins et al., 1993). However, these studies only used 17 surfaces and the relevance of these results have been contested by Bergmann Tiest and Kappers (2006) who have explored dimensionality with a total of 125 surfaces. Findings from this expanded database have suggested that there are at least four perceptual dimensions of surfaces (and likely more), although not all could be correlated specifically with named properties. We propose that some of this dimensionality could be attributed to non-textural properties such as compliance and thermal properties that might be obtained without the need for sliding movements. With specific regards to texture and sliding movements, the dimensions of sticky/slippery, rough/smooth, and coarse/fine seem to be the most salient descriptions of properties that make textures distinct, based on both the descriptive words that people use to describe textures and their utility as demonstrated by the experimental literature.

In Katz's (1925) original work he proposed a duplex theory for texture perception, hypothesizing that coarse textures can be discriminated spatially while fine textures are discriminated dynamically through sensed vibrations. This was prescient, as the structure and function of cutaneous mechanoreceptors was then unknown. We now know that vibrations and static pressure are sensed by separate populations of cutaneous mechanoreceptors (Knibestöl and Vallbo, 1970; Jones and Lederman, 2006). Artificial tactile sensors have developed along similar lines, offering either high spatial resolution or high temporal bandwidth. Reviews of the various tactile sensing technologies over the last 30 years can be found in (Nicholls and Lee, 1989; Howe, 1994; Lee and Nicholls,

1999; Dahiya et al., 2010). For dynamic tactile sensing and texture discrimination, a number of technologies have been introduced implementing accelerometers (Howe and Cutkosky, 1989, 1993), piezoelectric film (Tada et al., 2003) microphones (Edwards et al., 2008), and tri-axial MEMS force sensors (de Boissieu et al., 2009). More recently, many tactile sensors have introduced fingerprint-like ridges (Mukaibo et al., 2005; Oddo et al., 2009; Scheibert et al., 2009), which have been proposed to enhance the correlation of spatial frequency of explored textures with temporal patterns in the sensed vibrations.

The use of tactile sensors for artificial texture discrimination has received a great deal of attention in recent years. Tada et al. (2004) were able to demonstrate that signal variance of two different polyvinylidene difluoride (PVDF) films embedded at different depths in a complaint sensor could be used to distinguish among five different textures. Further development by this group expanded this analysis to an additional sensory dimension using an embedded strain gage (Hosoda et al., 2006). Mukaibo et al. (2005) developed a tactile sensor with fingerprints and embedded strain gages to discriminate surfaces based on roughness and friction. A force sensor with an elastic covering developed by de Boissieu et al. (2009) was used with sliding movements to identify 10 different kinds of paper using two different analytical approaches: the first utilized differences in Fourier coefficients in the recorded vibrations while the second used more direct signal features such as the mean, variance, and kurtosis of the signals as well as spectral properties in a neural network classifier. A similar approach was taken by Giguere and Dudek (2011) using accelerometers on a rigid tactile probe to classify driving surfaces based on their means, variance, and higher-order moments in a neural network. Oddo et al. (2011) used a robotic finger producing a stereotyped sliding movement to discriminate between three fine textured gratings ranging from 400 to 480  $\mu\text{m}$  based on their spectral properties. Jamali and Sammut (2011) analyzed Fourier components of vibrations measured from eight different textures using a novel method of majority voting to classify these textures with a high accuracy of 95%. This study took advantage of multiple exploratory movements, starting with three movements initially and adding movements until 80% or more of these movements indicated a particular texture. With exception to the last study that explored three different sliding velocities, all of these cases considered only a single exploratory movement. It has been demonstrated that multiple exploratory movements as well as multiple features can boost the performance of such a classifier for texture discrimination (Sinapov and Stoytchev, 2010). In a subsequent study by the same group 20 textures were explored with a fingernail-like tactile sensor measuring accelerations at five different exploratory movements. The frequency components from these different movements were used to obtain a classification performance increase from 65% using the best single exploratory movement to 80% for all five exploratory movements (Sinapov et al., 2011).

In all of these cases, the discrimination of textures with these artificial systems is for the most part a "passive" exploratory procedure. Force and speed are preset to some standard values and a fixed movement (or sequence of movements) is executed. Furthermore, the selection of signal processing measures is seemingly

arbitrary in many of these studies. Various methods are attempted and those that appear to yield the best performance are used as classifier input. Instead, we propose that findings from psychophysical literature can guide the development of more intuitive and useful signal measures.

As reviewed above, multiple signals, multiple exploratory movements, as well as repeated trials can boost classification performance. However, as the complexity of discrimination tasks increase beyond simply texture discrimination and more movements and signals are added to the repertoire, the feasibility of doing *everything* (especially for multiple trials) can become highly impractical if not completely infeasible. Instead, the task of discrimination can take advantage of a hypothesis-testing approach that we have proposed humans likely use when exploring objects (Loeb et al., 2011). Each successive exploratory movement can be used to reduce the set of possible candidates; this information can be used to determine the optimal *next* exploratory movement that would yield the best discrimination among these most likely candidates rather than the entire population. Such an approach would have advantages in reducing the number of exploratory movements needed to classify a texture or in the general case, any object. Here we introduce a novel algorithm where the selection of the exploratory movement becomes a critical process of the identification task. Using a database of prior experience, optimal exploratory movements are selected and executed to aid in the discrimination task.

## MATERIALS AND METHODS

An overview of Bayesian exploration is presented first (see Classification Theory and Strategy) in the context of a texture discrimination task, followed by a description of the BioTac multimodal tactile sensor (see Biomimetic Tactile Sensor) and the experimental apparatus used to control sliding movements when exploring textures (see Experimental Apparatus). The descriptive words humans use when discriminating textures are used to define quantifiable properties of textures (see Analytical Measures of Descriptive Texture Properties), followed by a method for determining the most useful exploratory movements to estimate those properties (see Selection of Set of Exploratory Movements). The final three Sections describe the classifier training over this refined set of movements (see Classifier Training and Data Collection), the methods employed for comparing performance of this classifier to human performance in discriminating pairs of similar textures (see Texture Discrimination and Comparison with Human Performance) and methods for absolute texture discrimination from a broad set of 117 textures (see Absolute Texture Identification).

## CLASSIFICATION THEORY AND STRATEGY

Classification is a topic of wide interest in artificial intelligence and is a subset of the larger fields of pattern recognition and machine learning. The goal of a classification task is to identify which class or classes best explains a set of observations. Many tools exist involving both supervised and unsupervised training (Jain et al., 2000). In the majority of classification problems, inputs are given and the class with the maximal posterior likelihood determines

the classification<sup>1</sup>. This introduces a fundamental deficiency in the typical approach to classification problems: the decision must be made with the currently available information. To compensate for this deficiency, it is common to collect as much information as possible before the classification is made. The time and effort required to produce each exploratory movement to collect tactile data suggests that this would be highly inefficient. Decisions are first required to determine which exploratory movements to make before any tactile information can be obtained. The selection of these movements would benefit greatly from iterative decision making, in which the observations of previous movements are used to identify the most likely candidates to select the next movement that is most likely to disambiguate them. Here we introduce a novel method of texture discrimination implementing these strategies. This method of *Bayesian exploration* should be generalizable to any identification task requiring such intelligence.

### Bayesian inference for discrimination of textures

Bayesian inference is a widely implemented statistical classification method used to estimate the likely causes of an observation after it has occurred. Considering a set of textures ( $T$ ) and the observable measurements that they generate ( $X$ ) when performing an exploratory movement ( $M$ ), we can estimate the likelihood that a given texture had caused these observations with Bayes' rule:

$$P(T_i|X, M_m) = \frac{P(X|T_i, M_m) P(T_i)}{P(X, M_m)} \quad (1)$$

Where  $T_i$  belongs to a set of textures  $T$ ,  $X$  is a set of observable properties (which are introduced in the later sections),  $M_m$  is a particular exploratory movement that gives rise to these sensed properties, and  $P(T_i)$  represents the prior probability of texture  $T_i$ .  $P(X, M_m)$  is the probability of observation  $X$  occurring given all known causes from the set  $T$  at exploratory movement  $M_m$  and can be found by the law of total probability:

$$P(X, M_m) = \sum_j P(X|T_j, M_m) P(T_j) \quad (2)$$

Substituting (2) into (1) yields a common formulation of Bayes' rule:

$$P(T_i|X, M_m) = \frac{P(X|T_i, M_m) P(T_i)}{\sum_j P(X, T_j, M_m) P(T_j)} \quad (3)$$

The probability of a measurement occurring given a known texture and exploratory movement can be estimated from its probability density function. In the absence of other evidence, the central limit theorem suggests that these values should fall within a normally distributed probability density function that can be defined according to a mean ( $\mu$ ) and standard deviation ( $\sigma$ ):

$$P(X|T_i, M_m) \propto p(X|T_i, M_m) = \frac{1}{\sqrt{2\pi\sigma_{i,m}^2}} e^{-\frac{(x-\mu_{i,m})^2}{2\sigma_{i,m}^2}} \quad (4)$$

<sup>1</sup>Other methods may use cost functions to reduce the occurrence of Type-I or Type-II errors for particular classes where such errors are detrimental.

It is important to note that the probability density function is not a true probability, but rather a density, and can take on a value greater than unity. However, this measure is proportional to the actual probability; the unknown scaling can be ignored as it is canceled out by the denominator of (3), which has the same scaling factor. The formulas (3) and (4) can be used to update the posterior probability of a texture given observation  $X$  from a normally distributed set of expected observations. In practice, as evidenced by human performance, multiple observations, and exploratory movements need to be made to refine this to an acceptable level of confidence before determining the most likely texture.

**Adaptive selection of optimal exploratory movements**

We have proposed that humans use a careful selection of exploratory movements to test hypotheses when exploring objects by touch (Loeb et al., 2011). Consider a simple example of identifying a brick by touch. Absent prior information about the object, a reasonable first exploratory movement might be an enclosure movement, yielding information about the object’s size and indicating that it is a large rectangular prism. Based on this information, the examiner may then conclude that it is either a brick or a block of wood. Useful subsequent movements to extract the most information between these two objects would probably focus on its mass, such as pushing or hefting the object.

The process of determining which exploratory movement is optimal requires a prediction of the perceived benefit based on prior experiences. A similar methodology has been presented by Rebguns et al. (2011), where movements and sensing actions are selected to reduce Shannon entropy. In that study exploratory movements cease when there is no perceived reduction of this entropy, a feature the authors refer to as “burying its head in the sand” to avoid getting additional information that might increase uncertainty. While the performance of this study was quite impressive, the concept of additional information being undesirable is peculiar. By contrast, our approach is not to infer the reduction of entropy; instead we simply select the movement that would best discriminate between likely objects. The decision to make this next movement or not depends on whether the information and a higher level of confidence is worth the time and energy required to make the exploratory movement.

To estimate which movement would best discriminate among likely objects, we can use prior experience to infer the expected similarity between signals from pairs of objects at each of these movements. Movements that produce the greatest difference in measured signals from different objects would be optimal for the discrimination task, while the movements that produce similar signals would not be useful. One suitable measure of this degree of confusion is the amount of overlap between two probability density functions. An estimation of this is provided by the Bhattacharyya coefficient, defined as:

$$BC = \int \sqrt{p_1(x) p_2(x)} dx \tag{5}$$

The Bhattacharyya coefficient varies between 0 and 1 depending on the overlapping region of the two probability density functions. For a given movement, observation, and pair of textures, a low

value would indicate no confusion (so this would be a very useful movement to make in order to disambiguate these objects), while a high value would indicate an undesirable movement because substantial ambiguity would remain. For all possible pairs of textures ( $i$  and  $j$ ) we can define an expected confusion probability matrix for each possible exploratory movement ( $m$ ) as:

$$C_{ij,m} = \int \sqrt{p(x|T_i, M_m) p(x|T_j, M_m)} dx \tag{6}$$

For normally distributed populations this reduces to:

$$C_{ij,m} = \sqrt{\frac{2\sigma_{i,m}\sigma_{j,m}}{\sigma_{i,m}^2 + \sigma_{j,m}^2}} e^{-\frac{(u_{i,m}-u_{j,m})^2}{4(\sigma_{i,m}^2 + \sigma_{j,m}^2)}} \tag{7}$$

We can estimate the expected uncertainty for a particular texture and movement ( $u_{i,m}$ ) that would remain after making an exploratory movement from this confusion probability matrix:

$$u_{i,m} = \frac{\sum_{j,j \neq i} C_{ij,m} P(T_j)}{\sum_j C_{ij,m} P(T_j)} \tag{8}$$

Equation 8 measures the degree of confusion between a specific texture and all other likely textures, weighted by their priors, divided by the total amount of weighted confusion including between that texture and itself. If no other textures produce overlapping probability distribution curves with this texture, the value then becomes zero, as there would be no expected uncertainty for this texture and movement combination.

The total expected uncertainty for all textures for a given exploratory movement ( $U_m$ ) can be estimated as:

$$U_m = \sum_i u_{i,m} P(T_i) \tag{9}$$

Substituting (8) into (9) yields:

$$U_m = \sum_i \left( \frac{\sum_{j,j \neq i} C_{ij,m} P(T_j)}{\sum_j C_{ij,m} P(T_j)} \right) P(T_i) \tag{10}$$

which, given the coefficient  $C_{ij,m}$  is equal to 1 when  $i$  is equal to  $j$ , can be shown to reduce to:

$$U_m = 1 - \sum_i \left( \frac{(P(T_i))^2}{\sum_j C_{ij,m} P(T_j)} \right) \tag{11}$$

The value from (11) can be used to determine which movement would produce the lowest expected uncertainty. We define the perceived benefit of making an exploratory movement as:

$$B_m = 1 - U_m^\alpha \tag{12}$$

Which depends on parameter  $\alpha$ , which we define as inversely proportional to the number of times an exploratory movement has been made previously ( $n$ ) for the current discrimination task:

$$\alpha = \frac{1}{n} \quad (13)$$

To promote diversity in exploratory movements and collect a richer database of information, we need to reduce the benefit of repeated movements that did not yield satisfactory discrimination performance in prior explorations. Because the uncertainty is a value that ranges from 0 to 1, a larger value of  $n$  reduces the benefit of a repeated movement. By calculating this benefit for all possible exploratory movements, the movement that produces the maximal benefit can be identified. The iterative selection and execution of these optimal exploratory movements when investigating an object is the process that we call Bayesian exploration.

### BIOMIMETIC TACTILE SENSOR

The BioTac® (SynTouch, Los Angeles, CA, USA; **Figure 1**) was designed to provide both robustness and sensitivity for multimodal tactile sensing. It consists of a rigid core that contains all sensory transducers, covered by an elastomeric skin. The space between the skin and the core is inflated with an incompressible liquid to give it a compliance that mimics human fingerpads. No transducers or electrical components are contained in the skin, making the design robust to grit, moisture, or other damage that typically plagues tactile sensors. The BioTac consists of three complementary sensory modalities (force, vibration, and temperature) that have been integrated into a single package. Contact forces distort the elastic skin and underlying conductive liquid, changing impedances of electrodes distributed over the surface of the rigid core (Wettels et al., 2008; Wettels and Loeb, 2011). Vibrations in the skin propagate through the fluid and are detected by the pressure sensor (Fishel et al., 2008). These vibrations can be amplified and filtered to obtain a dynamic (AC) pressure signal with even greater sensitivity than the human fingertip (Fishel and Loeb, 2012). Temperature and heat flow are transduced by a thermistor near the surface of the rigid core (Lin et al., 2009).

The BioTac exhibits high sensitivity to induced vibrations when sliding over textured surfaces (Fishel et al., 2008). More recent quantitative tests with controlled small impacts and applied vibrations demonstrated higher sensitivity than human fingertips (Fishel and Loeb, 2012). In this study it was demonstrated that the BioTac is capable of detecting small vibrations only a few nanometers in amplitude around its peak frequency sensitivity of 330 Hz, nearly two orders of magnitude better than human subjects. To achieve this sensitivity, the BioTac takes advantage of carefully designed signal processing electronics that allow a sensitivity near the theoretical noise floor of the pressure sensor. First the output from the piezoresistive pressure transducer (24PC15SMT, Honeywell) is amplified by a gain of 10 with a low-pass anti-aliasing filter (1040 Hz) obtain a measurement of fluid (DC) pressure (sensitivity: 21.8 mV/kPa). This is then passed through a band-pass filter (10–1040 Hz) and amplified with an additional gain of 99.1 to obtain a sensitivity of 2.16 mV/Pa for dynamic (AC) pressure. The background noise at this stage was found to be only 1.2 mV

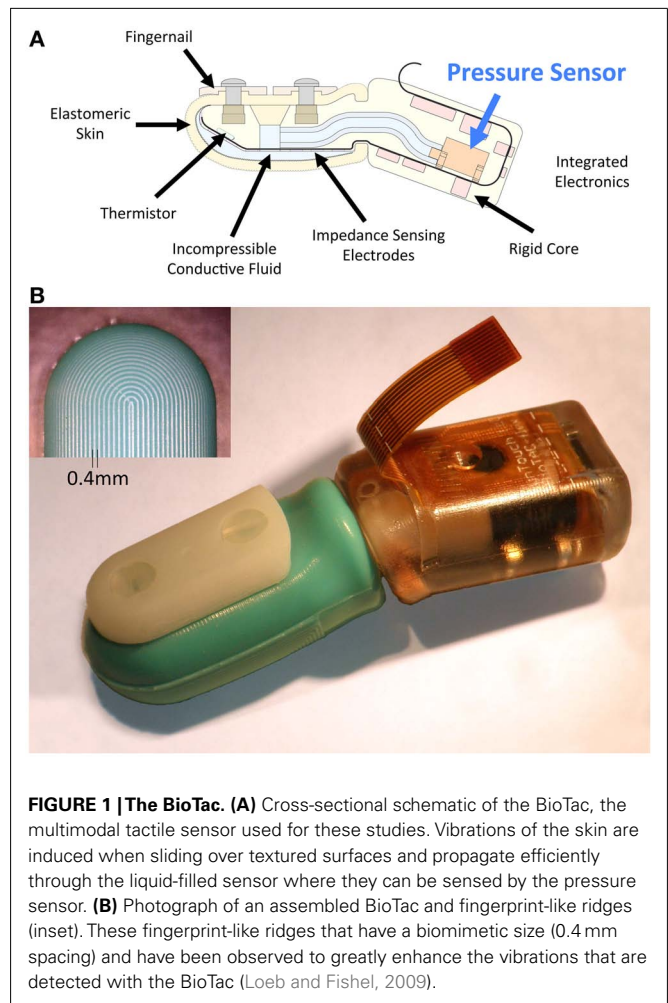


**FIGURE 1 | The BioTac.** (A) Cross-sectional schematic of the BioTac, the multimodal tactile sensor used for these studies. Vibrations of the skin are induced when sliding over textured surfaces and propagate efficiently through the liquid-filled sensor where they can be sensed by the pressure sensor. (B) Photograph of an assembled BioTac and fingerprint-like ridges (inset). These fingerprint-like ridges that have a biomimetic size (0.4 mm spacing) and have been observed to greatly enhance the vibrations that are detected with the BioTac (Loeb and Fishel, 2009).

(0.52 Pa of dynamic pressure). Dynamic (AC) pressure as well as static (DC) pressure were sampled at 2200 Hz and digitized with a resolution of 12 bits in the range of 0–3.3 V (AC Pressure is biased to 1.65 V) through onboard electronics inside the BioTac. Sampling and data transmission are controlled through a serial peripheral interface (SPI) protocol provided with the BioTac.

The compliance, shape and material properties of the liquid-inflated elastomeric skin (Silastic S, Dow Corning) give rise to a natural resonant frequency around 200–350 Hz, which happens to be similar to the peak sensitivity of the Pacinian corpuscles. The surface of the BioTac has a fingerprint-like pattern (cylindrical shaped ridges with a height of 0.2 mm and spacing of 0.4 mm) that has been observed to enhance the amplitude of these vibrations in the BioTac (Loeb and Fishel, 2009). Given its similarities to the mechanical properties and sensitivity of the human fingertip, the BioTac provides an opportunity to test theories of human texture discrimination (Loeb et al., 2011) and to explore if they can be used by artificial systems seeking to achieve similar performance in tactile object identification.

### EXPERIMENTAL APPARATUS

We hypothesize that humans utilize a variety of lateral sliding movements when exploring textures. The magnitude of contact

force and velocity of the sliding movement are the two most obvious parameters that define these movements. Compelling artificial texture percepts can be recreated based on only these two parameters of an exploratory movement (Romano and Kuchenbecker, 2011). The apparatus developed for these experiments is capable of precision control of contact force and sliding velocity while collecting sensory data from the BioTac as it explores a texture. The apparatus makes use of a stepper motor to set contact force and a precision linear stage to control the sliding velocity relative to the textured surface (Figure 2).

### Force Control with Stepper Motor

Normal force of the BioTac onto the explored texture is adjusted with a stepper motor (L4118 and SMC133, Nanotec) that positions a lever with a BioTac on the end (Figure 2). Observations indicated that the change in fluid pressure of the BioTac was linearly correlated with contact force (slope 11.5 mN/bit,  $R^2 = 0.995$ ) at forces less than 2 N (Figure 3). This was verified by pressing down on a force plate (Nano17, ATI) positioned to be at the same height as the textures. At forces greater than 2 N the skin of the BioTac comes into contact with the core and the relationship between contact force and fluid pressure is no longer linear. This relationship in the linear range was used to control the stepper motor in order to achieve the desired contact force prior to an exploratory movement. The BioTac was lowered slowly onto a texture (0.5 mm/s) while monitoring the actual DC pressure. When this value reached the target change in DC pressure, the stepper motor was stopped. The sliding movements and associated shear forces tended to produce modest changes in the DC pressure, but no adjustments were made to the stepper motor position while sliding and collecting vibration data to avoid introducing spurious vibrations.

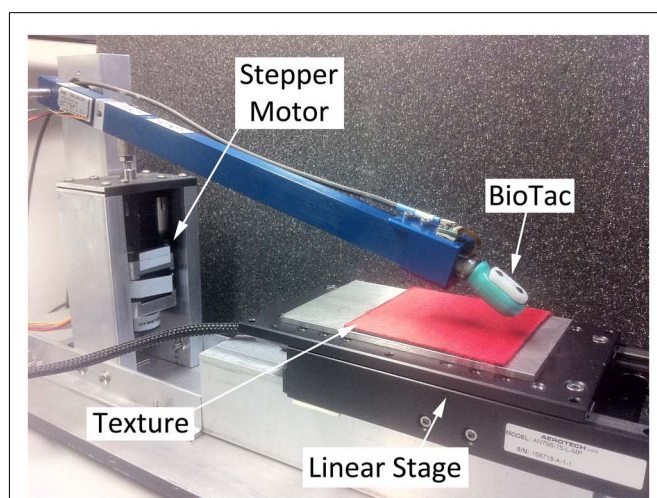


**FIGURE 2 | Texture exploration apparatus with the BioTac and texture.**

A stepper motor (left) is attached to a lever (blue) that can raise or lower the BioTac on textures. Adjusting the vertical position of the stepper motor provides control of contact force. To produce lateral motion, a special vibration-free linear stage is used to slide textures past the BioTac. Textures are adhered to flat, square magnets that can be mounted and dismantled rapidly on a steel plate attached to the linear stage.

### Velocity control with linear stage

Sliding velocity of the textures under the BioTac was controlled with a precision, low-vibration linear stage (ANT130, Aerotech). The high-quality cross-roller bearings of the motor produced extremely smooth sliding motions and no mechanical vibrations could be detected even with human touch while the stage was moving. A motion controller (Soloist, Aerotech) controlled sliding velocity and distance based on preset commands. Motor current and sliding velocity were sampled by the motion controller, which could be queried in LabVIEW using built-in software libraries provided by the manufacturer.

### Textures

A total of 117 textures were used in these experiments (Table 1). These were selected from a large library of everyday materials found in art supply, fabric, and hardware stores. Using a variety of commonly occurring textures provides a more realistic database of surfaces than have been previously used in other studies of psychophysical and artificial texture discrimination, which tend to use surfaces made from the same material varying along a single parameter such as spatial period. These textures were cut into 75 mm × 75 mm squares and attached to square magnets of the same size with adhesive backing. The magnetically backed textures could be rapidly mounted and dismantled to a steel plate attached to the linear stage.

### Software

The sampling of the BioTac, control of stepper motor and linear stage were done using LabVIEW (National Instruments). Sampling of the BioTacs was achieved using a USB/SPI adapter (Cheetah SPI, Total Phase) and software libraries developed by and available from SynTouch (Los Angeles, CA, USA). Both DC and AC pressure were sampled at 2200 Hz each. Data was sampled continuously and transmitted back to the computer in batches every 100 ms. The digital controls for the stepper motor were also updated every 100 ms through a DAQ card (NI USB-6218, National Instruments). Control of the linear stage was maintained continuously by the motion controller; the motor current and

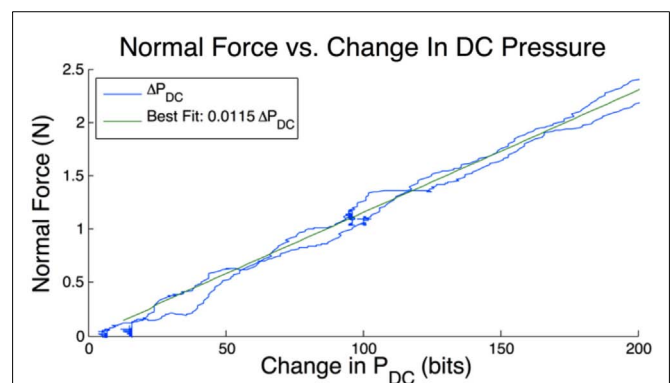


**FIGURE 3 | Relationship between normal force and change in DC pressure.** A single trial is shown in both loading and unloading (blue) as normal force increases and decreases on the tip of the BioTac. The best fitting line is shown in green and a correlation value of  $R^2 = 0.995$  is observed.

**Table 1 | List of 117 textures used in this study.**

#	Texture	#	Texture	#	Texture	#	Texture
1	Computer paper	31	Very soft foam	61	Lacquered vinyl	91	Corduroy
2	Linen paper	32	Marble	62	Smooth vinyl	92	Silk velvet
3	Smooth cardstock	33	Smooth tile	63	Canvas vinyl	93	Short-hair fur
4	Marble cardstock	34	Rough tile	64	Madrid vinyl	94	Velboa
5	Canvas cardstock	35	Natural stone laminate	65	Corinthian vinyl	95	Terry cloth
6	Double mulberry paper	36	Oak wood	66	PVC snakeskin	96	Velour
7	Vellum	37	Polished hickory	67	Coarse leather	97	Velvet
8	Cardboard	38	Balsa wood	68	Medium-coarse leather	98	Viscose challis
9	Foam board	39	Nylon plastic	69	Smooth leather	99	Cotton sateen
10	Velcro hooks	40	PVC plastic	70	Coarse suede	100	Burlap
11	Velcro eyes	41	Acrylic	71	Smooth suede	101	Hand-woven cotton
12	Acrylic felt	42	Graphite	72	Very soft suede	102	Cotton duck
13	Polyester felt	43	Alumina graphite	73	Crepe de chine	103	Bull denim
14	Stiffened felt	44	Milled aluminum	74	Silk satin	104	Jean denim
15	Velvet paper	45	Ground aluminum	75	Pimatex cotton	105	Denim twill
16	Canvas	46	Polished aluminum	76	Cotton jersey	106	Flannel
17	Foam sheet	47	Polyurethane rubber	77	Cotton crush	107	Pineapple fiber weave
18	Plastic paper	48	Neoprene rubber	78	Cotton interlock	108	Scenery canvas
19	Template plastic	49	Nitrile rubber	79	Cotton lycra	109	Silk noil
20	Plastic mesh (5 mm)	50	Buna-N rubber	80	Cotton velveteen	110	Scenery muslin
21	Tarp	51	Santoprene rubber	81	Coarse cotton	111	Linen cloth
22	Corkboard	52	Viton rubber	82	Soft cotton	112	Cotton gauze
23	Carpet	53	Haplion rubber	83	Upholstry vinyl	113	Bamboo rayon
24	Frosted glass	54	Silicone rubber	84	Charmeuse satin	114	Nylon fabric
25	Flemish glass	55	Plastic sheet	85	Cotton/silk blend	115	Hemp silk
26	Satin glass	56	Car vinyl	86	Lens-cleaning fabric	116	Rabbit fur
27	Frosty vue glass	57	Textured vinyl #1	87	Rayon	117	Leopard shag
28	Textured glass	58	Textured vinyl #2	88	Crushed satin		
29	Styrofoam	59	PVC vinyl	89	Raw silk		
30	Soft foam	60	Snakeskin vinyl	90	Crushed velvet		

Textures can be grouped into the following categories: 1–9: paper-like materials; 10–23: art supplies and miscellaneous materials; 24–28: types of glass; 29–31: types of foam; 32–35: tiles and laminates; 36–38: types of wood; 39–46: engineering materials; 47–54: types of rubber; 55–66: types of vinyl; 67–72: leathers and suedes; 73–83: cottons and silks; 84–99: other fabrics and textiles; 100–115: coarse weaves; 116–117: furs.

stage position and velocity were queried every 100 ms through software libraries developed by Aerotech. For each texture, the exploratory process was automated to produce multiple trials at each exploratory movement before proceeding to the next texture. Data were analyzed offline in MATLAB.

### ANALYTICAL MEASURES OF DESCRIPTIVE TEXTURE PROPERTIES

A system that uses orthogonal measurements as inputs is ideal for a machine classifier problem. Several machine learning algorithms exist to reduce unnecessary dimensionality of inputs, such as principle component analysis and other multidimensional scaling techniques (Jain et al., 2000). Moderate success discriminating a small numbers of textures has been achieved using various statistical measures and signal processing approaches as input to these classifiers. We hypothesized that reasonably orthogonal measures could be obtained by studying the language people use to describe textures. The human brain is a very effective classifier and language has evolved as a tool to describe the percepts associated with texture discrimination. For this study, we selected simple and

intuitive measures of descriptive properties frequently used in psychophysical literature exploring texture discrimination, bypassing many of the artificial and convoluted statistical techniques commonly used in classifier methods. Three distinct properties have been identified in literature: traction (sticky/slippery), roughness (rough/smooth), and fineness (coarse/fine).

#### Traction of texture

Descriptive words such as *slippery* and *sticky*<sup>2</sup> are commonly used to describe the resistance to movement when sliding over a texture. This dimension has been suggested to be relatively orthogonal to the perceptual dimension of roughness (Hollins et al., 1993). To measure this percept, we chose to use traction or resistance to motion, although other literature has reported that this force is correlated with the perception of roughness (Smith et al., 2002a).

<sup>2</sup>The descriptive word sticky is also used to describe adhesive properties. However, even in this context it still refers to resistance to movement, albeit away from the surface.

In physics, the kinetic coefficient of friction between two objects is typically used to quantify this property. It is important to note that when measuring traction, we are measuring the force required to slide the BioTac skin (Silastic S, Dow Corning) over the texture; the measured traction is a property of these two surface interactions. Amontons' first and second laws, as well as Coulomb's law of friction, state that the coefficient of friction multiplied by the normal force is equal to the maximal shear force that two objects will exert on one another when sliding. While this is an idealization that does not address some of the more complex properties of friction (i.e., viscosity), we propose that the measurement of average frictional force between the skin of the BioTac and explored texture while sliding can provide a useful measure in discriminating textures.

In our experimental testbed, the linear stage that produces sliding movement can be queried for instantaneous motor current. This was found to vary linearly with shear force by placing the stage at a 45° angle and attaching various weights to it. In dynamic sliding it was observed that initially a high amount of current was required to accelerate the stage from rest but only a low amount of current was required to overcome the dynamic friction within the stage in the unloaded state once the stage had reached its target velocity. When the BioTac was pushed against a texture sample on the stage, the motor current required to sustain constant velocity sliding increased linearly with the applied normal force. Given the linearity of this response, the average motor current from the stage while sliding was used to estimate the traction between the BioTac and textures being explored. This was simpler and more accurate than using the force-sensing modality of the BioTac itself, which can extract tangential force from the distributed change in impedance of its impedance sensing electrodes (Wettels and Loeb, 2011).

$$\text{Traction} \propto \text{Motor Current} \quad (14)$$

Examples of this signal and calculations are provided in **Figure 4**, frame B.

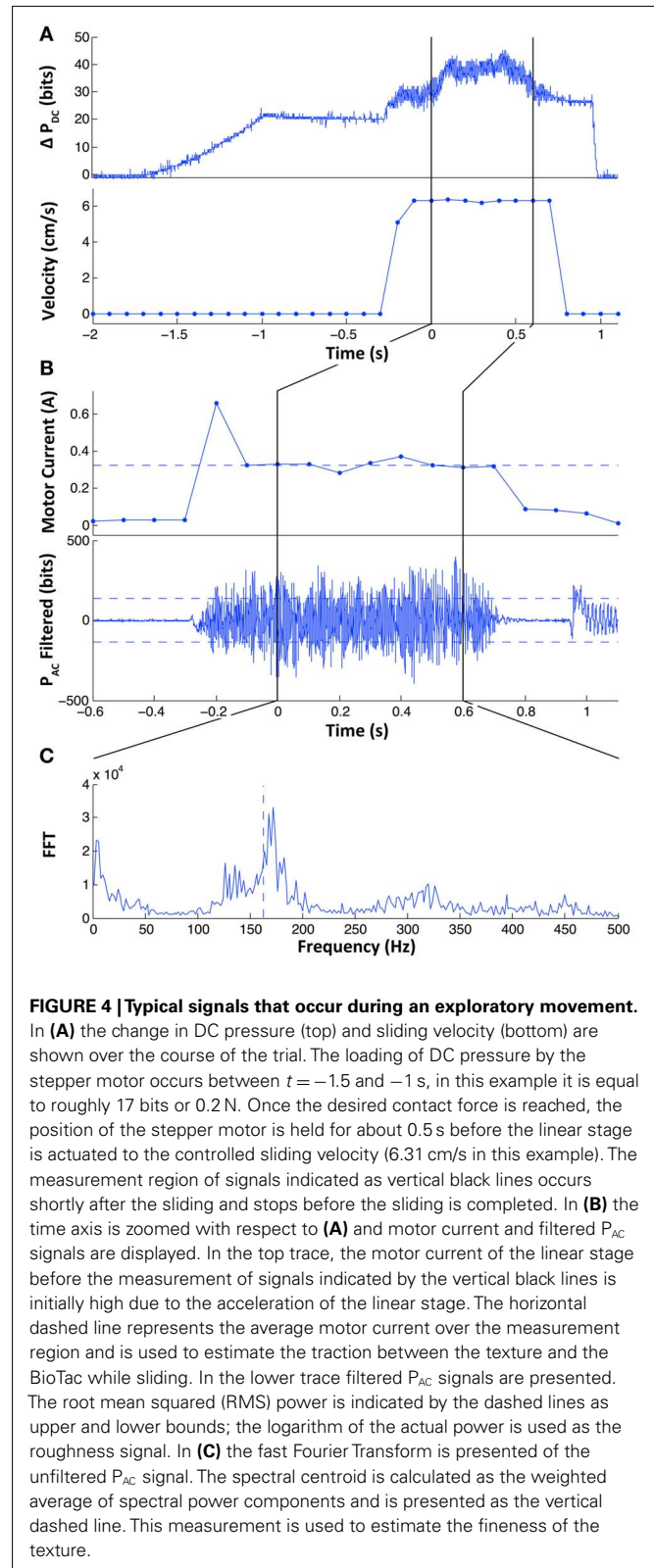
### Roughness of texture

When sliding over surfaces with different roughness properties with the BioTac, we observed that the amplitude of vibration as measured by the dynamic pressure sensor in the BioTac ( $P_{AC}$ ) was correlated with the perceived roughness of the texture, similar to the observations of (Bensmaïa and Hollins, 2005). In our own findings, smooth surfaces were found to produce virtually no vibrations, while rougher surfaces produced vibrations of much greater amplitudes. To quantify this, we computed the logarithm of signal power after subtracting the background noise with the equation:

$$\text{Power} = \frac{1}{N} \sum_{n=1}^N (\text{filt}(P_{AC}(n)))^2 \quad (15)$$

$$\text{Roughness} \propto \log(\text{Power} - \text{background noise}) \quad (16)$$

AC pressure was filtered with a 20–700 Hz digital band-pass filter (66th order FIR filter) to simulate the frequency response of the



Pacian corpuscles that are thought to mediate texture perception and eliminate low frequency oscillations from contributing to this estimate. An example of the filtered signal is shown in **Figure 4**,

frame B. It was also observed that even when locked in a fixed position, the stepper motor produced some background noise that was not consistent from trial to trial. By measuring this background noise power prior to sliding and subtracting it from the power while sliding we were able to obtain more consistent measurements of the signal power contributed from sliding alone. The logarithm of this signal was found to better reflect a more evenly distributed set of roughness properties with similar variances (as presented later in **Figure 5**). A similar justification for using the logarithm of surface amplitude in psychophysical discrimination of textures has been proposed by Bergmann Tiest and Kappers (2006).

### Fineness of texture

The role of spatial periodicity in the perception of textures has been explored in a number of studies. It has been observed that the

coarser textures produce lower-frequency vibrations when sliding over an object, while finer textures produce higher-frequency vibrations, suggesting the simple relationship:

$$f = \frac{v}{\lambda} \quad (17)$$

with  $\lambda$  equal to the spatial wavelength of the texture or fingerprints and  $v$  equal to the velocity of lateral motion. This is the operating principle of many algorithms for texture discrimination in artificial sensors (Mukaibo et al., 2005; Oddo et al., 2009, 2011; Scheibert et al., 2009). Our own findings have indicated that this relationship breaks down for finer textures and higher velocities (as presented later in **Figure 6**). Although not directly reported, this can be observed in the results from Mukaibo et al. for higher spatial frequencies and from Oddo et al. for higher velocities, in which the estimation of spatial wavelength becomes much more prone to errors when approaching these limits. The experiments of Scheibert et al. were conducted at very low exploratory speeds (0.02 cm/s), two to three orders of magnitude slower than common exploratory movements employed by humans (Dahiya and Gori, 2010), which is clearly not fast enough to observe this dynamic behavior. Furthermore, smoother surfaces have been demonstrated to be free of spectral harmonics, instead generating signals that represent  $1/f$  noise in the frequency domain (Wiertlewski et al., 2011). Measured frequencies do not always relate linearly to the spatial wavelength of the texture, particularly for fine or smooth textures, but the estimation of this frequency can still yield useful information about the relative fineness or coarseness of the texture.

We propose a measure of spectral centroid to determine the weighted frequency power of the vibrations recorded by the BioTac. The dynamic pressure is transformed into the frequency domain using the single-sided fast Fourier transform and the spectral centroid is calculated using the weighted average of the

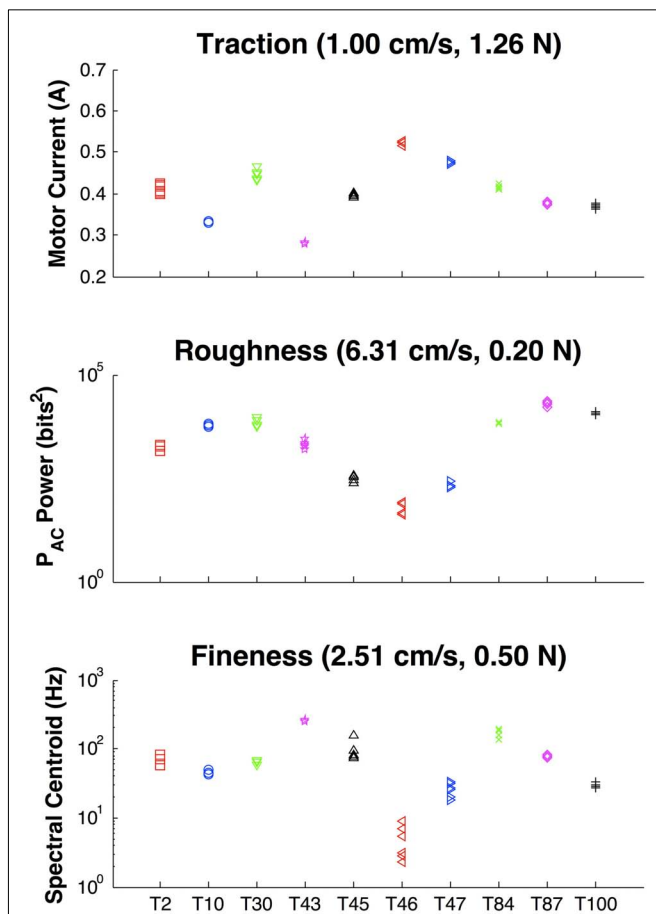


**FIGURE 5 | Measures of descriptive texture properties at their optimal exploratory movements.** Texture IDs: T2 = Linen Paper, T10 = Velcro Hooks, T30 = Foam, T43 = Graphite, T45 = Milled Aluminum, T46 = Polished Aluminum, T47 = Rubber, T84 = Satin, T87 = Rayon, T100 = Burlap. Top frame: Traction as measured from motor current to overcome sliding friction between the skin of the BioTac and the texture. Middle frame: roughness as measured from vibration power as recorded by the  $P_{AC}$  signal from the BioTac. Bottom frame: spectral centroid as measured by weighted spectral power of  $P_{AC}$  signal from the BioTac. Six trials are shown for each movement to demonstrate clustering of each signal.

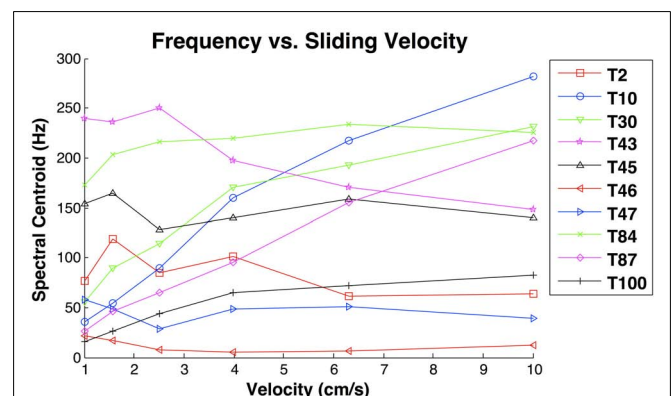


**FIGURE 6 | Spectral centroid as a function of sliding velocity at the lightest contact force (0.2 N).** Results indicate that only the spectral centroid of coarser textures (T10 = Velcro Hooks, T30 = Foam, T87 = Rayon, and T100 = Burlap) consistently increased as a function of velocity. Finer textures produced idiosyncratic functions of velocity, while the spectral centroid of graphite (T43) decreased as a function of velocity.

frequency power from the following equation:

$$SC = \frac{\sum (\text{fft}(P_{AC})^2 \times f)}{\sum \text{fft}(P_{AC})^2} \quad (18)$$

To smooth the frequency domain response, a sliding window was used to collect the Fourier transform at different sections of the signal, which were averaged and used for the spectral centroid estimation. Examples of this measurement are shown in **Figure 4**. A logarithmic scale of this measure is used as an input to the texture discrimination model. Note that this method does not attempt to compensate for the rather complex frequency response of the BioTac itself (Fishel and Loeb, 2012).

$$\text{Fineness} \propto \log(SC) \quad (19)$$

### Normality of Signals

The classifier discussed in Section “Classification Theory and Strategy” makes the assumption that signals arise from a normally distributed population. Due to the large number of textures explored, only a small number of trials could be collected for each of the exploratory movements. Therefore, a thorough analysis of the exact probability density function for these signals could not be conducted. We make the assumption that signals are normally distributed for the purposes of this study, however as more samples are collected a clearer understanding of the true probability density function would serve to improve the performance of this classifier. This will be even more important when classifying surfaces that have some heterogeneity in their textures.

### The curse of dimensionality

Additional input dimensions will typically improve performance of a classifier if they are well defined. In practice, however, it has been observed that additional dimensions will actually degrade performance of a classifier for a constant sample size, a property that has become known as the curse of dimensionality (Jain et al., 2000). To overcome this, an exponential increase in training data is required for each new dimension. To avoid the need for such a vast amount of training data, our model considers only univariate

distributions of a single property at each exploratory movement. Indeed, we have found that our classifier performance was severely degraded when considering all three properties at once for each exploratory movement using multidimensional probability density functions. The result was an algorithm that quickly converged in one or two exploratory movements but frequently to the wrong texture. As additional training is obtained, such a multidimensional approach would be optimal, but this is infeasible for the large number of textures used in this study. To avoid this shortcoming we only considered a single signal during an exploration movement. While this may not appear to take full advantage of all available information, it is actually preferable for a classifier with such limited experience, allowing it to focus solely on the property that it determines to be most relevant for a given exploration.

### SELECTION OF SET OF EXPLORATORY MOVEMENTS

While there exist infinite combinations of contact force and sliding velocities that can be used when exploring textures, experimental studies have demonstrated that individual subjects are quite consistent in reproducing exploratory movements in these tasks, although there is a high degree of variability among subjects (Smith et al., 2002b). This suggests that certain combinations of exploratory movement tend to be more efficient and that an individual person discovers and uses such combinations consistently. The internal representation of the objects in the external world could then be based on predictable sensations obtained when well-learned and, hence, dependable exploratory movements are made.

To identify these useful movements, 10 textures were chosen for the pilot study based on their perceived dissimilarity in the multidimensional space of identified texture properties (low/high traction, rough/smooth, coarse/fine; **Table 2**). Given the diversity of this sample, this was believed to represent most of the perceptual range of the complete set of 117 textures.

A total of 36 exploratory movements were chosen based on all combinations of six speeds and six forces. The ranges of these parameters were chosen to mimic the ranges humans typically use when exploring textures (1–10 cm/s, 0.2–2 N). Force ( $F$ ) and

**Table 2 | Textures used in exploratory movement pilot study and their perceived properties of traction, roughness, and fineness when explored by the human finger.**

ID	Name	Traction	Roughness	Fineness
T2	Linen paper	Med	Rough	Fine
T10	Velcro hooks	Low	Rough	Coarse
T30	Foam	High	Very rough	Coarse
T43	Graphite	Very low	Med	Fine
T45	Milled aluminum	Med	Smooth	Very fine
T46	Polished aluminum	Very high	Very smooth	No features
T47	Rubber	Very high	Smooth	No features
T84	Satin	Med	Med	Very fine
T87	Rayon	Med	Very rough	Med
T100	Burlap	Med	Very rough	Very coarse

*These samples were selected to represent the range of material properties to be expected over the larger population of textures.*

velocity ( $v$ ) at these six steps were calculated as a geometric series:

$$v_i = 10^{\frac{i-1}{5}} \times 1 \frac{cm}{s} \tag{20}$$

$$F_i = 10^{\frac{i-1}{5}} \times 0.2N \tag{21}$$

Using such a scale permits for comparisons to be made between exploratory movements that had equivalent frictional sliding power. For a given texture interacting with the BioTac skin, sliding power is proportional to the tangential force times sliding velocity. Given the assumptions of Amoltons' first law of friction, the tangential force would be proportional to the normal force for a given pair of surfaces with a constant coefficient of friction. With this set of parameters, pairs of force and velocity with equal sliding power could be found from the following equation:

$$P_a = F_i \times v_{a-i} \times \mu = 10^{\frac{a-2}{5}} \times \mu \times 20mW \tag{22}$$

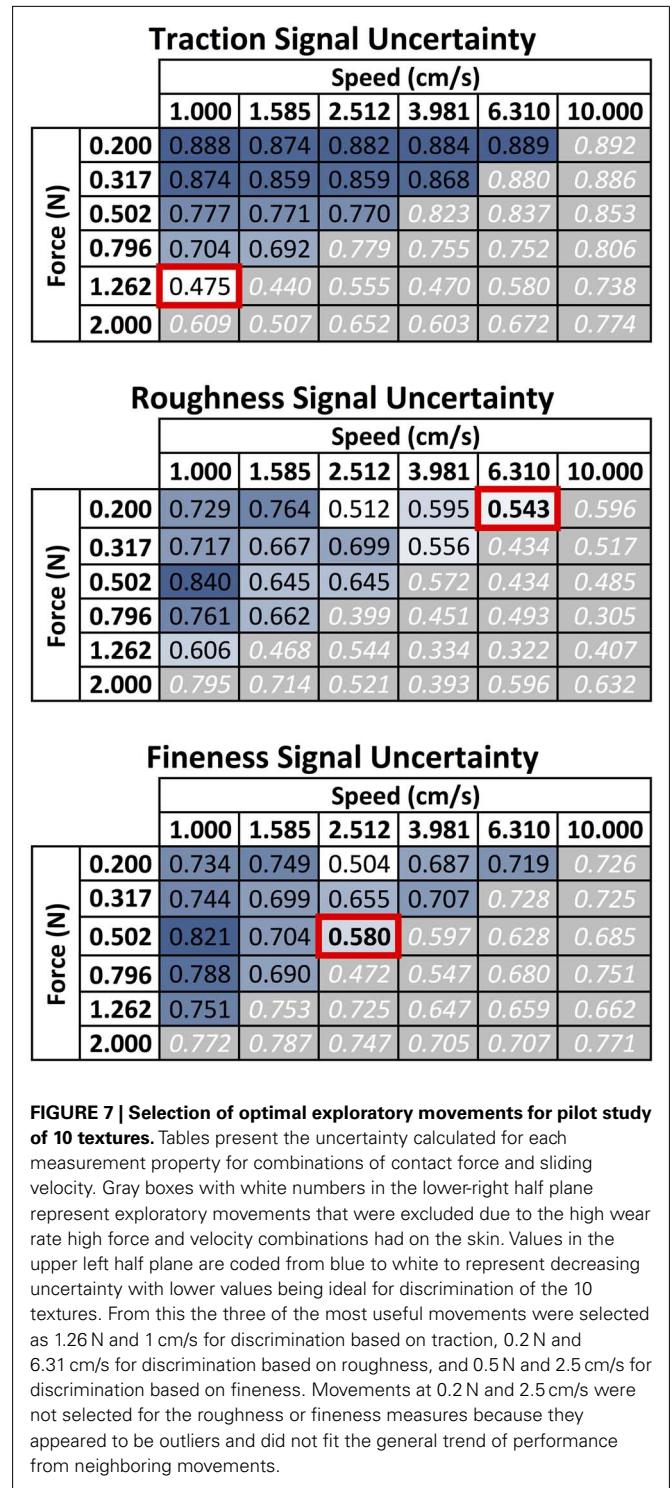
Six repetitions of the 36 movements were collected for each of the 10 textures. At each trial the starting location on the texture was randomized to ensure collected signals were properties of the texture itself and not necessarily an isolated feature on a given portion of the texture. Exploratory movements were automated by software and the data were saved to file for post processing. Data were collected for each of the exploratory movements for a particular texture before moving on to the next. The degree of uncertainty for each movement was analyzed for each signal property independently rather than as a multivariate system. This method was chosen to avoid the curse of dimensionality, as discussed in the previous section.

It was observed that high frictional sliding power exploratory movements (combinations of high force and velocity) led to an increase in skin wear and removal of fingerprints, resulting in substantial changes in the vibration signals recorded by the BioTac; these pairs of exploratory movement parameters were avoided. Of the remaining options, we selected three combinations, each of which provided the lowest uncertainty for one of the three properties (see **Figure 7**). These three *most useful* movements were used to explore the entire set of 117 texture samples.

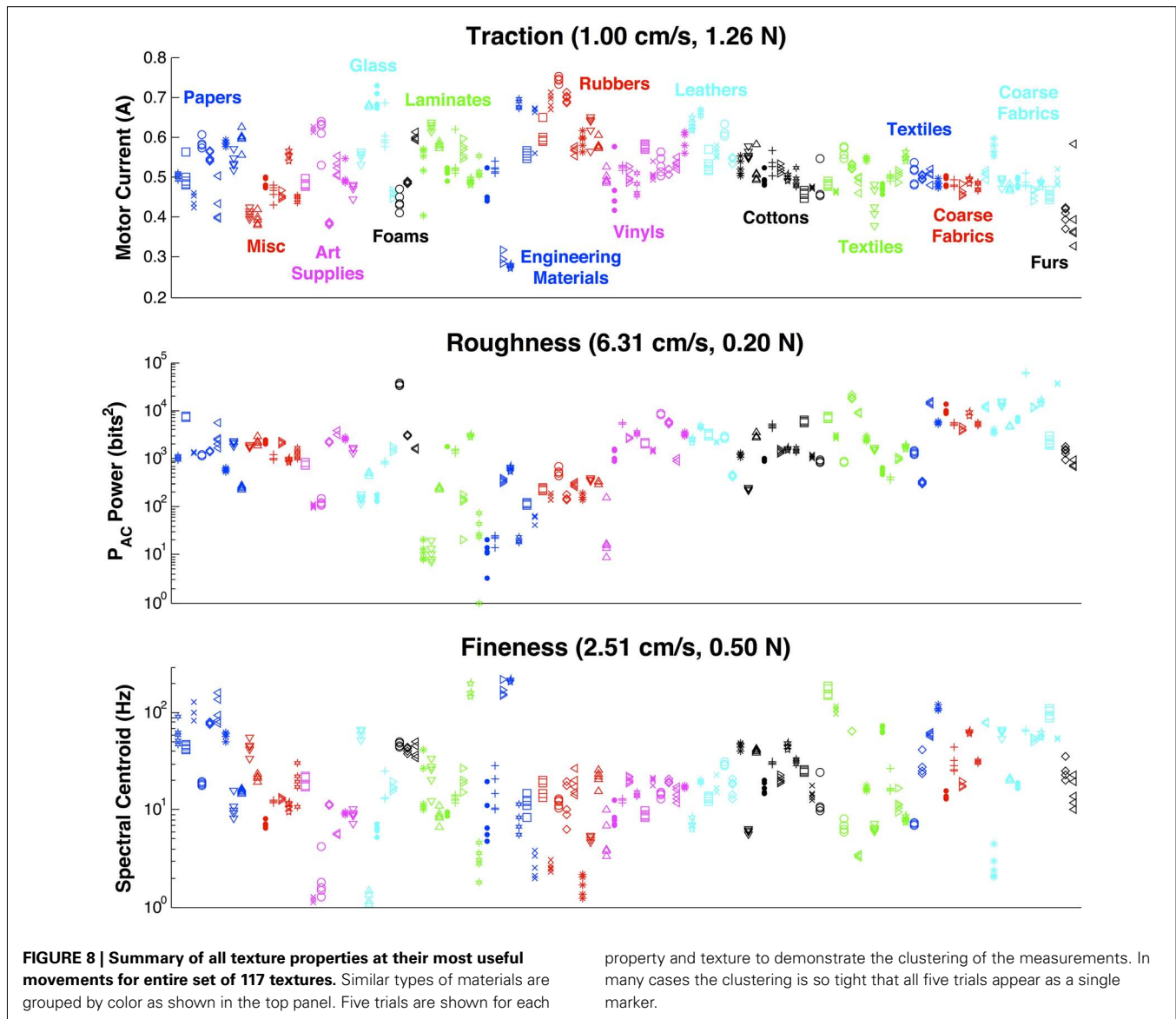
**CLASSIFIER TRAINING AND DATA COLLECTION**

Five trials were completed at each of the three selected exploratory movements for the entire set of 117 textures. All trials were completed on a single texture before moving to the next. During these trials, the skin was checked regularly to identify if the fingerprints were still intact. It was observed that fingerprint wear had a detrimental effect on the repeatability of data, particularly in the measurement of roughness from vibration power. To compensate for this, the skin of the BioTac was replaced if there were *any* visible signs of wear. With this approach we were able to avoid any signal drift resulting from wear, which was verified by comparing signals before and after the skin replacement. The skin of the BioTac was replaced two times under these conditions. Data collection for all 117 textures took roughly 20 h and spanned 4 days.

The data from these trials served to build a prior experience database that could be used to identify presented textures and to compute expected benefit of a given exploratory movement. During the course of these tests, three textures were damaged during



the higher force exploratory movements. Data for these textures were not used in the sample. Outputs of the various properties at their optimal movements are presented (**Figure 8**) along with the confusion probability matrices for all combinations of signals and movements (**Figure 9**). Signal correlation is presented to show the independence of each dimension (**Table 3**).



### TEXTURE DISCRIMINATION AND COMPARISON WITH HUMAN PERFORMANCE

Analyzing the resulting confusion probability matrices of the large texture dataset yielded surprising findings in the confusion between textures. Many pairs of textures that were perceived as difficult to discriminate by touch were readily distinguishable based on at least one dimension of the three calculated texture properties, while some pairs of textures that appeared simple to discriminate by human touch were determined to be more challenging to the artificial system based on the observed confusion matrices (Figure 9). Eight pairs of textures (16 textures total) were selected for a study of discriminability, including pairs that were perceived to be similar to human observers but not the artificial system, the reverse, or similar to both. Care was taken to select texture pairs that did not have other properties that were readily discriminable by other non-textural mechanisms such as compliance or thermal properties, for which human subjects would have an obvious

advantage (the BioTac does provide signals that can be used to estimate both properties (Lin et al., 2009; Su et al., 2012; but these were not used in this study).

Five human subjects consented to participate in a study to explore biological abilities to discriminate between similar textures. Prior to these experiments, subjects were informed that they would be presented with one of the eight pairs of textures at a time, which they could see and explore by sliding their fingers over them for as long as they desired in order to feel comfortable discriminating between the two textures in the pair. They were informed that after they were finished exploring, they would begin the testing phase and would not be allowed to explore both textures again. No additional guidance was provided on which properties or exploratory movements would be optimal for performing the discrimination task. They were also informed that when ready, they would have their vision occluded and be presented with a random selection of one of the two textures for four

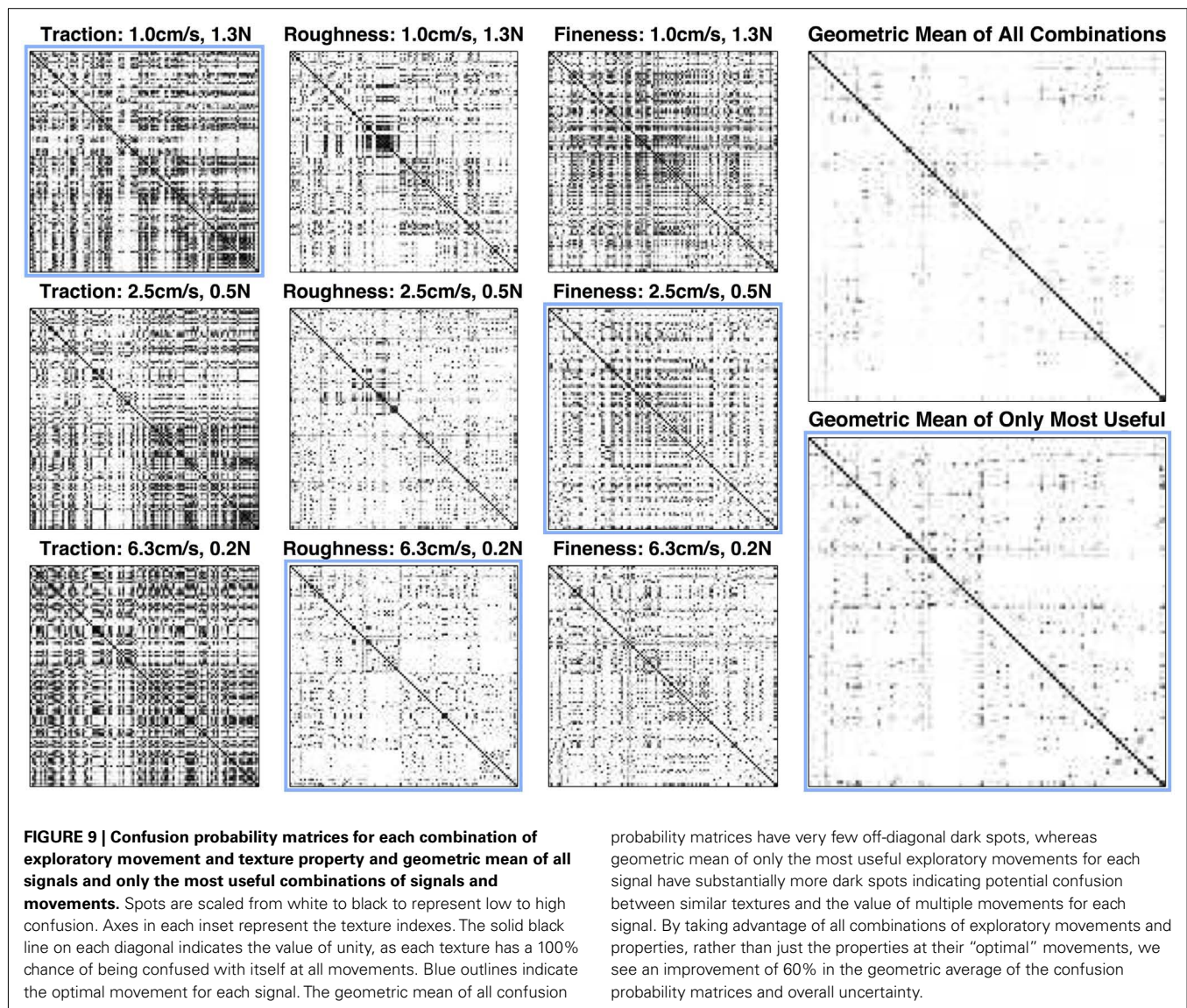


**FIGURE 9 | Confusion probability matrices for each combination of exploratory movement and texture property and geometric mean of all signals and only the most useful combinations of signals and movements.** Spots are scaled from white to black to represent low to high confusion. Axes in each inset represent the texture indexes. The solid black line on each diagonal indicates the value of unity, as each texture has a 100% chance of being confused with itself at all movements. Blue outlines indicate the optimal movement for each signal. The geometric mean of all confusion

probability matrices have very few off-diagonal dark spots, whereas geometric mean of only the most useful exploratory movements for each signal have substantially more dark spots indicating potential confusion between similar textures and the value of multiple movements for each signal. By taking advantage of all combinations of exploratory movements and properties, rather than just the properties at their "optimal" movements, we see an improvement of 60% in the geometric average of the confusion probability matrices and overall uncertainty.

trials. Subjects were aware that the selection of the presented texture was predetermined from a random number generator (i.e., it would not always be each texture twice for the four trials, by chance it could even be the same texture four times). The experimenter suggested that the subjects could call these textures A or B, however all subjects preferred to refer to the textures based on their visual properties (i.e., "the blue one"). For the testing phase, which started immediately after the exploratory phase, a small platform was placed in front of the subject where textures were to be placed. The platform was short and unobtrusive, allowing subjects to assume the same posture used in the exploratory phase. The experimenter placed the randomized texture on this platform and the subject held his finger over the texture until an auditory command was given to start exploration. After making exploratory movements (which ranged from two or three to dozens of movements depending on the difficulty the subject was experiencing), subjects notified the experimenter which of the two textures they thought they were touching. This was repeated for four trials for

each of the eight pairs of textures. While subjects were eager to know their performance, this was not disclosed to them until the completion of the experiment. Average performance across all five subjects for the eight texture pairs in terms of percentage of correct classifications (chance = 50%) is presented in **Table 4**.

Comparison in performance of humans with the artificial system in this discrimination task requires two separate populations of data, one to represent the information obtained in the exploratory phase and the other to represent novel information being encountered in the identification phase. This is commonly referred to in machine classifier problems as a training set and a validation set. The training set consists of data to be used as the *previous experience* that the Bayesian exploration algorithm refers to when encountering an unknown texture in order to determine optimal exploratory movements and to compute posterior probabilities after these movements. The original set of data obtained in the previous section was used to create this training set. A second set of novel data was collected and used as a validation set for the

**Table 3 | Correlation matrix between each texture property at each of the three movements.**

	Traction	Roughness	Fineness
<b>MOVEMENT 1 (1.00 cm/s, 1.26 N)</b>			
Traction	1.0000	-0.5564	-0.3560
Roughness	-0.5564	1.0000	0.2183
Fineness	-0.3560	0.2183	1.0000
<b>MOVEMENT 2 (2.51 cm/s, 0.50 N)</b>			
Traction	1.0000	-0.4916	-0.5100
Roughness	-0.4916	1.0000	0.3981
Fineness	-0.5100	0.3981	1.0000
<b>MOVEMENT 3 (6.31 cm/s, 0.20 N)</b>			
Traction	1.0000	-0.4019	-0.5472
Roughness	-0.4019	1.0000	0.5581
Fineness	-0.5472	0.5581	1.0000

same textures that were used in the human texture discrimination studies. Similar to the training set, five trials for each of the three exploratory movements were collected for these 16 textures.

The computational speed of computer processors made it attractive to analyze the performance of this artificial discrimination task offline in a *virtual* texture exploration. When performing a *virtual* exploratory movement, a randomly selected trial from the unseen validation set of the texture being explored was given to the classifier. Due to the high degree of randomness of these simulations, a total of 1000 simulations as described below for each of the eight pairs of textures were conducted to establish a more accurate measure of performance.

During a texture discrimination task for the artificial system, a pair of textures was selected and their prior probabilities were set equally to 50%. The probability for all other textures in the database was set to zero, effectively eliminating them from the classifier's decision process. One of the two textures was selected at random as the unknown texture to be identified by the system. The Bayesian exploration algorithm used data in its previous experience (from the training set) to decide which exploratory movement and signal would discriminate optimally between them. The signal from this movement in the validation set was delivered to the classifier and the posterior probabilities of the two textures were updated using Bayesian inference. The process of performing optimal combinations of exploratory movements and properties to measure through Bayesian exploration was repeated until one of the two textures converged to a probability of greater than 99.9%<sup>3</sup>. Data from these discrimination tasks was not added to the database. Results comparing the performance of human subjects

<sup>3</sup>The 99.9% convergence criterion for texture pairs was higher than the 99% used in the absolute classification task as discussed in the following section. It was found that when discriminating between a smaller number of textures (i.e., two as used in this experiment) the algorithm would quickly converge in only one or two movements and frequently to a wrong decision if the required probability threshold was not set to a high enough value. By increasing the required probability to a higher level, additional exploratory movements would be required, resulting in better overall classification performance. At this level most solutions converged to the correct values with a median of three exploratory movements with satisfactory results.

**Table 4 | Comparison of AB discrimination of similar texture pairs between human subjects and the Bayesian exploration classifier.**

Texture pairs	Percentage of correct classifications	
	Human subjects	Bayesian exploration
Computer paper (T1) vs. smooth cardstock (T3)	60%	<b>99.3%</b>
Buna-N rubber (T50) vs. silicone rubber (T54)	80%	<b>100.0%</b>
Acrylic felt (T12) vs. velour (T96)	90%	<b>100.0%</b>
Textured vinyl #1 (T57) vs. textured vinyl #2 (T58)	70%	<b>100.0%</b>
Pineapple fiber weave (T107) vs. linen cloth (T111)	<b>100%</b>	<b>100.0%</b>
Plastic paper (T18) vs. template plastic (T19)	85%	<b>97.7%</b>
Cotton duck (T102) vs. jean denim (T104)	90%	<b>100.0%</b>
Santoprene rubber (T51) vs. haplon rubber (T53)	75%	<b>100.0%</b>

*In all cases Bayesian exploration outperformed human subjects with many pairs of textures yielding 100% classification over the 1000 simulations for each pair (the best performance for each pair of textures is highlighted in bold).*

and the Bayesian exploration are presented as the percentage of correct identifications in **Table 4**.

### ABSOLUTE TEXTURE IDENTIFICATION

The new validation data from the 16 textures obtained in the previous section were also used against the entire set of 117 textures to evaluate the performance of absolute texture identification. The classifier was not aware of the 16 textures it was being presented and initially set the probabilities for all textures to the same value (1 divided by 117). The same process of Bayesian decision making to determine optimal pairs of exploratory movements and signals for virtual exploratory movements was followed as discussed in the previous section. The performance of this Bayesian exploration approach was compared with two alternative exploratory strategies. In the first, the most useful movements for each of these signals as determined in Section "Selection of Set of Exploratory Movements" were cycled; in the second, exploratory movement and signal combinations were randomly selected. A maximum of 10 exploratory movements were allowed and the classifier was run until any texture converged to greater than 99% probability or until the 10 exploratory movements were conducted. If not converged, the texture with the greatest probability after the 10 exploratory movements was determined to be the most likely candidate. A total of 8000 Monte Carlo simulations over the 16 textures were conducted and performance is presented as percentage of correct classifications (**Table 5**). Examples of the evolving probabilities of possible textures and the selected exploratory movements for some of these trials are shown in **Figure 10**.

**Table 5 | Summary of performance for absolute classification task for uninformed cycling, random selection, and Bayesian Exploration.**

Summary of performance	Uninformed cycling	Random selection	Bayesian exploration
Correct identifications	49.9%	84.1%	<b>95.4%</b>
And converged	36.4%	68.3%	<b>89.3%</b>
Median # of movements	10*	8	<b>5</b>
PERFORMANCE DETAIL			
Computer paper (T1)	0.0%	57.8%	<b>82.0%</b>
Smooth cardstock (T3)	0.0%	81.2%	<b>99.6%</b>
Buna-N rubber (T50)	58.0%	84.4%	<b>100.0%</b>
Silicone rubber (T54)	88.6%	86.6%	<b>99.6%</b>
Acrylic felt (T12)	<b>100.0%</b>	94.2%	96.4%
Velour (T96)	33.4%	83.4%	<b>100.0%</b>
Textured vinyl #1 (TS7)	<b>100.0%</b>	99.6%	<b>100.0%</b>
Textured vinyl #2 (T58)	0.0%	51.4%	<b>67.2%</b>
Pineapple fiber weave (T107)	99.2%	94.0%	<b>99.8%</b>
Linen cloth (T111)	14.2%	90.6%	<b>99.6%</b>
Plastic paper (T18)	27.6%	86.4%	<b>100.0%</b>
Template plastic (T19)	86.2%	88.0%	<b>94.4%</b>
Cotton duck (T102)	<b>100.0%</b>	99.2%	<b>100.0%</b>
Jean denim (T104)	26.6%	91.8%	<b>96.8%</b>
Santoprene rubber (T51)	3.0%	75.4%	<b>93.6%</b>
Haplon rubber (T53)	61.2%	80.8%	<b>97.6%</b>

A total of 8000 Monte Carlo simulations for 16 textures from unique validation data were compared against the training data from all 117 textures to determine which of the 117 textures best fit the observed data when performing virtual explorations. Results of Bayesian exploration are compared to uninformed cycling through exploratory movements between the three signals at their most useful movements and random selection of exploratory movements from all combinations of movements and signals. The percentage of correct identifications are shown for each. The algorithm that produced the best performance for each texture is displayed in bold. \*For the case of uninformed cycling the median number of movements to convergence could not be obtained as the simulation was stopped at 10 movements before half of the simulations could converge.

## RESULTS

### ANALYSIS OF DESCRIPTIVE TEXTURE PROPERTIES

In the pilot study of 10 textures, descriptive properties were found to reflect expected values. For instance, graphite produced the lowest measure for traction between the surface and the skin of the BioTac while polished aluminum and rubber had the highest. Foam, satin, rayon, and burlap produced the highest measures of roughness, while polished aluminum produced the lowest measure of roughness. In calculating the spectral centroid, the finer textures such as graphite and satin produced higher values while the coarser textures such as burlap and velcro produced lower values. Featureless textures such as polished aluminum and rubber tended to produce low spectral centroids as well due to their 1/f noise as discussed in (Wiertlewski et al., 2011). The exploratory movements that produced the most discriminability within the 10-texture dataset as calculated by the minimal uncertainty are presented in Figure 5.

A notable finding of these trials was that the spectral centroid did not scale with sliding velocity for all textures (Figure 6). Such

scaling was observed only for certain coarse textures that were also rough (Velcro hooks, foam, rayon, burlap). This constitutes additional evidence that fingerprints do not simply convert sliding velocity and spatial frequency into temporal signals as concluded by (Scheibert et al., 2009).

### IDENTIFYING THE MOST USEFUL EXPLORATORY MOVEMENTS

The most useful movement for each property was selected from the set of 36 movements (Figure 7). It was observed that combinations of high-power exploratory movements (high force and high velocity) resulted in a high rate of fingerprint wear on the BioTac's skin. These high wear movements (gray boxes with white text in Figure 7) were eliminated, although some appeared to be useful for discrimination (e.g., 6.31 cm/s and 1.26 N for discriminating roughness). As a general trend, it was observed that the ability to discriminate traction improved at lower velocities and higher forces, while the ability to discriminate roughness improved at higher velocities and lower forces. These findings supported our own intuition on the exploratory movements humans make to extract these properties. We propose that when humans make a movement to determine surface traction, they tend to use a high amount of force while slowly moving their finger. Presumably this is to maximize the amount of shear force sensed in the finger; it is easier to control these forces by moving slowly. Similarly in our experimental testbed, sliding at slower velocities produced more stable sliding forces as measured by the motor current; this resulted in more consistent measurements between multiple trials. To discriminate roughness, we have observed that humans tend to use very light forces while sliding over the surfaces of textures to feel their vibrations. Our observations with the BioTac have demonstrated a possible utility of this strategy. In general, faster velocities tend to produce higher amplitude vibration signals, while greater forces tend to dampen vibrations sensed by the BioTac. The findings of these two exploratory movements as the most useful for these properties in our artificial system provide additional support to these hypotheses about biological exploratory movements for perception of traction and roughness.

While a certain movement may be classified as generally “useful” for a given property, other movements may actually be more useful for discriminating a given pair of materials along this property. Because all properties are collected with each movement, the classification algorithm takes advantage of all nine combinations of available movements and material properties during its decision process of determining the optimal movement and signal to sense.

### TRAINING DATASET

The measured properties of the 117 textures were individually tightly clustered for repeated measures but spanned most of the three dimensional property space, an ideal situation for an efficient classifier. The complete set of measured properties for each signal at the most useful movement for that property is shown in Figure 8. In many cases, textures that had similar values for one property tended to be dissimilar along other dimensions, suggesting the utility of well-chosen next exploratory movements.

A graphical representation of confusion probability matrices was generated for each combination of movements and properties

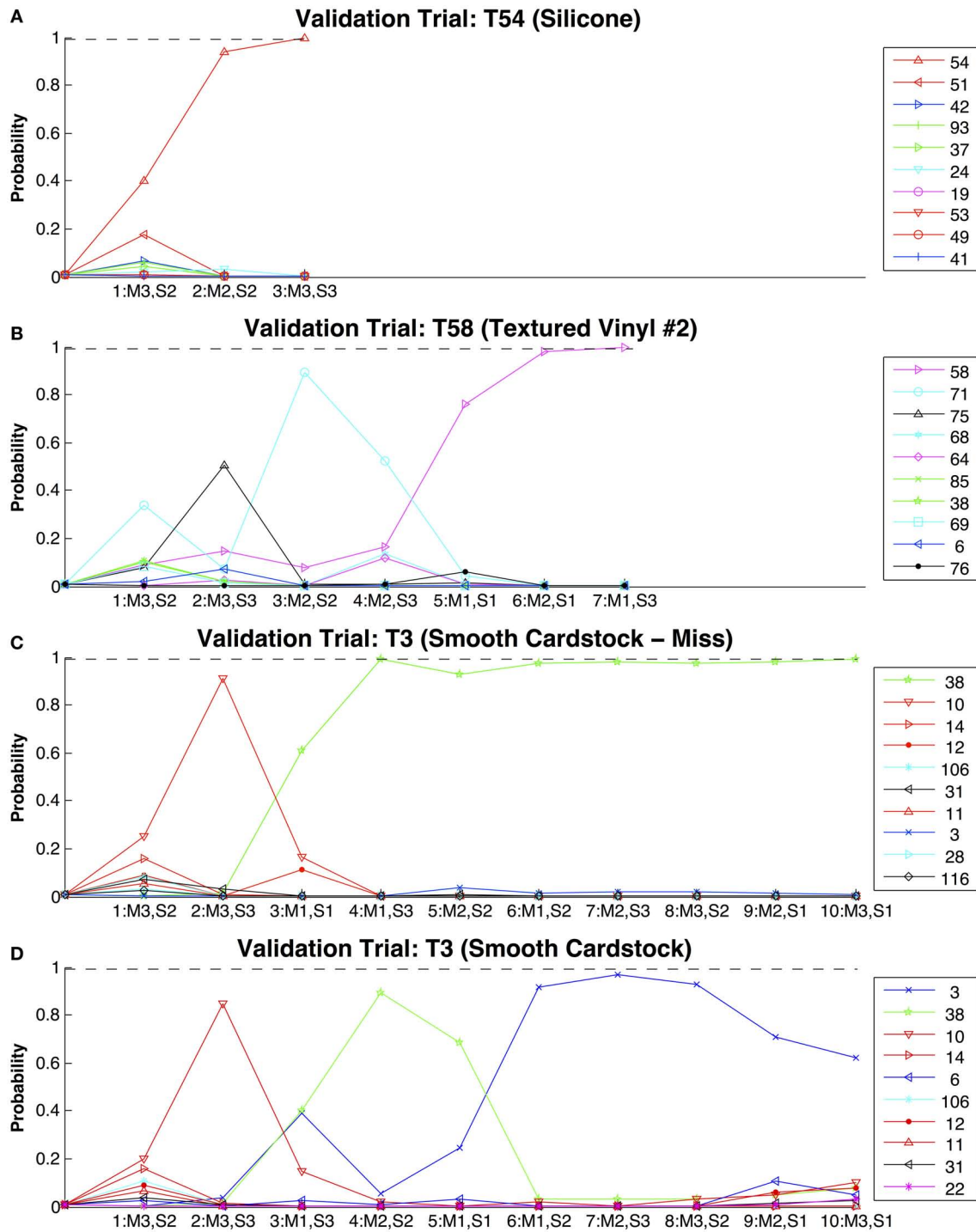


**FIGURE 10 | Evolution of estimated probabilities as virtual exploratory movements are made to identify textures from the entire training set of 117 textures.** In each of these plots the steps along the x-axis represent discrete exploratory movements, and the y-axis represents the estimated probabilities of likely texture candidates. The movement and signal taken at each step are indicated below the tick marks [Movements (M): 1 = 1.26 N, 1 cm/s; 2 = 0.5 N, 2.5 cm/s; 3 = 0.2 N, 6.31 cm/s. Signals (S): 1 = Traction, 2 = Roughness, 3 = Fineness]. The color-coded key for probability traces shows the numbers of the textures being classified in the validation trial.

Dashed line represents the 99% confidence required to end the simulation before all 10 movements are made. In (A) texture 54 (Silicone) was rapidly identified, as was the case for many of the simulations. In (B) texture 58 (Textured Vinyl #2) was eventually identified after a few initially more probable candidates were ruled out. In (C) texture three (smooth cardstock) is shown being misidentified as balsa wood (T38) and in (D) correctly identified, although with only 60% confidence at the end of the simulation. In both cases no texture reached a confidence of above 99% to stop the simulation so it ran for the complete 10 trials.

(Figure 9). The geometric mean (calculated by multiplying confusion probability matrices and taking the  $n$ th root of the result) for all of these movements and properties provides additional insight into which pairs of textures have the most confusion across all exploratory movements and properties. Results indicate that most textures are readily distinguishable with a few exceptions. When the confusion probability matrices are combined for only the optimal movements, there are considerably more off-diagonal dark spots representing textures that are likely to be confused. The identification algorithm chooses the combination of movement and signal type that will be most likely to discriminate among the most probable alternatives at any given point in the identification process.

Correlation between calculated texture properties were analyzed for all 117 textures for each movement and the average values for each movement are provided (Table 3).

An interesting finding was a strong negative correlation between roughness and traction. This can be observed in materials such as rubber and glass, which generally have smooth surfaces, yet produce a high amount of friction against the silicone skin of the BioTac. This contradicts (Smith et al., 2002a), who reported a strong positive correlation between friction and roughness for human fingertips, but did not include such a diverse set of materials.

#### TEXTURE DISCRIMINATION AND COMPARISON WITH HUMAN PERFORMANCE

Results of the performance for discriminating between two textures for both humans and our artificial algorithm are provided in Table 4. The performance of the classifier exceeded human performance for all pairs. The average performance of human subjects across all of the texture pairs was found to be 81.3% while the average performance of our classifier was found to be 99.6%. This result was quite unexpected, as human capabilities have previously been thought of as the “gold standard.” Our results in this study demonstrate that our artificial exploratory algorithm can surpass this capability even when the methods were designed to mimic the strategies that humans employ (but see Discussion).

#### ABSOLUTE TEXTURE CLASSIFICATION

The texture classification algorithm was validated by using it to identify the best match from the 117 textures in the database by selecting the most efficient sequence of exploratory movements from a novel set of data. Figure 10 shows a few examples of these simulations, which exhibit a wide range of sequences of exploratory movements and properties, depending on the actual texture being classified and those in the data set with which it might be most easily confused. In all cases the first movement is 0.2 N and 6.31 cm/s to determine texture roughness. This is due to all textures starting with equal probability (1 divided by 117). In this scenario, data from the training set has indicated that this first movement will produce the largest benefit. After information from this first movement is collected, each simulation went through a set of exploratory movements that was optimal for discriminating among the most likely candidates for the particular simulation.

This was found to be unique for each texture and even different between simulations of the same texture due to the random presentation of various trials from the validation dataset.

In this study we compared the Bayesian exploration algorithm with alternative algorithms such as cycling through the most useful movements for each signal and randomly selecting combinations of exploratory movements and signals to measure. A summary of performance for the 8000 Monte Carlo simulations of the 16 textures tested is provided (Table 5). Our Bayesian exploration algorithm was found to be superior in both classification accuracy and number of exploratory movements required to converge to 99% confidence. Furthermore the Bayesian exploration strategy was more likely to converge on the correct texture before reaching the maximum of 10 movements. Of the 16 textures explored for global classification among the set of 117 textures in these simulations, Bayesian exploration outperformed uninformed cycling and random selection for all but one of these textures.

## DISCUSSION

### SUMMARY OF FINDINGS

Previous investigations into the psychophysics of textures and their classification from sensory data have looked at a fairly narrow range of coarse textures and exploratory movements. This has resulted in simplistic classifiers based on one or two dimensions of the sensory information that tend to break down when extrapolated beyond their original data. Such circumscription makes study design more tractable but it may foreclose opportunities inherent in considering the larger problem. The large set of textures and large range of movements explored in this study forced us to develop systematic and scalable methods for dealing with a problem whose scale is more similar to that faced by the human nervous system. These methods extend conventional Bayesian decision making to encompass optimal strategies for acquiring the data for such optimal decision making, suggesting the term *Bayesian exploration*.

For this study we have found the method of Bayesian exploration to be far superior to other methods previously used for discriminating textures: de Boissieu et al. (2009) were able to demonstrate discrimination among 10 different textures with 62% performance classification; Giguere and Dudek (2011) were able to obtain a classification performance of 89.9–94.6% with 10 surfaces; Oddo et al. (2011) demonstrated a classification performance of 97.6% classification across three fine gratings; Jamali and Sammut (2011) demonstrated 95% classification across eight textures; Sinapov et al. (2011) demonstrated a classification performance of 95% across 20 different textures when using multiple exploratory movements. Bayesian exploration yielded a performance of 99.7% when choosing between two difficult textures, surpassing even human capabilities, and 95.4% when choosing from a database of 117 textures. Normally classification accuracy would be expected to decline as the number of possible textures increased.

A guiding principle throughout this study was biomimicry. We used a tactile sensor that shares many mechanical features with the human fingertip and we slid it over textured surfaces with exploratory movements similar to those that humans make when exploring textures. The exploratory movements and properties to

measure were also inspired by observations of human behavior and descriptive language humans use to describe textures. The Bayesian exploration algorithm intelligently selects the optimal exploratory movements to make based on current knowledge of what the texture may be and prior experience of which movement would best discriminate the likely possibilities, a method also inspired by theories of biological behavior (Loeb et al., 2011). Gratifyingly, we were able to obtain performance in discriminating texture that surpassed human capabilities for both accuracy and speed of classification.

The use of descriptive properties inspired by human language was probably important. The human brain is an outstanding classifier, so naturally one would expect it understands what makes textures different. Therefore, the language that humans use to describe textures are inherently low-hanging fruit for inspiring analytical measures of texture properties. In this study we implemented relatively simple algorithms for estimating these signal properties (motor current to estimate sliding force, vibration power to estimate roughness, vibration frequency to estimate coarseness). The performance of our classifier, even using this simplified set of inputs, far exceeded our expectations for such a large database of textures. This approach of language-guided signals may be useful for other artificial discrimination tasks.

There are, of course, substantial differences between our machine and a human hand or even other robotic systems. On the plus side, the human fingertip has a much richer set of sensors than the BioTac, which has a similar dynamic range but lacks the spatial resolution of the dynamic Meissner's receptors in the individual fingerprint ridges (Jones and Lederman, 2006). On the minus side, the movements of the human hand are subject to considerably more motor noise than our electrical motors (Jones et al., 2002; Jones and Lederman, 2006). Apparently these two differences tended to cancel each other in terms of overall performance. This may be a general property of the Bayesian strategy for selection of exploratory movements and interpretation of the resulting sensory data. Noise affecting either the movements or the sensory transduction is represented automatically in the database and biases the process away from choices that provide less useful information for any reason. Extending this algorithm to a complete robotic system working in unstructured environments is expected to degrade the quality of measured signals, which was enhanced by the careful design of a custom-built experimental apparatus. In particular, the actuators in humanoid robots are likely to be considerably noisier than our apparatus, introducing both variability into the exploratory movements and noise into the sensor signals. Additional training to better understand the characteristics of noise and variability is one way to compensate for this. We expect the Bayesian exploration method to be robust to this and evolve to make the most of available information.

#### CONSIDERATIONS FOR IMPROVING THE CLASSIFIER

The results presented in this study implement what is known in machine learning as supervised learning. A set of textures and their properties to measure were given to the classifier and it was told that the textures were unique and therefore belonged to separate classes. In the real world, the existence of discrete

entities must be inferred in the first place from the clustering of data points that may arise from the existence of multiple discrete entities, continuous gradations of material properties, or simply noise in the measurement system. Any novel sensory experience might be taken to be a distorted sampling of a previously known entity or a first example of a new entity. Such situations can be accommodated by extending the classification algorithm to continuously refine its experience for known textures as well as to identify when new textures are encountered and a new entity needs to be added to the database. One method to do this would be to calculate the Bhattacharya coefficient between the object currently being explored and the existing database of objects. If the newly observed data are not similar enough to known textures, a new class could be created. In addition to the distributions of the tactile data themselves, the classifier may be able to use other information such as the visual appearance (used by our subjects when first comparing the two similar textures in the discrimination task) or the probability that an entity could have changed or been replaced from one exploration to the next.

In our system, the internal representation of a texture's properties consists only of a mean value and a standard deviation for each property and each movement that can be made. After successfully identifying a texture, the system would benefit from adding these new data to its library so future encounters with the same texture will be identified more efficiently. Furthermore, as more explorations are made, the true probability density function could be identified, which may in fact deviate from the initially assumed normal distributions. This would serve to improve classifier performance. Adding these results to the system would also increase the amount of training data it has available, eventually enabling multivariate analysis as opposed to the univariate methods used in this study to avoid the curse of dimensionality (Jain et al., 2000). Updating the mean and standard deviation with the new data can accomplish this, but it is not trivial. If all observations are assumed to be equally valid regardless of when they occurred, then updating requires knowledge also of the previous number of experiences with that entity. If a new entity is created, it is possible, even likely, that a substantial number of the previous observations have been misclassified. Creating two new means and standard deviations from one previously learned distribution may not be feasible, in which case the algorithm will need to "forget" much of the old data and explore the two new entities intensively to create new internal representations.

Collecting data sufficient for multivariate analysis was impractical for the large number of textures employed in these experiments, but something like it may be feasible over the life of an organism or robotic system learning progressively about its world. We propose that a strategy of initially focusing only on salient properties for novice systems with little experience is preferable. As more experience is obtained, however, such systems could benefit from the efficiency of multivariate analysis.

#### CONSIDERATIONS FOR IDENTIFYING OBJECTS BY ALL AVAILABLE SENSORY MODALITIES

The strategies used in this study could be generally applied to a more diverse class of problems involving object identification.

As discussed in the introduction, texture discrimination is only a small subset of tools that humans employ when discriminating objects by touch, others include: compliance, thermal properties, shape, volume, and weight. The development of biologically inspired exploratory movements and signal measures for these properties would enhance the capabilities and performance of the system. Furthermore, these must be integrated with other exteroceptive modalities such as vision, sound, and smell. Iterative decisions must be made about other exploratory movements of the fingers, the eyes (e.g., saccadic gaze shifts), and other attentive mechanisms. Anthropomorphic robots provide both the need and the ability to implement biomimetic strategies for coping with such high dimensional data. In doing so, they may provide insights into those strategies that are difficult to obtain from studying biological systems alone.

## REFERENCES

- Bensmaïa, S., and Hollins, M. (2005). Pacinian representations of fine surface texture. *Percept. Psychophys.* 67, 842–854.
- Bergmann Tiest, W. M., and Kappers, A. M. L. (2006). Analysis of haptic perception of materials by multidimensional scaling and physical measurements of roughness and compressibility. *Acta Psychol. (Amst.)* 121, 1–20.
- Brisben, A. J., Hsiao, S. S., and Johnson, K. O. (1999). Detection of vibration transmitted through an object grasped in the hand. *J. Neurophysiol.* 81, 1548–1558.
- Dahiya, R. S., and Gori, M. (2010). Probing with and into fingerprints. *J. Neurophysiol.* 104, 1–3.
- Dahiya, R. S., Metta, G., Valle, M., and Sandini, G. (2010). Tactile sensing – from humans to humanoids. *IEEE Trans. Robot.* 26, 1–20.
- de Boissieu, F., Godin, C., Guilhamat, B., David, D., Serviere, C., and Baudois, D. (2009). “Tactile texture recognition with a 3-axial force MEMS integrated artificial finger,” in *Proceedings of Robotics: Science and Systems*, Seattle, 49–56.
- Edwards, J., Lawry, J., Rossiter, J., and Melhuish, C. (2008). Extracting textural features from tactile sensors. *Bioinspir. Biomim.* 3, 1–12.
- Fishel, J. A., and Loeb, G. E. (2012). “Sensing tactile microvibrations with the BioTac – comparison with human sensitivity,” in *IEEE/RAS-EMBS International Conference on Biomedical Robotics and Biomechanics*, Rome.
- Fishel, J. A., Santos, V. J., and Loeb, G. E. (2008). “A robust micro-vibration sensor for biomimetic fingertips,” in *IEEE/RAS-EMBS International Conference on Biomedical Robotics and Biomechanics*, Scottsdale, 659–663.
- Giguere, P., and Dudek, G. (2011). A simple tactile probe for surface identification by mobile robots. *IEEE Trans. Robot.* 27, 534–544.
- Hollins, M., Bensmaïa, S., and Washburn, S. (2001). Vibrotactile adaptation impairs discrimination of fine, but not coarse, textures. *Somatosens. Mot. Res.* 18, 253–262.
- Hollins, M., Faldowski, R., Rao, S., and Young, F. (1993). Perceptual dimensions of tactile surface texture: a multidimensional scaling analysis. *Percept. Psychophys.* 54, 697–705.
- Hollins, M., and Risner, S. R. (2000). Evidence for the duplex theory of tactile texture perception. *Percept. Psychophys.* 62, 695–705.
- Hosoda, K., Tada, Y., and Asada, M. (2006). Anthropomorphic robotic soft fingertip with randomly distributed receptors. *Robot. Auton. Syst.* 52, 104–109.
- Howe, R. D. (1994). Tactile sensing and control of robotic manipulation. *Adv. Robot.* 8, 245–261.
- Howe, R. D., and Cutkosky, M. R. (1989). “Sensing skin acceleration for slip and texture perception,” in *IEEE International Conference on Robotics and Automation*, Scottsdale, 145–150.
- Howe, R. D., and Cutkosky, M. R. (1993). Dynamic tactile sensing: perception of fine surface features with stress rate sensing. *IEEE Trans. Rob. Autom.* 9, 140–151.
- Jain, A. K., Duin, R. P. W., and Mao, J. (2000). Statistical pattern recognition: a review. *IEEE Trans. Pattern Anal. Mach. Intell.* 22, 4–37.
- Jamali, N., and Sammut, C. (2011). Majority voting: material classification by tactile sensing using surface texture. *IEEE Trans. Robot.* 27, 508–521.
- Johansson, R. S., Landström, U., and Lundström, R. (1982). Responses of mechanoreceptive afferent units in the glabrous skin of the human hand to sinusoidal skin displacements. *Brain Res.* 244, 17–25.
- Jones, K. E., Hamilton, A. F., and Wolpert, D. M. (2002). Sources of signal-dependent noise during isometric force production. *J. Neurophysiol.* 88, 1533–1544.
- Jones, L. A., and Lederman, S. J. (2006). *Human Hand Function*. New York: Oxford University Press.
- Katz, D. (1925). *The World of Touch*, trans. L. E. Krueger, 1989. Hillsdale, NJ: Lawrence Erlbaum.
- Knibestöl, M., and Vallbo, A. B. (1970). Single unit analysis of mechanoreceptor activity from the human glabrous skin. *Acta Physiol. Scand.* 80, 178–195.
- Lederman, S. J., and Klatzky, R. L. (1987). Hand movements: a window into haptic object recognition. *Cogn. Psychol.* 19, 342–368.
- Lederman, S. J., Loomis, J. M., and Williams, D. A. (1982). The role of vibration in the tactual perception of roughness. *Percept. Psychophys.* 32, 109–116.
- Lee, M. H., and Nicholls, H. R. (1999). Tactile sensing for mechatronics – a state of the art survey. *Mechatronics* 9, 1–31.
- Lin, C. H., Erickson, T. W., Fishel, J. A., Wettels, N., and Loeb, G. E. (2009). “Signal processing and fabrication of a biomimetic tactile sensor array with thermal, force and microvibration modalities,” in *IEEE International Conference on Robotics and Biomimetics*, Guilin, 129–134.
- Loeb, G. E., and Fishel, J. A. (2009). *The Role of Fingerprints in Vibrotactile Discrimination*. Whitepaper for DoD Physics of Biology, University of Southern California.
- Loeb, G. E., Tsianos, G. A., Fishel, J. A., Wettels, N., and Schaal, S. (2011). Understanding haptics by evolving mechatronic systems. *Prog. Brain Res.* 192, 129–144.
- Mountcastle, V. B., LaMotte, R. H., and Carli, G. (1972). Detection thresholds for stimuli in humans and monkeys: comparison with threshold events in mechanoreceptive afferent nerve fibers innervating the monkey hand. *J. Neurophysiol.* 35, 122–136.
- Mukaibo, Y., Shirado, H., Konyo, M., and Maeno, T. (2005). “Development of a texture sensor emulating the tissue structure and perceptual mechanism of human fingers,” in *IEEE International Conference on Robotics and Automation*, Barcelona, 2565–2570.
- Nicholls, H. R., and Lee, M. H. (1989). A survey of robot tactile sensing technology. *Int. J. Rob. Res.* 8, 3–30.
- Oddo, C. M., Beccai, L., Felder, M., Giovacchini, F., and Carrozza, M. C. (2009). Artificial roughness encoding with a bio-inspired MEMS-based tactile sensor array. *Sensors* 9, 3161–3183.
- Oddo, C. M., Controzzi, M., Beccai, L., Cipriani, C., and Carrozza, M. C. (2011). Roughness encoding for discrimination of surfaces in artificial active-touch. *IEEE Trans. Robot.* 27, 522–533.
- Rebguns, A., Ford, D., and Fasel, I. (2011). “InfoMax control for acoustic exploration of objects by a mobile robot,” in *AAAI Conference on Artificial Intelligence*, San Francisco, 22–28.

## ACKNOWLEDGMENTS

The authors would like to thank Raymond Peck for fabrication of the BioTac sensors and apparatus used in these tests and Michelle Willie and Lee Ann Lumilan for preparation of the texture samples. The authors would also like to thank the entire team at the Medical Device Development Facility at the University of Southern California and at SynTouch LLC, particularly Gary Lin, Matthew Borzage, Nicholas Wettels, David Groves, and Tomonori Yamamoto for their advice and assistance on this project. This research was supported by the Department of Defense Advanced Research Projects Agency contract D11PC20121.

## SUPPLEMENTARY MATERIAL

The Movies S1 and S2 for this article can be found online at <http://www.frontiersin.org/Neurorobotics/10.3389/fnbot.2012.00004/abstract>

- Romano, J. M., and Kuchenbecker, K. J. (2011). Creating realistic virtual textures from contact acceleration data. *IEEE Trans. Haptics*.
- Scheibert, J., Leurent, S., Prevost, A., and Debregeas, G. (2009). The role of fingerprints in the coding of tactile information probed with a biomimetic sensor. *Science* 323, 1503–1506.
- Sinapov, J., and Stoytchev, A. (2010). “The boosting effect of exploratory behaviors,” in *AAAI Conference on Artificial Intelligence*, Atlanta, 1613–1618.
- Sinapov, J., Sukhoy, V., Sahai, R., and Stoytchev, A. (2011). Vibrotactile recognition and categorization of surfaces by a humanoid robot. *IEEE Trans. Robot.* 27, 488–497.
- Smith, A. M., Chapman, C. E., Deslandes, M., Langlais, J., and Thibodeau, M. (2002a). Role of friction and tangential force variation in the subjective scaling of tactile roughness. *Exp. Brain Res.* 114, 211–223.
- Smith, A. M., Gosselin, G., and Houde, B. (2002b). Deployment of fingertip forces in tactile exploration. *Exp. Brain Res.* 147, 209–218.
- Su, Z., Fishel, J. A., Yamamoto, T., and Loeb, G. E. (2012). Use of tactile feedback to control exploratory movements to characterize object compliance. *Front. Neurobotics*.
- Tada, Y., Hosoda, K., and Asada, M. (2004). “Sensing ability of anthropomorphic fingertip with multi-modal sensors,” in *IEEE International Conference on Intelligent Robots and Systems*, Seattle, 1005–1012.
- Tada, Y., Hosoda, K., Yamasaki, Y., and Asada, M. (2003). “Sensing the texture of surfaces by anthropomorphic soft fingertips with multi-modal sensors,” in *IEEE International Conference on Intelligent Robots and Systems*, Las Vegas, 31–35.
- Wettels, N., and Loeb, G. E. (2011). “Haptic feature extraction from a biomimetic tactile sensor: force, contact location and curvature,” in *IEEE International Conference on Robotics and Biomimetics*, Phuket.
- Wettels, N., Santos, V. J., Johansson, R. S., and Loeb, G. E. (2008). Biomimetic tactile sensor array. *Adv. Robot.* 22, 829–849.
- Wiertelwski, M., Hudin, C., and Hayward, V. (2011). “On the 1/f noise and non-integer harmonic decay of the interaction of a finger sliding on flat and sinusoidal surfaces,” in *IEEE World Haptics Conference*, Istanbul, 25–30.
- Conflict of Interest Statement:** Both authors are equity partners in SynTouch, LLC, which manufactures and sells the BioTac sensors described in this article.

Received: 20 March 2012; paper pending published: 10 April 2012; accepted: 23 May 2012; published online: 18 June 2012.

Citation: Fishel JA and Loeb GE (2012) Bayesian exploration for intelligent identification of textures. *Front. Neurobot.* 6:4. doi: 10.3389/fnbot.2012.00004

Copyright © 2012 Fishel and Loeb. This is an open-access article distributed under the terms of the Creative Commons Attribution Non Commercial License, which permits non-commercial use, distribution, and reproduction in other forums, provided the original authors and source are credited.



# Learning tactile skills through curious exploration

Leo Pape<sup>1\*</sup>, Calogero M. Oddo<sup>2</sup>, Marco Controzzi<sup>2</sup>, Christian Cipriani<sup>2</sup>, Alexander Förster<sup>1</sup>, Maria C. Carrozza<sup>2</sup> and Jürgen Schmidhuber<sup>1</sup>

<sup>1</sup> Istituto Dalle Molle di Studi sull'Intelligenza Artificiale, Università della Svizzera Italiana, Lugano, Switzerland

<sup>2</sup> The BioRobotics Institute, Scuola Superiore Sant'Anna, Pisa, Italy

## Edited by:

Robyn Grant, University of Sheffield, UK

## Reviewed by:

Nathan F. Lepora, University of Sheffield, UK

Benjamin Kuipers, University of Michigan, USA

## \*Correspondence:

Leo Pape, Istituto Dalle Molle di Studi sull'Intelligenza Artificiale, Università della Svizzera Italiana, Lugano, Switzerland.  
e-mail: pape@idsia.ch

We present curiosity-driven, autonomous acquisition of tactile exploratory skills on a biomimetic robot finger equipped with an array of microelectromechanical touch sensors. Instead of building tailored algorithms for solving a specific tactile task, we employ a more general curiosity-driven reinforcement learning approach that autonomously learns a set of motor skills in absence of an explicit teacher signal. In this approach, the acquisition of skills is driven by the information content of the sensory input signals relative to a learner that aims at representing sensory inputs using fewer and fewer computational resources. We show that, from initially random exploration of its environment, the robotic system autonomously develops a small set of basic motor skills that lead to different kinds of tactile input. Next, the system learns how to exploit the learned motor skills to solve supervised texture classification tasks. Our approach demonstrates the feasibility of autonomous acquisition of tactile skills on physical robotic platforms through curiosity-driven reinforcement learning, overcomes typical difficulties of engineered solutions for active tactile exploration and underactuated control, and provides a basis for studying developmental learning through intrinsic motivation in robots.

**Keywords:** active learning, biomimetic robotics, curiosity, intrinsic motivation, reinforcement learning, skill learning, tactile sensing

## 1. INTRODUCTION

Complex robots typically require dedicated teams of control engineers that program the robot to execute specific tasks in restricted laboratory settings or other controlled environments. Slight changes in the task requirements or the robot's environment often require extensive re-programming, calibration, and testing to adjust the robot to the changed conditions. The implementation of these tasks could be sped up significantly if the robot autonomously develops and maintains some knowledge about its own capabilities and the structure of the environment in which it lives. Instead of placing the task of supplying the robot with such knowledge in the hands of the robot's creator, *curious* robots actively explore their own capabilities and the structure of their environment even *without an externally specified goal*. The structure found in the environment and its relation to the robot's own actions during curious exploration could be stored and used later to rapidly solve externally-specified tasks.

A formalization of the idea of curious exploratory behavior is found in the work of Schmidhuber (2010) and references therein. The theory of intrinsically-motivated learning developed in these works considers active machine *learning agents* that try to become more efficient in storing and predicting the observations that follow from their actions. A major realization of Schmidhuber (2010), is that curious behavior should not direct the agent toward just any unknown or unexplored part of its environment, but to those parts where it expects to *learn* additional patterns or regularities. To this end, the learning agent should keep track of its past learning *progress*, and find the relation between this progress and its own behavior. Learned behaviors

that lead to certain regular or predictable sensory outcomes, can be stored in the form of *skills*. Bootstrapping the skills learned in this fashion, the agent can discover novel parts of the environment, learn composite complex skills, and quickly find solutions to externally-specified tasks.

This work presents curiosity-driven, autonomous acquisition of tactile exploratory skills on a biomimetic robot finger equipped with an array of microelectromechanical touch sensors. We show that from active, curiosity-driven exploration of its environment, the robotic system autonomously develops a small set of basic motor skills that lead to different kinds of tactile input. Next, the system learns how to exploit the learned motor skills to solve supervised texture classification tasks. Our approach demonstrates the feasibility of autonomous acquisition of tactile skills on physical robotic platforms through curiosity-driven reinforcement learning, overcomes typical difficulties of engineered solutions for tactile exploration and underactuated control, and provides a basis for studying curiosity-driven developmental learning in robots.

Since both theory and practically-feasible algorithms for curiosity-driven machine learning have been developed only recently, few robotic applications of the curiosity-driven approach have been described in the literature thus far. Initial robotic implementations involving vision-based object-interaction tasks are presented in Kompella et al. (2011). A similar approach has been described by Gordon and Ahissar (2011) for a simulated whisking robot. Examples of alternative approaches to curiosity-driven learning on simple robots or simulators can be found in the work of Oudeyer et al. (2007); Vigorito and Barto (2010);

Konidaris et al. (2011); Mugan and Kuipers (2012). None of these works consider curiosity-driven development of tactile skills from active tactile exploration.

The rest of this work is organized as follows: section 2 presents the curiosity-driven learning algorithm and the tactile robotic platform used in the experiments. Section 3.1 illustrates the operation of the curiosity-driven reinforcement learning algorithm on a simple toy-problem. The machine learning approach for tactile skill learning presented here has not been published before, and will be described and compared to other approaches where relevant for tactile skill learning. Section 3.2 then shows the learning of basic tactile skills on the robotic platform and how these can be exploited in an externally-specified surface classification task. Section 4 discusses the results and the relevance of active learning in active tactile sensing.

## 2. MATERIALS AND METHODS

### 2.1. CURIOSITY-DRIVEN MODULAR REINFORCEMENT LEARNING

#### 2.1.1. Skill learning

The learning of tactile skills is done here within the framework of reinforcement learning (e.g., Kaelbling et al., 1996). A reinforcement learner (RL) addresses the problem which *actions* to take in which *states* in order to maximize its cumulative expected *reward*. The RL is not explicitly taught which actions to take, as in supervised machine learning, but must instead explore the environment to discover which actions yield the most cumulative reward. This might involve taking actions that yield less immediate reward than other actions, but lead to higher reward in the long-term. When using RLs for robot control, states are typically abstract representations of the robot's sensory inputs, actions drive the robot's actuators, and the rewards represent the desirability of the robot's behavior in particular situations. Learning different skills here is done with a *modular* reinforcement learning architecture in which each module has its own reward mechanism, and when executed, produces its own behavior.

Most modular reinforcement learning approaches address the question how to split up a particular learning task into subtasks each of which can be learned more easily by a separate module. In the curiosity-driven learning framework presented here, there is no externally-specified task that needs to be solved or divided. Instead, the modules should learn different behaviors based on the structure they discover in the agent's sensory inputs. This is done by reinforcement learning modules that learn behaviors that lead to particular kinds of sensory inputs or events, and then terminate. The different *kinds* of sensory events are distinguished by another module, which we here call an abstractor. An abstractor can be any learning algorithm that learns to represent the structure underlying its inputs into a few relevant components. This could for example be an adaptive clustering method, an autoencoder (e.g., Bourlard and Kamp, 1988), qualitative state representation (Mugan and Kuipers, 2012) or (including the time domain) a slow-feature analysis (Kompella et al., 2011). Each component of the abstractor is coupled to a RL module that tries to generate *stable* behaviors that lead to sensory inputs with the coupled abstractor state, and then terminates. The resulting modules learn the relation between the part of their sensory inputs that can be directly affected through their own actions, and the

abstract structure of their sensory inputs. In other words, the system learns different *skills* that specify *what* sensory events can occur, and *how* to achieve those events. As the behaviors learned by these modules depend on the ability of the system to extract the structure in its sensory input, and not on some externally-provided feedback, we call these modules intrinsically-rewarded skills (inSkills).

Apart from inSkills, we also use externally-rewarded skills (exSkills) that are learned through external reward from the environment, and a small number of other modules whose operation will be detailed below. Modules can take two kinds of actions (1) execute a *primitive* that translates directly into an actuator command and (2) execute another module. When the executed module collects sensory inputs with its corresponding abstractor state, it terminates and returns control to the calling module. The possibility of executing another module as part of a skill allows for cumulative learning of more complex, composite skills. In the initial learning stages, there is not much benefit in selecting another module as an action, as most modules have not yet developed behaviors that reliably lead to different sensory events. However, once the modules become specialized, they may become part of the policy of another module. To prevent modules from calling themselves directly, or indirectly via another module, the RL controller keeps track of the selected modules on a calling stack, and removes the currently executing module and its caller modules from the available action set. In this fashion, only modules that are not already on the calling stack can be selected for execution.

It is not uncommon for modular architectures to instantiate additional modules during the learning process. This comes at a disadvantage of specifying and tuning *ad-hoc* criteria for module addition and pruning. Instead, we use a learning system with a fixed number of modules, which has to figure out how to assign those modules to the task at hand. Although this system is by definition limited (but so is any physical system), flexibility, and cumulative learning are achieved through the hierarchical combination of modules; once the system acquires a new skill, it could use that skill as part of another skill to perform more complex behaviors.

During curious exploration of its environment, the learning agent is driven by a module that tries to improve the reliability of the inSkill behaviors. The idea of using the learning progress of the agent as reward is closely following the work of Schmidhuber (2010). However, the focus here is not so much on the ability of the abstractor predict or compress any observations, but on finding stable divisions of sensory inputs produced by the agent's behavior into a few components. The intrinsic reward is not just the learning progress of the abstractor, but also includes the improvement in the RL's ability to produce the different sensory events distinguished by the abstractor. In essence, the role of learning progress is taken over here by stability progress, which involves the distribution of the agent's limited computational and physical resources such that the most relevant (relative to the system's learning capabilities) sensory events can be reliably produced. This strong relation between distinct sensor abstractions and the ability to learn behaviors that lead to those abstractions has also been argued for by Mugan and Kuipers (2012).

### 2.1.2. Adaptive model-based reinforcement learning

Although the abstractors and RLs could in principle be instantiated with a range of different machine learning methods, in practice, especially in robotic practice, few algorithms can be successfully used. The main challenges for curiosity-driven learning on actual hardware are: (1) the algorithms have to learn from much smaller amounts of samples (in the order of  $10^2$ – $10^3$ ) than are typically assumed to be available in the machine learning literature (often more than  $10^4$  to solve even the simplest tasks); (2) typical machine learning approaches assume that training samples are generated from a stationary distribution, while the whole purpose of curiosity-driven learning is to make novel parts of the environment and action space available to the robot *during* and *as a result of* learning; (3) typical reinforcement learning algorithms assume a stationary distribution of the reward, while the intrinsic reward signal in curiosity-driven learning actually decreases as a result of learning the behavior that leads to this reward. None of these challenges is considered solved in the area of practical machine learning; mathematically optimal universal ways of solving them (Schmidhuber, 2006) are not practical. In the present work, we employ various machine learning techniques that have been proposed before in the literature, and introduce some new approaches we are not aware of having been described before. The main criterion for choosing the techniques described below was not their theoretical elegance, efficiency, or even optimality, but their robustness to the challenges addressed above.

To learn effectively from the small amount of samples that can be collected from the robotic platform, the learning system trains a Markov model from the collected data, and generates training data for the reinforcement learning algorithm from this model. A Markov model represents the possible states  $\mathcal{S}$  of its environment as a set of numbers  $s \in \mathcal{S}$ . In each state, a number of actions  $a \in \mathcal{A}$  are available that lead to (other) states  $s' \in \mathcal{S}$  with probability  $p(s'|s, a)$ . While a primitive action takes one timestep, skills taking several timesteps might also be selected as actions. The model therefore also stores the duration  $d(s, a, s')$  of an action in terms of the number of primitive actions.

The Markov model is further augmented to facilitate learning during the dynamic expansion of the agent's skills and exploration of the environment. For each module  $\mathcal{M}_j$  and each transition  $(s, a, s')$ , the model keeps track of: (1) the short-term reward  $r_j(s, a, s')$  provided by the module's reward system; (2) the probability  $z_j(s, a, s')$  of terminating the module's policy; (3) the long-term reward  $q_j(s, a, s')$  that changes on a slower timescale than the short-term reward. Instead of accumulating the Markov model's learned values over the whole learning history, all model values are updated with a rule that gives more weight to recently-observed values and slowly forgets observations that happened a long time ago:

$$m(s, a, s') \leftarrow (1 - w_*)m(s, a, s') + w_*v(s, a, s'), \quad (1)$$

with model values  $m = \{d, q, r, z\}$ , update weights  $w_* = \{w_d, w_q, w_r, w_z\}$ , and observed values  $v = \{d, q, r, z\}$ . The short-term rewards, termination probabilities, and transition durations are updated according to Equation 1 for every observation, while

the long-term reward is updated for all  $q(s, a, s')$  after processing of a number of samples equal to the reinforcement learning episode length. Transition probabilities are updated by adding a small constant  $w_p$  to  $p(s'|s, a)$ , and then rescaled such that  $\sum_{s' \in \mathcal{S}} p(s'|s, a) = 1$ . As the model values adjust to the changing skills, previously learned transitions become less likely. For efficiency reasons we prune model values  $d, p, r, z$  for which the transition probabilities have become very small ( $p(s'|s, a) < w_o$ ) after each model update. Together, these update rules ensure that the agent keeps adapting to newly acquired skills and changing dynamics of its expanding environment. Increasing (decreasing) the model parameters  $\{w_d, w_o, w_q, w_r, w_z\}$  leads to the development of more flexible (more stable) behaviors.

The values stored in the Markov model for each module are used by reinforcement learners to learn policies that maximize the cumulative module rewards. The RLs keep track of how much each state-action pair  $(s, a)$  contributes to the cumulative reward  $r$  when following the current action-selection policy. In reinforcement learning these state-action values are known as a  $Q$ -values:

$$Q(s, a) = \sum_{t=0}^{\infty} \gamma^t r(t), \quad (2)$$

where  $\gamma$  is a discount factor that weights the importance of immediate versus future rewards, and  $t$  is time. The RL selects actions  $a$  in state  $s$  according its current policy  $\pi(s)$ :

$$\pi(s) = \operatorname{argmax}_{a \in \mathcal{A}} Q^\pi(s, a). \quad (3)$$

An efficient algorithm for learning those  $Q$ -values is least-squares policy iteration (LSPI; Lagoudakis and Parr (2003)). LSPI represents the estimated  $Q$ -values as an  $\omega$ -weighted linear combination of  $\kappa$  features of state-action pairs  $\phi(s, a)$ :

$$\hat{Q}(s, a) = \sum_{j=1}^{\kappa} \phi_j(s, a) \omega_j, \quad (4)$$

where  $\omega_j$  are the parameters learned by the algorithm. The feature function  $\phi(s, a)$  used here represents state-action pairs as binary feature vectors of length  $\kappa = |\mathcal{S}| |\mathcal{A}|$ , with a 1 at the index of the corresponding state-action pair, and a 0 at all other indices. LSPI sweeps through a set of  $n$  samples  $D = \{(s_i, a_i, s'_i, r_i, p(s'_i | s_i, a_i)) \mid i = 1, \dots, n\}$  generated from the model, and updates its estimates of parameter vector  $\omega$  as:

$$\omega = A^{-1}b \quad (5)$$

$$A = \sum_{i=1}^n \left[ \phi(s_i, a_i) \left( \phi(s_i, a_i) - \sum_{s' \in \mathcal{D}} \gamma p(s' | s_i, a_i) \phi(s', \pi(s')) \right)^T \right] \quad (6)$$

$$b = \sum_{i=1}^n [\phi(s_i, a_i) r_i]. \quad (7)$$

Because actions with different durations are possible in our implementation, we slightly alter Equations 6 and 7 to take into

account the duration  $d_i$  of a transition, both in the discount factor  $\gamma$  and the module reward  $r_i$ :

$$A = \sum_{i=1}^n \left[ \phi(s_i, a_i) \left( \phi(s_i, a_i) - \sum_{s' \in D} \gamma^{d_i} p(s' | s_i, a_i) \phi(s', \pi(s')) \right) \right]^T \quad (8)$$

$$b = \sum_{i=1}^n \left[ \phi(s_i, a_i) \gamma^{d_i-1} r_i \right]. \quad (9)$$

### 2.1.3. Skill types

The curiosity-driven learning agent uses four different types of reinforcement learning modules:

An **explorer** module is a naive curiosity module that tries to find novel observations around previous novel observations, but does not exploit any further structure of the environment. The reward mechanism of an explorer uses the Markov model to keep track of the number of times a certain state was visited, and rewards transitions  $(s, a, s')$  inverse-proportionally to the number of times  $s'$  was visited:  $r_j(s, a, s') = e^{-c(\cdot, \cdot, s')}$ , where  $e$  is the natural logarithm base, and  $c(\cdot, \cdot, s')$  the number of times a transition led to  $s'$ . This leads to a policy that drives the agent toward yet unexplored parts of the environment, thus speeding up initial exploration.

**InSkill** modules exploit regularities in the environment to learn behaviors that lead to particular kinds of sensory events. Sensory inputs are grouped in an unsupervised manner by the abstractor into separate abstractor states  $y_j$ . The behavior that leads to each abstractor state  $y_j$  is learned by an individual reinforcement learning module  $\mathcal{M}_j$ . The reward mechanism of these RLs reflects the reliability with which a transition leads to a particular abstractor state. A reward of 1 is given when transition  $(s, a, s')$  leads to  $y_j$ , and a reward of 0 otherwise. In combination with the update rule in Equation 1, this yields high model reward values  $r_j(s, a, s')$  for transitions that reliably lead to the corresponding abstractor state  $y_j$ , and low model reward values otherwise. An inSkill terminates when a transition produces its coupled abstractor state. When a module terminates because of other reasons (e.g., reaching the maximum number of allowed timesteps), a failure reward  $-w_f$  (i.e., penalty) is added to  $r_j(s, a, \cdot)$ . The reason this penalty is given to all  $s' \in S$ , is that it is unknown to which state the transition would have led if the module had terminated successfully.

Note that no direct feedback exists between the ability of the abstractor to separate sensory events, and the ability of the RLs to learn behaviors that leads to those events (as is done in some RL approaches). However, there is a behavioral feedback in the sense that the total learning system favors behaviors that lead to those sensory events that can *reliably* be distinguished by the abstractor.

The skill **progressor** drives the overall behavior of the agent when running in curious exploration mode. The progressor executes those skills that are (re)adapting their expertise. Both increase and decrease in the long-term reward collected by

a skill implies it is adjusting to a more stable policy, so the progressor is rewarded for the absolute *change* in long-term reward of the inSkills:

$$r_i(\cdot, a_i, \cdot) = \sum_{(s, a, s') \in (S \times \mathcal{A} \times S)} \text{abs}(p(s' | s, a) \Delta q_i(s, a, s')). \quad (10)$$

and uses a fixed reward  $r_x$  for explorer modules.

An **exSkill** module learns to maximize externally-provided reward. Just as the other skills, exSkills can choose to execute other skills, thus exploiting skills that have been learned through the intrinsic reward system. Reward is given for reaching a designer-specified goal, which then also terminates the module.

Apart from the termination condition mentioned in the above description, all modules also terminate after a fixed maximum number of actions  $\tau_z$ .

All RL modules simultaneously learn from all samples (off-policy). However, modules that execute other modules as part of their own policy, learn about the actual behavior (on-policy) of the executed modules. While off-policy learning facilitates rapid learning of all modules in parallel, it also changes a module's behavior without its explicit execution, leading to potentially incorrect policies in modules that select the changed modules as part of their own policy. This issue is resolved as a side-effect of using a progressor, which is rewarded for, and executes the changing modules, leading to additional sampling of the changed modules until they stabilize.

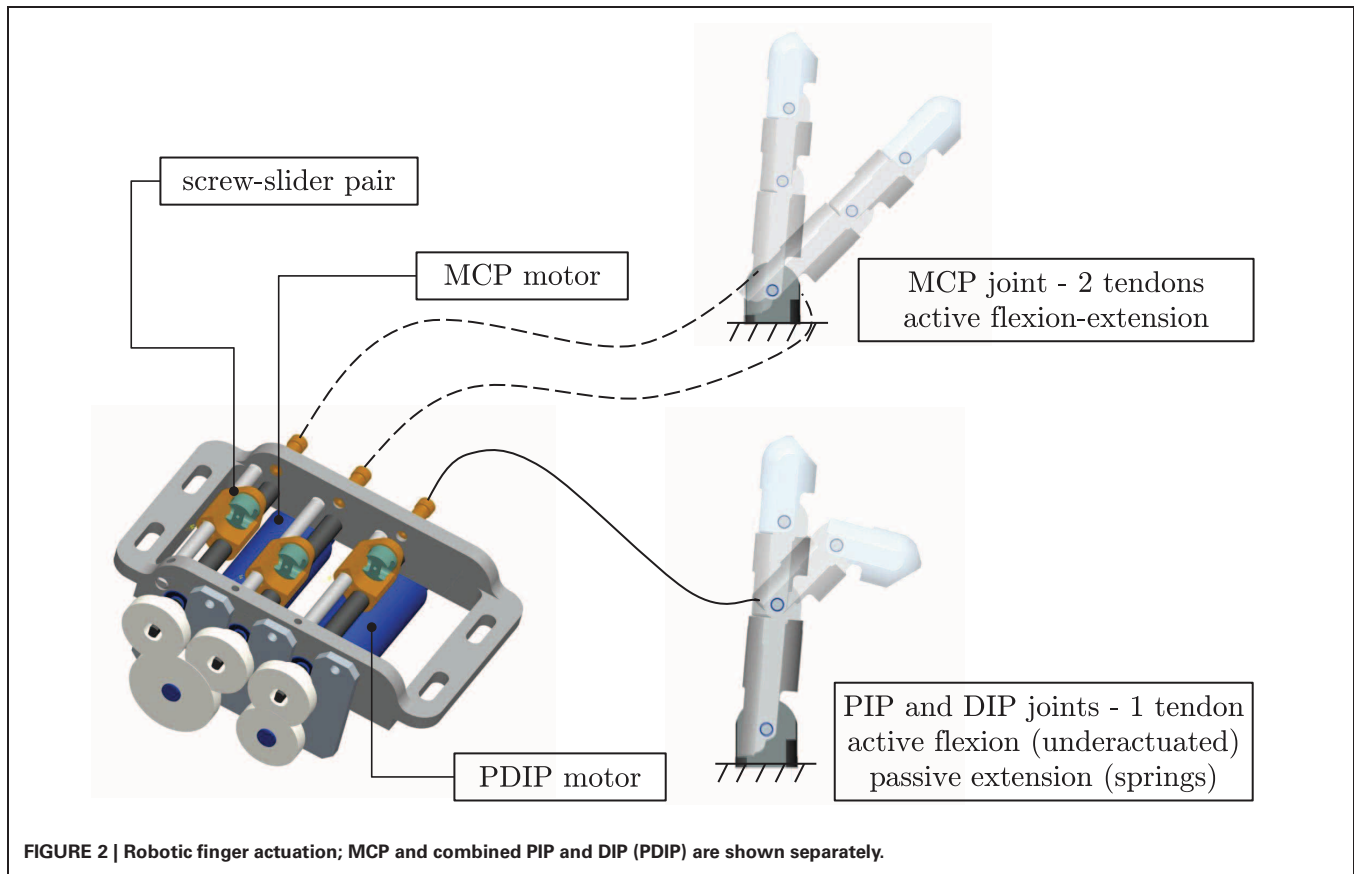
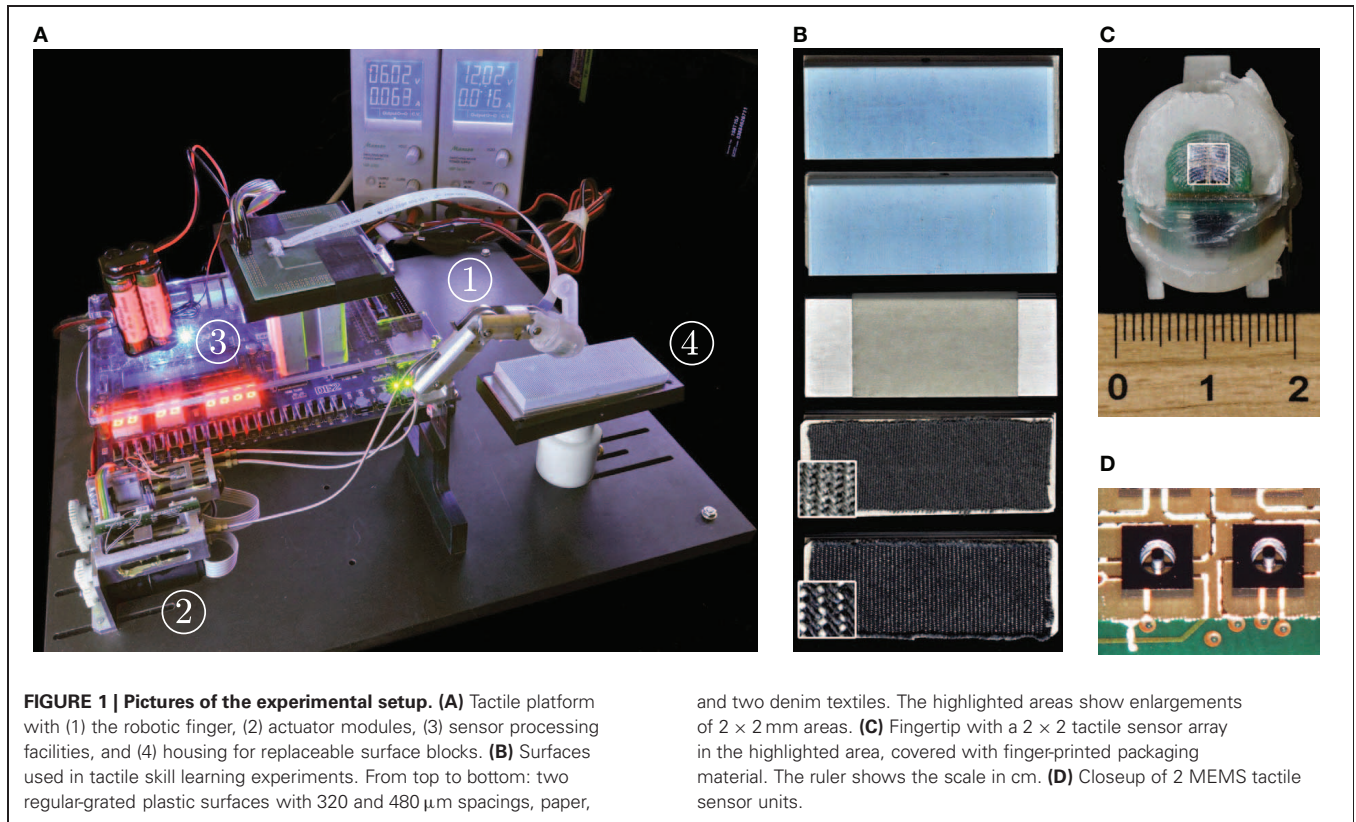
Apart from the exploration done by the explorer module, a fixed amount of exploration is performed in each module by selecting an untried action from the available action set with probability  $\epsilon$  instead of the action with the maximum Q-value. In case no untried actions are available for exploration, an action is selected with uniform probability from the available action set. Such a policy is called  $\epsilon$ -greedy.

## 2.2. ROBOTIC PLATFORM FOR TACTILE SKILL LEARNING

We use the curiosity-driven machine learning framework to investigate curiosity-driven learning of tactile skills on a robotic platform specifically designed for active tactile exploration. The platform (**Figure 1A**) consists of a robotic finger with a tactile sensor in its fingertip, actuation and processing units, and a housing for replaceable blocks with different surfaces. The details of each of those components are given in the remainder of this section.

### 2.2.1. Biomimetic robotic finger

The human-sized (Buchholz et al., 1992) biomimetic robotic finger used in the active learning experiments is composed of three phalanges and three flexion joints: a metacarpophalangeal (MCP) joint, a proximal interphalangeal (PIP) joint, and a distal interphalangeal (DIP) joint (see **Figure 2**). Unlike the natural finger, no abduction of the MCP joint is possible, since the task under investigation (i.e., an exploratory trajectory) requires the fingertip to move in two dimensions only. Like the natural finger, the robotic finger is driven by



tendons and underactuated; the three joints are actuated by just two motors. Underactuation reduces design complexity and allows self-adaptation and anthropomorphic movements similar to human exploratory tasks.

The finger is driven by two direct-current (DC) motors (model 1727, Faulhaber Minimotor; gear head ratio 14:1). One motor actively actuates the flexion and extension of the MCP joint by means of two lead screw pairs with opposite screw handedness (agonist-antagonist action, **Figure 2**). The second motor actuates the flexion of the PIP and DIP underactuated pair (PDIP hereafter) by pulling the tendon. Extension of the PDIP joints during tendon release is achieved passively through torsional springs housed inside the joints. The DC-motors are integrated with optical encoders that monitor the released tendon-length, enabling position control in motor space. Additionally, tension sensors are integrated in the tendons. Each motor is controlled by a low-level motion controller implementing position, tendon tension, torque (motor current) control, and monitoring. The low-level motion controllers are directly controllable by a host PC through a RS232 serial communication bus.

Due to the underactuated architecture and absence of joint-angle sensors, the kinematics of the finger are not unique and can only be solved by considering the dynamics of the robot and its interaction with the environment. Control and monitoring in motor space does not allow for unique control and monitoring in fingertip space, unless the full dynamic model of the finger and its interaction with the touched surface is computed. This makes it difficult to control the finger by means of conventional control strategies (Arai and Tachi, 1991).

### 2.2.2. Fingertip with MEMS tactile sensor array

The tip of the robotic finger holds a  $2 \times 2$  array of 3D microelectromechanical system (MEMS) tactile sensors (see also Oddo et al., 2011b) created with silicon microstructuring technologies. Each  $1.4 \text{ mm}^3$  sensor consists of four piezoresistors implanted at the roots of a cross-shaped structure measuring the displacement of the elevated pin (**Figure 1D**). The MEMS sensors are placed on a rigid-flex printed circuit board lodged in the fingertip (see **Figure 1C**). The resulting array has a density of  $72 \text{ units/cm}^2$  (i.e.,  $16 \text{ channels}/22.3 \text{ mm}^2$ ), similar to the  $70 \text{ units/cm}^2$  of human Merkel mechanoreceptors (Johansson and Vallbo, 1979).

The piezoresistor output signals are directly (without preamplification) acquired at a frequency of 380 Hz by a 16-channel 24-bit analog-to-digital converter (ADS1258, Texas Instruments) lodged in the distal phalanx. The digital signals acquired from the sensor array via the analog-to-digital converter are encoded as ethernet packets by C/C++ software routines running on a soft-core processor (Nios II, Altera) instantiated onboard a FPGA (Cyclone II, Altera), and broadcasted over an ethernet connection.

The outer packaging layer of the fingertip (**Figure 1C**) is made of synthetic compliant material (DragonSkin, Smooth-On) and has a surface with fingerprints mimicking the human fingerpad (i.e.,  $400 \mu\text{m}$  between-ridge distance; fingerprint curvature radius of  $4.8 \text{ mm}$  in the center of the sensor array; artificial epidermal ridge-height of  $170 \mu\text{m}$ ; total packaging thickness of  $770 \mu\text{m}$ ; Oddo et al., 2011a).

### 2.2.3. Platform

The robotic finger, control modules, and processing hardware are mounted on a platform together with a housing for replaceable surface samples (see **Figure 1A**). Five different surfaces are used in the tactile skill learning experiments (see **Figure 1B**): two regular-grated plastic blocks with grating-spacings of  $320$  and  $480 \mu\text{m}$  (labeled 'grating 320' and 'grating 480', respectively), a paper surface (labeled 'paper'), and two different denim textiles (labeled 'fine textile' and 'coarse textile').

The robotic finger and MEMS sensor are handled by separate control and readout modules. To achieve synchronization between finger movements and tactile sensory readouts, we implemented a real-time, combined sensory-motor driver in Java and .NET, which can be easily interfaced from other programming languages.

## 3. RESULTS

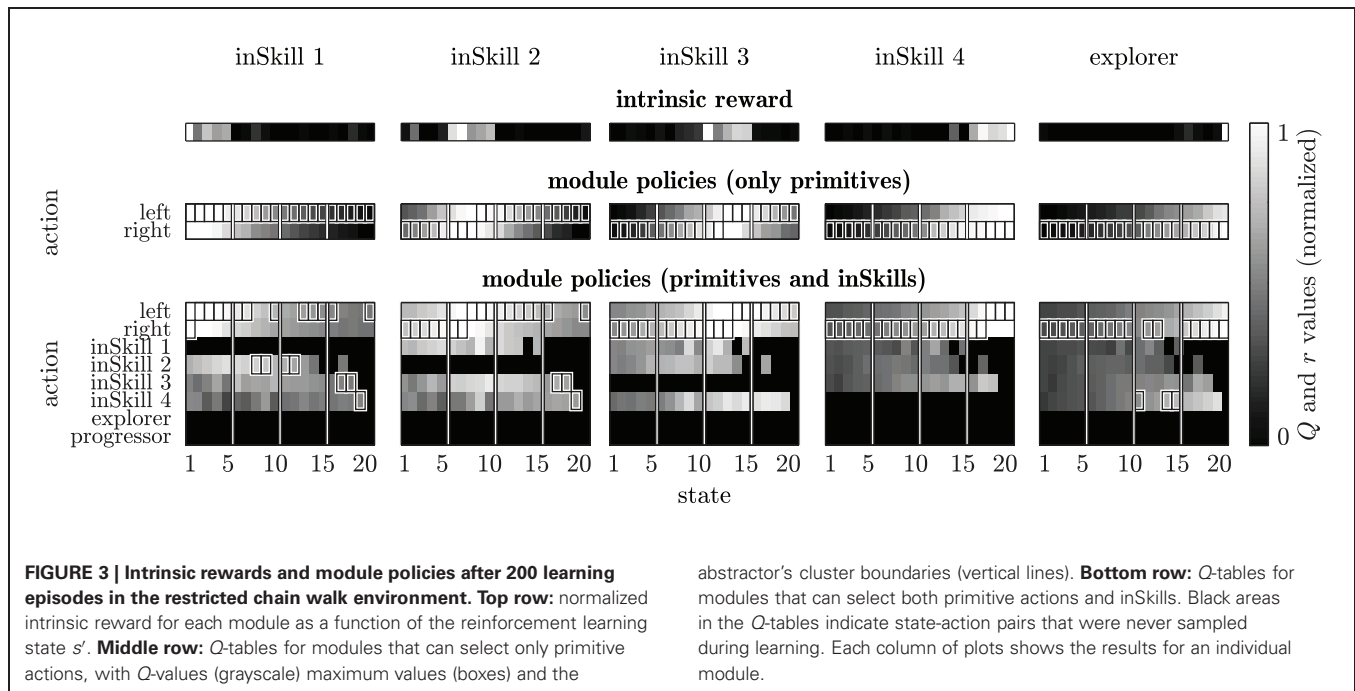
### 3.1. EXAMPLE: RESTRICTED CHAIN WALK

#### 3.1.1. Setup

We illustrate the relevant aspects of the curiosity-driven learning algorithm with a chain walk problem, an often-used toy-problem in reinforcement learning (e.g., Sutton and Barto, 1998). In the chain walk problem considered here, the learning agent is placed in a simulated environment in which it can move left or right between 20 adjacent states. Going left (right) at the left (right) end of the chain leaves the agent in the same state. The structure of the environment is rather obvious when presented in the manner of **Figure 3**; however, note that the agent does not know beforehand which actions lead to which states. Instead, it has to *learn* the effects of its actions by trying the actions one at a time.

Learning is done over a number of episodes in which the agent always starts in state 1 (left of each column in **Figure 3**), and interacts with the environment for a maximum of 25 timesteps. Limiting the chain walk task in this fashion forces the learning agent to address the three machine learning challenges discussed in section 2.1.2: (1) the agent can collect only a limited number of samples before it is sent back to state 1; (2) states cannot be equally sampled, as the agent needs to pass through states closer to state 1 to reach more distant states; (3) larger parts of the input space become available to both the RL and the abstractor as a result of learning, requiring the adjustment of the modules to the increasing input space.

In externally-rewarded chain walk tasks, reaching a particular state or states usually yields a reward. Here, however, we let the agent first explore the chain walk environment without providing any external reward. During this curiosity-driven exploration phase, the sensory input to both the RL and the abstractor is the current state. The abstractor divides the states seen thus far into a number of regions, and the RL modules have to learn policies for reaching each of those regions. In curious-exploration mode the agent thus learns skills for reaching different parts of the environment. These skills can later be used in externally-rewarded tasks where the agent is rewarded for reaching particular states. Instead of retrying all primitive actions starting from state 1 each episode, the agent can then use the learned skills to quickly reach different regions in the environment.



In real-world experiments many processes are going on that affect the learning agent to a certain extent, but cannot all be explicitly represented. The effect of these processes is often referred to as noise. To test the robustness of the learning agent against such noise, we incorporate some random processes in both the environment and the abstractor. To simulate noise in the environment, there is a 10% chance that a primitive action has the reverse effect (going right instead of left, and v.v.), and an additional 10% chance that a primitive has no effect at all (the agent stays in the same state). Abstractor noise is introduced by feeding a randomly selected state (instead of the current state) as input to the abstractor with a 10% chance every timestep.

The abstractor used for skill learning is a simple clustering algorithm that equally divides the states seen thus far into  $k$  parts  $y_1, \dots, y_k$ . The  $k$  corresponding inSkill modules  $\mathcal{M}_1, \dots, \mathcal{M}_k$  learn policies for reaching each of those parts. Rapid exploration of the environment is facilitated by an explorer module. The overall behavior of the agent is driven by a progressor module, which receives reward for the long-term inSkill change and a reward of  $r_x = 0.1$  for selecting the explorer module. In this fashion, the progressor switches to the explorer module once the stability progress of the inSkills becomes smaller than 0.1. Each episode starts with the execution of the progressor in state 1. The progressor selects to execute a module, which runs until it terminates by itself, or for a maximum of  $\tau_z$  steps in the environment. This is repeated until  $\tau_e$  environment steps (episode length) are executed. At the end of an episode, the samples collected during that episode are used to update the Markov model and the abstractor. Next, the new reinforcement learning policies are generated for each module from the model. A list of all parameter values used for this experiment is given in **Table 1**.

### 3.1.2. Skill learning

**Figure 4** shows an example of the intrinsic reward, the fastest learning modules, and the changing cluster boundaries of the abstractor during curious exploration with four inSkills. As becomes clear from this figure, the agent starts by learning policies for reaching the first few abstractor states (episodes 1–10, until marker (a)). Once it reaches state 15 at marker (a), the agent spends several episodes (11–30, marker (a)–(b)) adjusting modules 3 and 4, which are the modules that take the agent to the rightmost part of the known environment. At episode 30 (marker (b)), the inSkill modules have stabilized (i.e., all inSkills' intrinsic rewards  $< 0.1$ ), and the agent executes the exploration module. Using the learned skills for further exploration of the environment, the exploration module quickly manages to reach state 17 (episode 31, marker (b)). The abstractor adjusts its cluster distribution to the new observations, and the inSkills have to change their policies for reaching those clusters accordingly. This process is repeated at episode 57 (marker (c)), where the exploration policy is selected, and promptly takes the agent to the rightmost state (state 20). Due to the change in the abstractor's distribution, the inSkills change their policies again until their learning progress becomes less than 0.1 (episode 75, marker (d)), and the exploring module takes over. This switching between learning stable behaviors, and exploiting the stabilized behaviors to explore all transitions in the environment goes on until the environment is fully explored. After that, the agent continues to explore while the inSkills remain stable, indicating that the limit of the agent's learning capabilities in the environment is reached.

An example of the final RL policies for the four-inSkill chain walk task is plotted in **Figure 3**. The top row of this figure shows an equal distribution of the inSkill reward regions over the state space. The second row with the module's policies in

**Table 1 | Experimental parameters and their values.**

Symbol	Description	Chain walk	Tactile platform
$\mathcal{S}$	state set	$\{1, \dots, 20\}$	$\{1, \dots, 36\}$ , see <b>Figure 8</b>
$\mathcal{A}$	action set	{left, right}	see <b>Figure 8</b>
$k$	number of clusters/inSkill modules	{4, 7, 10}	5
$\epsilon$	reinforcement learning exploration rate	0.1	0.1
$\gamma$	reinforcement learning discount	0.95	0.95
$\kappa$	LSPI feature vector length	20	36
$r_x$	fixed exploration reward	0.1	0.2
$\tau_e$	episode length	25	25
$\tau_z$	maximum module timesteps	25	20
<i>Markov model update weights</i>			
$w_d$	duration update weight	0.2	0.2
$w_f$	action failure penalty	0.1	0
$w_o$	pruning threshold	0.01	0.01
$w_p$	transition probability update weight	0.33	0.33
$w_q$	long-term reward update weight	0.2	0.2
$w_r$	short-term reward update weight	0.2	0.2
$w_z$	termination probability update weight	0.2	0.2

case only primitive actions are allowed, makes clear that the inSkills correctly learn to go left (right) when they are to the right (left) of the reward regions. The bottom row of **Figure 3** shows the module's policies in case both primitives and inSkills could be selected as actions. Note that an inSkill cannot execute itself, the explorer or the progressor as part of its policy, as indicated by the absence of  $Q$ -values in **Figure 3**. During initial exploration, the selection of other modules happens quite often, because the transition probabilities of primitive actions are not yet sampled reliably. Once the transition probabilities are estimated more accurately during subsequent exploration, primitive actions become preferred over executing other modules, because the on-policy  $\epsilon$ -greedy behavior of the executed modules is less efficient than the optimal policy. After the whole environment is explored, some modules still select other inSkills in certain states. For example, inSkill 1 selects inSkill 2 for going left in states 8–9 and 11–12, and inSkills 1 and 2 select inSkill 3 for going left in states 17 and 18. Again, this is due to the low number of times those state-action (state-module) pairs are sampled during the 200 learning episodes.

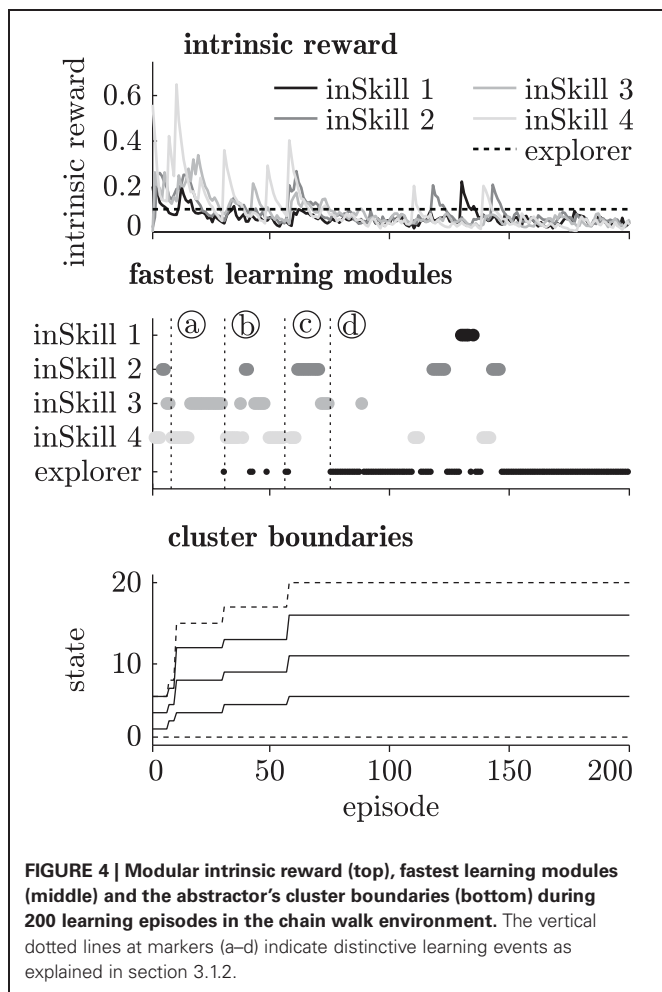
The explorer module (right column in **Figure 3**) learns policies for reaching the least-visited parts of the environment. This is still reflected in the exploring module's  $Q$ -values and reward after learning. More reward is obtained in states further away from the starting state 1, and  $Q$ -values are increasing with increasing distance from the starting state, because states further away from the starting state are visited less frequently.

### 3.1.3. Skill exploitation

To demonstrate the usefulness of the learned skills in an externally-rewarded chain walk task, we compare an agent with trained inSkills against two other learning agents that have no skill-learning capabilities (1) an agent with no additional modules and (2) an agent with a naive explorer module only. Note that

all agents still use an  $\epsilon$ -greedy policy as additional means of exploration. The externally-rewarded task for the agents is to reach any of the states in the furthest region (states 16–20), while starting from state 1. The main challenge is getting to this region by fast and efficient exploration. Once the reward region is reached for the first time, the RLs can usually extract the right policy instantly from the model. Each episode lasts only 25 timesteps, and each module can also run for a maximum of 25 timesteps (see **Table 1**). Together with the 20% chance of primitive failure (10% in the opposite direction and 10% no change) this makes the task particularly challenging. Even when the right policy is learned, the RL might not always reach any of the goal states during an episode due to action noise.

All experiments are repeated 500 times, and the results are averaged. **Figure 5** shows the average proportion of the total possible reward achieved as a function of the number of primitive actions taken during learning over 40 episodes. As becomes clear from this figure, the agent with no additional modules takes a long time to reach the target region. Eventually, the  $\epsilon$ -greedy policy will take this agent to the rewarding states, but on average it takes much longer than the 40 training episodes displayed here. The agent with the explorer module learns to reach the rightmost region much faster, because its explorer module drives it to previously unexplored regions. The agents with previously learned inSkills quickly reach the target region by simply selecting one of the previously learned skills that leads there. Agents with more inSkills collect the reward with less training examples because several modules lead to the rewarding region. Due to the difficulty of the task (20% action failure, 10% abstractor noise), it still takes these agents some episodes to reach the target region for the first time (e.g., less than half of the time for the four-inSkill agent during the first episode). However, the agents with previously-learned skills are still much faster in solving the externally-rewarded task than the other agents.

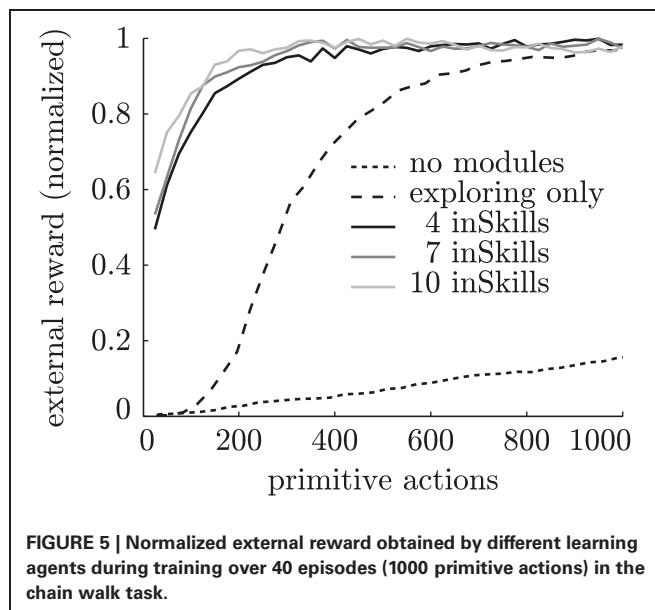


## 3.2. CURIOSITY-DRIVEN SKILL LEARNING ON THE ROBOTIC PLATFORM

### 3.2.1. Setup

The curiosity-driven learning algorithm is applied on the robotic tactile platform to learn the movements that lead to different kinds of tactile events. Here, tactile events are encoded as the frequency spectra of MEMS sensor-readouts during 0.33 s finger movements. We filter the MEMS signals with a high-pass filter with lower limit of 0.5 Hz because frequencies below this threshold do not reflect any information about the type (or presence) of sensor-surface contact. Additionally, we filter the signals with a 50 Hz notch filter to suppress power line noise. For various reasons (e.g., location relative to the fingerprints, DragonSkin becoming stuck inside the sensor after intensive use, general wear, 50 Hz distortions), some channels of the MEMS sensor gave less consistent readings than others. The spectra of the three best performing channels selected from visual inspection of the signals are used in the following.

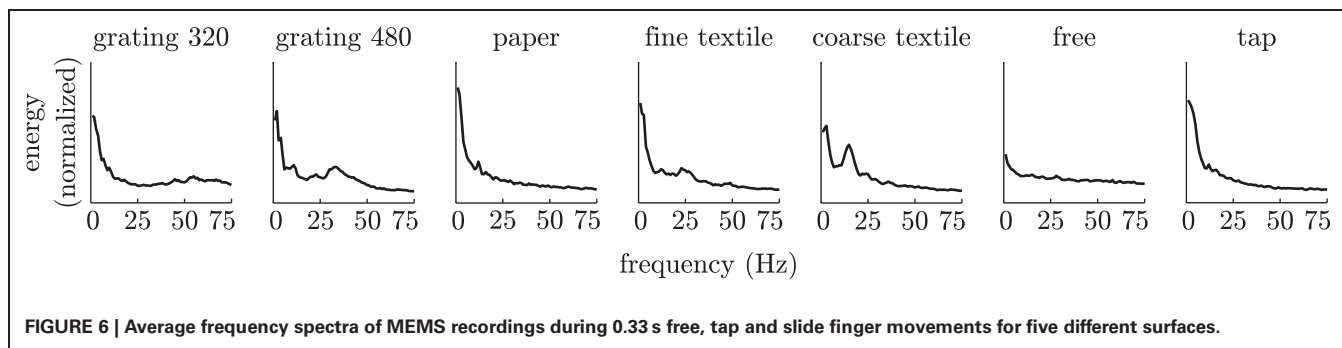
We expect that at least three different tactile events can be distinguished with the robotic platform: (1) movement without sensor-surface contact, which we call free movement, (2) tapping on a surface, and (3) sliding over a surface. To check our expectations, we programmed the finger to perform 50 repetitions of each of these movements in setups with five different surfaces. **Figure 6**



shows the frequency spectra of the MEMS signals averaged over 50 scripted free, tapping and sliding movements over the surfaces. Sliding movements generate spectra with a low-frequency peak caused by changes in pressure during sliding, and some additional spectral features at higher frequencies: grating 320 has a slight increase in energy around 55 Hz, grating 480 has a peak around 30 Hz, paper has no additional spectral features, fine textile has a peak around 25 Hz, and coarse textile has a peak around 12 Hz. Movements without sensor surface contact (free) yield an almost flat frequency spectrum, while tapping movements lead to spectra with a low-frequency peak and no other significant spectral features.

The frequency spectra are fed to an abstractor, whose task is to cluster similar sensory events and represent them as discrete tactile states. The abstractor used for distinguishing tactile events is a  $k$ -means clustering algorithm (Lloyd, 1982) that partitions the spectra into  $k$  clusters  $y_1, \dots, y_k$ , with  $k \in \{3, 4, 5\}$ . Although  $k$ -means clustering is an unsupervised method, it is still possible to calculate its classification accuracy on free, tapping and sliding events by assigning each cluster to the tactile event with the largest number of samples in that cluster. **Figure 7** shows the classification accuracies on free, tapping and sliding events for each surface individually. As becomes clear from this figure, the signals generated during free, tapping and sliding movements can be distinguished from each other by the  $k$ -means clusterers with reasonable accuracy (>90%). Using more than three (i.e., the number of different finger movements) clusters helps to better separate the different tactile events, usually because the difference between data generated during different types of sliding movements is larger than the difference between data collected from free and tapping movements.

The goal of the inSkill modules is to learn behaviors that produce MEMS signals belonging to the corresponding abstractor cluster. To learn finger behaviors, the RLs need some proprioceptive information from the finger, and needs to be able to



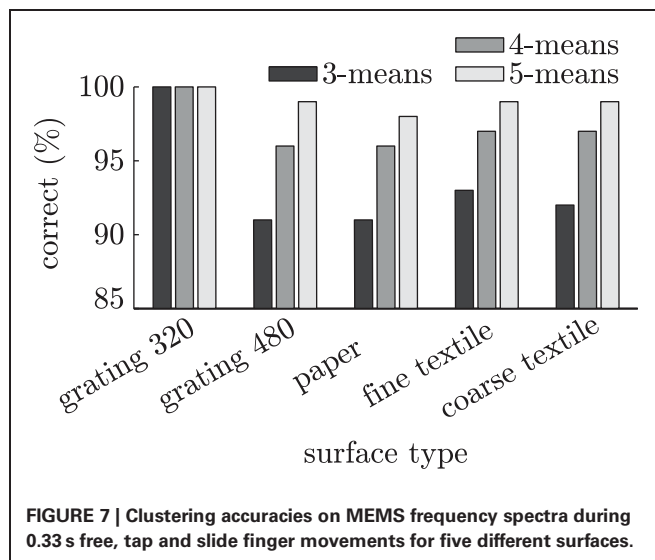
execute finger movements. We use a representation that might not be optimal for the learning algorithms, but greatly simplifies the graphical presentation of the tactile skill learning. The RLs are fed with the MCP and combined PDIP motor locations, discretized into six positions for each motor, yielding 36 states in total as depicted in **Figure 8**. The RLs can select from a total of eight primitive actions that set the torque of the MCP and the tension of the PDIP as presented in **Figure 8**. Each motor primitive lasts a fixed 0.33 s. Unlike the chain walk task, the adjacent states might not be directly reachable from each other, for example, closing the PDIP motor when it is half closed (third or fourth state column in **Figure 8**) might fully close it at the end of the transition (left state column in **Figure 8**). Note that many aspects of the robot's dynamics, such as the angles of the underactuated PIP and DIP joints, the precise encoder values, finger movement direction and velocity, cable tension in case of sensor-surface contact, etc., are not captured in this representation, and instead need to be absorbed by Markov model's transition probabilities. More complex representations using more state and action dimensions might facilitate faster learning, but do not lend themselves for an easily understandable presentation of tactile-skill learning.

The episodic learning scheme in the chain walk task is also applied for the robotic platform. At the episode start the finger is put in randomly selected encoder positions in the range (0.1–0.9) (MCP) and (0.1–0.5) (PDIP), which approximately covers the finger's movement range (see **Figure 8**). We use slightly shorter episode and module runtime lengths (20) than in the chain walk task to speed up the experiments. A list of all parameter values used for the robotic platform experiment is given in **Table 1**.

We run the curiosity-driven learning agent on the robotic platform using five inSkill modules, a naive explorer and a skill progressor. No external reward is provided to the agent yet. To allow for adaptation of the  $k$ -means clusterer during exploration and skill-learning, it is retrained every reinforcement learning episode on a buffer of the last 500 observations. Consistency of the cluster-means between each episode is enforced by initializing the  $k$ -means training algorithm with the most recent cluster-means.

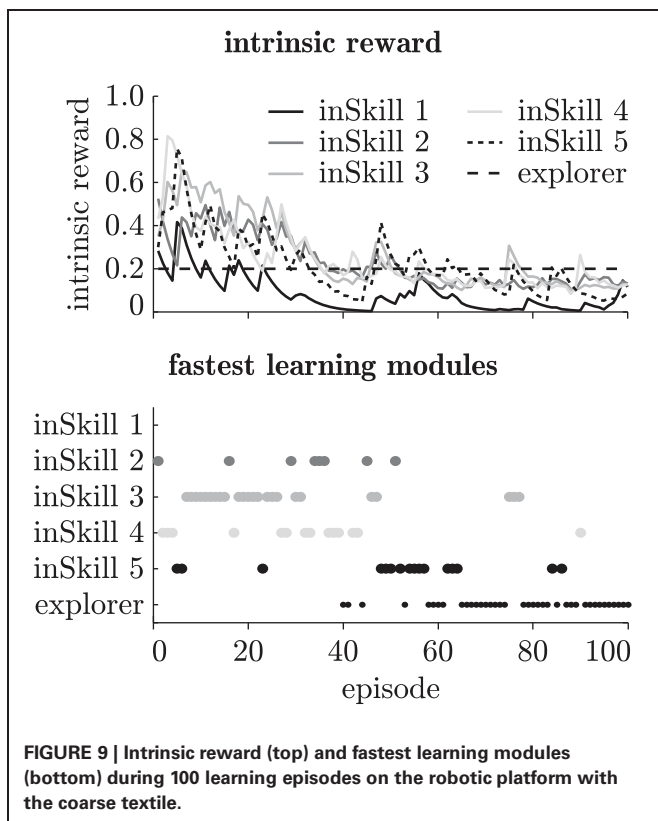
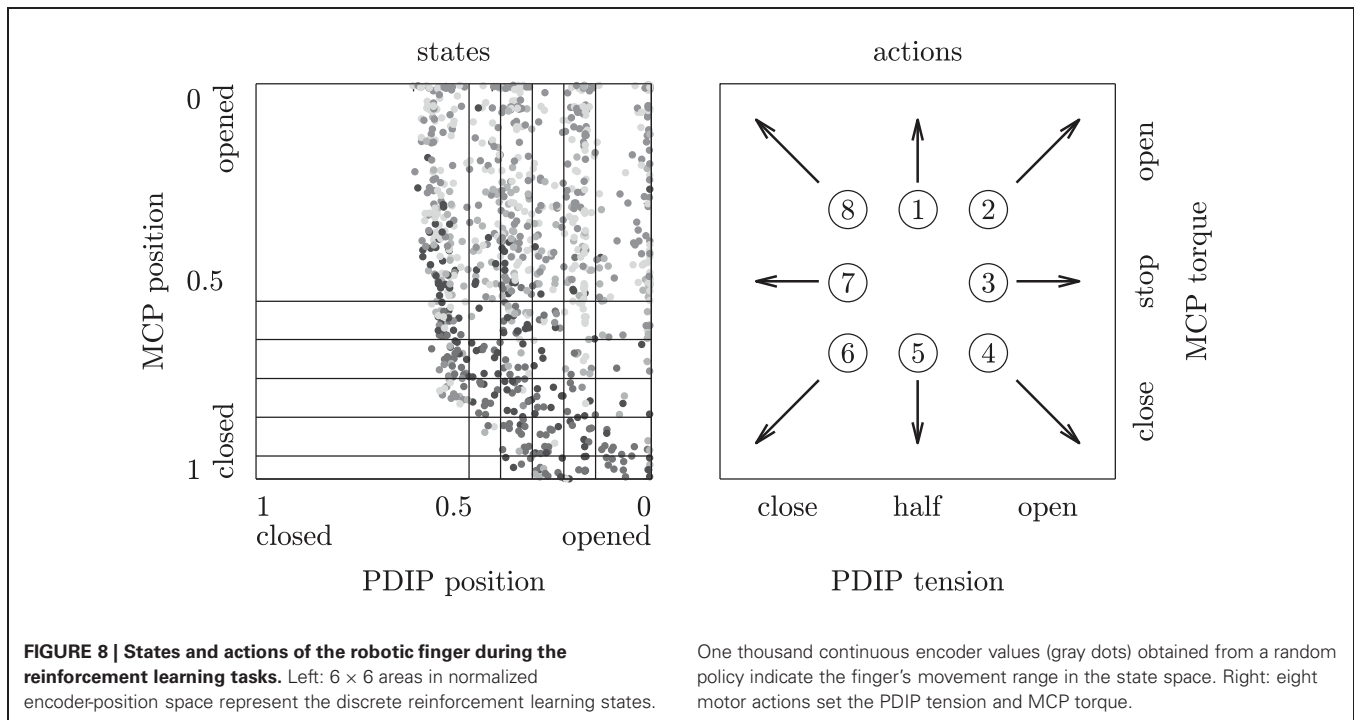
### 3.2.2. Skill learning

**Figure 9** shows an example of the intrinsic reward of the inSkills during curious exploration of the robotic platform with the coarse textile. The intrinsic reward generated by the progress of the inSkills decreases over time as the agent learns separate behaviors for generating different tactile events. Unlike in the chainwalk



task, little switching back and forth between skill learning and exploration occurs. Instead, the agent learns the inSkills without calling the explorer for explicit exploration, because it can easily reach all parts of the environment. After about 65 episodes, the inSkills stabilize, and the exploring module takes over, with a few short exceptions around episodes 75, 85, and 90. The learning progress in the inSkills around these episodes is due to the finger getting stuck (caused by faulty encoder readouts) in a pose where the sensors generated many samples for a single cluster. The curiosity-driven learning algorithm picks this up as a potentially interesting event, and tries to learn behaviors that reliably lead to such an event. However, after resetting the finger at the end of the episode, the encoders return the correct values again, and the learning agent gradually forgets about the deviating event.

**Figure 10** shows an example of the abstractor clusters and corresponding RL policies after 100 episodes of curiosity-driven learning in a setup with the coarse textile. Comparing the cluster-means of the inSkills learned during curious exploration to the frequency spectra of the scripted free, tapping and sliding movement in **Figure 6**, it becomes clear that the abstractor has learned a similar division of the MEMS frequency spectra. The almost flat frequency spectrum for inSkill 2 is very similar to the frequency spectrum of the scripted free movements, and the spectrum for



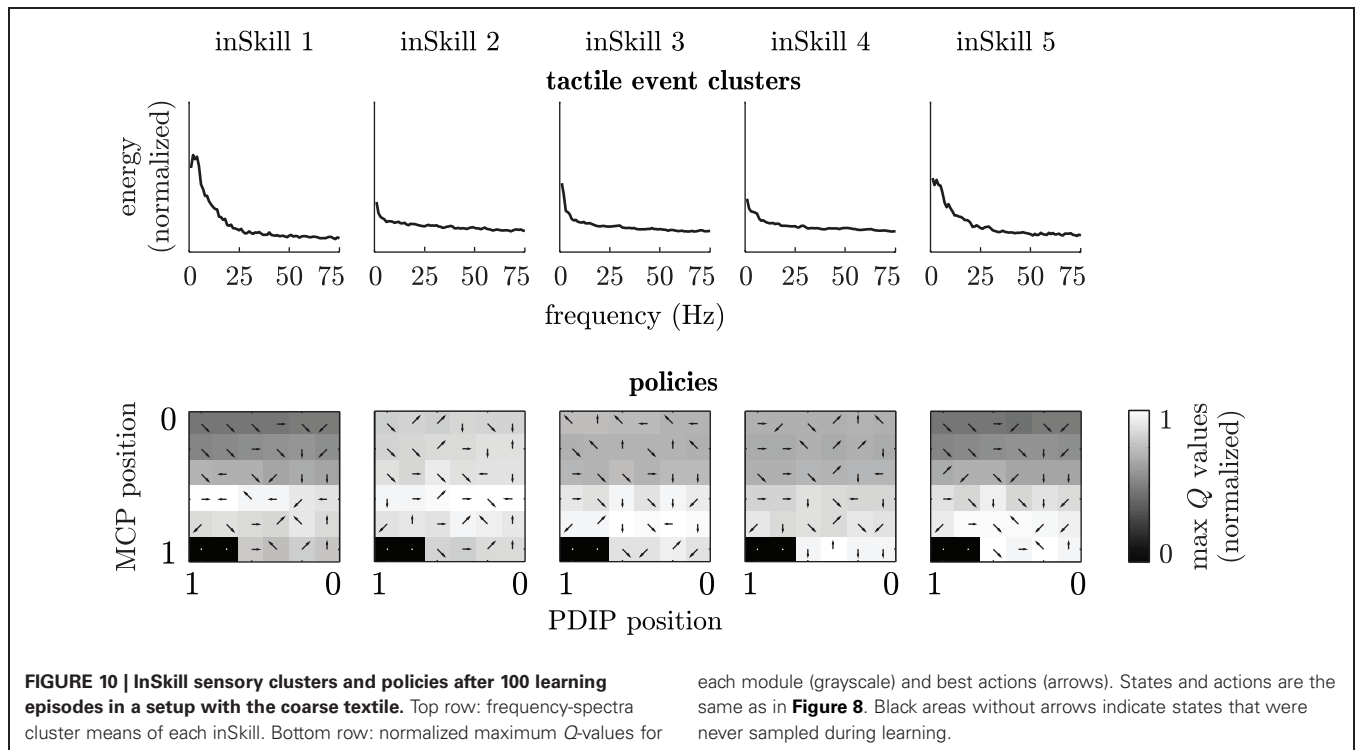
inSkill 1 has a similar low-frequency peak as the spectrum of the scripted tapping movement. The spectrum of inSkill 5 is most similar to the sliding spectrum of the coarse textile in **Figure 6**, but misses the characteristic peak around 12 Hz. The absence

of a clear peak for this inSkill is probably due to the combination of several sliding movements at different sensor angles and hence, different sensor-surface speeds, smearing out the spectral peaks over a larger range. The actual behaviors generated by these inSkills and the Q-tables in **Figure 10** indicate that the corresponding finger movements are also learned; the Q-values of inSkill 2 (free) have almost the same value throughout the state space, with slightly higher values with the finger away from the surface; inSkill 1 (tap) has two distinctive high Q-values for opening and closing the PDIP joints with the MCP joint halfway closed (middle-left in its Q-table); inSkill 5 (slide) obtains high Q-values with the MCP joint almost closed and opening and closing actions close to the surface (bottom-center in its Q-table).

The specialization of inSkills 3 and 4 is less obvious from **Figure 10**. However, the actual behavior of the inSkills indicated that inSkill 3 developed into a module for learning slight elastic deformations of the sensor packaging material while opening the finger close to the surface (while not actually touching anything), while inSkill 4 developed behavior that led to similar changes during closing movements.

In setups with the other four surfaces, the skill repertoire learned by the agent also contains distinct behaviors for free, tapping and sliding movements. Apart from these skills, a range of other consistent behaviors were learned, such as behaviors for breaking sensor-surface contact, behaviors that generate elastic deformation of the packaging material after sensor-surface contact, separate skills for sliding forward and sliding backward, hard and soft tapping, and tapping from different angles.

While the specialization of the skills changes during exploration of the environment, the exploration phase often involves the learning of skills in a particular order; first the agent learns



to distinguish between free and tapping movements, and as a result of improving its tapping skills, learns a sliding skill as well. During the learning of reliable tapping, the finger makes many movements with the sensor close to the surface. This leads to the discovery of sliding movements, and the learning of the associated sliding skill. The result of this sequence is visible in **Figure 9**, where the sliding skill (inSkill 5) is the last module that is learned (note that the final specialization happens for the inSkill with the highest number (5) is a coincidence; the order of the clusters is determined randomly).

### 3.2.3. Skill exploitation

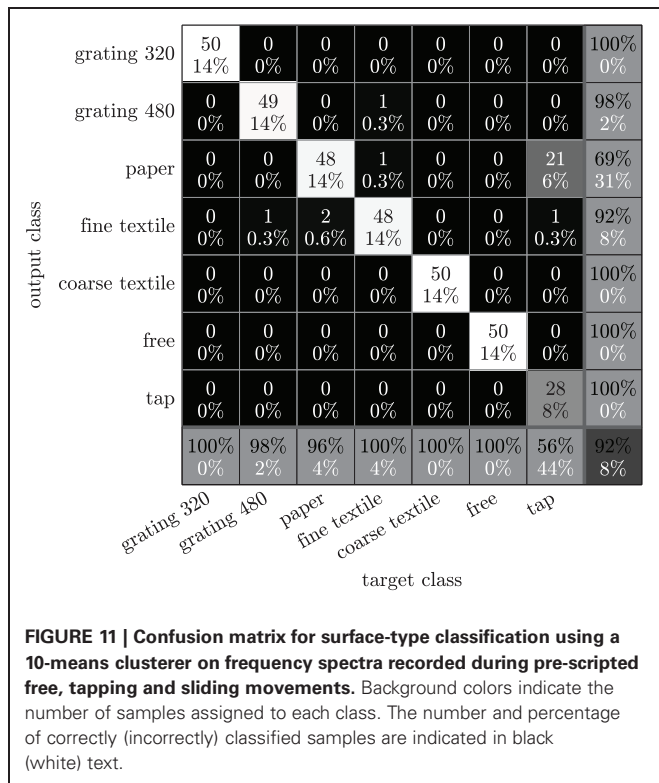
After autonomous learning of skills on the robotic platform, we test the usefulness of the learned skills in an externally-rewarded surface-classification task. The task for the robotic finger is to figure out which surface sample is placed on the platform. Instead of programming the finger to slide over the surface, the agent has to learn which of its movements generate the most distinguishing information about the surface sample. We compare the learning agent with previously learned tapping and sliding skills against a learning agent without such previously-learned skills.

To determine the different surface types in the externally-rewarded task, we compare the frequency spectra recorded during each finger movement with previously recorded frequency spectra during sliding movements over the different surfaces, tapping movements, and movements without sensor-surface contact. An external reward of 1 is provided when the recorded spectrum closely matched the frequency spectra of the surface placed on the platform and an external reward of 0

otherwise. After each correct classification, the module ends, and the finger is reset as in an episode start. Although the reward function does not directly represent misclassifications (i.e., the finger can continuously provide misclassification without penalty) due to the limited amount of time in each trial, more reward can be obtained if the finger makes correct classifications sooner.

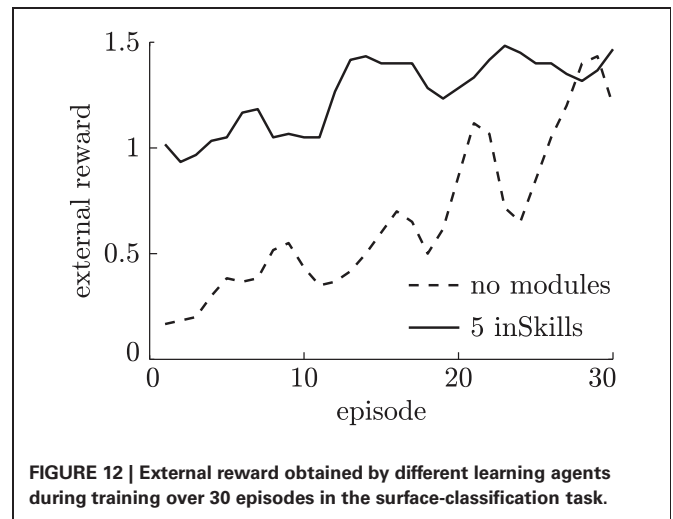
To give an indication of how difficult it is to distinguish the different surfaces during scripted sliding movements, we provide the frequency spectra recorded during sliding movements as well as during free and tapping movements to a 10-means clusterer, and compute the clustering accuracy as described before. As shown in **Figure 11**, the overall accuracy of 92% for distinguishing the different surfaces from each other, is not as high as the accuracy of distinguishing between free, tap and slide movements for each surface individually (**Figure 7**), but still is well above guess chance (14%). **Figure 11** further indicates that sliding movements over different surfaces can be accurately distinguished from each other, as well as from tapping and free movements. However, it is more difficult to distinguish sliding movements over paper from tapping movements, probably because the smooth paper surface produces almost no distinctive spectral features (compare also the frequency spectra for sliding over paper and tapping in **Figure 7**). Using slightly different numbers of clusters (between 7 and 15) changed the accuracies with only a few percentages.

During the externally-rewarded task, we keep training the skills learned during the curious exploration phase for two reasons: (1) skills used during autonomous exploration might be useful in quickly solving an externally-specified task, but might



not solve it directly. For example, a sliding skill might lead to sensor data that distinguishes a sliding movement from a tapping movement in a particular setup, but might not necessarily be good for distinguishing between different surface types. Still, some kind of sliding movement is probably required to distinguish between different surface types. An existing sliding skill could be easily adjusted to make slightly different movements that are better for distinguishing between surface types. We therefore add the external reward to inSkill modules that were active when the external reward was received, and adjust the modules' models and policies accordingly. (2) The dynamics of the robotic platform change during operation for various reasons (e.g., cable stretch, changes in ambient temperature and battery levels, general wear). While this might require repeated calibration in traditional approaches, the learning system used here is flexible enough to cope with those changes.

Learning in the externally-rewarded tasks is done over 30 episodes and repeated three times for each of the five surfaces described in section 2.2.3. **Figure 12** shows the average reward during training. As shown in this figure, agents that have previously learned inSkills learn to solve the externally-rewarded task much faster than the agent without such previously learned skills. The skills learned during the curious exploration phase are useful for the externally-rewarded task, but often do not solve it directly. Instead, the skills need to be (slightly) adjusted from skills that distinguish free, tap and slide movements for individual surfaces, into sliding movements that distinguish different surfaces. This skill adjustment is reflected in the increasing reward of the agent with previously-learned inSkills while it is learning to solve the externally-rewarded task.



#### 4. DISCUSSION

We presented a curiosity-driven modular reinforcement learning framework for autonomous learning of tactile skills on a tactile robotic platform. The learning algorithm was able to differentiate distinct *tactile events*, while simultaneously learning *behaviors* for generating those tactile events. The tactile *skills* learned in this fashion allowed for rapid learning of an externally-specified surface classification task. Our results highlight two important aspects of active tactile sensing: (1) exploratory tactile skills can be *learned* through intrinsic motivation (2) using previously-acquired tactile skills, an agent can learn which exploratory policies yield the most relevant tactile information about a presented surface.

A key aspect of the developmental learning system presented here is the ability to use previously-learned skills for reaching novel parts of the environment, and to combine skills into more complex composed skills. This bootstrapping of skills became apparent in the chain walk task, where modules used other modules to reach parts of the environment in case the transition probabilities of primitive actions were not accurately known. Also, during curious exploration of the tactile platform, the agent first learned to move the finger without sensor-surface contact, then learned to tap the finger on the surface, and finally learned the more difficult skill of sliding the finger over the surface while maintaining sensor-surface contact. After learning these skills, the agents kept exploring the environment in search for further things to learn, while maintaining a stable division of skills learned thus far.

The notion of *active* tactile sensing has recently been discussed in Prescott et al. (2011), who considered different interpretations: (1) the energetic interpretation, in which the information-relevant energy flow is from the sensor to the outer world being sensed; (2) the kinetic interpretation, in which the sensor touches rather than is being touched; and (3) the preferred interpretation by Prescott et al. (2011), which considers active sensing systems as purposive and information-seeking, involving control of the sensor apparatus in whatever manner suits the task. Our work fits best with the third interpretation,

because tactile information drives both the learning of tactile exploratory skills and the categorization of tactile stimuli. Note, however, that the exploratory dynamics are not directly used as kinaesthetic information provided to the texture classifier, but rather enter in the categorization chain as affecting sensor outputs. In future work, it would be interesting to study if and how tactile and kinaesthetic information could be fused for motor control and perceptual purposes during learning of exploratory skills.

A potentially interesting comparison could be made between the usage of sensory information during tactile exploration in humans and in the biomimetic robotic setup. In our experiments the algorithms were able to distinguish between different textures using the key spectral features of the sensor output. The human neuronal mechanisms and contributions of the different types of mechanoreceptors for distinguishing textural details (Yoshioka et al., 2007) are still highly debated. No agreement has been reached about the most informative mechanoreceptors (i.e., among Merkel, Meissner, Ruffini, and Pacini corpuscles) or about the coding strategy (e.g., temporal, spatial, spatiotemporal, intensity) used by humans to represent textural information. Various studies aimed at demonstrating that the Pacinian system encodes fine textures (Hollins et al., 2001; Bensmaïa and Hollins, 2003; Bensmaïa and Hollins, 2005). In particular, Hollins and Risner (2000) supported the Katz's duplex theory, according to which fine textures are supposed to be mediated by different classes of mechanoreceptors via vibrational cues for fine forms and via spatial cues for coarse forms. Conversely, Johnson and colleagues presented human psychophysical studies and complementary electrophysiological results with monkeys supporting a unified peripheral neural mechanism for roughness encoding of both coarse and fine stimuli, based on the spatial variation in the firing rate of Slowly Adapting type I afferents (SAI; Merkel) (Connor et al., 1990; Connor and Johnson, 1992; Blake et al., 1997; Yoshioka et al., 2001). Johansson and Flanagan (2009) introduced a hypothetical model of tactile coding based on coincidence detection of neural events, which may describe the neuronal mechanism along the human somatosensory chain from tactile receptors, passing through cuneate neurons up to the somatosensory cortex. What has been agreed on is that humans can detect up to microtextures (LaMotte and Srinivasan, 1991), and that the human perception of textures is severely degraded in case of lack of tangential motion between the fingertip and the tactile stimuli (Morley et al., 1983; Gardner and Palmer, 1989; Radwin et al., 1993; Jones and Lederman, 2006). This consolidated finding fits well the results presented in the current work: like human beings, the robotic finger also developed skills for sliding motions tangential to the tactile stimuli while seeking for information-rich experiences.

Recently, Fishel and Loeb (2012) obtained impressive texture classification accuracies on a large range of different textures, using an algorithm that selects the most discriminative exploratory motions from a set of tangential sliding movements with different forces and velocities. *That* variations in

high-level motion parameters like force and velocity are important for obtaining the most distinctive information is, however, not inferred by their learning algorithm. Our approach first learns how to make exploratory movements without any teacher feedback and without any knowledge of high-level parameters such as sensor-surface force and velocity. As in Fishel and Loeb (2012), our algorithm then learns to select exploratory movements that yield the most distinctive information about the presented textures. Whereas Fishel and Loeb (2012) learn to select pre-scripted exploratory movements, our algorithm can still refine the previously-learned exploratory movements during the learning of the supervised texture classification task.

A further comparison could be made between the exploratory behaviors learned by the biomimetic platform, and the learning of tactile exploratory procedures by human beings. There is a large body of literature about the exploratory procedures employed by humans when investigating an objects, including texture (e.g., Lederman and Klatzky, 2009, and references therein). Tapping and sliding tangentially over a surface are both used by human beings and learned by the robotic platform when gathering tactile information. Apart from using or selecting *existing* exploratory procedures it could also be interesting to study similarities in how these exploratory procedures are *learned* in human beings in the first place. The constraints of the biomimetic robotic finger make tapping easier to learn than sliding. Consequently, sliding is often learned after and as a result of tapping. Similar constraints in human beings might lead the same developmental trend (from tapping to sliding).

Although the robotic finger has just two controllable degrees of freedom, learning skills in an autonomous fashion already proved to be beneficial during learning of an additional externally-specified task. Moreover, the learning approach allowed for overcoming challenges in traditional engineered solutions to robotic control, such as the need of constant recalibration of the robotic platform to changing circumstances, and the absence of joint-angle sensors in the underactuated joints. We expect that autonomous acquisition of skills in robots will become increasingly important for autonomous learning in robots with more degrees of freedom and sensory capabilities.

## ACKNOWLEDGMENTS

This work was funded by the EU under projects NanoBioTouch (FP7-NMP-228844), IM-CLeVeR (FP7-ICT-231722), NanoBioTact (FP6-NMP-033287), and SmartHand (FP6-NMP4-CT2006-33423). Leo Pape acknowledges his colleagues at IDSIA for the many discussions about curiosity-driven learning in theory and practice. Calogero M. Oddo and Maria C. Carrozza acknowledge Dr. Lucia Beccai from CMBR IIT@SSSA for previous collaboration in the development of the biomimetic fingertip, and Prof. Johan Wessberg from the Department of Physiology of University of Gothenburg for meaningful discussions on the human somatosensory system. The authors thank the two reviewers for their constructive comments.

## REFERENCES

- Arai, H., and Tachi, S. (1991). Position control of a manipulator with passive joints using dynamic coupling. *IEEE Trans. Rob. Autom.* 7, 528–534.
- Bensmaïa, S. J., and Hollins, M. (2003). The vibrations of texture. *Somatosens. Mot. Res.* 20, 33–43.
- Bensmaïa, S. J., and Hollins, M. (2005). Pacinian representations of fine surface texture. *Percept. Psychophys.* 67, 842–854.
- Blake, D. T., Hsiao, S. S., and Johnson, K. O. (1997). Neural coding mechanisms in tactile pattern recognition; the relative contributions of slowly and rapidly adapting mechanoreceptors to perceived roughness. *J. Neurosci.* 17, 7480–7489.
- Bourlard, H., and Kamp, Y. (1988). Auto-association by multilayer perceptrons and singular value decomposition. *Biol. Cybern.* 59, 291–294.
- Buchholz, B., Armstrong, T. J., and Goldstein, S. A. (1992). Anthropometric data for describing the kinematics of the human hand. *Ergonomics* 35, 261–273.
- Connor, C. E., Hsiao, S. S., Phillips, J. R., and Johnson, K. O. (1990). Tactile roughness: neural codes that account for psychophysical magnitude estimates. *J. Neurosci.* 10, 3823–3826.
- Connor, E., and Johnson, K. O. (1992). Neural coding of tactile texture: comparison of spatial and temporal mechanisms for roughness perception. *J. Neurosci.* 12, 3414–3426.
- Fishel, J. A., and Loeb, G. E. (2012). Bayesian exploration for intelligent identification of textures. *Front. Neurobot.* 6:4. doi: 10.3389/fnbot.2012.00004
- Gardner, E. P., and Palmer, C. I. (1989). Simulation of motion of the skin. I. Receptive fields and temporal frequency coding by cutaneous mechanoreceptors of OPTACON pulses delivered to the hand. *J. Neurophysiol.* 62, 1410–1436.
- Gordon, G., and Ahissar, E. (2011). “Reinforcement active learning hierarchical loops,” in *International Joint Conference of Neural Networks (IJCNN)*, (San Jose, CA).
- Hollins, M., and Risner, S. R. (2000). Evidence for the duplex theory of tactile texture perception. *Percept. Psychophys.* 62, 695–705.
- Hollins, M., Bensmaïa, S. J., and Washburn, S. (2001). Vibrotactile adaptation impairs discrimination of fine, but not coarse, textures. *Somatosens. Mot. Res.* 18, 253–262.
- Johansson, R. S., and Flanagan, J. R. (2009). Coding and use of tactile signals from the fingertips in object manipulation tasks. *Nat. Rev. Neurosci.* 10, 345–359.
- Johansson, R. S., and Vallbo, A. B. (1979). Tactile sensibility in the human hand: relative and absolute densities of four types of mechanoreceptive units in glabrous skin. *J. Physiol.* 286, 283–300.
- Jones, L. A., and Lederman, S. J. (2006). “Tactile sensing,” in *Human Hand Function*, eds L. A. Jones and S. J. Lederman (New York, NY: Oxford University Press), 44–74.
- Kaelbling, L. P., Littman, M. L., and Moore, A. W. (1996). Reinforcement learning: a survey. *J. AI Res.* 4, 237–285.
- Kompella, V. R., Pape, L., Masci, J., Frank, M., and Schmidhuber, J. (2011). “AutoIncSFA and vision-based developmental learning for humanoid robots,” in *IEEE-RAS International Conference on Humanoid Robots*, (Bled, Slovenia).
- Konidaris, G. D., Kuindersma, S. R., Grupen, R. A., and Barto, A. G. (2011). “Autonomous skill acquisition on a mobile manipulator,” in *Proceedings of the Twenty-Fifth Conference on Artificial Intelligence (AAAI-11)*, (San Francisco, CA).
- Lagoudakis, M. G., and Parr, R. (2003). Least-squares policy iteration. *J. Mach. Learn. Res.* 4, 1107–1149.
- LaMotte, R. H., and Srinivasan, M. A. (1991). “Surface microgeometry: neural encoding and perception. Information processing in the somatosensory system,” in *Wenner-Gren International Symposium Series*, eds O. Franzen and J. Westman (New York, NY: Macmillan Press), 49–58.
- Lederman, S. J., and Klatzky, R. L. (2009). Haptic perception: a tutorial. *Atten. Percept. Psychophys.* 71, 1439–1459.
- Lloyd, S. P. (1982). Least squares quantization in PCM. *IEEE Trans. Inf. Theory* 28, 129–137.
- Morley, J. W., Goodwin, A. W., and Darian-Smith, I. (1983). Tactile discrimination of gratings. *Exp. Brain Res.* 49, 291–299.
- Mugan, J., and Kuipers, B. (2012). Autonomous learning of high-level states and actions in continuous environments. *IEEE Trans. Auton. Ment. Dev.* 4, 70–86.
- Oddo, C. M., Beccai, L., Wessberg, J., Backlund Wasling, H., Mattioli, E., and Carrozza, M. C. (2011a). Roughness encoding in human and biomimetic artificial touch: spatiotemporal frequency modulation and structural anisotropy of fingerprints. *Sensors* 11, 5596–5615.
- Oddo, C. M., Controzzi, M., Beccai, L., Cipriani, C., and Carrozza, M. C. (2011b). Roughness encoding for discrimination of surfaces in artificial active touch. *IEEE Trans. Rob.* 27, 522–533.
- Oudeyer, P. Y., Kaplan, F., and Hafner, V. (2007). Intrinsic motivation systems for autonomous mental development. *IEEE Trans. Auton. Ment. Dev.* 11, 265–286.
- Prescott, T. J., Diamond, M. E., and Wing, A. M. (2011). Active touch sensing. *Philos. Trans. R. Soc. Lond. B Biol. Sci.* 366, 2989–2995.
- Radwin, R., Jeng, O., and Gisske, E. (1993). A new automated tactility test instrument for evaluating hand sensory function. *IEEE Trans. Rehabil. Eng.* 1, 220–225.
- Schmidhuber, J. (2006). Developmental robotics, optimal artificial curiosity, creativity, music, and the fine arts. *Connect. Sci.* 18, 173–187.
- Schmidhuber, J. (2010). Formal theory of creativity, fun, and intrinsic motivation (1990–2010). *IEEE Trans. Auton. Ment. Dev.* 2, 230–247.
- Sutton, R., and Barto, A. (1998). *Reinforcement Learning: An Introduction*. Cambridge, MA: MIT Press.
- Vigorito, C. M., and Barto, A. G. (2010). Autonomous learning of high-level states and actions in continuous environments. *IEEE Trans. Auton. Ment. Dev.* 2, 132–143.
- Yoshioka, T., Gibb, B., Dorsch, A. K., Hsiao, S. S., and Johnson, K. O. (2001). Neural coding mechanisms underlying perceived roughness of finely textured surfaces. *J. Neurosci.* 21, 6905–6916.
- Yoshioka, T., Bensmaïa, S. J., Craig, J. C., and Hsiao, S. S. (2007). Texture perception through direct and indirect touch: an analysis of perceptual space for tactile textures in two modes of exploration. *Somatosens. Mot. Res.* 24, 53–70.

**Conflict of Interest Statement:** The authors declare that the research was conducted in the absence of any commercial or financial relationships that could be construed as a potential conflict of interest.

Received: 16 March 2012; accepted: 27 June 2012; published online: 23 July 2012.

Citation: Pape L, Oddo CM, Controzzi M, Cipriani C, Förster A, Carrozza MC and Schmidhuber J (2012) Learning tactile skills through curious exploration. *Front. Neurobot.* 6:6. doi: 10.3389/fnbot.2012.00006

Copyright © 2012 Pape, Oddo, Controzzi, Cipriani, Förster, Carrozza and Schmidhuber. This is an open-access article distributed under the terms of the Creative Commons Attribution License, which permits use, distribution and reproduction in other forums, provided the original authors and source are credited and subject to any copyright notices concerning any third-party graphics etc.

**Glossary of symbols.**


---

$\mathcal{A}$	action set
$A$	LSPI update matrix
$a$	action
$b$	LSPI update vector
$c$	transition count in Markov model
$D$	set of samples
$d$	transition duration
$e$	base of natural logarithm
$i$	index
$j$	module index
$k$	number of clusters / inSkill modules
$\mathcal{M}$	reinforcement learning module
$m$	Markov model value
$n$	number of samples
$o$	Markov model pruning threshold
$Q$	reinforcement learning state-action value
$p$	transition probability
$q$	long-term reward
$r$	short-term reward
$s, s'$	state
$\mathcal{S}$	state set
$t$	time
$v$	observed value
$w$	Markov model update weight
$y$	abstractor output
$z$	termination probability

---

$\Delta$	difference operator
$\epsilon$	reinforcement learning exploration rate
$\gamma$	reinforcement learning discount
$\kappa$	LSPI feature vector length
$\pi$	reinforcement learning policy
$\phi$	LSPI feature vector
$\omega$	LSPI weight
$\tau_e$	episode length
$\tau_z$	maximum module timesteps

---

**Glossary of acronyms.**


---

DC	direct current
DIP	distal interphalangeal
exSkill	externally-rewarded skill
inSkill	intrinsically-motivated skill
MCP	metacarpophalangeal
MEMS	microelectromechanical system
PDIP	combined PIP and DIP joints
PIP	proximal interphalangeal
RL	reinforcement learner

---



# Use of tactile feedback to control exploratory movements to characterize object compliance

Zhe Su<sup>1\*</sup>, Jeremy A. Fishel<sup>1,2</sup>, Tomonori Yamamoto<sup>2</sup> and Gerald E. Loeb<sup>1,2</sup>

<sup>1</sup> Department of Biomedical Engineering, Medical Device Development Facility, University of Southern California, Los Angeles, CA, USA

<sup>2</sup> SynTouch LLC, Los Angeles, CA, USA

## Edited by:

Tony J. Prescott, University of Sheffield, UK

## Reviewed by:

Antonio Novellino, *ett s.r.l.*, Italy  
Leslie S. Smith, University of Stirling, UK

## \*Correspondence:

Zhe Su, Department of Biomedical Engineering, Medical Device Development Facility, University of Southern California, Denney Research Building B6, 1042 Downey Way, Los Angeles, CA 90089, USA.  
e-mail: szhe.bme@gmail.com

Humans have been shown to be good at using active touch to perceive subtle differences in compliance. They tend to use highly stereotypical exploratory strategies, such as applying normal force to a surface. We developed similar exploratory and perceptual algorithms for a mechatronic robotic system (Barrett arm/hand system) equipped with liquid-filled, biomimetic tactile sensors (BioTac<sup>®</sup> from SynTouch LLC). The distribution of force on the fingertip was measured by the electrical resistance of the conductive liquid trapped between the elastomeric skin and a cluster of four electrodes on the flat fingertip surface of the rigid core of the BioTac. These signals provided closed-loop control of exploratory movements, while the distribution of skin deformations, measured by more lateral electrodes and by the hydraulic pressure, were used to estimate material properties of objects. With this control algorithm, the robot plus tactile sensor was able to discriminate the relative compliance of various rubber samples.

**Keywords:** compliance discrimination, exploratory movements, haptic perception, Barrett robot, biomimetic tactile sensor (BioTac<sup>®</sup>), haptic robotics

## INTRODUCTION

Humans interact with compliant objects to judge ripeness of fruits, the air pressure in bicycle tires or the quality of a mattress. Expert bakers judge the quality of flour by evaluating physical firmness or toughness of dough (Katz, 1937). During breast or prostate examinations, healthcare practitioners use their hands to locate and characterize a hard lump in soft tissue. Unlike visual features such as size and shape, compliance can only be appreciated via active or passive touch.

It is essential for social and personal assistive robots and prosthetic hands (a form of telerobot) to be able to perceive material properties such as compliance to handle household objects. The ability to interact with fragile objects is necessary particularly if such systems are designed to interact physically with humans. Compliance perception could also be beneficial to robot-assisted, minimally invasive surgeries by detecting a hidden tumor in an organ or a calcified artery in heart tissue (Yamamoto et al., 2009). A variety of tactile sensors have been designed to solve the tactile sensing problems in robotic manipulation and medicine (Webster, 1988), but their practical use is limited by the hostile environments to which robotic and prosthetic hands are typically exposed. The BioTac<sup>®</sup> is a robust and easy to repair tactile sensor that is capable of detecting point of contact, normal/tangential contact forces, and object spatial properties with impedance sensing electrodes (Wettels et al., 2008a; Wettels and Loeb, 2011), micro-vibrations associated with slip and textures through a hydro-acoustic pressure sensor (Fishel et al., 2008), and thermal fluxes with a thermistor (Lin et al., 2009).

Previous studies of compliance discrimination by robots used a combination of tactile and force sensors. (Takamuku et al., 2007) built a tendon-driven robot hand covered with strain gauges and a piezoelectric polyvinylidene fluoride (PVDF) skin.

By performing squeezing and tapping over objects with different material properties, the strain gauges in this tactile sensor enabled the discrimination of hardness of different materials. Campos and Bajcsy (1991) proposed a robotic haptic system architecture that performed haptic exploratory procedures based on Lederman and Klatzky (1987) psychophysical studies of human performance. Hardness of objects were determined by measuring the force required to produce a given displacement. Both studies focused on measuring contact force and indentation displacement to discriminate object hardness or compliance. An adaptive force/position control algorithm was tested on an industrial robot to maintain force along the normal direction to the surface while moving in tangential directions on a rubber ball with 10 cm radius and 5000 N/m stiffness (Villani et al., 2000). In this paper, we present the results of using information about distributed deformation of the elastic skin of our tactile sensor to discriminate compliance, a strategy that appears to be similar to that used by humans. This is made possible by using sensory feedback from a cluster of impedance sensing electrodes in the BioTac that are responsive to distributed forces. With these electrodes we were able to maintain a consistent orientation while applying normal forces to the surface of the object.

Subjective hardness/softness discrimination has been studied in psychophysical studies. Srinivasan and LaMotte (1995) showed that humans are efficient at discriminating subtle differences in softness under both active touch and passive touch with only cutaneous sensation but they are unable to discriminate even large differences during local cutaneous anesthesia. This suggests that tactile sensory information independent of proprioceptive information is necessary for discriminating softness of objects with deformable surface. Their studies also show that randomizing maximum force levels and indentation velocity in passive

touch does not seem to affect sensitivity. This indicates that compliance discrimination can be done without fine control of these movements. Instead, we propose that spatial distribution of skin could be the cue for compliance discrimination. Peine (1999) developed a taxonomy that classifies the surgeons' finger motion during palpation procedures. They found that surgeons apply various normal force with no lateral motion to sense the stiffness of body tissues. Lateral motion after applying heavy pressure was found to enhance the ability to detect hard lumps in soft tissue.

To acquire information about object properties, humans tend to perform stereotyped exploratory movements (Lederman and Klatzky, 1987). The exploratory movements to detect hardness are pressing and squeezing (Lederman and Klatzky, 1990). We have developed a haptic robot platform with a Barrett hand-wrist-arm system whose three fingers have been equipped with novel BioTac® multimodal tactile sensors. In this paper, we present algorithms for the control of human-like exploratory movements for pressing on and characterizing objects with various hardnesses (durometer values). When robot gradually presses its fingertip into rubber samples with compliant surfaces, it uses the sensory feedback from the tactile sensor (BioTac) to control both normal and tangential contact forces and to adjust the orientation of its fingertip to account for the potentially unknown orientation of contact surfaces and internal discontinuities such as buried lumps. The distributed deformation sensed by the BioTac can be used to estimate the compliance of the contact surface.

## MATERIALS AND METHODS

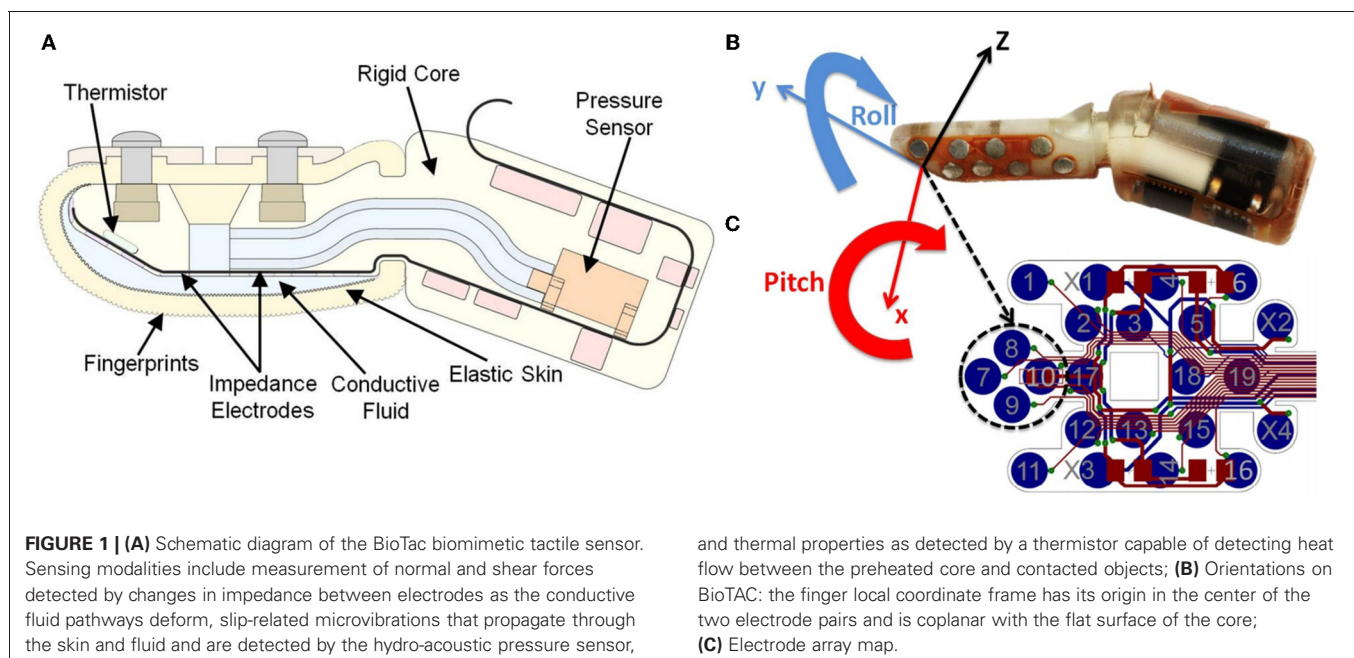
We present data from initial experiments with flat objects made from materials with varying hardness to demonstrate the simultaneous use of multimodal tactile sensor data to control exploratory movements and to interpret their results.

## EXPERIMENT SETUP

### Overview of the biomimetic tactile sensor (BioTac)

The BioTac (Figure 1A) consists of a rigid core housing all electronics and sensory components surrounded by an elastic skin that is inflated with an incompressible and conductive fluid. When the skin contacts an object, this fluid is displaced, resulting in distributed impedance changes in the electrode array on the surface of the rigid core. The impedance of each electrode tends to be dominated by the thickness of the fluid layer between the electrode and the immediately overlying skin. The skin has a pattern of asperities on its inner layer that gradually compress with increasing normal force, preventing object saturation (Wettels et al., 2008b). A MEMS pressure transducer measures hydrostatic pressure, which increases depending on the distribution of deformation in the elastic skin.

Similar to the human fingertip, the BioTac sensors are sensitive to tangential as well as normal forces. When performing a compliance movement it is desirable to apply forces normally and symmetrically to the object. For the haptic robot, this means servoing its end-effectors in the pitch and roll directions to orient a flat portion of the core of the BioTac that defines a local coordinate frame (Figure 1B). The sensory feedback is provided by four adjacent electrodes on this flat region whose impedance depends on compression of the skin against the electrode surface. These four adjacent electrodes are labeled electrode 7, 8, 9, and 10 on the electrode array map (Figure 1C). The pair of electrodes along the x-direction (8 and 9) and the pair of electrodes along the y-direction (7 and 10) are used for servocontrol of the pitch and roll, respectively, of the robotic fingertip. When the tactile sensor detects differences between these pairs of electrodes the error is corrected by adjusting the pitch or roll of the fingertip with the robot. The total contact force during indentation is estimated from the sum of impedance changes on all four electrodes. When pressing into a compliant object, the object has a tendency to wrap



around the finger and the resulting forces can be measured by lateral electrodes not on the flat surface (such as 17). Comparing this change with the relative magnitude of impedance changes in the central four electrodes can yield substantial information about the compliance of the object. Additional information from the fluid pressure can also be used to characterize these changes. The sensor signals that provide information about compliance depend also on the curvature of the surface of the object, which must be estimated simultaneously from the complete temporal profiles of all sensor signals (Wettels and Loeb, 2011).

### Testing materials

The levels of compliance for objects used in this experiment are classified by their durometers. The durometer is measured by the indentation depth into a material created by a given force on a standardized indenter with specific diameter. There are several scales of durometer depending on the diameter and configuration of the indenter, the spring forces applied on the tested materials. The samples in this experiment were all one inch thick and made from Neoprene rubber (50 Shore A) and polyurethane rubber (30 Shore A, 50 Shore 00, and 30 Shore 00), going from hard to soft.

### Experimental procedure

The experiments were conducted on the seven DOF Barrett WAM robot arm and four DOF Barrett Hand BH-280 equipped with the BioTac. In each trial, the robot pressed one digit against a rubber sample in an unknown orientation and position. The robot controller had no prior knowledge of the orientation of the surface; instead it used tactile sensory feedback to identify a contact surface and adjust its finger orientation while pressing onto the compliant surface (Figure 2A).

### ROBOT EXPLORATORY MOVEMENTS

The exploratory movement can be divided into three phases: (1) Reach to an object surface by controlling position in Cartesian coordinate system with smooth path movement. The desired position is either provided *a priori* or estimated by machine vision. (2) Maintain normal contact and orientation with the center of the fingertip by maintaining a symmetrical distribution of force on a cluster of tactile sensors. (3) Controlling the exploratory movement, which consists of pressing the fingertip gradually into the contact surface while maintaining normal orientation of the fingertip in the pitch and roll directions.

### Online orientation control using tactile sensor feedback

In order to maintain the orientation of the flat portion of the sensor while gradually pressing into a compliant surface, the desired orientation trajectory is generated by feedback signals on the two pairs of electrodes. These differential signals are used to incrementally increase or decrease current pitch and roll angles ( $\beta_c$ ,  $\gamma_c$ ) with very small increments ( $\Delta\beta$ ,  $\Delta\gamma$ ) in the finger local coordinates, respectively. From the new local roll-pitch angles ( $\beta$ ,  $\gamma$ ) in the finger local coordinate frame (shown in Figure 1B), the corresponding finger local rotation matrix  $\mathbf{R}_{\text{local}}$  can be derived and translated into rotation matrix in the robot base coordinates  ${}^B\mathbf{R}_{\text{Finger}}$  by premultiplying local rotation matrix with matrix  ${}^B\mathbf{R}_{\text{F}}$  which is the forward kinematic from fingertip to robot base. Instead of using roll-pitch-yaw angles for orientation control directly, a unit quaternion representation of orientation  $[\eta, \epsilon_1, \epsilon_2, \epsilon_3]$  is derived from the new rotation matrix, because of its singularities-free property (Yuan, 1988). This online orientation generation algorithm is shown in a pseudo-code, (Table 1).

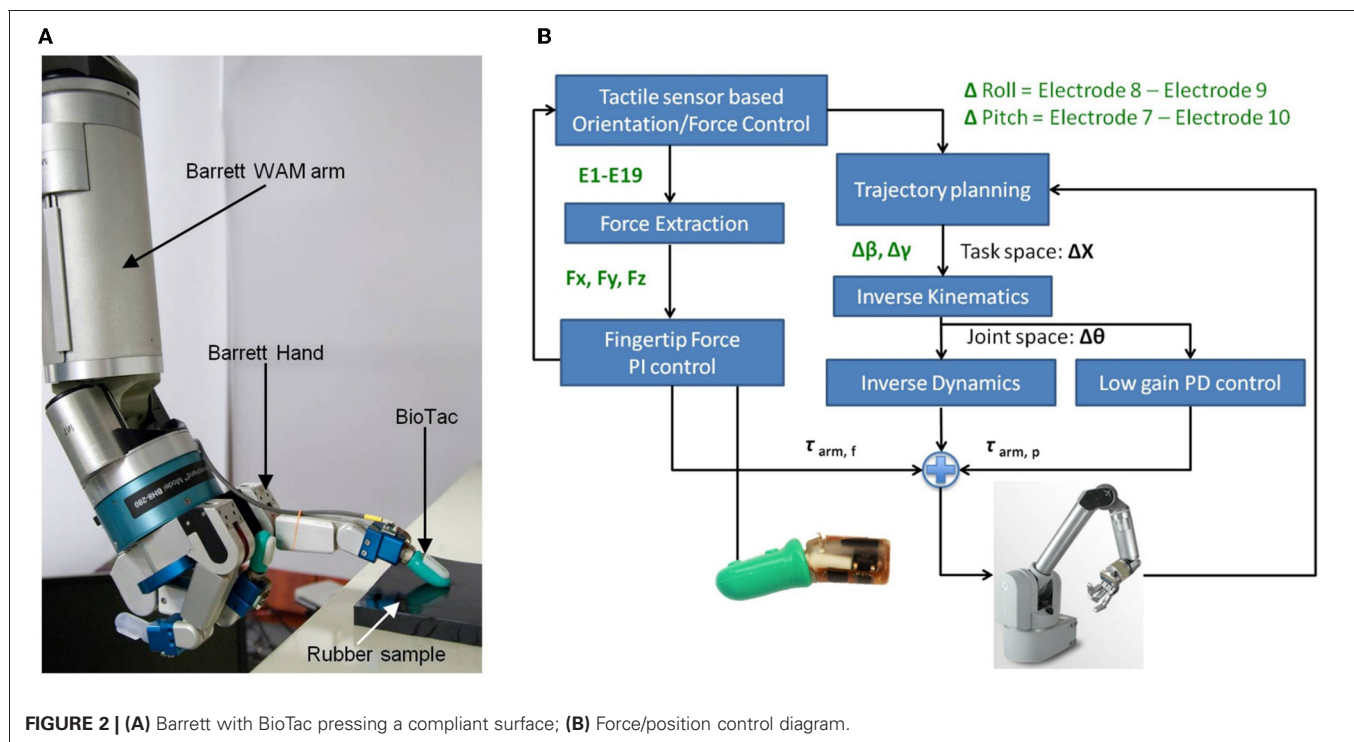


**Table 1 | Algorithm for online orientation generation using tactile sensor feedback.**


---

Algorithm online orientation generation using tactile sensor feedback  
( $E_8, E_9, E_7, E_{10}$ )

IF  $E_8 > E_9$  THEN  
 $\beta = \beta_c + \Delta\beta$

ELSEIF  $E_8 < E_9$  THEN  
 $\beta = \beta_c - \Delta\beta$

ENDIF

IF  $E_7 > E_{10}$  THEN  
 $\gamma = \gamma_c + \Delta\gamma$

ELSEIF  $E_7 < E_{10}$  THEN  
 $\gamma = \gamma_c - \Delta\gamma$

ENDIF

$\mathbf{R}_{\text{local}} = \text{RotationMatrix}(\beta, \gamma)$

${}^{\text{F}}\mathbf{R}_{\text{finger}} = {}^{\text{F}}\mathbf{R} * \mathbf{R}_{\text{local}}$

$[\eta, \epsilon_1, \epsilon_2, \epsilon_3] = \text{Quaternions}({}^{\text{F}}\mathbf{R}_{\text{finger}})$

---

The scalar  $\eta$  part and the vector part ( $\epsilon_1, \epsilon_2, \epsilon_3$ ) in a unit quaternion representation fulfill  $\eta^2 + \epsilon_1^2 + \epsilon_2^2 + \epsilon_3^2 = 1$ .

A velocity-based orientation control with quaternion feedback is written below:

$$\boldsymbol{\omega}_r = \boldsymbol{\omega}_d - \mathbf{K}_o \mathbf{e}_o \quad (1)$$

where  $\boldsymbol{\omega}_d$  is the desired angular velocities,  $\mathbf{K}_o$  is diagonal gain matrix and  $\mathbf{e}_o$  is the orientation error which is formulated using the unit quaternion (Yuan, 1988) as:

$$\mathbf{e}_o = \delta\boldsymbol{\epsilon} = \eta_d\boldsymbol{\epsilon} - \eta\boldsymbol{\epsilon}_d + [\boldsymbol{\epsilon}_d \times \boldsymbol{\epsilon}] \quad (2)$$

where  $[\boldsymbol{\epsilon}_d \times] = \begin{bmatrix} 0 & -\epsilon_{3d} & \epsilon_{2d} \\ \epsilon_{3d} & 0 & -\epsilon_{1d} \\ -\epsilon_{2d} & \epsilon_{1d} & 0 \end{bmatrix}$  and  $[\eta, \epsilon_1, \epsilon_2, \epsilon_3]$  is

the current orientation and  $[\eta, \epsilon_{1d}, \epsilon_{2d}, \epsilon_{3d}]$  is the desired orientation.

### Robot position control

The desired positions and orientation generated by the online trajectory generation using tactile sensory feedback is achieved by a velocity-based operational space controller together with an inverse dynamic law and PD feedback error compensation in joint space (Nakanishi et al., 2008). Inverse dynamics control enables low PD feedback gains for compliant control while ensuring high tracking performances. The control law is written as:

$$\boldsymbol{\tau}_{\text{arm, p}} = \mathbf{M}\ddot{\mathbf{q}}_d + \mathbf{h} + \mathbf{K}_p(\mathbf{q}_d - \mathbf{q}) + \mathbf{K}_d(\dot{\mathbf{q}}_d - \dot{\mathbf{q}}) \quad (3)$$

where  $\boldsymbol{\tau}_{\text{arm, p}}$  is computed vector of torques to track desired joint angles  $\mathbf{q}_d$  with measured current joint angles  $\mathbf{q}$ ,  $\mathbf{M}$  is rigid-body inertia matrix of the arm,  $\dot{\mathbf{q}}_d$  is the vector of desired joint velocity shown as:

$$\dot{\mathbf{q}}_d = \mathbf{J}^+(\dot{\mathbf{x}}_d + \mathbf{K}_x(\mathbf{x}_d - \mathbf{x})) + \mathbf{K}_{\text{post}}(\mathbf{I} - \mathbf{J}^+)(\mathbf{q}_{\text{post}} - \mathbf{q}) \quad (4)$$

where  $\mathbf{x}$  and  $\mathbf{x}_d$  are the measured and desired finger position and orientation,  $\mathbf{h}$  is the vector of Coriolis, centrifugal, and

gravitational forces,  $\mathbf{K}_p$ ,  $\mathbf{K}_d$ ,  $\mathbf{K}_x$ , and  $\mathbf{K}_{\text{post}}$  are diagonal gain matrices.  $\mathbf{J}$  is the end-effector Jacobian,  $\mathbf{J}^+$  denotes the pseudo-inverse of Jacobian and  $\mathbf{q}_{\text{post}}$  is the vector of default posture optimized in the nullspace of the end-effector motion. The desired joint acceleration  $\ddot{\mathbf{q}}_d$  and desired joint position  $\mathbf{q}_d$  are obtained by numerical differentiation and integration of the desired velocity  $\dot{\mathbf{q}}_d$ .

### Robot force control

Because the robot will press its end-effector onto compliant surfaces, external contact forces need to be taken into account. The external contact forces are obtained from the three force vectors on the BioTac extracted from impedance changes. They are used to compute torques in the joint space to account for the external contact forces by premultiplying them with Jacobian transpose, shown in Equation 5. The tracking of desired contact forces is achieved with a PI controller (Pastor et al., 2011)

$$\boldsymbol{\tau}_{\text{arm, f}} = -\mathbf{J}^T(\mathbf{F}_{\text{arm\_des}} - \mathbf{F}_{\text{arm}}) + \mathbf{K}_I \int_{t-\Delta t}^t (\mathbf{F}_{\text{arm\_des}} - \mathbf{F}_{\text{arm}}) dt \quad (5)$$

where  $\mathbf{F}_{\text{arm\_des}}$  is desired forces at the end-effector,  $\mathbf{F}_{\text{arm}}$  is the measured forces interpreted from BioTac,  $\mathbf{K}_I$  is a diagonal positive definite gain matrix and  $\Delta t$  is the time-window during which the force error is integrated. The integral controller will compensate for steady-state errors during contact. An overview of the presented control architecture is shown in **Figure 2B**.

### NORMAL AND TANGENTIAL FORCE EXTRACTION

During contact with an object, external forces deform the skin and fluid path around the impedance sensing electrodes. This deformation results in a distributed pattern of impedance changes on the electrodes. Previous studies have shown that both normal and tangential forces can be characterized from the impedance changes on the electrodes using machine learning techniques (Wettels et al., 2009; Wettels and Loeb, 2011). Here we present a simpler and more robust analytical algorithm to estimate normal and tangential forces.

The BioTac contains an array of 19 impedance sensing electrodes distributed over the surface of the core, which has a coordinate frame aligned with its long axis (**Figure 3**). Each impedance sensing electrode was determined to have the highest sensitivity to forces applied normally to its surface. The normal vectors to each of these electrodes in 3-axis coordinate space can be weighted with the change in impedance of these electrodes to determine an estimate of tri-axial force. We calculate the  $x$ ,  $y$  and  $z$  force vectors from these electrodes with the following equation:

$$\begin{bmatrix} F_x \\ F_y \\ F_z \end{bmatrix} = \begin{bmatrix} S_x & 0 & 0 \\ 0 & S_y & 0 \\ 0 & 0 & S_z \end{bmatrix} \times \begin{bmatrix} N_{1,x} & \cdots & N_{19,x} \\ N_{1,y} & \cdots & N_{19,y} \\ N_{1,z} & \cdots & N_{19,z} \end{bmatrix} \\ \times \left( \begin{bmatrix} E_1 \\ \cdots \\ E_{19} \end{bmatrix} - \begin{bmatrix} E_{1,\text{rest}} \\ \cdots \\ E_{19,\text{rest}} \end{bmatrix} \right)$$

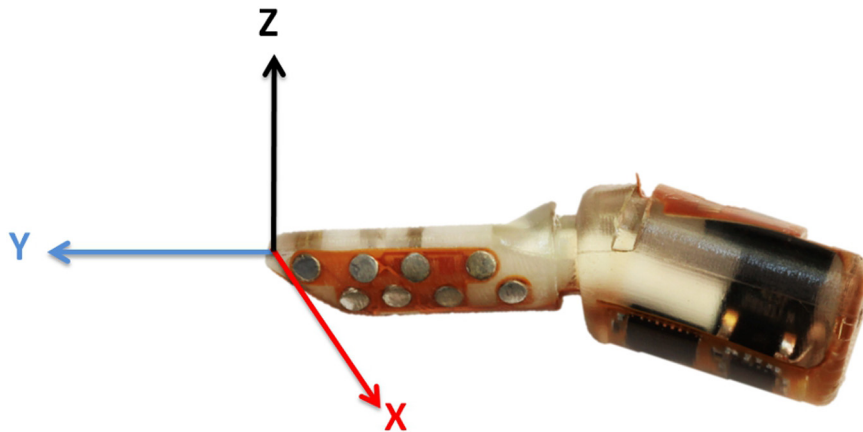


FIGURE 3 | Coordinate frame of BioTAC: each impedance sensing electrode has a specific orientation in the BioTAC coordinate frame.

where  $[F_x, F_y, F_z]$  is the three dimensional force vectors on the BioTAC,  $[E_1 \cdots E_{19}]$  and  $[E_{1, \text{rest}} \cdots E_{19, \text{rest}}]$  are the measured impedance changes and resting impedance values on the BioTAC,

$\begin{bmatrix} N_{1, x} & \cdots & N_{19, x} \\ N_{1, y} & \cdots & N_{19, y} \\ N_{1, z} & \cdots & N_{19, z} \end{bmatrix}$  is a matrix in which each column is calcu-

lated normal vector for each impedance sensing electrode surface from the geometry of the rigid core, the  $S_x$ ,  $S_y$  and  $S_z$  are scaling values for  $x$ - $y$ - $z$  three dimensional vectors to transform these arbitrary units into engineering units (N).

## RESULTS

### FORCE EXTRACTION

The scaling factor for each of the three dimensional estimated force vectors from the BioTAC were calibrated on a 6-axis force plate (HE6x6-16, ATMI). We found that using the above-mentioned normal/tangential force calibration method was computationally efficient and achieved a low root-mean-squared (rms) error that exceeded performance of the neural network and machine learning techniques described in (Wettels et al., 2009; Wettels and Loeb, 2011). **Figure 4** shows the actual forces (blue) measured from force plate and the predicted force vectors (red) extracted from BioTAC by manually pressing and sliding the BioTAC on the force plate. While pressing and sliding the BioTAC, the flat portion of the BioTAC was kept parallel with the surface of the force plate, similar to the orientation goal of the servocontroller for the exploratory poking movements. The rms errors for these sample movements were less than 10% of the applied forces in each axis.

### PRESSING WITH ORIENTATION UNCERTAINTY

Typical behavior of the system poking a surface with unknown orientation is illustrated in **Figure 5**. The top two plots show the impedances of the pairs of electrodes along  $x$  and  $y$  direction (E8 vs. E9, E7 vs. E10) on the flat portion of the core of the BioTAC, which is the desired center of contact. The differential signals between those two pairs of electrodes are also displayed in the two middle plots in **Figure 5**. After the initial contact (around 0.5–1 s),

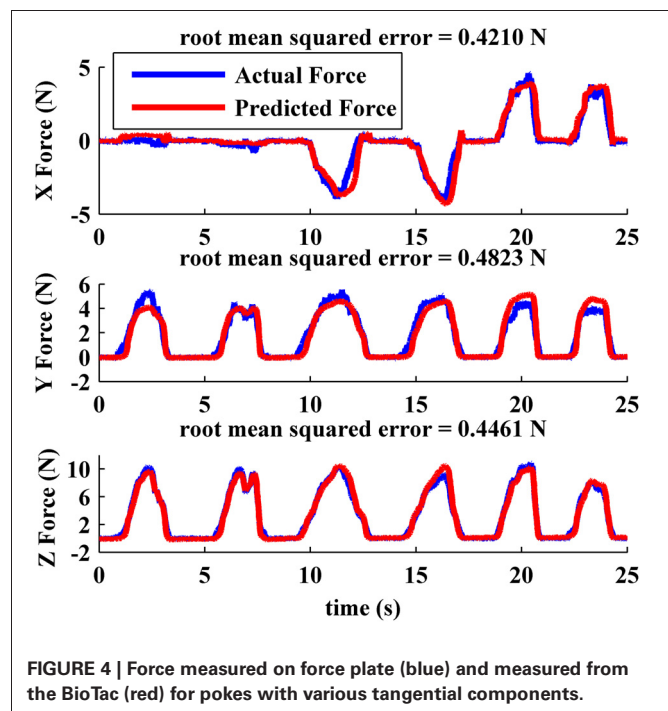


FIGURE 4 | Force measured on force plate (blue) and measured from the BioTAC (red) for pokes with various tangential components.

the robot gradually pressed the BioTAC into the compliant surface. A small asymmetry in the  $x$ -direction pair triggered the small correction to the roll angle that occurred at about 2–2.5 s and a larger correction at 4.5–5 s, shown in the bottom left plot. A larger asymmetry in the  $y$ -direction pair triggered a large pitch angle correction at 4–6 s, shown in the bottom right plot. The correction to pitch angle was relatively slow because it involved most of the proximal joints of the Barrett arm and it actually resulted in the second correction to the roll angle.

While the robot performed a pressing behavior, its contact force on the compliant surface was controlled by using tangential and normal force feedback extracted from the impedance electrode array on the BioTAC. **Figure 6** shows that the robot pressed

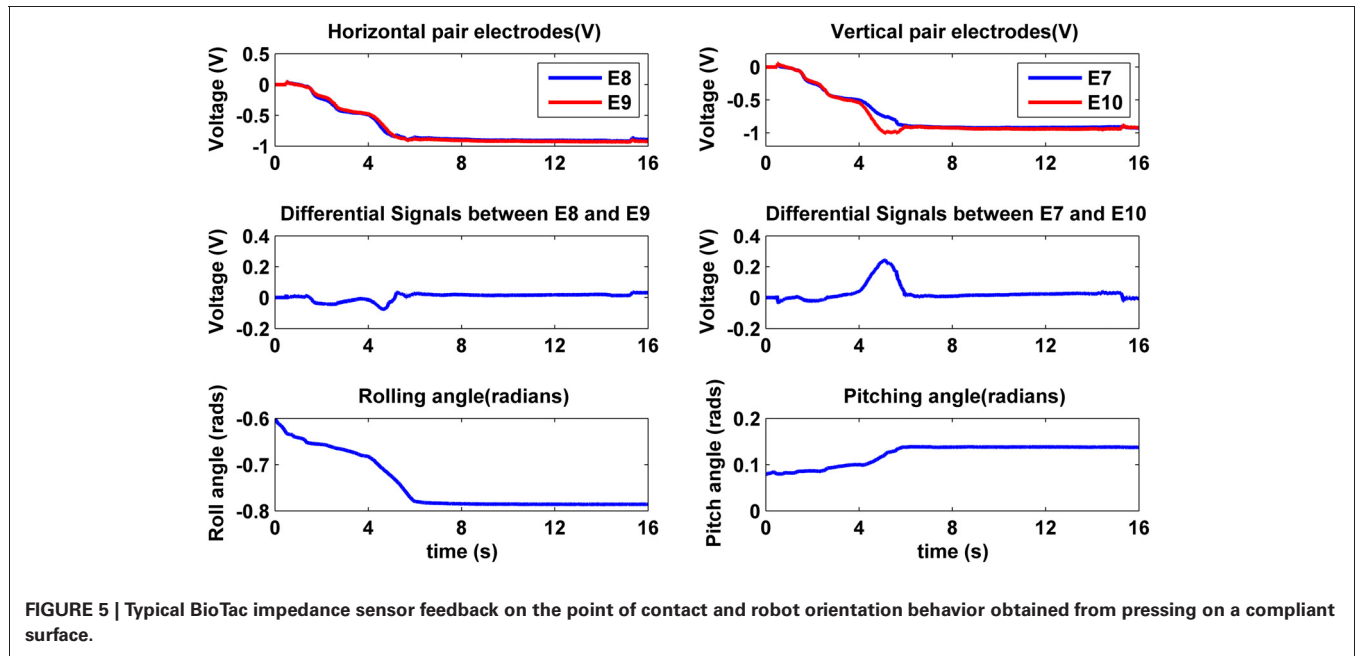


FIGURE 5 | Typical BioTac impedance sensor feedback on the point of contact and robot orientation behavior obtained from pressing on a compliant surface.

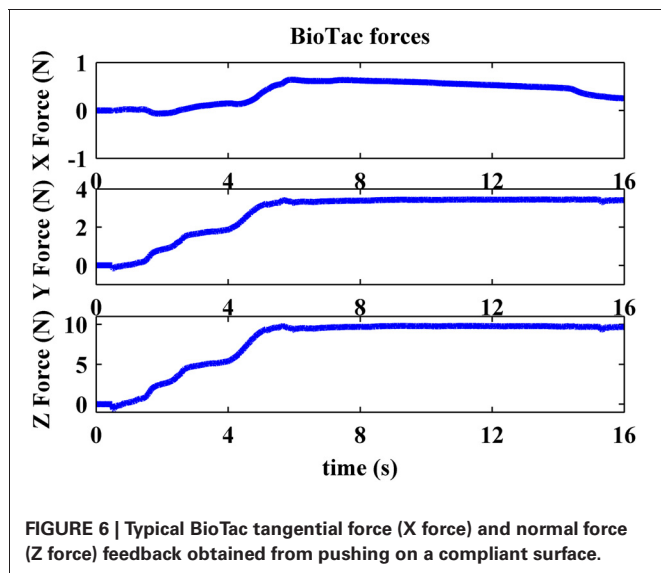


FIGURE 6 | Typical BioTac tangential force (X force) and normal force (Z force) feedback obtained from pushing on a compliant surface.

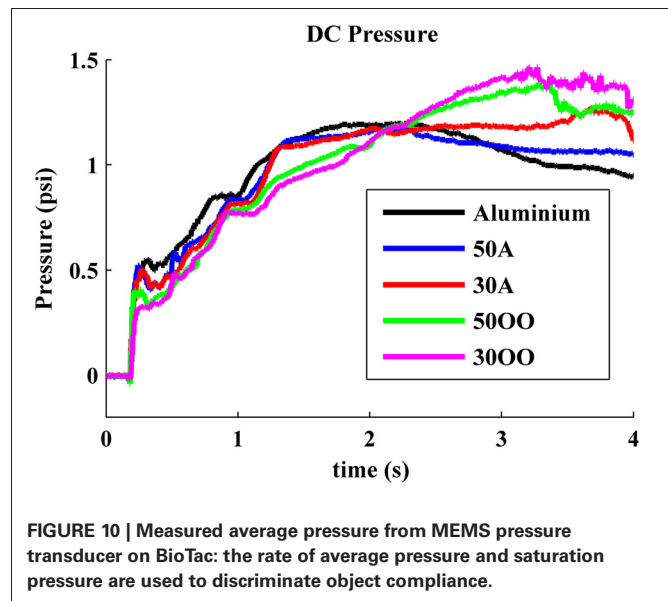
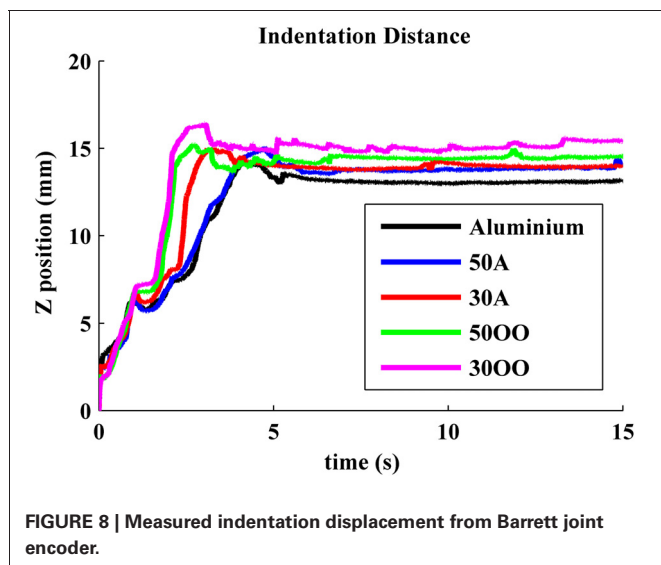
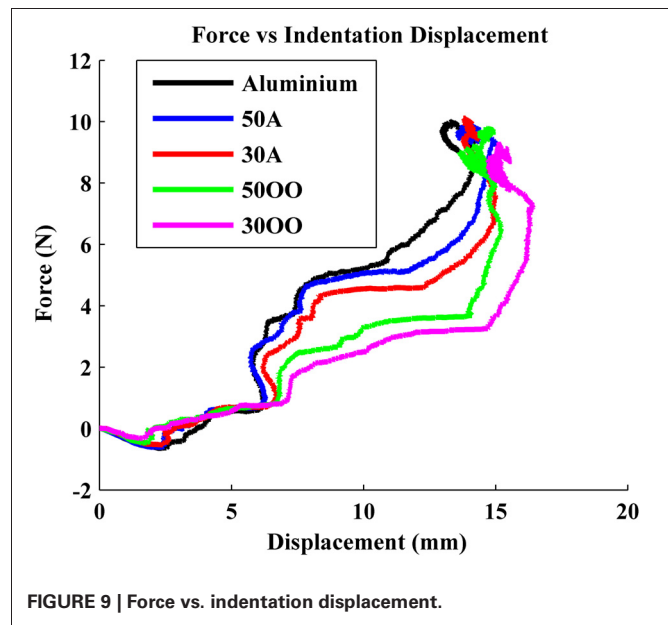
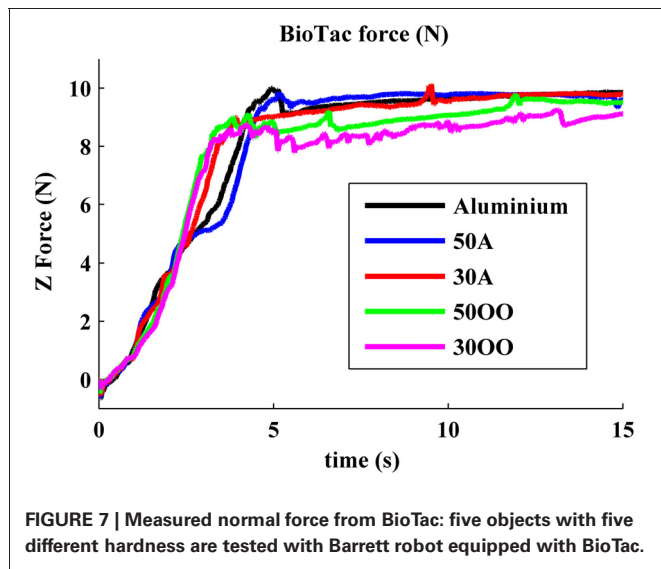
10 N on the compliant surface and kept its lateral tangential force (X Force) close to zero. The axial tangential force of 4 N is what would be expected given the 30° tilt of the flat portion of the fingertip with respect to the long axis of the BioTac. Stretch between the BioTac elastic skin and the compliant rubber sample caused by two rolling movements (around 2–2.5 s and 4.5–5 s in Figure 5) created a positive tangential force on the sensor, but the force controller gradually decreased the tangential force to close to zero by the end of the movements shown in Figure 6.

**COMPLIANCE DISCRIMINATION**

**Force and displacement**

Previous experiments showed that force and indentation displacement can be used in compliance discrimination when

actively palpating with a tool (LaMotte, 2000). Thus, the ratio between force and indentation displacement can also provide information for the perception of compliance, especially for compliant objects covered with non-deformable surfaces, such as piano keys. During our experiment, the robot is controlled to apply 10 N in the normal direction onto five objects, consisting of an aluminum plate and four progressively softer rubber samples with durometer Shore 50A, Shore 30A, Shore 5000, and Shore 3000. Shore 50A is as hard as a pencil eraser and shore 3000 is a little bit softer than a racquet ball. When the robot was actively pressing the BioTac onto five objects with various hardnesses, normal forces and indentation displacement were measured from BioTac and robot joint encoders, respectively, as shown in Figures 7 and 8. The initial rates of rise of force were similar for all materials, but it took the robot longer to reach 10 N on soft materials 5000 and 3000 because it needed to constantly adjust its fingertip orientation to keep its fingertip orthogonal to the surface of soft materials. In Figure 8, we observe that the softer materials have more indentation displacement than the harder materials. The indentation displacement was measured by the position sensors in the robot actuators. It reflects the sum of indentation of the skin of the BioTac plus indentation of the object being probed plus stretching of the fine stainless-steel cables that link the motors to the joints. Figure 9 shows that indentation displacement trajectories were similar for all materials up to about 6 mm and 1 N, which were due to displacement of the elastic skin on the BioTac and the initial stretching on the finger joints, which explain a nearly linear relationship between force and displacement. From 6 mm to 12 mm, indentation displacement trajectories diverged as a result of the deformation of rubber samples with different compliance properties and stretching of cables in the robot. At about 15 mm and 10 N, they reconverged because they were then dominated by the stretching of the cables in the robot



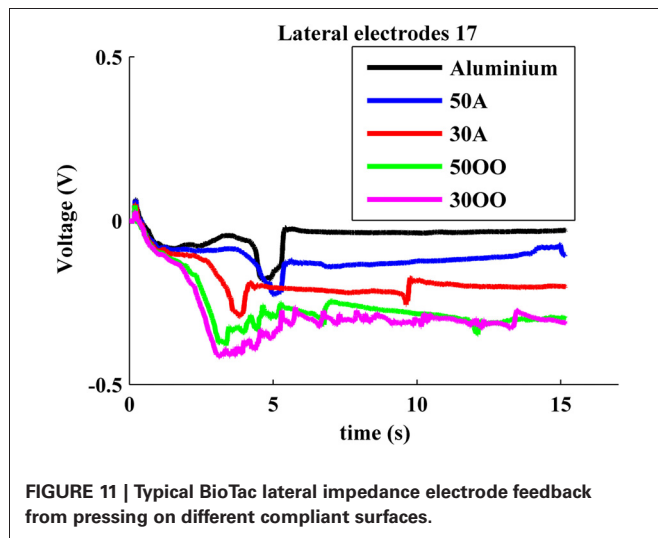
wrist subjected to large external forces from the compressed samples.

### Deformation

In light of the complex combination of factors that contributes to apparent indentation displacement of the fingertip, it would be desirable to use temporal variations of average pressure and spatio-temporal variations of distributed skin deformation, as proposed for human discrimination of hardness by Srinivasan and LaMotte (1995). Both types of tactile information are available from the BioTac. The MEMS pressure transducer measures the average pressure of the fluid inside the space between the elastic skin and rigid core. The spatio-temporal variations of distributed deformation are provided by the impedance electrode array, especially from lateral electrodes adjacent to the central four electrodes used for controlling the applied force.

When the BioTac was pressed against hard materials (e.g., the aluminum plate and shore A 50 and shore A 30 rubber samples),

fluid pressure plateaued or actually declined after normal force reached 2.87 N (around 2 s in **Figure 10**). This saturation is caused by the rigid object pushing the elastic skin against the rigid core on BioTac. The first part of the increasing fluid pressure reflects the compliance of the BioTac skin and fluid pressure, which grows nonlinearly after the skin contacts the core. The curves diverge before that occurs if and when the object compliance exceeds the BioTac compliance. As shown in **Figure 9** (1–2 s), harder objects created a higher rate of average pressure changes in the BioTac. When BioTac pressed objects with softer surface, the soft surface not only pushed the elastic skin against the rigid core more gradually, but also progressively enveloped the side of the BioTac fingertip. This created higher saturation pressures for softer surfaces (around 2–3 s in **Figure 10**).



The tendency of soft surfaces to envelop the fingertip as they are deformed can be seen also in the impedances of more lateral electrodes such as #17 (Figure 11). The BioTac actually measures the current admitted into the electrode from a test pulse applied to various reference electrodes distributed in the fingertip, so a decrease in measured voltage from an initial value reflects an increase in electrode impedance. For the lateral electrode #17, the impedance initially increased similarly for all materials as increasing force was applied at the fingertip and the skin deformed, but the curves diverged as the more compliant materials deformed and enveloped the skin further from the centroid of contact. The reorientation movement that the robot made to correct pitch to maintain normal force (4.5–5 s in Figure 5) resulted in the transients in lateral electrode impedance at that time (Figure 11), which were particularly pronounced for the hard materials. After the robot corrected its orientation and reached its maximum contact force, the resting voltage on the lateral electrode reflected the compliance of the object.

## REFERENCES

- Campos, M., and Bajcsy, R. (1991). "A robotic haptic system architecture," in *Proceedings of the 1991 IEEE International Conference on Robotics and Automation*, (Sacramento, CA), 338–343.
- Fishel, J. A., Santos, V. J., and Loeb, G. E. (2008). "A robust micro-vibration sensor for biomimetic fingertips," in *Proceedings of the IEEE International Conference on Biomedical Robotics and Biomechatronics*, (Scottsdale, AZ), 659–663.
- Katz, D. (1937). Studies on test baking: III. The human factor in test baking: a psychological study. *Cereal Chem.* 14, 382–396.
- LaMotte, R. H. (2000). Softness discrimination with a tool. *J. Neurophysiol.* 83, 1777–1786.
- Lederman, S. J., and Klatzky, R. L. (1987). Hand movements: a window into haptic object recognition. *Cogn. Psychol.* 19, 342–368.
- Lederman, S. J., and Klatzky, R. L. (1990). "Haptic exploration and object representation," in *Vision and Action: The Control of Grasping*, ed M. Goodale (New Jersey, NJ: Ablex), 98–109.
- Lin, C. H., Erickson, T. W., Fishel, J. A., Wettels, N., and Loeb, G. E. (2009). "Signal processing and fabrication of a biomimetic tactile sensor array with thermal, force and microvibration modalities," in *Proceedings of the IEEE International Conference on Robotics and Biomimetics*, (Guilin), 129–134.
- Nakanishi, J., Cory, R., Mistry, M., Peters, J., and Schaal, S. (2008). Operational space control: a theoretical and empirical comparison. *Int. J. Rob. Res.* 27, 737–757.
- Pastor, P., Righetti, L., Kalakrishnan, M., Schaal, S. (2011). "Online movement adaptation based on previous sensor experiences," in *Proceedings of the IEEE/RSJ International Conference on Intelligent Robots and Systems (IROS)*, (San Francisco, CA, USA).
- Peine, W. J. (1999). *Remote Palpation Instruments for Minimally Invasive Surgery*. Ph.D. dissertation, Harvard University, United States. (Dissertations and Theses: A&I database, publication No. AAT 9921526.).
- Srinivasan, M. A., and LaMotte, R. H. (1995). Tactual discrimination of softness. *J. Neurophysiol.* 73, 88–101.
- Takamuku, S., Gómez, G., Hosoda, K., and Pfeifer, E. (2007). "Haptic discrimination of material properties by a robotic hand," in *Proceedings of the 6th IEEE International Conference on Development and Learning*, (London), 1–6.
- Villani, L., Natale, C., Siciliano, B., and de Wit, C. C. (2000). An experimental study of adaptive force/position control algorithms for an industrial robot. *IEEE Trans. Control Syst. Technol.* 8, 777–786.
- Webster, J. G. (1988). *Tactile Sensors for Robotics and Medicine*. New York, NY: John Wiley and Sons.
- Wettels, N., Fishel, J. A., Su, Z., Lin, C. H., and Loeb, G. E. (2009). "Multi-modal synergistic tactile

## DISCUSSION

The tactile sensors available in the BioTac have properties similar to those in human fingertips and can be used to measure compliance of objects, but only if there is accurate control of the exploratory movement. Those same sensors can be used to control the exploratory movements, using tactile feedback control that may also be similar to what humans use when deciding how to palpate an unknown object. The preliminary results presented here are a first step in designing algorithms that can enable robots to produce the range of exploratory movements and the percepts that humans achieve thereby.

In this paper, the BioTac was controlled to explore flat compliant objects. Compliant objects that have curved surfaces or inhomogeneities in material properties will generate different responses in the sensors, whose interpretation may require additional exploratory movements. The tactile-based control of exploratory movements presented here should enable systematic exploration of such unknown objects regardless of their location or orientation with respect to the robot hand.

Systematic datasets need to be generated by poking the BioTac into objects with various curvatures and various compliances to develop a more complete perceptual algorithm. In previous studies, the impedance sensing electrodes of the BioTac could be used to make coarse determinations of radius of curvature of rigid objects (Wettels and Loeb, 2011). Humans tend to follow the contour of objects to perceive their precise shapes (Lederman and Klatzky, 1990). Palpation of hard objects buried in soft tissues probably reflects a combination of tactile-driven movements to determine the orientation of hard surfaces and kinesthesia to keep track of the location and size of those surfaces (Peine, 1999). In the future, we will combine pressing and contour-following exploratory movements to facilitate the perception of both compliance and shape of objects. Eventually, tactile information from exploratory movements must be fused with machine vision to permit location, characterization, identification, and dexterous manipulation of objects in the environment.

- sensing,” in *Tactile Sensing in Humanoids—Tactile Sensors and Beyond Workshop, 9th IEEE-RAS International Conference on Humanoid Robots*. (Paris).
- Wettels, N., and Loeb, G. E. (2011). “Haptic feature extraction from a biomimetic tactile sensor: force, contact location and curvature,” in *IEEE-ROBIO*, (Phuket, Thailand).
- Wettels, N., Santos, V. J., Johansson, R. S., and Loeb, G. E. (2008a). Biomimetic tactile sensor array. *Adv. Robot.* 22, 829–849.
- Wettels, N., Smith, L. M., Santos, V. J., and Loeb, G. E. (2008b). “Deformable skin design to enhance response of a biomimetic tactile sensor,” in *IEEE International Conference on Biomedical Robotics and Biomechanics*, (Scottsdale, AZ), 132–137.
- Yamamoto, T., Vagvolgyi, B., Balaji, K., Whitcomb, L. L., and Okamura, A. M. (2009). “Tissue property estimation and graphical display for teleoperated robot-assisted surgery,” in *IEEE Transactions on Haptics*, (Kobe), 4239–4245.
- Yuan, J. (1988). Closed-loop manipulator control using quaternion feedback. *IEEE J. Rob. Autom.* 4, 434–440.
- Conflict of Interest Statement:** Jeremy A. Fishel and Gerald E. Loeb are equity partners in SynTouch, LLC, which manufactures and sells the BioTac sensors described in this article. Zhe Su and Tomonori Yamamoto have no commercial or financial relationships that could be construed as a potential conflict of interest.
- Received: 20 March 2012; paper pending published: 13 April 2012; accepted: 10 July 2012; published online: 26 July 2012.
- Citation: Su Z, Fishel JA, Yamamoto T and Loeb GE (2012) Use of tactile feedback to control exploratory movements to characterize object compliance. *Front. Neurobot.* 6:7. doi: 10.3389/fnbot.2012.00007
- Copyright © 2012 Su, Fishel, Yamamoto and Loeb. This is an open-access article distributed under the terms of the Creative Commons Attribution License, which permits use, distribution and reproduction in other forums, provided the original authors and source are credited and subject to any copyright notices concerning any third-party graphics etc.



# Texture-induced vibrations in the forearm during tactile exploration

Benoit Delhay<sup>1,2</sup>, Vincent Hayward<sup>3</sup>, Philippe Lefèvre<sup>1,2</sup> and Jean-Louis Thonnard<sup>1\*</sup>

<sup>1</sup> Institute of Neuroscience, Université Catholique de Louvain, Brussels, Belgium

<sup>2</sup> Institute of Information and Communication Technologies, Electronics and Applied Mathematics, Université Catholique de Louvain, Louvain-la-Neuve, Belgium

<sup>3</sup> Institut des Systèmes Intelligents et de Robotique, Université Pierre-et-Marie Curie, Paris, France

## Edited by:

Robyn Grant, University of Sheffield, UK

## Reviewed by:

Irina Skalióra, Biomedical Research Foundation of the Academy of Athens, Greece

Georges Debregeas, Centre National de la Recherche Scientifique, France

## \*Correspondence:

Jean-Louis Thonnard, Institute of Neuroscience, Université Catholique de Louvain, Avenue Mounier 53, bte 53.02, 1200 Brussels, Belgium.  
e-mail: jean-louis.thonnard@uclouvain.be

Humans can detect and discriminate between fine variations of surface roughness using active touch. It is hitherto believed that roughness perception is mediated mostly by cutaneous and subcutaneous afferents located in the fingertips. However, recent findings have shown that following abolishment of cutaneous afferences resulting from trauma or pharmacological intervention, the ability of subjects to discriminate between textures roughness was not significantly altered. These findings suggest that the somatosensory system is able to collect textural information from other sources than fingertip afference. It follows that signals resulting of the interaction of a finger with a rough surface must be transmitted to stimulate receptor populations in regions far away from the contact. This transmission was characterized by measuring in the wrist vibrations originating at the fingertip and thus propagating through the finger, the hand and the wrist during active exploration of textured surfaces. The spectral analysis of the vibrations taking place in the forearm tissues revealed regularities that were correlated with the scanned surface and the speed of exploration. In the case of periodic textures, the vibration signal contained a fundamental frequency component corresponding to the finger velocity divided by the spatial period of the stimulus. This regularity was found for a wide range of textural length scales and scanning velocities. For non-periodic textures, the spectrum of the vibration did not contain obvious features that would enable discrimination between the different stimuli. However, for both periodic and non-periodic stimuli, the intensity of the vibrations could be related to the microgeometry of the scanned surfaces.

**Keywords:** texture, roughness, vibration, touch

## INTRODUCTION

Humans have the ability to detect fine features of textured surfaces and to discriminate between them using *direct, active finger touch* (Katz, 1925/1989; Sathian et al., 1989; Connor et al., 1990; Libouton et al., 2010). During this exploration mode, the tactile roughness discrimination is believed to be mediated through two combined mechanisms. Firstly, a spatial code represents texture information spatially, through the distributed activation of populations of adjacent mechanoreceptors. This channel is thought to rely on slowly adapting (SA1) mechanoreceptors (Connor et al., 1990 and Connor and Johnson, 1992) and the density of the mechanoreceptors naturally limits its resolution. Secondly, a temporal code represents the time-dependent variations of the finger-surface interaction due to their relative movement. Depending on the temporal frequency of the stimulation, either rapidly adapting (RA) or Pacinian (PC) systems are thought to encode these vibrations (Muniak et al., 2007). Textured surfaces can also be felt *indirectly*, namely by actively exploring a surface through a probe being held in the hand (indirect touch) (Klatzky and Lederman, 1999; Yoshioka et al., 2007). During this second scanning mode, roughness is necessarily encoded through vibrations transmitted through the probe to receptors in the hand.

Yoshioka et al. (2007) compared the roughness discrimination during direct and indirect touch exploration of various textured surfaces encountered in daily life (e.g., corduroy, paper, and rubber). The authors found that (1) the roughness discrimination was similar in both scanning modes and (2) the perceived roughness was correlated with the vibratory power measured on the probe. In a more recent study the same group reported that the roughness constancy was preserved in both direct and indirect touch. However, this constancy was not preserved during passive scanning, indicating the importance of hand movement and proprioception (Yoshioka et al., 2011).

Recent findings in direct active finger touch (Libouton et al., 2012) have shown that the tactile roughness discrimination performance was unaffected by entrapment or traumatic section of the median nerve at the wrist. They confirmed this finding in healthy subjects who were given an anesthetic ring bloc and were still capable to perform a tactile roughness discrimination task. The authors concluded that if the innervation of the finger pad was compromised, information about textures could be captured and encoded by remote mechanoreceptors located in more proximal tissues, where the innervation was intact. In this case, they

suggested that the finger might act like a probe, transmitting the vibrations to remote receptors.

The Pacinian afferents are the primary receptors encoding these cutaneous vibrations (Hollins and Bensmaïa, 2007; Johansson and Flanagan, 2009). They are present in the subcutaneous layer of the skin but are also found near tendons, periarticular and interosseus ligaments and muscles (Mountcastle, 2005). The discovery of Hunt (1961) highlighted the existence of very sensitive RA vibration receptors being situated in the interosseus nerve of the hind limb of cats. These receptors that respond to vibrations transmitted through the footpad act “almost like a seismograph.” Hunt (1961) characterized them as Pacinian corpuscles having a very high sensitivity. As a consequence, very small vibrations transmitted through the skin and soft tissues, even applied at a considerable distance, readily evoked vigorous discharges of these Pacinian corpuscles.

The findings of Libouton et al. (2012) may be viewed as an instance of perceptual constancy, that is, subjects with de-afferented extremities tended to maintain a stable perception of roughness in spite of profound changes in the conditions under which it was acquired. Roughness constancy is a remarkably robust phenomenon, it is therefore more informative to identify when constancy breaks down rather than when it occurs. The invariant quantity that is perceived can be represented by a function  $s(x, y)$  that represents the profile of surface. The perceptual task faced by the brain is to acquire specific attributes of  $s$  through a complex transduction process involving tribology, contact mechanics and other physics. For simplicity, and without loss of generality to the foregoing argument, let us consider one dimension only. A contact, then, is represented by an interval,  $\bar{x}$ , that represents the region of contact (which can vary from 1 cm for a bare finger to a few  $\mu\text{m}$  for a sharp probe). During scanning the felt signal is driven by  $s(\bar{x}(t))$  through the physics of the probe-surface interaction. From the chain rule,  $s(\bar{x}(t))$  has a temporal gradient of the form,  $s'(\bar{x}) d\bar{x}/dt = s'(\bar{x}) \bar{v}(t)$ , that is, the product of the surface gradient filtered through the surface contact with the relative velocity of the contact region. This expression, *ceteris paribus*, makes the ambiguous character of the stimulation evident; shifting the spatial spectrum of a surface has the same effect as changing the scanning velocity. The surface spatial gradient *per se*,  $s'(x)$ —available through direct finger contact but not through a probe—varies through time when there is relative movement. It may or it may not participate in the perception of specific attributes of the surface. It is known, however, that the brain can estimate  $\bar{v}$  from this quantity (Essick et al., 1988). To further clarify the quantities involve, let us call  $v$  the surface scanning velocity obtained through limb movement to distinguish it from  $\bar{v}$  acquired through skin afference. Using these definitions, **Table 1** summarizes qualitatively previous behavioral results regarding roughness constancy. All these results are uniformly explained by the brain's ability to learn and maintain time-free representations of surfaces of the form  $s(x)$ , termed *spatiotopic*, accessed through the temporal gradients,  $s'(\bar{x}) v(t)$  or  $s'(\bar{x}) \bar{v}(t)$ , if and only if the scanning velocity is available (cases 6 and 8 in **Table 1**). This observation, when related to the findings of Libouton et al. (2012), motivates the present study aimed at determining how

subjects with de-afferented extremities could have access to  $s'(\bar{x}) v(t)$ .

Taken together these findings suggest that the somatosensory system, provided that sufficient information is available, is able to collect textural information from other sources than fingertip afferences. Vibrations generated during the scanning of textured surfaces were hypothesized to propagate through the finger and the hand, and stimulate receptors populations in regions far away from the contact region. If present in regions that are not affected by the subject trauma or by pharmacological intervention, these vibrations may explain the ability to perceive the main features of textures scanned with a finger, that is, without the benefits of the skin in contact with the surface. Moreover, there is nothing against the possibility of healthy subject to take advantage of this information too.

This hypothesis was tested in the present study by recording the vibrations propagating in the finger, hand, and wrist of subjects during active exploration of textured surfaces with the fingertip. In addition, the spectrum and the magnitude of the measured vibrations taking place in the forearm tissues were analyzed in order to test whether they were correlated to the characteristics of the explored texture surfaces.

## MATERIALS AND METHODS

### SUBJECTS

Six healthy volunteers participated in the study (four males and two females, ranging in age from 25 to 30 years, five over the six subjects were right-handed). They were asked to carefully wash their right hand 10 min before the experiment. All the subjects gave their informed consent and the local ethical committee approved the experimental protocol.

### STIMULI

Periodic and non-periodic rough surfaces were used in the present study for a total of eight different textures. Five periodic stimuli with known spectral characteristics and three sandpapers with ISO scaling of the different roughness levels were compared.

The five different grooved surfaces were made of polyurethane resin. The grating was of periodic square waveform. The spatial period of the waves was chosen between 0.16 mm and 1.6 mm. It is assumed that textures with spatial period under 200  $\mu\text{m}$  need relative movement to be felt (“duplex theory,” Hollins and Risner, 2000 and Hollins and Bensmaïa, 2007). With the chosen range of spatial period, we covered thus the two side of this theory. The profile of the wave form is shown on **Figure 1**. All five samples had the same dimension ratio. Following the classical studies (Taylor and Lederman, 1975), the groove width was three times the ridge width, and was equal to the groove depth. **Table 2** summarizes the geometrical dimensions of the five periodic stimuli.

Three different sandpaper grit sizes (P80, P240, P800) were used with P80 being the coarser and P800 the thinner (see **Table 3**).

### APPARATUS

A force platform was designed in order to securely fix the different stimuli and measure the contact forces (normal and tangential to the surface). A schematic view of the apparatus is shown on

**Table 1 | Tabulation of previous results relating to texture constancy which are all explained by the brain's ability to access specific attributes of the invariant surface descriptor  $s(x)$  through the temporal gradient  $s'(\bar{x}) v(t)$ .**

Study and main condition	Task	Movement generation	Quantities available				Constancy		
			$s'(x(t))$	$s(\bar{x}(t))$	$v(t)$	$\bar{v}(t)$	Case		
Katz (1925/1989), natural surfaces. Lederman (1981) gratings of constant periodicity; bare finger.	Roughness estimation	Self	yes	yes	yes	yes	yes	(1)	
		External	yes	yes	no	yes			
Lamb (1983), Meftah et al. (2000), raised dots constant periodicity, bare finger.	Spatial period discrimination	Self	yes	yes	yes	yes	yes	(2)	
	Roughness estimation	External	yes	yes	no	yes			
Hughes et al. (2007), raised dots with spatial period <i>gradient</i> , bare finger.	Spatial period <i>gradient</i> discrimination	Self	yes	yes	yes	yes	yes	(3)	
Lawrence et al. (2007), gratings of constant periodicity; bare finger, rigid probe.	Roughness estimation	Self	Finger	yes	yes	yes	yes	yes	(4)
			Probe	yes	no	yes	no		
Wiertlewski et al. (2011a), natural surfaces, bare finger via causality inversion.	Identification and spatial period discrimination	Self	yes	no	yes	no	yes	(5)	
		External	yes	no	no	no	no	(6)	
Yoshioka et al. (2011) natural surfaces; bare finger, rigid probe	Roughness estimation	Self	Finger	yes	yes	yes	yes	yes	(7)
			Probe	yes	no	yes	no		
		External	Finger	yes	yes	no	yes	no	(8)
Probe	yes	no	no	no					
Libouton et al. (2012) natural surfaces; de-afferented extremities	Roughness estimation	Self	yes	no	yes	no	yes	(9)	

If  $v(t)$  is inaccessible, constancy breaks down (cases 6, 8).

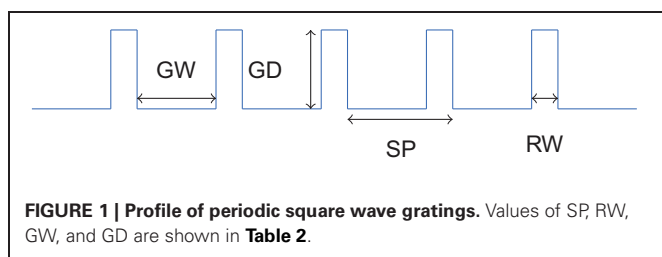


**Table 2 | Set of periodic stimuli used for the experiment: geometrical dimensions of the grooved surfaces made of polyurethane resin.**

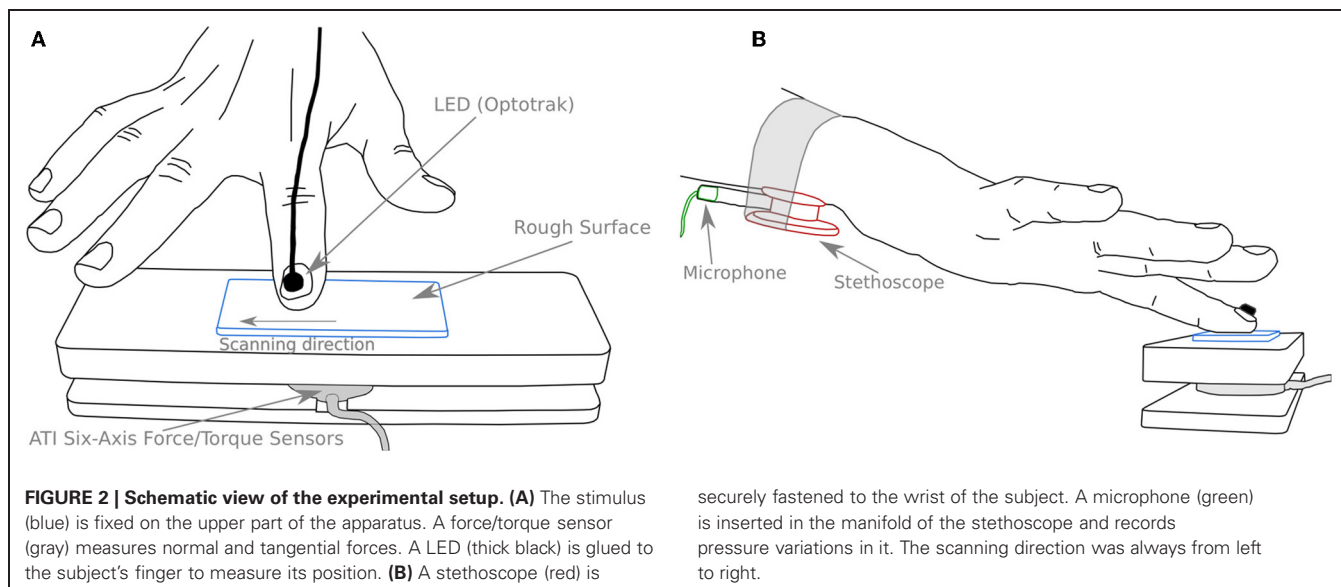
Spatial period (SP = $\lambda$ ) ( $\mu\text{m}$ )	Ridge Width (RW) ( $\mu\text{m}$ )	Groove Width (GW) ( $\mu\text{m}$ )	Groove Depth (GD) ( $\mu\text{m}$ )
P1 160	40	120	120
P2 240	60	180	180
P3 400	100	300	300
P4 800	200	600	600
P5 1600	400	1200	1200

**Figure 2.** A forces and torques transducer (Mini40 F/T transducer, ATI Industrial Automation, NC, USA) was placed between the table and the support in order to measure the normal and tangential force (NF and TF, respectively) applied by the finger

**Table 3 | Set of sandpapers used for the experiment: geometrical properties.**

ISO/FEPA grit designation ( $\mu\text{m}$ )	Average particle diameter	Roughness ( $\mu\text{m}$ )
P800	22	Very fine
P240	58	Medium
P80	201	Coarse

during scanning. The stimuli were fixed in the center of the apparatus (see Figure 2A). The position of the subject's finger was measured by means of an optical tracking system with LED markers bonded to the nail (Optotrak, Northern Digital Inc., Waterloo, Ontario, Canada). The vibrations created by the scanning of the rough surfaces were recorded using a stethoscope (Classic II S.E., 3 M Littmann, Neuss, Germany) with the bell side fastened under the flexor tendons of the wrist, where the best signal could be recorded (see Figure 2B). The pressure variations caused by the normal displacement of the skin under the stethoscope bell was sensed by a high sensitivity microphone (4060 Omnidirectional Hi-Sens, DPA Microphones, Allerød, Denmark) inserted in the manifold of the stethoscope (see Figure 2B). A computer display was placed in front of the subject in order to give him/her a feedback of the NF applied on the rough surface and of the velocity of the finger during the scanning.



## EXPERIMENTAL PROCEDURE

The subject was sitting comfortably in front of the apparatus. He/she was first instructed to perform several scans, from left to right on the textured surface using the right index finger. During these strokes, he/she was asked to maintain the NF and the scanning velocity constant and as close as possible to an instructed value.

Three different NF (1, 2, and 4 N) and three different exploration velocities (50, 100, and 150 mm/s) were instructed (nine different conditions). The forces and velocities were chosen in order to correspond to values adopted naturally during tactile exploration (see Gamzu and Ahissar, 2001; Smith et al., 2002; Libouton et al., 2010; Skedung et al., 2011). Given these scanning velocities, we expected to find the fundamental frequencies for periodic stimuli ranging from 30 Hz to 1 kHz ( $f = v/\lambda$ ). For the sandpapers, the NF was restricted to 1 N because higher forces caused skin irritation. In each condition, a block of acquisition was triggered for 15 sec once the subject was trained thereby capturing from 3 to 10 scanning movements depending on the scanning velocity.

## DATA ACQUISITION

The acquisition was realized using a custom made Labview software. The forces and sound signals were acquired with a digital-to-analog, analog-to-digital data acquisition system (DAQ 6071E, National Instruments, Austin, TX, USA). The sound signal was first amplified (K1803, universal mono preamplifier, Velleman) before being acquired at 20 kHz. The forces and the position of the finger were acquired at a sample frequency of, respectively, 1 kHz and 500 Hz. A trigger signal allowed synchronization of the finger position with the force and sound signals.

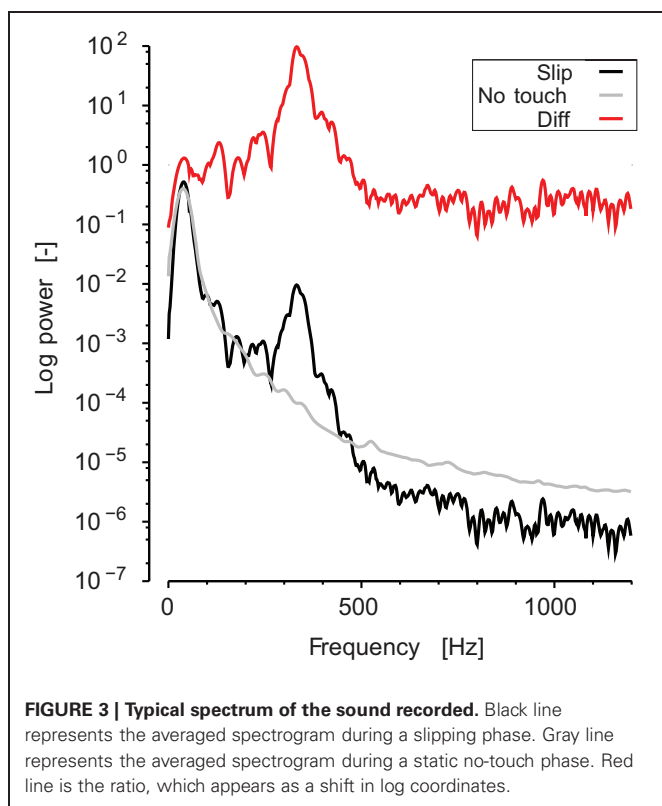
## DATA PROCESSING

The processing was done using a custom made Matlab software. The forces and positions were first low-pass filtered with

a fourth-order, zero phase-lag Butterworth filter with a cutoff frequency at 30 Hz. This frequency was chosen to remove high frequency noise but permitted to keep a high temporal resolution. The sound was high-pass filtered (fourth order, zero-lag Butterworth) with a cutoff frequency of 25 Hz in order to remove DC component and low-frequency physiological artifacts (heart-beat, muscles contractions). The speed and acceleration along the scanning direction were derived from the position of the finger.

From each block of trials, we retained the three strokes that best complied with the following three conditions. The NF applied had to be in the range of the targeted force  $\pm 30\%$ . There was no stick and slip during the movement (a stick and slip was detected by the presence of high peaks in the acceleration profile). The speed had to be maintained approximately constant for a range of 12 mm. The mean NF and TF, the mean coefficient of dynamic friction,  $\mu = TF/NF$ , and the mean scanning velocity were then computed for each stroke. Due to the variability of the velocity adopted by each subject, we then separated all strokes into two velocity categories. The first category was ranging from 30 to 120 mm/s and the second was ranging from 120 to 250 mm/s. An estimate of the vibrations power was obtained by computing the root mean square (RMS) of the sound magnitude for each stroke.

The analysis of the vibrations frequency content recorded at the wrist was conducted as follows. First, the short time Fourier transform (i.e., the spectrogram,  $\Phi$ ) of the sound was computed for each stroke. The width of the short-time window was 50 ms and the overlap was 45 ms (thus, a spectrum vector was computed every 5 ms). The frequency range was defined from 30 Hz to 1200 Hz. Using the same short-time windows, we computed the spectrogram of the sound during static and no contact periods for each block. This spectrum was averaged over time, and then subtracted from each stroke spectrogram in order to extract the signal due to the stroke itself for each trial (see **Figure 3**).



Second, we estimated the peak of intensity in each window of the spectrogram and extracted its corresponding frequency.

For periodic stimuli, the energy was expected to be precisely located at the mechanical fundamental frequency,  $f_0 = v/\lambda_0$ . The frequency of the peak in the spectrum was simply computed at each instant ( $t_i$ ) from,

$$f_p(t_i) = \arg \max_f (\Phi(t_i, f)). \quad (1)$$

The spatial period of the surface explored was estimated by computing the ratio between the scanning velocity and the frequency of the peak in the spectrum,

$$\hat{\lambda} = \frac{v}{f_p}. \quad (2)$$

For non-periodic stimuli, no precise peak of intensity was expected. In order to get an estimation of the centroid of energy in the spectrogram, we computed the median frequency of the spectrum,

$$\text{such that } \sum_{f=30}^{f_p(t_i)} \Phi(t_i, f)^2 = \sum_{f=f_p(t_i)}^{1200} \Phi(t_i, f)^2, \quad (3)$$

and the estimate of the spatial periodicity of the surface was computed in the same way as for the periodic stimuli.

## RESULTS

### TYPICAL TRIALS

Two typical traces are shown in **Figure 4**. They illustrate the temporal evolution of the measured variables during the scanning of periodic grating (**A**) and sandpaper (**B**). The target NF was 2 N for the periodic grating and 1 N for the sandpaper. The target scanning velocity was 150 mm/s for both. The upper panel shows the evolution of the NF (black line) and the TF (gray line). The central panel reports the finger scanning velocity. The lower panel shows the spectrogram of the sound recorded at the subject wrist. The subject touched the surface and adjusted the NF while progressively increasing the TF. Once the ratio TF/NF reached the static coefficient of friction, the finger started to slip at a nearly constant velocity. During the slip phase (gray box), vibrations propagated through the finger and hand tissues up to the wrist. For the periodic stimuli (see **Figure 4A**), the energy of the spectrum was concentrated around the fundamental frequency  $f_0 = v/\lambda_0$  and there was energy in the harmonics also. For sandpaper (**Figure 4B**), the energy of the spectrum is spread over a very wide range during the whole slip. One can notice that at the beginning of the slip, there is a high peak of sound intensity, which is spread over a wide range of frequencies in both conditions.

### SPECTRAL ANALYSIS

The peak intensity frequencies ( $f_p$ ) are plotted as a function of velocity for subject S3 (**Figure 5**). Each color corresponds to a different periodic stimulus. The thick line represents theoretical fundamental,  $\lambda_0 = v/f_0$ , and data points are  $f_p$  values computed for each window in the short time Fourier transform. Most of the points are found around the fundamental frequency and  $f_p$  was found correlated with the spatial periodicity of the stimuli up to 1.2 kHz. These results confirm the presence of vibrations correlated with the spatial periodicity of the stimuli and the scanning velocity.

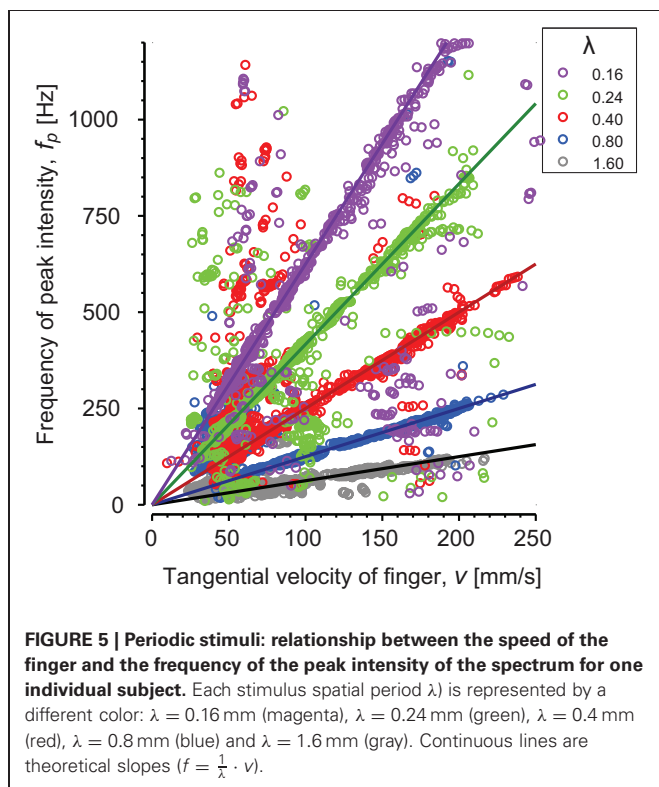
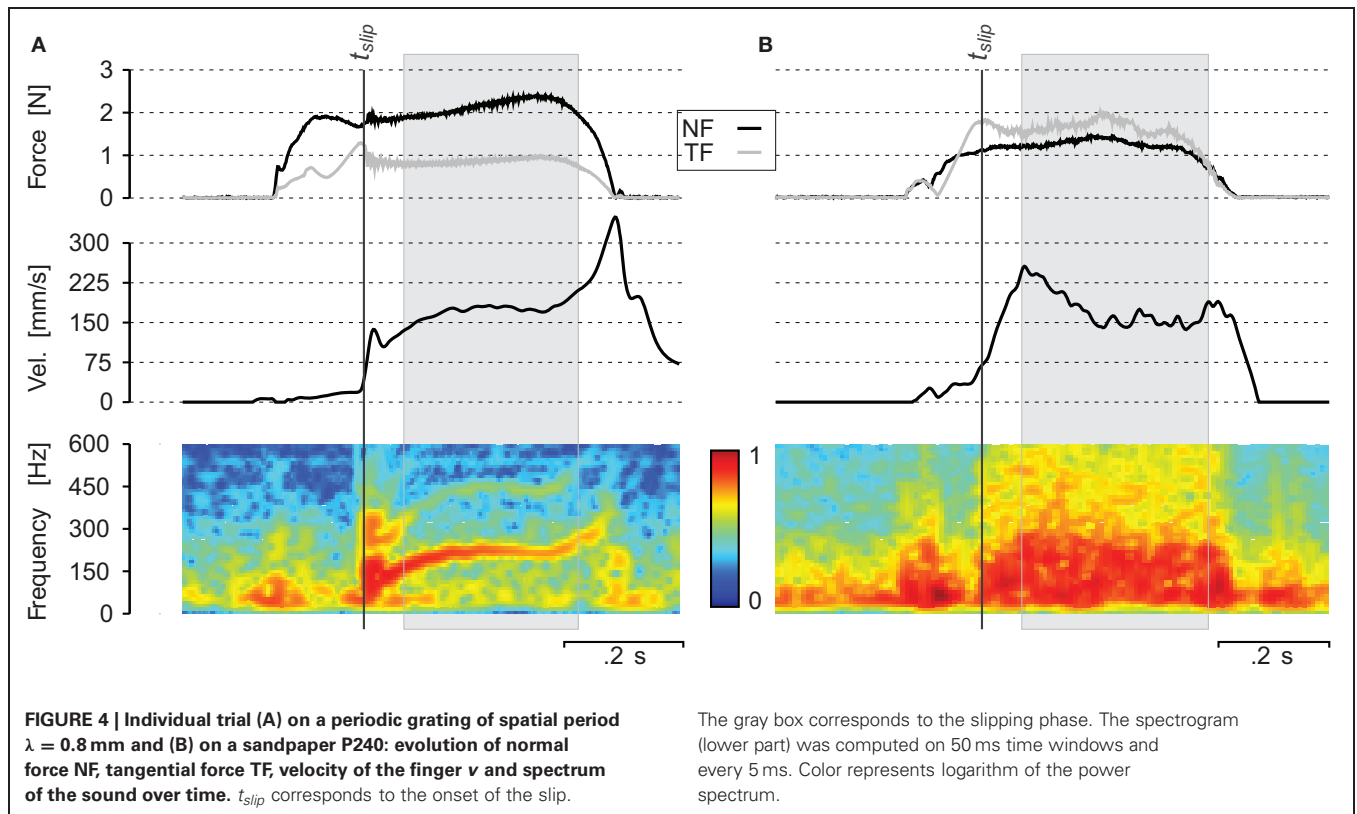
The histograms of spatial period estimates are plotted on **Figure 6** for all trials (six subjects, three NF and two velocities) performed with the five different stimuli ( $0.16 \text{ mm} < \lambda < 1.60 \text{ mm}$ ). The dashed lines are aligned on the actual spatial period of each stimulus. It can be clearly seen that the principal mode of the estimate of the spatial period for each surface is aligned on the actual spatial period. For some trials,  $\hat{\lambda}$  was also found on the second, third or next harmonics (see **Figures 6C** and **D**). The principal modes observed for each stimulus and the numbers of observations are summarized in **Table 4**.

Spectral information related to sandpapers is summarized in **Table 4**. In contrast with the periodic stimuli, the identified spatial period varied much more within the same sandpaper grit size. Furthermore, there was no significant difference in the principal mode observed between the different grit sizes.

From the spectrum analysis, we could thus extract relevant information for the discrimination of periodic stimuli but not for sandpaper.

### VIBRATION MAGNITUDE

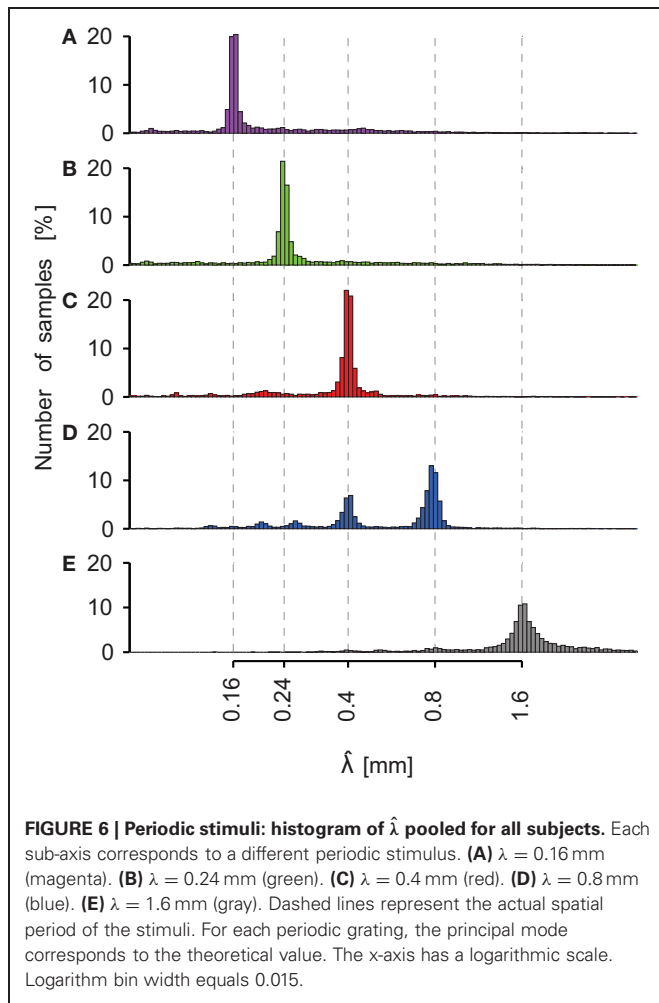
The RMS intensity of the sound was computed for each stroke. This parameter was computed as an indicator of the vibration magnitude transmitted up to the wrist. Assuming that the cavity



pressure is uniform (the wave length of the vibrations is more than 30 cm at 1 kHz), the skin average displacement over the surface of the belt aperture was of the order of  $0.3 \mu\text{m}$  (see **Table 5**). For periodic stimuli, a two ways ANOVA (no interaction term) revealed a significant effect of NF ( $p < 0.001$ ) but not of velocity on the vibrations magnitude. The larger the force, the more intense was the vibration. A linear regression revealed a significant slope of 0.13 of the logarithm of intensity as a function of the NF. For sandpapers, we found no effect of velocity.

The logarithm of the intensity is plotted on **Figure 7** as a function of the five stimuli's spatial period (**A–C**) and the three sandpaper's grit size (**B–D**). The range of RMS values varied a lot across subjects. Before pooling the data of all subjects, the data of each individual were normalized with respect to a specific condition:  $\lambda = 0.4$ , NF = 2 N and  $v = 100$  mm/s for periodic stimuli and P240, NF = 1 N and  $v = 100$  mm/s for sandpapers. Normalization factors are shown in **Table 5** for each subject.

**Figure 7** presents data for all speeds and forces pooled together in black lines. The effect of NF (**Figures 7A,B**) and finger velocity (**Figures 7C,D**) is shown in colored lines. For periodic stimuli, the logarithm of the RMS magnitude increased linearly with the logarithm of the spatial period (slope = 0.24,  $p < 0.001$ , all forces pooled). The slope was significant for each level of force separately ( $p = 0.029$ ,  $p < 0.001$ , and  $p = 0.003$  for NF equal to 1, 2, and 4 N, respectively). There was a significant pair wise difference



between each of P1-P2-P3 and P5 ( $p < 0.05$ , Tukey's test) and between P1 and P4 ( $p < 0.05$ , Tukey's test).

For sandpapers (**Figure 7B**), the grit size induced a significant increase of the vibration RMS ( $p < 0.05$ ).

**COEFFICIENT OF FRICTION**

The coefficient of dynamic friction is plotted on **Figure 8** as a function of the five stimuli's spatial period **(A)** and the three sandpaper's grit size **(B)**. For the periodic stimuli the coefficient of friction was small (around 0.5) and constant across the different stimuli ( $p = 0.86$ ).

The dynamic friction was much higher for the sandpapers, ranging from 0.9 for P800 to 1.3 for P80. We found a significant pair wise difference between P80 and P800 ( $p = 0.04$ , Tukey's test).

**DISCUSSION**

Libouton et al. (2012) suggested that the somatosensory system was able to collect roughness from other sources of information than fingertip afferences. The authors highlighted that the tactile roughness discrimination performance was unaffected by entrapment or traumatic section of the median nerve at the wrist. As a consequence, they concluded that, if the innervation of the finger pad was compromised, information about textures could be captured and encoded by remote mechanoreceptors located in more proximal tissues where the innervation was intact. We attempted to explain the mechanism through which humans can detect textured surfaces and discriminate between them when the innervation of the finger pad is radically compromised.

To this end, we recorded vibrations in the range from 30 Hz upto 1.2 kHz taking place in subjects' wrist tissues while they explored textured surfaces. Our results demonstrate the propagation of vibratory waves produced by the finger pad interaction

**Table 4 | Principal modes for the estimate of spatial period  $\hat{\lambda}$  for periodic and non-periodic stimuli.**

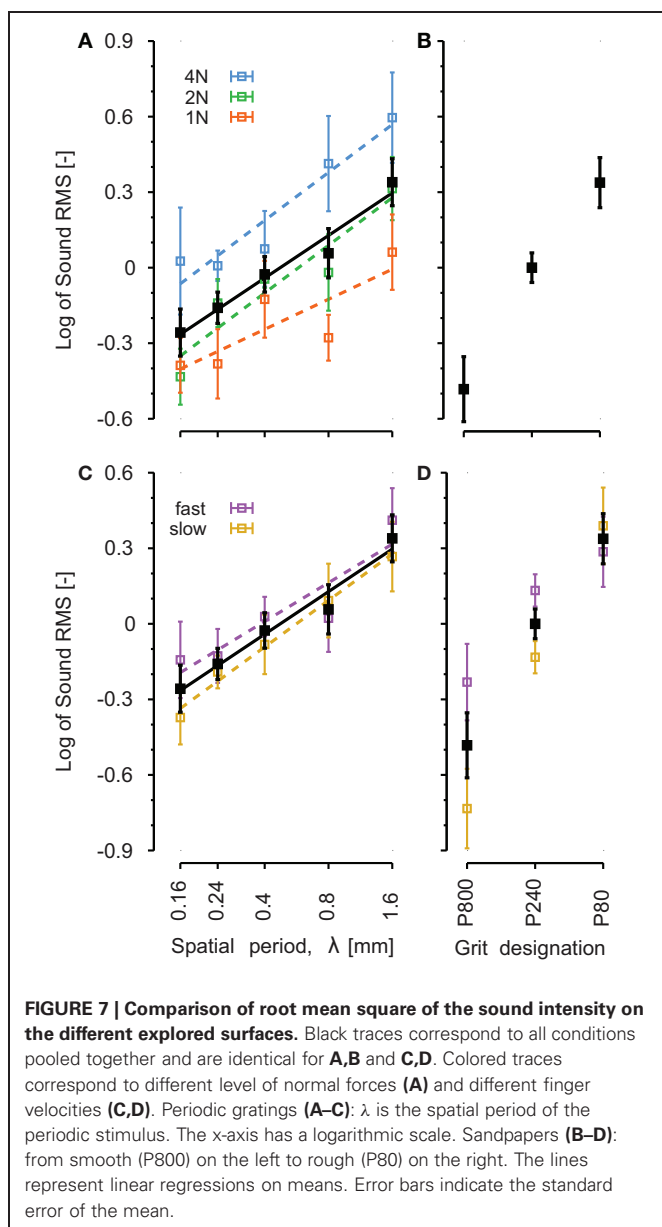
	Periodic gratings					Sandpapers		
	P1	P2	P3	P4	P5	P800	P240	P80
Principal mode (mm)	0.163	0.237	0.394	0.804	1.64	0.269	0.288	0.279
Percentage of observations (%)	57.49	59.78	68.02	49.42	59.73			

The percentage of observations corresponds to the fraction of the observations that have a spatial period within  $\pm 20\%$  of the spatial period of the stimuli.

**Table 5 | Normalization factors for pressure variation and skin displacement for each subject (corresponding to 0 in the log scale of Figure 7).**

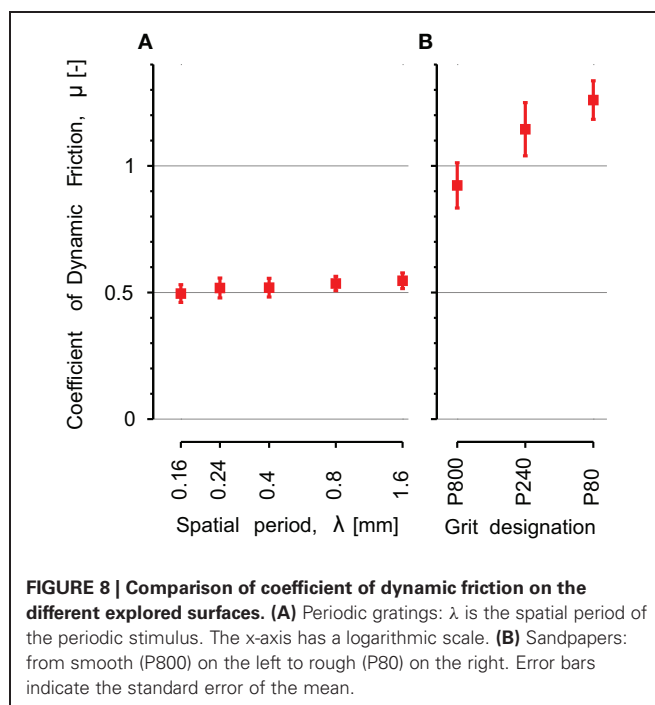
	S1	S2	S3	S4	S5	S6
<b>GRATINGS</b>						
Pressure variation (Pa)	2.52	2.78	0.47	2.00	1.63	1.12
Skin displacement ( $\mu\text{m}$ )	0.35	0.39	0.06	0.28	0.23	0.16
<b>SANDPAPER</b>						
Pressure variation (Pa)	3.18	2.37	3.08	1.99	2.06	2.38
Skin displacement ( $\mu\text{m}$ )	0.44	0.33	0.43	0.28	0.29	0.33

The skin displacement was computed according to  $\partial V = -\beta V \partial p$ , with  $\beta$  being the air compressibility,  $V$  the belt volume and  $p$  the pressure. We considered the stethoscope belt as a cylinder, and the skin acting like a piston.



with a textured surface to at least the wrist regions. We found that the vibration spectral energy was located on the fundamental frequency plus harmonics for periodic stimuli. This frequency, together with the fingertip velocity, corresponded to the spatial period of the stimulus. We did not find any obvious features that could reflect the grit size in the spectra for sandpapers. We also found that the coefficient of dynamic friction varied according to the sandpapers' grit sizes but remained constant across the different polyurethane gratings. These results corroborate the findings of Wiertelowski et al. (2011b) who measured the vibrations taking place at the finger-surface interface and found that the transformation of the surface geometry into vibrations was strongly non-linear, causing both frequency spread and background noise.

The present results show that the biomechanics of hand tissues can transmit surface interaction signals far away from the contact, up to the forearm, and probably much beyond. The



likely mechanical paths are bone conduction (Corso, 1963), tendon conduction (Pourcelot et al., 2005), surface Rayleigh waves (Liang and Boppart, 2010), shear waves in the bulk (von Gierke et al., 1951); or a combination thereof. Our results establish the possibility for the somatosensory system to combine information from multiple modalities and from distributed locations in order to assess properties of the characteristics of an unknown texture, using the fingertips as a distant probe and through a variety of different mechanisms yet to be described.

When rubbing a finger against sand paper, the spatial periodicity of the vibration signal in the wrist was in the range of the fingerprint periodicity, i.e., near 0.3 mm (see **Table 4**), suggesting that the fingerprints could make a spectral selection due to their intrinsic periodicity (Martinot, 2006; Prevost et al., 2009; Scheibert et al., 2009). For the periodic stimuli, some estimates of the spatial period were around 0.4 mm, especially for 0.8 mm gratings (see **Figure 4D**), which could also be linked to the fingerprint periodicity although a more likely explanation is simply a frequency doubling effect in a preferred range due to the presence of two edges per period of the stimulus.

It was hypothesized that the Pacinian channel could encode vibratory intensity (Hollins and Bensmaïa, 2007). This population of receptors is indeed a good candidate to encode scanned textures through remotely transmitted signals. Moreover, the exquisite sensitivity of the Pacinian corpuscle makes them good candidates for picking up signals having travelled over considerable distances (Hunt, 1961), see Hamann (1995) for a review. Significant vibrations in the wrist imply that, in healthy subjects, very large populations of receptors can be stimulated throughout the hand and the arm.

In the present study we have demonstrated that vibrations generated during the scanning of textured surfaces propagate through the finger and hand and stimulate receptor populations

in regions far away from the contact region at least up to the wrist. The spectrum and the magnitude of the measured vibrations have to be considered as the best predictors of roughness discrimination. These findings have important implications in providing realistic sensory feedback for prosthetic-hand users. Indeed, it suggests that advanced prosthetic arms, equipped with sensory feedback, could partially restore the tactile sensation of amputees, through the activation of the remote mechanoreceptive system. Therefore, the transmission and reception of vibratory stimuli related to texture to the remaining stump becomes a major priority in the conception of future prosthetic hands.

## CONCLUSION

We showed the presence of high frequency vibrations in the wrist of subjects exploring rough surfaces. The vibratory power is the best predictor of the texture roughness sensed remotely. It accounts for both periodic and non-periodic surfaces, with very different frictional properties. This result is consistent with perceptual studies carried on either with fingertip touch or with

probe scanning. Moreover, we showed that the frequency content of periodic stimuli contained also potential information to encode roughness. Thus, many questions remain unclear about the contribution of the spectral content of the vibrations in the perceived roughness. Finally, friction may contribute to refine perception of roughness.

## ACKNOWLEDGMENTS

The authors would like to thank the subjects for their kind participation, Simon Johnson and Bill Ranken from Unilever R&D Port Sunlight for providing the gratings, Vincent Théate for his technical support and Anne Klöcker for revision of the manuscript. This research was supported by a grant from Prodex, ESA (European Space Agency), PAI, FNRS, FRSM, ARC (BELGIUM), and a grant from the Commission of the European Union under Contract N° EU-FP7-NMP4-SL-2009-228844, NanoBioTouch. Additional funding was from the European Research Council, Advanced Grant PATCH, agreement No. 247300 awarded to Vincent Hayward.

## REFERENCES

- Connor, C. E., Hsiao, S. S., Phillips, J. R., and Johnson, K. O. (1990). Tactile roughness: neural codes that account for psychophysical magnitude estimates. *J. Neurosci.* 10, 3823–3836.
- Connor, C. E., and Johnson, K. O. (1992). Neural coding of tactile texture: comparison of spatial and temporal mechanisms for roughness perception. *J. Neurosci.* 12, 3414–3426.
- Corso, J. F. (1963). Bone-conduction thresholds for sonic and ultrasonic frequencies. *J. Acoust. Soc. Am.* 35, 1738–1743.
- Essick, G. K., Franzen, O., and Whitsel, B. L. (1988). Discrimination and scaling of velocity of stimulus motion across the skin. *Somatosens. Mot. Res.* 6, 21–40.
- Gamzu, E., and Ahissar, E. (2001). Importance of temporal cues for tactile spatial-frequency discrimination. *J. Neurosci.* 21, 7416–7427.
- Hamann, W. (1995). Mammalian cutaneous mechanoreceptors. *Prog. Biophys. Mol. Biol.* 64, 81–104.
- Hollins, M., and Bensmaïa, S. J. (2007). The coding of roughness. *Can. J. Exp. Psychol.* 61, 184–195.
- Hollins, M., and Risner, S. R. (2000). Evidence for the duplex theory of tactile texture perception. *Percept. Psychophys.* 62, 695–705.
- Hughes, B., Wang, J., Rosic, D., and Palmer, K. (2007). “Texture gradients and perceptual constancy under haptic exploration,” in *Second Joint EuroHaptics Conference and Symposium on Haptic Interfaces for Virtual Environment and Teleoperator Systems. World Haptics 2007*, (Tsukuba, Japan: IEEE), 66–71.
- Hunt, C. C. (1961). On the nature of vibration receptors in the hind limb of the cat. *J. Physiol.* 155, 175–186.
- Johansson, R. S., and Flanagan, J. R. (2009). Coding and use of tactile signals from the fingertips in object manipulation tasks. *Nat. Rev. Neurosci.* 10, 345–359.
- Katz, D. (1925/1989). *The world of touch*, ed L. E., Krueger, Trans. Hillsdale, NJ: Erlbaum [Original work published in 1925].
- Klatzky, R. L., and Lederman, S. J. (1999). Tactile roughness perception with a rigid link interposed between skin and surface. *Percept. Psychophys.* 61, 591–607.
- Lamb, G. D. (1983). Tactile discrimination of textured surfaces: psychophysical performance measurements in humans. *J. Physiol.* 338, 551–565.
- Lawrence, M. A., Kitada, R., Klatzky, R. L., and Lederman, S. J. (2007). Haptic roughness perception of linear gratings via bare finger or rigid probe. *Perception* 36, 547–557.
- Lederman, S. J. (1974). Tactile roughness of grooved surfaces: the touching process and effects of macro- and microsurface structure. *Percept. Psychophys.* 16, 385–395.
- Lederman, S. J. (1981). The perception of surface roughness by active and passive touch. *Bull. Psychon. Soc.* 18, 253–255.
- Liang, X., and Boppart, S. A. (2010). Biomechanical properties of *in vivo* human skin from dynamic optical coherence elastography. *IEEE Trans. Biomed. Eng.* 57, 953–959.
- Libouton, X., Barbier, O., Berger, Y., Plaghki, L., and Thonnard, J.-L. (2012). Tactile roughness discrimination of the finger pad relies primarily on vibration sensitive afferents not necessarily located in the hand. *Behav. Brain Res.* 229, 273–279.
- Libouton, X., Barbier, O., Plaghki, L., and Thonnard, J.-L. (2010). Tactile roughness discrimination threshold is unrelated to tactile spatial acuity. *Behav. Brain Res.* 208, 473–478.
- Martinot, F. (2006). *Caractérisation du Rôle de la Dynamique du Toucher Dans la Perception de Textures*. Ph.D. thesis, Université des Sciences et Technologies de Lille, Lille.
- Meftah, E. M., Belingard, L., and Chapman, C. E. (2000). Relative effects of the spatial and temporal characteristics of scanned surfaces on human perception of tactile roughness using passive touch. *Exp. Brain Res.* 132, 351–361.
- Mountcastle, V. B. (2005). *The Sensory Hand. Neural Mechanisms in Somatic Sensation*. London, England and Cambridge, MA: Harvard University Press.
- Muniak, M. A., Ray, S., Hsiao, S. S., Dammann, J. F., and Bensmaïa, S. J. (2007). The neural coding of stimulus intensity: linking the population response of mechanoreceptive afferents with psychophysical behavior. *J. Neurosci.* 27, 11687–11699.
- Pourcelot, P., Defontaine, M., Ravarya, B., Lematre, M., and Crevier-Denoix, N. (2005). A non-invasive method of tendon force measurement. *J. Biomech.* 38, 2124–2129.
- Prevost, A., Scheibert, J., and Debrégeas, G. (2009). Effect of fingerprints orientation on skin vibrations during tactile exploration of textured surfaces. *Commun. Integr. Biol.* 2, 422–424.
- Sathian, K., Goodwin, A. W., John, K. T., and Darian-Smith, I. (1989). Perceived roughness of a grating: correlation with responses of mechanoreceptive afferents innervating the monkey's fingerpad. *J. Neurosci.* 9, 1273–1279.
- Scheibert, J., Leurent, S., Prevost, A., and Debrégeas, G. (2009). The role of fingerprints in the coding of tactile information probed with a biomimetic sensor. *Science* 323, 1503–1506.
- Skedung, L., Danerlöv, K., Olofsson, U., Michael Johansson, C., Aikala, M., Kettle, J., Arvidsson, M., Berglund, B., and Mark Rutland, W. (2011). Tactile perception: finger friction, surface roughness and perceived coarseness. *Tribol. Int.* 44, 505–512.
- Smith, A. M., Chapman, C. E., Deslandes, M., Langlais, J.-S., and Thibodeau, M.-P. (2002). Role of friction and tangential force variation in the subjective scaling of tactile roughness. *Exp. Brain Res.* 144, 211–223.
- Taylor, M. M., and Lederman, S. J. (1975). Tactile roughness of grooved surfaces: a model and the effect of friction. *Percept. Psychophys.* 17, 23–36.
- von Gierke, H. E., Oestreicher, H. L., Franke, E. K., Parrack, H. O., and von Wittern, W. W. (1951). Physics of vibrations in living tissues. *J. Appl. Physiol.* 4, 886–900.

- Wiertlewski, M., Lozada, J., and Hayward, V. (2011a). The spatial spectrum of tangential skin displacement can encode tactual texture. *IEEE Trans. Rob.* 27, 461–472.
- Wiertlewski, M., Hudin, C., and Hayward, V. (2011b). “On the 1/f noise and non-integer harmonic decay of the interaction of a finger sliding on flat and sinusoidal surfaces,” in *World Haptics Conference (WHC), 2011*, (Istanbul, Turkey: IEEE), 25–30.
- Yoshioka, T., Bensmaïa, S. J., Craig, J. C., and Hsiao, S. S. (2007). Texture perception through direct and indirect touch: an analysis of perceptual space for tactile textures in two modes of exploration. *Somatosens. Mot. Res.* 24, 53–70.
- Yoshioka, T., Craig, J. C., Beck, G. C., and Hsiao, S. S. (2011). Perceptual constancy of texture roughness in the tactile system. *J. Neurosci.* 31, 17603–17611.
- Conflict of Interest Statement:** The authors declare that the research was conducted in the absence of any commercial or financial relationships that could be construed as a potential conflict of interest.
- Received: 28 March 2012; paper pending published: 16 April 2012; accepted: 19 June 2012; published online: 06 July 2012.*
- Citation: Delhaye B, Hayward V, Lefèvre P and Thonnard J-L (2012) Texture-induced vibrations in the forearm during tactile exploration. Front. Behav. Neurosci. 6:37. doi: 10.3389/fnbeh.2012.00037*
- Copyright © 2012 Delhaye, Hayward, Lefèvre and Thonnard. This is an open-access article distributed under the terms of the Creative Commons Attribution License, which permits use, distribution and reproduction in other forums, provided the original authors and source are credited and subject to any copyright notices concerning any third-party graphics etc.



# Rasch-built measure of pleasant touch through active fingertip explorations

Anne Klöcker<sup>1</sup>, Carlyne Arnould<sup>2</sup>, Massimo Penta<sup>1</sup> and Jean-Louis Thonnard<sup>1\*</sup>

<sup>1</sup> Institute of Neuroscience, Université Catholique de Louvain, Brussels, Belgium

<sup>2</sup> Department of Occupational Therapy, Paramedical Category, Haute Ecole Louvain en Hainaut, Montignies-sur-Sambre, Belgium

## Edited by:

Pavel M. Itskov, Champalimaud Foundation, Portugal

## Reviewed by:

Helena Backlund Wasling, Gothenburg University, Sweden  
Ekaterina Vinnik, Champalimaud Foundation, Portugal

## \*Correspondence:

Jean-Louis Thonnard, Institute of Neuroscience, Université Catholique de Louvain, Tour Pasteur, 53 Avenue Mounier (B1.53.04), 1200 Brussels, Belgium.  
e-mail: jean-louis.thonnard@uclouvain.be

**Background:** Evidence suggests that somatic sensation has a modality for pleasant touch. **Objective:** To investigate pleasant touch at the fingertip level (i.e., glabrous skin site) through the elaboration of a linear unidimensional scale that measures (i) various materials according to the level of pleasantness they elicit through active fingertip explorations and (ii) subjects according to their pleasantness leniency levels. **Subjects:** We enrolled 198 healthy subjects without any neurological disease. **Methods:** Blindfolded subjects actively explored 48 materials with their index fingertips and reported the perceived pleasantness of each on a 4-level scale. The fingertip moisture levels on each subject were measured before the experimental session. Data were analyzed using the Rasch model. **Results:** We elaborated unidimensional linear scale that included 37 materials according to their pleasantness of touch. The pleasantness level of 21 materials was perceived differently, depending on the fingertip moisture levels of the subjects. **Conclusion:** Based on our findings, we formulated a *Pleasant Touch Scale*. Fingertip moisture levels appeared to be a major factor for (un)pleasant feelings during active exploration.

**Keywords:** active touch, pleasantness, Rasch model, latent variable measurement, friction, moisture

## INTRODUCTION

The hand is the key organ of the sense of touch (Lundborg, 2005), making sensation fundamental to hand function. Four major modalities of somatic sensation have been described: (i) discriminative touch, (ii) proprioception, (iii) nociception, and (iv) temperature sense (Lundborg, 2005), although studies over the last decade have suggested the existence of a supplementary modality, namely *pleasant touch* (Johansson et al., 1988; Nordin, 1990; McGlone et al., 2007; McGlone and Reilly, 2010).

Studies investigating pleasant touch at hairy skin sites have suggested that C-tactile nerve fibers (CT-fibers) play a fundamental role in the detection and transmission of pleasant stimuli applied to the skin (Olausson et al., 2002, 2010; McGlone et al., 2007; Essick et al., 2010; Morrison et al., 2011). These CT-fibers were identified during microneurography recordings from infra- and supraorbital nerves (Johansson et al., 1988; Nordin, 1990). CT-fibers were later observed in other hairy skin areas, such as the arm (Vallbo et al., 1999). However, they seem to be missing from glabrous skin sites, such as the fingertips (McGlone and Reilly, 2010; Olausson et al., 2010). Studies investigating pleasant touch at glabrous skin sites frequently used either magnitude estimation (ME) or categorical rating procedures. The results of such studies suggested that soft and smooth materials were perceived as more pleasant than rough materials (Major, 1895; Ripin and Lazarsfeld, 1937; Ekman et al., 1965; Verrillo et al., 1999).

Pleasant touch may be described as a positive sensation induced by cutaneous stimulation. Hence, pleasant touch cannot be directly observed or measured and may be regarded as a *latent variable* rather than an observable variable. Observable variables can be directly quantified and typically generate linear measures (e.g.,

the grain size of sandpapers can be measured in micrometers). Latent variables can only be measured indirectly (e.g., pain, intelligence, or pleasant touch), generally by using a questionnaire or a set of stimuli (Thurstone, 1928; Rasch, 1960; Tesio et al., 2007). Questionnaires usually provide ordinal scores, rather than linear scores, with no constant unit. For example, pleasant touch could be assessed by presenting various stimuli to a subject and asking the subject to rate these stimuli on the basis of a 4-level response scale, e.g., “very unpleasant” (scored 0), “unpleasant” (scored 1), “pleasant” (scored 2), and “very pleasant” (scored 3). Two major issues would, however, prevent the widespread uniform use of numbers resulting from such a response scale. First, the scores would be ordinal, meaning that equal differences (e.g., from scores of 0–1 and 2–3) would not necessarily represent the same change/quantity of pleasant touch. Second, the scores attributed to the stimuli would not necessarily be unidimensional; thus, adding these individual scores may result in a total score that conceals numerous unrelated dimensions (e.g., color, hardness, roughness, temperature, mental representation). As a consequence, quantitative comparisons of these ordinal scores are not possible (Merbitz et al., 1989; Wright and Linacre, 1989). Nevertheless, probabilistic measurement models can be used to determine linear and unidimensional measures from ordinal scores, the most promising being the Rasch model (Rasch, 1960). The Rasch model is a prescriptive model, rather than a descriptive one, requiring that solely the location of the item (e.g., the amount of pleasantness elicited by a stimulus) and the ability of a subject (e.g., the “satisfaction level” induced by perception of a stimulus) determine the probabilities of category choices on the response scale. When applied to pleasant touch, this measurement framework can be

used to construct a linear and unidimensional *Pleasant Touch Scale* assessing (i) each stimulus according to its level of pleasantness and (ii) each subject according to his/her leniency level, defined as a subject's "satisfaction level" induced by perception of the stimulus.

The aim of this study was to investigate pleasant touch at a glabrous skin site through the elaboration of a gradual hierarchy of stimuli eliciting pleasant touch (i.e., the *Pleasant Touch Scale*). This unidimensional linear scale was designed (i) to quantify the pleasantness level elicited by various materials during direct active fingertip explorations and to grade these materials by pleasantness level and (ii) to quantify the pleasantness leniency level of subjects and to grade them by pleasantness leniency level. The elaboration of such a *Pleasant Touch Scale* may contribute to knowledge of pleasant touch at glabrous skin sites. Indeed, the *quantitative* information obtained by this scale may provide objective insight of the characteristics (of subjects and/or materials) that influence pleasant touch. Consequently, future research on pleasant touch may refer to such scale and specifically examine the characteristics that influence pleasantness or unpleasantness.

## MATERIALS AND METHODS

The present study was approved by the Biomedical Ethical Commission of the Faculty of Medicine of the Université catholique de Louvain.

### SUBJECTS

We enrolled 198 healthy subjects, 74 males and 124 females, aged between 20 and 70 (mean age,  $39.5 \pm 13.4$  years).

### INSTRUMENT

To elaborate the *Pleasant Touch Scale*, we selected 48 materials, encountered in everyday life, based on three perceptual tactile dimensions (i.e., hard vs. soft, rough vs. smooth, and sticky vs. slippery; Hollins et al., 1993, 2000; Yoshioka et al., 2007). Of these 48 stimuli, 26 had been used in studies dealing with the discriminative aspect of touch (Major, 1895; Hollins et al., 1993, 2000; Bergmann Tiest and Kappers, 2006; Yoshioka et al., 2007; Yoshioka and Zhou, 2009). The remaining 22 materials included everyday life materials such as baking paper, cast, cling film, and tights. Each selected material was glued onto an aluminum plate, 77 mm long and 32 mm wide.

### PROCEDURE

Before each experiment, the index fingertip moisture level of each subject was measured using the Corneometer®CM 825. The subjects were blindfolded, and each of the 48 materials was placed in random order in front of the subjects. The subjects were instructed to place the pulp of their dominant index finger on the selected material and to explore its surface through slow lateral sliding movements. No specific instructions on the normal force to apply to each material or on the speed of sliding were provided. Exploration of each material could be repeated as many times as required, after which each subject was asked to rate the material's pleasantness level on a 4-level scale: (0) very pleasant, (1) pleasant, (2) unpleasant, or (3) very unpleasant (**Figure 1**). Subjects hesitating between categories (1) pleasant and (2) unpleasant were



**FIGURE 1 | Illustration of the experimental procedure.** The subject was seated in front of the material fixation device, and 48 materials were successively explored with the pulp of the index finger.

instructed to choose "unpleasant" as soon as the material was not perceived as being pleasant or "pleasant" as soon as the material was not perceived as unpleasant. Each subject's total score could range from 0 (i.e., all materials rated as very pleasant,  $48 \times 0$ ) to 144 (i.e., all materials rated as very unpleasant,  $48 \times 3$ ). Similarly, the total score of each material could range from 0 (i.e., all subjects rated it as very pleasant,  $198 \times 0$ ) to 594 (i.e., all subjects rated it as very unpleasant,  $198 \times 3$ ).

### DATA ANALYSIS

Data were analyzed using the Rasch Unidimensional Measurement Models software (RUMM2020). The rating scale model was preferred to the partial credit model, since it yields better fit of the data to the model (Wright, 1999).

The Rasch model is a *probabilistic* model elaborated by the Danish mathematician Rasch (1960). The Rasch model allows the elaboration of unidimensional and linear scales for latent variables (e.g., pain, intelligence, or pleasant touch) by locating subjects and items along a *single* underlying linear scale (Rasch, 1960; Wright and Stone, 1979; Tennant et al., 2004; Tennant and Conaghan, 2007). This model was originally elaborated to analyze dichotomous data (i.e., two response categories per item such as "yes/no" or "pass/fail"). The model formulates the probability of success of a subject with a given ability on an item with a given difficulty. No other parameter besides the subject's ability (i.e., his/her location) and the item's difficulty (i.e., its location) is needed to determine the expected response. In this sense the model is unidimensional as it involves only one latent dimension of the subjects.

Later on, the model was expanded to accommodate polytomous response formats (i.e., more than two response categories per item such as “very low/low/moderate/high/very high”; Wright and Masters, 1982; Andrich, 1988). For polytomous response formats, the model prescribes that the probability of endorsing any response to an item depends solely on the subject’s ability, the item’s difficulty, and the threshold difficulties, where thresholds (i.e., “boundaries” between successive categories) are the locations on the underlying scale at which successive responses become the most probable if subjects of increasing ability answer a given item (Andrich, 1978a,b; Wright and Masters, 1982; Tennant et al., 2004; Tennant and Conaghan, 2007).

When applied to touch related pleasantness perception, the Rasch model prescribes that the probability that a subject selects a given response category (i.e., pleasantness category) for a given item (i.e., material) depends solely on (i) the subject’s pleasantness leniency level, (ii) the material’s pleasantness level, and (iii) the threshold locations. Based on the estimated subject leniency and the material pleasantness, the expected response of a subject to an item can be computed by the model. The similarity between the observed and expected responses to any item is reported by the software, through a  $\chi^2$  fit statistic (Andrich et al., 2004). Materials with a significant  $\chi^2$  value indicate that the difference between the observed and expected responses was too high to be random; they do not fit the unidimensional scale defined by the other materials and can be eliminated. In addition, the hypothesized order of the response categories (i.e., “very pleasant,” “pleasant,” “unpleasant,” and “very unpleasant”) must be empirically verified. Items presenting disordered thresholds between successive response categories indicate that the subjects were unable to discriminate the four response categories, allowing these items to be eliminated (Andrich, 1996). The resulting scale is defined in logits (log-odds-units), a unit defined as the natural logarithm of the odds of success (i.e., the pass/fail probability ratio) of a subject to an item and which is constant throughout the measurement scale. Consequently, at any level of the measurement scale, a 1-logit difference in an item’s pleasantness level indicates a constant ratio of its odds of being pleasant ( $e^1 = 2.71$ ) for any subject, whereas a 2-logit difference indicates the odds of being pleasant at a ratio of  $e^2 = 7.39$ , etc. The origin of the scale is conventionally set at the average material pleasantness level.

### MATERIAL SELECTION

Based on the 48 original materials, successive analyses were performed to select materials (i) presenting ordered response categories and (ii) fitting a unidimensional scale.

#### Ordered response scale

The subjects were asked to report their pleasantness perception on a 4-level scale: (0) very pleasant, (1) pleasant, (2) unpleasant, or (3) very unpleasant. To control the order of response categories, whether successive categories represent decreasing pleasantness levels was verified for each material. If the response categories were ordered, the thresholds were located in the anticipated order. Provided that the anticipated order of response categories was verified, less lenient subjects should have selected a higher response

for any given material, whereas subjects selecting a higher response to a given material should be less lenient. However, a reversed order of the thresholds between successive response categories indicated that the response scale was not used as expected (Tennant, 2004). If the categories were not distinguished by the sample, the concerned categories were collapsed into a single category (Tennant and Conaghan, 2007).

#### Unidimensional scale

Different statistic methods are available to test the fit of the data to the model requirements. This study used item  $\chi^2$  fit statistics. In this statistical method, the squared standardized residuals (i.e., the difference between the response expected by the model and the observed response by the subject) of all subjects are summed, leading to a  $\chi^2$  value for each material. Subsequently, a significance test was used to evaluate whether the  $\chi^2$  was too high to be attributed to random variation. A  $p$ -value of the item fit statistics of  $<0.05$  indicated a misfitting item that may threaten the concept of unidimensional (Tennant and Conaghan, 2007). There are two types of misfits, *underfit* and *overfit*. Underfitted items violate the unidimensionality concept as the subjects’ answers to these items are influenced by variables other than the measured one (Penta et al., 2005). An overfitted item does not necessarily represent a threat to the unidimensionality concept (Penta et al., 2005). Indeed, the response patterns of overfitted items are more deterministic than those predicted by the Rasch model. However, in contrast to underfitted items, the pleasantness levels of overfitted items can be predicted from each subject’s pleasantness leniency level (Penta et al., 2005). As a consequence, only underfitted items (i.e., materials) were eliminated from this study.

#### DIFFERENTIAL ITEM FUNCTIONING

Once satisfactory metric properties were achieved for the whole sample, the invariance of the pleasantness hierarchy of items within the sample was tested through a differential item functioning (DIF) analysis. DIF occurs if subjects of distinct subgroups (e.g., males vs. females) with the same leniency level perceive any given material differently (Tennant et al., 2004). In this study, DIF was investigated according to (i) gender, (ii) age ( $\leq 37$  vs.  $>37$  years, the median age of the subjects), and (iii) fingertip moisture level ( $\leq 70$  vs.  $>70$  arbitrary units, or “a.u.,” the median moisture level). To investigate DIF, each subgroup was divided into five class intervals (CI) of decreasing pleasantness leniency levels, and two-way analysis of variance (ANOVA) was computed on the standardized residuals of the different CIs (Andrich et al., 2004). Factors analyzed in two-way ANOVA included (i) subject subgroups (e.g., males vs. females) and (ii) CIs of decreasing pleasantness leniency. A significant subgroup’s main effect indicated a uniform DIF, occurring if the standardized residuals change significantly from one subgroup to another and evolve in parallel. In such a case, the relative difficulty of the item would differ between these subgroups (Smith, 1992). An item displaying a uniform DIF may be deleted or split into as many specific items as there are subject subgroups; each specific item would therefore have a difficulty peculiar to the corresponding subject’s subgroup (Tennant et al., 2004).

## RELIABILITY OF THE PLEASANT TOUCH SCALE

To assess the reliability of the *Pleasant Touch Scale*, a separation reliability index was computed for the items and subjects (Wright and Masters, 1982). The Item Separation Index enables the number of material pleasantness levels that may statistically be distinguished within the sample to be calculated. The Person Separation Index enables the number of statistically distinguished subject pleasantness leniency levels using the selected materials to be calculated. A higher item/person separation index indicates better separation of the measures (Wright and Masters, 1982).

## RESULTS

Successive Rasch analyses were performed to construct the final *Pleasant Touch Scale*. Of the 48 original materials (*hereafter* items), 11 showed disordered thresholds, indicating that our 198 subjects were unable to discriminate among the four levels of pleasantness for these items. As the subjects were unable to discriminate between “unpleasant” and “very unpleasant,” these categories were merged into one category, “unpleasant,” and the entire data set was reanalyzed using a 3-level scale: (0) very pleasant, (1) pleasant, and (2) unpleasant. Two items, however, adhesive UHU® Patafix and microfiber dust cloth, still presented disordered thresholds and were deleted from further consideration. Rasch analysis showed that six items (i.e., tissue carpet, thermal isolation, sponge, antislip carpet, velcro, and plastic door mat) did not fit a unidimensional scale and were therefore also eliminated, which resulted in a 40-item scale. No significant DIF based on age and gender was observed for any item, but invariance investigation of the items according to the subjects’ levels of fingertip moisture showed that 17 items shared a common location for low and high moisture level subgroups, whereas the other 23 items presented a DIF. These 23 items elicited different levels of pleasantness when touched by subjects with dry (i.e.,  $\leq 70$  a.u.) and wet (i.e.,  $> 70$  a.u.) skin. Each of these 23 items was therefore split into two different items with locations specific to fingertip moisture level, one each for subjects with dry and wet skin. After the splitting procedure, four split items and one common item showed underfitting (i.e., teflon high moisture, teflon low moisture, crepe paper high moisture, crepe paper low moisture, and corduroy), and were therefore removed. Consequently, the final *Pleasant Touch Scale* includes 58 items, of which (i) 16 items share a common location in low and high moisture level subgroups and (ii) 42 items have locations specific to the fingertip moisture level.

## METRIC PROPERTIES OF THE PLEASANT TOUCH SCALE

The calibration of the 58 items of the *Pleasant Touch Scale* is presented in **Table 1**, in which the items were ordered from the most unpleasant at the top (“sandpaper\_LM”) to the most pleasant at the bottom (“paper\_160 g/m<sup>2</sup>”). Items followed by “\_LM” and “\_HM” are split items with pleasantness locations specific to subjects with low and high fingertip moisture levels, respectively. The pleasantness levels of the 58 materials covered a range of 6.91 logits (range:  $-4.47$  to  $2.44$  logits), indicating that the odds of pleasing any particular subject was in a ratio higher than 1000:1 (i.e.,  $e^{6.91}$ :1) between the most and least pleasant items. This pleasantness range was arbitrarily centered at 0 logits. **Table 1** also shows the pleasantness level of each material expressed in percent, with 0 and 100%

indicating the least and most pleasant materials, respectively. Furthermore, the table presents the standard errors (SE) associated with the estimations of the pleasant levels of the different items (mean: 0.18 logits; range: 0.36 logits). The item fit statistics ( $\chi^2$  with associated  $p$ -values) indicate that all 58 items contribute to the definition of a unidimensional scale. Finally, **Table 1** also shows the perceptual tactile dimension of each material.

## DESCRIPTION OF THE PLEASANT TOUCH SCALE

**Figure 2** illustrates the structure of the final *Pleasant Touch Scale*. The lower part shows the relationship between the total ordinal raw score and the subjects’ linear pleasantness leniency levels. As the data were analyzed using a 3-level scale, the subjects’ ordinal raw scores ranged from 0 (i.e., subjects finding all 58 materials very pleasant,  $0 \times 58$ ) to 116 (i.e., subjects finding all 58 materials unpleasant,  $2 \times 58$ ). The relationship between total score and pleasantness leniency levels was roughly linear for total scores between 25 and 90. In this area, an increase of 1 point in total raw score represents always the same progression in pleasantness measures. For example, increases from 40 to 41 and from 60 to 61 correspond to increases in pleasantness leniency of 0.05 logits. Outside this central range, a 1 point increase in total ordinal raw score did not correspond to the same progression in linear pleasantness measures. Indeed, an increase in total raw score from 114 to 115 corresponded to 0.55 logits, whereas an increase from 5 to 6 corresponded to 0.28 logits. This large difference in the progression of the pleasantness leniency levels for a same increase in total ordinal raw score illustrates the non-linearity of the raw scores (Wright and Stone, 1979; Arnould et al., 2004).

The upper part of **Figure 2** shows that the distribution of pleasantness leniency levels in subjects ranged from  $-2.62$  to  $3.42$  logits, indicating that their odds of leniency levels are in a ratio over 400:1 (i.e.,  $e^{6.04}$ :1) between the most and the least lenient subject. Subjects on the left represent the most lenient (i.e., “the most easy to please”) and those on the right represent the least lenient (i.e., “the least easy to please”). The average subject location was 0.68 logits (SD: 0.88 logits), indicating that overall, the subjects found the materials more unpleasant than pleasant. In addition, the distribution shows that the pleasantness leniency of subjects with wet fingers (blank bars in **Figure 2**) and dry fingers (black bars in **Figure 2**) alternate on the *Pleasant Touch Scale*. This indicates a lack of relationship between fingertip moisture and pleasantness leniency [ $t$ -test,  $t = -0.849$ ;  $p$  (two-tailed) = 0.397].

The middle part of **Figure 2** shows items of the *Pleasant Touch Scale*, representing the most unpleasant at the top to the most pleasant at the bottom. Each line presents the most probable response of the subjects to the different items of the *Pleasant Touch Scale* as a function of their pleasantness leniency levels. For example, to find the material “tights” very pleasant, a subject would have to have a leniency level of  $\leq -0.378$  logits. A subject with a leniency level  $\geq 2.516$  logits would be expected to find this same material unpleasant. Subjects with leniency levels between  $-0.378$  and  $2.516$  logits would be expected to find “tights” pleasant.

The expected responses of the subjects to each item are obtained by comparing the pleasantness leniency levels of the subjects to the pleasantness level of each item. For example, a subject with a total raw score of 58, corresponding to a pleasantness

**Table 1 | Description of materials of the pleasant touch scale.**

Code	Material description	Pleasantness (logits)	Pleasantness (%)	SE (logits)	Residual (z)	Fit ( $\chi^2$ )	df	p-Value	Perceptual dimension
1.	Sandpaper LM	-4.47	0.00	0.48	-0.12	4.32	4.00	0.36	Rough
2.	Rough sponge_LM	-4.19	4.05	0.40	0.50	3.58	4.00	0.47	Rough
3.	Sandpaper_HM	-2.45	29.23	0.30	0.03	5.28	4.00	0.26	Rough
4.	Silicon_LM	-2.44	29.38	0.27	-0.37	4.55	4.00	0.34	Sticky
5.	Silicon_HM	-2.23	32.42	0.24	1.32	3.38	4.00	0.50	Sticky
6.	Latex	-1.88	37.48	0.17	-0.67	2.00	4.00	0.74	Sticky
7.	Wax	-1.73	39.65	0.17	1.22	3.98	4.00	0.41	Sticky
8.	Cling film	-1.49	43.13	0.15	-0.36	3.34	4.00	0.50	Sticky
9.	Rough sponge_HM	-1.43	43.99	0.23	0.26	3.14	4.00	0.53	Sticky
10.	Carbon paper_HM	-1.19	47.47	0.20	-0.51	2.30	4.00	0.68	Slippery
11.	Linen	-1.12	48.48	0.14	1.48	4.80	4.00	0.31	Rough
12.	Leather chamois_LM	-0.84	52.53	0.19	2.02	6.03	4.00	0.20	Sticky
13.	Tesa tape_HM	-0.75	53.83	0.19	-0.36	2.05	4.00	0.73	Smooth
14.	Carbon paper_LM	-0.71	54.41	0.19	-0.14	1.78	4.00	0.78	Slippery
15.	Wood_LM	-0.64	55.43	0.18	0.51	5.79	4.00	0.22	Hard
16.	Leather chamois_HM	-0.60	56.01	0.19	0.79	0.86	4.00	0.93	Sticky
17.	Plastic_HM	-0.59	56.15	0.19	-0.17	2.28	4.00	0.69	Smooth
18.	Argil_LM	-0.57	56.44	0.18	1.23	4.63	4.00	0.33	Hard
19.	Plexiglass_HM	-0.51	57.31	0.17	0.25	3.19	4.00	0.53	Hard
20.	Glass_HM	-0.26	60.93	0.16	2.57	3.49	4.00	0.48	Hard
21.	Aluminium_HM	-0.19	61.94	0.18	-0.35	1.25	4.00	0.87	Hard
22.	Tile_HM	-0.18	62.08	0.16	0.37	6.95	4.00	0.14	Hard
23.	Argil_HM	-0.15	62.52	0.17	0.46	3.98	4.00	0.41	Hard
24.	Wood_HM	-0.13	62.81	0.19	0.39	4.60	4.00	0.33	Hard
25.	Chipboard_LM	-0.10	63.24	0.19	0.19	4.34	4.00	0.36	Hard
26.	Cork	0.06	65.56	0.13	-0.29	1.74	4.00	0.78	Hard
27.	Table cloth_HM	0.20	67.58	0.17	-0.81	4.05	4.00	0.40	Slippery
28.	Plexiglass_LM	0.26	68.45	0.15	0.88	3.29	4.00	0.51	Hard
29.	Marble_HM	0.28	68.74	0.15	1.88	4.54	4.00	0.34	Hard
30.	Plastic_LM	0.39	70.33	0.15	0.15	4.40	4.00	0.35	Smooth
31.	Tesa tape_LM	0.40	70.48	0.15	0.24	4.20	4.00	0.38	Smooth
32.	Glass_LM	0.43	70.91	0.15	1.50	2.87	4.00	0.58	Hard
33.	Cast_LM	0.46	71.35	0.18	-0.09	7.46	4.00	0.11	Hard
34.	Silk	0.52	72.21	0.13	-0.69	3.32	4.00	0.51	Smooth
35.	Transparent paper_HM	0.57	72.94	0.15	0.50	2.75	4.00	0.60	Slippery
36.	Viscose tissue	0.60	73.37	0.12	0.99	7.78	4.00	0.10	Rough
37.	Paper_250 (g/m <sup>2</sup> _HM)	0.62	73.66	0.16	-0.32	2.97	4.00	0.56	Smooth
38.	Chipboard_HM	0.63	73.81	0.17	0.25	5.80	4.00	0.21	Hard
39.	Foam	0.63	73.81	0.12	1.14	4.87	4.00	0.30	Soft
40.	Cotton tissue_LM	0.66	74.24	0.18	0.06	0.52	4.00	0.97	Rough
41.	Table cloth_LM	0.68	74.53	0.16	0.08	3.27	4.00	0.51	Slippery
42.	Aluminum_LM	0.70	74.82	0.17	-0.10	1.27	4.00	0.87	Hard
43.	Tile_LM	0.81	76.41	0.17	0.79	2.30	4.00	0.68	Hard
44.	Cast_HM	0.87	77.28	0.19	1.14	4.03	4.00	0.40	Hard
45.	Tights	1.07	80.17	0.13	-0.87	3.10	4.00	0.54	Slippery
46.	Paper_250 (g/m <sup>2</sup> _LM)	1.08	80.32	0.17	0.24	0.83	4.00	0.93	Smooth
47.	Marble_LM	1.12	80.90	0.16	0.07	0.64	4.00	0.96	Hard
48.	Cotton tissue_HM	1.17	81.62	0.19	-0.17	3.50	4.00	0.48	Rough
49.	Paper 70 (g/m <sup>2</sup> )	1.22	82.34	0.14	-1.10	6.36	4.00	0.17	Smooth
50.	Paper 120 (g/m <sup>2</sup> _LM)	1.23	82.49	0.19	-0.50	2.50	4.00	0.64	Smooth

(Continued)

Table 1 | Continued

Code	Material description	Pleasantness (logits)	Pleasantness (%)	SE (logits)	Residual (z)	Fit ( $\chi^2$ )	df	p-Value	Perceptual dimension
51.	Transparent paper_LM	1.40	84.95	0.18	-0.76	5.40	4.00	0.25	Slippery
52.	Baking paper	1.49	86.25	0.13	-0.83	9.86	4.00	0.04	Smooth
53.	Synthetic tissue	1.50	86.40	0.13	-1.77	11.19	4.00	0.02	Smooth
54.	Velvet	1.74	89.87	0.12	0.51	4.43	4.00	0.35	Soft
55.	Cellular rubber	1.83	91.17	0.13	-0.30	8.26	4.00	0.08	Soft
56.	Paper_120 (g/m <sup>2</sup> _HM)	1.86	91.61	0.20	-0.18	2.60	4.00	0.63	Smooth
57.	Paper_80 (g/m <sup>2</sup> )	1.89	92.04	0.14	-0.60	5.19	4.00	0.27	Smooth
58.	Paper 160 (g/m <sup>2</sup> )	2.44	100.00	0.14	-0.27	1.58	4.00	0.81	Smooth

Items are ordered from least to most pleasant.

SE, standard error; df, degree of freedom; LM, low fingertip moisture; HM, high fingertip moisture.

leniency level of 0 logit, has the highest probability of finding (i) items 1 (“sandpaper\_LM”) through 9 (“rough sponge\_HM”) and 12 (“leather chamois”) unpleasant, (ii) items 10 (“carbon paper\_HM”) through 11 (“linen”), 13 (“tesa tape\_HM”) through 46 (“paper 250 g/m<sup>2</sup>\_LM”), and 48 (“cotton tissue\_HM”) through 53 (“synthetic tissue”) pleasant, and (iii) items 47 (“marble\_LM”) and 54 (“velvet”) through 58 (“paper\_160 g/m<sup>2</sup>”) very pleasant (see middle part of Figure 2).

#### RELIABILITY OF THE PLEASANT TOUCH SCALE

The material separation coefficient was equal to 0.98, indicating that 10.14 material pleasantness levels could be statistically distinguished by the sample. The reliability subject separation coefficient was equal to 0.88, indicating that 3.97 subject pleasantness leniency levels could be statistically distinguished using the selected materials (Wright and Masters, 1982).

#### DISCUSSION

We have described here the construction of a linear, unidimensional *Pleasant Touch Scale*, which quantifies (i) the level of pleasantness elicited in subjects by various materials during direct active fingertip explorations and (ii) the pleasantness leniency level of subjects. To construct this scale, 198 healthy subjects successively explored 48 different materials and reported their perception of pleasantness using a 4-level pleasantness scale. The collected data were analyzed using Rasch model. The initial analysis indicated that subjects did not discriminate between “unpleasant” and “very unpleasant.” Consequently, these two categories were merged, and the data were analyzed using three response levels. In addition, several materials had to be eliminated because they did not fit the unidimensional scale defined by the other items. This indicates that the pleasantness levels of these materials were influenced by dimensions other than pleasantness, suggesting that subjects associated the sensation of these materials with, for example, positive or negative events in their lives. The investigation of the invariance of the scale showed that the levels of pleasantness of more than half of the items differed according to the moisture levels on the subjects’ fingertips. Indeed, each of these DIF items was perceived differently, depending on whether subjects had dry or wet skin, and could therefore be split into two items with different locations specific to fingertip moisture level. The final *Pleasant Touch*

*Scale* orders 58 items – 16 with a common location in subjects with low and high moisture levels and 42 with locations specific to the fingertip moisture level – arranged according to their levels of pleasantness and 198 subjects arranged according to their levels of pleasantness leniency.

In this study, the data were collected using a category rating (CR) scale. Indeed, each stimulus was initially rated on a 3-level scale, yielding ordinal scores. An alternative data collection procedure would be ME. In contrast to CR, ME is an unlimited rating scale method, allowing subjects to freely choose a number reflecting their perception of a (set of) stimulus (stimuli), without pre-setting rating categories (Stevens, 1975). ME was initially designed, i.a. to yield ratio level scales, although this remains unclear (Wills and Moore, 1994). Indeed, both ME and CR have been found to yield ordinal scores (Wills and Moore, 1994), with both methods generating data/scores lacking essential psychometric properties (i.e., linearity and unidimensionality), precluding the objective and quantitative comparison of the measured variable. Therefore, in order to allow objective comparisons of the measured variable (e.g., pleasantness leniency level), the data/scores obtained through both scaling methods must be transformed into linear and unidimensional measures. Furthermore, compared with CR scale procedures, it has been suggested that the ME methods increase response variability, lowering the power of a test (Mellers, 1983). We therefore collected data using a CR scale, followed by transformation into linear unidimensional measures through Rasch model analysis.

The hierarchy of items sharing the same pleasantness level regardless of the fingertip moisture levels of the subjects indicates that rough and sticky items are more unpleasant to explore than smooth, slippery, or soft items. Indeed, the most unpleasant materials were “latex,” “wax,” “cling film,” and “linen,” while the most pleasant ones are “silk,” “viscose tissue,” “foam,” “tights,” “paper (70 g/m<sup>2</sup>),” “baking paper,” “synthetic tissue,” “velvet,” “cellular rubber,” “paper (80 g/m<sup>2</sup>),” and “paper (1690 g/m<sup>2</sup>).” Similarly, other studies have found that soft and smooth materials were rated as most pleasant to touch, whereas rough materials were perceived as unpleasant (Major, 1895; Ekman et al., 1965; Essick et al., 1999, 2010; Verrillo et al., 1999).

Subjects with high fingertip moisture levels perceived *rough and sticky materials as more pleasant* than subjects with low fingertip

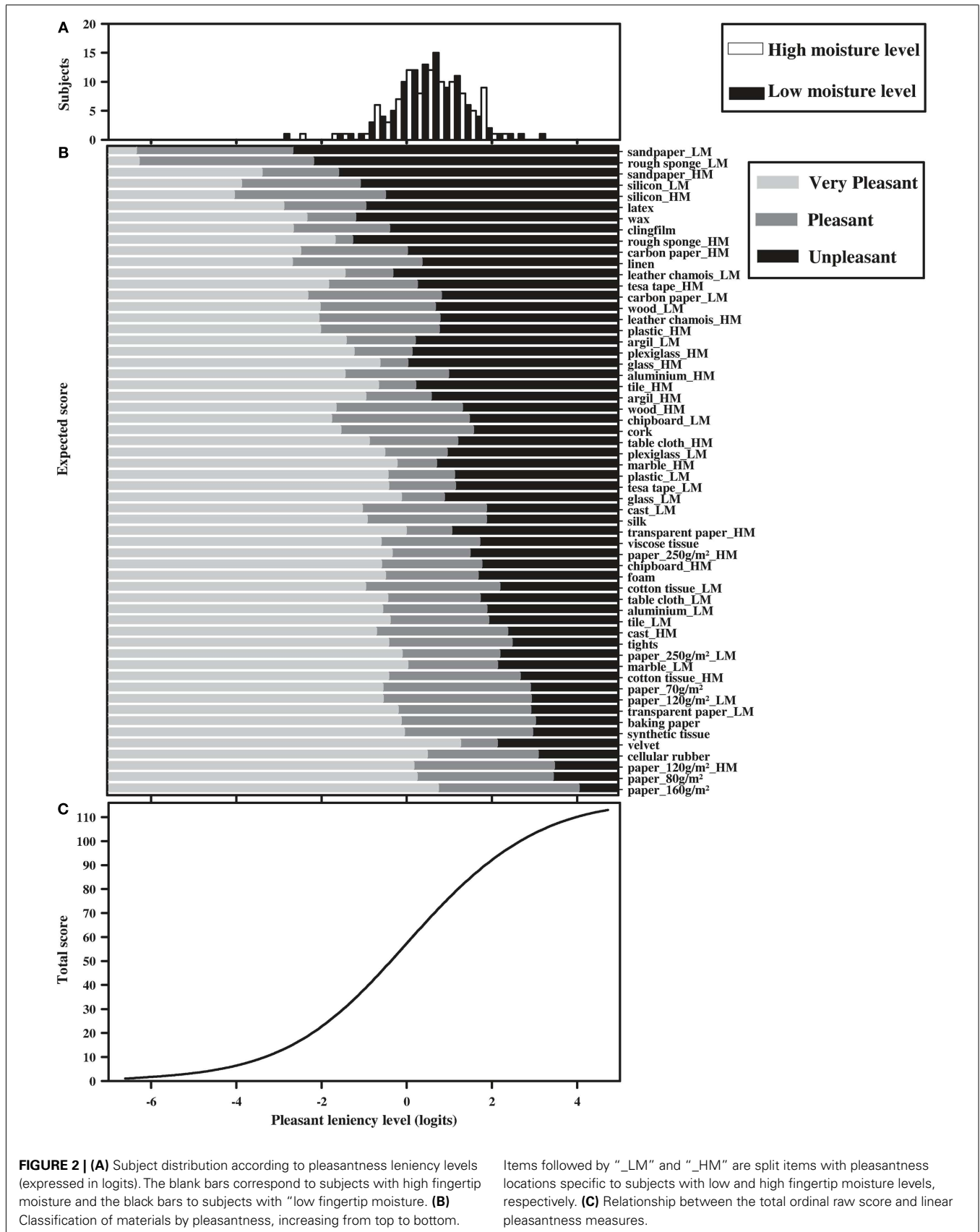


**FIGURE 2 | (A)** Subject distribution according to pleasantness leniency levels (expressed in logits). The blank bars correspond to subjects with high fingertip moisture and the black bars to subjects with "low fingertip moisture. **(B)** Classification of materials by pleasantness, increasing from top to bottom.

Items followed by "\_LM" and "\_HM" are split items with pleasantness locations specific to subjects with low and high fingertip moisture levels, respectively. **(C)** Relationship between the total ordinal raw score and linear pleasantness measures.

moisture levels. Increased fingertip moisture was found to increase the dynamic coefficient of friction (i.e., the ratio between friction and normal force during slippage; André et al., 2011) until a certain moisture threshold (Nacht et al., 1981; Tomlinson et al., 2007; Gerhardt et al., 2008). Similarly, skin hydration can increase finger's adhesion to a contacting surface, decreasing the probability of occurrence of slippage (André et al., 2011). Above the before mentioned moisture threshold, however, a further increase of skin hydration decreases the coefficient of friction (Tomlinson et al., 2007), due to the accumulation of a thin layer of moisture between the explored surface and the skin. Consequently, it may be hypothesized that rough and sticky materials, perceived as more pleasant if fingertip moisture was high, were materials that allowed fingertip moisture to accumulate to a very high level on their surfaces, resulting in the formation of a thin layer of moisture between the explored material and the skin of the fingertip. This may decrease the dynamic coefficient of friction of sticky materials and the roughness perception of rough materials, increasing the perceived pleasantness. This last assumption is strengthened by studies highlighting that the rough nature of rough materials are less perceived with higher skin hydration (Verrillo et al., 1998, 1999).

Conversely, subjects with high fingertip moisture levels perceived *smooth materials as less pleasant* than subjects with low fingertip moisture levels. It may be hypothesized that these smooth materials assimilated lower levels of moisture on their surfaces and failed to reach the moisture threshold above which the coefficient of friction decreases. The accumulated moisture may increase the

dynamic coefficient of friction, leading to a less pleasant perception of the explored materials, which are perceived as stickier.

Finally, hardness was found to be unrelated to the perception of pleasantness, with some (e.g., tile\_LM, cast\_HM, marble\_LM) perceived as pleasant and others (e.g., wood\_LM, argil\_LM, plexiglass\_HM) as unpleasant. Rather, pleasantness was more dependent on roughness and stickiness than on hardness.

The aim of this study was to investigate pleasant touch of glabrous skin. Results suggest that a subject's pleasantness leniency level, elicited by active touch, may be defined as a latent trait common among subjects. The *Pleasant Touch Scale* is a unidimensional and linear scale, ordering materials according to their level of pleasantness and healthy subjects according to their level of pleasantness leniency. Consequently, our findings provide *objective* insights into the characteristics of materials and subjects that influence pleasant touch. Indeed, we found that (i) smooth and soft materials are perceived as more pleasant than rough and sticky materials and (ii) the level of fingertip moisture influences the perception of pleasantness. Furthermore, this scale may be useful in future studies, aimed, for example, at determining correlations between the pleasantness levels of materials and the dynamics of active touch.

## ACKNOWLEDGMENTS

We are grateful for the kind participation of all subjects. This work was supported by a grant from the Commission of the European Union under Contract No. EU-FP7-NMP4-SL-2009-228844, NanoBioTouch.

## REFERENCES

- André, T., Levesque, V., Hayward, V., Lefevre, P., and Thonnard, J. L. (2011). Effect of skin hydration on the dynamics of fingertip gripping contact. *J. R. Soc. Interface* 103, 402–408.
- Andrich, D. (1978a). Application of a psychometric rating model to ordered categories which are scored with successive integers. *Appl. Psychol. Meas.* 2, 581–594.
- Andrich, D. (1978b). Rating formulation for ordered response categories. *Psychometrika* 43, 561–573.
- Andrich, D. (1988). *Rasch Models for Measurement*. Newbury: SAGE Publications.
- Andrich, D. (1996). Category ordering and their utility. *Rasch Meas. Trans.* 9, 464–465.
- Andrich, D., Sheridan, B. E., and Luo, G. (2004). *Rasch Unidimensional Measurement Models (RUMM): A Windows Based Computer Program*. Perth: Murdoch University.
- Arnould, C., Penta, M., Renders, A., and Thonnard, J. L. (2004). ABILHAND-Kids: a measure of manual ability in children with cerebral palsy. *Neurology* 63, 1045–1052.
- Bergmann Tiest, W. M., and Kappers, A. M. (2006). Analysis of haptic perception of materials by multidimensional scaling and physical measurements of roughness and compressibility. *Acta Psychol. (Amst.)* 121, 1–20.
- Ekman, G., Hosman, J., and Lindstroem, B. (1965). Roughness, smoothness, and preference: a study of quantitative relations in individual subjects. *J. Exp. Psychol.* 70, 18–26.
- Essick, G. K., James, A., and McGlone, F. P. (1999). Psychophysical assessment of the affective components of non-painful touch. *Neuroreport* 10, 2083–2087.
- Essick, G. K., McGlone, F., Dancer, C., Fabricant, D., Ragin, Y., Phillips, N., Jones, T., and Guest, S. (2010). Quantitative assessment of pleasant touch. *Neurosci. Biobehav. Rev.* 34, 192–203.
- Gerhardt, L. C., Strassle, V., Lenz, A., Spencer, N. D., and Derler, S. (2008). Influence of epidermal hydration on the friction of human skin against textiles. *J. R. Soc. Interface* 5, 1317–1328.
- Hollins, M., Bensmaia, S., Karlof, K., and Young, F. (2000). Individual differences in perceptual space for tactile textures: evidence from multidimensional scaling. *Percept. Psychophys.* 62, 1534–1544.
- Hollins, M., Faldowski, R., Rao, S., and Young, F. (1993). Perceptual dimensions of tactile surface texture: a multidimensional scaling analysis. *Percept. Psychophys.* 54, 697–705.
- Johansson, R. S., Trulsson, M., Olsson, K. A., and Westberg, K. G. (1988). Mechanoreceptor activity from the human face and oral mucosa. *Exp. Brain Res.* 72, 204–208.
- Lundborg, G. (2005). "Sensation and Sensorimotor Integration in Hand Function," in *Nerve Injury and Repair: Regeneration, Reconstruction, and Cortical Remodelling*. Elsevier.
- Major, D. R. (1895). On the affective tone of simple sense impressions. *Am. J. Psychol.* 7, 57–77.
- McGlone, F., and Reilly, D. (2010). The cutaneous sensory system. *Neurosci. Biobehav. Rev.* 34, 148–159.
- McGlone, F., Vallbo, A. B., Olausson, H., Loken, L., and Wessberg, J. (2007). Discriminative touch and emotional touch. *Can. J. Exp. Psychol.* 61, 173–183.
- Mellers, B. A. (1983). Evidence against "absolute" scaling. *Percept. Psychophys.* 33, 523–526.
- Merbitz, C., Morris, J., and Grip, J. C. (1989). Ordinal scales and foundations of misinference. *Arch. Phys. Med. Rehabil.* 70, 308–312.
- Morrison, I., Loken, L. S., Minde, J., Wessberg, J., Perini, I., Nennesmo, I., and Olausson, H. (2011). Reduced C-afferent fibre density affects perceived pleasantness and empathy for touch. *Brain* 134, 1116–1126.
- Nacht, S., Close, J. A., Yeung, D., and Gans, E. H. (1981). Skin friction coefficient – changes induced by skin hydration and emollient application and correlation with perceived skin feel. *J. Soc. Cosmet. Chem.* 32, 55–65.
- Nordin, M. (1990). Low-threshold mechanoreceptive and nociceptive units with unmyelinated (C) fibres in the human supraorbital nerve. *J. Physiol. (Lond.)* 426, 229–240.
- Olausson, H., Lamarre, Y., Backlund, H., Morin, C., Wallin, B. G., Starck, G., Ekholm, S., Strigo, I., Worsley, K., Vallbo, A. B., and Bushnell, M. C. (2002). Unmyelinated tactile afferents signal touch and project to insular cortex. *Nat. Neurosci.* 5, 900–904.
- Olausson, H., Wessberg, J., Morrison, I., McGlone, F., and Vallbo, A. (2010). The neurophysiology of unmyelinated tactile afferents. *Neurosci. Biobehav. Rev.* 34, 185–191.

- Penta, M., Arnould, C., and Decruynaere, C. (2005). *Développer et interpréter une échelle de mesure. Applications du modèle de Rasch*. Belgium: Mardaga.
- Rasch, G. (1960). *Probabilistic Models for Some Intelligence and Attainment Tests*. Chicago: Mesa Press.
- Ripin, R., and Lazarsfeld, P. F. (1937). The tactile-kinaesthetic perception of fabrics with emphasis on their relative pleasantness. *J. Appl. Psychol.* 21, 198–224.
- Smith, R. M. (1992). *Applications of Rasch Measurement*. Chicago: Mesa Press.
- Stevens, S. S. (1975). *Psychophysics: Introduction to its Perceptual, Neural, and Social Prospects*. New York: John Wiley & Sons.
- Tennant, A. (2004). Disordered thresholds: an example from the functional independence measure. *Rasch Meas. Trans.* 17, 945–948.
- Tennant, A., and Conaghan, P. G. (2007). The Rasch measurement model in rheumatology: what is it and why use it? When should it be applied, and what should one look for in a Rasch paper? *Arthritis Rheum.* 57, 1358–1362.
- Tennant, A., Penta, M., Tesio, L., Grimby, G., Thonnard, J. L., Slade, A., Lawton, G., Simone, A., Carter, J., Lundgren-Nilsson, A., Tripolski, M., Ring, H., Biering-Sorensen, F., Marincek, C., Burger, H., and Phillips, S. (2004). Assessing and adjusting for cross-cultural validity of impairment and activity limitation scales through differential item functioning within the framework of the Rasch model: the PRO-ESOR project. *Med. Care* 42(Suppl. 1), 137–148.
- Tesio, L., Simone, A., and Bernardinello, M. (2007). Rehabilitation and outcome measurement: where is Rasch analysis-going? *Eura. Medicophys.* 43, 417–426.
- Thurstone, L. L. (1928). Attitudes can be measured. *Am. J. Sociol.* 33, 529–554.
- Tomlinson, S. E., Lewis, R., and Carré, M. J. (2007). Review of the frictional properties of finger-object contact when gripping. *J. Eng. Tribol.* 221, 841–850.
- Vallbo, A. B., Olausson, H., and Westberg, J. (1999). Unmyelinated afferents constitute a second system coding tactile stimuli of the human hairy skin. *J. Neurophysiol.* 81, 2753–2763.
- Verrillo, R. T., Bolanowski, S. J., Checkosky, C. M., and McGlone, F. P. (1998). Effects of hydration on tactile sensation. *Somatosens. Mot. Res.* 15, 93–108.
- Verrillo, R. T., Bolanowski, S. J., and McGlone, F. P. (1999). Subjective magnitude of tactile roughness. *Somatosens. Mot. Res.* 16, 352–360.
- Wills, C. E., and Moore, C. F. (1994). A controversy in scaling of subjective states: magnitude estimation versus category rating methods. *Res. Nurs. Health* 17, 231–237.
- Wright, B. D. (1999). Model selection: rating scale or partial credit? *Rasch Meas. Trans.* 12, 641–642.
- Wright, B. D., and Linacre, J. M. (1989). Observations are always ordinal; measurements, however, must be interval. *Arch. Phys. Med. Rehabil.* 70, 857–860.
- Wright, B. D., and Masters, G. N. (1982). *Rating Scale Analysis. Rasch Measurement*. Chicago: Mesa Press.
- Wright, B. D., and Stone, M. H. (1979). *The Measurement Model. In Best Test Design. Rasch Measurement*. Chicago: Mesa Press.
- Yoshioka, T., Bensmaia, S. J., Craig, J. C., and Hsiao, S. S. (2007). Texture perception through direct and indirect touch: an analysis of perceptual space for tactile textures in two modes of exploration. *Somatosens. Mot. Res.* 24, 53–70.
- Yoshioka, T., and Zhou, J. (2009). Factors involved in tactile texture perception through probes. *Adv. Robot.* 23, 747–766.

**Conflict of Interest Statement:** The authors declare that the research was conducted in the absence of any commercial or financial relationships that could be construed as a potential conflict of interest.

Received: 13 March 2012; paper pending published: 30 April 2012; accepted: 30 May 2012; published online: 21 June 2012.

Citation: Klöcker A, Arnould C, Penta M and Thonnard J-L (2012) Rasch-built measure of pleasant touch through active fingertip explorations. *Front. Neurobot.* 6:5. doi: 10.3389/fnbot.2012.00005

Copyright © 2012 Klöcker, Arnould, Penta and Thonnard. This is an open-access article distributed under the terms of the Creative Commons Attribution Non Commercial License, which permits non-commercial use, distribution, and reproduction in other forums, provided the original authors and source are credited.



# Whisker encoding of mechanical events during active tactile exploration

Yves Boubenec<sup>1</sup>, Daniel E. Shulz<sup>1</sup> and Georges Debrégeas<sup>2\*</sup>

<sup>1</sup> Unité de Neurosciences Information et Complexité, UPR 3293, Centre National de la Recherche Scientifique, Gif-sur-Yvette, France

<sup>2</sup> FRE3231 Laboratoire Jean Perrin, Centre National de la Recherche Scientifique, UPMC Université Paris 6, Paris, France

## Edited by:

Blythe Towal, California Institute of Technology, USA

## Reviewed by:

Mitra J. Hartmann, Northwestern University, USA

Garrett B. Stanley, Georgia Institute of Technology, USA

Jason Ritt, Boston University, USA

## \*Correspondence:

Georges Debrégeas, FRE3231 Laboratoire Jean Perrin, Centre National de la Recherche Scientifique, UPMC Université Paris 6, 24 rue Lhomond, 75005 Paris, France.  
e-mail: georges.debregeas@lps.ens.fr

Rats use their whiskers to extract a wealth of information about their immediate environment, such as the shape, position or texture of an object. The information is conveyed to mechanoreceptors located within the whisker follicle in the form of a sequence of whisker deflections induced by the whisker/object contact interaction. How the whiskers filter and shape the mechanical information and effectively participate in the coding of tactile features remains an open question to date. In the present article, a biomechanical model was developed that provides predictions of the whisker dynamics during active tactile exploration, amenable to quantitative experimental comparison. This model is based on a decomposition of the whisker profile into a slow, quasi-static sequence and rapid resonant small-scale vibrations. It was applied to the typical situation of a rat actively whisking across a solid object. Having derived the quasi-static sequence of whisker deformation, the resonant properties of the whisker were analyzed, taking into account the boundary conditions imposed by the whisker/surface contact. We then focused on two elementary mechanical events that are expected to trigger significant neural responses, namely (1) the whisker/object first contact and (2) the whisker detachment from the object. Both events were found to trigger a deflection wave propagating upward to the mystacial pad at constant velocity of  $\approx 3\text{--}5$  m/s. This yielded a characteristic mechanical signature at the whisker base, in the form of a large peak of negative curvature occurring  $\approx 4$  ms after the event has been triggered. The dependence in amplitude and lag of this mechanical signal with the main contextual parameters (such as radial or angular distance) was investigated. The model was validated experimentally by comparing its predictions to high-speed video recordings of shock-induced whisker deflections performed on anesthetized rats. The consequences of these results on possible tactile encoding schemes are briefly discussed.

**Keywords:** exploration, rat, resonance, tactile, vibration, vibrissae, whiskers, whisking

## INTRODUCTION

The vibrissal system of the rat is one of the prominent model systems for investigating the mechanisms of sensory information processing in the tactile modality. Rats use their whiskers to sense their close environment and gather information about object features such as location (Krupa and Nicolelis, 2001; O'Connor et al., 2010a), shape (Brecht and Merzenich, 1997; Polley et al., 2005), texture (Carvell and Simons, 1990; Morita et al., 2011), and size (Anjum et al., 2006). Active movements of body, head (Milani et al., 1989; Carvell and Simons, 1990; Towal and Hartmann, 2006; Mitchinson et al., 2007) or whiskers themselves during whisking (Welker, 1964; Carvell and Simons, 1990; Berg and Kleinfeld, 2003) induce contact between the whisker and the probed environment. This mechanical interaction elicits sequences of whisker deflection. Each whisker is embedded in a follicle in the skin (Ebara et al., 2002), where mechanoreceptors transduce whisker base deflections into neural signals (Lichtenstein et al., 1990; Szwed et al., 2006). Neurons along the

trigeminal pathway respond to various aspects of the whisker base movements, such as high acceleration events (Jadhav et al., 2009; Lottem and Azouz, 2009; Jadhav and Feldman, 2010), whisker speed (Arabzadeh et al., 2004), average noise level (Arabzadeh et al., 2005), or characteristic features of the whisker motion spectra (Hipp et al., 2006). These different properties of the whisker base dynamics are then processed by the central nervous systems to extract relevant features of the environment. In order to decipher the underlying neural code, one needs to relate the dynamics of the whisker to the physical and geometrical characteristics of the contacting surface. This amounts to understanding the way the whisker carries and shapes information from the contact point to the follicle.

Consider a typical exploration task during which a rat whisks across an object (**Figure 1**). This sequence can be broken up into three consecutive phases. First, the whisker rotates freely in air; second, it slides over the object and is submitted to a frictional contact at the whisker tip; the whisker then detaches and pursues

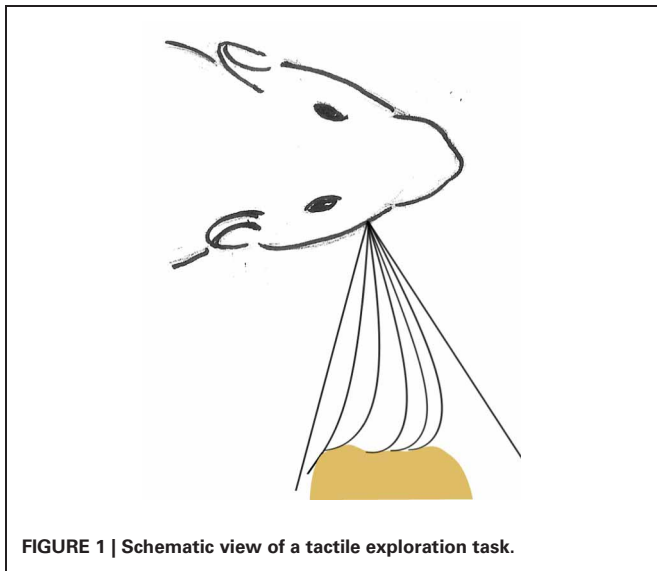


FIGURE 1 | Schematic view of a tactile exploration task.

its motion in air (no contact). Recently, several groups have studied how the rat could extract the contour of an object from the time evolution of the torque at the base of each of its whiskers (Kaneko et al., 1998; Scholz and Rahn, 2004; Clements and Rahn, 2006; Kim and Möller, 2007; Solomon and Hartmann, 2010). The encoding mechanism requires proprioceptive information (the angular position of the whisker with respect to the snout) and the knowledge of the relationship between the radial distance and the resulting torque in the follicle. This relationship was derived by computing the successive equilibrium profiles of the whiskers for a non-frictional contact. Due to the slender geometry of the whisker, any change in the contact configuration (during the first contact or following the whisker detachment from the object) is expected to trigger a burst of whisker oscillations ignored in these quasi-static descriptions. During the sliding phase itself, stick-slip instabilities are bound to occur, which should also result in brief vibrating episodes. Several studies have suggested that these mechanical events are encoded by specific mechanoreceptors. In particular, Szwed et al. (2003) established that distinct populations of trigeminal ganglion neurons specifically respond to first contact and/or detachment. Other works (Ritt et al., 2008; Wolfe et al., 2008; Jadhav et al., 2009; Lottem and Azouz, 2009) have further suggested that surface roughness may in large part be encoded by the rate of discrete high acceleration events elicited by stick-slip instabilities at the whisker/object contact. Notice that analogous mechanical events, separating different action phases, have been shown to play a central role in the planning and control of manipulation tasks in the context of active human touch (Johansson and Flanagan, 2009).

In the present article, we focused on the encoding of the first contact and detachment events by the whisker. A biomechanical model is developed to quantitatively predict the sequence of whisker deformation that these events elicit in realistic conditions of tactile exploration. Specific predictions of the model were validated through high-speed video recordings of shock-induced whisker deflections. By investigating how various contextual parameters (such as radial and angular distance or friction

coefficients) control the mechanical signature at the whisker base, we aimed to understand what information can be extracted by the neural system. The consequence of these results on possible tactile encoding schemes are discussed, which we believe may be of interest to the fields of whisker tactile perception as well as neurorobotics.

## RESULTS

Our biomechanical approach is based on a decomposition of the whisker dynamics into rapid small amplitude resonant oscillations superimposed onto a slow (quasi-static) sequence of deformation. The oscillating term is further decomposed along a series of resonant modes whose spatial and temporal properties are computed numerically.

In a first section, we describe the quasi-static evolution of the whisker as it is swept across a rectangular obstacle. In the second section, the mode decomposition scheme used to describe the rapid dynamics of the whisker is presented. Two distinct mechanical events are then successively examined: (1) the initial contact (shock) between the whisker and the object; (2) the detachment of the whisker from the object. In both cases, the precise time-sequence of the whisker dynamics can be accurately predicted. A particular focus is put on the time-evolution of the moment at the whisker base (in the follicle) as it constitutes the relevant peripheral input for the mechanoreceptors.

### QUASI-STATIC EVOLUTION OF A WHISKER SCANNED ACROSS A RECTANGULAR OBJECT

In this first section, the quasi-static evolution of the whisker, i.e., the series of equilibrium configurations, is calculated as it is swept across a rectangular object. Several robotics studies analyzed the shape of a whisker submitted to a contact force. Most of those works used numerical solutions to determine whisker profiles (Scholz and Rahn, 2004; Clements and Rahn, 2006; Solomon and Hartmann, 2010). In the limit of small deflections, a small angle approximation can be used which yields an analytical solution to this mechanical problem (Birdwell et al., 2007). A large majority of those works, however, ignored any frictional interaction between the whisker and the substrate in their theoretical derivations. Nevertheless a few studies performed with artificial whiskers investigated the influence of frictional interactions for predicting radial distance (Solomon and Hartmann, 2008) and local object shape (Schroeder and Hartmann, 2012) during whisker touch. Here, we numerically derive the quasi-static sequence of whisker deflection as it is swept across an obstacle, taking into account the frictional force. In line with physiological observations made in rats (Voges et al., 2012) and other whisker-bearing animals (Williams and Kramer, 2010), the whisker is modeled as a truncated tapered rod. We denote  $L$  the length of the non-truncated cone,  $b$  the maximum (base) radius and  $\alpha = b/L$  the cone angle (Figure 2A). In order to simplify the equations governing the whisker mechanics, the whisker profiles are described using a curvilinear coordinate  $s$  defined as the normalized arc length such that the cone tip (the end of the non-truncated whisker) position defines the origin  $s = 0$  and the whisker base is located at  $s = 1$ . The radius of the whisker at position  $s$  thus reads  $r(s) = \alpha sL$ . In this coordinate, the whisker

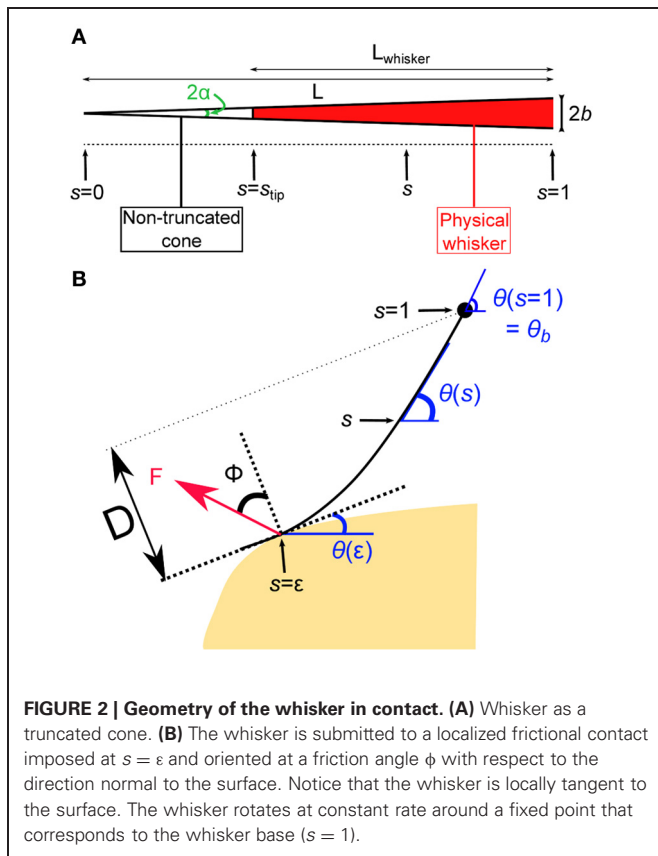


**FIGURE 2 | Geometry of the whisker in contact. (A)** Whisker as a truncated cone. **(B)** The whisker is submitted to a localized frictional contact imposed at  $s = \epsilon$  and oriented at a friction angle  $\phi$  with respect to the direction normal to the surface. Notice that the whisker is locally tangent to the surface. The whisker rotates at constant rate around a fixed point that corresponds to the whisker base ( $s = 1$ ).

physical tip is located at  $s_{tip} = 1 - L_{whisker}/L$ . Note that, owing to the truncation of the whiskers,  $L$  can be significantly larger than the actual whisker length  $L_{whisker}$ .

The whisker profile is described in curvilinear angular coordinates as  $\theta = \theta(s)$  (Figure 2B). The whisker is embedded in the pad tissue down to 4–5 mm (Ebara et al., 2002), which strongly constrains the angular position of the whisker base. Although the pad does exhibit some level of elastic compliance, as established by Jenks et al. (2010) in awake rats (Jenks et al., 2010), here we assume the anchorage to be strictly rigid and thus impose  $\theta(1) = \theta_b$ . The whisking process is modeled by imposing a rotation of the whisker around its base at constant rate  $\gamma$ . The base angle  $\theta_b = \theta(s = 1)$  thus grows linearly with time such that  $\theta_b(t) = \gamma t$ . The whisker is considered linearly elastic with a uniform Young's modulus  $E$  and density  $\rho$ . Any intrinsic (spontaneous) curvature and out-of-plane deformations are also ignored. When in contact with the object, the whisker is submitted to a frictional force  $F$  which is assumed to apply at a single point located at  $s = \epsilon$  along the whisker. The present analysis is restricted to configurations where  $\epsilon > s_{tip}$ , which constrains the whisker to be locally tangent to the object surface. The orientation of the force  $F$  with respect to the direction normal to the whisker at  $s = \epsilon$  is set by the friction angle  $\phi = \tan^{-1}(\mu)$  where  $\mu$  is the friction coefficient (Persson, 2000). Within these hypothesis, the equation governing the whisker bending moment equilibrium reads (see “Methods” for the detailed derivation):

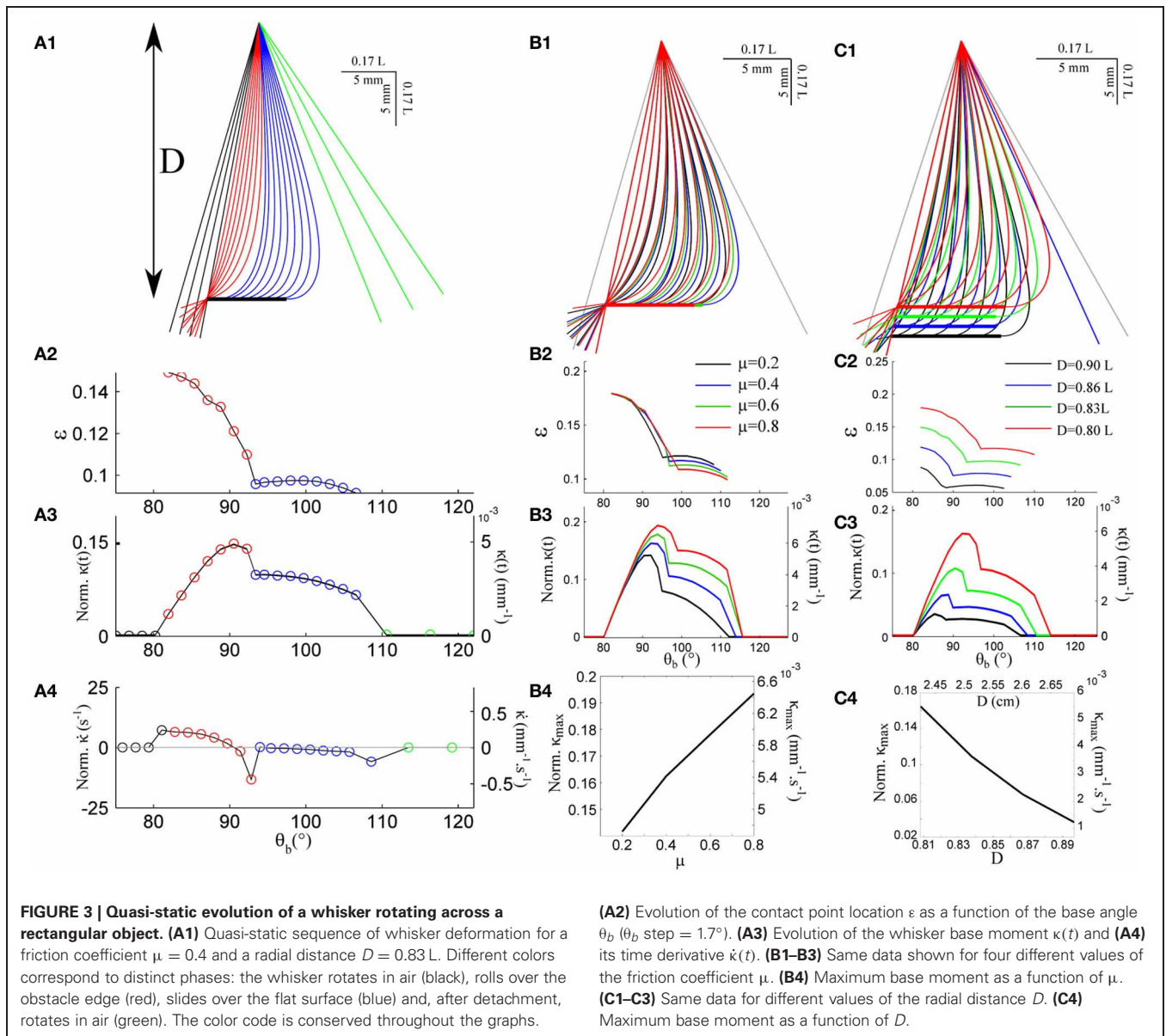
$$(s^4 \theta')' - \tilde{F} \cos(\phi - \theta + \theta(\epsilon)) = 0 \quad (1)$$

where  $\tilde{F} = 4F/(\pi\alpha^4 EL^2)$  is an adimensional force. The single contact point hypothesis further imposes that the moment is null at the contact point such that  $\theta'(\epsilon) = 0$ . For given values of  $\theta_b$  (imposed by the rotation of the whisker base), the friction angle  $\phi$  and the contact point  $\epsilon$ , one can numerically compute a series of equilibrium whisker profiles by imposing different values of the contact angle  $\theta(\epsilon) < \theta_b$ . This method is first used to derive the quasi-static evolution of the whisker as it rolls over the edge of the rectangular obstacle. In this regime, the position of the contact point on the object is fixed. This condition yields, for each whisking angle  $\theta_b$ , a unique solution associated with a contact location  $\epsilon$  along the whisker. As  $\theta_b$  increases, the contact angle  $\theta(\epsilon)$  decreases and eventually vanishes. This time marks the onset of a second phase during which the whisker slides along the surface of the object. In this second regime, the contact angle  $\theta(\epsilon)$  is null while the radial distance  $D$  (the distance from the whisker base to the free surface) remains constant. Again, a unique solution, associated with a contact location  $\epsilon$ , is obtained for each whisking angle  $\theta_b$ . When the contact point reaches the edge of the object, the whisker snaps off and then continues to rotate in air at a constant rotation rate.

Figure 3A shows the quasi-static evolution of the whisker profile for a friction coefficient  $\mu = 0.4$ , a radial distance  $D = 0.83L$ , and a rotation rate  $\gamma = 400^\circ/s$ . During this sequence, the contact point position along the whisker varies within a small range  $0.08 < \epsilon < 0.15$  (Figure 3A2). The graphs A3 and A4 display the evolution of the base moment  $\kappa(t) = \theta'(s = 1)$  and its time-derivative  $\dot{\kappa}(t)$ . In all graphs, and throughout the article, double scales are used in order to show the data both in reduced (all lengths being normalized by  $L$ ) and physical units. For the latter, a typical whisker length  $L = 3$  cm is used. Figure 3B displays similar traces for various friction coefficients  $\mu = \{0.2, 0.4, 0.6, 0.8\}$ . This range should encompass most physical situations (Persson, 2000). Although the associated profiles appear quite similar, increasing the friction coefficient yields a significant amplification of the base moment signal  $\kappa(t)$  as shown in Figure 3B4. One may notice that the effect becomes significant when the whisker is sufficiently deformed while the different graphs collapse in the early moments following the initial contact, i.e., when the whisker is essentially straight. The friction coefficient also controls the time (or base angle) at which the whisker detaches from the object. Although these frictional effects are significant, the base moment  $\kappa(t)$  appears to be mostly controlled by the radial distance  $D$  as shown in Figure 3C. Reducing this distance by 10% yields a five-fold increase of the maximum base moment experienced during the exploratory sequence. It thus seems unlikely that this quantity provides significant cue for the discrimination of surfaces exhibiting different frictional properties.

### WHISKER RESONANT DYNAMICS

The preceding section addressed the quasi-static evolution of the whisker as it is swept across a rectangular object. This sequence is expected to be valid for a massless whisker or at infinitely slow scanning speed (Quist and Hartmann, 2012). For a real whisker, however, inertia effects will induce significant deviations. In particular, the contact and detachment processes, which mark the



transition between distinct mechanical conditions at the whisker tip, will trigger brief episodes of oscillations.

These dynamic modulations are treated perturbatively in the form of a small displacement  $u(s, t)$  normal to the quasi-static profile sequence (see **Figure 4A**). We assume that both the quasi-static deformation and dynamic oscillations amplitude remain sufficiently moderate such that a small angle approximation ( $\theta(s) \ll 1$ ) can be implemented. The validity of this hypothesis, for both mechanical events, will be discussed *a posteriori*. In this limit, the classical Euler–Bernoulli equation that governs the force equilibrium normal to the whisker can be expanded around the quasi-static profile, yielding for  $u(s, t)$  (see Weaver et al., 1990):

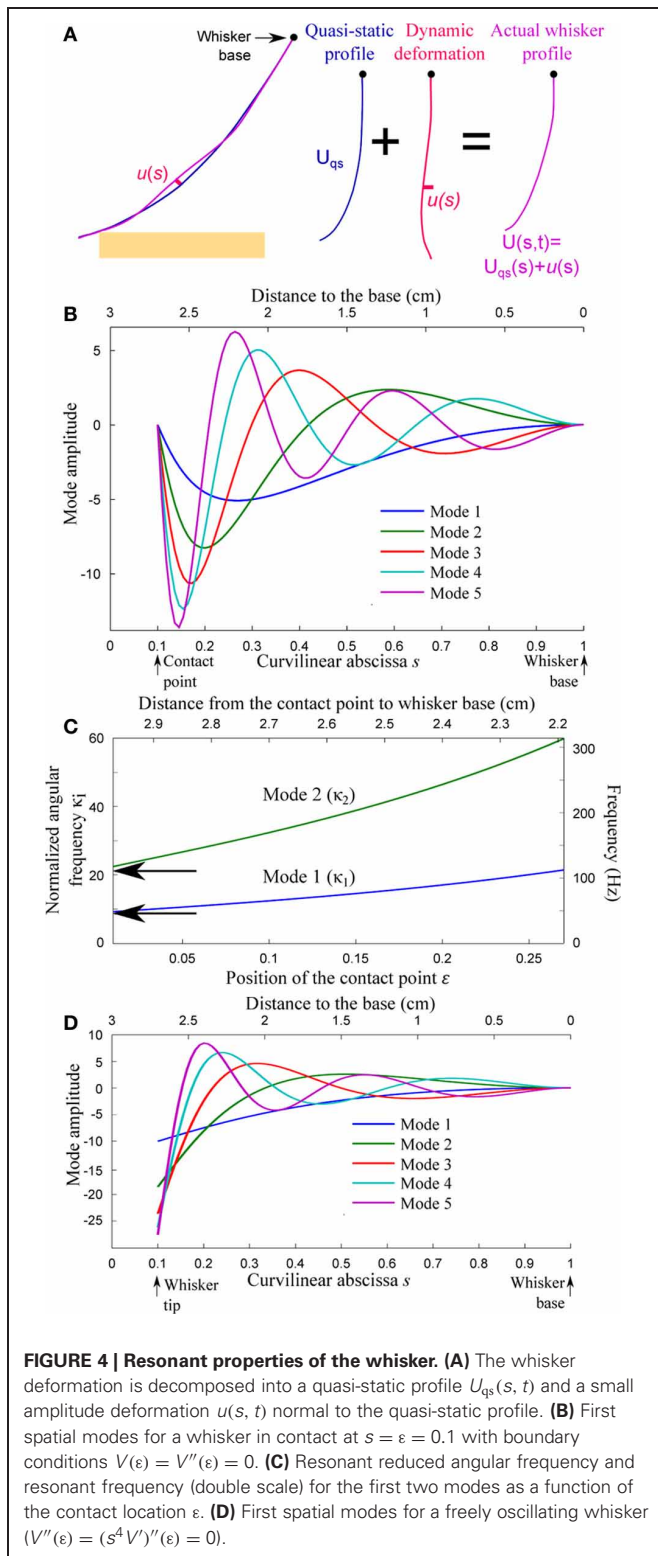
$$\frac{\partial^2}{\partial s^2} \left( EI \frac{\partial^2 u}{\partial s^2} \right) + \rho A \frac{\partial^2 u}{\partial t^2} = 0 \quad (2)$$

where  $A = \pi r^2$  is the whisker section area. This equation is re-written in reduced coordinates (all distances being expressed in unit of the ideal non-truncated whisker length  $L$ ) in the form:

$$\frac{\partial^2}{\partial s^2} \left( s^4 \frac{\partial^2 u}{\partial s^2} \right) + k^2 s^2 \frac{\partial^2 u}{\partial t^2} = 0 \quad (3)$$

where  $k = 2\sqrt{\rho/E}L/\alpha$  is a time-scale characterizing the mechanical resonance of the isolated whisker: the fundamental resonance frequency of the freely vibrating whisker reads  $f_{FRF} = 1.39/k$ . In this expression, all lengths are expressed in units of  $L$ . Equation (3) is classically solved by separation of time and space variables:  $u(s, t) = V(s)q(t)$ . The spatial term  $V(s)$  obeys the following equation:

$$(s^4 V'')'' - k^2 \omega^2 s^2 V = 0 \quad (4)$$



The choice of boundary conditions (discussed below) sets the series of admissible angular frequencies  $\omega_i (i = 1, 2, \dots) = \kappa_i/k$  and corresponding resonant spatial modes  $V_i(s) (i = 1, 2, \dots)$ . Each mode is associated with a harmonic equation

of motion that reads:

$$\ddot{q} + \omega_i^2 q = 0 \tag{5}$$

In the absence of any knowledge on the underlying mechanism, dissipative processes are accounted for by introducing a linear damping term in the time-dependent Equation (5) with a mode-independent damping ratio  $\zeta$ . The dynamic equation is thus rewritten as:

$$\ddot{q} + 2\zeta\omega_i\dot{q} + \omega_i^2 q = 0 \tag{6}$$

Within this hypothesis, the general solution for the freely oscillating whisker finally reads:

$$u(s, t) = \sum_i V_i(s) \left( \alpha_i \cos(\sqrt{1-\zeta^2}\omega_i t) + \beta_i \sin(\sqrt{1-\zeta^2}\omega_i t) \right) e^{-\zeta\omega_i t} \tag{7}$$

### DEPENDENCE OF THE WHISKER RESONANCE FREQUENCY ON THE CONTACT POINT LOCATION

The resonant spatial modes  $V_i(s)$  and associated angular frequencies  $\omega_i$  depend on the boundary conditions. As already mentioned, the whisker is assumed to be rigidly anchored at its base, which imposes  $V(1) = V'(1) = 0$ . The different phases of the exploration correspond to distinct boundary conditions at the whisker tip.

- (a) As the whisker rolls over the object's edge, the maintained contact imposes a constant position of the whisker at  $s = \epsilon$ . Ignoring the inertia of the whisker tip (the region  $s_{tip} < s < \epsilon$ ), the moment at contact is null. The boundary conditions thus read  $V(\epsilon) = V''(\epsilon) = 0$ .
- (b) As the whisker slides onto the object's flat surface, the maintained frictional contact imposes both a constant position and orientation of the whisker at  $s = \epsilon$ , so that  $V(\epsilon) = V'(\epsilon) = 0$ .
- (c) After detachment of the whisker from the object, the whisker oscillates freely in air. This yields a null moment and null force condition at the whisker tip, such that  $V''(\epsilon) = (s^4 V'')'(\epsilon) = 0$ .

For each value of the contact location  $\epsilon$  in the range  $0.01 < \epsilon < 0.2$ , the first five modes  $V_{1-5}(s)$  and associated adimensional angular frequencies  $\kappa_{1-5}$  are numerically computed using Mathematica v8.0 (Wolfram Research). **Figures 4B,D** display the spatial resonant modes obtained for  $\epsilon = 0.1$  and boundary conditions (a) and (c), respectively. Their strong asymmetry results from the tapered geometry of the whiskers. The resonant normalized angular frequencies  $\kappa_1$  and  $\kappa_2$  are shown in **Figure 4C** as a function of  $\epsilon$  for boundary conditions (a). Both angular frequencies are found to increase as the contact point moves toward the base. The arrows indicate the corresponding angular frequencies for an isolated (freely vibrating) whisker. In order to express the resonant frequencies  $f_i = \kappa_i/(2\pi k)$  in physical units (right axis scale), a typical time-scale  $k$  is computed using data from the literature (Hartmann et al., 2003). This value  $k = 30.4$  ms is conserved throughout the article.

The slender geometry of the whisker confers it the property of a resonant oscillator, which thus acts as a mechanical band-pass filter. Neimark et al. observed resonance when shaking the whisker near its tip with a piezoelectric actuator (fixed–fixed boundary conditions) (Neimark et al., 2003). Although the boundary conditions were different between those data (fixed–fixed) and our model (fixed–pinned), the frequencies they reported for  $\beta$  and C1 fell within our predicted range (Figure 4C). Owing to their various lengths, the resonant frequencies of the freely vibrating whiskers span a wide range across the pad. This observation led Neimark et al. to propose a tonotopic scheme for texture encoding in which each whisker would transduce one particular spatial wavelength (Neimark et al., 2003). The present model may in part explain why this encoding scheme hypothesis failed to receive experimental validation so far. The effective resonant frequencies varies with the location of the contact point along the whisker and the way that the whisker is pinned and/or fixed at the contact point (see Figure 4C). The optimal transduction frequencies in real sensing situations, rather than being whisker specific, are thus expected to vary by a factor of up to 3 over the course of a single sensing task. It is tempting to suggest in reverse that the instantaneous resonant frequency may used by the rat to extract information about the distance from the pad to the touched object. However, the dependence being relatively weak (owing to the tapered geometry of the whisker), the spectral characteristic of the whisker dynamic is unlikely to play a significant role in the precise determination of radial distance.

### SHOCK AGAINST THE OBJECT’S EDGE

The resonant modes are now used to investigate the dynamics induced by the shock of the whisker against the object’s edge. The whisker initially rotates in air at constant angular velocity  $\gamma$  around the whisker base. At time  $t = 0$ , the whisker makes contact with the object’s edge at a position  $s = \epsilon$  along the whisker. In line with previous observations (Hartmann et al., 2003), the collision is assumed to be inelastic such that the whisker tip remains in constant contact with the object at  $t > 0$  (no rebound). The duration of the shock-induced oscillation is expected to damp out over a time period of order  $\tau/\zeta$ , where  $\tau$  is the period of the fundamental mode. During this time, the contact point location  $\epsilon$ , deduced from the quasi-static sequence, varies by less than 0.02 (0.002 after one resonant period). We ignore this minute change and assume  $\epsilon$  to be constant, which allows one to describe the oscillating dynamics on a well-defined series of resonant modes.

The whisker profile  $U(s, t)$  at time  $t > 0$  is decomposed as  $U(s, t) = U_{qs}(s, t) + u(s, t)$  where  $U_{qs}(s, t)$  is the quasi-static profile evolution and  $u(s, t)$  characterizes the shock-induced dynamics. By introducing this decomposition in Equation (3),  $u(s, t)$  is found to obey the dynamic equation (see “Methods”):

$$\frac{\partial}{\partial s^2} \left( s^4 \frac{\partial^2 u}{\partial s^2} \right) + k^2 s^2 \frac{\partial^2 u}{\partial t^2} = -k^2 s^2 \ddot{U}_{qs}(s, t) \quad (8)$$

One thus needs to compute the second time-derivative of the quasi-static profile  $\ddot{U}_{qs}(s, t)$ . Prior to the shock, the whisker experiences a solid rotation at constant rotation rate  $\gamma$ .

Immediately after the shock, within the small deflection approximation, the quasi-static profile also evolves linearly in time (see “Methods”). The expression of  $\ddot{U}_{qs}(s, t)$  can thus be written as:

$$\ddot{U}_{qs}(s, t) = \delta(t)\gamma\bar{U}(s) \quad (9)$$

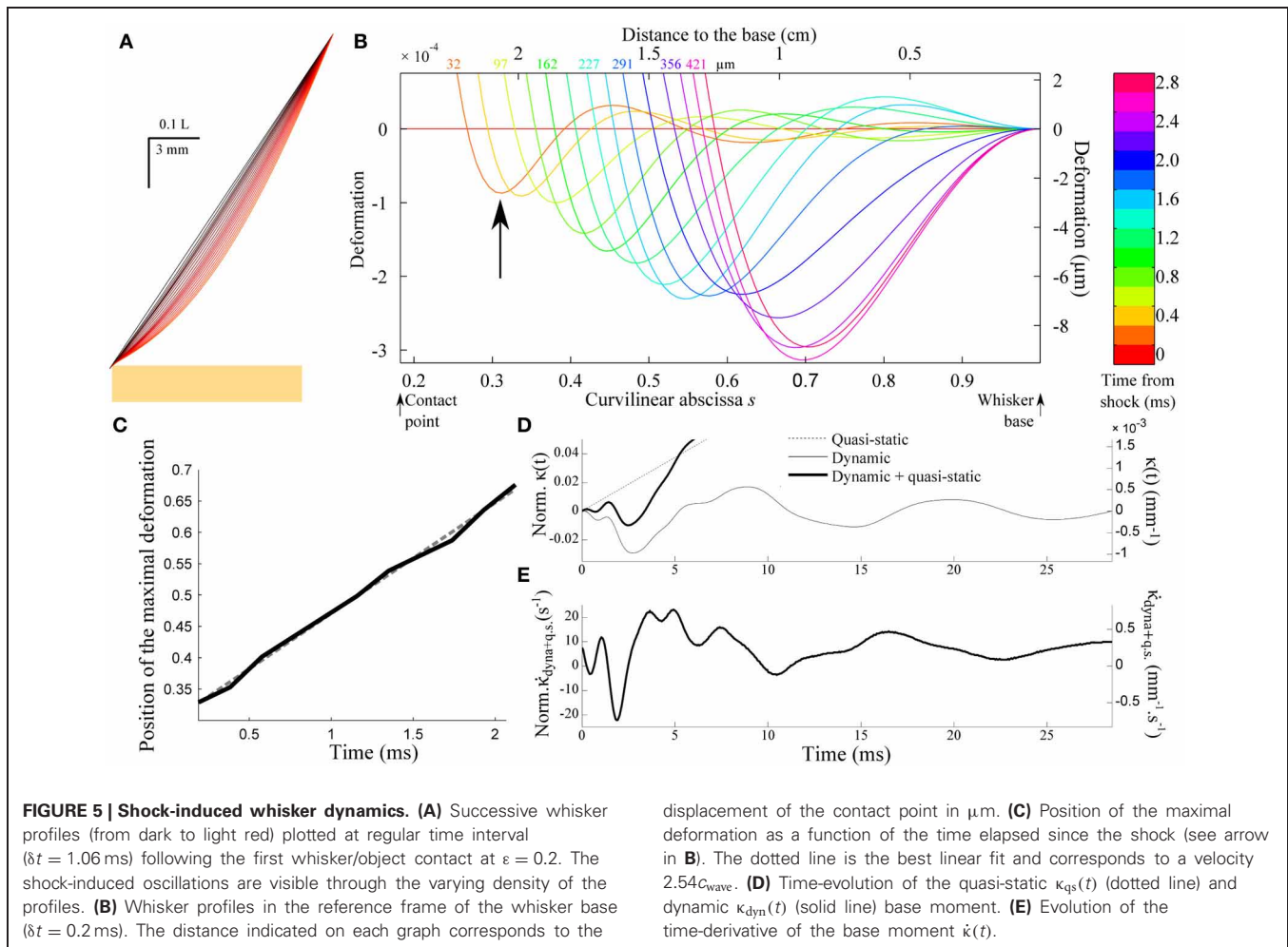
where  $\delta(t)$  is the Dirac function and  $\bar{U}(s)$  is a normalized profile that depends on  $\epsilon$  and  $\gamma$  (see “Methods” for analytical derivation). The dynamic term  $u(s, t)$  is decomposed onto the resonant modes  $V_i(s)$  corresponding to boundary conditions  $V(\epsilon) = V''(\epsilon) = 0$ , in the form  $u(s, t) = \sum_i q_i(t)V_i(s)$ . Projecting expression (Equation 8) onto each mode  $V_i(s)$ , and using the orthogonality of the resonant modes, the mode amplitudes  $q_i(t)$  are found to obey the dynamic equation [see Equations (36–41) in “Methods”]:

$$\begin{aligned} \ddot{q}_i + 2\zeta\omega_i\dot{q}_i + \omega_i^2 q_i &= - \int_{\epsilon}^1 s^2 \ddot{U}_{qs}(s, t) V_i(s) ds \\ &= -\delta(t)\gamma \int_{\epsilon}^1 s^2 \bar{U}(s) V_i(s) ds \end{aligned} \quad (10)$$

Notice that, as indicated before, a damping term is added to account for dissipative processes. After integration, the complete shock-induced dynamics reads:

$$\begin{aligned} U(s, t > 0) &= \gamma t \bar{U}(s) - \gamma \sum_i V_i(s) \left( \int_{\epsilon}^1 s^2 \bar{U}(s) V_i(s) ds \right) \\ &\quad \times \frac{e^{-\zeta\omega_i t} \sin(\sqrt{1-\zeta^2}\omega_i t)}{\sqrt{1-\zeta^2}\omega_i} \end{aligned} \quad (11)$$

Figure 5A shows the successive whisker profiles for a contact located at  $\epsilon = 0.2$ . The damping factor is set at  $\zeta = 0.1$ , consistent with values reported in the literature for the fundamental mode (Hartmann et al., 2003; Neimark et al., 2003). Figure 5B displays the same sequence in the reference frame of the whisker base (the imposed rotation of the whisker base has been subtracted). This graph illustrates how the shock at the tip of the whisker triggers a wave of deflection that travels up to the whisker base. Notice that the first maximum (indicated by an arrow in Figure 5B) is negative, i.e., opposite to the long time scale whisker deflection induced by the object. The position of the first minimum displays a linear dependence with the time elapsed since the shock (Figure 5C). This constant wave velocity results from the tapered geometry, since a  $\sqrt{t}$  dependence is expected in the case of a cylindrical rod (Audoly and Neukirch, 2005). From dimensional analysis of Equation (3), the wave velocity is expected to be of order  $c_{wave} = \alpha c$  where  $\alpha$  is the cone angle and  $c = \sqrt{E/\rho}$  is the sound velocity in the bulk material. The apparent wave velocity obtained by linear fitting on graph C is consistently found to be  $2.54c_{wave}$  (5.02 m/s in physical units). Figure 5D shows the evolution of the moment  $\kappa(t) = \partial^2 U / \partial s^2 (s = 1, t)$  at the base of the whisker (black solid line). The graph also displays both the dynamic ( $\kappa_{dyn}(t) = \partial^2 u / \partial s^2 (s = 1, t)$ , gray solid line) and quasi-static ( $\kappa_{qs}(t) = \partial^2 U_{qs} / \partial s^2 (s = 1, t)$ , dotted line) components for comparison. Although the maximum amplitude of the deflection wave is of the order of 15  $\mu\text{m}$ , i.e., a small fraction



of the whisker base diameter, it yields a significant negative dip in the whisker base curvature dynamics. The time-derivative  $\dot{\kappa}(t)$  signal (Figure 5E) in turn exhibits a clear signature of the whisker/object contact in the form of large amplitude oscillation with a peaked maximum occurring at a time  $\tau_{\text{peak}} \approx 4$  ms after the shock.

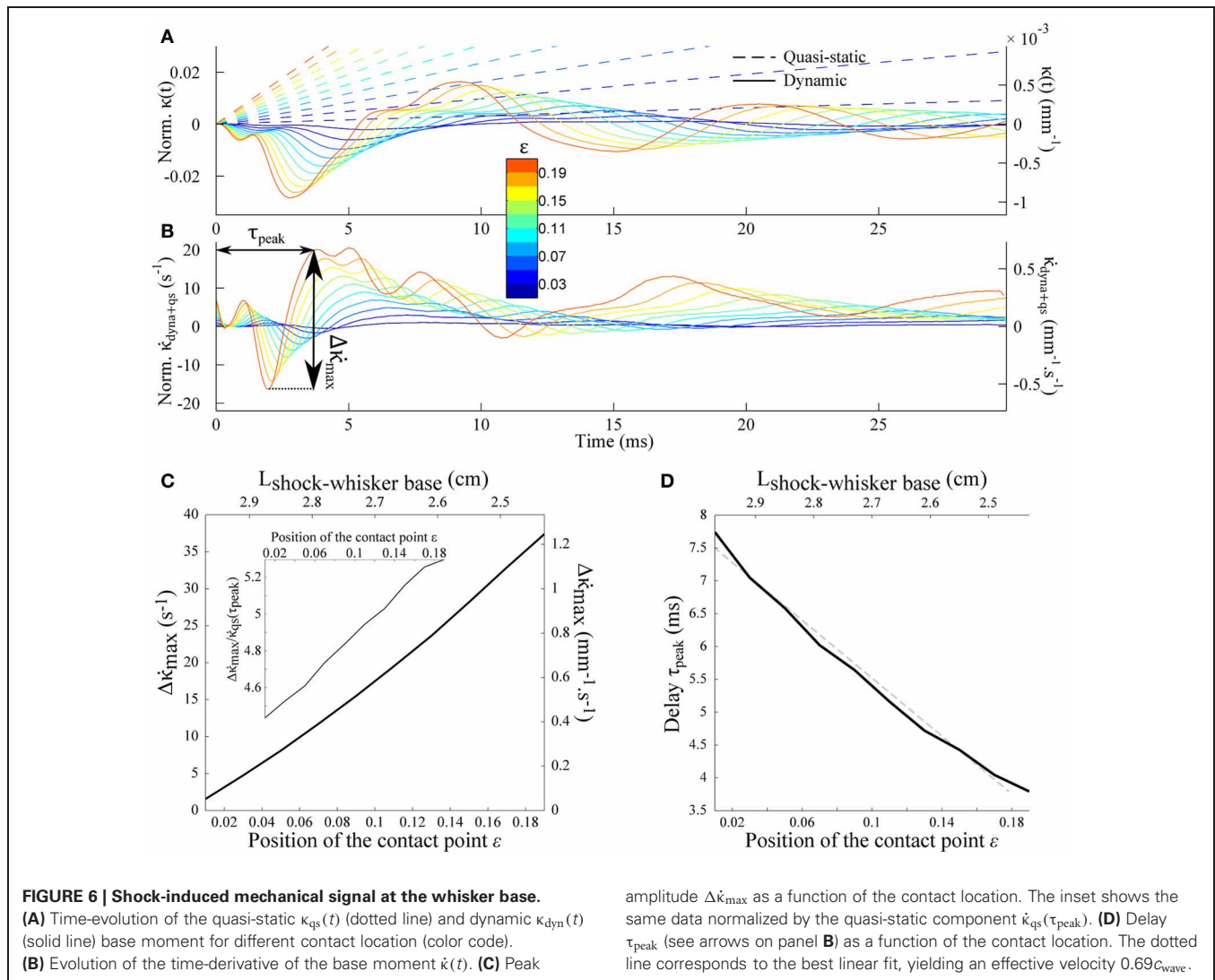
Equation (11) indicates that the peak amplitude  $\Delta \dot{\kappa}_{\text{max}}$  should be linearly proportional to the rotation rate  $\gamma$ . It also increases as the contact point moves toward the whisker base i.e., for shorter radial distances (Figures 6A–C). Notice that the peak amplitude remains larger than the quasi-static value  $\dot{\kappa}_{\text{qs}}(\tau_{\text{peak}})$  (Inset). The last graph of Figure 6 shows the delay  $\tau_{\text{peak}}$  between the shock event and the arrival of the mechanical signal at the whisker base as a function of the contact location. The dependence is quasi-linear within the range of  $\epsilon$  explored, which allows us to extract an approximate velocity  $0.69c_{\text{wave}}$  (1.36 m/s in physical units) of the same order as the wave velocity determined in Figure 5.

In the range of parameters explored, the maximum angular deflection of the whisker during the process is 0.06. This value validates the small angle hypothesis underlying the present analysis (Birdwell et al., 2007).

#### EXPERIMENTAL MEASUREMENTS OF SHOCK-INDUCED OSCILLATION

These predictions are tested experimentally on an anesthetized rat using high-speed videography (see “Methods”). The rat, and thus the whisker base, are maintained fixed while a thin bar is moved at constant speed  $V_{\text{bar}} = 60$  mm/s against the whisker tip (Figure 7A). We used a constant speed and not a tap since in that case a sudden acceleration would happen, which is a different condition and ethologically more unlikely to happen. The bar is vertical and fixed by its edge to a rectilinear motor. During the early instants following the shock, which are analyzed here, the whisker did not slip onto the bar such that the contact point along the whisker can be considered invariant. Whisker movements are captured using a bird’s-eye view high-speed camera operating at 2.5 kHz (Figure 7A). Whisker centerline profiles are tracked within each frame between the fur and the bar with a custom-designed semi-automatic script. The shock-induced whisker deflection profile  $U(s, t)$  is obtained by subtracting, for each frame, the whisker intrinsic profile as determined from images recorded before the shock.

The resulting sequence of shock-induced whisker deflections is shown in Figure 7B for a  $\beta$  whisker (length 46 mm) during the first 3 ms from the instant of collision. Consistent with the

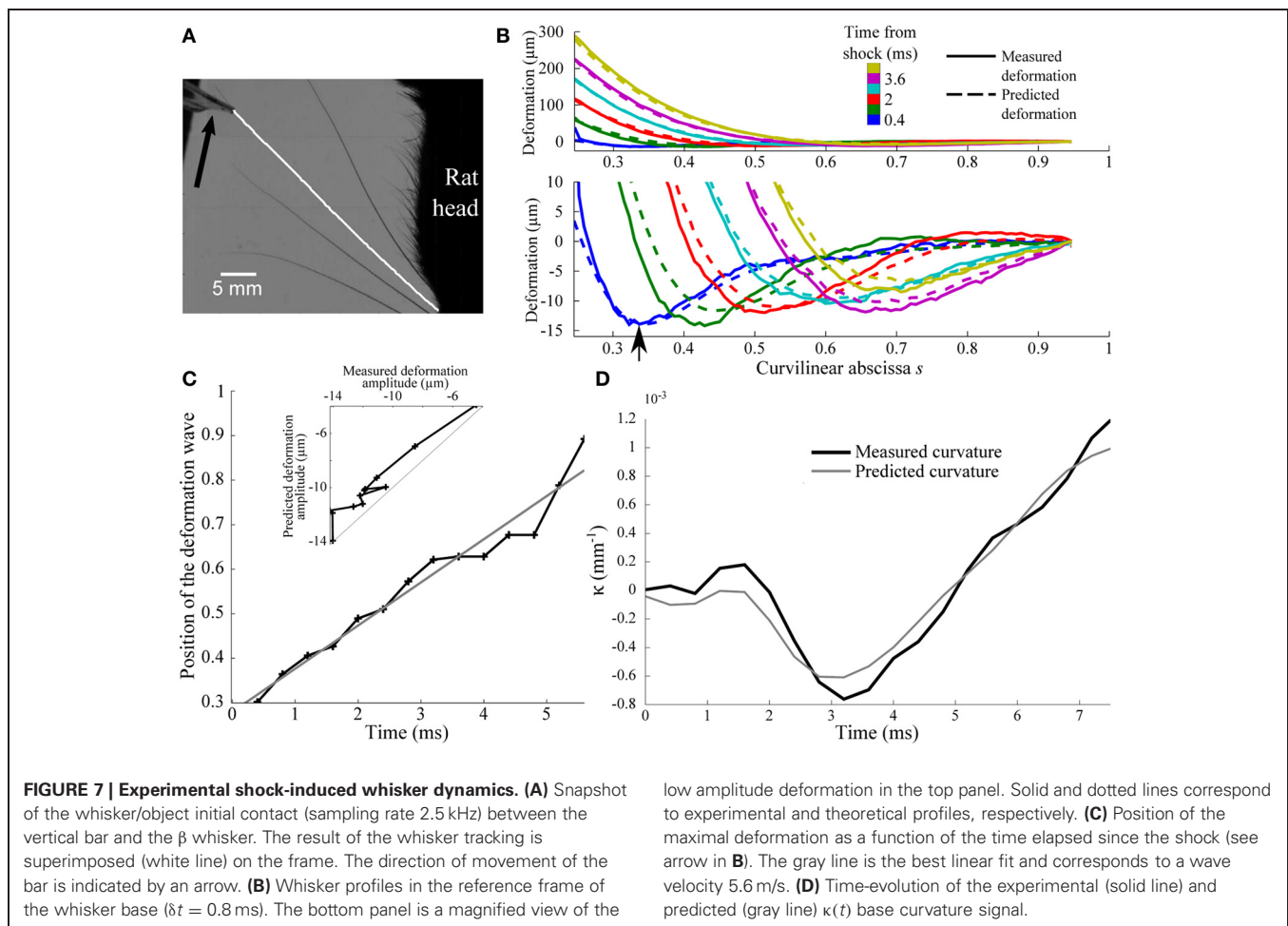


model, a deflection wave is observed characterized by a negative maximum deflection propagating upward. As expected, the wave appears to propagate at constant speed as indicated by the linear dependence of the location of the maximum deflection with time (**Figure 7C**). This allows us to extract an effective wave velocity equal to 5.6 m/s, in close agreement with the typical value predicted before.

In order to more quantitatively compare these results with the biomechanical model, we decomposed the whisker dynamics into rapid resonant oscillations superimposed onto a slow quasi-static sequence of deformation imposed by the moving bar. The quasi-static evolution  $U_{qs}(s, t)$  is first evaluated using the profiles measured at long time scale, i.e., when the relative contribution of the dynamic oscillation is expected to be negligible ( $t > 8$  ms). As expected, in this regime,  $U_{qs}(s, t)$  can be linearized as  $U_{qs}(s, t) = V_{bar}t\bar{U}(s)$ . The normalized profile  $\bar{U}(s)$  is well fitted by the static theoretical profile in the limit of small deflection (see “Methods”). The best fit yields a value of  $\epsilon = 0.25$ . Using the long time-scale normalized profile  $\bar{U}(s)$ , the complete sequence of whisker deflection  $U(s, t)$  is computed using the same scheme as described

earlier [adapted to the linear displacement configuration (see “Methods”)]. The comparison, for each parameter, is shown in **Figures 7B–D**. The model quantitatively captures not only the wave propagation dynamics ( $r^2 = 0.96, p < 2.10^{-9}$ ) (**Figure 7C**), but also the amplitude of the maximum deflection ( $r^2 = 0.94, p < 2.10^{-8}$ ) (inset in **Figure 7C**) and, most importantly, the base curvature signal ( $r^2 = 0.94, p < 2.10^{-8}$ ) (**Figure 7D**).

Identical measurements were performed for a C1 whisker (length 36 mm;  $\epsilon = 0.15$ ). The wave dynamics was found consistent with the model prediction ( $r^2 = 0.95, p < 10^{-5}$ ) with a wave velocity of 5.8 m/s, close to the value obtained for the  $\beta$  whisker. The measured wave amplitude appeared significantly lower than predicted during the first ms following the shock, resulting in low values of correlation for this parameter ( $r^2 = 0.41, p = 0.06$ ). After this initial period, however, a very consistent match was recovered ( $r^2 = 0.97, p < 5.10^{-5}$ ). The measured curvature signal at the whisker base being rather unaffected by the early deflections of the whisker tip, it was found to agree with the prediction for all the duration of the process ( $r^2 = 0.65, p = 0.0027$ ).



### CONSEQUENCE FOR EVENT-BASED OBJECT POSITION ENCODING

As the rat repetitively whisks onto an object, it produces a series of shocks. The present work demonstrates that each of them triggers, a few ms after contact, a characteristic signature in the base curvature signal which can be quantitatively predicted using a first order mechanical model of the whisker. The resulting mechanical stimulation at the whisker pad should be sufficiently intense to trigger a clear neural response. As displayed in **Figure 7**, the whisker peak base curvature is of the order of  $10^{-3} \text{ mm}^{-1}$  and its maximum time-derivative varies up to  $1 \text{ mm}^{-1} \cdot \text{s}^{-1}$ . Stimuli of comparable intensity have been shown to elicit reliable cortical discharges (O'Connor et al., 2010b; Huber et al., 2012).

Notice that the peak in the base curvature time derivative has an opposite sign and a larger amplitude compared to the long-time component, which may explain how so-called touch cells may specifically respond to first contact (Szwed et al., 2003). It has been recently proposed that these cells may mediate the coding of object angular position with respect to the pad through the precise timing of the shock event within the whisking cycle (Knutsen and Ahissar, 2009). The present biomechanical analysis allows us to estimate how the pre-neural whisker transduction contributes to the horizontal resolution of such an encoding scheme.

If one assumes that the neural response is triggered by the maximum of  $\dot{\kappa}(t)$ , the jitter  $\Delta T$  in the mechanoreceptor response

(the dispersion in spike timing) should be a fraction of the fundamental resonant period, i.e., a few ms. With a characteristic rotation rate during whisking of order  $\gamma = 400^\circ$ , this yields an angular resolution of  $\gamma \Delta T \approx 1^\circ$  consistent with available behavioral data (Knutsen et al., 2006). This crude evaluation implicitly ignores the lag between the shock and the arrival of the deflection wave at the whisker base that elicits the mechanoreceptors' response. This delay was shown to be of the order of  $c_{\text{wave}} L_{\text{contact-base}}$  where  $L_{\text{contact-base}}$  is the arc length between the contact point and the whisker base. This lag effect induces an additional error of up to a few degrees on the angular position of the object if its radial distance is unknown.

One may therefore suggest that the radial distance is evaluated using a parallel coding channel. One possible scenario, as originally proposed by Szwed et al. (2003), relies on the intensity of the mechanical signal which appears to decay rapidly with the radial distance, as shown in **Figure 6C**. By combining both information (timing and intensity of the shock-induced whisker base mechanical signal), a precise localization of the object can be recovered (Knutsen and Ahissar, 2009).

### DETACHMENT

We now turn to the detachment process that occurs when the whisker tip reaches the second edge of the object. We note  $t = 0$

the time at which the whisker snaps off. At  $t > 0$ , the whisker detaches from the object then oscillates freely in air. The profile is decomposed as  $U(s, t) = U_{qs}(s, t) + u(s, t)$  where  $U_{qs}(s, t)$  is the quasi-static evolution. The continuity of the position and velocity profiles at time  $t = 0$  imposes:

$$u(s, t = 0) = \Delta U_{qs}(s) \quad (12)$$

$$\dot{u}(s, t = 0) = \Delta \dot{U}_{qs}(s) \quad (13)$$

where  $\Delta U_{qs}(s) = U_{qs}(s, 0^-) - U_{qs}(s, 0^+)$  and  $\Delta \dot{U}_{qs}(s) = \dot{U}_{qs}(s, 0^-) - \dot{U}_{qs}(s, 0^+)$ . The term  $u(s, t)$  is decomposed along the resonant modes with boundary conditions  $V''(\epsilon) = (s^4 V'')'(\epsilon) = 0$  as in Equation (7):

$$u(s, t) = \sum_i V_i(s) (\alpha_i \cos(\sqrt{1-\zeta^2} \omega_i t) + \beta_i \sin(\sqrt{1-\zeta^2} \omega_i t)) e^{-\zeta \omega_i t} \quad (14)$$

Projecting Equations (12) and (13) on each spatial mode, the coefficients  $\alpha_i$  and  $\beta_i$  can be written, in the limit  $\zeta \ll 1$ :

$$\alpha_i = \int_{\epsilon}^1 s^2 \Delta U_{qs}(s) V_i(s) ds \quad (15)$$

$$\beta_i = \frac{1}{\omega_i} \int_{\epsilon}^1 s^2 \Delta \dot{U}_{qs}(s) V_i(s) ds \quad (16)$$

In order to obtain an expression of  $\Delta U_{qs}$  and  $\Delta \dot{U}_{qs}$ , the quasi-static profiles are computed at time  $\{-\delta t, 0^-, 0^+, \delta t\}$  with  $\delta t \ll 1/\gamma$ . This allows us to obtain linearized expressions of the quasi-static profile sequences around  $t = 0$ , before and after the shock, in the form:

$$U_{qs}(s, t < 0) = U_{qs}(s, 0^-) + \frac{U_{qs}(s, 0^-) - U_{qs}(s, -\delta t)}{\delta t} t \quad (17)$$

$$U_{qs}(s, t > 0) = U_{qs}(s, 0^+) + \frac{U_{qs}(s, \delta t) - U_{qs}(s, 0^+)}{\delta t} t \quad (18)$$

This yields:

$$\Delta U_{qs}(s) = U_{qs}(s, 0^-) - U_{qs}(s, 0^+) \quad (19)$$

$$\Delta \dot{U}_{qs}(s) = \frac{1}{\delta t} (U_{qs}(s, 0^-) - U_{qs}(s, -\delta t) - U_{qs}(s, \delta t) + U_{qs}(s, 0^+)) \quad (20)$$

**Figure 8A** shows the evolution of the whisker profile just after the detachment, for different base angle  $\theta_b$  at detachment. When the quasi-static evolution is subtracted (**graph B**), one recovers a wave propagation mechanism qualitatively similar to that observed after the shock (wave speed of order 3.5 m/s). This event produces a characteristic signature at the whisker base shown in **Figures 8B,C**. Notice that the mechanical signal is rather insensitive to the whisker base angle prior to the detachment.

As indicated earlier, the present analysis is based on the assumption that the whisker remains weakly deformed during the

whole process. As shown in **Figure 8A**, this hypothesis becomes valid only a few hundreds of microseconds after the event is triggered. At very early time, and for large angular and small radial distances to the object, the tip of the whisker exhibits large deflection angle. However, owing to the conical shape of the whisker, the large deformation appears to be confined to the very end of the whisker: in the range of configurations explored, 80% of the whisker, i.e., 99% of the mass, displays a deflection angle smaller than 0.5. The small angle approximation should therefore provides a reasonable first order approximation of the detachment dynamics for all situations explored.

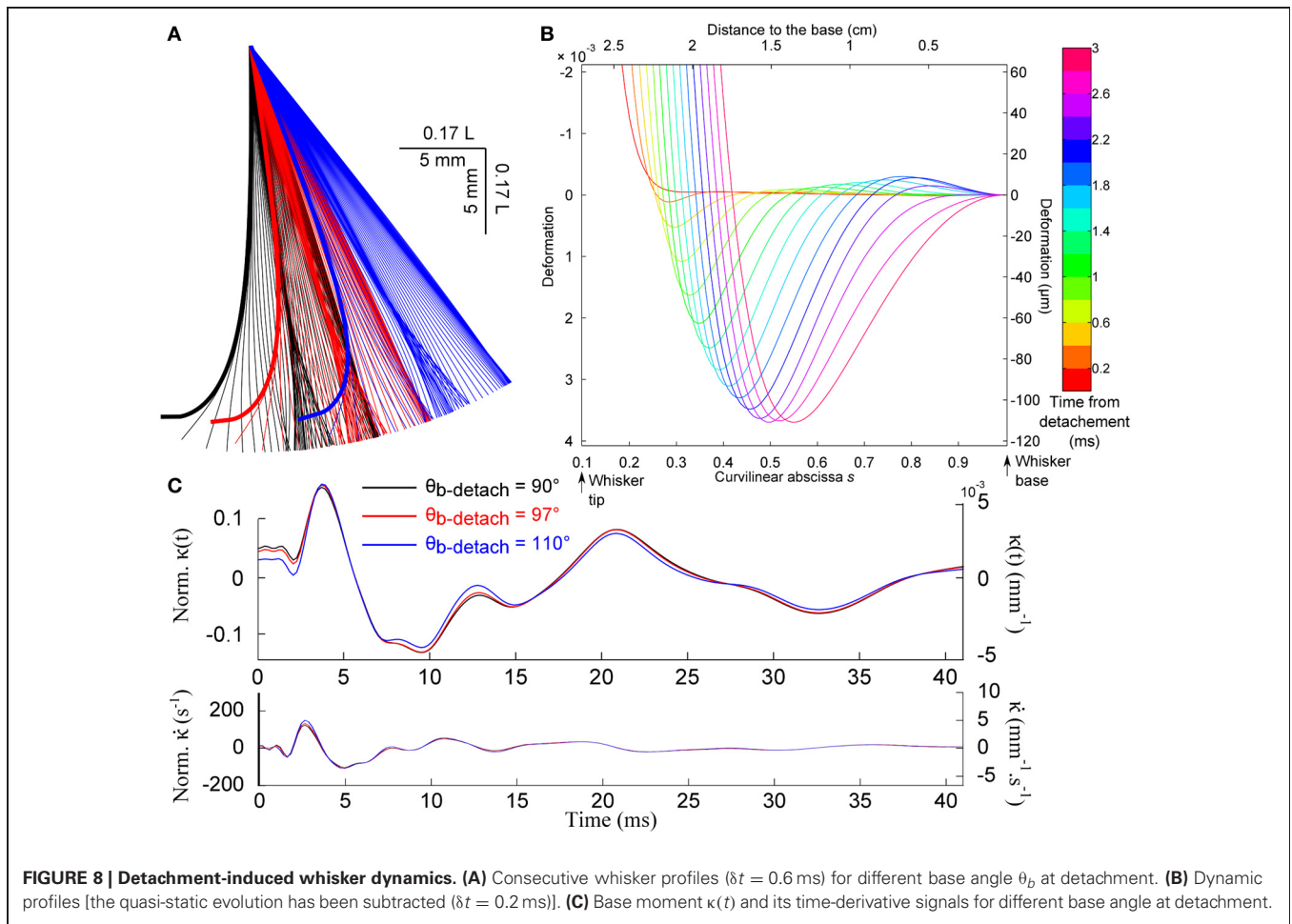
The whisker detachment from the object also triggers a deflection wave that propagates upward at a speed comparable to that observed for the shock event. The resulting signal at the whisker base appears to be  $\approx 10$  times more intense than for the shock. It should thus trigger significant neural response, as confirmed by the existence of so-called detachment cells whose response is specifically triggered by such events (Szwed et al., 2003). Our study shows that an increase in the friction coefficient delays the detachment process (**Figure 3B**). The precise timing of the detachment-induced signal may thus provide an indication on the surface frictional properties. Such a scenario would however, require the independent knowledge of the angular position of the object edge.

#### VIBRISAE CAN BE ASSUMED TO BE UNIFORMLY DAMPED OVER ALL SPATIAL MODES

A key assumption in the development of the present model is that the damping coefficient of the vibrissa is constant over all spatial modes. Previous experimental studies, however, have shown that magnification ratio increases with mode number (Hartmann et al., 2003; Neimark et al., 2003). Specifically, the bottom plot of Figure 4 of Hartmann et al. (2003), and Figure 4 of Neimark et al. (2003) (e.g., the  $\beta$  whisker) both show an increase in peak magnitude with mode number. Note that Neimark et al. chose to plot the curve assuming constant amplitude (instead of constant acceleration), so each peak must be scaled by the frequency squared to demonstrate the increase with mode number. This experimental finding has until now been unexplained, although Hartmann et al. (2003) suggested that it was likely in part due “to nonlinear effects of viscous and/or hysteretic damping.”

Here we show that, at odds with the authors’ proposed interpretation, a linearly damped model of whisker with a mode-independent damping ratio, as assumed in the present work, allows one to correctly capture this measurement. It also illustrates how the mode-decomposition approach introduced in the present study, may allow to quantitatively re-analyze earlier data on whisker dynamics.

Throughout the calculation, we use the same notation as in the present article. The text indicates that the whisker has a length  $L_{\text{whisker}} = 53$  mm, a base radius  $b = 105 \mu\text{m}$  and a tip radius  $r_{\text{tip}} = 5.5 \mu\text{m}$ . Assuming a conical shape, this yields  $\epsilon = r_{\text{tip}}/b = 0.05$ . Using the Young modulus  $E = 3.02$  GPa and  $\rho = 1.14$  mg/mm<sup>3</sup> indicated in the article, the values for the (undamped) resonant frequencies can be computed and read:  $F_i = \{37.9, 93.4, 175.4$  Hz}. The whisker base is forced with a



sinusoidal motion [Figure 9A reproduced from Hartmann et al. (2003)], starting at  $t = 0$ :

$$A_{\text{base}}(t) = A_{\text{base}} \sin(\omega t) \tag{21}$$

The whisker response is derived using the same scheme as detailed in the present article. The displacement sequence is broken into  $U(s, t) = U_{\text{qs}}(s, t) + u(s, t)$  where the first term represents the massless whisker response:  $U_{\text{qs}}(s, t) = A_{\text{base}} \sin(\omega t)$ . The dynamic term can thus be written as:

$$\begin{aligned} u(s, t) &= \sum_i V_i(s) \int_{\epsilon}^1 s^2 V_i(s) ds \int_0^t G(t-t') \ddot{U}_{\text{qs}}(s, t') dt' \tag{22} \\ &= -A_{\text{base}} \sum_i V_i(s) \int_{\epsilon}^1 s^2 V_i(s) ds \int_0^t G(t-t') \omega^2 \\ &\quad \times \sin(\omega t') dt' \tag{23} \end{aligned}$$

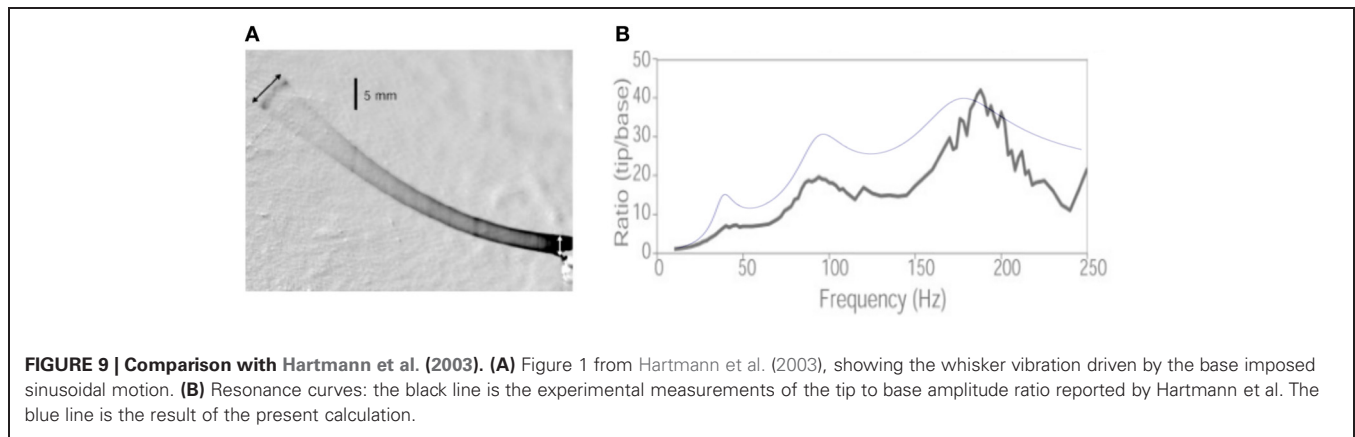
where  $G(t)$  is the Green's function of the resonant system (Equation 49).

The time-dependent term in Equation (23) can be analytically integrated. It oscillates at the driving frequency with an absolute peak-to-peak amplitude that can be written as  $2F(\omega/\omega_i, \zeta)$ .

Due to the resonant nature of the system, the spectrum is dominated by the closest resonant mode. We thus approximate the maximal amplitude of the response signal with the sum of the maximal amplitude of each mode signal. The ratio between the whisker tip oscillation amplitude (the peak-to-peak amplitude of signal  $U(s, t)$  measured at  $s = \epsilon$ ) and the driving base amplitude  $2A_{\text{base}}$  thus reads:

$$R(\omega) \approx 1 + \sum_i \left[ V_i(\epsilon) \int_{\epsilon}^1 s^2 V_i(s) ds \right] F(\omega/\omega_i, \zeta) \tag{24}$$

The dependence of the maxima of the response signal with mode number thus depends primarily on the series of prefactors  $V_i(\epsilon) \int_{\epsilon}^1 s^2 V_i(s) ds$ , such that no conclusion can be drawn without prior knowledge of the resonant spatial modes. In the present case, this prefactor reads, for the first three modes: {3.7, 6.5, 7.6} and thus does increase with the mode number. Notice that the evolution of the peak amplitude results from the conical shape of the whisker—it would decrease for a cylindrical rod. Figure 9B compares the prediction obtained for a damping ratio of 0.15 (a characteristic value given by the authors) identical for all three modes. Although no adjustable parameter has been used to produce this plot, it does captures the evolution of the whisker tip



response. The slight over-estimation of the two first modes can be due to the fact that the whisker displays significant spontaneous curvature, such that the small angle limit is not strictly valid.

It thus appears that the data reported in previous experimental studies (Hartmann et al., 2003; Neimark et al., 2003) are, to first order, consistent with a linear damping model with a unique damping ratio for all modes.

## DISCUSSION

The biomechanical model presented here provides a generic method to describe the mechanical transduction operated by the whisker in realistic conditions of exploration. The theoretical approach consists of successively computing the slow (quasi-static) evolution of the whisker and the rapid resonant dynamics. It provides prediction of the complete whisker deflection, and in particular of the mechanical signal elicited in the follicle which conveys the relevant peripheral input for the mechanoreceptors. It is therefore directly amenable to experimental comparison as illustrated in the present article in the case of first contact. In this configuration, we were able to characterize the dynamic of the deflection wave with micron-scale resolution by subtracting the static configuration of the whisker prior to the event. For the detachment case, the deflection wave proved to be difficult to observe with such precision owing to the continuous evolution of the whisker quasi-static profile prior to the event.

Beyond the specific context in which it is implemented in the present study, this biomechanical model may constitute a useful tool for understanding the neural encoding of tactile information. It may in particular guide the type of stimuli that needs to be played at the whisker base during electrophysiological recordings in the somatosensory cortex. It should also find direct applications in robotic rats by easing the development of decoding algorithms allowing one to extract relevant physical information from the whisker inputs (Kim and Möller, 2007). This approach, unlike finite-element models, allows one to clearly identify the consequences of whiskers' resonant properties.

The model is based on several simplifying assumptions and should therefore be considered as a first order description of the whisker dynamics. First, the whisker spontaneous curvature and out-of-plane deflections are ignored. For moderately curved whisker, the spontaneous curvature can be accounted for when

deriving the quasi-static sequence by modifying Equation (1) as explained in the "Methods" section. The prediction of the dynamic model itself does not depend on the resting state. However, for largely deformed whisker, the paradigmatic scenario envisioned here might be changed. In particular, the hypothesis of a shock normal to the whisker axis might be unrealistic for strongly concave-forward whiskers (Quist and Hartmann, 2012). For such vibrissae, the out-of-plane deflections are bound to be also significant.

Second, the whisker is assumed to exhibit a conical shape and to be linearly elastic, with uniform density and elastic modulus. It has been recently reported that the Young's modulus  $E$  may vary significantly along the whisker, owing to its internal structure (Quist et al., 2011), although conflicting results exist (Carl et al., 2012). However, one should notice that the modulus appears in the equation through the bending stiffness which scales as  $r^4E$  ( $r$  whisker radius), so that the most critical hypothesis should actually lie in the conical shape assumption. Indeed, a 10% deviation to the conical shape is expected to induce a larger deviation than a 40% variation of  $E$  along the whisker.

Third, the model assumes linear damping, characterized by a unique parameter  $\zeta$  in the dynamic equation. This *ad-hoc* introduction of a damping term is not based on any sort of physical modeling and reflects the absence of prior knowledge on the nature of dissipative processes. At least five different mechanisms may contribute to damping: visco-elastic dissipation in the whisker itself, mechanical radiation in the tissue, air friction, interfacial dissipation at the whisker/substrate contact, visco-elastic dissipation in the follicle. In the absence of well-established mechanical descriptions of the dissipative mechanism, it is common for lightly damped systems (i.e., effective damping ratio  $<0.2$ ) to assume proportional damping (Weaver et al., 1990), as done in the present work. One should notice that typical damping ratios reported in the literature for the fundamental mode lies in the range  $0.1 < \zeta < 0.2$  such that the resonant system is well within the underdamped limit. As a result, the resonant frequency is not strongly affected by the precise choice of the damping ratio. During the review process, one of the referees pointed to us that the linear damping hypothesis with a unique damping ratio appears at odds with resonance curves experimentally obtained by Hartmann et al. on isolated whiskers (Hartmann et al., 2003).

When re-analyzed using the resonant modes description, these data are in fact consistent with this hypothesis as demonstrated in the “Methods” section.

Within this set of hypothesis, it appears that the whisker transduction mechanism depends on the whisker intrinsic properties through only three independent parameters: (1) the length of the equivalent non-truncated whisker  $L$  (2) the wave velocity  $c_{\text{wave}} = \alpha\sqrt{E/\rho}$  that characterizes the speed at which information is conveyed from the whisker tip to the follicle, and (3) the damping factor  $\zeta$  that reflects the dissipative processes (the intrinsic time-scale  $k$  is the product  $2c_{\text{wave}}L$ ). Notice that the Young’s modulus  $E$ , the density  $\rho$ , and the cone angle  $\alpha$  vary in a small range across the whisker pad (Hartmann et al., 2003; Carl et al., 2012; Voges et al., 2012) so that  $c_{\text{wave}}$  should weakly depend on the whisker identity. Similarly, the values reported for the damping factor appear to lie within a rather small range (Hartmann et al., 2003; Neimark et al., 2003). When displayed in reduced coordinates (all lengths being expressed in units of  $L$ ), the present results should therefore provide a reasonable description of the rapid whisker dynamics, regardless of the whisker identity.

The last and most limiting hypothesis of the proposed dynamic model is that its validity requires the whisker deflection to remain small. For large deflections, the dynamic equation should include additional terms that reflect the coupling between the quasi-static (deformed) state and the oscillating dynamic. This correction might become significant when one attempts to describe situations in which the whisker vibrates around strongly pre-deformed configurations, such as encountered during exploration of textured surfaces for instance. At the expense of significant mathematical developments, it should be possible to derive the resonant spatial modes in this regime and then implement the same theoretical scheme. However, as illustrated with the detachment process, the whisker tapered shape tends to confine the large deflection to the very end of the whisker even for large angular distances. One may thus hope that this first order description provides a good approximation in most realistic exploratory conditions. We postpone the discussion of this regime of whisker oscillations during sliding to a forthcoming publication.

## METHODS

### EQUILIBRIUM PROFILE OF A FRICTIONAL WHISKER

The whisker is modeled as a slender tapered rod of length  $L$  and maximum base radius  $b$ . The cone angle  $b/L$  is noted  $\alpha$ . The whisker base is rigidly clamped with a fixed angle  $\theta(s=1) = \theta_b$  and submitted to a frictional force  $F$  assumed to be applied at a single point located at  $s = \varepsilon$  along the whisker. The present analysis is restricted to configurations where  $\varepsilon > s_{\text{tip}}$  which constrains the whisker to be locally tangent to the object surface. The orientation of the friction force  $F$  with respect to the direction normal to the whisker at  $s = \varepsilon$  is set by the friction angle  $\phi = \tan(\mu)$  where  $\mu$  is the friction coefficient (see **Figure 2B**). Forces balance along the whisker yields an expression for the normal  $N(s)$  and tangential force  $T(s)$  at location  $s > \varepsilon$ :

$$N(s) = F \cos(\phi - \theta + \theta(\varepsilon)) \quad (25)$$

$$T(s) = F \sin(\phi - \theta + \theta(\varepsilon)) \quad (26)$$

The momentum equilibrium further imposes:

$$\frac{\partial M}{\partial s} - N(s) = 0 \quad (27)$$

where the bending moment can be expressed as  $M(s) = EI\theta'$ ,  $I = \frac{\pi\alpha^4 s^4}{4}$  is the area moment of inertia and  $E$  is the Young’s modulus. From Equations (25) and (27), one obtains the dimensionless static equilibrium equation:

$$(s^4\theta')' - \tilde{F} \cos(\phi - \theta + \theta(\varepsilon)) = 0 \quad (28)$$

where all distances are scaled by the length of the non-truncated cone  $L$  and the reduced force  $\tilde{F} = 4F/(\pi\alpha^4 EL^2)$ . Notice that the intrinsic in-plane whisker curvature  $\theta'_{\text{int}}(s)$  could be taken into account by substituting the first (derivative) term by  $(s^4(\theta' - \theta'_{\text{int}}))'$ . In the present study, the intrinsic whisker curvature is supposed to be null. Equation (28) is solved numerically using Mathematica v8.0 (Wolfram Research) through integration of the following equation:

$$\frac{\partial}{\partial s} \left( \frac{(s^4\theta')'}{\cos(\phi - \theta + \theta(\varepsilon))} \right) = 0 \quad (29)$$

We assume the whisker to be rigidly clamped in the pad such that  $\theta(1) = \theta_b$ . The friction force is assumed to apply at a single location so that the bending momentum is null at the contact point:  $\theta'(\varepsilon) = 0$ . For any values of the friction coefficient  $\mu$ , maximum angle  $\theta_b$ , and contact point location  $\varepsilon$ , one finds a unique solution when further imposing the contact angle  $\theta(\varepsilon) < \theta_b$ .

For weakly deformed whiskers, a small angle approximation of Equation (29) can be used which reads, in Cartesian coordinates:

$$(s^4 U'')'' = 0 \quad (30)$$

### ORTHOGONALITY OF THE RESONANT MODES

Multiplying Equation (4) for mode  $i$  by  $sV_j$  and integrating between  $\varepsilon$  and 1 gives the equality:

$$\int_{\varepsilon}^1 (s^4 V_i'')'' V_j ds = k^2 \omega_i \int_{\varepsilon}^1 s^2 V_i V_j ds \quad (31)$$

Integrating the left member by parts (twice) yields:

$$[(s^4 V_i'')' V_j]_{\varepsilon}^1 - [s^4 V_i'' V_j']_{\varepsilon}^1 + \int_{\varepsilon}^1 s^4 V_i'' V_j'' ds = k^2 \omega_i \int_{\varepsilon}^1 s^2 V_i V_j ds \quad (32)$$

The boundary conditions involve that the bracket terms are null. One can rewrite the same expression by swapping  $i$  and  $j$ . If we now subtract both equations, we obtain:

$$(\omega_i^2 - \omega_j^2) \int_{\varepsilon}^1 s^2 V_i V_j ds = 0 \quad (33)$$

The spatial mode  $V_i(s)$  are normalized such that  $\int_{\epsilon}^1 s^2 V_i^2 ds = 1$ . This yields the orthogonality property of the resonant modes:

$$\int_{\epsilon}^1 s^2 V_i V_j ds = 0 \text{ for } i \neq j$$

$$\int_{\epsilon}^1 s^2 V_i V_i ds = 1 \text{ for } i = j \tag{34}$$

This relationship has practical consequences. First, let's consider a dynamic evolution of the whisker in the form:  $u(s, t) = \sum_i q_i(t) V_i(s) ds$ . The amplitude of mode  $i$  can be directly computed as:

$$q_i(t) = \int_{\epsilon}^1 s^2 V_i(s) u(s, t) ds \tag{35}$$

Second, if we now consider a situation where the whisker oscillates through the application of a distributed normal force gradient  $f(s, t)$ , Equation (3) reads:

$$\frac{\partial}{\partial s^2} \left( s^4 \frac{\partial^2 u}{\partial s^2} \right) + k^2 s^2 \frac{\partial^2 u}{\partial t^2} = f(s, t) \tag{36}$$

Introducing the mode decomposition in this equation, we write:

$$\sum_i [(s^4 V_i'')'' q_i + k^2 s^2 V_i \ddot{q}_i] = f(s, t) \tag{37}$$

The modes  $V_i$  being solutions of Equation (4), the equation can be written as:

$$\sum_i s^2 V_i [\ddot{q}_i + \omega_i^2 q_i] = \frac{1}{k^2} f(s, t) \tag{38}$$

Projecting this equation on the spatial mode  $V_i(s)$  and using the orthogonality property, one obtains the dynamic equation for the mode amplitude  $q_i(t)$ :

$$\ddot{q}_i + \omega_i^2 q_i = \frac{1}{k^2} \int_{\epsilon}^1 f(s, t) V_i(s) ds \tag{39}$$

**COUPLING THE WHISKER'S RAPID DYNAMICS TO ITS QUASI-STATIC EVOLUTION**

The whisker displacement  $U(s, t)$  is decomposed in the form  $U(s, t) = U_{qs}(s, t) + u(s, t)$  where  $U_{qs}(s, t)$  describes the quasi-static evolution. By introducing this decomposition in Equation (3), one obtains the dynamic equation for  $u(s, t)$ :

$$\frac{\partial^2}{\partial s^2} \left( s^4 \frac{\partial^2 u}{\partial s^2} + s^4 \frac{\partial^2 U_{qs}}{\partial s^2} \right) + k^2 s^2 \left( \frac{\partial^2 u}{\partial t^2} + \frac{\partial^2 U_{qs}}{\partial t^2} \right) = 0 \tag{40}$$

We assume  $U_{qs}(s, t)$  to obey the small deflection equilibrium Equation (30):  $(s^4 U_{qs}'')'' = 0$ . The resonant component of the whisker deflection thus obeys the dynamic equation:

$$\frac{\partial^2}{\partial s^2} \left( s^4 \frac{\partial^2 u}{\partial s^2} \right) + k^2 s^2 \frac{\partial^2 u}{\partial t^2} = -k^2 s^2 \ddot{U}_{qs}(s, t) \tag{41}$$

Using the mode-decomposition  $u(s, t) = \sum_i q_i(t) V_i(s)$  and the orthogonality of the resonant modes [see Equations (36) and (39)], the amplitude of each mode  $q_i(t)$  is found to obey the dynamic equation:

$$\ddot{q}_i + 2\zeta\omega_i \dot{q}_i + \omega_i^2 q_i = - \int_{\epsilon}^1 s^2 \ddot{U}_{qs}(s, t) V_i(s) ds \tag{42}$$

This approach is implemented in the case of a shock. Prior to the shock, the whisker experiences a solid rotation at constant rotation rate  $\gamma$  which simply reads:  $U_{qs}(s, t < 0) = \gamma(1 - s)t$ . Integrating Equation (30) with boundary conditions  $U(1) = 0, U'(1) = \gamma t, U(\epsilon) = U''(\epsilon) = 0$ , one obtains the evolution of the quasi-static profile immediately after the shock:

$$U_{qs}(s, t > 0) = \gamma t \frac{(1 - s)(2s^2 + \epsilon^2(1 + s) - \epsilon s(3 + s))}{2(1 - \epsilon)^2 s^2} \tag{43}$$

Based on these two expressions, one can compute the second time-derivative of the quasi-static profile  $\ddot{U}_{qs}(s, t)$ :

$$\ddot{U}_{qs}(s, t) = \delta(t)\gamma\bar{U}(s) \tag{44}$$

where  $\delta(t)$  is the Dirac function and  $\bar{U}(s)$  is a normalized profile that reads:

$$\bar{U}(s) = \dot{U}_{qs}(s, 0^+) - \dot{U}_{qs}(s, 0^-) = \frac{\epsilon(1 - s)^2(\epsilon - 3s + 2s\epsilon)}{2(1 - \epsilon)^2 s^2} \tag{45}$$

In order to integrate Equation (42), one needs to compute the Green's function  $G(t)$ , i.e., the response of the dynamic system, initially at rest, to a Dirac of unit force:

$$\left( \frac{d^2}{dt^2} + 2\zeta\omega_i \frac{d}{dt} + \omega_i^2 \right) G(t) = \delta(t) \tag{46}$$

with boundary conditions  $G(t < 0) = G'(t < 0) = 0$ . For  $t > 0$ , the general solution reads:

$$G(t > 0) = \left( \alpha \cos(\sqrt{1 - \zeta^2}\omega_i t) + \beta \sin(\sqrt{1 - \zeta^2}\omega_i t) \right) e^{-\zeta\omega_i t} \tag{47}$$

In order to determine  $\alpha$  and  $\beta$ , we integrate Equation (46) between  $0^-$  and  $0^+$ , once and twice:

$$(G'(0^+) - G'(0^-)) + 2\zeta\omega_i (G(0^+) - G(0^-)) = 1$$

$$(G(0^+) - G(0^-)) = 0 \tag{48}$$

These two equations and the boundary conditions impose  $G(0^+) = 0$  and  $G'(0^+) = 1$ . The solution thus finally reads:

$$\text{For } t > 0: G(t) = \frac{1}{\omega_i \sqrt{1 - \zeta^2}} e^{-\zeta\omega_i t} \sin(\omega_i \sqrt{1 - \zeta^2} t)$$

$$\text{For } t < 0: G(t) = 0 \tag{49}$$

The mode amplitude  $q_i(t)$  of the dynamic component associated with the event occurring at time  $t = 0$  simply follows, for  $t > 0$ :

$$q_i(t) = - \left( \int_{\epsilon}^1 s^2 \bar{U}(s) V_i(s) ds \right) G(t) \quad (50)$$

### SURGICAL PREPARATION AND WHISKER STIMULATION FOR *In vivo* EXPERIMENTS

Experiments were conducted in conformity with French (JO 2001-464) and European legislation (86/609/CEE) on animal experimentation. An adult male Wistar albino rat (318 g) was anesthetized with urethane (1.5 g/kg, i.p.). Body temperature was maintained at 37°C. The scalp was retracted after a subcutaneous injection of a local anesthetic (Lidocaine 1%). The skull was then cemented to a metal bar. A 1 mm thick metal bar was moved by a linear stepper motor (Linear Motor MLL302, Systro GmbH) at a speed  $V_{\text{bar}} = 60$  mm/s. The bar contacted the whisker near its tip. The whiskers were trimmed at the end of the experiment, and their diameters were measured at different positions, from base to tip. This allowed us to determine the length  $L$  of the ideal (non-truncated) cone.

### HIGH-SPEED VIDEOGRAPHY OF WHISKER DEFLECTIONS

Whisker movements were recorded at a frame rate of 2.5 kHz with a high-speed camera (Photron Fastcam SA3/105 mm f-2.8 DG Macro Sigma; pixel resolution 55  $\mu\text{m}$ ) mounted vertically above the animal. Whiskers were illuminated from below using a backlight (SSLUB, Phlox and PP520, Gardasoft). The camera produces bird's-eye view movies of the whiskers. We choose to study whiskers  $\beta$  and C1 whose curvature plane are essentially horizontal and can thus be entirely imaged with the present optical configuration (Figure 7A).

### WHISKER TRACKING

Detecting the shock-induced deflection wave, whose typical amplitude is of the order of a few tens of microns, required subpixel determination of the whisker centerline profile in each frame. The whisker deflected by the object was tracked using a semi-automated algorithm written in Python. We subtracted the average background image from each frame in the movie. Whisker centerline profiles were then extracted: we scanned all columns of each movie frame in order to extract the pixel of maximal intensity defining the approximate position of the whisker. The precise position of the whisker centerline in each column of the frame was then defined as the barycenter (each pixel is

weighted by its intensity) of the pixels surrounding the pixel of maximal intensity (center position  $\pm 2$  pixel). In order to extract the shock-induced deflection sequence (Figure 7B), the whisker profile determined before the shock was subtracted to each post-shock profile. The deflection sequence was then smoothed using a five pixel wide sliding window. This procedure yields a spatial resolution of  $\approx 1$   $\mu\text{m}$  on the shock-induced whisker deflection.

### ANALYSIS OF EXPERIMENTAL DATA

Our experimental configuration slightly differed from that considered in the model. In the latter, the whisker rotated at constant speed across a fixed obstacle. In the experiment, the whisker was fixed, and the obstacle was moved linearly at constant speed  $V_{\text{bar}}$ . For this shock configuration, it is easy to show that Equation (11) becomes:

$$U(s, t > 0) = V_{\text{bar}} t \bar{U}(s) - V_{\text{bar}} \sum_i V_i(s) \left( \int_{\epsilon}^1 s^2 \bar{U}(s) V_i(s) ds \right) \times \frac{e^{-\zeta \omega_i t} \sin(\sqrt{1 - \zeta^2} \omega_i t)}{\sqrt{1 - \zeta^2} \omega_i} \quad (51)$$

The back-illumination geometry combined with the bird's-eye optics results in a shadow region in the vicinity of the object that prevented the tracking of the whisker down to the whisker/object contact point. Similarly, the fur hampered a proper observation of the whisker near the skin. As a consequence, the positions  $s = \epsilon$  and  $s = 1$  could not be determined from the images, and were thus left as free parameters. The wave speed was determined by linear fitting the position of the first deflection minimum as a function of the time elapsed since the first contact (Figure 7C). The four first resonant modes were used to fit the data. Fitting was performed with Matlab's `fminsearch` function. Correlation between experimental and theoretical data was assessed with Pearson's correlation test on the first 3 and 5 ms for C1 and  $\beta$  whiskers, respectively.

### ACKNOWLEDGMENTS

We thank D. Golomb and S. Neukirch for stimulating discussions, V. Ego-Stengel and L. Bourdieu for helpful comments on the manuscript and E. Coudert for drawing. This work was supported by CNRS, ANR (project TRANSTACT 0294) and EU 7th Framework Program under grant N° 269921 (BrainScales).

### REFERENCES

- Anjum, F., Turni, H., Mulder, P. G. H., van der Burg, J., and Brecht, M. (2006). Tactile guidance of prey capture in truscan shrews. *Proc. Natl. Acad. Sci. U.S.A.* 103, 16544–16549.
- Arabzadeh, E., Panzeri, S., and Diamond, M. E. (2004). Whisker vibration information carried by rat barrel cortex neurons. *J. Neurosci.* 24, 6011–6020.
- Arabzadeh, E., Zorzin, E., and Diamond, M. E. (2005). Neuronal encoding of texture in the whisker sensory pathway. *PLoS Biol.* 3:e17. doi: 10.1371/journal.pbio.0030017
- Audoly, B., and Neukirch, S. (2005). Fragmentation of rods by cascading cracks: why spaghetti does not break in half. *Phys. Rev. Lett.* 95, 095505.
- Berg, R. W., and Kleinfeld, D. (2003). Rhythmic whisking by rat: retraction as well as protraction of the vibrissae is under active muscular control. *J. Neurophysiol.* 89, 104–117.
- Birdwell, J. A., Solomon, J. H., Thajchayapong, M., Taylor, M. A., Cheely, M., Towal, R. B., et al. (2007). Biomechanical models for radial distance determination by the rat vibrissal system. *J. Neurophysiol.* 98, 2439–2455.
- Brecht, M., and Merzenich M. M. (1997). Functional architecture of the mystacial vibrissae. *Behav. Brain Res.* 84, 81–97.
- Carl, K., Hild, W., Mampel, J., Schilling, C., and Witte, H. (2012). Characterization of static properties of rat's whisker system. *IEEE Sens. J.* 12, 340–349.
- Carvell, G. E., and Simons, D. J. (1990). Biometric analyses of vibrissal tactile discrimination in the rat. *J. Neurosci.* 10, 2638–2648.
- Clements, T. N., and Rahn, C. D. (2006). Three dimensional contact imaging with an actuated whisker. *IEEE Trans. Rob. Autom.* 22, 844–848.
- Ebara, S., Kumamoto, K., Matsuura, T., Mazurkiewicz, J. E., and Rice,

- F. L. (2002). Similarities and differences in the innervation of mystacial vibrissal follicle-sinus complexes in the rat and cat: a confocal microscopic study. *J. Comp. Neurol.* 449, 103–119.
- Hartmann, M. J., Johnson, N. J., Towal, R. B., and Assad, C. (2003). Mechanical characteristics of rat vibrissae: resonant frequencies and damping in isolated whiskers and in the awake behaving animal. *J. Neurosci.* 23, 6510–6519.
- Hipp, J., Arabzadeh, E., Zorzin, E., Conrath, J., Kayser, C., Diamond, M. E., et al. (2006). Texture signals in whisker vibrations. *J. Neurophysiol.* 95, 1792–1799.
- Huber, D., Gutnisky, D. A., Peron, S., O'Connor, D. H., Wiegert, J. S., Tian, L., et al. (2012). Multiple dynamic representations in the motor cortex during sensorimotor learning. *Nature* 484, 473–478.
- Jadhav, S. P., and Feldman, D. E. (2010). Texture coding in the whisker system. *Curr. Opin. Neurobiol.* 20, 313–318.
- Jadhav, S. P., Wolfe, J., and Feldman, D. E. (2009). Sparse temporal coding of elementary tactile features during active whisker sensation. *Nat. Neurosci.* 12, 792–800.
- Jenks, R. A., Vaziri, A., Bolori, A.-R., and Stanley, G. B. (2010). Self-motion and the shaping of sensory signals. *J. Neurophysiol.* 103, 2195–2207.
- Johansson, R. S., and Flanagan, J. R. (2009). Coding and use of tactile signals from the fingertips in object manipulation tasks. *Nat. Rev. Neurosci.* 10, 345–359.
- Kaneko, M., Kanayama, N., and Tsuji, T. (1998). Active antenna for contact sensing. *IEEE Trans. Rob.* 14, 278–291.
- Kim, D., and Möller, R. (2007). Biomimetic whiskers for shape recognition. *Rob. Auton. Syst.* 55, 229–243.
- Knutsen, P. M., and Ahissar, E. (2009). Orthogonal coding of object location. *Trends Neurosci.* 32, 101–109.
- Knutsen, P. M., Pietr, M., and Ahissar, E. (2006). Haptic object localization in the vibrissal system: behavior and performance. *J. Neurosci.* 26, 8451–8464.
- Krupa, D. J., and Nicolelis, M. A. L. (2001). Behavioral properties of the trigeminal somatosensory system in rats performing whisker-dependent tactile discriminations. *J. Neurosci.* 21, 5752–5763.
- Lichtenstein, S. H., Carvell, G. E., and Simons, D. J. (1990). Responses of rat trigeminal ganglion neurons to movements of vibrissae in different directions. *Somatosens. Mot. Res.* 7, 47–65.
- Lottem, E., and Azouz, R. (2009). Mechanisms of tactile information transmission through whisker vibrations. *J. Neurosci.* 29, 11686–11697.
- Milani, H., Steiner, H., and Huston, J. P. (1989). Analysis of recovery from behavioral asymmetries induced by unilateral removal of vibrissae in the rat. *Behav. Neurosci.* 103, 1067–1074.
- Mitchinson, B., Martin, C. J., Grant, R. A., and Prescott, T. J. (2007). Feedback control in active sensing: rat exploratory whisking is modulated by environmental contact. *Proc. Biol. Sci.* 274, 1035–1041.
- Morita, T., Kang, H., Wolfe, J., Jadhav, S. P., and Feldman, D. E. (2011). Psychometric curve and behavioral strategies for whisker-based texture discrimination in rats. *PLoS ONE* 6:e20437. doi: 10.1371/journal.pone.0020437
- Neimark, M., Andermann, M., Hopfield, J., and Moore, C. (2003). Vibrissa resonance as a transduction mechanism for tactile encoding. *J. Neurosci.* 23, 6499–6509.
- O'Connor, D. H., Clack, N. G., Huber, D., Komiyama, T., Myers, E. W., and Svoboda, K. (2010a). Vibrissa-based object localization in head-fixed mice. *J. Neurosci.* 30, 1947–1967.
- O'Connor, D. H., Peron, S. P., Huber, D., and Svoboda, K. (2010b). Neural activity in barrel cortex underlying vibrissa-based object localization in mice. *Neuron* 67, 1048–1061.
- Persson, B. (2000). *Sliding Friction: Physical Principles and Applications*. Nanoscience and Technology. New York, NY: Springer.
- Polley, D. B., Rickert, J. L., and Frostig, R. D. (2005). Whisker-based discrimination of object orientation determined with a rapid training paradigm. *Neurobiol. Learn. Mem.* 83, 134–142.
- Quist, B. W., Faruqi, R. A., and Hartmann, M. J. Z. (2011). Variation in young's modulus along the length of a rat vibrissa. *J. Biomech.* 44, 2775–2781.
- Quist, B. W., and Hartmann, M. J. Z. (2012). Mechanical signals at the base of a rat vibrissa: the effect of intrinsic vibrissa curvature and implications for tactile exploration. *J. Neurophysiol.* 107, 2298–2312.
- Ritt, J., Andermann, M., and Moore, C. I. (2008). Embodied information processing: vibrissa mechanics and texture features shape micro-motions in actively sensing rats. *Neuron* 57, 599–613.
- Scholz, G. R., and Rahn, C. D. (2004). Profile sensing with an actuated whisker. *IEEE Trans. Rob. Autom.* 20, 124–127.
- Schroeder, C. L., and Hartmann, M. J. (2012). Sensory prediction on a whiskered robot: a tactile analogy to “optic flow”. *Front. Neurobot.* 6:9. doi: 10.3389/fnbot.2012.00009
- Solomon, J. H., and Hartmann, M. J. Z. (2008). Artificial whiskers suitable for array implementation: accounting for lateral slip and surface friction. *IEEE Trans. Rob.* 24, 1157–1167.
- Solomon, J. H., and Hartmann, M. J. Z. (2010). Extracting object contours with the sweep of a robotic whisker using torque information. *Int. J. Rob. Res.* 29, 1233–1245.
- Szwed, M., Bagdasarian, K., and Ahissar, E. (2003). Encoding of vibrissal active touch. *Neuron* 40, 621–630.
- Szwed, M., Bagdasarian, K., Blumenfeld, B., Barak, O., Derdikman, D., and Ahissar, E. (2006). Responses of trigeminal ganglion neurons to the radial distance of contact during active vibrissal touch. *J. Neurophysiol.* 95, 791–802.
- Towal, R. B., and Hartmann, M. J. (2006). Right-left asymmetries in the whisking behavior of rats anticipate head movements. *J. Neurosci.* 26, 8838–8846.
- Voges, D., Carl, K., Klauer, G., Uhlig, R., Schilling, C., Behn, C., et al. (2012). Structural characterization of the whisker system of the rat. *IEEE Sens. J.* 12, 332–339.
- Weaver, W., Timoshenko, S., and Young, D. H. (1990). *Vibration Problems in Engineering*. Hoboken, NJ: Wiley-IEEE.
- Welker, W. (1964). Analysis of sniffing of the albino rat. *Behaviour* 22, 223–244.
- Williams, C. M., and Kramer, E. M. (2010). The advantages of a tapered whisker. *PLoS ONE* 5:e8806. doi: 10.1371/journal.pone.0008806
- Wolfe, J., Hill, D. N., Pahlavan, S., Drew, P. J., Kleinfeld, D., and Feldman, D. E. (2008). Texture coding in the rat whisker system: slip-stick versus differential resonance. *PLoS Biol.* 6:e215. doi: 10.1371/journal.pbio.0060215

**Conflict of Interest Statement:** The authors declare that the research was conducted in the absence of any commercial or financial relationships that could be construed as a potential conflict of interest.

Received: 28 March 2012; accepted: 18 October 2012; published online: 06 November 2012.

Citation: Boubenec Y, Shulz DE and Debrégeas G (2012) Whisker encoding of mechanical events during active tactile exploration. *Front. Behav. Neurosci.* 6:74. doi: 10.3389/fnbeh.2012.00074  
Copyright © 2012 Boubenec, Shulz and Debrégeas. This is an open-access article distributed under the terms of the Creative Commons Attribution License, which permits use, distribution and reproduction in other forums, provided the original authors and source are credited and subject to any copyright notices concerning any third-party graphics etc.



# Sensory prediction on a whiskered robot: a tactile analogy to “optical flow”

Christopher L. Schroeder<sup>1</sup> and Mitra J. Z. Hartmann<sup>1,2\*</sup>

<sup>1</sup> Department of Biomedical Engineering, Northwestern University, Evanston, IL, USA

<sup>2</sup> Department of Mechanical Engineering, Northwestern University, Evanston, IL, USA

## Edited by:

Robyn Grant, University of Sheffield, UK

## Reviewed by:

Quan Zou, University of Nevada, USA

Gerald Loeb, University of Southern California, USA

## \*Correspondence:

Mitra J. Z. Hartmann, Mechanical Engineering Department, Biomedical Engineering Department, Northwestern University, 2145 Sheridan Road, Evanston, IL 60208, USA.  
e-mail: m-hartmann@northwestern.edu

When an animal moves an array of sensors (e.g., the hand, the eye) through the environment, spatial and temporal gradients of sensory data are related by the velocity of the moving sensory array. In vision, the relationship between spatial and temporal brightness gradients is quantified in the “optical flow” equation. In the present work, we suggest an analog to optical flow for the rodent vibrissal (whisker) array, in which the perceptual intensity that “flows” over the array is bending moment. Changes in bending moment are directly related to radial object distance, defined as the distance between the base of a whisker and the point of contact with the object. Using both simulations and a 1×5 array (row) of artificial whiskers, we demonstrate that local object curvature can be estimated based on differences in radial distance across the array. We then develop two algorithms, both based on tactile flow, to predict the future contact points that will be obtained as the whisker array translates along the object. The translation of the robotic whisker array represents the rat’s head velocity. The first algorithm uses a calculation of the local object slope, while the second uses a calculation of the local object curvature. Both algorithms successfully predict future contact points for simple surfaces. The algorithm based on curvature was found to more accurately predict future contact points as surfaces became more irregular. We quantify the inter-related effects of whisker spacing and the object’s spatial frequencies, and examine the issues that arise in the presence of real-world noise, friction, and slip.

**Keywords:** rat, vibrissae, prediction, tactile flow

## INTRODUCTION

As an animal moves through the environment, the spatial and temporal gradients of sensory data it acquires are related through the velocity of its moving sensory surfaces. This relationship is represented by the “complete derivative” (Munson et al., 2009), and represents a mathematically inviolate description of information flow over moving sensory surfaces.

In the field of visual neuroscience, the complete derivative has been termed the “optical flow” equation. The optical flow equation relates spatial and temporal intensity (brightness) gradients to the velocity of the animal (Barron et al., 1994; Beauchemin and Barron, 1995; Horn and Schunck, 2003). Recent papers have formalized the idea of “tactile flow” to describe the flow of strain energy density across the hand (Bicchi et al., 2008; Scilingo et al., 2008), and bending moment (torque) at the whisker base across the rodent vibrissal (whisker) array (Gopal and Hartmann, 2007; Hartmann, 2009).

Notably, the optic and tactile flow equations are typically used by assuming that the animal makes use of spatial and temporal gradients of brightness (vision) or strain energy (tactile) to compute the velocity of its sensor array.

We recently proposed a complementary scheme: namely, if the animal already knows its own velocity, then it can use the complete derivative to predict future sensory data (Gopal and

Hartmann, 2007; Hartmann, 2009). Computing the complete derivative at multiple spatial scales would allow the animal to predict the stimulus that it will measure in the next sensory instant and provide a mechanism to distinguish between externally-generated and self-generated motion.

In the present work, we used the rat vibrissal system as a model to examine the plausibility of using the complete derivative to predict upcoming sensory data. Rats actively brush and tap their whiskers (vibrissae) against objects to tactually explore the environment. During detailed exploration of objects, rats move their vibrissae rhythmically, between 5 and 25 Hz (Welker, 1964; Berg and Kleinfeld, 2003). During navigation behaviors, however, rats often hold their whiskers out in a relatively static position as they follow along a wall or tunnel.

The present work was designed to investigate tactile flow across the vibrissal array in this type of translational navigation behavior. We used both simulations and a 1 by 5 array of artificial vibrissae (hardware) to investigate the plausibility of using the complete derivative to predict upcoming whisker-object contact points.

## METHODS

Our initial investigations were performed in simulation, and we then investigated the real-world issues that arise with implementation on a 1 × 5 array of robotic whiskers.

## ALGORITHMS FOR THE DETERMINATION OF RADIAL DISTANCE, SLOPE, AND CURVATURE

### Radial distance determination using translations instead of rotations

Radial object distance is defined as the Euclidean distance between the base of a vibrissa and the point at which it makes contact with an object. Previous work has shown that an object's contour can be extracted by continuous rotation of a vibrissa against an object (Kaneko et al., 1998; Solomon and Hartmann, 2010). As the vibrissa "sweeps" against the object through a rotation, measurement of the bending moment (torque) at the vibrissa base permits the radial object distance to be continuously computed, and the object contour thereby inferred. This technique was empirically validated with sweeps of a vibrissa past three differently shaped objects (Solomon and Hartmann, 2010). The rotational sweep models vibrissal motion during typical "whisking" behavior, in which the rat rotates its vibrissae at their base.

During wall-following behavior, however, rats do not always whisk, but sometimes keep their vibrissae protracted against the wall. This behavior is better modeled as a relative translation between vibrissa and object, rather than as a rotation. Although Solomon and Hartmann (2010) developed equations to describe the translational sweep of a vibrissa past an object, the equations were not validated in hardware.

In the present study, we experimentally validate the translation equations developed in Solomon and Hartmann (2010) and use them to extract object contours. Equations 1–3 below provide only a brief overview of the differences between radial distance extractions during rotation versus translation. A more complete description of radial distance extraction based on rotation is provided in Solomon and Hartmann (2010).

As shown in previous work (Kaneko et al., 1998; Solomon and Hartmann, 2006, 2008, 2010, 2011; Birdwell et al., 2007) the radial distance  $r_0$  to the initial contact point on an object can be calculated using

$$r_0 = k \frac{\phi_0}{M_0} \quad (1)$$

where  $k = 3EI$ ,  $E$  is the elastic modulus of the vibrissa,  $I$  is the area moment of inertia,  $\phi_0$  is a small pushing angle beyond initial contact (typically about  $3^\circ$ ), and  $M_0$  is the bending moment at the vibrissa base.

Once the radial distance  $r_0$  to the initial contact point is calculated, the whisker undergoes either a small rotation ( $d\phi$ ) or translation ( $dL$ ). Radial distance at the current time step ( $r_i$ ) can then be calculated based on estimates of radial distance at previous time steps.

The procedures for calculating  $r_i$  after a translation or rotation are quite similar, but they differ in the calculation of the magnitude of the vector  $\bar{\delta}_{i-1}$ , perpendicular to the longitudinal axis of the vibrissa at the contact point. With the x-axis defined to be parallel to the vibrissa at  $t = t_0$ , Solomon and Hartmann (2010) define  $\bar{\delta}_{i-1}$  for rotation as:

$$\bar{\delta}_{i-1} = -r_{i-1} \cdot d\phi \cdot \begin{bmatrix} \sin \phi_{i-1} \\ \cos \phi_{i-1} \end{bmatrix}. \quad (2)$$

where  $r_{i-1}$  is the radial distance at the previous time step (before rotation),  $d\phi$  is the incremental rotation, and  $\phi_{i-1}$  is the angle between the vibrissa base at time  $t_0$  and the base at time  $t_{i-1}$  (after rotation).

In contrast,  $\bar{\delta}_{i-1}$  for translation is defined by:

$$\bar{\delta}_{i-1} = \begin{bmatrix} 0 \\ dL \end{bmatrix}. \quad (3)$$

where  $dL$  is the incremental linear movement between time steps. It is important to note that the base of each vibrissa is fixed perpendicular to the direction of linear movement for this definition of  $\bar{\delta}_{i-1}$ .

The value of  $\bar{\delta}_{i-1}$  is then used to calculate the next radial distance  $r_i$ , regardless of whether the whisker was translated or rotated. For a detailed explanation of this calculation, please refer to **Figure 4** of Solomon and Hartmann (2010) and Equations 6–11 also in Solomon and Hartmann (2010).

### Computing object slope and curvature from radial distances

The local slope ( $\mu$ ) and the local curvature ( $\kappa$ ) of an object can be calculated based on radial distance measurements. To calculate either  $\mu$  or  $\kappa$ , we first define our coordinate system as shown in **Figure 1**. The distance  $ds_i$  is the distance the base-point of the whisker has translated in timestep  $i$ , and the direction of  $ds$  is always coincident with the rat's velocity. Radial distance estimates at multiple time points, the angle  $d\theta$ , and the distance  $ds$  can then

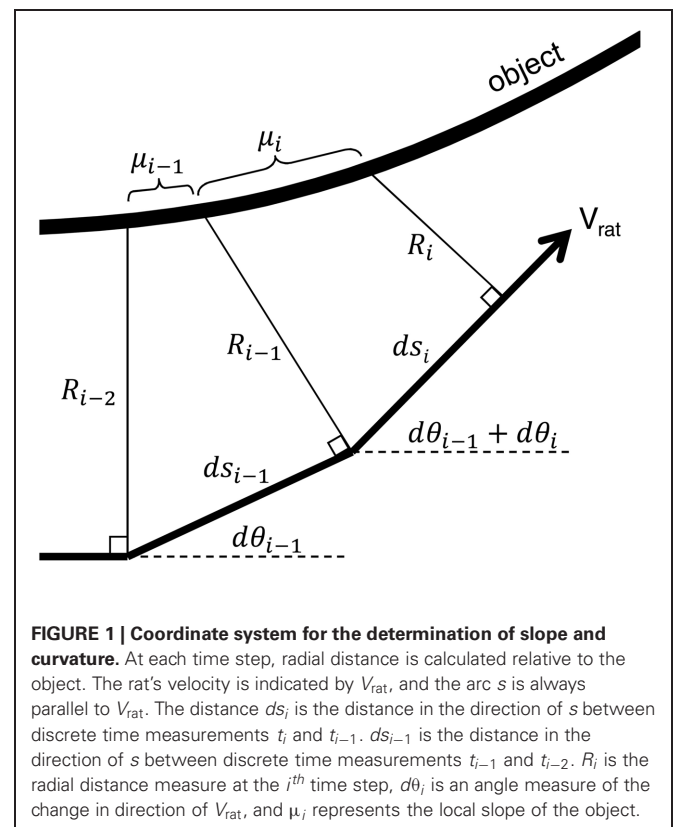


**FIGURE 1 | Coordinate system for the determination of slope and curvature.** At each time step, radial distance is calculated relative to the object. The rat's velocity is indicated by  $V_{rat}$ , and the arc  $s$  is always parallel to  $V_{rat}$ . The distance  $ds_i$  is the distance in the direction of  $s$  between discrete time measurements  $t_i$  and  $t_{i-1}$ .  $ds_{i-1}$  is the distance in the direction of  $s$  between discrete time measurements  $t_{i-1}$  and  $t_{i-2}$ .  $R_i$  is the radial distance measure at the  $i^{th}$  time step,  $d\theta_i$  is an angle measure of the change in direction of  $V_{rat}$ , and  $\mu_i$  represents the local slope of the object.

be used to find the slope  $\mu_i$  at each time step:

$$\mu_i = \frac{R_i - R_{i-1} + ds_i(d\theta_{i-1} + d\theta_i)}{ds_i - R_i(d\theta_{i-1} + d\theta_i) + R_{i-1}d\theta_{i-1}} \quad (4)$$

Slope  $\mu_i$  is defined by the differences between radial distance measures ( $R_i$  and  $R_{i-1}$ ) divided by the distance traveled ( $ds_i$ ). Each  $d\theta$  term accounts for changes in the rat velocity vector between radial distance measurements.

Calculation of curvature is similar, but requires us to first calculate the slope  $\mu_{i-1}$  obtained in timestep  $i-1$ :

$$\mu_{i-1} = \frac{R_{i-1} - R_{i-2} + ds_{i-1}d\theta_{i-1}}{ds_{i-1} - R_{i-1}d\theta_{i-1}} \quad (5)$$

Curvature is then defined using both  $\mu_i$  and  $\mu_{i-1}$ :

$$\kappa_i = \frac{\left| \frac{\mu_i - \mu_{i-1}}{ds_i} \right|}{[1 + (\mu_i)^2]^{\frac{3}{2}}} \quad (6)$$

This equation is simply the discretized version of the definition of curvature measured in 2D Cartesian coordinates. Notably, the commonly-used simplification of Equation 6 that assumes  $\mu_i$  is small compared to unity (and therefore reduces the equation to just the numerator) was empirically found to be inaccurate. The small slope assumption does not always hold in our calculations.

When the rat's heading does not change significantly between timesteps,  $d\theta_i$  and  $d\theta_{i-1}$  are both zero and Equation 4 can be simplified to:

$$\mu_i = \frac{R_i - R_{i-1}}{ds_i} \quad (7)$$

where  $R$  and  $s$  still represent differences between radial distance measures ( $R_i$  and  $R_{i-1}$ ) over the distance traveled ( $ds_i$ ). Equation 5 can be similarly simplified and Equation 6 remains the same.

### Calculating slope and curvature based on radial distances measured with multiple whiskers

So far, we have described the sensory data obtained by a single whisker over time. Equations 4–7 apply equally well, however, to multiple whiskers making simultaneous contact with an object, at different locations on the object. In this case, the subscript  $i$  in Equations 4–7 should be interpreted to mean the  $i^{\text{th}}$  whisker, instead of the  $i^{\text{th}}$  timestep. **Figure 2** illustrates this idea. **Figure 2A** illustrates that calculation of slope and curvature with a single vibrissa requires memory of the data acquired on the previous timestep. In contrast, **Figure 2B** illustrates that calculation of slope and curvature with multiple vibrissae can be achieved within a single time step. This second method is equivalent to the rat integrating information across vibrissae within the array. In practice, calculation of slope and curvature can occur over both a single whisker (with memory) and multiple whiskers (at different spatial locations) simultaneously.

### PREDICTION OF FUTURE POINTS OF CONTACT AND FUTURE CURVATURE OVER TWO DIFFERENT SPATIAL SCALES

Equations 1–7 define the calculations used to find radial distance, local object slope, and local object curvature. Using these calculated values, we now show that it is possible to make predictions about the sensory data the animal will receive.

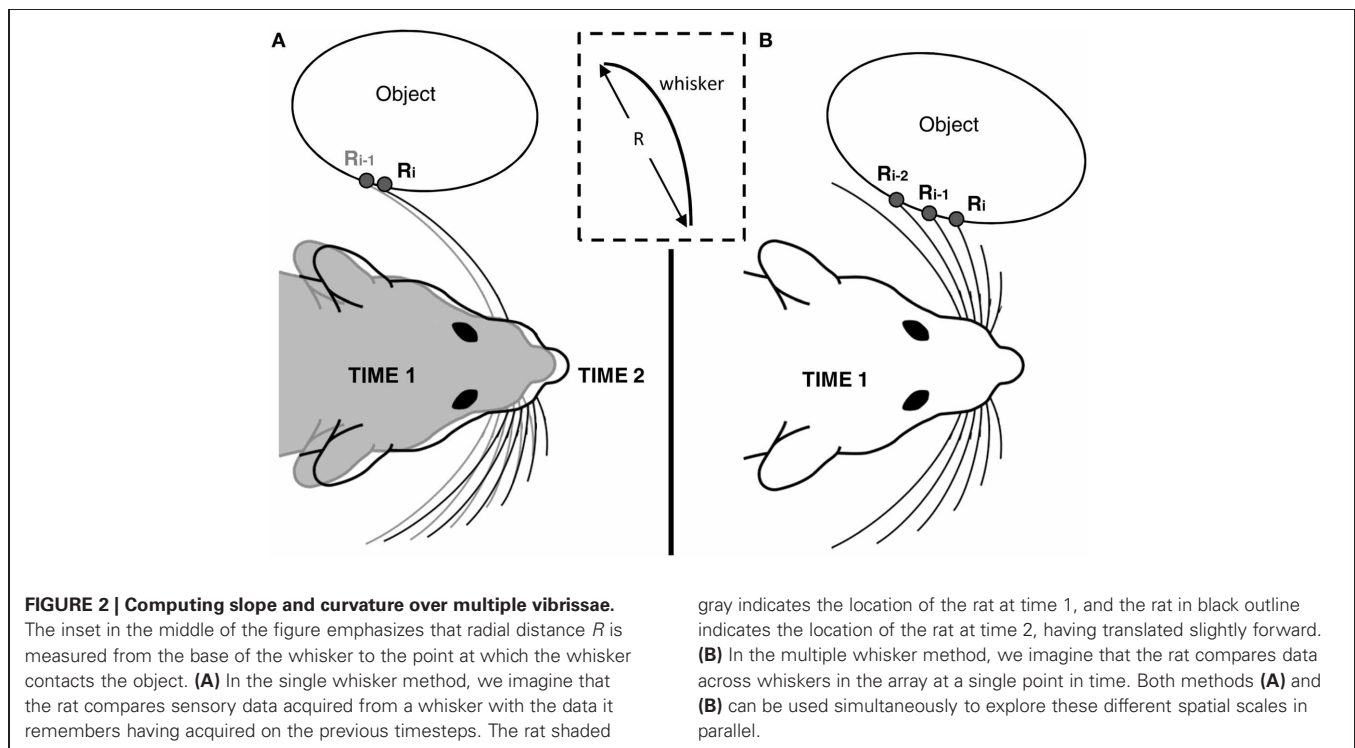


**FIGURE 2 | Computing slope and curvature over multiple vibrissae.** The inset in the middle of the figure emphasizes that radial distance  $R$  is measured from the base of the whisker to the point at which the whisker contacts the object. **(A)** In the single whisker method, we imagine that the rat compares sensory data acquired from a whisker with the data it remembers having acquired on the previous timesteps. The rat shaded

gray indicates the location of the rat at time 1, and the rat in black outline indicates the location of the rat at time 2, having translated slightly forward. **(B)** In the multiple whisker method, we imagine that the rat compares data across whiskers in the array at a single point in time. Both methods **(A)** and **(B)** can be used simultaneously to explore these different spatial scales in parallel.

### “Tactile flow” permits prediction of sensory data

Because animals control the movements of their limbs, they control the velocity with which sensory data flow over their sensory surfaces (Gopal and Hartmann, 2007; Bicchi et al., 2008; Nemenman et al., 2008; Scilingo et al., 2008; Hartmann, 2009). The time evolution of the flow field in space and time can be written via the complete derivative as shown in Equation 8.

$$\frac{dA_{sen}}{dt} = \frac{\partial A_{env}}{\partial t} + V \bullet \nabla A_{sen} \quad (8)$$

In this equation,  $A$  is any quantity that is being measured (intensity, temperature, etc.), and the vector  $V$  is the relative velocity between the sensory surface and the environment. The first term on the right represents intrinsic fluctuations in  $A$ , that is, changes in the environment. If environmental fluctuations are slow on the time scale of the animal’s movements, that term becomes zero and the progression of gradients is almost completely deterministic. New information flows over the edges of the sensory surface, but thereafter, values may be computed by calculating the spatial gradients of  $A$  across the sensor. Equation 8 provides an inviolate mathematical description of information flow over moving sensory surfaces. The equation is not a model, it is necessarily true, in the same way that distance is equal to velocity integrated over time. Computing the terms of the complete derivative at multiple spatial and temporal scales would allow the animal to predict the stimulus that it will measure in the next sensory instant.

### Interpreting “tactile flow” for an array of vibrissae

In this paper, we choose to represent “tactile flow” through radial distance of contact along the rat whisker because radial distance is directly related to changes in bending moment at the vibrissal base (Kaneko et al., 1998; Solomon and Hartmann, 2006). Prediction of future radial distances is possible by choosing radial distance ( $R$ ) as the main parameter in the complete derivative shown in Equation 8. If the object being explored is static on the timescale of the animal’s movements, then the first term on the right side of Equation 8 will be zero. In the context of the rat vibrissal system, we can therefore rewrite Equation 8 as follows:

$$\frac{R_{i+1} - R_i}{(t_{i+1} - t_i)} = 0 + V \frac{R_i - R_{i-1}}{ds_i} \stackrel{\text{def}}{=} V\mu_i \quad (9)$$

where  $R_{i+1}$  is the radial distance of the future point of contact,  $R_i$  is the current radial distance,  $t_{i+1}$  and  $t_i$  are the times at which the radial distances are measured,  $V$  is the translational velocity of the rat,  $ds_i$  is the distance traveled in the last time step, and  $\mu_i$  is the current slope. Rearranging the equation and substituting  $\mu_i$  as in the last term above yields:

$$R_{i+1} = R_i + V\mu_i(t_{i+1} - t_i) \quad (10)$$

Thus it is clear that future radial distance can be estimated from the current slope.

If the slope of the object is changing, we expect the current curvature of the object to be able to give a better estimate of future radial distance. To use curvature, we first predict the future slope

of the object, and then use that predicted slope to predict future radial distance. The future slope  $\mu_{i+1}$  is found by choosing  $\mu$  as the parameter in Equation 8, as shown in Equation 11:

$$\frac{\mu_{i+1} - \mu_i}{(t_{i+1} - t_i)} = 0 + V \frac{\mu_i - \mu_{i-1}}{ds_i} \quad (11)$$

The simplification that  $\kappa_i = \frac{\mu_i - \mu_{i-1}}{ds_i}$  was empirically found to generate significant error in our results. Therefore, in Equation 11 we replace  $\frac{\mu_i - \mu_{i-1}}{ds_i}$  with the full equation for  $\kappa_i$  as shown in Equation 6, yielding:

$$\mu_{i+1} = \mu_i + V\kappa_i(t_{i+1} - t_i) = \mu_i + V \frac{\left| \frac{\mu_i - \mu_{i-1}}{ds_i} \right|}{\left[ 1 + (\mu_i)^2 \right]^{\frac{3}{2}}} (t_{i+1} - t_i) \quad (12)$$

where  $\mu_{i+1}$  is the local object slope at the future point of contact,  $\mu_i$  is the current local object slope,  $V$  is the translational velocity of the rat,  $\kappa_i$  is the current local object curvature, and  $t_{i+1}$  and  $t_i$  are the times at which the radial distances used to calculate slope and curvature are measured. When Equation 12 is substituted into Equation 10 (with  $\mu_{i+1}$  replacing  $\mu_i$ ), we obtain an equation that estimates future radial distance based on both current slope and current curvature:

$$R_{i+1} = R_i + V(\mu_i + V\kappa_i(t_{i+1} - t_i))(t_{i+1} - t_i) \quad (13)$$

Finally, in the type of wall following behavior and environmental exploration in which prediction would be most useful to a rat, it is more likely that significant changes in calculated local object slope and local object curvature are due to measurement error than due to abrupt changes in the object. To decrease the sensitivity of predicted radial distance to measurement error, we average the local slope and curvature as follows:

$$\mu_{\text{avg}} = \frac{1}{(N-1)} \sum_i^{N-1} \mu_i \quad (14)$$

$$\kappa_{\text{avg}} = \frac{1}{(N-2)} \sum_i^{N-2} \kappa_i \quad (15)$$

where  $\mu_{\text{avg}}$  is the average slope,  $\kappa_{\text{avg}}$  is the average curvature,  $N$  is either the number of past time steps (c.f., **Figure 2A**) or the number of vibrissae being used (**Figure 2B**),  $\mu_i$  is the local object slope between each radial distance measurement, and  $\kappa_i$  is the local object curvature between each calculated slope value. Substituting Equations 14 and 15 into Equations 10 and 13 yields:

$$R_{i+1} = R_i + V\mu_{\text{avg}}(t_{i+1} - t_i) \quad (16)$$

and

$$R_{i+1} = R_i + V(\mu_i + V\kappa_{\text{avg}}(t_{i+1} - t_i))(t_{i+1} - t_i) \quad (17)$$

### Simultaneous prediction with single and multiple vibrissae

As illustrated in **Figure 2**, local object slopes and curvatures can be computed either using a single whisker (with memory) or

using multiple whiskers (distributed in space). For each of these two spatial scales, we can use either Equation 16 or Equation 17 to predict future contact points. We note that the use of multiple vibrissa permits the calculation of slope and curvature within a single timestep. In contrast, two or three timesteps are required to calculate slope and curvature using a single vibrissa. In addition, multiple vibrissae can be used to rapidly compute surface gradients on a larger spatial scale than would be possible with a single whisker. Using a single whisker would require memory of a duration equal to the inter-whisker-spacing divided by the velocity of the array, in order to obtain slope and curvature estimates at a spatial scale comparable to those obtained by multiple whiskers. Thus, there is a tradeoff between spatial scale and memory. Of course, computations can be done at both spatial scales (single and multiple whiskers) simultaneously.

### HARDWARE METHODS

Radial object distance is defined as the Euclidean distance between the base of a vibrissa and the point of object contact (Szwed et al., 2003; Birdwell et al., 2007). Previous work has shown that an object's contour can be extracted by continuous rotation of a vibrissa against an object (Solomon and Hartmann, 2010). As the vibrissa "sweeps" against the object through a rotation, measurement of the bending moment at the vibrissa base permits the radial object distance to be continuously computed, and the object contour thereby inferred. This technique was empirically validated with sweeps of a vibrissa past three differently shaped objects (Solomon and Hartmann, 2010). This same study demonstrated that a similar algorithm would work for translation of the vibrissa instead of rotation, but the translation technique was not empirically validated.

#### *Vibrissa and vibrissa array design*

The present work used a single horizontal row of a five by five array of vibrissae (Figure 3A). Vibrissae were constructed from Nitinol wire 4 cm in length and 500  $\mu\text{m}$  in diameter. Nitinol wire was chosen because it is highly elastic and tends not to kink. Each wire was mounted in a 4 mm x 4 mm rectangular aluminum block with a strain gauge (Omega Engineering) attached to each block face (Figure 3B). This vibrissa design allows for a 2-D measure of strain, but in the present study the measured strain in the vertical plane was negligible compared to the strain in the plane of object translation (the horizontal plane).

#### *Linear actuation*

A linear actuation system was built to model the forward (translational) movement of a rat as it explores its environment. Because the vibrissa array was tethered with power and signal cables, it was easier to translate an object past the stationary vibrissa array than it was to translate the array past the object. In the present work, these two paradigms are equivalent because we are concerned only with relative velocity between the array and object. This study did not explore methods to distinguish between self-generated versus external movements.

As shown in Figure 4, a wheeled cart carried a test object along a track a fixed distance from the vibrissa array. The motion of the cart was controlled by an Animatics SmartMotor. The programmable motor controller and associated 4000 count/rev

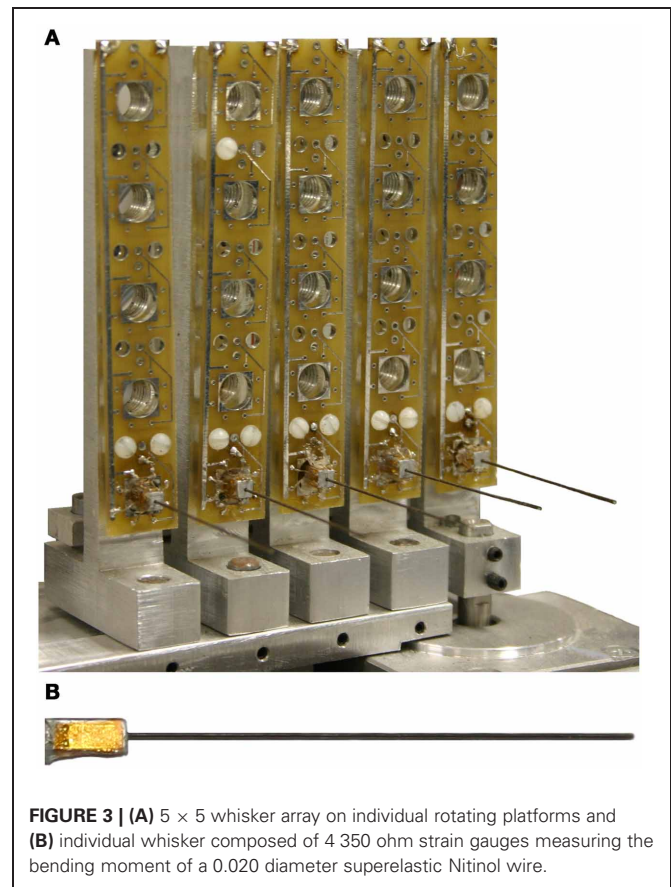


**FIGURE 3 | (A)** 5 × 5 whisker array on individual rotating platforms and **(B)** individual whisker composed of 4 350 ohm strain gauges measuring the bending moment of a 0.020 diameter superelastic Nitinol wire.

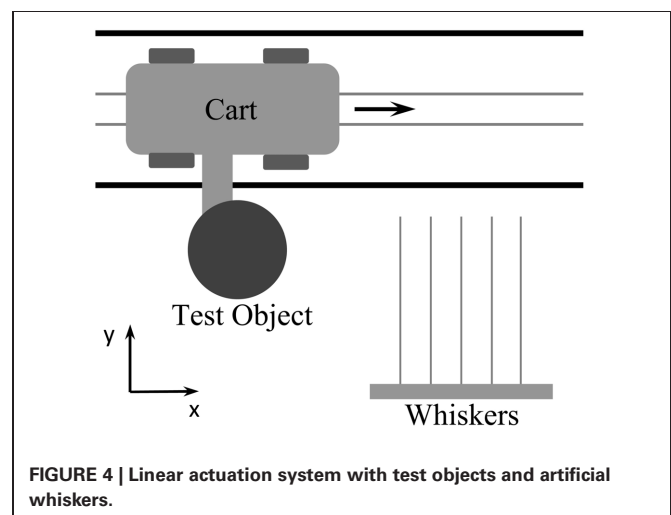


**FIGURE 4 | Linear actuation system with test objects and artificial whiskers.**

encoder allowed accurate position measurements within 10  $\mu\text{m}$ . In practice, however, we only found it necessary to calculate position to within 0.1 mm. Similarly, velocity was calculated to within 0.1 mm/sec. These levels of accuracy were chosen because noise dominated the measurement error below these thresholds, causing there to be no appreciable difference in position measurement with increasing accuracy.

### Device calibration

The two strain gauges for each sensing dimension on each vibrissa were arranged in a half Wheatstone bridge so the bending of the vibrissa created a change in voltage at the output of the circuit. The resting output was zeroed with a potentiometer. The actual value of the voltage output depended on circuit parameters such as gain, so it was necessary to calibrate the voltage output to the curvature at the base of the vibrissa. To calibrate the voltage to the curvature, the vibrissa was rotated against a peg placed at a known distance from the vibrissa base. For cylindrical homogenous vibrissae, curvature and moment differ only by a scaling factor. Given the known angular deflection of the cylindrical vibrissa and the distance between the base and peg, Solomon and Hartmann have shown that the moment can be calculated based on Euler-Bernoulli beam theory (Solomon and Hartmann, 2010).

Once a vibrissa has been calibrated, the voltage recorded from that vibrissa is converted to moment at the base of the vibrissa. The radial distance  $r_0$  to the initial contact point is calculated using Equation 1.

### Error calculations in simulation and hardware

To quantify the accuracy of radial distance prediction using each method, prediction error was defined as:

$$E_{pred} = \frac{1}{N} \sum_{i=1}^N \left| \frac{PRD_i - MRD_i}{MRD_i} \right| \quad (18)$$

where  $E_{pred}$  is the prediction error,  $N$  is the number of samples in a trial,  $PRD_i$  is the predicted radial distance for each sample, and  $MRD_i$  is the measured radial distance for each sample.  $E_{pred}$ , which we define as prediction error, is the mean absolute error of the prediction. It is mean absolute percent error (MAPE) when multiplied by 100. For simulated results,  $MRD_i$  is chosen to be accurate to machine precision. This choice results in a prediction error that solely measures the accuracy of the prediction algorithm for a given set of parameters. In hardware,  $MRD_i$  is calculated using the measured bending moment  $M$  as shown in Equation 1. In this case, prediction error  $E_{pred}$  is affected both by measurement error as well as the accuracy of the prediction algorithm. In practice, however, errors in radial distance extraction (measurement errors) were small compared to errors in prediction.

## RESULTS

As described in *Methods*, we use both Equation 16 (prediction using slope) and Equation 17 (prediction using curvature) to predict upcoming radial distance, and we use the two equations at different spatial scales.

### PREDICTION: SIMULATION RESULTS

In all simulations in this section, we assume “perfect” radial distance extraction at time 1, and then calculate slope and curvature to predict radial distance at time 2. In other words, we do not simulate whisker deflection. The goal of this section is to verify that the use of either slope or curvature is sufficient for the prediction of future radial distance. Simulation will also show whether the

increased mathematical complexity required by the use of local curvature leads to significantly increased predictive accuracy over the simpler equation for local slope.

In these simulations, the data collection method (i.e., single vibrissa or multiple vibrissa) is irrelevant, as the main difference between the two methods is spatiotemporal scale—the simulated objects can be made to arbitrary size and the sampling rate can be increased or decreased arbitrarily.

To quantify prediction error from the use of Equations 16 and 17, we simulated translation of the whiskers past several differently sized cylinders. We then quantified how well the predicted values matched actual values. The results of this simulation are shown in **Figure 5**. As expected, both local object curvature and local object slope were good predictors of future radial distance, with error less than  $0.1 \pm 0.07\%$  for each method. In these simulations, the error results only from discretization of slope and curvature.

**Figure 6** shows the results of simulating vibrissa contact with two different objects. Predictions about the future shape of the object were made using both Equations 16 and 17. The accuracy of these predictions for these simulated objects gives insight into the accuracy of each prediction method and shows the advantages and disadvantages of prediction using these two different equations.

In **Figure 6A**, local object slope and local object curvature were both used to make predictions about future contact points on an object that contained several gradual changes in curvature. Predictions using both slope and curvature were reasonably accurate over the object surface, with prediction errors of  $6.37 \pm 6.81\%$  for prediction using local object slope and  $3.02 \pm 1.52\%$  for prediction using local object curvature. In this first example, there is a clear advantage to choosing prediction using local object curvature. This simulation illustrates that prediction based on local object curvature is more accurate than prediction based on local object slope when curvature changes gradually.

The second test object (**Figures 6B,C**) had a location at which curvature abruptly changed—that is, an edge. **Figure 6B** shows that prediction using local object slope (Equation 16) acts similarly to a low pass filter with respect to change in curvature, resulting in a relatively accurate prediction. **Figure 6C**,

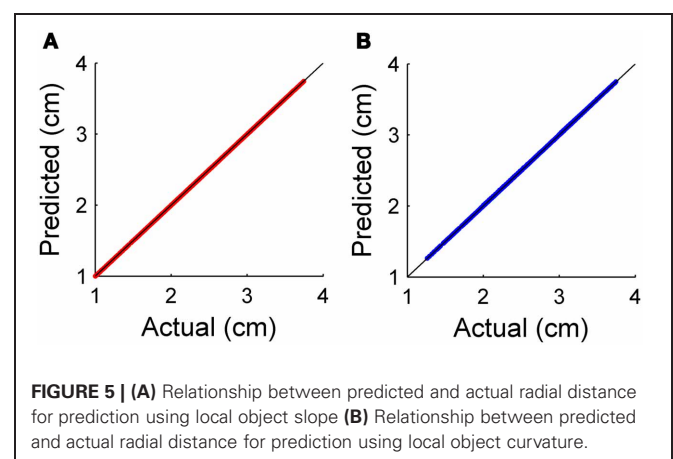
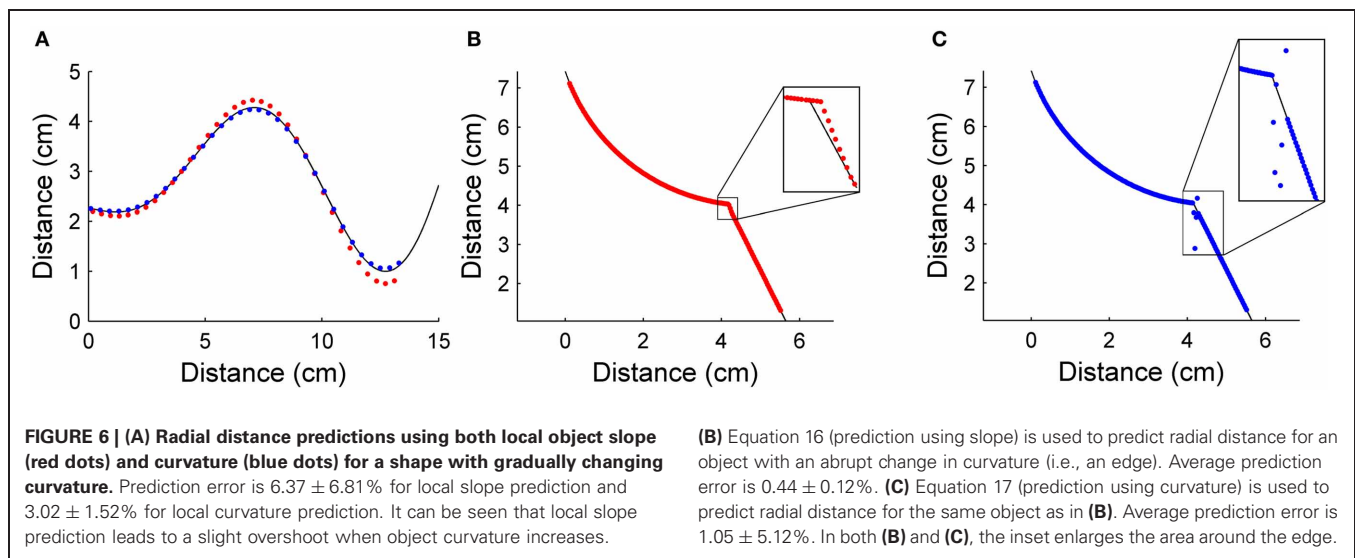


**FIGURE 5 | (A)** Relationship between predicted and actual radial distance for prediction using local object slope **(B)** Relationship between predicted and actual radial distance for prediction using local object curvature.



in contrast, shows that prediction using local object curvature (Equation 17) was accurate until the abrupt change was reached, at which point there was a spike in the absolute percent error of the prediction. The prediction error of  $0.44 \pm 0.12\%$  for prediction using local object slope was lower than the prediction error of  $1.05 \pm 5.12\%$  for prediction using local object curvature.

In summary, these simulation results demonstrate that local object curvature more accurately predicts future contact points on regions of objects with no distinct edges, but that when objects have distinct edges, prediction using local object slope is more accurate. Of course, this in turn raises the question of what it means for an object to have a “distinct edge.” Mathematically, it must be an edge in the sense that there is a discontinuity in the curvature between measurements, which is clearly related to the spatial scale of the object relative to the spacing of the whiskers. We investigate this in the next section.

### IMPORTANCE OF WHISKER SPACING

The spacing between the whiskers on the object surface places limits on the maximum curvature that can be sensed. Equation 19 defines  $\kappa_{\max}$ , the maximum discriminable curvature:

$$\kappa_{\max} = \frac{1}{r} = \frac{1}{d + \Delta} \quad (19)$$

where  $r$  is the radius of the osculating circle defining  $\kappa_{\max}$ ,  $d$  is the vibrissa spacing, and  $\Delta$  is an arbitrarily small distance.

In the present work, we assumed that the spacing between the whiskers on the object surface was approximately equal to the spacing between them at their base. This is a reasonable approximation for the present work, in which the whiskers are parallel to each other, but is unlikely to be valid for the real rat.

**Figure 7A** illustrates the relationship expressed in Equation 19. The distance  $\Delta$  is added to the vibrissa spacing because a force must be applied to the vibrissae to find a contact point. The limiting case is finding the curvature of a cylinder with radius  $r$  and  $\Delta = 0$ . With vibrissae spaced at  $d = r$ , the object could only apply a force to bend at most two of the vibrissae. In order to make

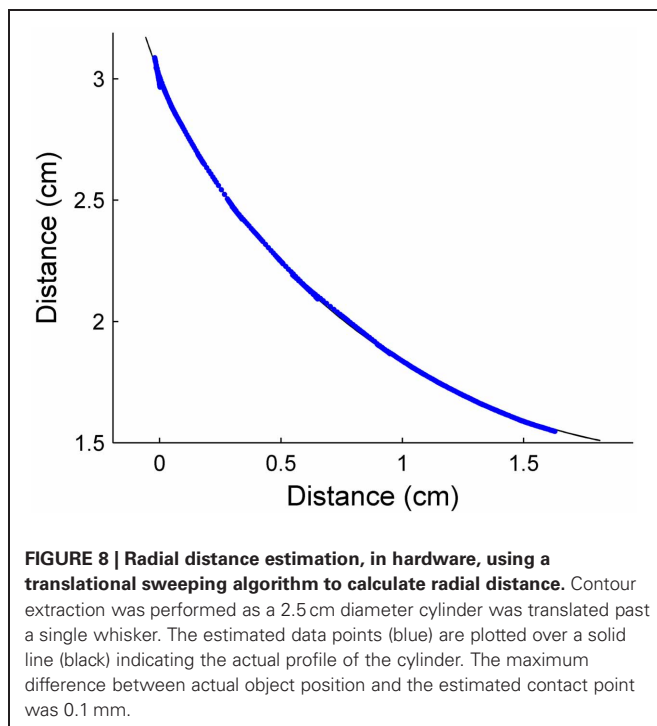
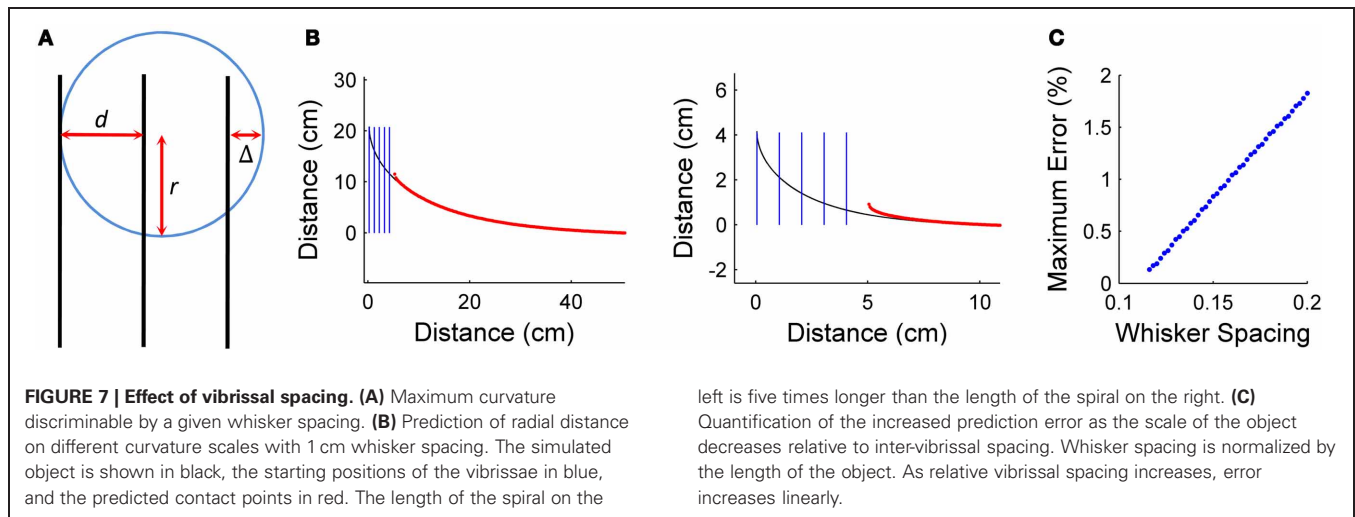
a discrete curvature approximation, a minimum of three contact points are required to define curvature. Therefore,  $\Delta$  must be strictly greater than zero if the measurement of curvature is desired.

To demonstrate the effect of relative vibrissa spacing on prediction error, prediction was simulated over hyperbolic spirals of various sizes. The hyperbolic spiral was chosen as the test object because it can be translated past the vibrissa array in such a way that curvature decreases approximately linearly. In these simulations, the multiple-vibrissa prediction method was used, with vibrissa spacing set to 1 cm. The size of the spiral test object was decreased for each case to illustrate the effect of relative vibrissa spacing.

**Figure 7** shows the simulated test object on two different length scales, as vibrissa spacing stays constant. The left side of **Figure 7B** shows an object large on the scale of inter-vibrissa spacing, while the right side of **Figure 7B** shows an object small on the scale of inter-vibrissa spacing. **Figure 7C** illustrates that prediction error increases as the test object decreases in size. This increase in error is unsurprising, and occurs for two reasons. First, the relative change in distance between the most forward measurement and the predicted radial distance is more pronounced as the object decreases in size. More importantly, the spacing between vibrissae defines the resolution of the array, and it is decreasing relative to the change in curvature that is occurring. This simulation illustrates the importance of vibrissa spacing to prediction—though gradual curvature changes can be accurately predicted with good spatial resolution, prediction suffers when resolution decreases.

### HARDWARE RESULTS: VALIDATION OF THE TRANSLATIONAL SWEEP ALGORITHM

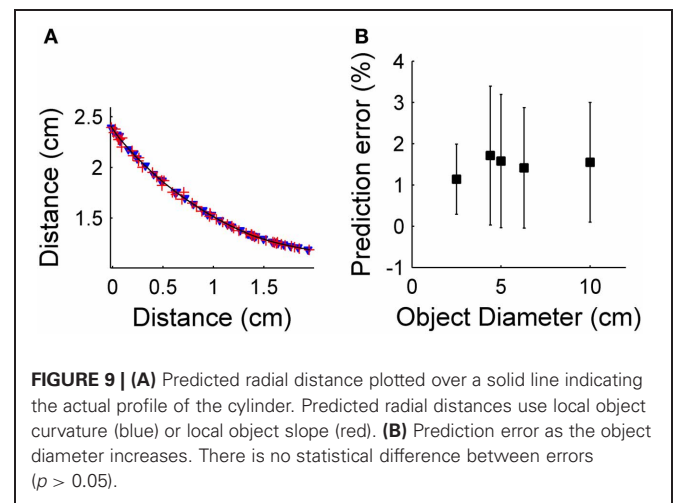
We next aimed to validate these simulation results in hardware. However, before we could do so, we needed to experimentally validate the translational sweep algorithm proposed by Solomon and Hartmann (2010). We implemented the translational sweep algorithm on our hardware array of whiskers (see *Methods*) to extract



the contour of an object as it was translated past one or more vibrissae in the array. **Figure 8** shows results from a trial in which a 2.5 cm diameter cylinder was translated past a single vibrissa at a velocity of 2 cm/s. The maximum difference between the actual object position and the estimated contact point at any given time was 0.1 mm, within the limits of measurement error.

#### HARDWARE RESULTS: IMPLEMENTATION OF PREDICTION WITH A SINGLE VIBRISSA: OBJECT OF CONSTANT CURVATURE

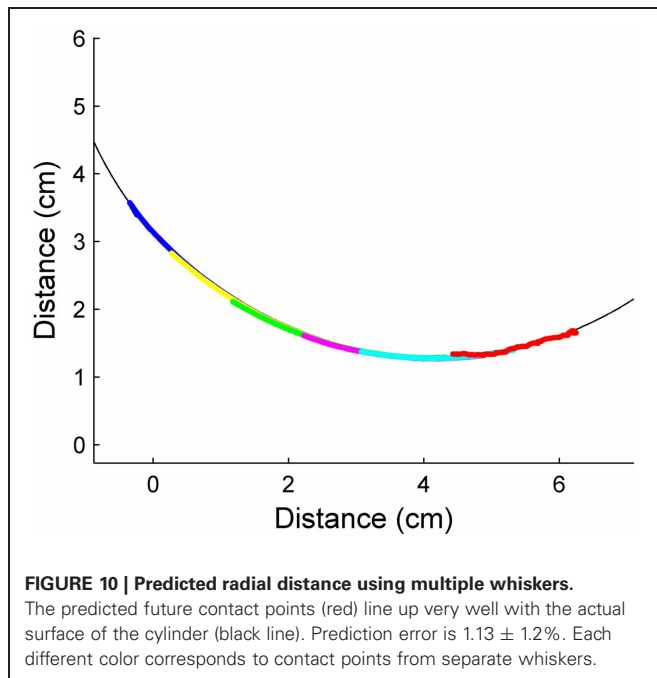
Having validated the translational sweep algorithm, we next aimed to test the two prediction methods in hardware. **Figure 9A** presents the same contour extraction data as in **Figure 8**, but here we also apply the prediction algorithms. Specifically, **Figure 9A** shows the contact points prediction using local object



slope (Equation 16) and prediction using local object curvature (Equation 17). These predictions are plotted over a curve representing the actual surface of the cylinder. Using different numbers of past time steps did not significantly affect the accuracy of the prediction, which stayed fixed at an average level of  $1.3 \pm 1.25\%$  for prediction using local object slope, and an average level of  $1.1 \pm 0.96\%$  for prediction using local object curvature (**Figure 9B**). Prediction error was calculated according to Equation 18. Because there was no difference between numbers of past time steps used, five points were used for the rest of the single-vibrissa experiments presented in this paper. In the second part of this experiment, cylinders with diameters of 2.5 cm, 4.4 cm, 5.0 cm, 6.3 cm, and 10 cm were passed by the array at a velocity of 2 cm/s. As expected, there is no significant effect of object diameter on prediction error. The error across the trials for prediction using local object curvature was  $1.40 \pm 1.43\%$ .

#### HARDWARE IMPLEMENTATION OF PREDICTION WITH MULTIPLE VIBRISSAE: OBJECT OF CONSTANT CURVATURE

Neurons in the trigeminal nuclei have receptive fields that include multiple vibrissae, which may enable the rat to estimate the surface gradient at a single time point. For this technique to



be viable, the chosen vibrissae must all be touching the object at once. The spacing between adjacent vibrissae in the final design of the array (Figure 3) is 1.5 cm. To ensure there were times when all five vibrissae touched the test object concurrently, only the 10 cm diameter cylinder was used for these constant curvature trials. Figure 10 shows the predicted future contact points for the vibrissa array as the array moves forward. Each predicted point is 1.5 cm further along the object than the lead vibrissa was at the time of the point's prediction. Since the five points of contact come from five different vibrissae, the predicted curvature gradient is implemented over a much larger spatial scale. Small errors in distance estimation result in larger deviations in the predicted future radial distance estimate.

#### HARDWARE IMPLEMENTATION OF PREDICTION WITH A SINGLE VIBRISSAE: OBJECT WITH ABRUPT CURVATURE CHANGE

The results of the previous two sections show that prediction using local object curvature can accurately predict future contact points for an object with constant curvature. In the world, however, such objects are rarely found. We did not implement prediction using the multiple vibrissa method on this object because the main difference between the spatial scales over which we were making abrupt changes was better represented by the single vibrissa method.

To show the effect of abrupt changes in object curvature on prediction, a simple case was examined. Figure 11A shows the test object. The object has three distinct constant curvatures with no smoothing transition from one to the next. The radii of curvature for the sections were 2.5 cm, 3.2 cm, and 2.2 cm. The object was moved past the vibrissa array using linear actuation at a velocity of 2 cm/s. Prediction was performed using local object curvature for each vibrissa, with predicted contact points shown in Figure 11B.

It can be seen from Figure 11C that the absolute percent error of the prediction remains small during the first section of constant curvature. At the transition to the second curvature, the absolute percent error increases, with the maximum value more than quadrupling the prediction error during the first section. Once the vibrissa has been able to sense the second curvature for a short time, absolute percent error returns to baseline. The second transition is similar to the first. A closer examination of Figure 11B shows fewer predicted points during the times when the algorithm is least accurate. The reason for this is that the vibrissa slips quickly over the concavity in the object, covering the distance more quickly than during slip-free data collection. This longitudinal slip causes a significant increase in error in the estimation of distance.

#### HARDWARE IMPLEMENTATION OF PREDICTION WITH MULTIPLE VIBRISSAE: OBJECT WITH GRADUAL CURVATURE CHANGE

We tested the hardware vibrissa array with a section of a hyperbolic spiral that had an approximately linear decrease in curvature as the object was translated past the whiskers.

Figure 12 shows the estimate of predicted future radial distance when the vibrissa array was passed by an object with gradually changing curvature. Figure 12A shows the actual object. Figure 12B shows a trial using the single vibrissa method, which corresponds to the situation where spacing between the data points is small relative to the change in curvature. The prediction error of  $0.97 \pm 1.4\%$  is very similar to the error for an object with constant curvature ( $1.1 \pm 0.96\%$ ). In Figure 12C, the vibrissa base points were evenly spaced at 1.5 cm intervals, and the multiple vibrissa method was used. This increase in spacing mirrored the decrease in size of the object in the simulations, and resulted in an increase in prediction error. Since the gradual change in curvature is from high curvature to lower curvature, the predicted future contact points lie mostly inside the actual curve. Prediction error for this trial was  $12.7 \pm 7.11\%$ , though the error decreases to  $11.9 \pm 6.97\%$  when the largest outlier is removed.

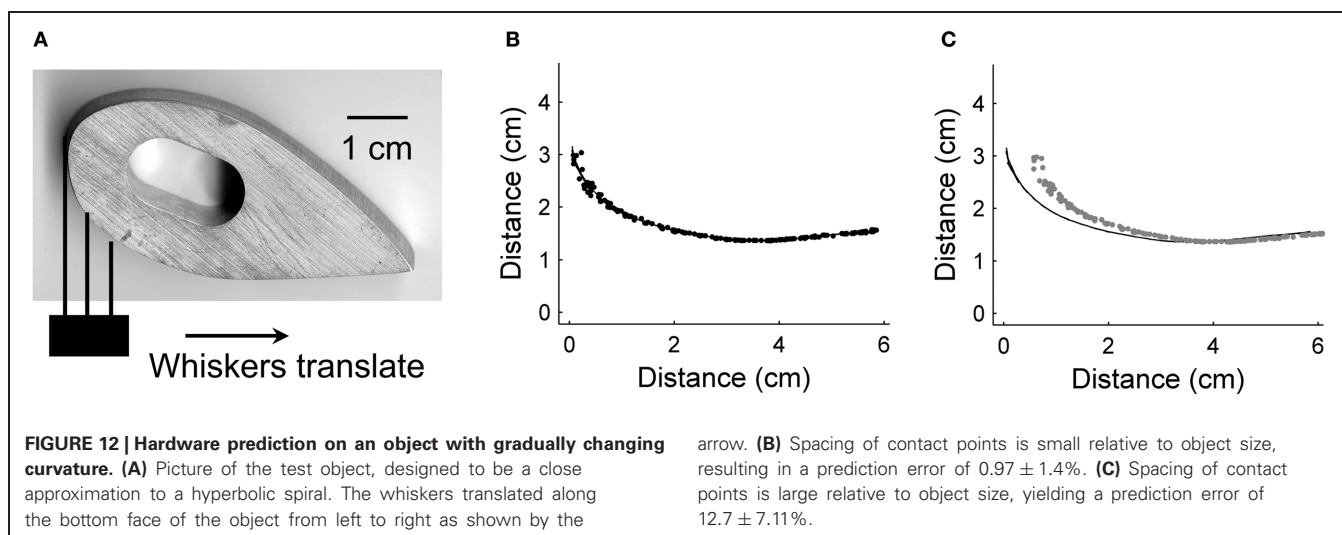
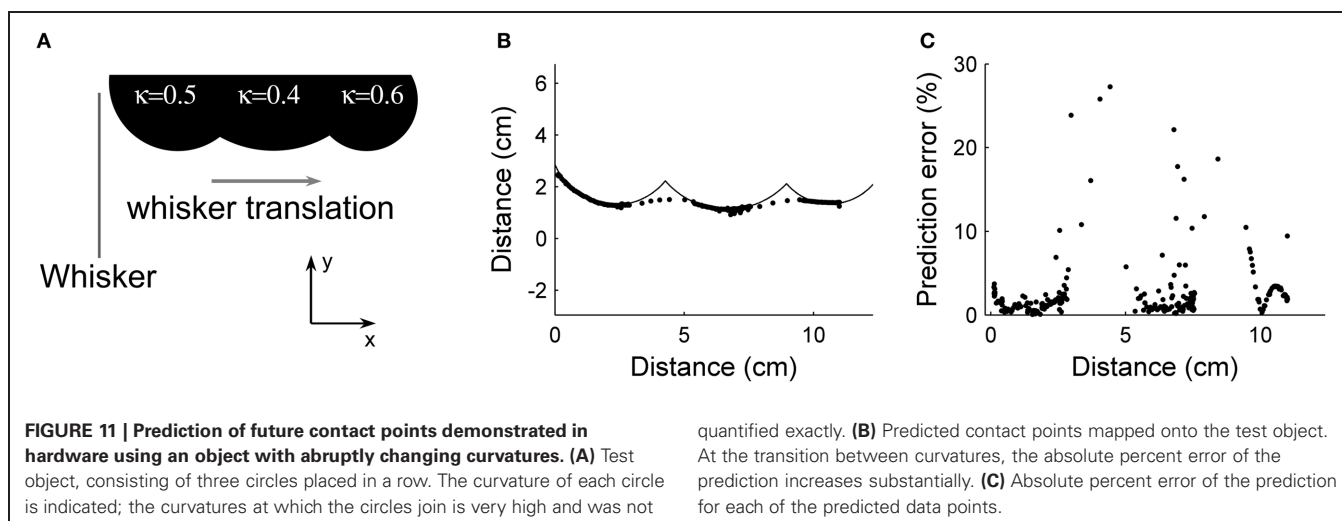
## DISCUSSION

This paper has demonstrated that simple algorithms can be used to predict future contact points on an object. Prediction is accurate for objects that have constant and/or gradually changing curvature as long as the distance between vibrissae is small relative to the change in curvature. Abrupt changes in object curvature result in jumps in absolute percent error of the prediction.

#### PREDICTION ALGORITHM PERFORMANCE

Two different algorithms for prediction were described in the results section. Prediction using local object slope is only accurate when the curvature being measured does not change much between estimated contact points, but it can accommodate for abrupt changes in curvature (e.g., an edge). Prediction using local object curvature was shown to be more accurate for both objects with constant curvature and objects with gradual changes in curvature.

In all cases, vibrissa spacing makes a difference in accuracy of prediction. This result is hardly surprising, since the limiting factor is essentially sensor resolution. The main advantage of



widely spaced vibrissae is the ability to predict further ahead in space. Since information about the sensed object is spread over a wider distance, it is more likely that the estimated curvature will be a reflection of the overall curvature of the object rather than a measurement of a local deviation from the actual object curvature.

These observations lead to the hypothesis that vibrissa spacing represents a trade-off between accuracy and predictive utility. For wall following, we anticipate that the rat will protract its vibrissae far forward and maximize spacing between the tips, because predictive sensing over a large spatial scale is important. For edge detection tasks, accuracy becomes more important so we anticipate that the vibrissal tips will be spaced more closely together.

#### A COMPUTATIONAL MECHANISM FOR THE INSTANT DETECTION OF MOTION

Motion detection, as well as the ability to distinguish self-movement from environmental movement, is critical to animal survival. Behaviors such as escape or predation must link motion

detection to immediate motor action. For these behaviors, the quality of the sensory data obtained is largely irrelevant, as long as it is sufficient to trigger the appropriate motor action. We suggest that a mismatch between predicted and actual sensory input may serve to direct attention.

In this work, we have presented specific examples of how calculating terms of the total derivative might be used by a moving rat to track an object within its vibrissal sensory array. If an object is moving in the vibrissal field, there will be a mismatch between actual and predicted input that is exactly equal to how the world is changing in time. In the next time step, the animal can use this mismatch to compute the relative velocity between its own movements and movements in the world. In other words, the animal can compare predicted and actual sensory data obtained to estimate the quantity  $\frac{\delta A_{env}}{\delta t}$ . Of course, if the fluctuations in the environment (i.e., movements of objects in the world) are unpredictable, then the animal will never succeed in finding an accurate estimate. Because objects on the scale of the rat are strongly dominated by inertial forces, however, many changes in the world will have predictable temporal trajectories (e.g., a rolling tin can).

## ADVANTAGES OF USING PREDICTION DURING WALL FOLLOWING BEHAVIOR

During wall-following behavior, a rat maintains a small separation between itself and the wall while traveling at a relatively high velocity. The rat can maintain this separation even when walls curve, however, since the rat has mass, and it moves at a high velocity, changing direction takes time and energy. Following a curving wall would be easier if the rat could predict the future wall profile using its vibrissae. More specifically, if a rat could use just radial distance measures to predict the upcoming wall contour, it could start to change direction sooner, reducing inertial delays and saving energy. Encoding by its vibrissa array to determine where the wall was likely to be in the future, it would save energy and allow the rat to travel along the wall at a higher velocity. With these prediction algorithms that prediction could be accomplished at a very low level of processing. The algorithms presented here suggest that this type of prediction could be achieved with a very low level of computation.

## POSSIBLE IMPROVEMENTS IN VIBRISSA SENSING/PREDICTION

An examination of the results presented in **Figure 11** shows predicted data points that are spaced much less densely in the concave regions of the object. Data are less dense in these sections because the vibrissa slips, and because only the tip of the vibrissa contacts during part of the movement. When the vibrissa tip is the only part of the vibrissa that contacts the object, radial

distance cannot be accurately calculated with our algorithm. For artificial whiskers like the ones presented in this work, these sorts of tip contacts can occur at several radial distances near the full whisker length. In order to calculate radial distance for tip contacts, we need a measure of the axial force being applied to the vibrissa tip, where axial force is defined along the axis of the vibrissa. Future versions of the vibrissa array presented in this paper will be able to sense axial force along with bending moments at the vibrissa base.

The artificial whiskers used in this work were cylindrical, but real rat whiskers taper linearly. Tapering the whisker confers at least two advantages. First, whisker taper increases sensitivity to small contact forces (Williams and Kramer, 2010; Solomon and Hartmann, 2011). Second, when used in conjunction with an axial force sensor (not used in the present work), a tapered whisker ensures that the mappings between bending moment and axial force are one-to-one with radial distance and  $\theta_{push}$ , the angle through which the whisker has rotated against the object (Solomon and Hartmann, 2011).

## ACKNOWLEDGMENTS

This work was funded by NSF award IOS-0818414 and NSF CAREER award IOS-0846088 to Mitra J. Z. Hartmann and NSF EFRI-0938007 (Liu, PI). Christopher L. Schroeder was sponsored by NSF IGERT # DGE-0903637: Integrative Research in Motor Control and Movement (Hale, PI).

## REFERENCES

- Barron, J. L., Fleet, D. J., and Beauchemin, S. S. (1994). Performance of optical flow techniques. *Int. J. Comput. Vis.* 12, 43–77.
- Beauchemin, S. S., and Barron, J. L. (1995). The computation of optical flow. *ACM Comput. Surv.* 27, 433–467.
- Berg, R. W., and Kleinfeld, D. (2003). Rhythmic whisking by rat: retraction as well as protraction of the vibrissae is under active muscular control. *J. Neurophysiol.* 89, 104–117.
- Bicchi, A., Scilingo, E. P., Ricciardi, E., and Pietrini, P. (2008). Tactile flow explains haptic counterparts of common visual illusions. *Brain Res. Bull.* 75, 737–741.
- Birdwell, J. A., Solomon, J. H., Thajchayapong, M., Taylor, M. A., Cheely, M., Towal, R. B., Conradt, J., and Hartmann, M. J. Z. (2007). Biomechanical models for radial distance detection by rat vibrissae. *J. Neurophysiol.* 98, 2439–2455.
- Gopal, V., and Hartmann, M. J. Z. (2007). Using hardware models to quantify sensory data acquisition across the rat vibrissal array. *Bioinspir. Biomim.* 2, S135–S145.
- Hartmann, M. J. Z. (2009). Active touch, exploratory movements, and sensory prediction. *Integr. Comp. Biol.* 49, 681–690.
- Horn, B. K. P., and Schunck, B. G. (2003). Determining optical flow. *Artif. Intell.* 17, 185–203.
- Kaneko, M., Kanayama, N., and Tsuji, T. (1998). Active antenna for contact sensing. *IEEE Trans. Rob. Autom.* 14, 278–291.
- Munson, B. R., Young, D. F., Okiishi, T. H., and Huebsch, W. W. (2009). *Fundamentals of Fluid Mechanics*. Hoboken, NJ: John Wiley and Sons, Inc.
- Nemenman, I., Lewen, G. D., Bialek, W., and Van Steveninck, R. R. D. (2008). Neural coding of natural stimuli: information at sub-millisecond resolution. *PLoS Comput. Biol.* 4:e1000025. doi: 10.1371/journal.pcbi.1000025
- Scilingo, E. P., Sgambelluri, N., and Bicchi, A. (2008). “The role of tactile flow in processing dynamic haptic stimuli” in *Sense of Touch and its Rendering: Progress in Haptics Research Book Series*, eds A. Bicchi, M. Buss, M. O. Ernst, and A. Peer (Heidelberg, Berlin: Springer-Verlag Berlin), 39–60.
- Solomon, J. H., and Hartmann, M. J. Z. (2006). Robotic whiskers used to sense features. *Nature* 443, 525.
- Solomon, J. H., and Hartmann, M. J. Z. (2008). Artificial whiskers suitable for array implementation: accounting for lateral slip and surface friction. *IEEE Trans. Rob.* 24, 1157–1167.
- Solomon, J. H., and Hartmann, M. J. Z. (2010). Extracting object contours with the sweep of a robotic whisker using torque information.. *Int. J. Rob. Res.* 29, 1233–1245.
- Solomon, J. H., and Hartmann, M. J. Z. (2011). Radial distance determination in the rat vibrissal system and the effects of Weber’s law. *Philos. Trans. R. Soc. Lond. B Biol. Sci.* 366, 3049–3057.
- Szwed, M., Bagdasarian, K., and Ahissar, E. (2003). Encoding of vibrissal active touch. *Neuron* 40, 621–630.
- Welker, W. I. (1964). Analysis of sniffing of the albino rat. *Behaviour* 22, 223–244.
- Williams, C. M., and Kramer, E. M. (2010). The advantages of a tapered whisker. *PLoS ONE* 5:e8806. doi: 10.1371/journal.pone.0008806

**Conflict of Interest Statement:** The authors declare that the research was conducted in the absence of any commercial or financial relationships that could be construed as a potential conflict of interest.

Received: 19 March 2012; paper pending published: 11 April 2012; accepted: 20 July 2012; published online: 22 October 2012.

Citation: Schroeder CL and Hartmann MJZ (2012) Sensory prediction on a whiskered robot: a tactile analogy to “optical flow”. *Front. Neurobot.* 6:9. doi: 10.3389/fnbot.2012.00009

Copyright © 2012 Schroeder and Hartmann. This is an open-access article distributed under the terms of the Creative Commons Attribution License, which permits use, distribution and reproduction in other forums, provided the original authors and source are credited and subject to any copyright notices concerning any third-party graphics etc.



# The effect of whisker movement on radial distance estimation: a case study in comparative robotics

Mathew H. Evans<sup>1\*</sup>, Charles W. Fox<sup>1</sup>, Nathan F. Lepora<sup>1</sup>, Martin J. Pearson<sup>2</sup>, J. Charles Sullivan<sup>2</sup> and Tony J. Prescott<sup>1</sup>

<sup>1</sup> Department of Psychology, Sheffield Centre for Robotics, University of Sheffield, Sheffield, UK

<sup>2</sup> Bristol Robotics Laboratory, University of the West of England, Bristol, UK

## Edited by:

Blythe Towal, California Institute of Technology, USA

## Reviewed by:

Karen Moxon, Drexel University, USA

Joseph H. Solomon, Northwestern University, USA

## \*Correspondence:

Mathew H. Evans, Department of Psychology, University of Sheffield, Western Bank, Sheffield, S10 2TN, South Yorkshire, UK.

e-mail: mat.evans@shef.ac.uk

Whisker movement has been shown to be under active control in certain specialist animals such as rats and mice. Though this whisker movement is well characterized, the role and effect of this movement on subsequent sensing is poorly understood. One method for investigating this phenomena is to generate artificial whisker deflections with robotic hardware under different movement conditions. A limitation of this approach is that assumptions must be made in the design of any artificial whisker actuators, which will impose certain restrictions on the whisker-object interaction. In this paper we present three robotic whisker platforms, each with different mechanical whisker properties and actuation mechanisms. A feature-based classifier is used to simultaneously discriminate radial distance to contact and contact speed for the first time. We show that whisker-object contact speed predictably affects deflection magnitudes, invariant of whisker material or whisker movement trajectory. We propose that rodent whisker control allows the animal to improve sensing accuracy by regulating contact speed induced touch-to-touch variability.

**Keywords:** active sensing, touch, whisker, robot, biomimetic, comparative, perception, classification

## 1. INTRODUCTION

Many robots have been developed for understanding whisker sensing (Prescott et al., 2009; Evans et al., 2012). Though each has expanded our understanding in certain ways, it is difficult to apply the results in a general way to other paradigms or wider applications. Choices made in the development of robotic hardware specify the kind of questions that can be answered by that platform. For example, robots with high degrees of freedom allow research into the effects of whisker movement on sensing, but this movement is not precise enough to expose the underlying mechanisms of whisker sensing.

A complementary robotics approach, similar to approaches used in the biological sciences (Kappers et al., 1936; Kardong, 2006), allows the development of robots where the results from one platform can inform the experiments on another. Great progress can be made, both by performing experiments on appropriate platforms and ensuring that results inform general conclusions. Results from robotics in turn may provide insights for neuroscience. A key example where such an approach may be fruitful is in understanding the effect whisker movement has on sensing.

In this paper we will briefly introduce rodent whisker movement control, and whiskered robots that model these systems will be reviewed. A comparative robotics approach is described, outlining a path for addressing some of the questions from biology in a more explicit and effective manner. Specifically, what is the effect of whisker movement on radial distance estimation?

### 1.1. ACTIVE WHISKER TOUCH SENSING IN RODENTS

Whiskers are found in almost all terrestrial mammals, *Homo Sapiens* excepted, and some marine mammals (Ahl, 1986). Although whiskers are hairs, their structure is highly specialized, with regards to their surface structure and mechanical properties, in transferring contact information to the hair follicle for tactile sensing (Chernova and Kulikov, 2011). For example, whiskers vary in length, thickness, shape, and stiffness between species depending on animal size or how the whiskers are used (Sarko et al., 2011).

Rats typically have around 30 prominent whiskers on each cheek (or mystacial pad), arranged in a regular grid of rows and columns (Ahl, 1986). These large *macro-vibrissae* vary in length and width across the whisker pad, from the largest [2–40 mm in length (Diamond et al., 2008)] in the most caudal column down to the smallest in the rostral column. A dense array of 40–70 smaller *micro-vibrissae* (a few mm in length) are located around the lips (Brecht et al., 1997). Physical differences between the whiskers affect their mechanical properties, such as their bending and damping characteristics (Hartmann et al., 2003), which could have repercussions for sensing, a critical consideration when building artificial whiskers.

Whiskers can only encode information about objects when they make contact with them. To gather information about the world, rodents sweep their whiskers through the air, and bring them on to surfaces in the environment. This back and forth sweeping movement of the whiskers [called “whisking” (Welker, 1964)] has been the subject of a great deal of research. A single

“whisk” is defined as one cycle of whisker protraction (forward movement) and retraction (backward movement), and without perturbation rats typically whisk in short bouts of  $\approx 10$  cycles, at around 5–8 Hz (Carvell and Simons, 1990).

Though initially thought to be very regular (Semba and Komisaruk, 1984), recent studies using optoelectronic monitoring techniques (Bermejo et al., 2002) and high speed videography (Sachdev et al., 2002; Towal and Hartmann, 2006) has revealed that rat whisking can be highly irregular and complex. It is full of asynchronies, where different whiskers are protracted by different amounts (Sachdev et al., 2002) and asymmetries, where the whiskers on either side of the head are moved out of phase with one another (Towal and Hartmann, 2006). These irregular movements are thought to be the result of active sensing strategies (Hartmann, 2001; Berg and Kleinfeld, 2003; Mitchinson et al., 2007).

Among other parameters (Towal and Hartmann, 2008), rats control the spread and contact force of whiskers to ensure even, light contacts across the whisker array. Specifically, rats seem to use particular strategies for sensing, such as the rapid cessation of protraction upon initial contact with a surface, and contact induced asymmetry in the whisker movements, where a whisker contact on one side of the rat’s head causes an increase in the protraction of whiskers on the side contra-lateral to contact (Grant et al., 2009). Together these efforts are grouped into a strategy described as minimal impingement (hereafter MI), maximal contact (Mitchinson et al., 2007).

In addition, head movement greatly effects the velocity of whisker contacts (Grant et al., 2009), and whisker movement is controlled to sweep space in anticipation of head movement (Towal and Hartmann, 2006). Though some have been identified (Grant et al., 2009), it remains unclear which components of whisker movement are actively controlled by the rat, which are artefacts arising from limitations of biological systems, and which if any are important for sensing. For example, do rats change their whisking frequency to improve the discrimination of particular surfaces, or because their muscles cannot maintain high frequencies of whisking for prolonged periods of time?

## 1.2. ACTIVE WHISKER TOUCH SENSING IN ROBOTS

A number of software and hardware models have been developed to better understand whisker sensing. There are many reasons why modeling a system is an important step toward understanding, and why synthetic models (models built in software or hardware) in particular are so useful (Rosenblueth and Wiener, 1945; Mitchinson et al., 2010). For example, in a model whisker movement can be precisely controlled to determine the effects any changes have on whisker deflections and subsequent analysis.

Whiskers have been modeled simply as elastic beams (Salisbury, 1984; Young et al., 2003). Though progress has been made very recently in more precise computational modeling of whiskers (Quist and Hartmann, 2012), their small size make accurate simulation difficult. A more straightforward method is to build artificial whiskers and mount them on robots. Whiskered robots have been broadly reviewed recently in Prescott et al. (2009). Specifically focusing on whisker actuation mechanisms, and the effect these have on sensing, early models were static and

provided binary contact vs. no contact reports (Schiebel et al., 1986; Jung and Zelinsky, 1996). Hinged whiskers were used to infer the location of tip contact through potentiometer readings (Russell, 1992). Emulating earlier modeling work, elastic beam equations have been used by a number of researchers to infer the location of contact along an artificial whisker, and in turn the curvature of a surface with whiskers mounted on robots (Russell and Wijaya, 2003, 2005), rotational DC motors (Kim and Moller, 2004, 2007), or a set screw (Solomon and Hartmann, 2006). In a unique design Wilson and Chen (1995) used a pair of pressurized tubes laid end to end as a whisking mechanism, and a closed loop control system to infer whisker tip contact location in space.

In more biomimetic (Vincent et al., 2006) robots (such as in, Seth et al., 2004; Fend et al., 2005; Meyer et al., 2005; Pearson et al., 2007; Lepora et al., 2012b) multiple degrees of freedom are included as whiskers are often actuated, as well as being mounted on mobile robot platforms. This increased whisker movement makes texture discrimination difficult (Fend et al., 2003), especially in conditions where whisker motion varies from trial to trial (Fox et al., 2009). To address this point further more complex whiskered robots, with individually actuated whiskers have been developed in recent years for investigating biomimetic whisker control strategies (such as MI discussed earlier, Pearson et al., 2011), and how these strategies may improve texture discrimination (Lepora et al., 2010b; Sullivan et al., 2012).

## 1.3. WHISKER MATERIALS

The material a whisker is made from has a critical influence on the way a whisker interacts with a surface, and as a result the nature of the deflections created at the whisker base (Hartmann et al., 2003). Whiskers are specialized sensory elements for aiding tactile sensing in the hair follicle, differing in structure from other mammalian hairs to ensure strength and stiffness (Chernova and Kulikov, 2011; Sarko et al., 2011). Rat whiskers have evolved to have excellent mechanical properties for transferring tactile information to the follicle during sensory exploration (Chernova and Kulikov, 2011). Specifically, rat whiskers are stiff when moved in air but bend in contact and are highly damped with damping ratios  $\zeta$  of 0.11:0.19 and Young’s modulus  $E$  of  $\approx 3$ –4 GPa (Hartmann et al., 2003). This ensures that the whiskers do not oscillate when whisked in air, which can add noise to the deflection signal and make contacts difficult to detect. This damping also increases when the whisker is in the animal, as observed in that contact induced oscillations are smaller in whisking rats than isolated whiskers (Hartmann et al., 2003). Whiskers are tapered, which has certain advantages [some are described in detail by Williams and Kramer (2010)], so it is important that artificial whiskers taper if they are to appropriately mimic the biological system. In artificial systems whisker material and morphology have also been shown to be important for texture discrimination (Lungarella et al., 2002; Fend et al., 2006).

## 1.4. RADIAL DISTANCE TO CONTACT ESTIMATION

Estimating the radial distance to contact (in this paper, from the base of the whisker) allows an agent to determine whether an object has made contact with a whisker at the tip or the shaft, which is important for texture discrimination, and to

discriminate between contacts with the surfaces or corners of objects. Measuring the location in space of multiple contacts over time allows an agent to reconstruct the contours of an object or perimeters of the environment (Fox et al., 2012). Radial distance estimation has been demonstrated in rodents (Szwed et al., 2006), and approached by many researchers. Theoretically, radial distance to contact estimation along a beam is a solved problem (Solomon and Hartmann, 2006, 2011), as long as whisker movement is precisely controlled and the physical properties such as size, taper, and elasticity are known. In an applied robotic setting these parameters are not always known precisely, therefore a more data-driven approach is appropriate (Evans et al., 2010a; Lepora et al., 2010a). In this paper we use a feature-based radial distance estimation method, essentially extracting analogous information to the bending moment at peak protraction, but using regression to determine the relationship between this value and radial distance to contact.

Feature-based classification involves finding invariant features in the data that correspond to parameters in the real world. For example, using scale invariant feature transformation (SIFT) algorithms in vision (Lowe, 1999; Juan and Gwun, 2010). Feature extraction has also been demonstrated in biological sensing systems. Frog prey capture is based on the principle of feature detection, with responses elicited for any object matching the size and angular velocity of a fly (Lettvin et al., 1959). In the rat whisker system some researchers have reported cells that respond to “kinetic features” in whisker deflections (Petersen et al., 2008). An advantage of this approach is that it reveals how different whisker movement patterns affect the extracted features, and may allow the measurement of numerous features to classify a range of whisker-object contact parameters simultaneously in future.

### 1.5. A COMPARATIVE ROBOTICS APPROACH

As robots become more complex, they become more difficult to control. As this progression continues it may be difficult to conduct experiments that address fundamental questions about whisker-object interactions. In this paper we present a complementary robotics approach. Here, a group of different robots are used to address the same problem of radial distance to contact estimation, allowing a direct comparison of whisker materials and actuation methods. This approach may help in understanding radial distance to contact estimation more generally, invariant of whisker material or actuation method.

Three robots were used for comparison. Firstly, an XY positioning robot moves objects onto an artificial whisker sensor in an accurate and highly repeatable manner, allowing the collection of large amounts of whisker deflection data. This approach provides the opportunity for a better understanding of the nature of whisker-object contacts (expanding on previous preliminary work in Evans et al., 2010a,b). Data collected on the XY positioning robot is used to systematically train and test a classifier under a range of contact conditions, and extract features for radial distance to contact and contact speed estimation. Secondly, SCRATCHbot (an acronym of Spatial Cognition and Representation through Active TouCH, Pearson et al., 2010) is a mobile whiskered robot which approximates the degrees of movement of an exploring rat. Actuated whiskers are mounted on

an articulated “neck,” which is in turn fixed to a mobile base. SCRATCHbot is used here in a “head-fixed” protocol to show how the classifier and features developed on the XY positioning robot can be applied to data from a less restricted whisking robot. Thirdly, CrunchBot is a mobile whiskered robot with stationary whiskers (Fox et al., 2011). This robot has fewer degrees of freedom than SCRATCHbot, allowing more straightforward robot control and data collection in a mobile setting. Testing the feature-based classifier on CrunchBot evaluates whether this approach can be robustly implemented on a mobile robot. In addition to separate actuation methods, all three robot platforms utilize different whisker materials. This change allows for the comparison of whisker materials in the same radial distance estimation task, and tests the classifier’s robustness to this change. A great deal of effort was made to find materials for artificial whiskers that would match the mechanical properties of real whiskers at different scales, such as stiffness and bending characteristics. Additional concerns are toughness and the ability to appropriately shape the whisker.

## 2. MATERIALS AND METHODS

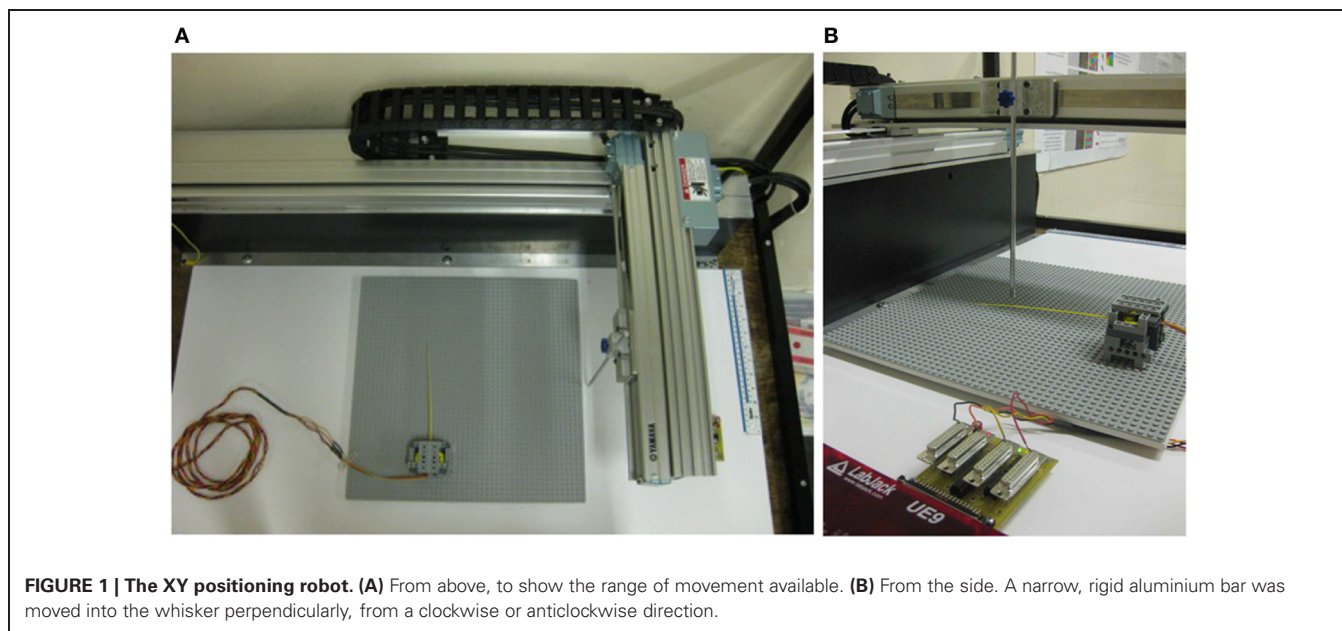
### 2.1. ROBOT PLATFORMS

#### 2.1.1. XY positioning robot platform

A Cartesian robot (see **Figure 1**) was chosen as it is capable of a wide range of movement, is very accurate and can move at speeds which approximate scaled rat-whisker velocities. Deflections for the whisker are streamed to a PC, and can be processed in real time to control subsequent movement of the positioning robot. The robot (Yamaha-PXYX, Yamaha Robotics) has a movement range of 350 × 650 mm, and can move up to 720 mm/s. Repeatability of the robot is ±0.01 mm, and the maximum load it can carry is 1.5 kg. Objects are carried by the robot into an artificial whisker fixed to the table, as this allows us to control the contact as carefully as possible. Moving the whisker into an object would subject the sensor to trajectory-dependent accelerations that would cause more complex effects such as whisker oscillations. Subsequent robots described in this paper allow for exploring these trial to trial variations and their effect on sensing. A controller (Yamaha RCX 222, 2-axis robot controller) takes instructions from a PC through an RS232 cable, and the controller interprets the instructions, completes path integration, and drives the motors. Instructions for the robot are generated inside a MATLAB (mathworks.com) loop, and can be easily updated during robot operation, depending on the whisker input.

#### 2.1.2. SCRATCHbot robot platform

The SCRATCHbot robot platform (**Figure 2A**) consists of a head-mounted whisker array, a mobile body housing computing means, motors and power supply, and an articulated neck allowing free movement of the head independent from the body. For this experiment we focus only on the head. Six independent columns of three whiskers, arranged in two arrays of nine whiskers either side of the head, are independently driven by a DC motor and gearbox. Whiskers in a column are mechanically coupled, but columns themselves are capable of independent rotational (anterior–posterior) whisk-like movement. Movements and data collection are coordinated by independent



micro-controllers. A central PC-104+ reconfigurable computing platform, including a closely coupled array of FPGAs and a single board computer, handled all sensor and motor coordination.

### 2.1.3. CrunchBot robot platform

CrunchBot (**Figure 2B**) consists of an iRobot Create base (irobot.com) with an extended cargo bay to accommodate a netbook PC. This netbook is used for autonomous control of the robot, running Ubuntu 10.10 on a single-core Intel Atom processor. The netbook hosts a Player server (playerstage.sourceforge.net) providing high-level, networked API interfacing to the Create's serial port commands. Rapid prototyped ball joint mountings fixed to an adjustable metal bar individually hold six static artificial whiskers. The whiskers are positioned at angles to fan out across the width of the robot while covering any blind spots. Radial distance estimation and basic motor control can run in real time on the netbook, reading the raw data from the circular buffer.

## 2.2. ARTIFICIAL WHISKERS

Three different materials were used in the fabrication of whiskers for the three robot platforms. Each whisker is made on an Envisiontec Perfactory rapid prototyping machine (envisiontec.de). The XY positioning robot whisker was made from flexible Acrylonitrile butadiene styrene (ABS) plastic ( $E \approx 1.63$  GPa,  $\zeta \approx 0.07$ ), 185 mm long, 2 mm diameter at the base, 0.5 mm at the tip. SCRATCHbot whiskers are identical in shape and size to those on the XY positioning robot, but are made from the fiberglass material ( $E \approx 25$  GPa,  $\zeta \approx 0.5$ ). CrunchBot whiskers were made from Nanocure RC25 ( $E \approx 4.89$  GPa,  $\zeta \approx 0.2$ ) and were smaller in size, 160 mm in length, 1.45 mm diameter at the base tapering linearly to 0.3 mm at the tip. All whiskers are straight, but may curve slightly due to gravity perpendicular to the plane of movement, and are linearly tapered. Each whisker was mounted at the

base into a short, polyurethane rubber (Poly 74-20 RTV from Polytec, synergym.co.il) filled, inflexible tube called a follicle case (see **Figure 3**).

A magnet was bonded to the base of the whisker shaft in such a way that when the follicle case/whisker shaft assembly was located into the whisker mount (see **Figure 3**), the magnet was positioned directly above a tri-axis Hall effect sensor integrated circuit (IC, Melexis MLX90333 [www.melexis.com](http://www.melexis.com)). Hall effect sensors measure the change in voltage across a conductor in response to changes in the strength of a nearby magnetic field. The tri-axis Hall effect sensor used here can measure the voltage changes in three orthogonal axes, i.e.,  $x$  and  $y$  across the plane of the sensor, and  $z$  upwards toward the whisker. As forces are applied to the whisker shaft, the moment experienced at the base will rotate the magnet around a pivot point, nominally in the center of the polyurethane bearing. The sensor output voltage provides information about the magnitude of whisker deflection whether the whisker is moving or not, therefore the information is useful for static as well as dynamic classification approaches. When the whisker is deflected the movement of the magnet is proportional to whisker bending.

## 2.3. DATA COLLECTION

### 2.3.1. XY positioning robot data collection

Deflections of the whisker were transmitted through the Hall effect sensors to a LabJack UE9 USB data acquisition card (labjack.com) at a rate of 1 kHz for each of the  $x$  and  $y$  directions. Each trial lasted 4 s. This data was sent to a computer through the BRAHMS middleware (brahms.sourceforge.net) for analysis in MATLAB.

A MI control policy (observed in rats and discussed in Section 1.1) was implemented. In contrast to passive deflections, this policy keeps the amplitude and duration of whisker deflection within a limited range, and also keeps whisker ringing after contact to a minimum. An additional benefit is that the forces acting

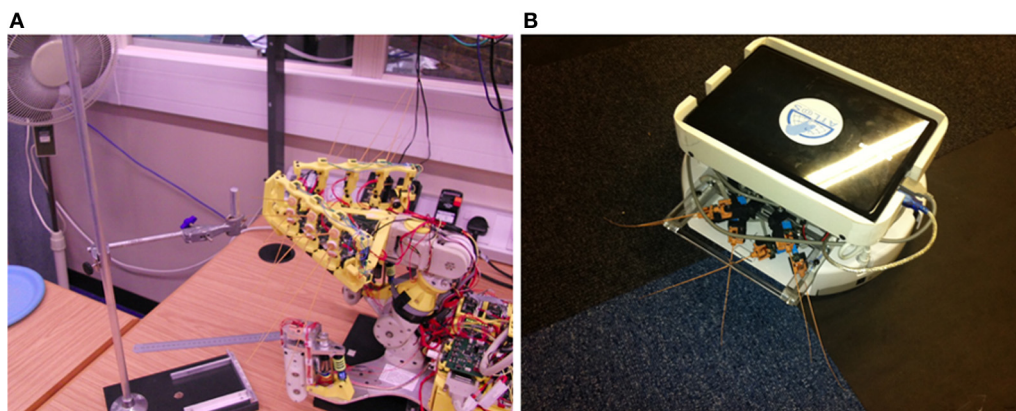


**FIGURE 2 | (A)** The SCRATCHbot whiskered mobile robot. To collect data for this experiment the robot platform was kept stationary while it whisked into a pole at varying radial distances to contact, and whisk speed. **(B)** The CrunchBot mobile whiskered robot.

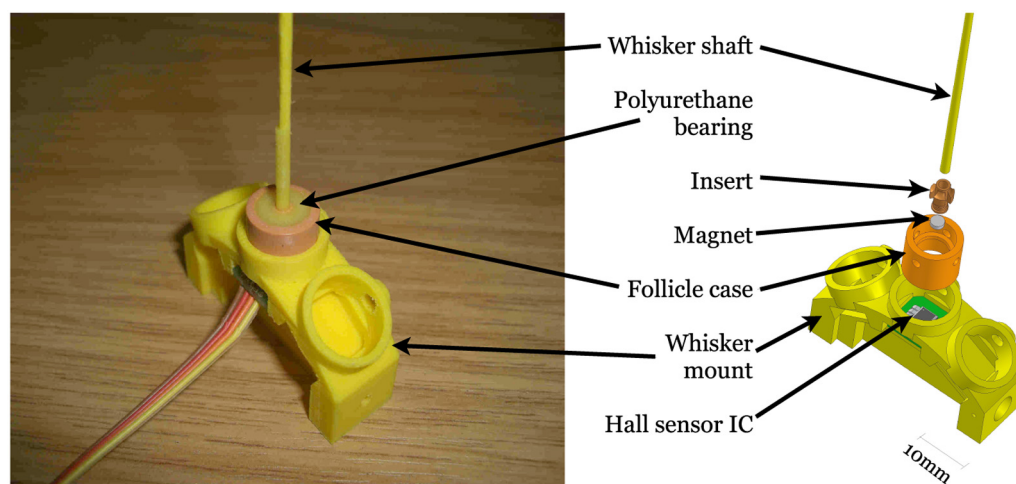


**FIGURE 3 | Diagram of whisker follicle sensor construction.** CrunchBot whisker follicles differ slightly in shape, but operate in exactly the same way.

on the whisker are much smaller, meaning whisker breakage is less likely, even in high speed collisions.

MI was implemented by instructing the robot to move an object (here a narrow, rigid, cylindrical bar) into the whisker at a given speed until a deflection magnitude threshold ( $0.05\text{ V}$ ) is crossed, at which point the robot retracts the object as fast as possible ( $720\text{ mm/s}$ ). Temporal latency for the loop is  $\approx 300\text{ ms}$  from initial contact due to the controller duty cycle.

Preliminary investigations showed that contacts could be made over a radial distance range of  $80\text{--}180\text{ mm}$  without saturating the Hall effect sensor, or the bar slipping past the whisker tip before a retraction. Object speed ranged from  $36\text{--}216\text{ mm/s}$ . Contacts were sampled at radial distance intervals of  $1\text{ mm}$ , and speed intervals of  $\approx 7\text{ mm/s}$  over the previously described ranges, respectively. In total 101 radial distances and 26 speeds were sampled, giving 2626 different radial distance and speed combinations. Contact combinations were randomly interleaved during data collection to limit any order effects, such as changing

whisker properties across trials. For each contact combination, the whisker was deflected by the robot in both a clockwise and anticlockwise directions ( $-ve$  and  $+ve$  in  $x$ , see **Figure 1**), ensuring that the whisker did not undergo plastic deformations. The experiment was performed twice (two runs of clockwise and anticlockwise, generating four separate sets in total) to generate sufficient data for training the classifier. Data from each trial was stored separately. Deflections from the clockwise robot movement trials ( $-ve$  in  $x$ ) were multiplied by  $-1$ , so data from all trials were directly comparable. Trials were ordered into arrays by speed and radial distance to contact. Each trial was aligned to peak deflection, and cut down to only  $325\text{ ms}$  either side of the peak deflection.

### 2.3.2. SCRATCHbot data collection

A single column of whiskers from a SCRATCHbot head was used for this experiment. The upper and lower whiskers were removed, and the dorsal–ventral axis of the whisker was set

to 90° (horizontal). A vertical aluminium bar (13 mm cross-sectional diameter) was positioned at three different radial distances (70, 100, and 130 mm) at an azimuthal angle of 135° (180° = dead-ahead). The whisker was driven around the azimuthal axis (anterior–posterior) using a sinusoidal whisking pattern, with a retraction-protraction range of 60° (from 90° to 150°). The frequency of whisking was set at 2, 4, and 6 Hz, giving nine conditions in total. Eight contacts were made in each condition, four were used for training the classifier and four for testing (36 contacts for both training and testing). Data was streamed to the onboard computer through BRAHMS, and stored for later analysis. The whisker drive controller received no sensory feedback from the whisker sensor itself, only using the absolute measurement of theta to close a PID controller.

### 2.3.3. CrunchBot data collection

Data from the six whiskers was collected using an FPGA configured as a bridge to a USB 2.0 interface. Up to 28 whiskers can be connected to this FPGA bridge at one time. Using the vendor provided software driver and API (Cesys GmbH <http://www.cesys.com/en/home.html>), a user can request the data from all whiskers at minimum intervals of 500  $\mu$ s (a sample rate of 2 kHz).

A “body whisk” behavior was included in the robot program to ensure consistent contact forces and speed. As the whiskers were not actuated the whole robot must rotate in a systematic way to simulate the whisking behavior of rats. Upon initial contact with an object the robot first reverses away a short distance before rotating at 15° per second toward the object for 1 s, then rotating at 15° per second away from the object for 1 s. This allows this whiskers to move over the surface of the contact object, collecting data about the radial distance (or in other experiments the orientation and texture of the surface). After the whisk the robot reverses again to clear the object, then rotates in a random direction and moves forward again. The whisker sweep during the contact phase is similar to a sinusoidal whisk.

For the verification of radial distance estimation a square cornered object was used. The robot was set in motion on a trajectory that would ensure the corner of the object would make contact with a particular whisker at a specific radial distance. The robot would then perform the body whisk movement, and the data would be stored. A dataset was collected for each whisker, consisting of five contacts at each of six points along the whisker (10 mm intervals over a 50 mm range) from the tip of the whisker. Though the whisker is 160 mm long, only 140 mm is external to the “follicle.”

## 2.4. FEATURE-BASED RADIAL DISTANCE ESTIMATION WITH UNCERTAIN CONTACT SPEEDS

To successfully implement a feature-based classifier, appropriate features must first be found and extracted. Inspection of the whisker data showed that Hall effect sensor output voltage at peak deflection (proportional to bending moment  $M$ ) could be used as a feature for radial distance discrimination at a given speed.

Feature  $f_1$  can be defined as

$$f_1 = \max_t M(t), \quad (1)$$

where  $M(t)$  is the deflection magnitude varying with time, measured by the Hall effect sensor in volts. Note that  $t(f_1)$  is the time at  $\max_t M(t)$ .

Similarly, contact speed could be discriminated using deflection duration. Deflection duration was taken as the width of the deflection peak (prominent initial deflection in each trace of **Figure 4**). Deflection duration was measured using a threshold crossing on the sensor output. When Hall effect sensor output exceeded  $\gamma = 0.05$  V a timer was initiated ( $t_1$ ), and when Hall output subsequently fell below this threshold the timer was stopped ( $t_2$ ). Feature  $f_2$  (measured in ms) can thus be defined as,

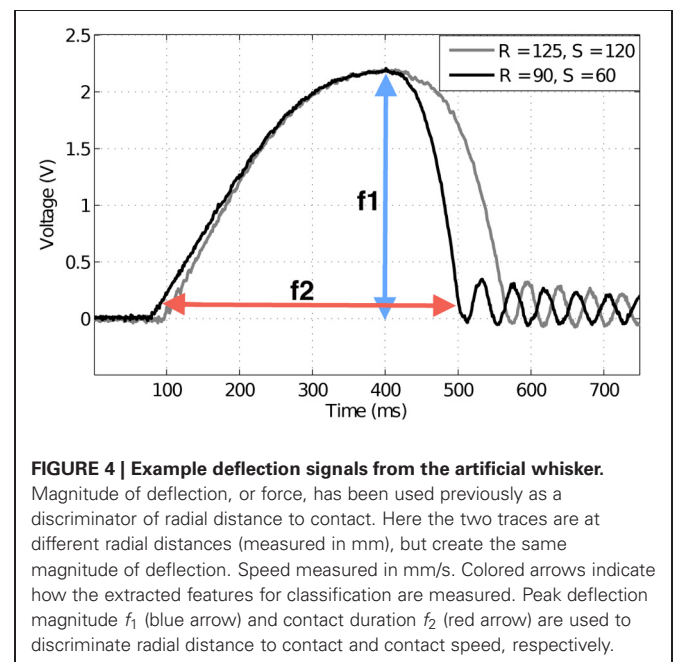
$$t_1 = \min\{t : M(t) \geq \gamma\}, \quad (2)$$

$$t_2 = \min\{t : M(t) \leq \gamma, t_2 > t_1\}, \quad (3)$$

$$f_2 = t_2 - t_1, \quad (4)$$

where  $\gamma$  is the threshold. Colored arrows in **Figure 4** give examples of these measurements.

A model was generated of the relationship between each pair of features and the corresponding contact properties with polynomial regression (using `polyfitn` in MATLAB, [bit.ly/polyfitN](http://bit.ly/polyfitN)). Using linear least squares a model is generated that can be used to classify new data. Three arguments are required for the model, an array of independent variable values, an array of dependent variable values, and a model specification, namely the degree of the polynomial. A fifth degree polynomial was chosen as preliminary studies showed it provided good results. The independent variables in this instance were features  $f_1$  and  $f_2$ . To find both radial distance and speed, two models were developed, with dependent variables of radial distance and speed, respectively.



The same polynomial regression operation was repeated on data from SCRATCHbot, though fewer summary statistics were generated as the dataset was smaller than that generated on the XY positioning robot.

On CrunchBot a linear regression was used. As robot motion is controlled, whisker contact speed variability is low between trials and a linear regression is sufficient for classification in this instance. To find an estimate of radial distance  $r$ ,

$$r = a_1 f_1 + a_0, \quad (5)$$

was fitted to the data with a linear-in-the-parameters regression on the line, giving a least-squares fit for  $(a_0, a_1)$  for each whisker. Due to the small dataset size a “leave one out” protocol was used for classifier testing of CrunchBot. Four out of five contacts at each radial distance was used to train the classifier, with the remaining contact used for testing. This process was repeated using a different test contact each time. For each robot a mean absolute error statistic is given, which is more informative than mean error alone.

### 3. RESULTS

#### 3.1. XY POSITIONING ROBOT

**Figure 5** shows histograms of classification errors for both radial distance (**A**) and speed (**B**), and a scatterplot of the errors for each sample in the test set. Mean  $\mu$  and standard deviation  $\sigma$  for radial distance and speed estimation errors was 1.2, 7.9 mm and 3.3, 25.8 mm/s, respectively. The mean absolute error was 6.2 mm and 20.4 mm/s for radial distance and speed, respectively. **Figure 6** shows mean classification error for radial distance error, with respect to true radial distance (**A**), and for contact speed, with respect to true contact speed (**B**).

**Figure 7** shows a contour plot of the extracted features  $f_1$  and  $f_2$ . While deflection magnitude is proportional to radial distance to contact for a given speed (**Figure 7A**), the precise degree of deflection is ambiguous without a separate measure of contact speed. On data generated on the XY positioning robot the

duration of contact can provide this additional measure. This figure is examined further in Section 4.

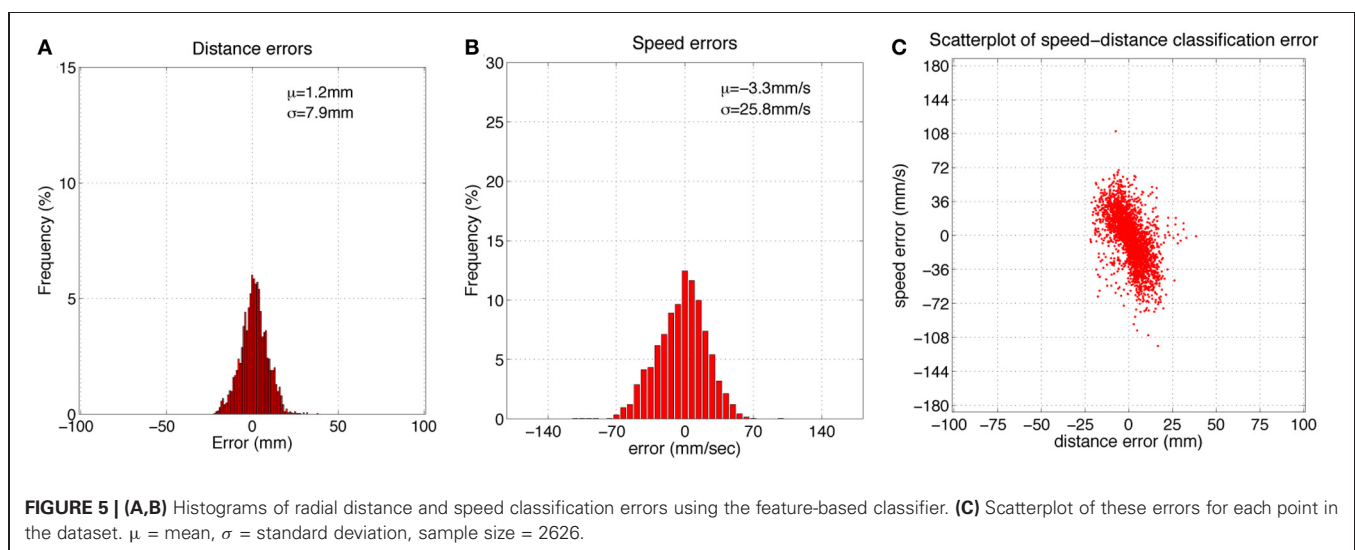
#### 3.2. SCRATCHbot

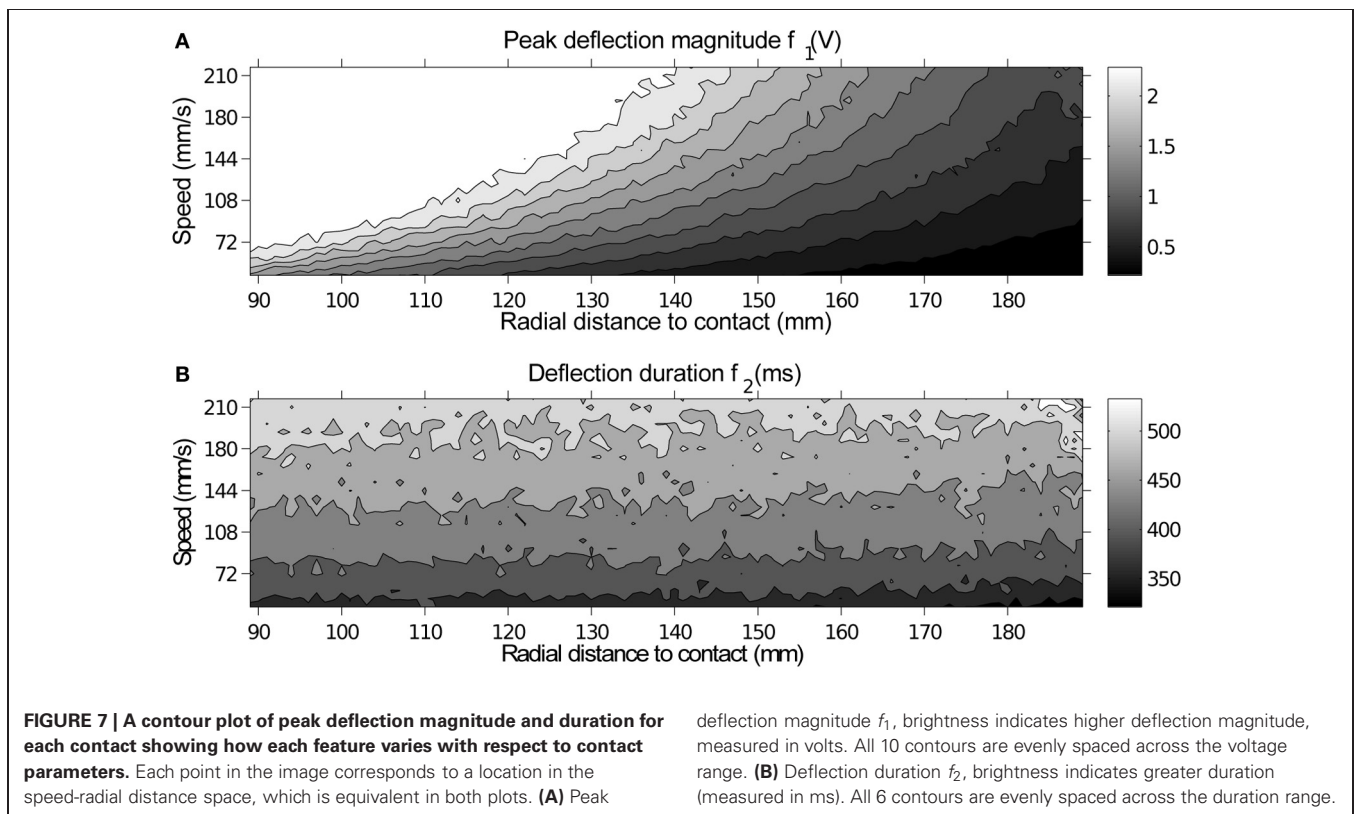
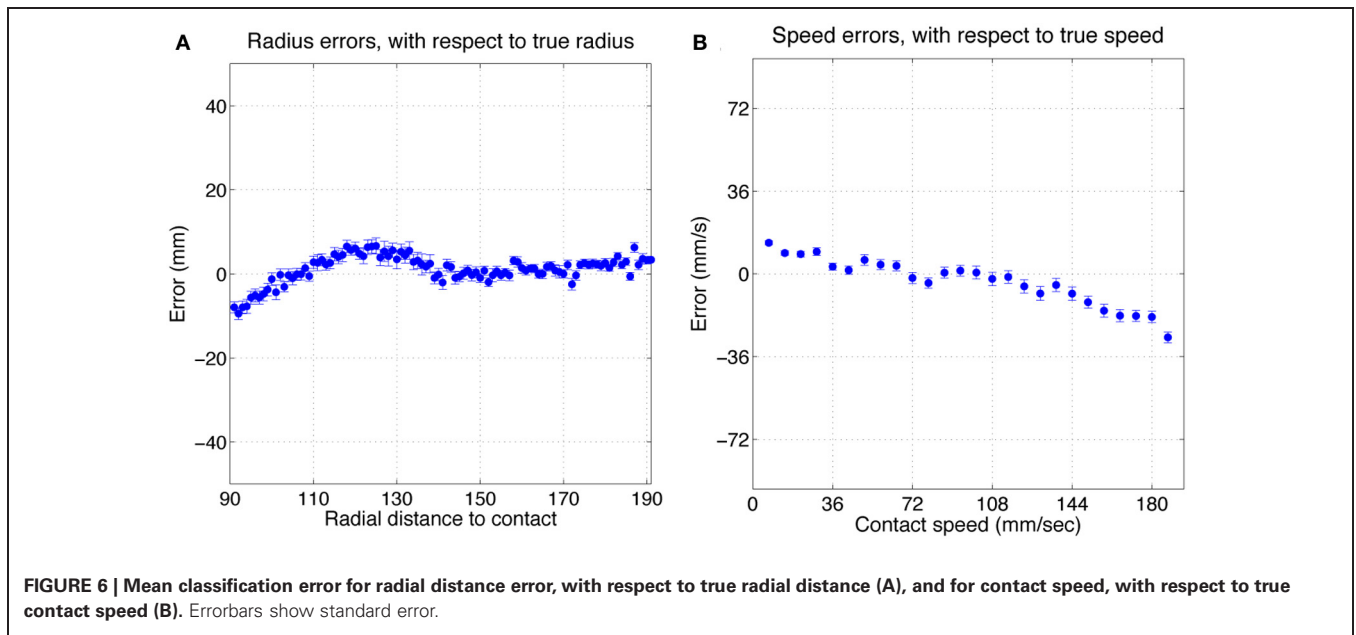
Results from SCRATCHbot show that the features and classifier developed on the XY positioning robot also apply to data collected from a whisking robot. As **Figure 8** shows, classification performance is almost perfect, with only one mis-classification of speed in the 36 contact test-dataset. **Figure 9** demonstrates that a key difference between data from SCRATCHbot and the XY positioning robot is the way whisker speed affects contact duration. Contact duration on the XY positioning robot increases as object speed increases, as object retraction is controlled by a feedback loop of a fixed duration. The faster the object moves, the further the whisker is deflected before a retraction is initiated. This increases contact duration in proportion to an increase in speed. Since SCRATCHbot is performing active whisking onto a static object, increased whisk speed results in a shorter contact duration. However, though the direction of the relationship is reversed, whisk speed still predictably affects contact duration. As in the XY positioning robot data, whisking at the same speed but different radial distances affects peak deflection magnitude (as can be seen in **Figure 9B**). Taking contact duration into account with a feature-based classifier allows accurate radial distance estimation at different whisk speeds.

#### 3.3. CRUNCHBOT

Typical whisker deflections from CrunchBot are shown in **Figure 10**. Peak deflection magnitude for each contact is shown in **Figure 11**. Mean absolute error for radial distance estimation is shown in Table below.

	Whisker 1 (mm)	Whisker 2 (mm)	Whisker 3 (mm)	Whisker 4 (mm)	Combined (mm)
$\mu$ abs. Err	4.11	1.89	1.28	3.30	2.65

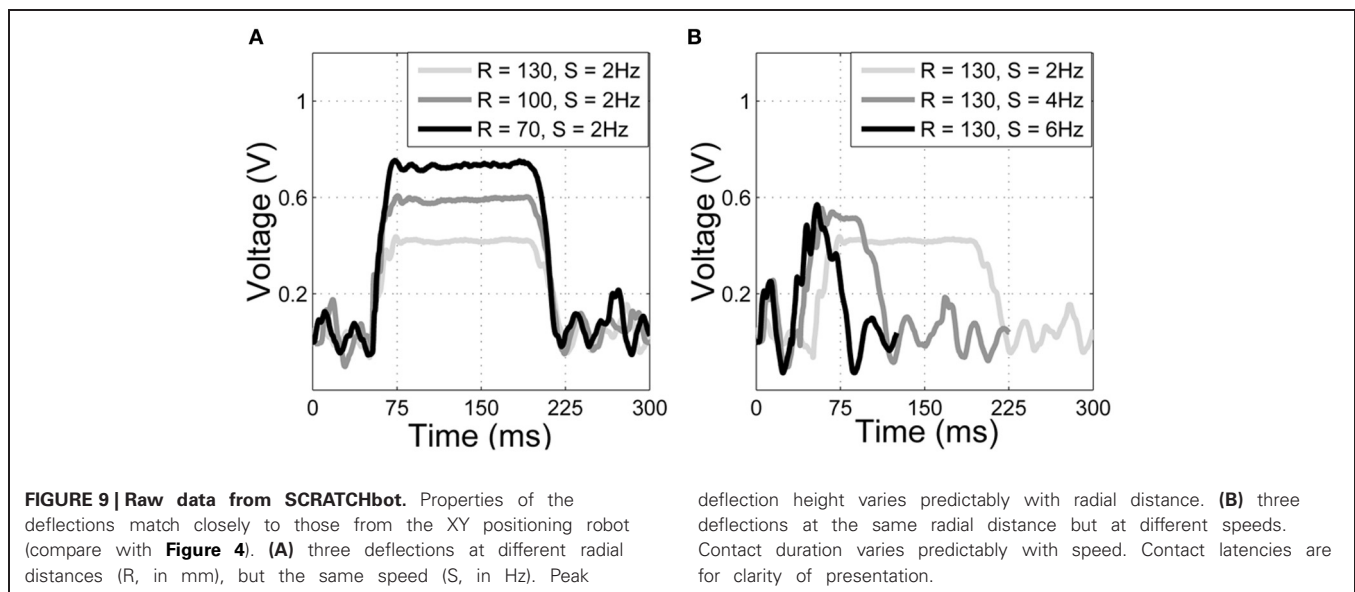
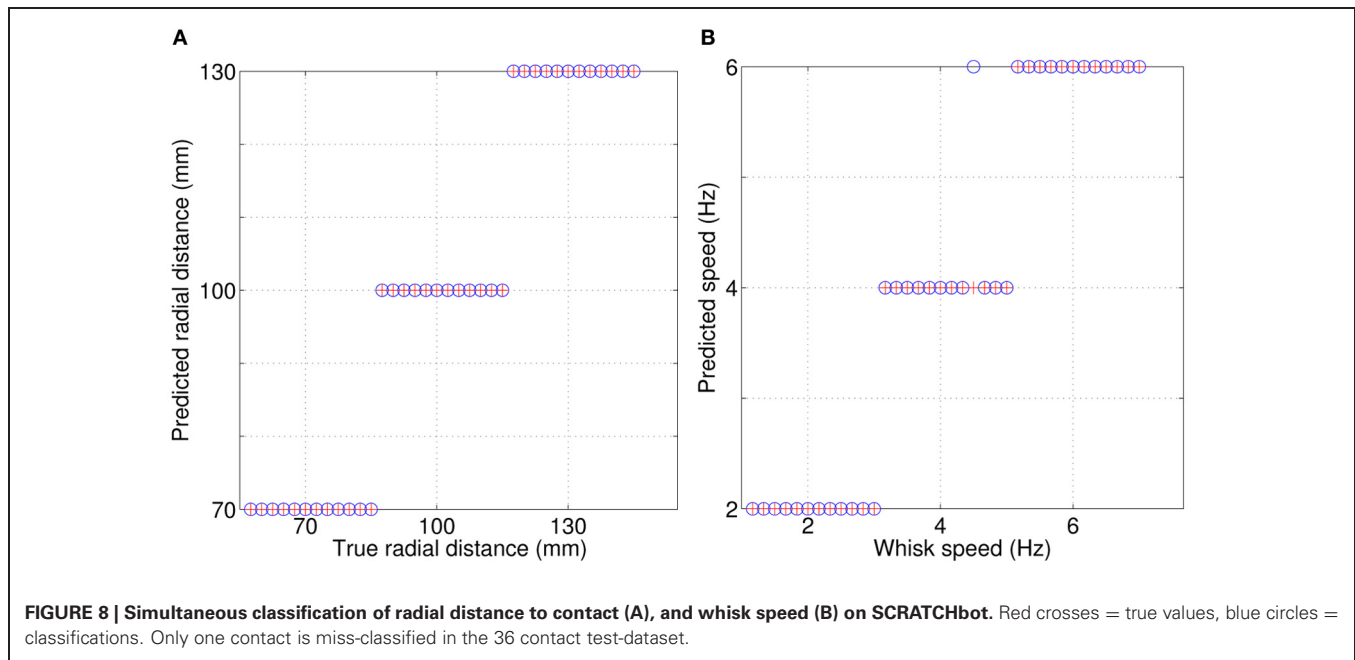




Mean absolute error is very low, typically less than 5 mm over the 50 mm range tested. For some whiskers classification error is even lower, below 2 mm. These results compare favorably with results from controlled conditions on the XY positioning robot (Section 3.1) where speed was variable. This indicates that the noise in the odometry is low enough to ensure a consistent contact force and speed on this mobile robot.

#### 4. DISCUSSION

Deflection magnitude is proportional to radial distance to contact, a relationship that is preserved across robot platforms, regardless of whisker material or actuation method. Whisker-object contact speed also affects deflection magnitude in a predictable manner on both the XY positioning robot and whisking SCRATCHbot. Controlling the whisker movement allows a very



simple linear regression-based radial distance estimation method to be successfully implemented on CrunchBot, a mobile robot.

#### 4.1. COMPARISON AND SYNTHESIS ACROSS ROBOT PLATFORMS

It may have been assumed that the relationship between whisker deflection, for a given radial distance to contact, and contact speed would be linear. However, though the relationship may be linear for a certain radial distance to contact, that linear relationship does not hold for all contact locations along the whisker. This can be seen on data from the XY positioning robot in **Figure 7**.

Inspection of **Figure 5C** reveals that classification errors on XY positioning robot data are not completely random. There is an interaction between the parameters, which can be seen as a

skewing in alignment of the errors: positive errors in radial distance estimation occur more often with negative errors in speed estimation, and vice versa. A more detailed look at these effects can be seen in **Figure 6**. This figure shows how classification errors vary across each parameter range. The systematic trends reflect the fact both speed and radial distance are classified simultaneously. Both contact speed and radial distance estimation is best (error is lowest) in the middle of each range. Large radial distances are over estimated (negative errors on the left side of **Figure 6A**) and small radial distances are underestimated (positive errors on the right side of **Figure 6A**). The opposite effect is seen for contact speed (**Figure 6B**), where large contact speeds are underestimated and low contact speeds are overestimated.

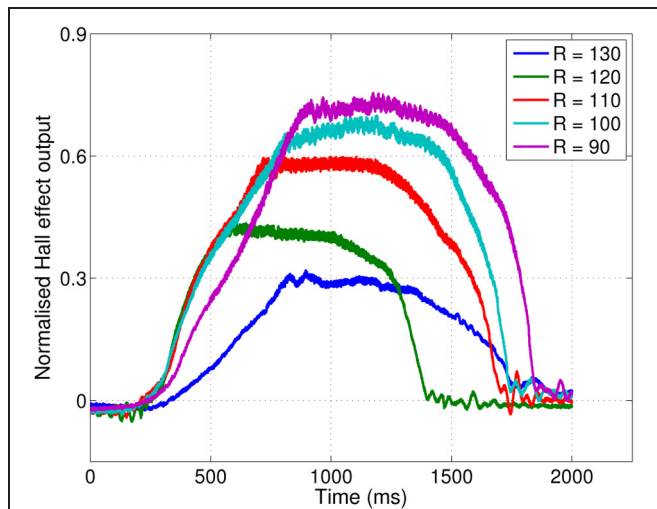


**FIGURE 10 | Radial distance to contact affects deflection magnitude on the mobile CrunchBot robot.** Five deflections at different radial distances ( $R$ , in mm), but the same speed. Peak deflection height varies predictably with radial distance.

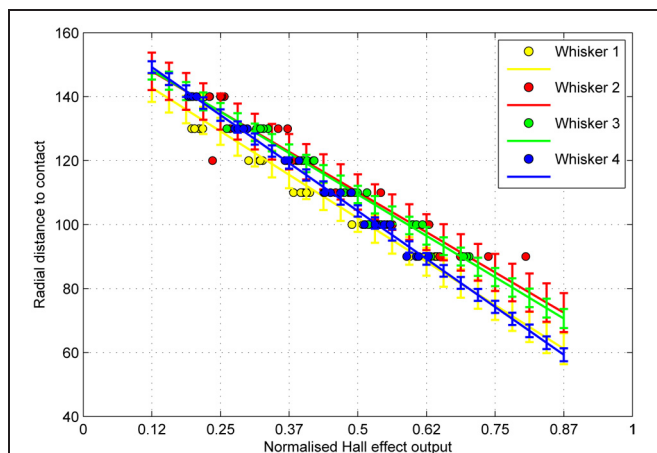


**FIGURE 11 | Radial distance to contact for a given magnitude of whisker deflection (dots), and estimates of the standard deviation of the error in predicting future observations (errorbars) for each whisker.** Sample size = 30 contacts per whisker, 120 in total. Radius measured in mm.

These effects can be explained by looking at how the extracted features change across the parameter space in **Figure 7**. A positive classification error of speed i.e., a jump from a dark to light area in **Figure 7B**, would result in a corresponding negative classification error of radial distance i.e., a jump from a dark to light area in **Figure 7A**. More transparently an increase in contact speed results in an increase in contact duration ( $f_2$ ), while an increase in radial distance to contact results in a reduction in deflection magnitude. Misclassifications as the deflection “grows” in both height and duration would result in an over-estimation of speed and an underestimation of radial distance and vice versa. A prediction of this work for biological whisker systems is that rats would

overestimate the radial distance to contact when contact speed is lower than expected, for example, as an object moves away from the rat.

All three robotic platforms presented here use different whisker materials and control strategies. These differences affect the temporal pattern of whisker deflections, which can be seen in **Figures 4, 9, and 10**. Whisker mechanical properties affect the initial rate of deflection change, and contact induced oscillations. Stiff fiberglass SCRATCHbot whiskers (**Figure 9**) result in a sharp initial increase in deflection and larger oscillations in between contacts. On the XY positioning robot and CrunchBot (**Figures 4 and 10**, respectively) robot movement speed changes throughout the contact, slowing down as peak deflection is approached, resulting in differences in gross deflection shape. While previously work has shown that whisker movement affects texture discrimination (Evans et al., 2009; Lepora et al., 2012a; Sullivan et al., 2012), our results show that such changes do not affect the key features extracted for radial distance estimation with the feature-based method presented here. Successful classification of radial distance on a particular robot platform does require the classifier to be trained on data from that robot, but the underlying principles are invariant for whisker material and robot movement. Specifically, that radial distance to contact affects the magnitude of peak deflection, and this is modulated predictably by contact speed.

#### 4.2. RELATION TO OTHER STUDIES OF RADIAL DISTANCE ESTIMATION

These are the first published results of whisker-based contact speed estimation. As rats carefully control whisker motion, and as consequence contact speed, it may not be immediately apparent why this discrimination is important. Objects in the environment sometimes move and, for example, when a shrew is hunting crickets it needs to determine both the location and movement of that prey animal to execute an accurate fatal attack (Anjum et al., 2006). Another consideration is that rats have no spindles in their whisking muscles, and therefore do not have accurate proprioception of their whiskers (Diamond et al., 2008; Mameli et al., 2010). Since accurate radial distance estimation is dependent on well characterized contact speed, a signal-based method, such as the contact duration feature approach presented here, is of potentially great importance. From a robotics perspective this kind of tactile movement tracking may be useful for other tasks, such as in tactile manipulation.

It is difficult to determine how much better or worse the feature-based approach presented here is over previous whisker-based radial distance estimation methods. These are the first results where contact speed is both variable and unknown. On data collected on the XY positioning robot we report a mean absolute discrimination error of 6.17 mm with a 185 mm whisker. This is a normalized accuracy of 3.4% of whisker length. In a real-time application on board a mobile robot we report an average mean absolute discrimination error of 2.65 mm with a 160 mm whisker. This is a normalized accuracy of 1.65% of whisker length.

With fixed contact speed and a static beam equation-based method (Solomon and Hartmann, 2010) report contact localization accuracy between 0.3 and 0.88 mm on different surfaces with a 50 mm whisker. This is a normalized accuracy of  $\approx 1\%$  of

whisker length. This approach is more accurate than the results presented in the present paper, but reported under very different conditions (contact speed was very carefully controlled, slow, and not variable across trials). Further research is required to determine whether a similar approach would be successful in a more applied mobile robot setting, or under conditions of variable contact speed.

Rats have demonstrated radial distance estimation up to an accuracy of 2.5 mm (Krupa et al., 2001), which, with a 50–60 mm whisker, is a normalized accuracy of  $\approx 4\text{--}5\%$  of whisker length. These findings indicate that the feature-based approach presented here compares favorably with the performance of rats, even in the strict conditions of single whiskers making single object contacts and variable contact speed.

The results compare less favorably with typical range finding methods in robotics, such as laser range finders, or a Microsoft Kinect camera, which are both capable of sub-millimeter accuracy over short ranges (Khoshelham, 2011). Therefore the key contribution of whisker sensors for robotics is unlikely to be contact localization for its own sake, but in a wide range of other applied settings. Firstly, whiskers are useful in environments where other localization methods are impaired, for example, in smoky and dusty environments or underwater. Secondly, whiskers are small, low powered and can be manufactured cheaply, making them ideal for implementation as arrays on mobile robots. Finally, accurate characterization of contact properties such as localization and speed are essential for subsequent surface discriminations, as previous results have shown that whisker-based texture discrimination is improved when contact location and whisker movement are taken into account (Fend, 2005; Evans et al., 2009; Fox et al., 2009). A feature-based approach, as demonstrated here, could in principle provide a texture classifier with the necessary contact localization and speed information for improved discrimination. The integration of multiple texture reports over time into a local map of an object would also be dependent on accurate contact localization. This would be an extension of the tactile SLAM work published previously (Fox et al., 2012), and an area we hope to pursue in the future.

Hall effect sensors have some advantages over other sensing methods. Hall effect sensors are robust to damage, especially when housed in a rubber filled follicle, which is an important consideration when measuring whisker deflections as they are constantly striking objects in the environment. Hall effect sensors are also relatively inexpensive, and can be made quite small which makes them ideal for application to large arrays of whiskers. It has been proposed that rats determine radial distance to contact by encoding the bending of whiskers through moments at the base (Szwed et al., 2006). The Hall effect sensor is not a direct model of the rat follicle sinus, and does not report pure moments or forces at the whisker base but a combination of these properties along with whisker rotation angle about a pivot. Using a completely hard follicle rubber would remove the angular component of the deflection, but the sensor would no longer be able to measure bending. A whisker sensor could feasibly be designed that more closely models the physical structure of the rat follicle sinus, but it would remain an approximation. The artificial whiskers presented here capture the important aspects of contact

induced deflections at both high and low frequencies, which is sufficient for understanding the abstracted principles of whisker sensing.

### 4.3. IMPLICATIONS FOR UNDERSTANDING BIOLOGICAL WHISKER SYSTEMS

Exploring active whisker movement in artificial systems highlights that active whisker control may be similar to aspects of eye movement control in active vision (Aloimonos et al., 1988). The field of active vision explores how the eyes may be moved to efficiently search an environment. The difference between active vision and active touch is in the scale of the movements with respect to the environment. In active vision the sensors can be moved to search a whole environment, for tasks such as scene identification of mapping (Davison and Murray, 2002). Active whisker touch can only be used over a very local region of the environment, therefore active whisker control may be thought of as analogous to micro-saccades for gaze stabilization (Collewyn and Kowler, 2008) or pupil diameter and lens focus, for luminance and depth of field control in the eye (Koss and Wang, 1972; Takehiko and Haruo, 1991). In vision optic flow and retinal slip can be used as an error signal for corrective eye movements for smooth pursuit (De Brouwer et al., 2001). Similarly, a measure of contact duration may be used by the rat as an error signal to correct whisker movements.

## 5. CONCLUSION

In this paper we have shown that a similar complementary approach can be successfully pursued in robotics. Certain experiments are much easier to perform on robots with fewer degrees of freedom, such as the XY positioning robot. The results from these experiments can save a great deal of time when implementing classifiers onboard mobile robots such as CrunchBot, or robots with high degrees of freedom such as SCRATCHbot. Mobile robot experiments can then generate predictions for biological systems, or drive further XY positioning robot research. This approach, and indeed these robots, could be used to answer a broad array of questions about active touch in the future.

We have shown that in each of the robots presented here, regardless of whisker material or actuation method, the radial distance to contact can be determined from peak deflection magnitude. In addition the speed of contact also predictably affects the amplitude of whisker deflection in each of these robots. By taking the speed of contact into account, radial distance estimation can be accurately performed in a range of settings. We predict that if whiskered mammals are using deflection amplitude (or degree of bending) to determine the radial distance to contact, the contact induced signal will change if the animal whisks at a different speed or force, and that this must be taken into account for accurate discriminations.

## ACKNOWLEDGMENTS

The authors would like to thank the EPSRC doctoral training scheme, a University of Sheffield/EPSRC Doctoral Prize Fellowship, and European Framework 7 Grants BIOTACT (ICT-215910), and EFAA (ICT-270490) for funding this research. The authors would also like to thank the reviewers for their constructive appraisals.

## REFERENCES

- Ahl, A. (1986). The role of vibrissae in behavior: a status review. *Vet. Res. Commun.* 10, 245–268.
- Aloimonos, J., Weiss, I., and Bandyopadhyay, A. (1988). Active vision. *Int. J. Comput. Vis.* 1, 333–356.
- Anjum, F., Turni, H., Mulder, P., van der Burg, J., and Brecht, M. (2006). Tactile guidance of prey capture in Etruscan shrews. *Proc. Natl. Acad. Sci. U.S.A.* 103, 16544–16549.
- Berg, R., and Kleinfeld, D. (2003). Rhythmic whisking by rat: retraction as well as protraction of the vibrissae is under active muscular control. *J. Neurophysiol.* 89, 104–117.
- Bermejo, R., Vyas, A., and Zeigler, H. (2002). Topography of rodent whisking—i. Two-dimensional monitoring of whisker movements. *Somatosen. Mot. Res.* 19, 341–346.
- Brecht, M., Preilowski, B., and Merzenich, M. (1997). Functional architecture of the mystacial vibrissae. *Behav. Brain Res.* 84, 81–97.
- Carvell, G., and Simons, D. (1990). Biometric analyses of vibrissal tactile discrimination in the rat. *J. Neurosci.* 10, 2638–2648.
- Chernova, O. F., and Kulikov, V. F. (2011). Structural differences between the shafts of mammalian vibrissae and hairs and their causes. *Dokl. Biol. Sci.* 438, 182–185.
- Collwijn, H., and Kowler, E. (2008). The significance of microsaccades for vision and oculomotor control. *J. Vis.* 8, 1–21.
- Davison, A., and Murray, D. (2002). Simultaneous localization and map-building using active vision. *IEEE Trans. Pattern Anal. Mach. Intell.* 24, 865–880.
- De Brouwer, S., Missal, M., and Lefevre, P. (2001). Role of retinal slip in the prediction of target motion during smooth and saccadic pursuit. *J. Neurophysiol.* 86, 550–558.
- Diamond, M., von Heimendahl, M., Knutsen, P., Kleinfeld, D., and Ahissar, E. (2008). ‘where’ and ‘what’ in the whisker sensorimotor system. *Nat. Rev. Neurosci.* 9, 601–612.
- Evans, M., Fox, C., Pearson, M., Lepora, N., and Prescott, T. (2010a). “Whisker-object contact speed affects radial distance estimation,” in *Robotics and Biomimetics (ROBIO), 2010 IEEE International Conference* (Tianjin, China), 720–725.
- Evans, M. H., Fox, C. W., Pearson, M. J., and Prescott, T. J. (2010b). “Tactile discrimination using template classifiers: towards a model of feature extraction in mammalian vibrissal systems,” in *Proceedings of the 11th International Conference on Simulation of Adaptive Behaviour (SAB). FROM ANIMALS TO ANIMATS 11. Lecture Notes in Computer Science, Vol. 6226/2010* (Paris, France), 178–187.
- Evans, M. H., Fox, C. W., Pearson, M. J., and Prescott, T. J. (2009). “Spectral template based classification of robotic whisker sensor signals in a floor texture discrimination task,” in *Proceedings of Towards Autonomous Robotic Systems (TAROS 2009)*, eds T. Kyriacou, U. Nehmzow, C. Melhuish, and M. Witkowski (Derry, Northern Ireland), 19–24.
- Evans, M., Pearson, M., Lepora, N., Prescott, T., and Fox, C. (2012). “Whiskered texture classification with uncertain contact pose geometry,” in *Intelligent Robots and Systems (IROS), 2012 IEEE/RSJ International Conference* (Vilamoura, Algarve, Portugal), 7–13.
- Fend, M. (2005). “Whisker-based texture discrimination on a mobile robot,” in *Advances in Artificial Life* (Canterbury, UK), 302–311.
- Fend, M., Bovet, S., and Hafner, V. (2005). The artificial mouse—a robot with whiskers and vision. *Signal [V]* 5, 6.
- Fend, M., Bovet, S., and Pfeifer, R. (2006). On the influence of morphology of tactile sensors for behavior and control. *Rob. Auton. Syst.* 54, 686–695.
- Fend, M., Bovet, S., Yokoi, H., and Pfeifer, R. (2003). “An active artificial whisker array for texture discrimination,” in *Proceedings of the IEEE/RSJ International Conference on Intelligent Robots and Systems IROS2003, Vol. 2* (Las Vegas, NV).
- Fox, C., Evans, M., Lepora, N., Pearson, M., Ham, A., and Prescott, T. (2011). “Crunchbot: a mobile whiskered robot platform,” in *TAROS’11 Proceedings of the 12th Annual Conference on Towards Autonomous Robotic Systems* (Sheffield, UK), 102–113.
- Fox, C., Evans, M., Pearson, M., and Prescott, T. (2012). “Tactile slam with a biomimetic whiskered robot,” in *Robotics and Automation (ICRA), 2012 IEEE International Conference* (IEEE), 4925–4930.
- Fox, C., Mitchinson, B., Pearson, M., Pipe, A., and Prescott, T. (2009). Contact type dependency of texture classification in a whiskered mobile robot. *Auton. Robots* 26, 223–239.
- Grant, R., Mitchinson, B., Fox, C., and Prescott, T. (2009). Active touch sensing in the rat: anticipatory and regulatory control of whisker movements during surface exploration. *J. Neurophysiol.* 101, 862–874.
- Hartmann, M. (2001). Active sensing capabilities of the rat whisker system. *Auton. Robots* 11, 249–254.
- Hartmann, M., Johnson, N., Towal, R., and Assad, C. (2003). Mechanical characteristics of rat vibrissae: resonant frequencies and damping in isolated whiskers and in the awake behaving animal. *J. Neurosci.* 23, 6510–6519.
- Juan, L., and Gwon, O. (2010). A comparison of SIFT, PCA-SIFT and SURF. *Int. J. Image Process.* 3, 143–152.
- Jung, D., and Zelinsky, A. (1996). “Whisker based mobile robot navigation,” in *Intelligent Robots and Systems’ 96, IROS 96, Proceedings of the 1996 IEEE/RSJ International Conference*, Vol. 2 (IEEE) (Beijing, China), 497–504.
- Kappers, C., Huber, G., and Crosby, E. (1936). The comparative anatomy of the nervous system of vertebrates including man. *J. Nerv. Ment. Dis.* 84, 709–711.
- Kardong, K. (2006). *Vertebrates: Comparative Anatomy, Function, Evolution*. Boston, MA: McGraw-Hill Higher Education.
- Khoshelham, K. (2011). “Accuracy analysis of kinect depth data,” in *ISPRS Workshop Laser Scanning, Vol. 38* (Calgary, AB), 1.
- Kim, D., and Moller, R. (2004). “A biomimetic whisker for texture discrimination and distance estimation,” in *From Animals to Animats 8, Proceedings of the International Conference on the Simulation of Adaptive Behaviour*, eds S. Schaal, A. Ijspeert, A. Billard, S. Vijayakumar, J. Hallam, and J.-A. Meyer, (MIT Press), 140–149.
- Kim, D., and Moller, R. (2007). Biomimetic whiskers for shape recognition. *Rob. Auton. Syst.* 55, 229–243.
- Koss, M., and Wang, S. (1972). Brainstem loci for sympathetic activation of the nictitating membrane and pupil in the cat. *Am. J. Physiol.* 222, 900.
- Krupa, D., Matell, M., Brisben, A., Oliveira, L., and Nicolelis, M. (2001). Behavioral properties of the trigeminal somatosensory system in rats performing whisker-dependent tactile discriminations. *J. Neurosci.* 21, 5752–5763.
- Lepora, N., Evans, M., Fox, C., Diamond, M., Gurney, K., and Prescott, T. (2010a). “Naive bayes texture classification applied to whisker data from a moving robot,” in *Neural Networks (IJCNN), The 2010 International Joint Conference* (Barcelona, Spain), 1–8.
- Lepora, N. F., Pearson, M. J., Mitchinson, B., Evans, M. H., Fox, C. W., Pipe, A. G., et al. (2010b). “Naive Bayes novelty detection for a moving robot with whiskers,” in *Robotics and Biomimetics (ROBIO), 2010 IEEE International Conference* (IEEE) (Tianjin, China), 131–136.
- Lepora, N., Fox, C., Evans, M., Diamond, M., Gurney, K., and Prescott, T. (2012a). Optimal decision-making in mammals: insights from a robot study of rodent texture discrimination. *J. R. Soc. Interface* 9, 1517–1528.
- Lepora, N., Sullivan, J., Mitchinson, B., Pearson, M., Gurney, K., and Prescott, T. (2012b). “Brain-inspired bayesian perception for biomimetic robot touch,” in *Robotics and Automation (ICRA), 2012 IEEE International Conference* (IEEE) (St. Paul, MN), 5111–5116.
- Lettvin, J., Maturana, H., McCulloch, W., and Pitts, W. (1959). What the frog’s eye tells the frog’s brain. *Proc. IRE* 47, 1940–1951.
- Lowe, D. (1999). “Object recognition from local scale-invariant features,” in *Computer Vision, 1999. The Proceedings of the Seventh IEEE International Conference*, Vol. 2 (IEEE) (Kerkyra, Greece), 1150–1157.
- Lungarella, M., Hafner, V., Pfeifer, R., and Yokoi, H. (2002). “An artificial whisker sensor for robotics,” in *Proceedings of the IEEE/RSJ International Conference on Intelligent Robots and Systems (IROS)* (Lausanne, Switzerland), 2931–2936.
- Mameli, O., Stanzani, S., Mulliri, G., Pellitteri, R., Caria, M., Russo, A., et al. (2010). Role of the trigeminal mesencephalic nucleus in rat whisker pad proprioception. *Behav. Brain Funct.* 6:69. doi: 10.1186/1744-9081-6-69.
- Meyer, J., Guillot, A., Girard, B., Khamassi, M., Pirim, P., and Berthoz, A. (2005). The psikharpax project: towards building an artificial rat. *Rob. Auton. Syst.* 50, 211–223.
- Mitchinson, B., Martin, C., Grant, R., and Prescott, T. (2007). Feedback control in active sensing: rat exploratory whisking is modulated by environmental contact. *Proc. Biol. Sci.* 274, 1035–1041.
- Mitchinson, B., Pearson, M., Pipe, A., and Prescott, T. (2010). “Biomimetic robots as scientific models: a view from the whisker tip,” in *Neuromorphic and*

- Brain-based Robots*, ed J. Krichmar (Cambridge, UK: MIT Press).
- Pearson, M., Mitchinson, B., Pipe, A., and Prescott, T. (2011). Biomimetic vibrissal sensing for robots. *Philos. Trans. R. Soc. B.* 366, 3085–3096.
- Pearson, M., Pipe, A., Melhuish, C., Mitchinson, B., and Prescott, T. (2007). Whiskerbot: a robotic active touch system modeled on the rat whisker sensory system. *Adapt. Behav.* 15, 223.
- Pearson, M. J., Mitchinson, B., Welsby, J., Pipe, A. G., and Prescott, T. J. (2010). “SCRATCHbot: active tactile sensing in a whiskered mobile robot,” in *Proceedings of the 11th International Conference on Simulation of Adaptive Behaviour (SAB). FROM ANIMALS TO ANIMATS 11. Lecture Notes in Computer Science, Vol. 6226/2010* (Paris, France), 93–103.
- Petersen, R., Brambilla, M., Bale, M., Alenda, A., Panzeri, S., Montemurro, M., et al. (2008). Diverse and temporally precise kinetic feature selectivity in the VPM thalamic nucleus. *Neuron* 60, 890–903.
- Prescott, T., Pearson, M., Mitchinson, B., Sullivan, J., and Pipe, A. (2009). Whisking with robots from rat vibrissae to biomimetic technology for active touch. *IEEE Rob. Autom. Mag.* 16, 42–50.
- Quist, B., and Hartmann, M. (2012). Mechanical signals at the base of a rat vibrissa: the effect of intrinsic vibrissa curvature and implications for tactile exploration. *J. Neurophysiol.* 107, 2298–2312.
- Rosenblueth, A., and Wiener, N. (1945). The role of models in science. *Philos. Sci.* 12, 316–321.
- Russell, R. (1992). “Using tactile whiskers to measure surface contours,” in *Proceedings of the IEEE International Conference on Robotics and Automation* (Nice, France), 2, 1295–1299.
- Russell, R., and Wijaya, J. (2003). “Object location and recognition using whisker sensors,” in *Australasian Conference on Robotics and Automation* (Citeseer), 761–768.
- Russell, R., and Wijaya, J. (2005). Recognising and manipulating objects using data from a whisker sensor array. *Robotica* 23, 653–664.
- Sachdev, R., Sato, T., and Ebner, F. (2002). Divergent movement of adjacent whiskers. *J. Neurophysiol.* 87, 1440–1448.
- Salisbury Jr., J. (1984). Interpretation of contact geometries for force measurements. *Proc. IEEE Int. Conf. Robot. Automat.* 1, 240–247.
- Sarko, D., Rice, F., and Reep, R. (2011). Mammalian tactile hair: divergence from a limited distribution. *Ann. N.Y. Acad. Sci.* 1225, 90–100.
- Schiebel, E., Busby, H., and Waldron, K. (1986). “Design of a mechanical proximity sensor,” in *Robotics and Automation Proceedings 1986 IEEE International Conference* (San Francisco, CA).
- Semba, K., and Komisaruk, B. R. (1984). Neural substrates of two different rhythmical vibrissal movements in the rat. *Neuroscience* 12, 761–774.
- Seth, A., McKinstry, J., Edelman, G., and Krichmar, J. (2004). “Texture discrimination by an autonomous mobile brain-based device with whiskers,” in *Proceedings of the IEEE International Conference on Robotics and Automation ICRA2004* (New Orleans, LA), 4925–4930.
- Solomon, J., and Hartmann, M. (2006). Biomechanics: robotic whiskers used to sense features. *Nature* 443:525. doi: 10.1038/443525a
- Solomon, J., and Hartmann, M. (2010). Extracting object contours with the sweep of a robotic whisker using torque information. *Int. J. Robot. Res.* 29, 1233–1245.
- Solomon, J., and Hartmann, M. (2011). Radial distance determination in the rat vibrissal system and the effects of weber’s law. *Philos. Trans. R. Soc. B Biol. Sci.* 366, 3049–3057.
- Sullivan, J., Mitchinson, B., Pearson, M., Evans, M., Lepora, N., Fox, C., et al. (2012). Tactile discrimination using active whisker sensors. *IEEE Sens. J.* 12, 350–362.
- Szwed, M., Bagdasarian, K., Blumenfeld, B., Barak, O., Derdikman, D., and Ahissar, E. (2006). Responses of trigeminal ganglion neurons to the radial distance of contact during active vibrissal touch. *J. Neurophysiol.* 95, 791–802.
- Takehiko, B., and Haruo, T. (1991). Cerebral cortical and brainstem areas related to the central control of lens accommodation in cat and monkey. *Comp. Biochem. Physiol. C* 98, 229–237.
- Towal, R., and Hartmann, M. (2006). Right-left asymmetries in the whisking behavior of rats anticipate head movements. *J. Neurosci.* 26, 8838–8846.
- Towal, R. B., and Hartmann, M. J. Z. (2008). Variability in velocity profiles during free-air whisking behavior of unrestrained rats. *J. Neurophysiol.* 100, 740–752.
- Vincent, J., Bogatyreva, O., Bogatyrev, N., Bowyer, A., and Pahl, A. (2006). Biomimetics: its practice and theory. *J. R. Soc. Interface* 3, 471.
- Welker, W. (1964). Analysis of sniffing of the albino rat. *Behaviour* 22, 223–244.
- Williams, C., and Kramer, E. (2010). The advantages of a tapered whisker. *PLoS ONE* 5:e8806. doi: 10.1371/journal.pone.0008806
- Wilson, J., and Chen, Z. (1995). A whisker probe system for shape perception of solids. *J. Dyn. Syst. Meas. Control* 117, 104.
- Young, W., Budynas, R., and Roark, R. (2003). *Roark’s Formulas for Stress and Strain*. 7th Edn. (Beijing, China: Tsinghua University Press.).

**Conflict of Interest Statement:** The authors declare that the research was conducted in the absence of any commercial or financial relationships that could be construed as a potential conflict of interest.

Received: 19 March 2012; accepted: 10 December 2012; published online: 02 January 2013.

Citation: Evans MH, Fox CW, Lepora NF, Pearson MJ, Sullivan JC, and Prescott TJ (2013) The effect of whisker movement on radial distance estimation: a case study in comparative robotics. *Front. Neurobot.* 6:12. doi: 10.3389/fnbot.2012.00012

Copyright © 2013 Evans, Fox, Lepora, Pearson, Sullivan, and Prescott. This is an open-access article distributed under the terms of the Creative Commons Attribution License, which permits use, distribution and reproduction in other forums, provided the original authors and source are credited and subject to any copyright notices concerning any third-party graphics etc.



# The role of orienting in vibrissal touch sensing

Robyn A. Grant\*, Anna L. Sperber and Tony J. Prescott

Department of Psychology, University of Sheffield, Sheffield, UK

## Edited by:

Blythe Towal, California Institute of Technology, USA

## Reviewed by:

Michael Brecht, Humboldt University Berlin, Germany  
D. Caroline Blanchard, University of Hawaii at Manoa, USA  
Asaf Keller, University of Maryland School of Medicine, USA

## \*Correspondence:

Robyn A. Grant, Active Touch Laboratory, Department of Psychology, University of Sheffield, Western Bank, Sheffield, S10 2TN, UK.  
e-mail: r.a.grant@sheffield.ac.uk

Rodents, such as rats and mice, are strongly tactile animals who explore the environment with their long mobile facial whiskers, or macrovibrissae, and orient to explore objects further with their shorter, more densely packed, microvibrissae. Although whisker motion (whisking) has been extensively studied, less is known about how rodents orient their vibrissal system to investigate unexpected stimuli. We describe two studies that address this question. In the first we seek to characterize how adult rats orient toward unexpected macrovibrissal contacts with objects and examine the microvibrissal exploration behavior following such contacts. We show that rats orient to the nearest macrovibrissal contact on an unexpected object, progressively homing in on the nearest contact point on the object in each subsequent whisk. Following contact, rats “dab” against the object with their microvibrissae at an average rate of approximately 8 Hz, which suggests synchronization of microvibrissal dabbing with macrovibrissal motion, and an amplitude of 5 mm. In study two, we examine the role of orienting to tactile contacts in developing rat pups for maintaining aggregations (huddles). We show that young pups are able to orient to contacts with nearby conspecifics before their eyes open implying an important role for the macrovibrissae, which are present from birth, in maintaining contact with conspecifics. Overall, these data suggest that orienting to tactile cues, detected by the vibrissal system, plays a crucial role throughout the life of a rat.

**Keywords:** orienting, whisking, huddling, tactile fovea, development, active sensing, superior colliculus

## INTRODUCTION

Orienting behaviors are a generic aspect of animal sensing; for example, in vision (Land et al., 1999), hearing (Heffner, 1997), echolocation (Valentine et al., 2002), and touch (Catania and Kaas, 1997). Orienting can be defined as bringing your sensory apparatus to a point of interest. In describing orienting as an investigatory reflex, Pavlov (1927) made the following comment:

As another example of a reflex which is very much neglected we may refer to what may be called the investigatory reflex. I call it the “What-is-it?” reflex. It is this reflex which brings about the immediate response in man and animals to the slightest changes in the world around them, so that they immediately orientate their appropriate receptor organ in accordance with the perceptible quality in the agent bringing about the change, making full investigation of it.

(p. 140)

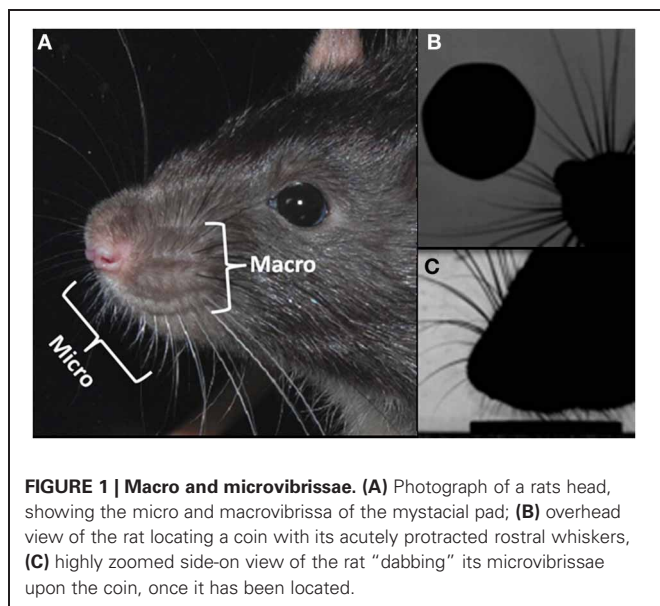
What is interesting here is that Pavlov proposes that it is not just the orient that is important, but also the subsequent exploration movements that contribute to the effective investigation of a stimulus.

Rodents, such as rats and mice, are strongly tactile animals who scan the environment with their long facial whiskers, or *macrovibrissae*, and orient to explore objects further with their shorter, and more densely packed, *microvibrissae* (Brecht et al., 1997; Hartmann, 2001; Grant et al., 2009). Rats have been found to modify their macrovibrissal movements in response to contact, in a manner that appears to regulate the force, number and

durations of whisker-surface contacts (Carvell and Simons, 1990; Mitchinson et al., 2007; Grant et al., 2009); vibrissal tactile sensing is, therefore, often seen as a paradigmatic example of an active sensing system (Prescott et al., 2011). Observations from as early as Vincent (1912) and Welker (1964) have described rats “nosing” an object, or directing their nose toward an object, but the orienting movements have yet to be fully described; hence in this article we will seek to better characterize both orienting movement to vibrissal touch, and aspects of subsequent exploration movements, in both adult and neonatal rats, in order to examine some hypotheses about the role of orienting in active vibrissal touch.

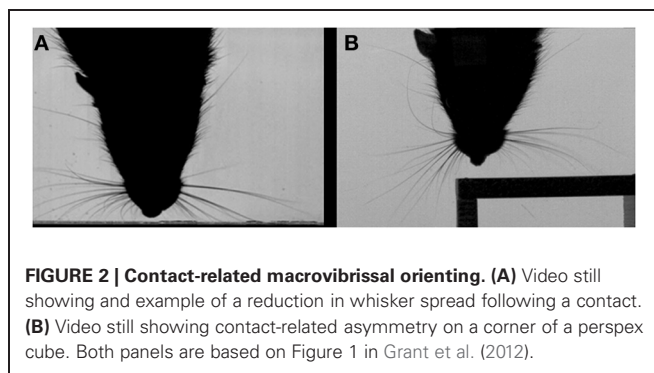
## ORIENTING IN VIBRISSAL TOUCH

Vibrissae, in rodents, are the prominent hairs positioned on the upper lip, mystacial pad, lower lip, brow, cheeks, and forelegs (Ahl, 1986). It is the mystacial vibrissae that have excited the most interest, in particular, the tapered macrovibrissae, which are independently moveable vibrissae via intrinsic musculature (**Figure 1A**). The macrovibrissae are not to be confused with the microvibrissae, which are much shorter (<7 mm) and not independently mobile (**Figure 1A**). The microvibrissae are also much more numerous—Brecht et al. (1997) counted 90–140 whiskers—and are not solely found on the mystacial pad, but also on the lower jaw and on the inside of the upper lip on the furry buccal pad (Welker, 1964; Brecht et al., 1997). When freely exploring animals contact an object with their macrovibrissae (**Figure 1B**), they tend to position the microvibrissal region on the items they are investigating (**Figure 1C**; see also Brecht et al., 1997;



Hartmann, 2001). Indeed, the macro and microvibrissae are often employed together in tasks to discriminate between different textures and shapes (Brecht et al., 1997; Hartmann, 2001), and it has been suggested that the macrovibrissae sample spatially in order to orient the microvibrissae. The average whisker density in the microvibrissae array ( $87/\text{cm}^2$ ) is considerably higher than that of the macrovibrissae ( $2/\text{cm}^2$ ; Brecht et al., 1997) consistent with this notion that the microvibrissae provide a high resolution sampling area and acting as a tactile "fovea." The position and small size of the microvibrissae have caused difficulties in studying them, and their use is, therefore, poorly characterized relative to that of the macrovibrissae. Methodological limitations may, therefore, be leading to an underemphasize, in the experimental literature, on the importance of the microvibrissae in rodent tactile sensing.

The orienting behavior that rats perform with their macrovibrissae has been proposed to conform to a "maximal contact" active sensing strategy (Mitchinson et al., 2007; Grant et al., 2009), such that following a contact, as many whiskers as possible are positioned on to the surface, so as to extract more information. Several aspects of whisker control contribute to promote the number of whisker contacts such as the reduction in whisker spread following an initial contact (Figure 2A). Mitchinson et al. (2007), found that in addition to controlling the whiskers so as to increase contact, the movements of the vibrissae may also be regulated so as to "minimize impingement"—the amount of bending of the whiskers against the contacted surface. Hence, when a rat contacts the corner of a perspex block, the macrovibrissae appear to orient with respect to the surface, according to a combined "minimal impingement/maximal contact" control strategy, such that the whiskers ipsilateral to the corner gently touch the surface, whilst those contralateral to the surface "reach round" so as to make additional contacts (Figure 2B) (Mitchinson et al., 2011). In this way the macrovibrissae almost take on the shape of the object in order to better extract certain properties from it. The macrovibrissae can also be oriented ahead of a head rotation,



which also gives rise to asymmetry of the whisker fields (Towal and Hartmann, 2006).

In the remainder of this article we describe two studies intended to improve our understanding of the role of orienting in vibrissal touch sensing. In study one, we seek to characterize how adult rats orient toward unexpected contacts on their long vibrissae. We follow Brecht et al. (1997), in assuming that rats will seek to explore a novel object with both their macro- and micro-vibrissae, and that the microvibrissae on the chin and lips can be considered to form a central foveal zone. Orienting, therefore, should consist of moving this fovea to locations of interest on detected objects, then exploring at these locations using motions that appropriately stimulate the microvibrissae. We look both at how macrovibrissal contacts are used to select the initial location for microvibrissal placement, and at how, having oriented, the animals move their short vibrissae to explore across the target surface. In study two, we examine the role of orienting to vibrissal contacts in developing rat pups for maintaining aggregations (huddles). Close contact with conspecifics is critical for the survival of young rat pups in order to maintain body temperature and gain access to food. Orienting at this age, therefore, requires successfully detecting the presence of nearby conspecifics and effectively judging in which direction to move in order to maintain or increase contact. Results of both studies provide new evidence that orienting to tactile cues, detected by the vibrissal system, plays a critical role throughout the life of a rat.

## STUDY 1: ORIENTING AND DABBING IN ADULT RATS

In this study we seek to characterize how adult rats orient toward unexpected macrovibrissal contacts with objects, we also examine the microvibrissal exploration behavior following such contacts. Data was recorded in two different settings, one to encourage orienting to a vertical block, the other to encourage exploration through palpation or "dabbing" of a horizontal surface with the microvibrissae. Henceforth these will be referred to as the "orienting" and "dabbing" data-sets.

## MATERIALS AND METHODS

### Animals

Data was collected using seven male Royal College of Surgeons (RCS) rats, aged 9–13 months and weighing 334–377 g. All animals had genetic retinal degeneration (dystrophy). These animals exhibit normal whisking behavior but also almost completely

blind and rely solely on tactile stimuli from their whiskers during testing (Hetherington et al., 2000). Hetherington et al. (2000) found that there was a tactile deficit in an RCS rat's ability to orient to a stimulus on their flank. However, they also tested their ability to orient to a stimulus in the whisker field and found no difference between RCS rats and other strains. In addition, quantification of whisker movements in our laboratory of dystrophic and non-dystrophic RCS animals and of sighted Hooded Lister rats suggest that whisking control in dystrophic animals does not deviate in any marked way from that of normally sighted rats. Therefore, although rats usually use their whiskers in the context of vision, there is no evidence that RCS rats have any deficit in tactile acuity of the whisker system, or use their whiskers in a different way. The rats were kept at 22°C in a 12-h light/dark cycle and had unrestricted access to food and water. All procedures were approved by the local Ethics Committee and UK Home Office, under the terms of the UK Animals (Scientific Procedures) Act of 1986.

### Procedures

Data collection took place in a 40 × 40 cm rectangular viewing arena with a glass floor, ceiling and front wall. It was illuminated from below by a custom-built high-power light box. Digital

high-speed video recordings were made with a Photron Fastcam PCI at 500 frames per second with a shutter speed of 0.5 ms, f-stop 22 and a resolution of 1024 × 1024 pixels. The camera was installed above the arena and thus produced an overhead view. To provide the camera with a second viewpoint, a front-silvered mirror was placed behind the glass front wall, suitably angled to offer a side-on view (as per Grant et al., 2009). Before each session the camera was positioned so that it looked straight down the front wall in the overhead view and the mirror was set at an angle of approximately 45° so that the camera looked along the floor in the side-on view. After precisely positioning the camera, a calibration tool with known dimensions was placed in the arena and recorded to serve as a reference for converting pixels to mm. One of two rectangular cuboids (*blocks*) made of transparent acrylic glass was placed in the arena and affixed to the floor with blue tack.

For recording of the orienting data-set a block with 2.0 × 2.8 × 7.65 cm edge length and a 50 mm lens were employed (as in **Figure 3**). To observe “dabbing” the block had the dimensions of 2.45 × 3.0 × 1.35 cm and a 120 mm lens was used (as in **Figure 4**). While the taller block offered a bigger area for the orienting behavior, the smaller block size provided a surface at a suitable height to encourage microvibrissal exploration.

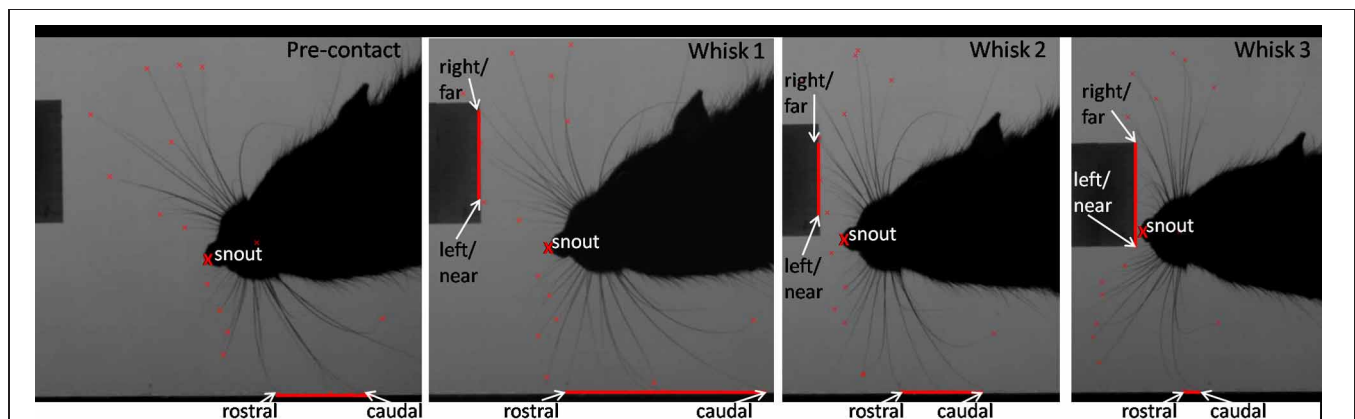


**FIGURE 3 | An example of the tracked points measured during orienting.** Example video stills from pre-contact whisk to a microvibrissal contact in whisk 3. Whisk 1: the rat has just contacted the block. Second whisk: the rat orients toward the block. Third whisk and microvibrissal contact: the nose is now touching the block. The red lines correspond to the

area of whiskers contacting the wall and perspex block. The rat moves away from the wall and toward the novel perspex block. The snout position and the positions of the whiskers on the block (right, left, near, and far), and the wall (rostral and caudal) will be to construct our measures, which we describe below.



**FIGURE 4 | Example of the tracked nose during the dabbing clips, shown in three example video-stills.**

## Recording

Data was collected in daily sessions in which each rat was individually placed in the viewing arena and allowed to freely explore its surroundings. During exploration, recordings of 1.6 s length were taken opportunistically when the rat contacted one of the perspex blocks. Only one perspex block was used in a recording session, and we alternated between the orienting block and the dabbing block on a daily basis. Generally, 12 clips were recorded for each animal per session. When a rat showed no exploratory behavior for more than 5 min, however, recording of that animal was discontinued for that session. A total of 129 clips were recorded for the orienting behavior (15–25 per animal) and 172 for the dabbing behavior (13–35 per animal).

## Data selection

Clips were selected for further analysis as follows. By manually inspecting the videos, frame by frame, the times (frames) of maximum macrovibrissal protraction were identified separately for the right and left whisker arrays this allowed each clip to be decomposed as a series of whisk cycles (“whisks”). Microvibrissal contact in both the orienting data-set and the dabbing data-set was inferred when the snout tip touched the block, which could generally be discerned in the side-on camera view.

For the orienting data-set the clips were required to have an initial whisk cycle in which there was no whisker contact with the block, termed a *pre-contact whisk*, to ensure that the first macrovibrissal contact with the block was always recorded. Each clip also had to provide a clear view of the rat making contact with the object, first with the macrovibrissae and subsequently with its microvibrissae. Eighty-four clips were discarded, most of them because the pre-contact whisk was missing (28 clips). In 18 clips there was no orientation or microvibrissae contact and in 10 clips the animal’s snout was obscured by the block in the side-on view. In total, 45 clips (2–11 per animal) in the orienting data-set match the criteria for further analysis. In these clips the initial microvibrissal contact occurred in either the 3rd or 4th whisk following the initial pre-contact whisk, therefore clips were analyzed for either 3 (12 clips) or 4 (9 clips) consecutive whisk cycles.

For the dabbing data-set the clips were required to include at least one complete episode in which the tip of the animal’s snout approached the block, made microvibrissal contact, and then withdrew—defined as a “dab.” The snout tip was required to be visible at all times. One Hundred clips were rejected, due to the snout being obscured (59 clips) or the rat showing no dabbing behavior (18 clips), this left a total of 72 (4–15 per animal) clips for further analysis in the dabbing data-set.

## Data analysis

Selected clips were examined by eye on an LCD monitor using uncompressed video and a purpose-built whisker tracking/analysis tool (as used by Mitchinson et al., 2007; Grant et al., 2009). In each clip, for both the orienting and dabbing data-sets, the corners of the block were identified in both the overhead and the side-on view to provide accurate information about the block’s position.

## Analysis of the orienting data-set

Each clip can be decomposed into a sequence of whisks. We refer to the  $i$ th whisk in the sequence where  $i \in \{0, 1, 2, 3, 4\}$  whisk 0 is

the pre-contact whisk and the snout contacts the block in either whisk 3 or whisk 4. We focus on the frames in which the whiskers are identified to be at maximum protraction, an example of which is shown in **Figure 3**. The vector position of the snout tip ( $s$ ) and of the locations of key whisker-object contact locations are determined by visual inspection and marked as shown in the example frames (**Figure 3**). For each sequence these locations are then used to define the following measures:

$s_{Final}$ : The position of the snout tip in the  $i$ th whisk and in the *final* whisk, the latter defines the point of microvibrissal contact.

$p_i^{bk}, p_i^{wk}$ : A point  $k$  on the block ( $b$ ) or wall ( $w$ ) identified in an image frame corresponding to the  $i$ th whisk.

$p_i^{bLeft}, p_i^{bRight}, p_i^{bNear}, p_i^{bFar}, p_i^{wRost}, p_i^{wCaud}$ : Respectively, the positions of the left-most and right-most macrovibrissal contacts points on the block, the nearest and furthest macrovibrissal block contact points, and the most rostral and most caudal contact points on the wall; all as determined by visual inspection of the relevant frames for whisk  $i$ . Note that, since the block is to the right of the wall, the leftmost and nearest contacts points are often the same, and the rightmost and furthest contact points are often the same.

$p_i^{bMid}, p_i^{wMid}$ : The mid-point of contacts with the block ( $b$ ) or wall ( $w$ ) calculated as the vector average of the left-most and right-most contacts points on the block and of the most rostral and most caudal contact points on the wall, i.e.,  $p_i^{bMid} = \frac{1}{2} \sum_k (p_i^{bLeft} + p_i^{bRight})$ ,  $p_i^{wMid} = \frac{1}{2} (p_i^{wRost} + p_i^{wCaud})$ .

$d_i^{bk}, d_i^{wk}$ : The distance from the snout tip to a given point on the block or wall, e.g.,  $d_i^{bNear} = \|s_i - c_i^{bNear}\|$ ,  $d_i^{wMid} = \|s_i - c_i^{wMid}\|$ .

$d_{ij}^{bk}$ : We wish to be able to compare the snout position in whisk  $i$ , with whisker contact position in a previous whisk cycle  $j$ , we, therefore, define  $d_{ij}^{bk} = \|s_i - c_j^{bk}\|$ . For instance  $d_{32}^{bNear} = \|s_3 - c_2^{bNear}\|$  is the distance from the snout position in whisk 3 to the nearest macrovibrissal contact position on the block in the preceding whisk 2.

To examine whether animals orient away from the wall and toward the block we perform repeated measures ANOVA for the measures  $d_i^{bMid}$  and  $d_i^{wMid}$  for  $i = 1, \dots, 4$ . To examine whether the rat orients toward the nearest, furthest, or intermediate point of contact on the block, and to the position detected in the initial contact (whisk 1) or in the most recent contact (whisk  $i - 1$ ) we looked at values of  $d_{i1}^{bk}$  for the positions *near*, *far*, and *mid*, and  $d_{i(i-1)}^{bk}$  for  $l = 1, \dots, 3$ . We also performed a regression of the  $y$ -coordinate of the final microvibrissal contact position  $s_{Final}$  with the  $y$ -coordinate of  $p_1^{bNear}, p_1^{bFar}, p_1^{bMid}, p_{(Final-1)}^{bNear}, p_{(Final-2)}^{bNear}$ . All data was checked to ensure normal distributions (Kolmogorov–Smirnov Test) and equal variances (Levene’s Test) before running the ANOVA and regression analyses.

## Analysis of the dabbing data-set

The tip of the snout was tracked in every fourth frame in both the side-on view (**Figure 4**) and the side-on view, with intervening values computed by interpolation. The change in  $y$  co-ordinate

of the snout position over time was then used to detect the “dabbing” motion for which measures of dab amplitude and frequency were calculated as follows.

Dab frequency was estimated using an autocorrelogram of the tracked vertical position. Specifically, the time series was smoothed using a zero-phase low-pass filter (boxcar) with a cut-off frequency of 16 Hz, which is well above the highest expected dab frequency from looking at the footage, this removes the high-frequency information. The first peak (maximum) in the autocorrelation of this smoothed time series was then identified automatically to give a first estimate of signal period. This estimate was then refined by gradient ascent on the unsmoothed autocorrelation series to locate the nearest peak to that found automatically in the smoothed.

To estimate the dab amplitude we first removed the mean value from the vertical nose position time series then computed the root mean square value to give the root-mean-square (RMS) dabbing amplitude. These time series were approximately sinusoidal, so we were able to estimate the “peak-to-peak dab amplitude” by multiplying the RMS dabbing amplitude by  $2\sqrt{2}$  (Chatfield, 2003). This estimate of amplitude is reasonably robust to departures from a purely sinusoidal pattern.

## RESULTS

### Rats orient toward unexpected object contacts

As show in **Figure 5**, when animals make an unexpected contact with an object, they will orient toward that object over successive whisk cycles (repeated measures ANOVA for  $d_i^{bMid}$  and  $i = 1, \dots, 4$ : [ $F_{(3, 33)} = 54.8, p = 0 < 0.001$ ], *post-hoc* tests:  $d_1^{bMid} > d_2^{bMid} > d_3^{bMid} > d_4^{bMid}$ ). At the same time they also gradually move away from the wall that was previously being followed (repeated measures ANOVA for  $d_i^{wMid}$  and  $i = 1, \dots, 4$ : [ $F_{(2, 18)} = 0.91, p = 0.010$ ], *post-hoc* tests:  $d_1^{wMid}, d_2^{wMid}, d_3^{wMid} < d_4^{wMid}$ ). This occurs even when the rat is contacting the wall and the block with whiskers on the same side of the face.

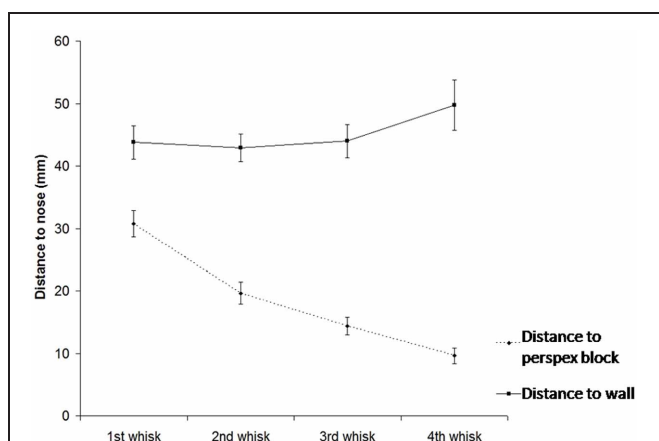


**FIGURE 5 | Position of the snout (S) relative to the mid-point of contacts wall and with the block (as detected by the macrovibrissae) over subsequent whisks.** The graph shows that animals toward the block over time indicating orienting toward the unexpected object, gradually moving away from the wall as they do so.

### Rats orient toward the closest whisker-object contact position

**Figure 6** shows that animals tend to orient toward the nearest initial whisker-object contact position rather than the furthest initial contact point or the mid-point of the initial contacts. An example of orienting was given in **Figure 3** which shows the whiskers positioned at maximum protraction for a sequence of four whisks, with initial macrovibrissal contact shown in the second frame, and microvibrissal (snout) contact in the final frame. Across the series the animal can be seen to move away from the wall and toward the nearest whisker contacts.

**Figure 7** and regression analyses (see **Table 1**) indicate that the animal may progressively home in on the position of the nearest macrovibrissal contact in preceding whisks. This result should be taken with some caution, however, since the most recent contact could be a better predictor simply because it is more proximal in time. Confirmation that the trajectory was been updated/corrected on a per-whisk basis could be found if the head position could be observed to fluctuate on the same time-scale as the whisk cycles. Informal observations of the whisker and head movements in all the 59 tracked orient examples did not identify any clear examples of such correctional movements. However, even in the absence of such evidence, per-whisk corrections could be taking place, these might either be too small to be apparent or may be obscured by some smoothing process that affects the orienting behavior.

### Dabbing occurs at a behaviorally relevant frequency

If head movements during an orient are relatively smooth, once the microvibrissae touch the block, head movements become very different. In the case of contact with a horizontal surface, the head moves up and down in a rhythmic movement referred to as palpating or dabbing. As shown in **Figure 8** the analysis of our dabbing data-set found that these movements occur at around 8 Hz ( $7.8 \pm 3.3$  Hz) and at amplitudes of around 5 mm

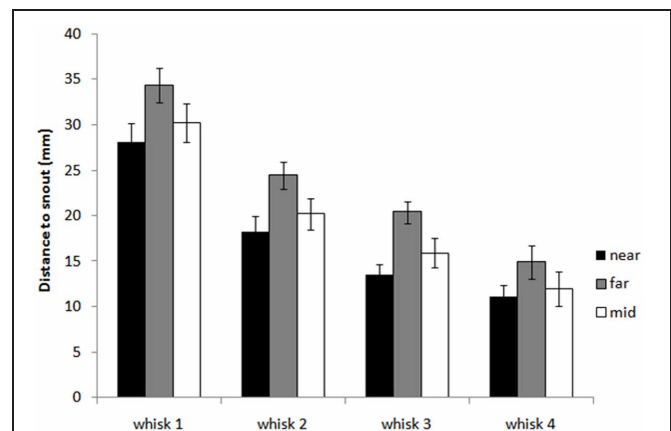


**FIGURE 6 | Distance from the snout tip in each whisk cycle to the nearest, furthest, and mid-point of block contacts in the initial contact whisk.** The graph shows histograms of the distances  $d_{i1}^{bNear}$ ,  $d_{i1}^{bFar}$  and  $d_{i1}^{bMid}$  for whisks  $i = 1, \dots, 4$ , averaged for X clips. The plot shows that as the animal orients toward the block, in whisks 2, 3, and 4, it moves toward the nearest initial point of contact rather than the furthest point or an intermediate point.

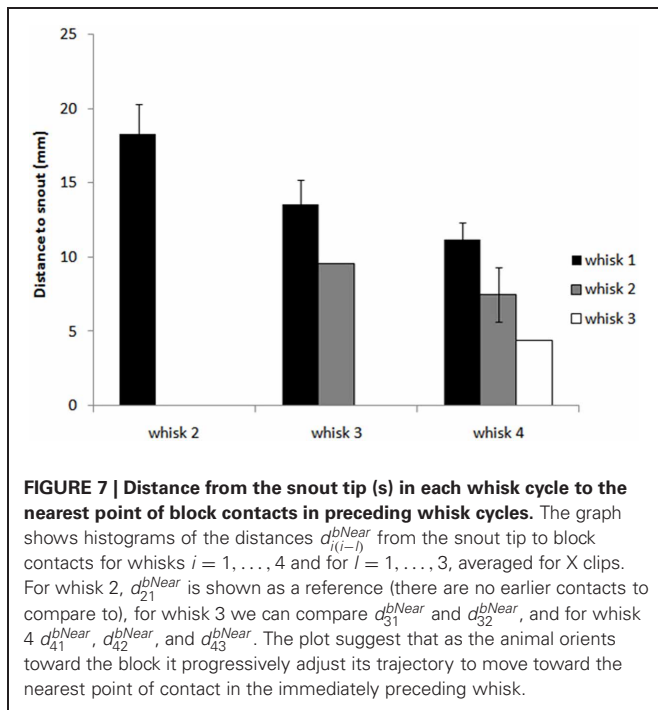


**Table 1 | Regression analyses for the  $y$ -coordinate of the microvibrissal contact position ( $s_{Final}$ ) with the  $y$ -coordinate of vibrissal contact positions in the first and subsequent contact whiskers.**

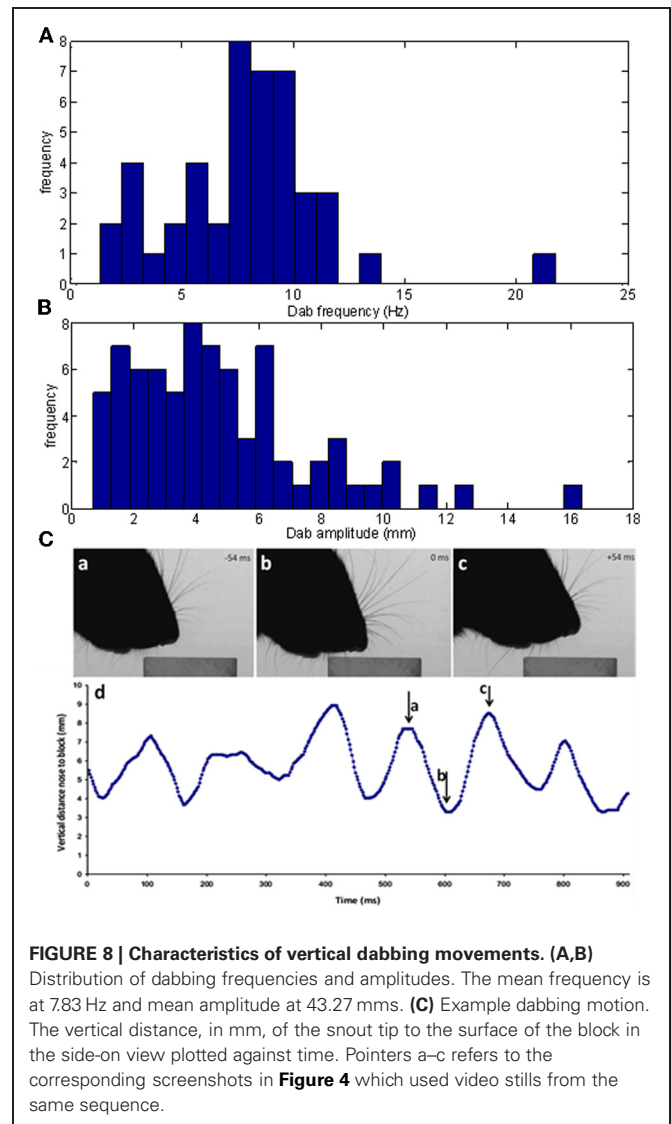
	$p_1^{bNear}$	$p_1^{bFar}$	$p_1^{bMid}$	$p_{(Final-2)}^{bNear}$	$p_{(Final-1)}^{bNear}$
$R^2$	0.758	0.522	0.673	0.886	0.901

A linear regression model of the  $y$ -coordinate of the final microvibrissal contact position  $s_{Final}$  with the  $y$ -coordinate of  $p_1^{bNear}$ ,  $p_1^{bFar}$ ,  $p_1^{bMid}$ ,  $p_{(Final-1)}^{bNear}$ ,  $p_{(Final-2)}^{bNear}$  shows that the microvibrissal contact may occur toward the closest whisker contact of preceding whiskers and the best predictors are the contact points nearest to the snout tip.

( $4.7 \pm 3.1$ ). Dabbing is thus on a behaviorally relevant timescale compared to the movements of the macrovibrissae which likewise occurs at a frequency of around 8 Hz (Mitchinson et al., 2011).

For example, **Figure 8C** shows the vertical position of the snout tip throughout an example video clip; panels **A–C** show example video stills corresponding to the arrows on the graph. We can see here that the snout tip is moving in a rhythmic manner. The video stills show that when the snout tip is away from the block (panels **A** and **C**), the macrovibrissae are retracted and lifted up, but when the head is brought down to palpate the block, the macrovibrissae are protracted and moved downwards to also touch the block. Between dabs the microvibrissae do not always lose contact with the object but rather may be moved along the surface (**Figure 8C**), suggesting that dabbing does not necessarily create absolutely discrete tactile impressions.

**Figure 9** shows three further example dabbing sequences. When dabbing over a block the microvibrissae are moved across the surface, and can sample block edges (**Figure 9B**) and surfaces (**Figures 9A,C**). Informally we have observed that, following an



orient, the rat may make just the one dab or, if it appears to be interested in actively exploring the object, this is followed by a variable number of others (we have seen up to eight dabs). The number of dabs and the duration of this exploratory behavior is likely to be dependent on both the alertness and motivation of the rat, and the novelty of the stimuli, the effects of such variables could be investigated in future research.

## STUDY 2: ORIENTING IN DEVELOPMENT

In study two, we examine the role of orienting to vibrissal contacts in developing rat pups for maintaining aggregations (huddles), a behavior that is critical for effective thermoregulation in juvenile animals. Behavior was recorded in two settings. First, we filmed rat pups in their home-cage, using a normal speed camera, interacting with and orienting to conspecifics. As is typical for this type of study quantification of behavior was performed by trained observers using standardized ordinal scales (Sullivan et al., 2003; Grant et al., 2012). To further examine orienting movements in relation to contacts, we also made some high-speed video

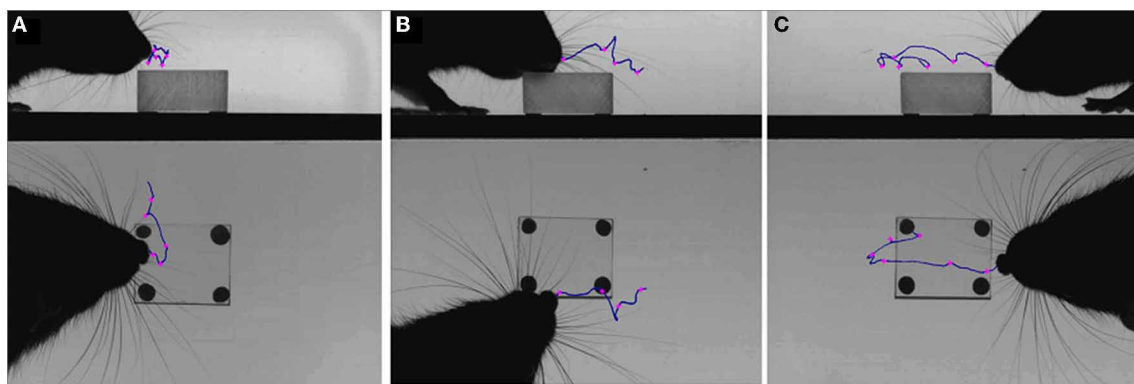


**FIGURE 9 | Dabbing trajectories and microvibrissae contacts.** High-speed video frames from three different clips (A–C) overlaid with the trajectory of the nose (blue lines) and the microvibrissae contacts (pink crosses) during a bout of dabbing.

recording of pup behavior in a setup that was intended to approximate conditions in the home-cage whilst allowing appropriate back-lighting for high-speed videography.

## MATERIALS AND METHODS

### Animals

Four litters were used in this study, two dystrophic RCS litters and two Hooded Lister litters. The RCS animals have a specific mutation that causes a gradual degeneration of the retina, with the consequence of loss of vision in the mature animal at around 17 weeks of age (Hetherington et al., 2000; McGill et al., 2004), but are normal at the ages tested here (i.e., the rats are able to see as soon as their eyes open and throughout this study). In the adult RCS rat there is no deficit in their ability to orient to a stimulus in the whisker field (Hetherington et al., 2000). Using these two strains gives us a wider distribution of litter sizes, from 6 to 11 animals, as the RCS animals tend to have smaller litters (6 and 8 pups per litter in this study) than the Hooded Listers (7 and 11 pups per litter in this study). Animals were kept in their home cage with both their parents and all their litter-mates present throughout experimentation. The pups were on a 12:12 light schedule and kept at 22°C, with water and food *ad libitum*. All procedures were approved by the local Ethics Committee and UK Home Office, under the terms of the UK Animals (Scientific Procedures) Act, 1986.

### Procedures

This study employed a form of *focal sampling*, where an individual is scored for a catalogue of behaviors over a limited time period (Altmann, 1974; Martin and Bateson, 1993). Specifically, two individual focal pups were selected at random, one male and one female—eight in total, from each litter and identified from their litter-mates with a marker pen bar on their tail. Animals were filmed between P2 and P21, every day where possible (where the animals are born on P0 and P1 is the subsequent day). The pups were filmed at 25fps using a *Casio Exilim* camera in their home cage in the lab for approximately 8 min per litter. This took place at around 9.30 a.m. each day, with the lid of the cage removed for clear viewing. Sixty-six clips were collected in this

way. 9.30 a.m. was selected as a good time of day as there were minimum disturbances to the animal houses in the morning, in addition, informal observations suggested that the animals were more active in the mornings.

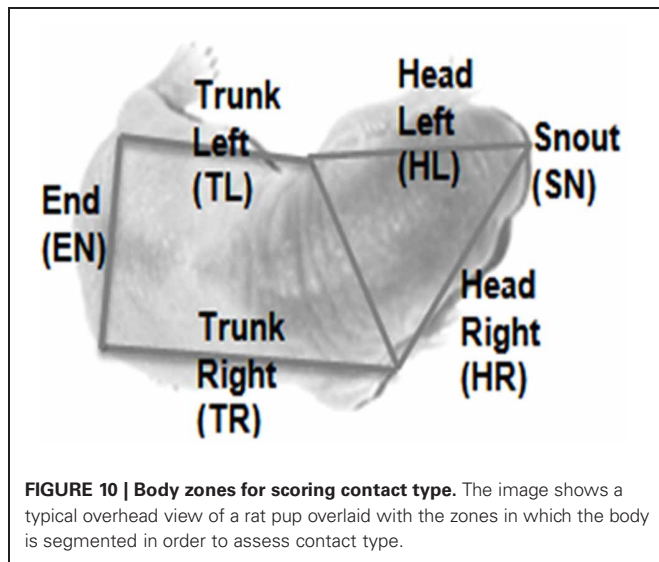
Two focal pups in each of the two RCS litters, one male and one female, were also filmed using high-speed videography at P5 and P6. Previous studies have indicated how important realistic temperatures and textures are in eliciting huddling behaviors (Campbell and Raskin, 2004). In order for the focal pup to be clearly visible in the camera view, we therefore put the rest of the litter in a soft material net, with holes of around 4 mm. This meant that the focal pup was in contact with its littermates directly through the holes and would receive tactile cues similar to those obtained in the nest. The netted huddle was placed into a glass experimental arena and the focal pup was positioned to the right of the huddle, approximately 50 mm away. The recording setup and camera were otherwise similar to that used in the high-speed videography element of study one. 1.6 s clips were recorded manually using a trigger whenever the focal pup contacted the netted huddle, an example clip can be seen in **Figure 13**. When the focal pup moved out of the field of view, it was placed back in to the starting position. Clips were collected in this way to qualitatively illustrate huddling behaviors.

### Data analysis

A 40 s sampling time (1000 frames) was selected to provide high sample numbers at a relevant time-scale for the types of behavior (orienting and huddling) we are interested as determined by reviewing pilot footage. At each 40 s interval, each of two focal pups in each litter was given a score on the following measures:

*Huddle size (H1)*: the number of animals in the focal pup's huddle or "aggregon" (a group of pups that are in contact with each other), scored between 1 and  $n$  (the total number of pups in the litter).

*Contact type (H2)*: Whereabouts on the body the focal pup it is in contact with its conspecifics, scored either 1 or 0 for six zones as shown in **Figure 10**.



*Movement direction (H3):* The direction of movement of the focal pup in the subsequent 1 s of footage, scored in one of six possible directions (including no movement).

*Huddling behavior (H4):* The type of huddling behavior engaged in for the next 15 s, scored in one of four categories for the Hooded Lister litters only. Further details of each of the ordinal scales are given in **Table 2**.

This analysis provided 10–20 data points for each scale, per day, per focal animal.

The principle analysis was to look at the effect of *Contact Type* on the subsequent movement direction of the pup; for instance, which way would the pup move if there was a contact at head-left? For this analysis, a mixed-model ANOVA was carried out with *Contact Type* on the focal pup as a within variable (SN, HL, HR, EN, TL, TR) and *Movement Direction* (none, left, right, forward)

and age (immature P2–09, transitory-adult P10–21) as between factors. All the data was checked that it was normally distributed (Kolmogorov–Smirnov Test) and had equal variances (Levene’s Test).

## RESULTS

### *Young rat pups turn toward contacts with conspecifics*

As shown in **Figure 11A**, we found that younger rat pups (P2–10) turn toward conspecifics in their huddle, more frequently than would be expected by chance. Specifically, pups that are contacted on the snout (sn) are more likely to move forward, those contacted on the left of the head (hl) to orient toward the left, and those on the right of the head (hr) toward the right. Older animals (P11–21, **Figure 11B**) showed no consistent pattern in their responses, possibly because their behavior is becoming too complex to be adequately described by an analysis of the type used here. One reason for the loss of consistency is the general reduction in huddling in older animals. Specifically, and in line with earlier studies (Schank and Alberts, 2000; Schank, 2008), we found that older animals (P18+) spend less time in huddles and were, therefore, less likely to be found in contact with conspecifics (**Figure 10C**).

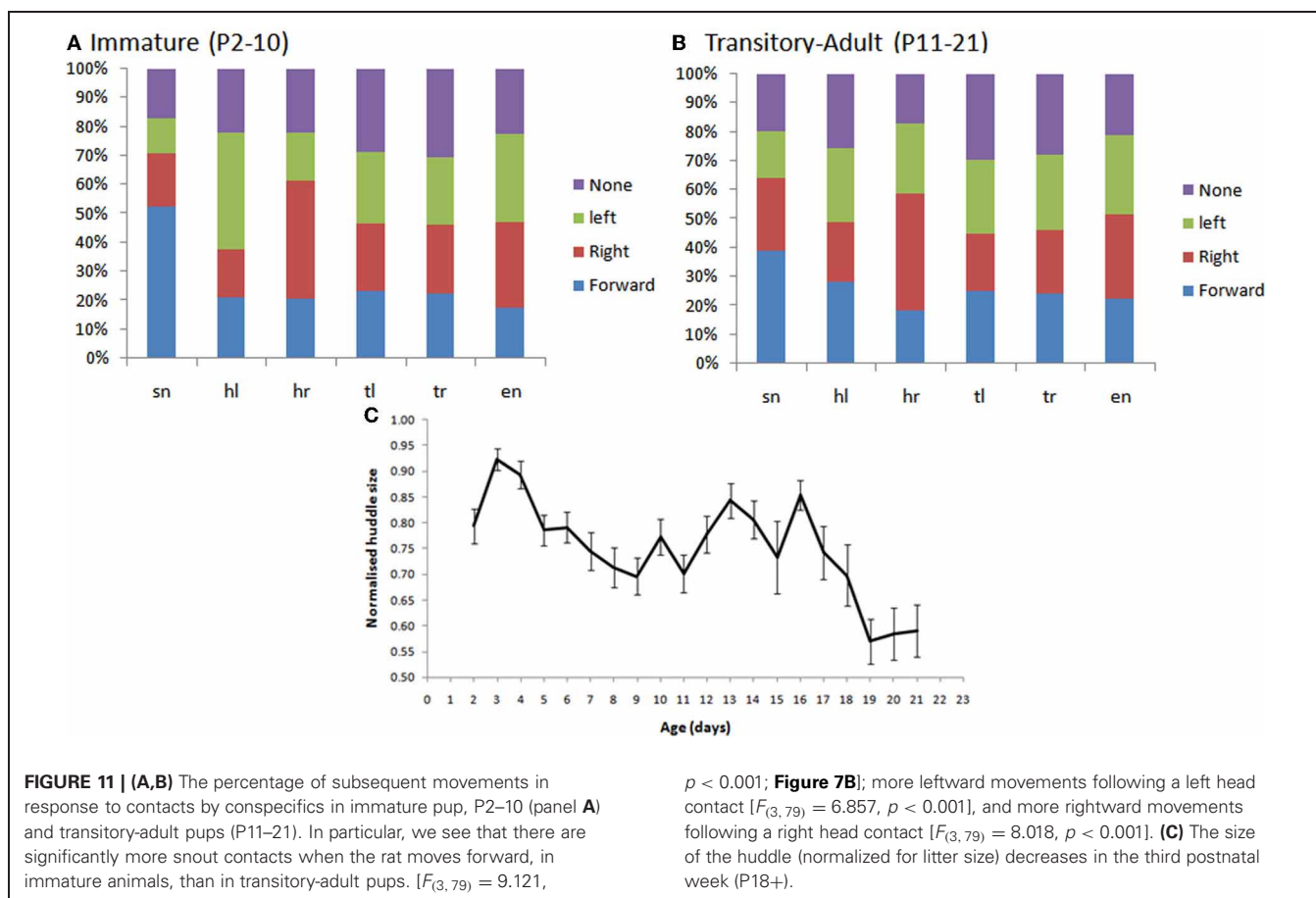
### *Rat pups dig in to the huddle, or move in and around it, from P2–10*

In a subset of animals (Hooded Lister pups) we also looked at the types of huddling behavior engaged in by animals that were in contact with conspecifics. Specifically, we observed whether the pup moved in-and-around the huddle, buried itself deeper into the huddle, or moved away from the huddle. As shown in **Figure 12A**, prior to P12, movement with respect to the huddle, where present, tended to involve moving in and around the huddle, or digging-in—burying under other animals in the huddle. At later ages, beginning from P10 pups move away from the huddle in some clips showing the beginnings of exploratory behavior. **Figure 12B**, shows that the “digging-in” behavior is more

**Table 2 | Ordinal scales for scoring orienting behavior during rat pup huddling.**

	Measure	Scored	Description
H1	Huddle size	$(1 - n)/n$	How many pups are in the aggregon (huddle) of the focal pup, normalized to litter size ( $n$ )
H2	Contact type	Score = 0 or 1 for each of SN, HR, HL, TR, TL, EN	Records where contacts are on a focal pup. Contacts could be trunk left (TL), end (EN), trunk right (TR), head left (HL), head right (HR) and snout (SN) for head contacts that were “straight on.” See <b>Figure 9</b> for an indication of how these zones are identified in the overhead camera view
H3	Movement direction	Score = 1 for one of None, Left, Right, Forward, Other	The global direction of the focal pups’ movements, in the 1 s immediately following the start of the observation period
H4	Subsequent behavior	Score = 1 for one of None, Digging, In-and-around, Away	Records the behavior that follows the contact and initial movement: no movement with respect to huddle position, digging in to the huddle, moving in and around the huddle, moving away from the huddle. Scored for the 15 s immediately following the start of the observation period for the Hooded Lister pups only

*Ordinal scales for coding locomotion and huddling, from home cage footage of neonatal rats. All measures except were developed specifically for the current study other than H1 which is taken from Schank and Alberts (1997).*



frequent when there is a snout contact (**Figure 11B**), suggesting a possible tactile trigger for this behavior.

Examples of huddling can be seen in the video stills in **Figure 13**, taken from two different filming sessions. Panels **A,B** shows P2 pups in a huddle. The focal pup (indicated by the asterisk) is being contacted by its conspecifics on its head left and head right (**Figure 13A**). The pup then begins to dig into the huddle, which can be seen by its extended rear legs (**Figure 13B**). **Figure 13C** shows a P7 pup being contacted on head right, it turns toward the contact (**Figure 13D**) and moves further into the huddle.

The home cage study demonstrates that young pups will orient toward conspecifics at an age before they eyes have opened, however, this does not confirm specifically that the trigger for the orienting movement will have been a vibrissal contact. At this age, the vibrissae are extremely fine hairs and impossible to observe in home cage video footage of this type. To confirm a role for whiskers in orienting we, therefore, examined pup orienting behavior in our high-speed video footage where we filmed pups interacting with a netted huddle of conspecifics. These recordings indicated that vibrissal contacts can serve as a trigger for orienting movements. For example, In **Figure 14**, a P6 rat pup can be seen making whisker contacts with the netted huddle on the left side of its head (0–0.19 s). It then “noses” around the huddle until the snout is positioned into a gap, and then starts to “dig” into the huddle.

## DISCUSSION

In study one, we showed that rats orient to the nearest macrovibrissal contact on an unexpected object, progressively homing in on the nearest contact point on the object in each subsequent whisk. Although it is not surprising that rats choose to move toward the nearest contact point it is at least logically possible that they might target the average position of vibrissal contacts on the object, therefore it is useful to confirm that the nearest contact point is generally preferred. Targeting the nearest point has two benefits. First the animal will be able to approach that point more quickly than any other point, second, it will expend less energy and be detoured less from its previous path in doing so, than if any other point of contact is targeted. Therefore, the strategy adopted by the animal is clearly an efficient one for rapidly approaching and finding out about novel objects.

The midbrain superior colliculus is widely considered to play a crucial role in orienting toward spatial targets (Benedetti, 1991; Hemelt and Keller, 2007; Cohen et al., 2008). That we are suggesting that the rat might be orienting to closest whisker contacts appears consistent with Cohen et al.’s (2008) findings that the colliculus responds most strongly to early contacts. In our study the closest contacts tended to occur on the more rostral whiskers, which do tend to contact surfaces before the more the caudal whiskers, which make contact with points more distal from the snout tip as they are swept forward. Benedetti (1991) found that whiskers more central to the visual field project to larger areas

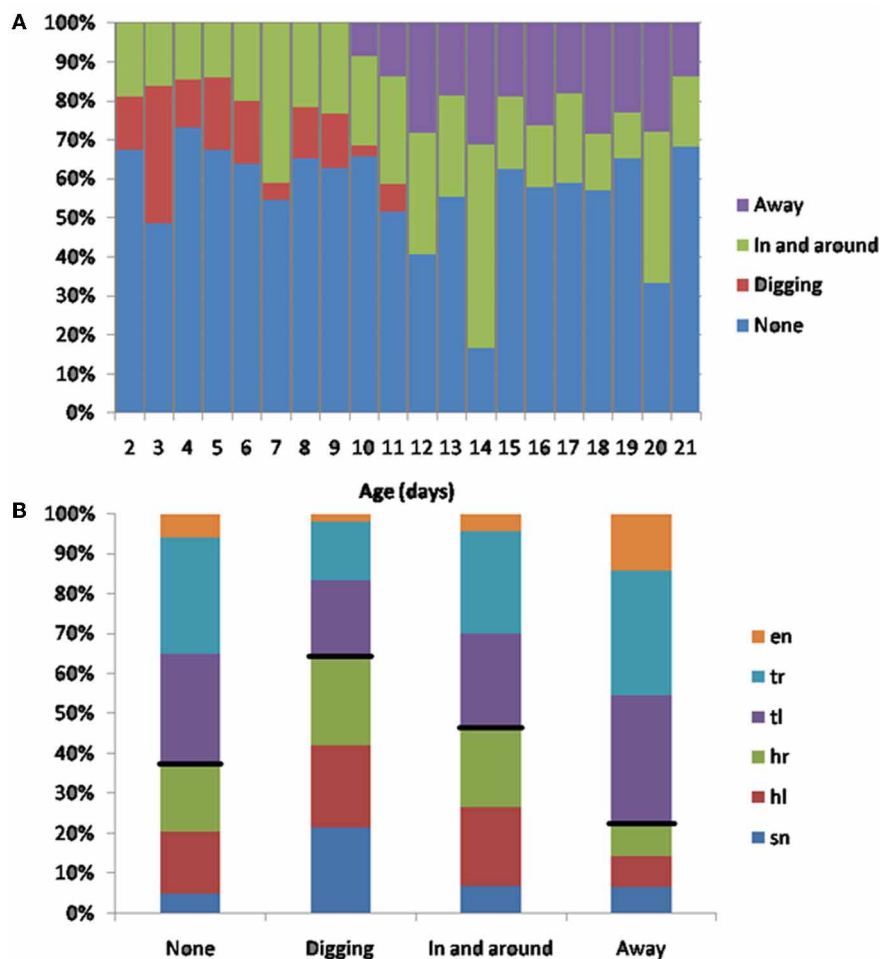


**FIGURE 12 | (A)** Subsequent behaviors following contact. Younger animals (<P12) tend to move in and out of the huddle, or to engage in digging in to the huddle. Older animals spend more time moving away from the huddle (>P10), and no time digging against each other. **(B)** The percentage of contact types for each behavior. Digging tends to occur after

more snout contacts (indicated by a larger blue bar in the digging category), moving away tends to occur after more trunk contacts (indicated by smaller blue, red and green bars in the away category). Black lines indicate the division between head and trunk contacts.

in the colliculus, again this could potentially also lead to greater preference for rostral whiskers in selecting the target for orienting movements.

Following contact, rats “dab” against the object with their microvibrissae at an average rate of  $\sim 8$  Hz which is consistent with Hartmann (2001) who showed evidence of the synchronization of microvibrissal dabbing with macrovibrissal motion. Here we have provided additional evidence concerning the amplitude of the dabbing motion which was found to be around 5 mm in our data, though very variable. Further examination of microvibrissal contact patterns would be useful to understand better how animals are using this high-resolution region of the vibrissal sensing system.

In study two, we examined the role of orienting to tactile contacts in developing rat pups for maintaining aggregations (huddles). The successful maintenance of huddling is crucial for the survival of young rat pups, so they can successfully feed and stay warm. Sullivan et al. (2003) previously showed that the loss

of vibrissae could impair effective huddling behavior. That vibrissae are already present at birth and can solicit head turning in very young animals (see also Grant et al., 2012) is further evidence that the vibrissae play an important role in maintaining contact with conspecifics. In the current study we have provided evidence consistent with the hypothesis that young pups are able to orient to contacts with nearby littermates before their eyes open. High-speed video footage confirms that contacts on the vibrissae are a likely candidate for the tactile triggers underlying this behavior. Interestingly, the superior colliculus appears to mature relatively slowly in young rat pups not reaching adult-like activity levels until the third week. The mechanisms underlying orienting in young rat pups, therefore, remain to be identified. It might be that the low numbers of unorganized somatosensory units in the colliculus are sufficient to drive these simple behaviors, alternatively brainstem systems outside the colliculus may be adequate to co-ordinate some forms of orienting. In addition, these behaviors seem to be only elicited by realistic whisker contacts, for example



**FIGURE 13 | Video stills of P2 and P7 pups in their home cage.**

(A) A P2 focal pup moves forward following contacts on its head left and head right; (B) 3.2 seconds later, the pup starts to dig in to the huddle, indicated by the extended rear limbs. (C) A P7 focal pup has

been contacted on its head right; (D) 4.3 seconds later the pup has oriented right toward the contacts and starts to move in and around the huddle. In each still the focal pup is indicated by an asterisk (\*).

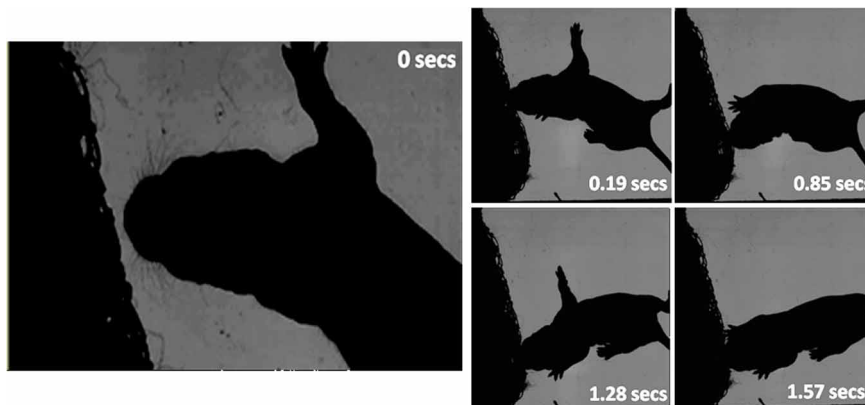


**FIGURE 14 | High-speed frames showing a P6 rat interacting with a netted huddle.** The first whisker contact is at 0 s on head left. The pup continues to move its head forward into the contact, which causes a

deeper snout contact (0.19 s). The pup “dabs” its head in to the huddle (0.85 s), positions into a gap (1.28 s) and starts to dig further into the huddle (1.57 s).

rat pups cannot orient toward whisker deflections with a wooden rod until after eye-opening (around P12; Sullivan et al., 2003). Indeed Campbell and Raskin (2004) showed that for a rat pup to show normal huddling behaviors it has to make contact with something warm, soft, and fluffy. These factors are all crucial for a young pup to successfully turn toward conspecifics and their

whiskers may play a role in identifying the tactile characteristics of conspecifics as well as locating them in nearby space.

Although the colliculus is the proposed primary candidate for mediating macrovibrissal orienting (Benedetti, 1991; Hemelt and Keller, 2007; Cohen et al., 2008), little is known about the pathways that convey information from the microvibrissae once they

have been contacted (Deschênes et al., 2012). Both the micro and macrovibrissae are represented extensively in the cortex, the macrovibrissae by the barrels, and the microvibrissae by a group of micro barrels, rostral to the barrel field (Benison et al., 2006; Deschênes et al., 2012). The high density of the microvibrissae and their large representation in the somatosensory cortex suggests that they do function as a high-resolution tactile sensor and supports Brecht et al.'s (1997) proposition that they function in object recognition tasks and feature detection. The orienting of the microvibrissae to objects, and their repeated touches, maximizes the number of whisker contacts with an object. In neonatal rats, this might be key to identifying textures and soft surfaces, so that they can huddle and thermoregulate effectively. In adults, the microvibrissae could aid in discriminating tactile cues such as

texture and shape (Brecht et al., 1997), which may be important for adult rats to identify food items, precisely locate objects such as insect prey for biting, and to navigate effectively around their environment.

## ACKNOWLEDGMENTS

The authors would like to thank Kendra Arkley and Dr. Ben Mitchinson for their help with the data and ideas for this paper. In study two, we would like to thank Dr. Ehud Forno for his suggestions and Dr. Lauren Hayes who collected some of the data. We are also extremely grateful for contributions from the animal staff, Marion Simkins and Dr. Len Hetherington, and the workshop staff, Andy Ham. Work for these studies was funded by an EPSRC DTA grant, and as part of the BIOTACT FP7 Bio-ICT project.

## REFERENCES

- Ahl, A. S. (1986). The role of vibrissae in behavior - a status review. *Vet. Res. Comm.* 10, 245–268.
- Altmann, J. (1974). Observational study of behaviour: sampling methods. *Behaviour* 49, 227–267.
- Benedetti, F. (1991). The postnatal emergence of a functional somatosensory representation in the superior colliculus of the mouse. *Dev. Brain Res.* 60, 51–57.
- Benison, A. M., Ard, T. D., Crosby, A. M., and Barth, D. S. (2006). Temporal patterns of field potentials in vibrissae/barrel cortex reveal stimulus orientation and shape. *J. Neurophysiol.* 95, 2242–2251.
- Brecht, M., Preilowski, B., and Merzenich, M. M. (1997). Functional architecture of the mystacial vibrissae. *Behav. Brain Res.* 84, 81–97.
- Campbell, B. A., and Raskin, L. A. (2004). Canalization of arousal in the preweanling rat: effects of amphetamine on aggregation with surrogate stimuli. *Dev. Psychobiol.* 14, 127–137.
- Carvell, G. E., and Simons, D. J. (1990). Biometric analyses of vibrissal tactile discrimination in the rat. *J. Neurosci.* 10, 2638–2648.
- Catania, K. C., and Kaas, J. H. (1997). Somatosensory fovea in the star-nosed mole: behavioral use of the star in relation to innervation patterns and cortical representation. *J. Comp. Neurol.* 387, 215–233.
- Chatfield, C. (2003). *The Analysis of Time Series: An Introduction*, 6th Edn. London: Chapman and Hall.
- Cohen, J. D., Hirata, A., and Castro-Alamancos, M. A. (2008). Vibrissa sensation in superior colliculus: wide-field sensitivity and state-dependent cortical feedback. *J. Neurosci.* 28, 11205–11220.
- Deschênes, M., Moore, J. D., and Kleinfeld, D. (2012). Sniffing and whisking in rodents. *Curr. Opin. Neurobiol.* 22, 243–250.
- Grant, R. A., Mitchinson, B., Fox, C. W., and Prescott, T. J. (2009). Active touch sensing in the rat: anticipatory and regulatory control of whisker movements during surface exploration. *J. Neurophysiol.* 101, 862–874.
- Grant, R. A., Mitchinson, B., and Prescott, T. J. (2012). The development of whisker control in rats in relation to locomotion. *Dev. Psychobiol.* 54, 151–168.
- Hartmann, M. (2001). Active sensing capabilities of the rat whisker system. *Auton. Robots* 11, 249–254.
- Heffner, R. S. (1997). Comparative study of sound localization and its anatomical correlates in mammals. *Acta Otolaryngol. (Stockh.) Suppl.* 532, 46–53.
- Hemelt, M. E., and Keller, A. (2007). Superior sensation: superior colliculus participation in rat vibrissa system. *BMC Neurosci.* 8, 12.
- Hetherington, L., Benn, M., Coffey, P. J., and Lund, R. D. (2000). Sensory capacity of the royal college of surgeons rat. *Invest. Ophthalmol. Vis. Sci.* 41, 3979–3983.
- Land, M. F., Mennie, N., and Rusted, J. (1999). The roles of vision and eye movements in the control of activities of daily living. *Perception* 28, 1311–1328.
- Martin, B., and Bateson, P. (1993). *Measuring Behaviour: An Introductory Guide*, 2nd Edn. Cambridge: Cambridge University Press.
- McGill, T. J., Douglas, R. M., Lund, R. D., and Prusky, G. T. (2004). Quantification of spatial vision in the royal college of surgeons rat. *Invest. Ophthalmol. Vis. Sci.* 45, 932–936.
- Mitchinson, B., Grant, R. A., Arkley, K. P., Perkon, I., and Prescott, T. J. (2011). Active vibrissal sensing in rodents and marsupials. *Philos. Trans. R. Soc. Lond. B Biol. Sci.* 366, 3037–3048.
- Mitchinson, B., Martin, C. J., Grant, R. A., and Prescott, T. J. (2007). Feedback control in active sensing: rat exploratory whisking is modulated by environmental contact. *Proc. Biol. Sci.* 274, 1035–1041.
- Pavlov, I. P. (1927). *Conditioned Reflexes: An Investigation of the Physiological Activity of the Cerebral Cortex*, Trans. G.V. Anrep. London: Oxford University Press.
- Prescott, T. J., Diamond, M. E., and Wing, A. M. (2011). Active touch sensing. *Philos. Trans. R. Soc. Lond. B Biol. Sci.* 366, 2989–2995.
- Schank, J. C. (2008). The development of locomotor kinematics in neonatal rats: an agent-based modeling analysis in group and individual contexts. *J. Theor. Biol.* 254, 826–842.
- Schank, J. C., and Alberts, J. R. (1997). Self-organized huddles of rat pups modeled by simple rules of individual behavior. *J. Theor. Biol.* 189, 11–25.
- Schank, J. C., and Alberts, J. R. (2000). The developmental emergence of coupled activity as cooperative aggregation in rat pups. *Proc. R. Soc. Biol. Sci.* 267, 2307–2315.
- Sullivan, R. M., Landers, M. S., Flemming, J., Vaught, C., Young, T. A., and Jonathan Polan, H. (2003). Characterizing the functional significance of the neonatal rat vibrissae prior to the onset of whisking. *Somatosens. Mot. Res.* 20, 157–162.
- Towal, R. B., and Hartmann, M. J. (2006). Right-left asymmetries in the whisking behavior of rats anticipate head movements. *J. Neurosci.* 26, 8838–8846.
- Valentine, D. E., Sinha, S. R., and Moss, C. F. (2002). Orienting responses and vocalizations produced by microstimulation in the superior colliculus of the echolocating bat, *Eptesicus fuscus*. *J. Comp. Physiol. A Sens. Neural Behav. Physiol.* 188, 89–108.
- Vincent, S. B. (1912). The function of the vibrissae in the behaviour of the white rat. *Behav. Monogr.* 1, 1–82.
- Welker, W. I. (1964). Analysis of sniffing in the albino rat. *Behavior* 22, 223–244.

**Conflict of Interest Statement:** The authors declare that the research was conducted in the absence of any commercial or financial relationships that could be construed as a potential conflict of interest.

Received: 20 March 2012; paper pending published: 19 April 2012; accepted: 20 June 2012; published online: 09 July 2012.

Citation: Grant RA, Sperber AL and Prescott TJ (2012) The role of orienting in vibrissal touch sensing. *Front. Behav. Neurosci.* 6:39. doi: 10.3389/fnbeh.2012.00039

Copyright © 2012 Grant, Sperber and Prescott. This is an open-access article distributed under the terms of the Creative Commons Attribution License, which permits use, distribution and reproduction in other forums, provided the original authors and source are credited and subject to any copyright notices concerning any third-party graphics etc.



# Tactile experience shapes prey-capture behavior in Etruscan shrews

Farzana Anjum and Michael Brecht\*

Bernstein Center for Computational Neuroscience, Humboldt University, Berlin, Germany

**Edited by:**

Robyn Grant, University of Sheffield, UK

**Reviewed by:**

D. Caroline Blanchard, University of Hawaii at Manoa, USA

Paul M. Nealen, Indiana University of Pennsylvania, USA

**\*Correspondence:**

Michael Brecht, Bernstein Center for Computational Neuroscience, Humboldt University, Philippstrasse 13 Haus 6, Berlin 10115, Germany.  
e-mail: michael.brecht@bccn-berlin.de

A crucial role of tactile experience for the maturation of neural response properties in the somatosensory system is well established, but little is known about the role of tactile experience in the development of tactile behaviors. Here we study how tactile experience affects prey capture behavior in Etruscan shrews, *Suncus etruscus*. Prey capture in adult shrews is a high-speed behavior that relies on precise attacks guided by tactile Gestalt cues. We studied the role of tactile experience by three different approaches. First, we analyzed the hunting skills of young shrews' right after weaning. We found that prey capture in young animals in most, but not all, aspects is similar to that of adults. Second, we performed whisker trimming for 3–4 weeks after birth. Such deprivation resulted in a lasting disruption of prey capture even after whisker re-growth: attacks lacked precise targeting and had a lower success rate. Third, we presented adult shrews with an entirely novel prey species, the giant cockroach. The shape of this roach is very different from the shrew's normal (cricket) prey and the thorax—the preferred point of attack in crickets—is protected by a heavy cuticle. Initially shrews attacked giant roaches the same way they attack crickets and targeted the thoracic region. With progressive experience, however, shrews adopted a new attack strategy targeting legs and underside of the roaches while avoiding other body parts. Speed and efficiency of attacks improved. These data suggest that tactile experience shapes prey capture behavior.

**Keywords:** whisker, vibrissa, experience, shrew, *Suncus etruscus*, object recognition

## INTRODUCTION

The somatosensory system of mammals is a classic system for studying neural plasticity. Neurophysiological and anatomical analysis demonstrated that somatosensory cortical maps are highly plastic, both during development (Van der Loos and Woolsey, 1973; Simons and Land, 1987) and in adult animals (Buonomano and Merzenich, 1998). Neural plasticity can be induced by peripheral lesions, passive sensory experience, and training on sensory tasks. Much of the research on neural plasticity of the somatosensory system has focused on the rodent S1/barrel cortex (Woolsey and Van der Loos, 1970) and our knowledge about the neural mechanisms underlying the development of the somatosensory system is impressive (Feldman and Brecht, 2005).

While our knowledge of the development of barrel cortex physiology and anatomy is fairly detailed, we know less about the development of behavioral capacities and natural whisker-mediated behaviors (Brecht, 2007). A notable exception is the work of Simons and colleagues (Carvell and Simons, 1995, 1996) that analyzed the perceptual consequences of barrel cortex plasticity. Specifically these authors demonstrated that whisker deprivation not only leads to alterations in neural responses but also is associated with a loss in tactile acuity in a texture discrimination task. Other author demonstrated that unilateral whisker trimming greatly impacts on behavioral lateralization (Meyer and Meyer, 1992; Aggestam and Cahusac, 2007) and that partial

whisker removal can affect the bilateral synchrony of whisker movements (Sellien et al., 2005).

In the present work, we sought to study the role of experience in shaping biologically relevant tactile behaviors. To this end we analyzed the role of tactile experience in the prey capture behavior of the Etruscan shrews. Earlier work (Anjum et al., 2006) has shown that adult shrews capture very large prey in complete darkness. This behavior involves very fast and precise whisker-guided attacks. Experiments with artificial prey replica with Etruscan shrews and with the American water shrew, *Sorex palustris* (Catania et al., 2008) have shown that shape cues are sufficient triggers to initiate attacks.

In particular we posed the following questions: (1) how similar or different is the behavior of young shrews, at the time of weaning, in comparison to the adults? (2) How does whisker deprivation in the first weeks of life affect prey capture in adult shrews? (3) Are adult shrews capable of adapting to a novel prey?

We find that tactile experience has a profound influence on prey capture behavior and that even adult shrews can adopt entirely novel prey capture strategies.

## MATERIALS AND METHODS

### ETRUSCAN SHREWS

Capture, handling, and maintenance of Etruscan shrews have been described in detail before (Anjum et al., 2006). Data

presented here refer to 18 animals (four females, 14 males; four wild captures, 14 captive born in our colony). Etruscan shrews were captured under a permit of the local government (permit no. N 6085/T-A31, Firenze, Italy) in the provinces Firenze and Livorno and all our procedures complied with German regulations on animal welfare and were approved by an ethics committee.

## PREY

### Crickets

Crickets were obtained from a local vendor (Gekonja, Berlin). We fed mainly juvenile and adult specimen of two cricket species, field crickets (*Gryllus assimilis*), and house crickets (*Acheta domestica*). They were maintained in our facility in a temperature regulated room and fed with fruit, salad leaves, and vitamin-fortified dry fish food.

### Giant cockroaches

The giant cockroach, *Blaberus giganteus*, is naturally found in the rainforests of South America. Giant cockroaches were bred and housed in glass terrariums with soft wood bedding and egg crates for hiding. They were maintained on fruits, lettuce, dry fish, and dog food, and supplied with water. We used the juveniles, about fourth instar larval stage. The body lengths were between 1.5 and 3.0 cm and thus matched the size of crickets normally fed to the shrews.

The giant roach larvae used in our experiments are burrow in soil and are only found in humid rainforests of South America. They are quite different in appearance from the common cockroach larvae to our knowledge quite different from insects found in shrew habitat in Italy. Since we do not know the detailed prey history of our wild-trapped shrews, we cannot exclude that they encountered somewhat similar prey before. The data shown in the result section argue against this idea, however. Both wild-trapped shrews and captive-bred shrew improved in hunting efficiency after experience with giant cockroaches.

The mass of crickets and giant cockroaches overlapped and ranged from 0.5 to 2 g. In size (body-length) matched animals' crickets were about 20% heavier. Besides crickets and roaches we fed animals also on mealworms (larvae of the mealworm beetle, *Tenebrio molitor*). Mealworms were occasionally supplied as an alternative to crickets and were given to breeding females as a source of fat. Animals were fed between 1 and 2 h prior to dimming of the lights every day and typically received slightly more cricket/mealworms than they would consume. The only exception from this *ad libitum* regime was made with animals that were presented with giant cockroaches. These animals were presented with giant cockroaches and after filming these encounters they received an additional five mealworms per day. This regime was chosen to increase the motivation to hunt giant cockroaches.

## YOUNG SHREWS

Shrews were weaned at postnatal day 21–23. The whole litter was moved into a new terrarium and animals were filmed from the very first day of weaning. Crickets were offered in an arena (measuring 12 × 12 cm) and also in the terrarium.

## WHISKER REMOVAL

After birth whiskers of the young animals were trimmed every other day. All pups of a litter were briefly removed from the parents' terrarium. In half of the animals whisker trimming (all whiskers) was done by restraining/holding the animals firmly by the neck muscles and cutting the whiskers very close to the skin with a sharp pair of small spring scissors using magnifying glasses for a better view. The other half of the litter (the control animals) was handled and held the same way for similar lengths of time, except that the whiskers were not cut. The weights of the pups were noted on every occasion of whisker trimming and their weight gain was comparable to that of the controls. Litters in which we performed whisker removal, were weaned slightly later than normal at postnatal day P25 and whiskers were trimmed for the last time on the day of weaning. Whisker deprived animals and control animals were housed separately but received the same number and similar sized crickets and mealworms (larvae of the mealworm beetle, *T. molitor*) for the next 4 weeks. Animal were filmed 4 weeks later; at this time whiskers were fully re-grown. Whisker re-growth was assessed under the microscope and documented by photographs (**Figure 3A**).

## EXPERIENCE WITH NOVEL PREY

In the experiments relating to novel prey, we housed animals individually and carefully monitored every single prey encounter. To this end giant cockroaches were offered in an arena (7.5 × 7.5 cm), one at a time and all encounters were videotaped under infrared illumination. Five shrews (four wild captured, one captive born from our colony) were used for this experiment. Shrews were regarded as "naïve" during their initial encounters with roaches. Therefore, the data from the first 4–6 roaches that were captured were termed "naïve." Animals were considered to be "experienced," when they had captured over 50 roaches over a period of at least 8 weeks. Because animals required several attacks to capture/kill a giant cockroach, all "experienced" shrews had placed several hundred attacks on giant cockroaches.

## VIDEO RECORDINGS, ANALYSIS, AND CLASSIFICATION OF ATTACKS

Videotaping and frame-by-frame analysis have been described in detail before (Anjum et al., 2006). In brief, encounters with prey were staged in custom-made acrylic arenas and videotaped in complete darkness using infrared illumination with an infrared sensitive video camera. The Scion Image (version 1.63) software was used for frame-by-frame analysis of attack clips. The shrew's approach toward the prey, which was followed by a rapid protraction of its rostrum toward the cricket resulting in a putative bite was counted as a completed attack. Aborted attacks started off in the same way, the shrew approached the prey, got as close as 0.5 cm or closer but did not make rapid protractions of the rostrum, therefore not biting the insect. Aborted attacks occurred either because the crickets were successful in escaping or because the shrew did not strike.

## RESULTS

### PREY CAPTURE IN YOUNG SHREWS

Shrew pups weaned between P21 and P23 were capable of hunting independently.

### Attack histograms

Prey captures in shrews are complex chains of events. To develop a quantitative grip on prey capture behavior, we derived measurements from a very large number of attacks. As described previously (Anjum et al., 2006), we first determined in a frame-by-frame-analysis of attack video, the endpoint of each attack and noted to which of nine cricket body parts attacks were directed. Accordingly, the cricket body was divided into nine parts, legs, cerci, posterior-, medial-, and anterior abdomen, posterior- and anterior thorax, head, and the antennae. The data were displayed as attack histograms (Figure 1). The attack histogram of adults (Figure 1A) showed that almost three quarters of attacks targeted the thorax (358 of a total of 456 attacks). Young animals also showed a tendency to attack the thorax (Figure 1B), but the preference was not as strong as adults. The number of attacks on the thorax (144 attacks) was about the same in number as the attacks on the remaining body parts (155 attacks). The fraction of attacks placed on the thorax (79%) in adults was significantly different from the fraction of thorax attacks (48%) in young animal (Fisher's exact test,

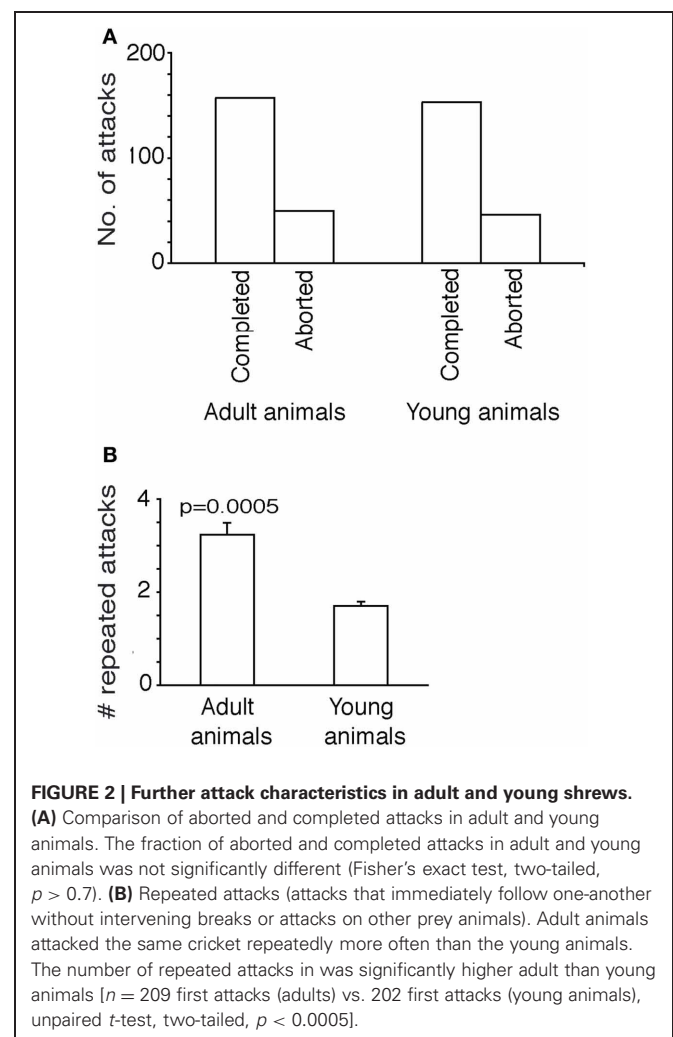
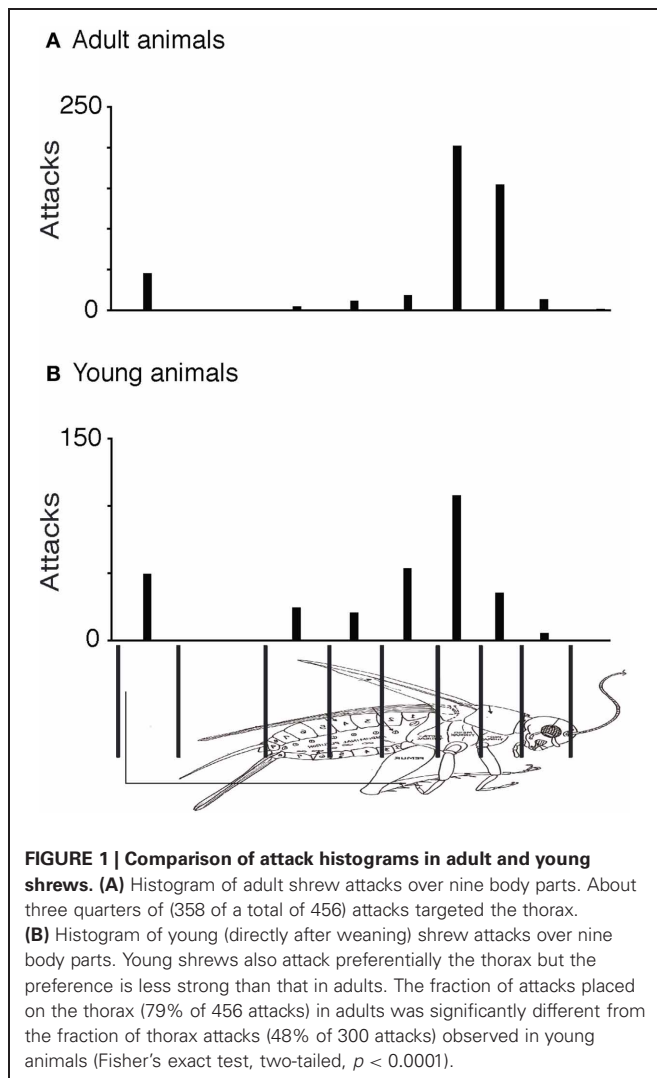
two-tailed,  $p < 0.0001$ ). Unlike adults young animals placed a large number of attacks (18% of total attacks) on the anterior abdomen.

### Completed and aborted attacks

Young animals also have a similar success rate, i.e., similar and statistically not different (Fisher's exact test, two-tailed,  $p > 0.7$ ) fraction of aborted attacks and completed attacks (Figure 2A).

### Repeated attacks

Adult shrews have the tendency to repeatedly attack the same cricket and even on the same body part of the cricket, supposedly using short-term memories of prior attack positions to guide further attacks (Anjum et al., 2006). Apparently this was a more efficient way of hunting as the prey that was attacked more often and recurrently, without getting time to recover from the trauma of the previous attack could be immobilized faster. In Figure 2B we show the number of immediately successive attacks shrews would place on a specific cricket. On average the adults would place 3.2 attacks on each cricket they initiated a first attack on, significantly more than young



shrews, who placed only 1.5 attacks on each cricket they initiated a first attack on [ $n = 209$  (adults) vs. 202 (young animals), unpaired  $t$ -test, two-tailed,  $p < 0.0005$ ]. The number of repeated attacks increases with the persistence with which a shrew attacks a specific prey animal; apparently young shrews more easily lose track of their prey or get more easily distracted by other prey.

### Cricket size

The prey capture behavior of the young shrews also seems to differ from the adults in the size of the crickets that they prefer to attack. Young animals preferentially attacked smaller crickets (1.5–1.75 cm) and preferentially left larger crickets ( $\geq 2$  cm) behind (data not shown). Adults, in contrast, attacked crickets of all sizes (data not shown).

### WHISKER DEPRIVATION

Whisker trimming leads to severe deficits in prey capture in adult shrews (Anjum et al., 2006). In the context of the present study we wanted to determine how the lack of whisker experience in early life affects prey capture capabilities. To this end we trimmed whiskers for 3–4 weeks and then allowed them to regrow. **Figure 3A** shows comparison between the whiskers of an untrimmed control animal (left), a whisker-trimmed animal at the end of the deprivation period (**Figure 3A** middle) and the same animal after whisker-regrowth (**Figure 3A** right). There was no visible difference in the vibrissae of the control animal or the deprived animal with fully re-grown whiskers.

### Attack histograms

In spite of the vibrissae of the deprived animals re-growing to normal lengths and distribution, whisker-deprived animals performed poorly in prey capture. Compared to controls (**Figure 3B**) whisker-deprived animals lacked the precise targeting of attacks to the thorax (**Figure 3C**). In whisker-deprived animals, attacks were more or less evenly distributed over the entire cricket body and only 22% (101 out of 459) of attacks targeted the thorax. The fraction of attacks placed on the thorax (79% of 456 attacks) in control adults was significantly higher in controls than the fraction of thorax attacks (22% of 459 attacks) in deprived animals (Fisher's exact test, two-tailed,  $p < 0.0001$ ).

### Completed and aborted attacks

The success rate of attacks was markedly lowered by whisker-deprivation. In controls only 32% of attacks were aborted and the remainder was completed. In contrast in whisker-deprived animals 57% of attacks were aborted (**Figure 4A**) and this difference was significant (Fisher's exact test, two-tailed,  $p < 0.05$ ).

### Repeated attacks and cricket size

The controls attacked each cricket repeatedly, on an average 3.2 consequent attacks on the same cricket while the test animals did only two times (**Figure 4B**) (unpaired  $t$ -test, two-tailed  $p = 0.0004$ ). There was no significant difference in the size of the crickets attacked between the controls and test animals (data not shown).

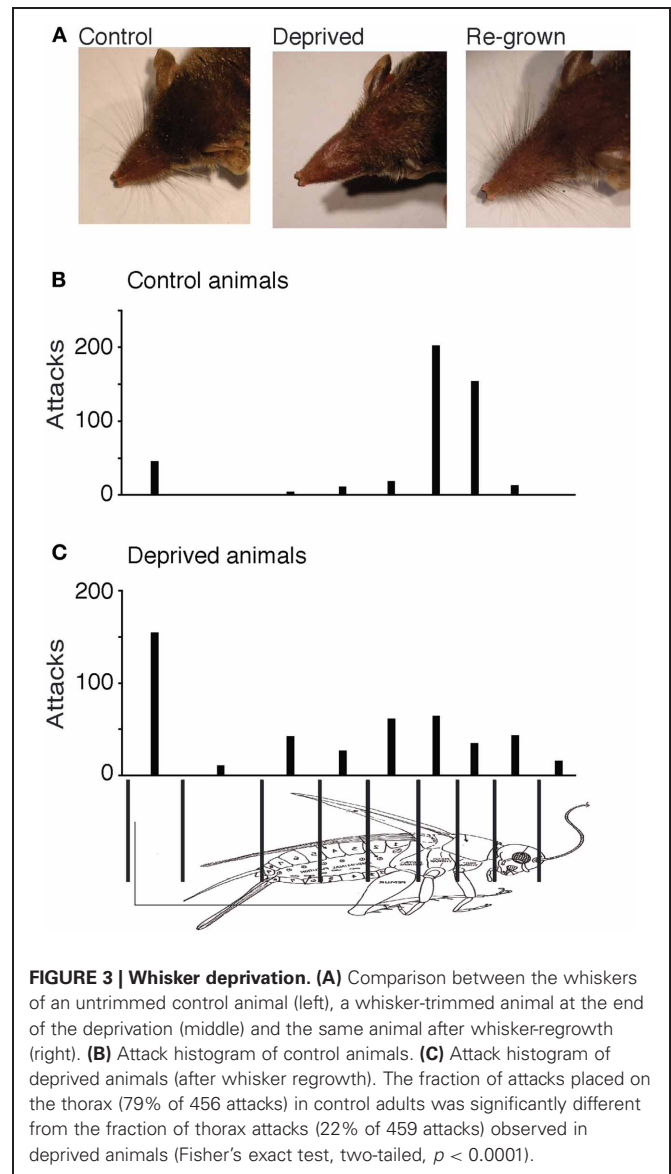


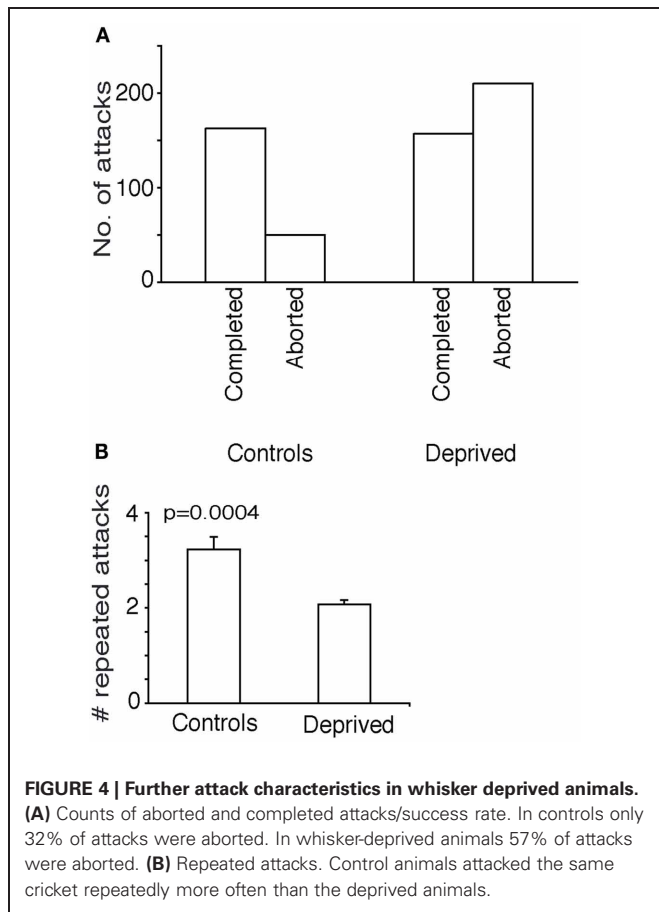
**FIGURE 3 | Whisker deprivation. (A)** Comparison between the whiskers of an untrimmed control animal (left), a whisker-trimmed animal at the end of the deprivation (middle) and the same animal after whisker-regrowth (right). **(B)** Attack histogram of control animals. **(C)** Attack histogram of deprived animals (after whisker regrowth). The fraction of attacks placed on the thorax (79% of 456 attacks) in control adults was significantly different from the fraction of thorax attacks (22% of 459 attacks) observed in deprived animals (Fisher's exact test, two-tailed,  $p < 0.0001$ ).

### EXPERIENCE WITH NOVEL PREY

When shrews were first exposed to the novel prey specimen—the giant cockroach—they did not attack giant roaches. Only after exposing the shrews to giant roaches for 3–8 days at their regular feeding times the shrews placed their first attack attempts on roaches.

### Attack histograms

The giant cockroach differs in important ways from the shrew's normal cricket prey (**Figure 5A**). It has a very tough cuticle all over the dorsal surface of the body, but has a much softer/tender ventral side. Its appendages, namely the cerci, legs, and antennae and even the head are somewhat placed below this shield-like cuticle. Only a part of the posterior legs and antennae can be found to be sticking out of the body making it difficult for the shrews to get a grip/be able to bite.



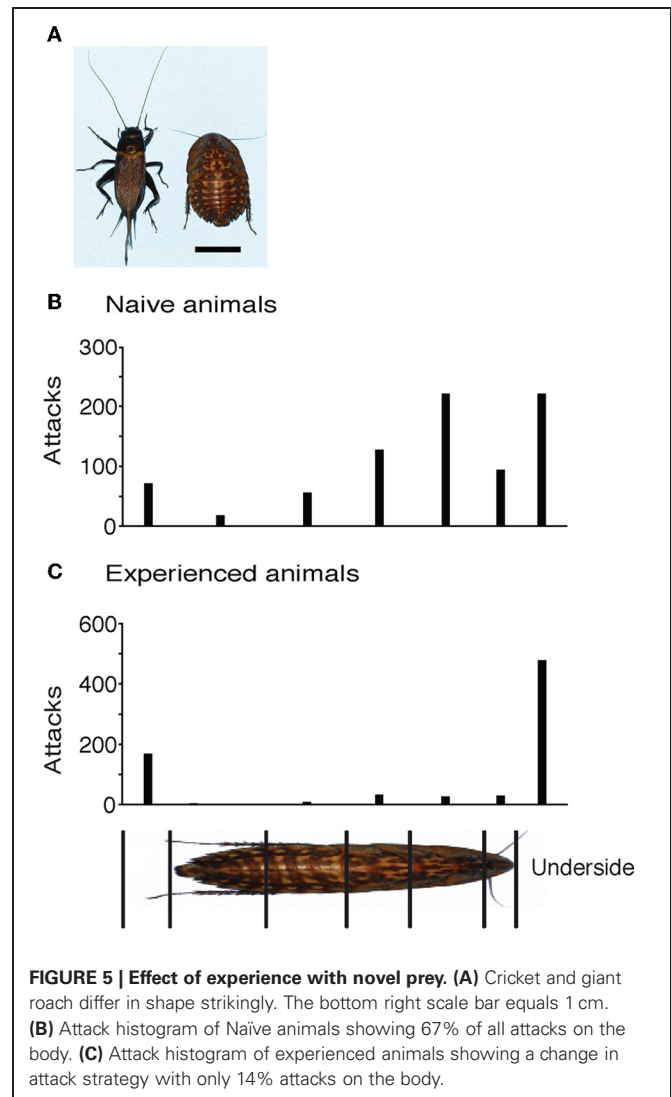
When first exposed to a giant roach, shrews attacked it with a similar pattern as they placed attacks on crickets. The attack histogram in **Figure 5B** shows data pooled from five inexperienced shrews. Of the 815 analyzed attacks, 521 were placed on the body (64%) and 294 on the legs and underside. A large portion of the attacks on the body were on the anterior body of the roach, similar to the attack pattern that normal shrews show for crickets. After experience with more than 50 roaches, the attack pattern radically changed. Now the same shrews attacked the body less and legs and under side more often (**Figure 5C**). Of the 756 attacks analyzed, only 106 were on the body (14%), and 650 on the legs and body. The change in distribution of on body- vs. non-body directed attacks in naïve vs. experienced animals was highly significant (Fisher's exact test, two-tailed  $p < 0.0001$ ).

#### Completed and aborted attacks

Early after the exposure to the new insect, shrews were quite unsuccessful in their attempts to attack the giant roaches and 62% of the attacks were aborted (**Figure 6A**). With experience, shrews became more efficient and only 33% of attacks were aborted.

#### Attack durations

The increase in efficiency of attacks with experience also reflected in a decrease of the time required for immobilizing and picking up the roach (**Figure 6B**). The time taken by each naive shrew



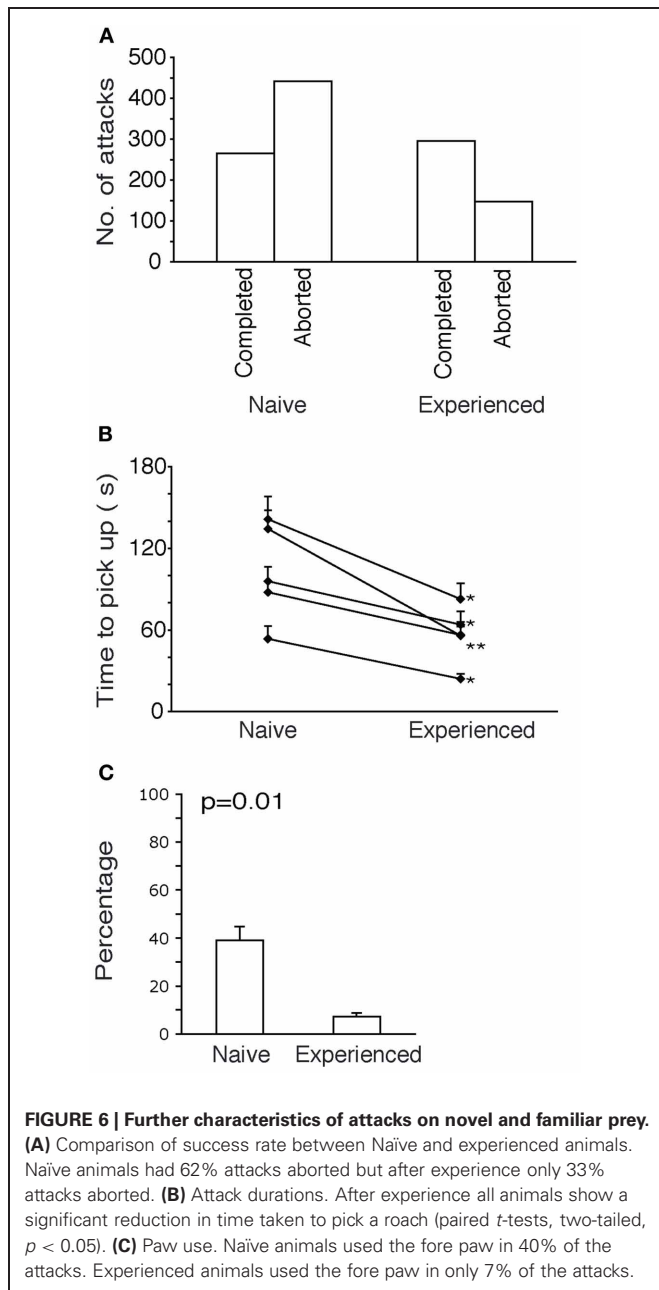
(in seconds) is shown to reduce with experience. All reductions in time taken to pick up the roach were found to be significant.

#### Paw-use

In the initial attacks of shrews on the giant roaches, the shrews displayed attack behaviors not commonly seen in attacks on crickets. Specifically the shrews used one or both of their forepaws in attacks on roaches. This behavior disappeared with progressive experience. In **Figure 6C**, a comparison of frequency of paw-usage before and after experience is shown. Before experience, shrews used the paw in 40% of the attacks and after experience only 7% of the attacks employed the paw.

## DISCUSSION

Three lines of evidence presented here suggest that shrew tactile behaviors are not hardwired, but are modified by tactile experience. First, the hunting behavior of young animals differs in subtle but significant ways from the hunting behavior of adults. Second, postnatal whisker deprivation has devastating effects on



the shrews' hunting capabilities. Third, we find that adult shrews are able to radically alter their prey capture strategies in response to novel prey.

### YOUNG ANIMALS

The prey capture behavior of young shrews directly after weaning was largely similar to the adults. The young animals attacked the anterior abdomen more often than the adults thereby demonstrating a slight lack of precision in targeting. Further experience with attacking crickets might improve attack precision. Moreover young shrews pursue individual crickets less persistently than adult shrews do. Again this change in attack strategy might come about by additional experience.

The similarity of prey capture behavior of young shrews after weaning and adults may be viewed as evidence that tactile experience is not required for prey capture behaviors. An alternative interpretation, which seems more consistent with our other findings (in particular the deprivation data), is that shrews already may have acquired considerable tactile experience prior to weaning. There are other behaviors, like nest building in female rats (Nováková, 1977), which are known to be partially acquired. Females that were prematurely weaned, there by deprived of early experience, nested, and handled the young differently from those weaned normally. As early as P14, the shrew pups have been seen moving about the cages along with the parents. According to our informal observations pups have been spotted tugging at a cricket, more likely hunted by the parents. Perhaps such experience acquired already in the nest contributed to the advanced hunting abilities of young animals directly after weaning. Young shrew may also acquire tactile experience through social behaviors in the nest such as play-fighting. It is not known if and to what extent shrews' play-fight, but in rats this behavior relies on tactile cues (Siviy and Panksepp, 1987) and there is evidence pointing to a role of somatosensory cortex in play-fighting (Panksepp et al., 1994).

### WHISKER DEPRIVATION IN EARLY LIFE

The strong effects that whisker deprivation in the early post natal life has on the prey capture behavior indicates that shrews could be actually acquiring/learning prey capture skills, that may account for the pups accompanying parents on hunting expeditions at nightfall (in shrew rooms). We analyzed prey capture behavior soon after their vibrissae regained their normal lengths. The effects were very similar to those in adult-vibrissae-deprived shrews (Anjum et al., 2006) in diminished precision/attack targeting, and reduced rates of successful attacks. There are known to be critical periods in rats (Simons and Land, 1987; Fox, 1992) and mice (Van der Loos and Woolsey, 1973; Weller and Johnson, 1975) during neonatal life when deprivation of tactile experience/whiskers leads to lasting effects even after months of experience with regrown whiskers. In shrews, the critical period of learning from tactile experience could be in early post natal life/through out the first 3 weeks after birth, which the pups spend growing with their parents. Etruscan shrews are known to have a life span between 1 and 1.5 years. One month long experience with regrown whiskers was insufficient to gain normal hunting skills of an adult.

### NOVEL PREY

The shrews attacked roaches initially in the same way they attack the crickets. Later, however, they adopted a new strategy: they attacked the legs and flipped the roach onto it's back and attacking the soft underside immobilizing it/making it defenceless. This change in strategy markedly increased the efficiency of attacks on the new prey. Our results imply that adult shrews are able to learn new behaviors through continued contact/interaction with a novel prey. All five shrews displayed the same change in the strategy; the most effective way of attacking a roach. The ability of Etruscan shrews to adapt to a new prey and the ability to

implement novel prey capture strategies could be highly adaptive in environments with changing prey populations.

### THE ROLE OF WHISKERS IN ATTACK BEHAVIORS

Our findings on the role of shrew whiskers in prey capture go well with a large body of literature suggesting a more general role of whiskers in attacks and aggressive behaviors. In rats whisker are required in attacks on mice (Thor and Ghiselli, 1975), play a significant role in controlling maternal aggression (Kolunie and Stern, 1990) and both in aggressive and non-aggressive social behaviors (Thor, 1976; Blanchard et al., 1977; Sarna et al., 2000; Brecht and Freiwald, 2011; Wolfe et al., 2011).

### THE ROLE OF EXPERIENCE IN THE SOMATOSENSORY SYSTEM

Our finding that shrew tactile behaviors are modified by tactile experience is in line with a large body of work on the ontogeny of the rodent somatosensory systems (Feldman and Brecht, 2005). Specifically, we hypothesize that the large primary somatosensory cortices of nocturnal rodents like rats and mice (Welker, 1971; Brecht and Freiwald, 2011), Etruscan shrews (Roth-Alpermann et al., 2010) as well of other shrew species (Catania et al., 1999) might serve as repositories for tactile learning. Numerous neurophysiological studies have demonstrated that whisker deprivation both in young and adult rodents can rapidly alter neuronal response properties. As far as available, the behavioral evidence (Carvell and Simons, 1995) also indicated performance on tactile tasks is compromised by disrupted tactile experience. Brief periods of altered sensory experience in

adult rats have shown to bring about significant changes in the functional properties of the S1 neurons (Diamond et al., 1993). We have rich information about the neuronal consequences of whisker deprivation. Specifically we know that whisker deprivation leads to massive alterations in the primary somatosensory cortex. At the same time we know little to nothing about the neural mechanism that represent more subtle changes in experience like the knowledge of a novel prey specimen. It remains to be seen if such knowledge is also reflected with changes of response properties in primary somatosensory cortex, or if such knowledge leads to alterations in higher-order processing stations as suggested from studies in the visual system (Logothetis et al., 1995).

### CONCLUSION

Our results on the tactile behaviors in Etruscan shrews resemble experience-dependence of visual behaviors in cats or monkeys. Visual experience plays an important role in the maturation of the visual system (Hubel and Wiesel, 1970; Hensch, 2004). Similarly, auditory behaviors like song-learning in birds have been shown to depend on experience (Brainard and Doupe, 2002). It is important to note, however, that—even in vertebrates—not all behaviors that require complex sensorimotor integration require experience. For example, electrosensory system of some electric fish seems to be largely hardwired (Vieta and Heiligenberg, 1991). Etruscan shrews display some of the most sophisticated tactile behaviors known to date (Anjum et al., 2006) and our present results suggest that these behaviors are shaped by experience.

### REFERENCES

- Aggestam, F., and Cahusac, P. M. (2007). Behavioural lateralization of tactile performance in the rat. *Physiol. Behav.* 91, 335–339.
- Anjum, F., Turni, H., Mulder, P. G., van der Burg, J., and Brecht, M. (2006). Tactile guidance of prey capture in Etruscan shrews. *Proc. Natl. Acad. Sci. U.S.A.* 103, 16544–16549.
- Bender, K., Allen, C. B., and Feldman, D. E. (2006). Synaptic basis for deprivation-induced synaptic weakening in rat somatosensory cortex. *J. Neurosci.* 26, 4155–4165.
- Blanchard, R. J., Takahashi, M. K., Fukunaga, K. K., and Blanchard, D. C. (1977). Functions of the vibrissae in the defensive and aggressive behavior of the rat. *Aggr. Behav.* 3, 231–240.
- Brainard, M. S., and Doupe, A. J. (2002). What songbirds teach us about learning. *Nature* 417, 351–358.
- Brecht, M. (2007). Barrel cortex and whisker-mediated behaviors. *Curr. Opin. Neurobiol.* 17, 408–416.
- Brecht, M., and Freiwald, W. A. (2011). The many facets of facial interactions in mammals. *Curr. Opin. Neurobiol.* 22, 259–266.
- Buonomano, D. V., and Merzenich, M. M. (1998). Cortical plasticity: from synapses to maps. *Annu. Rev. Neurosci.* 21, 149.
- Carvell, G. E., and Simons, D. J. (1995). Task- and subject-related differences in sensorimotor behavior during active touch. *Somatosens. Mot. Res.* 12, 1–9.
- Carvell, G. E., and Simons, D. J. (1996). Abnormal tactile experience early in life disrupts active touch. *J. Neurosci.* 16, 2750–2757.
- Catania, K. C., Hare, J. F., and Campbell, K. L. (2008). Water shrews detect movement, shape and smell to find prey underwater. *Proc. Natl. Acad. Sci. U.S.A.* 105, 571–576.
- Catania, K. C., Lyon, D. C., Mock, O. B., and Kaas, J. H. (1999). Cortical organization in shrews: evidence from five species. *J. Comp. Neurol.* 410, 55–72.
- Diamond, M. E., Armstrong-James, M., and Ebner, F. F. (1993). Experience-dependent plasticity in adult rat barrel cortex. *Proc. Natl. Acad. Sci. U.S.A.* 90, 2082–2086.
- Feldman, D. E., and Brecht, M. (2005). Map plasticity in somatosensory cortex. *Science* 310, 810–815.
- Fox, K. (1992). A critical period for experience dependent plasticity in somatosensory cortex. *J. Neurosci.* 12, 1826–1838.
- Hensch, T. K. (2004). Critical period regulation. *Annu. Rev. Neurosci.* 27, 549–579.
- Hubel, D. H., and Wiesel, T. N. (1970). The period of susceptibility to the physiological effects of unilateral eye closure in kittens. *J. Physiol.* 206, 419–436.
- Kolunie, J. M., and Stern, J. M. (1990). Maternal aggression: disruption by perioral anesthesia in lactating Long-Evans rats (*Rattus norvegicus*). *J. Comp. Psychol.* 104, 352–360.
- Logothetis, N. K., Pauls, J., and Poggio, T. (1995). Shape representation in the inferior temporal cortex of monkeys. *Curr. Biol.* 5, 552–563.
- Meyer, M. E., and Meyer, M. E. (1992). The effects of bilateral and unilateral vibrissotomy on behavior within aquatic and terrestrial environments. *Physiol. Behav.* 51, 877–880.
- Nováková, V. (1977). Significance of the weaning period for natality and maternal behaviour of laboratory rats. *Physiol. Bohemoslov.* 26, 303–309.
- Panksepp, J., Normansell, L., Cox, J. F., and Siviy, S. M. (1994). Effects of neonatal decortication on the social play of juvenile rats. *Physiol. Behav.* 56, 429–443.
- Roth-Alpermann, C., Anjum, F., Naumann, R., and Brecht, M. (2010). Cortical organization in the Etruscan shrew (*Suncus etruscus*). *J. Neurophysiol.* 104, 2389–2406.
- Sarna, J. R., Dyck, R. H., and Whishaw, I. Q. (2000). The Dalila effect: C57BL6 mice barber whiskers by plucking. *Behav. Brain Res.* 108, 39–45.
- Sellen, H., Eshenroder, D. S., and Ebner, F. F. (2005). Comparison of bilateral whisker movement in freely exploring and head-fixed adult rats. *Somatosens. Mot. Res.* 22, 97–114.
- Simons, D. J., and Land, P. W. (1987). Early experience of tactile stimulation influences organization of somatic sensory cortex. *Nature* 326, 694.
- Siviy, S. M., and Panksepp, J. (1987). Sensory modulation of juvenile play in rats. *Dev. Psychobiol.* 20, 39–55.
- Thor, D. H. (1976). Enhanced social docility in male hooded rats by dermal cautery of the vibrissal pads. *Aggr. Behav.* 2, 39–53.
- Thor, D. H., and Ghiselli, W. B. (1975). Suppression of mouse

- killing and apomorphine induced social aggression in rats by local anesthesia of the mystacial vibrissae. *J. Comp. Physiol. Psychol.* 88, 40–46.
- Van der Loos, H., and Woolsey, T. A. (1973). Somatosensory cortex: structural alterations following early injury to sense organs. *Science* 179, 395.
- Viete, S., and Heiligenberg, W. (1991). The development of the jamming avoidance response (JAR) in *Eigenmannia*: an innate behavior indeed. *J. Comp. Physiol. A* 169, 15–23.
- Welker, C. (1971). Microelectrode delineation of fine grain somatotopic organization of (Sml) cerebral neocortex in albino rat. *Brain Res.* 26, 259–275.
- Weller, W. L., and Johnson, J. I. (1975). Barrels in cerebral cortex altered by disruption in newborn but not five-day old mice (*Cricetidae* and *Muridae*). *Brain Res.* 83, 504–508.
- Wolfe, J., Mende, C., and Brecht, M. (2011). Social facial touch in rats. *Behav. Neurosci.* 125, 900–910.
- Woolsey, T. A., and Van der Loos, H. (1970). The structural organization of layer IV in the somatosensory region (SI) of mouse cerebral cortex. The description of a cortical field composed of discrete cytoarchitectonic units. *Brain Res.* 17, 205–242.
- Conflict of Interest Statement:** The authors declare that the research was conducted in the absence of any commercial or financial relationships that could be construed as a potential conflict of interest.
- Received: 09 March 2012; paper pending published: 29 March 2012; accepted: 28 May 2012; published online: 12 June 2012.
- Citation: Anjum F and Brecht M (2012) Tactile experience shapes prey-capture behavior in Etruscan shrews. *Front. Behav. Neurosci.* 6:28. doi: 10.3389/fnbeh.2012.00028
- Copyright © 2012 Anjum and Brecht. This is an open-access article distributed under the terms of the Creative Commons Attribution Non-Commercial License, which permits non-commercial use, distribution, and reproduction in other forums, provided the original authors and source are credited.



# An insect-inspired bionic sensor for tactile localization and material classification with state-dependent modulation

Luca Patanè<sup>1</sup>, Sven Hellbach<sup>2,3</sup>, André F. Krause<sup>3</sup>, Paolo Arena<sup>1</sup> and Volker Dürr<sup>2,3\*</sup>

<sup>1</sup> Dipartimento di Ingegneria Elettrica Elettronica e Informatica, University of Catania, Catania, Italy

<sup>2</sup> Lehrstuhl für Biologische Kybernetik, Fakultät für Biologie, Universität Bielefeld, Bielefeld, Germany

<sup>3</sup> Cognitive Interaction Technology – Center of Excellence, Universität Bielefeld, Bielefeld, Germany

## Edited by:

Tony J. Prescott, University of Sheffield, UK

## Reviewed by:

Suguru N. Kudoh, Kwansai Gakuin University, Japan

Hiroaki Wagatsuma, Kyushu Institute of Technology, Japan

## \*Correspondence:

Volker Dürr, Lehrstuhl für Biologische Kybernetik, Fakultät für Biologie, Bielefeld University, Universitätsstr. 25, 33615 Bielefeld, Germany.  
e-mail: volker.duerr@uni-bielefeld.de

Insects carry a pair of antennae on their head: multimodal sensory organs that serve a wide range of sensory-guided behaviors. During locomotion, antennae are involved in near-range orientation, for example in detecting, localizing, probing, and negotiating obstacles. Here we present a bionic, active tactile sensing system inspired by insect antennae. It comprises an actuated elastic rod equipped with a terminal acceleration sensor. The measurement principle is based on the analysis of damped harmonic oscillations registered upon contact with an object. The dominant frequency of the oscillation is extracted to determine the distance of the contact point along the probe and basal angular encoders allow tactile localization in a polar coordinate system. Finally, the damping behavior of the registered signal is exploited to determine the most likely material. The tactile sensor is tested in four approaches with increasing neural plausibility: first, we show that peak extraction from the Fourier spectrum is sufficient for tactile localization with position errors below 1%. Also, the damping property of the extracted frequency is used for material classification. Second, we show that the Fourier spectrum can be analysed by an Artificial Neural Network (ANN) which can be trained to decode contact distance and to classify contact materials. Thirdly, we show how efficiency can be improved by band-pass filtering the Fourier spectrum by application of non-negative matrix factorization. This reduces the input dimension by 95% while reducing classification performance by 8% only. Finally, we replace the FFT by an array of spiking neurons with gradually differing resonance properties, such that their spike rate is a function of the input frequency. We show that this network can be applied to detect tactile contact events of a wheeled robot, and how detrimental effects of robot velocity on antennal dynamics can be suppressed by state-dependent modulation of the input signals.

**Keywords:** bionic sensor, forward model, insect antenna, material classification, spiking network, tactile localization, tactile sense

## INTRODUCTION

The sense of touch is a prime source of information about object features within the near-range environment. Many animals carry actively moveable tactile sensors with which they explore and sample the ambient space (Prescott et al., 2011). Of these, the whiskers of mammals (Diamond et al., 2008; Mitchinson et al., 2011) and the antennae (or feelers) of insects and crustaceans (Staudacher et al., 2005) are amongst the most elaborate sensory structures for active tactile exploration. Thus, it is not surprising that a number of artificial tactile sensing systems have been developed that capture important aspects of mammal whiskers or insect antennae.

Pioneering studies on contact sensing with actuated passive probes were loosely inspired by whiskers or antennae. They either used torque or vibration sensors at the base of an otherwise non-sensorized beam to infer contact location from bending (e.g., Tsujimura and Yabuta, 1992; Kaneko et al., 1998) or resonant behavior of the beam (e.g., Ueno et al., 1998). More recently,

whisker-inspired sensor arrays have been developed for shape recognition in a stationary system (Solomon and Hartmann, 2006), but also for active exploration of objects by mobile robot platforms (e.g., Pearson et al., 2007, 2011). Insect-inspired applications with active feelers include tactually mediated decision-making for climbing *versus* tunnelling in a cockroach-inspired robot (Lewinger et al., 2005). All of these approaches have in common that the probe itself is a non-sensorized beam, and that tactile information is gathered by active exploration of the environment.

Mammal whiskers are hairs and, as such, are well-modeled by a non-sensorized beam held by a sensorized shaft. In contrast, insect antennae are multimodal and highly sensorized limbs of the head. As limbs, they contain at least two joints actuated by muscles, and may carry thousands of individual sensors in modalities as different as smell, taste, hygroreception (for humidity), thermoreception (for temperature), and touch (reviewed by Staudacher et al., 2005). Bionic analogs of insect

antennae therefore should be sensorized probes. To date, the most elaborate insect-inspired sensorized antennae are passive, at least in the sense that they do not actively sample the space around the robot “body.” As yet, they have been applied successfully in a tactile course-control paradigm inspired by wall-following behavior of cockroaches (Lee et al., 2008). The underlying principle is to infer the distance to the wall from a series of bending-sensitive elements (Cowan et al., 2003; Lamperski et al., 2005) that may even be tuneable in order to account for different functional properties along the probe (Demir et al., 2010).

Here, we propose an insect-inspired active tactile sensor that complements the approaches mentioned above by considering a sensorized and actively moveable probe suitable for tactile exploration on a mobile robot platform. The present paper has three objectives: (i) first it will review the measurement principle underlying vibration-based tactile localization (Lange et al., 2005, patented by Lange and Reimann, 2005) and material classification (Dürr et al., 2007). (ii) Second, it will demonstrate the implementation of this measurement principle by means of Artificial Neural Networks, ANNs (Hellbach et al., 2010), including considerations of the resource-performance trade-off (Hellbach et al., 2011). (iii) Thirdly, it will demonstrate the applicability of the system on a mobile robot, using a spiking neural network (Arena and Patanè, 2012) allowing for state-dependent modulation for separating self-induced stimulation from external stimulation.

The latter concerns a general problem of sensory systems in moving bodies, and also concerns technical applications in which self-motion of a system interferes with and potentially confounds the analysis of sensor readings. Whereas in animals and humans, the mechanisms underlying the separation of self-induced and external stimulation are often summarized by the terms *corollary discharge* and/or *efference copy* (different variants of such mechanisms are reviewed by Crapse and Sommer, 2008), in technical systems, they typically involve the definition of a forward model (see Karniel, 2002, for distinction of three variants of

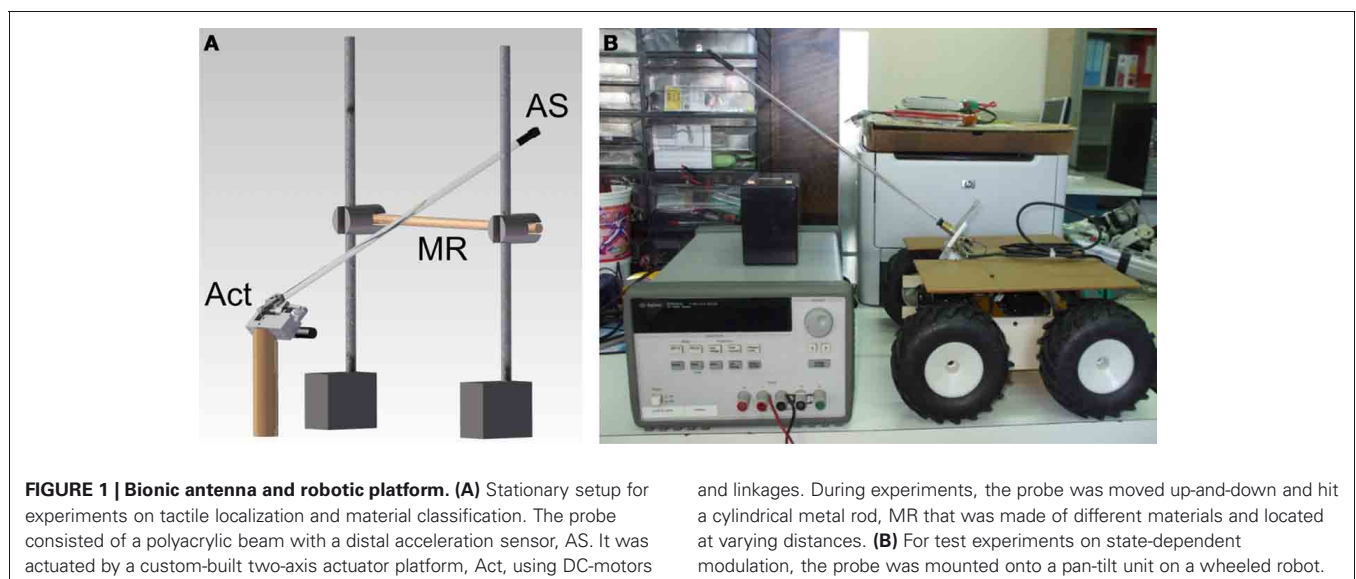
forward models). In more general terms, such mechanisms not only concern dealing with self-induced sensory input, but also predicting the behavior of a dynamical system in general, including its motor output. Several studies have addressed the analogies of predictive forward models in physiological and technical systems, (e.g., Miall and Wolpert, 1996; Mehta and Schaal, 2002; Schröder-Schetelig et al., 2010), including the putative role of forward models in insect neurobiology (Webb, 2004). In the context of active tactile sensing in insects, Gebhardt and Honegger (2001) described descending interneurons that are sensitive to antennal movement and whose responsiveness changes in the presence of antennal motor activity. Although the underlying mechanism has not been identified in the antennal system, it is reminiscent of a well-known mechanism in the auditory pathway of the same insect species (Poulet and Hedwig, 2002, reviewed by Poulet and Hedwig, 2007).

In analogy to the mechanism discovered by Poulet and Hedwig, the present study implements a simple forward model in the form of state-dependent modulation which, according to the classification scheme of Crapse and Sommer (2008), belongs to the lower-order corollary discharge mechanisms for “central control of sensation.” The core of the model is a spiking neural network consisting of a sensory array of resonate neurons. This sensory array extracts the relevant information related to contact events registered by the antenna. During self-motion of the robot, the motor speed command, i.e., the motor activity, is used to predict the strength of modulation of the input to the sensory array, thus adapting the sensory processing to the current “behavioral state.” We show how such activity- or state-dependent modulation allows separation of self-induced antennal stimulation from stimulation related to active touch.

## MATERIALS AND METHODS

### BIONIC ANTENNA

The bionic feeler used throughout this study (Figure 1) captured three major characteristics of the stick insect antenna:



(i) it is a beam-like structure actuated by two rotary joints (Dürr et al., 2001); (ii) it is compliant but also stiff enough to maintain its shape during self-motion (Dirks and Dürr, 2011); and (iii) it is vibration-sensitive (Westmark and Dürr, 2009). The probe consisted of a 33 cm polyacrylic tube that carried a distal two-axis acceleration sensor (Analog Devices ADXL210E). It was mounted to the actuator platform *via* a threaded electric plug connector, allowing simple exchange of probes without affecting the actuator platform. For the experiments on tactile localization and material classification, the actuator platform consisted of two orthogonal axes, each one driven by a 6V DC motor (Faulhaber 1331T 006SR). The linkage was designed to mimic the action range of the stick insect antenna, amounting to 90° in the vertical range, centered 10° above the horizon, and to 80° horizontal range centered 40° to the side. Two rotary position sensors (muRata SV01A potentiometers) monitored the orientation of the probe, thus supplying the two angles required for representing 3D contact location in a spherical coordinate system. The third dimension required for this representation, i.e., distance along the probe, was to be inferred from the sensor readings of the acceleration sensor (see below). For initial experiments, antennal movement was controlled by manual switching of a voltage source, and sensor readings were registered using an AD converter system (CED 1401 power, controlled by Spike2, Cambridge Electronics Design). For acquisition of larger data-sets, as necessary for ANN training, antennal movement control as well as sensor read-out were implemented on an embedded system (ATMEL AT90CAN128), with the raw sensor signal being available *via* RS232C for further processing in Matlab (The Mathworks). Angular positioning of the probe was limited by slack in the motors and amounted to approximately 7° (5 mm at the distal end of the probe). Total length of the feeler was 413 mm. Total weight was 175 g, including both motors.

#### PRE-PROCESSING, DETECTION OF CONTACT EVENTS, AND PARAMETER EXTRACTION

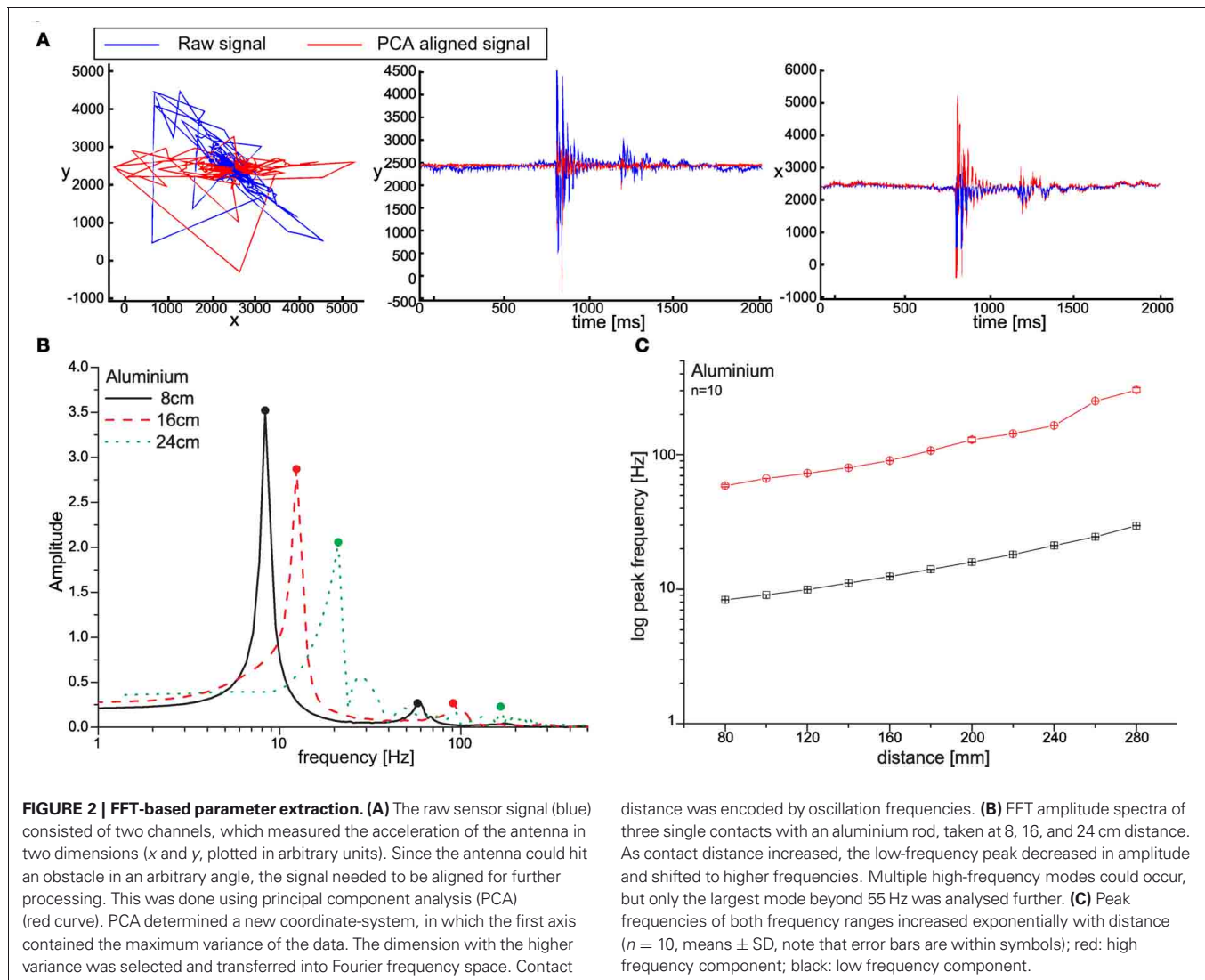
The distal acceleration sensor provided readings corresponding to two orthogonal dimensions, such that the actual oscillation of the antennal tip was projected onto the corresponding dimension vectors of the sensor. Because of this, sensor readings depended on the orientation of the sensor with respect to the antennal movement direction at the time of a contact event. To align the rotated oscillation with a single axis, principle component analysis, PCA, was applied. PCA computes a set of eigenvectors which are oriented with respect to the principal axes of the data distribution. The matrix of eigenvectors  $E$  can be used directly as an affine transform matrix applied to the data:  $X_{\text{rotated}} = E \cdot X$ . Here, the first dimension of the rotated data  $X_{\text{rotated}}$  contained the part of the data with the largest variance. For all experiments reported in this paper, only this part was used for further processing (Figure 2A).

As a first test for proof of principle in contact localization and material classification, we constrained the movement to the vertical axis and analysed sensor readings upon contact with one of two horizontal test rods (Figure 1A) made of either aluminium ( $\varnothing = 11.8$  mm) or wood ( $\varnothing = 9.6$  mm). For subsequent detailed

analysis of performance in classification of multiple materials, test rods were made of the following eight materials: aluminium, stainless steel, wood, copper, brass, polyoxymethylene (POM), polyvinylchloride (PVC), and acrylic glass. In these experiments, all test rods were 12 mm in diameter. Whenever an impact of the antenna on an obstacle occurred (contact event), the acceleration sensor recorded the damped harmonic oscillation of the antennal tip. Thus, for processing information relevant to contact events it was necessary (i) to detect the corresponding damped oscillation and (ii) to retrieve the relevant information for describing the properties of the oscillation recorded. In the stationary system, the contact could be detected easily and reliably by means of a simple threshold for the acceleration. For detecting the end of the oscillation, the local maxima over time were considered. The end point was defined as the time at which the amplitude of these maxima decreased below 10% of the maximum amplitude. Only the data within the window between the detected start and end points was processed further. In a first step, the mean signal amplitude was subtracted. Next, the frequency content of the damped oscillation was determined by means of a Fast Fourier Transform (FFT, using FFT algorithms of Matlab or MathCad, Adept Scientific). The result of the FFT was used in two different variants for further processing (see neural network section “Neural Network for Localization and Material Classification”). In case of the “parametric variant” the FFT result was used to extract six parameters that captured the most important signal properties. In the “FFT variant,” the entire amplitude spectrum of the FFT was used without further pre-processing. Whereas the parametric variant was used for proof of principle and for sensitivity analysis of distinct parameters, the FFT variant was used to find the best performance possible in case of maximum information available.

As the typical frequency spectrum of a contact-related signal contained two distinct peaks (Figure 2B), the purpose of parameter extraction was to describe the two corresponding frequency components in terms of their amplitude,  $A$ ; frequency,  $F$ ; and decay time constant,  $\tau$ . For contact events along the proximal three quarters of the probe, it was sufficient (i) to divide the FFT spectrum in two parts (using 55 Hz as a fixed boundary between low- and high-frequency components), (ii) to determine the peak frequency,  $F$ , within each part of the spectrum, and (iii) then reconstruct the signal corresponding to these frequency components, only (using inverse FFT-algorithms of Matlab or MathCad). The peak frequencies depended on the contact location following a logarithmic function (Figure 2C).

Damping was quantified by estimating the decay time constant from the local extreme points of the damped oscillation. The most satisfying results were obtained with the following algorithm: after decomposition of the recorded signal into a pair of low- and high-frequency components as described above for steps (i) to (iii), (iv) local extreme points were extracted with a minimum interval (e.g., 3 ms) and minimum absolute amplitude (e.g., 15 mV). Next, (v) the amplitudes of the extreme points were rectified and log-transformed. Finally, (vi) a linear regression yielded the amplitude,  $A$ , and time constant,  $\tau$ , of a first-order exponential decay function.



## NEURAL NETWORK FOR LOCALIZATION AND MATERIAL CLASSIFICATION

ANN were programmed and trained either by use of custom-written software (for proof of principle) or by use of the Neural Networks Toolbox of Matlab. For distance estimation and material classification tasks, we used simple feed-forward ANNs, either single- or multi-layered perceptrons. For proof of principle using the parametric variant, a single ANN was used for combined distance estimation and the distinction of two materials (wood *versus* aluminium). Several different combinations of input parameters were tested, as will be elaborated in the results section. In the FFT variant, separate networks were used for localization and material classification, although in principle, both could be combined into a single ANN. Input to the FFT variants was either the entire Fourier spectrum (509 frequency components) or the result of the dimension reduction algorithm (see below). Best results for distance estimation were obtained using a 3-layered ANN with 20 neurons for the first hidden layer and 5 for the second layer. For material classification a two-layered

network with 51 neurons in the hidden layer was sufficient. All networks were trained by use of a gradient descent method.

For reducing the input dimension in a data-driven manner, we used non-negative matrix factorization (NMF, Lee and Seung, 1999). Two other algorithms that, like NMF, also compute a vector basis transformation were tested too (PCA and Partial Least Squares, Schwartz et al., 2009), but will not be presented here. The main reason for using NMF was that it produces a set of basis vectors that, when applied to the input, has similar computational properties as a set of band-pass filters. Most importantly, it attenuates or amplifies each input component with positive scaling factors only. This property makes the solution physiologically plausible, as it captures the frequency-selective attenuation which is typical for sensory processing (e.g., Braddick et al., 1978). It arises due to the constraint of the NMF algorithm, allowing non-negative basis vector components only. In contrast, algorithms such as PCA and PLS produce basis vectors with negative components and, therefore, do not capture the computational properties of band-pass filters.

## ROBOTIC PLATFORM

The robotic system used for the implementation of the feed-forward strategies, consisted of a custom-built, dual-drive roving platform equipped with a pan-tilt actuated bionic-antenna, as shown in **Figure 1A**. The pan-tilt unit consisted of two Dynamixel motors (i.e., High-performance networked actuators for robots RX-64, <http://www.robotis.com/xr/>) controlled through an RS485 serial bus. The same motors were used also to actuate the four robot wheels. The low-level distributed control system was based on three main boards: (i) an 8-bit Atmega-based board used to handle the ADXL321 sensor; the  $x$  and  $y$  signals coming from the sensor were sampled with a 10-bit ADC at a sampling rate of 1 kHz, before being transferred to a PC *via* a USB connection; (ii) a 128-bit Atmega-based board was used to control the pan-tilt system of the antenna; in the simplest case, the two motors followed a limit cycle with a period of two seconds; (iii) the main board, based on a 128-bit Atmega microcontroller,

was used to control the movements of the roving platform and received commands from or exchanged data with a remote PC through a wireless connection.

## SPIKING NEURAL MODEL

The sensory data acquired with the robotic platform was processed by a spiking neural network model. The model combined linear sensory arrays of spiking neurons and a central pattern generator (CPG) model for driving the pan-tilt unit (**Figure 3**). After a pre-processing stage, the sensory information was fed into a one-dimensional array of spiking sensory neurons. Through plastic synapses, their output was then conveyed to the motor neurons that control the muscle/motor system. The scheme proposed in **Figure 3** refers to the general case in which the robot is equipped with two antennae, even though in the experiments described here, sensor data were acquired from a single antenna only.

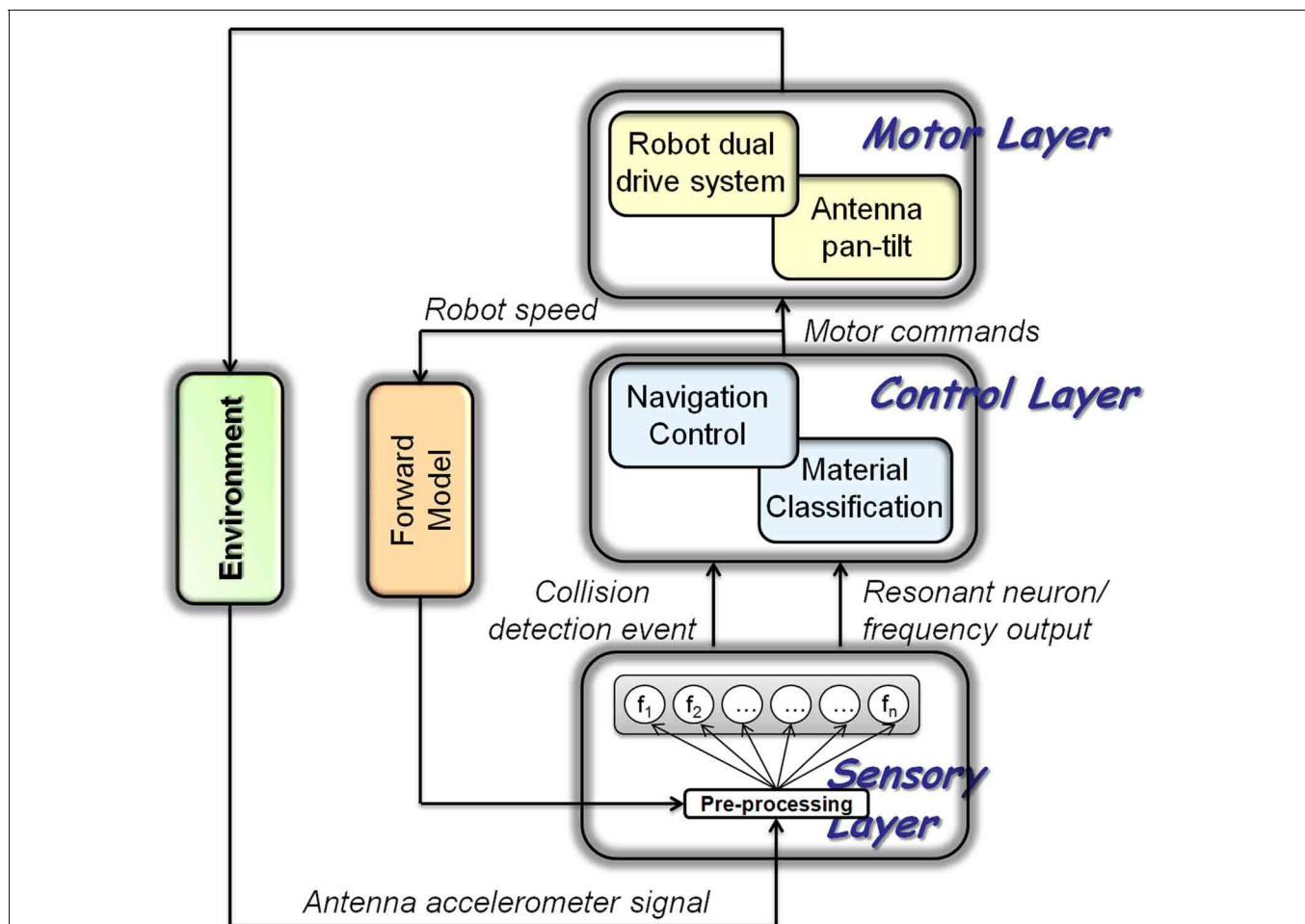


**FIGURE 3 |** Block diagram of the control architecture, designed for the integration of the bionic antennae in a roving platform. The neural network was characterized by multiple layers: (i) A Sensory Layer used for sensory pre-processing and extraction of the frequency spectrum of the acquired signal, based on an array of resonate-and-fire neurons; (ii) a Control Layer where a high-level navigation controller could be introduced together with the material classification network, and (iii) a Motor Layer, used to

actuate both robot wheels and the pan-tilt unit of the antenna. Details of the Motor Layer and the Navigation Control unit of the Control Layer are beyond the scope of this paper. The presence of a forward model for self-motion compensation has been considered by using a sensory gating strategy. The commands for speed were used to modify the pre-processing of the antennal acceleration sensor in order to compensate for self-induced sensor readings.

As described above, the sensory information acquired with the two-axis accelerometer was pre-processed using PCA and normalized. The pre-processed signal was used as input current for a series of resonate-and-fire neurons. Each neuron was tuned to resonate at a specific frequency in the interval from 7 to 30 Hz. The high-frequency band necessary for material classification was not used in the robot experiments, as we concentrated on distance estimation only. The array of resonate neurons used to process the sensory signals for each antenna represented a linear sensory array encoding the contact location along the antenna. Whereas neuron  $f_1$  provided information about the lowest frequency component (dominated by self-stimulation), neurons  $f_2$ – $f_n$  provided information about increasingly higher frequency components and were associated with contact detection of increasingly distal locations along the probe (with increasing  $n$  in  $f_n$ ). The array of resonate-and-fire neurons provided input to the control layer, of which only one part will be explained in this paper (Material Classification). Whereas the Navigation Control unit determined the appropriate movement direction upon tactile contact (e.g., away from the contacted obstacle), the Material Classification unit provided information about the contacted obstacle.

On the wheeled robot, the antenna was actuated with a pan-tilt system controlled by the Motor Layer that mediated the information from the Control Layer. The current speed of the robot could be used to modulate the cycle frequency of the antennae in order to reduce possible shadow areas, thus avoiding collisions with obstacles.

Within the spiking network within the Sensory Layer shown in **Figure 3**, each unit is an Izhikevich-type spiking neuron (Izhikevich, 2003). The neuron model is represented by the following differential equations:

$$\begin{aligned}\dot{v} &= k(0.04x^2 + 5v + 140 - u + I) \\ \dot{u} &= ak(bv - u)\end{aligned}$$

with the spike-resetting

$$\text{if } v \geq 0.03, \text{ then } \begin{cases} v \leftarrow c \\ u \leftarrow u + d \end{cases}$$

where  $v$  is the membrane potential of the neuron,  $u$  is a recovery variable, and  $I$  is the synaptic current. By choosing the parameters  $a$ ,  $b$ ,  $c$ , and  $d$ , different kinds of neural dynamics can be obtained. To show a resonate-and-fire behavior the neuron parameters were set to the following standard values:  $a = 0.1$ ,  $b = 0.26$ ,  $c = -60$  and  $d = -1$ . The parameter  $k$  was used to select the resonate frequency in each neuron. All other neurons behaved like class I neurons, in which the output spike rate was proportional to the input current (the adopted parameters were  $a = 0.02$ ,  $b = -0.1$ ,  $c = -55$  and  $d = 6$ ).

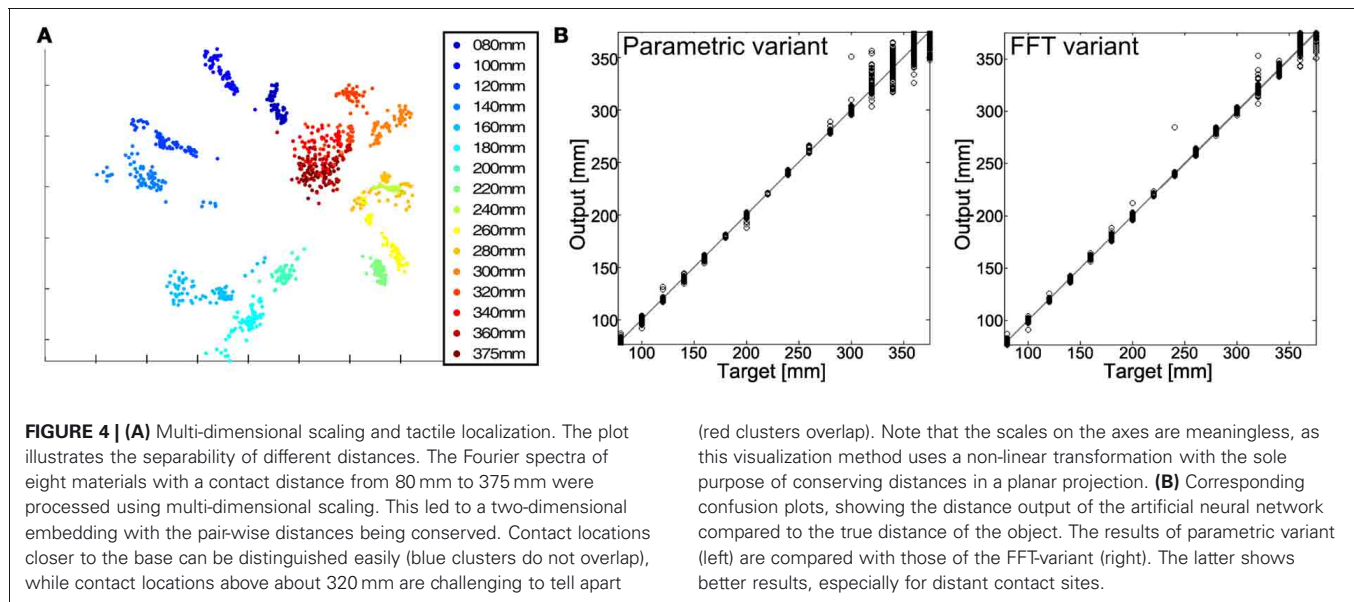
## RESULTS

### TACTILE CONTACT LOCALIZATION

When the antenna hits an object, the acceleration sensor recorded the impact in the form of an abrupt, steep signal followed by a damped harmonic oscillation. The latter can be explained by

the vibration of the free end of the probe, i.e., the part between the contact site and the tip. Accordingly, the fundamental frequency of the oscillation increased with increasingly distal contact events, i.e., with decreasing length of the vibrating free end of the probe (**Figures 2B** and **C**). The FFT amplitude spectra of the recorded oscillations always showed a salient low-frequency peak, followed by one or more high-frequency modes. In order to obtain good understanding of the main signal parameters and their relevance for the sensing process, we first limited the analysis to the two largest modes only, using their peak frequency, amplitude and decay time constant as parameters. Peak frequencies,  $F$ , of both modes increased exponentially with contact distance,  $d$  (**Figure 2C**, low frequency:  $\log F = 0.0268 \cdot d + 0.69$ ; high frequency:  $\log F = 0.0305 \cdot d + 1.52$ ), and linear regression models of the log-transformed frequencies explained more than 98% of the total variance of the data (low frequency:  $r^2 = 0.995$ ; high frequency:  $r^2 = 0.987$ ). Peak frequencies of the low-frequency peaks had approximately three times lower standard deviation than those of high-frequency peaks, indicating that the low-frequency peaks were more reliable for estimation of contact distance. Judged from the standard deviation of the low frequency peaks, the linear regression model allowed an average precision of 6.2 mm for estimates based on a single contact event.

A major problem of this parametric variant of sensory processing was that the frequency of the first harmonics became increasingly unreliable for distal contact sites due to an decrease of the signal-to-noise-ratio. Nevertheless, we tested the performance of tactile localization with an ANN receiving two frequency peaks of the FFT spectrum as input, and producing a distance estimate at its output. For comparison, we used the entire amplitude spectrum of the FFT, thus increasing the input dimension from 4 to 509. The results are shown in **Figure 4**. The fact that vibration-based distance estimation of contact events generally worked well is reflected by the disjunct clusters of input vectors after multi-dimensional scaling (**Figure 4A**, note that multi-dimensional scaling is used for visualization purposes only, not for quantitative analysis). As yet, this graph reveals that clusters corresponding to increasingly distal contact locations overlapped more and more, suggesting that it should become increasingly hard for an ANN to separate the corresponding input vectors. In other words, since the network had to find a mapping from frequency values to distance, performance was expected to deteriorate for distal contact locations. The regression plots in **Figure 4B** confirm this. Compared to the precision estimate based on the linear regression models mentioned above, performance increased for both ANN variants. For the parametric peak search variant, the root mean squared error (rmse) of 2.93 mm, equivalent to 0.7% of the antenna length. For the FFT variant, performance improved to an rmse of 1.71 mm, equivalent to 0.4% of the antenna length. This improvement was not due to altered network size (owing to more input dimensions), because using the lower frequency band only (halving the input) yielded similar results as those of the parametric variant, whereas ten-fold sub-sampling the input spectrum (tenth input size) produced classification results that did not differ from those obtained from the entire spectrum. In summary, this shows that (i) the



upper frequency band is important for good performance in vibration-based tactile localization, and (ii) that extraction of a single high-frequency mode is either not sufficient or not reliable enough for achieving the best performance in tactile localization.

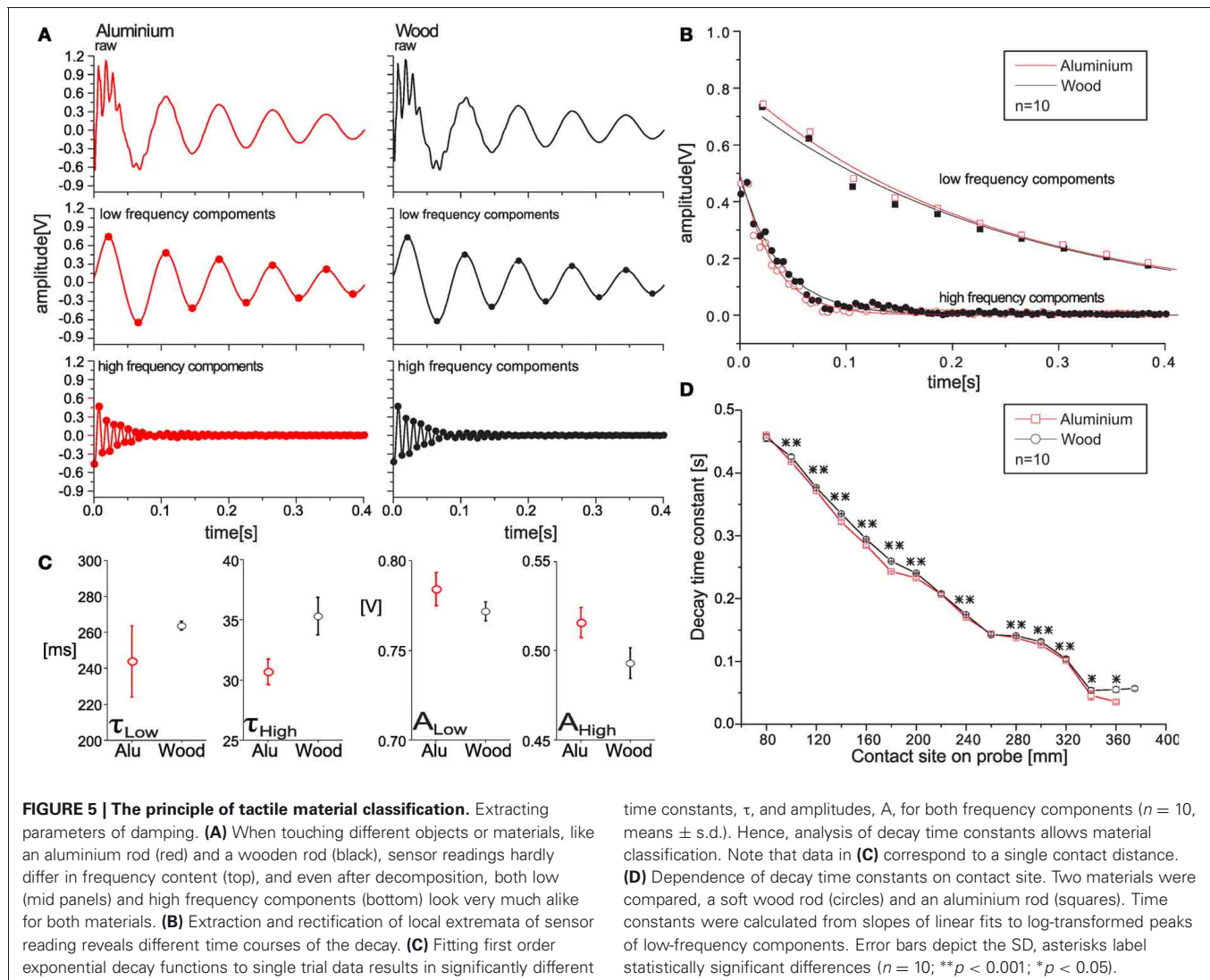
#### TACTILE MATERIAL CLASSIFICATION

Apart from tactile localization of objects, we were interested in exploiting information arising through physical interaction of the contacting materials. For example we were hoping to distinguish different material-specific properties through differences in energy dissipation. In a first approach, we used the parametric variant of signal analysis and tested its applicability for tactile material classification. **Figure 5** summarizes the proof of principle: the materials wood and aluminium could be distinguished reliably by comparing the decay time constants of the damped harmonic oscillations. This suggested that an ANN could be used for tactile classification of several materials, even if the signals recorded had identical peak frequencies (because of identical contact location on the probe), and very subtle differences in signal time course only (e.g., see time courses in **Figure 5A**). In our proof of principle experiment, extraction and rectification of the local extreme points revealed robust differences in decay time constants that could be measured reliably by fitting a first-order exponential decay function (**Figure 5B**). Amplitudes and time constants of the fit functions differed in a statistically significant manner for both the low- and high-frequency signal component ( $t$ -test;  $\tau_{\text{low}}$ :  $t = 3.140$ ,  $p = 0.0057$ ;  $\tau_{\text{high}}$ :  $t = 7.736$ ,  $p < 0.001$ ;  $A_{\text{low}}$ :  $t = -3.683$ ,  $p = 0.0017$ ;  $A_{\text{high}}$ :  $t = -5.934$ ,  $p < 0.001$ ; **Figure 5C**). A remarkable feature of the algorithm was the low variability of the results. For example, the coefficient of variation of the decay time constant of the low-frequency component,  $\tau_{\text{low}}$ , was less than 1%. Owing to the small variability, measurements from different materials could be distinguished with great reliability.

Potential problems of classification based on decay parameters could occur as decay time constants changed with frequency

and, thus, contact distance. To test whether it was possible to distinguish time constants at any contact location, we compared signals recorded for contacts on wood and aluminium, varying contact location from 80 to 375 mm. For both materials, decay time constants decreased with contact distance. The dependence was almost linear (**Figure 5D**). Time constants of the two materials were statistically different at all but four contact sites. On the background of having shown that tactile distance estimation by an ANN could be very reliable, it was clear that the decrease of time constant as a function of contact location was possible too. This suggested that material classification independent of contact site should be possible for an ANN, using either the parametric or the FFT variant.

In a first step of ANN-based material classification, we tested whether a two-layered perceptron could be trained to predict both the contact distance and the correct one of two materials (wood and aluminium). **Figure 6A** shows the network and the dependence of its performance on the number of hidden layer neurons. For identifying the most relevant input parameter for material classification, the ANN was trained with different sets of input parameters. If only the amplitude and frequency of the low-frequency component were used as input parameters, overall performance was bad (*blue line* in **Figure 6A**), mainly because errors in material classification were many. Performance improved if amplitude and frequency of the high-frequency component were included as well, but best performance (particularly for very small ANNs with few hidden neurons) was obtained if the decay time constant of the low-frequency component was included (*red and black lines* in **Figure 6A**, respectively). We did not include the decay time constant of the high frequency component because this was too unreliable to determine for distant contact locations where oscillation frequencies were very high (despite the fact that  $\tau_{\text{High}}$  proved to be a reliable at proximal contact sites, as seen in **Figure 5C**). For the best ANN with five input, eight hidden and two output neurons (equivalent to 56 synaptic weights, only), the precision in distance estimation



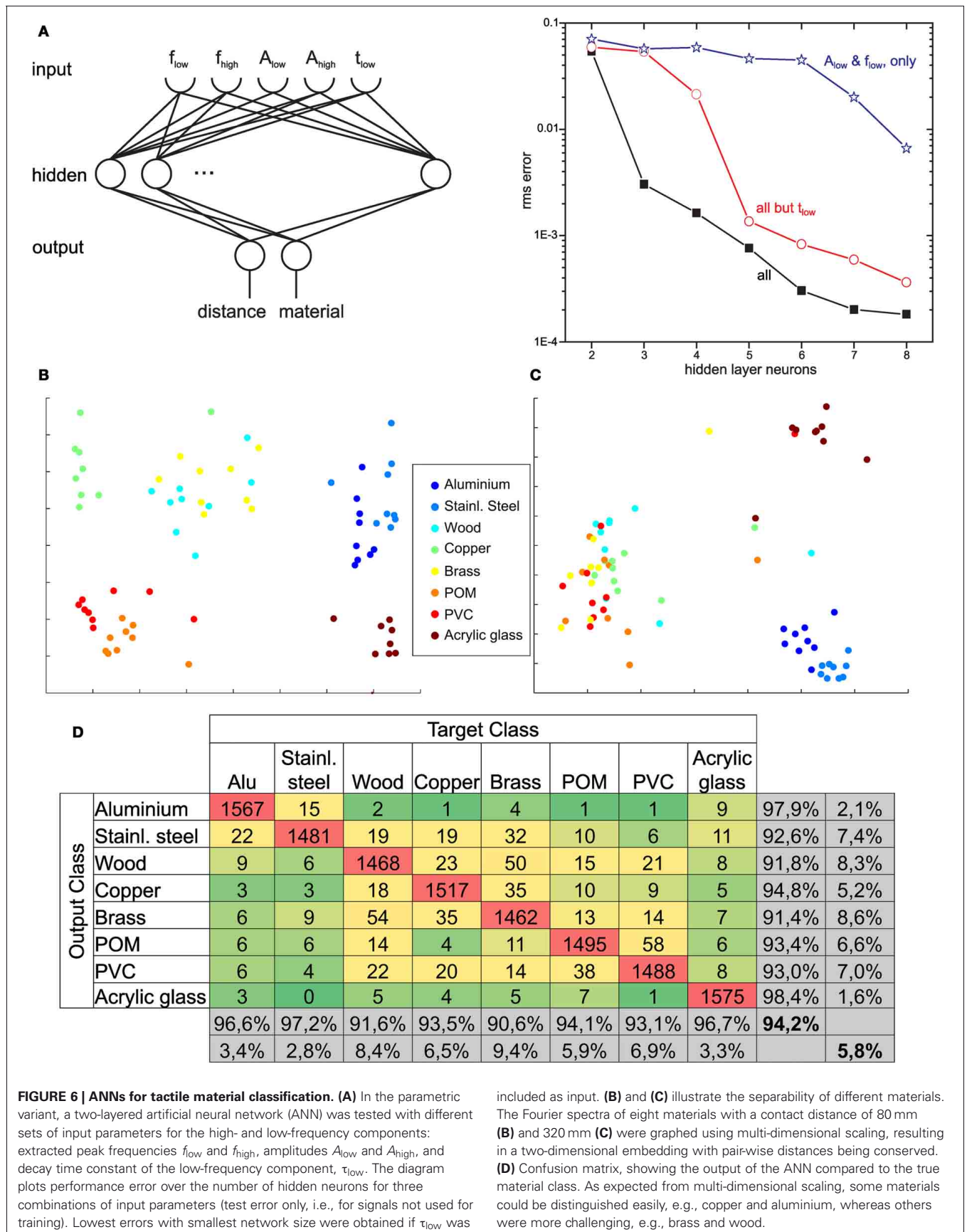
was  $\pm 4$  mm, with 87% correct material assignments for single contact events.

For testing the performance of material classification with several materials, we used eight cylindrical test rods made of different materials, including four metals and three plastics. Thus, the selection of materials included samples that were expected to be discriminated easily, e.g., aluminium and PVC, as well as samples that were expected to be much harder to distinguish, e.g., the two kinds of plastic. The experiments were carried out such that antennal contact occurred at 16 positions along the probe, ranging from 80 to 360 mm in steps of 20 mm, and at 375 mm. For each pair of material and contact location, contact events were recorded 100 times, yielding a total of 1600 sample measurements per material and 80 per contact distance. Multidimensional scaling of the input vectors for the FFT variant revealed that data points related to the same material clustered well, but with varying degree of overlap for selected material pairs (e.g., see brass and wood in **Figure 6B**). Moreover, overlap of clusters depended on contact location, as revealed by the different

graphs for 80 mm and 320 mm in **Figures 6B** and **C**). When using the entire amplitude spectrum of the FFT as input, overall performance in material classification was very good, amounting to 94.2% of correct assignments for single contact events. As yet, performance was not equally good for all materials, as reflected by the confusion matrix in **Figure 6D**, where correct assignments are shown in red, low error numbers are shown in dark green, and increasingly larger error numbers are shown in light green and yellow. For example, wood and aluminium were confused only rarely, while brass and wood appeared to be more difficult to discern (brass was confused with another material in 9.4% of cases, wood was confused in 8.4% of cases; both of these materials were most likely confused with each other).

#### REDUCING NETWORK DIMENSIONALITY WHILE MAINTAINING PERFORMANCE

As the results above showed that the FFT variant was clearly superior to the parametric variant, the question remained which parts of the FFT spectrum were needed and which ones were not.



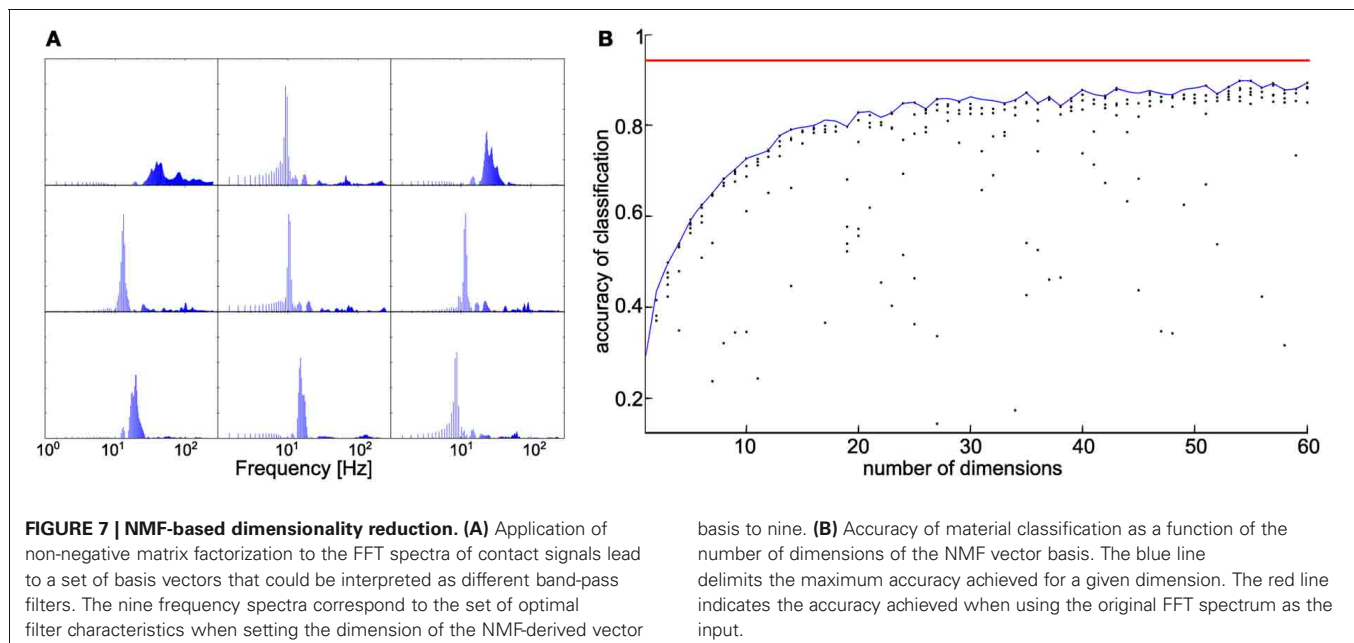
As the FFT variant used 509 input dimensions, the resulting ANN was large, requiring considerably more computational resources than the parametric variant. Thus, there was a clear resource-performance trade-off, and we were interested to assess how performance decreased with systematic reduction of input dimension. As preliminary results had already suggested that ten-fold sub-sampling of the FFT spectrum had little effect on distance estimation (see above), we sought the most efficient combination in inputs in a data-driven manner. For this, we applied non-negative matrix factorization, NMF, with varying numbers of output dimensions. A representative result of NMF with nine dimensions is shown in **Figure 7A**. The number of nine dimensions was chosen for a better visualization, only. However, with a larger number of dimensions the shown band-pass filter like characteristics stays the same. The nine basis vectors are drawn as frequency spectra, emphasizing the analogy to a set of band-pass filters. The corresponding nine-dimensional input to the ANN was then computed by the dot products of the 509-dimensional FFT spectrum of the measured signal with each one of the basis vectors shown. Thus, the number of basis vectors is equal to the number of input dimensions of the ANN. **Figure 7B** shows how material classification improves with number of input dimensions, where several training sessions were done for each number of input dimensions, in order to avoid random effects. The performance when using the un-filtered, entire FFT spectrum was used as reference. The results for reduced input dimension asymptotically approached the results of the entire spectrum. For more than 30 input dimensions, performance in material classification was at least 86% correct assignments. From 30 onwards, the improvement of performance became smaller. Compared to the reference performance of 94.2% correct assignments with 509 inputs, the performance with 30 inputs was reduced by 8% only, while the amount of data was reduced by 95%. Taken together, robust classification of eight materials can

be achieved by appropriately filtering the measured tactile contact signal by 30 non-linear band-pass filters obtained through NMF.

### SENSORY DATA PROCESSING IN SPIKING NEURAL NETWORK

Until this point, the sensor data was always pre-processed by FFT. Although the sensory encoding of stimuli in the frequency domain is common in various sensory systems, including mechanoreceptive and visual systems, FFT is not a biologically plausible algorithm, so we strived to replace FFT by a bionic method of information processing. For this we used a frequency-encoding sensory array based on resonate-and-fire neurons. By appropriate parameter adjustment of a single resonate-and-fire neuron, it is possible to tune selective band-pass filters (Izhikevich, 2003). Here, we exploited this property to determine the specific frequency selectivity for each neuron in a linear sensory array, such that each neuron was responsive to a narrow band of frequencies only. The frequency tuning of the neurons is shown in **Figure 8** where the responses of neurons with preferred frequencies at 7 Hz and 23 Hz are shown for two different sinusoidal input signals. Each neuron was responsive to the corresponding frequency and was silent to other inputs. The frequency selectivity is shown in **Figures 8 G,H** where the role of the parameters  $I$  and  $b$  was analysed for a neuron tuned to resonate at 7 Hz. By changing the amplitude of the input current,  $I$ , the neuron could either resonate in a wide range of frequencies or be excited in a narrow band around 7 Hz. Parameter  $b$  was responsible for the spike rate of the neuron.

After pre-processing with PCA, the signal was low-pass filtered to remove high-frequency disturbances (above 30 Hz). The data was then centred on zero by subtracting the mean value. This was done off-line but can be performed on-line too, e.g., by use of sliding window operations. Finally, the signal was transformed into a train of pulses of unit amplitude (**Figure 8I**), thus removing amplitude differences in the input to the resonate neurons



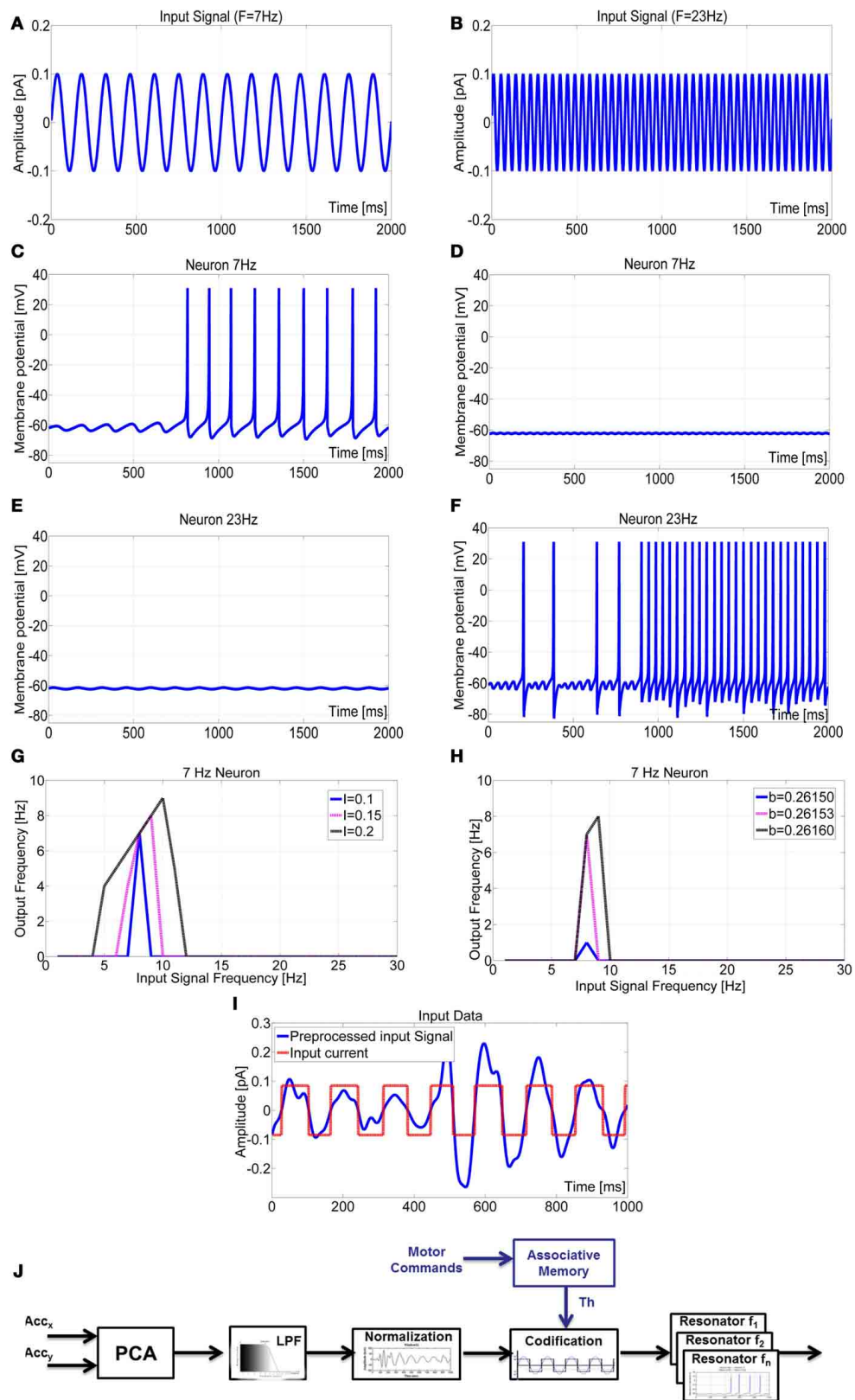


**FIGURE 8 | Behavior of two neurons tuned to stimulus frequencies of 7 Hz (A) and 23 Hz (B).** Membrane potential of the 7 Hz neuron showed

excitation in response to the sinusoidal stimulus with frequency 7 Hz (C) but no response to frequency 23 Hz (D). The opposite was true for the 23 Hz (Continued)

**FIGURE 8 | Continued**

neuron (E),(F). Tuning of frequency selectivity depended on parameters  $k$  and  $b$ , but also on the input amplitude  $I$ . This is illustrated for the 7 Hz neuron. Parameter  $k$  was used to select the frequency of interest (for 7 Hz:  $k = 0.3425$ ). The input amplitude  $I$  modified the window in which the neuron was active (G), and parameter  $b$  determined the spike rate (H). (I) The

pre-processed input signal was codified with a square-wave signal with an amplitude range  $[-0.085$  to  $0.085]$ . This improved the detection performance of the resonate neuron. (J) Block scheme of the signal elaboration from the sensory data acquisition to the neuron input current generation. An associative memory was considered to modulate the signal pre-processing depending on the robot motor command.

that could affect frequency selectivity (which is a function of  $I$ , see **Figure 8G**). Among the different methods tested, this square-wave transformation proved most efficient, as the zero-crossings became triggering events for spikes. The result was a codification of input frequency only, supporting narrow-band frequency selectivity in each neuron within the sensory array.

### SPIKING-BASED PROCESSING AND FORWARD MODEL BY SENSORY GATING

Experiments carried out with the bionic antenna being mounted to the robotic platform generated a wide variety of sensor data that was used to test state-dependent modulation of sensory processing. During motion, frequency analysis of the pre-processed sensor readings revealed an evident peak around 7.8 Hz (note that high frequency signals with  $f > 30$  Hz were not considered in this analysis). The presence of frequency components in the band 7–8 Hz is evident even in absence of tactile contacts. This activity represents the natural oscillation frequency of the sensory probe due to the robot/antenna motion. Still, antennal contact with an external object could be detected by a marked, impulsive response in the sensor reading. Upon registering a contact event, the antenna was maintained in contact with the obstacle for one second and a frequency analysis was performed. For this, the FFT-based analysis used so far was replaced by the spiking neural network architecture described in **Figure 3**, with appropriate parameter tuning as explained in **Figure 8**.

Analyzing the first results obtained using this pre-processing strategy, it was evident that, in some cases, low-amplitude fluctuations could create artifacts that erroneously caused a resonate neuron to fire a spike. To avoid this problem, a threshold for the signal amplitude was added, thus discarding sub-threshold fluctuations. The value of the threshold was critical because an inaccurate choice could lead to the presence of multiple false positives, or, on the contrary, to missing of all contact events (false negatives). Since most of the noise that made the threshold necessary was introduced by self-motion of the robot, this could be predicted from the motor commands assigned to the robot drives. In a first attempt to adaptively select an appropriate threshold value, we determined its dependence on robot speed. Indeed, if the robot drove on a plane surface, a simple speed-dependent threshold improved contact detection performance. Context-dependent setting of this threshold value allowed for state-dependent modulation of the sensitivity to contact events.

The effect of threshold modulation on the sensory array of resonate neurons is shown in **Figure 9**. It summarizes two experiments in which the robot antenna touched obstacles several times. The rows in **Figure 9** correspond to two different driving

speeds (Low speed  $v = 12$  cm/s; High speed  $v = 27$  cm/s). When the signal codification through the square-wave was performed without a threshold modulation ( $Th = 0$ ), contact events were detected erroneously, owing to the noise introduced by robot motion. Increasing the threshold can filter out disturbances, but too high thresholds can filter out contact signals, too. In the example shown, the optimal value of  $Th$  was strongly dependent on the speed of the robot, being more than five-fold as high for the fast speed than for the low speed. As yet, doubling  $Th$  led to a loss of true positives, irrespective of driving speed.

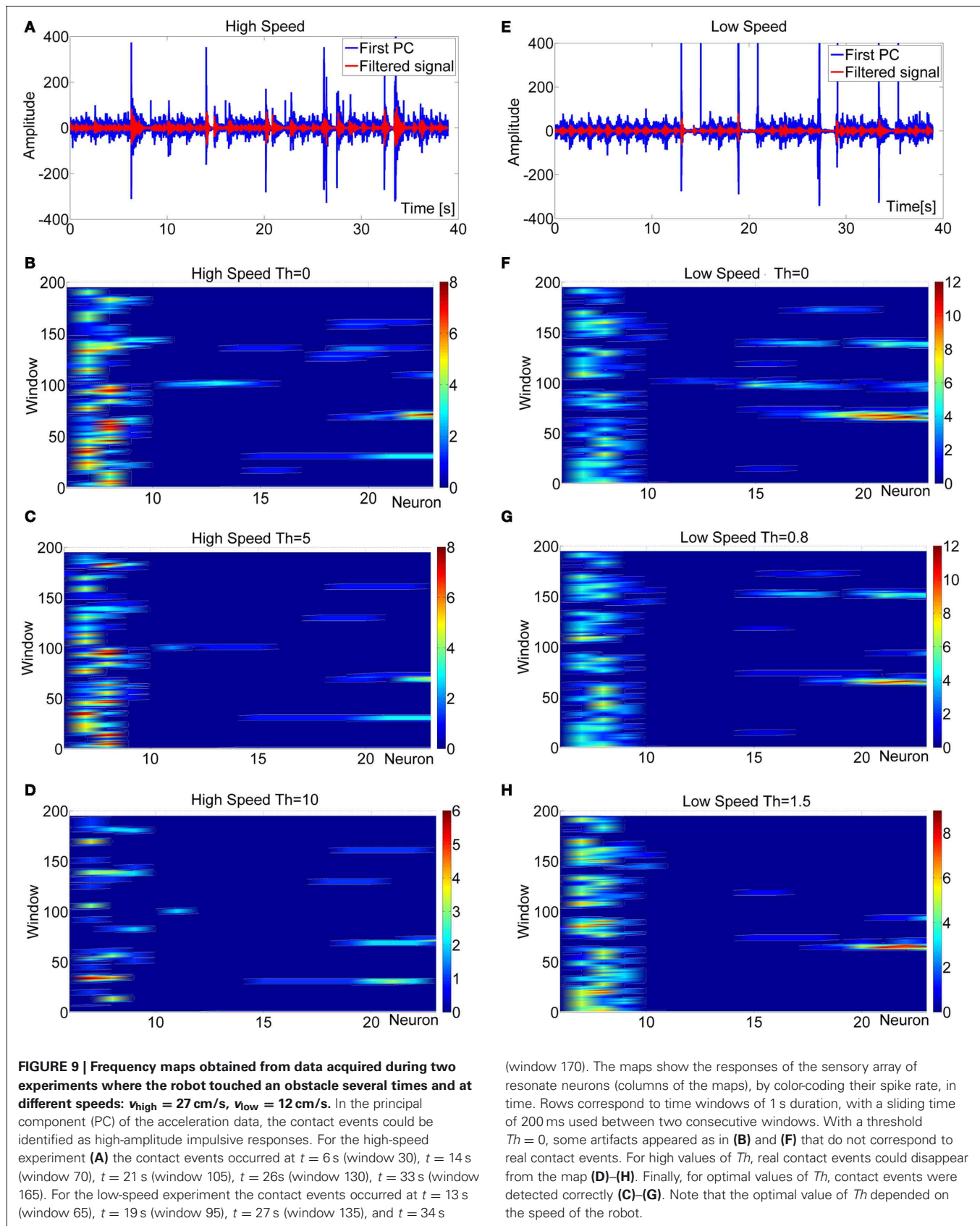
A more detailed example of a robot experiment is shown in **Figure 10**, where the response properties of two resonate neurons in the sensory array during a non-contact episode (**Figures 10 B,D,F**) and a contact event (**Figures 10 C,E,G**) are juxtaposed. In this experiment, the robot was moving at low speed on flat terrain and a tactile contact occurred after 5.5 s. During self-motion without tactile contacts, the 7 Hz neuron fired spikes continuously, whereas neurons tuned to higher frequencies remained silent. Upon tactile contact with the obstacle, the pattern of activity within the sensory array shifted to higher frequencies, and the 17 Hz neuron was most active. The frequency map (**Figure 10H**) shows the time course of neural activity within the entire sensory array: the initial frequency band of 7–8 Hz indicates that the robot moved and, therefore, caused self-stimulation at the resonance frequency of the probe. The contact event was detected by an abrupt termination of the 7 Hz activity and simultaneous occurrence of a new peak at much higher frequencies. As soon as the robot was stopped in response to tactile contact, neural activity ceased in both high and low frequency neurons.

## DISCUSSION

With this study, we present a bio-inspired tactile sensor for active tactile localization and material classification, suitable for application on a mobile robot platform. Two neural information processing modules were proposed for these purposes: a multi-layered perceptron for analysis of the frequency spectrum of the vibration signal recorded, and a spiking neural network that can provide the frequency spectrum and lends itself for state-dependent modulation of sensory processing during self-motion.

### TACTILE LOCALIZATION AND MATERIAL CLASSIFICATION

The measurement technique is simple, accurate, and robust. It is simple because the use of a single sensor per antenna, it is accurate because contact localization can achieve as little as 0.4% deviation from linearity over a measurement distance of some 40 cm, and it is robust because it allows for correct classification of eight materials in up to 94% of cases with a single contact



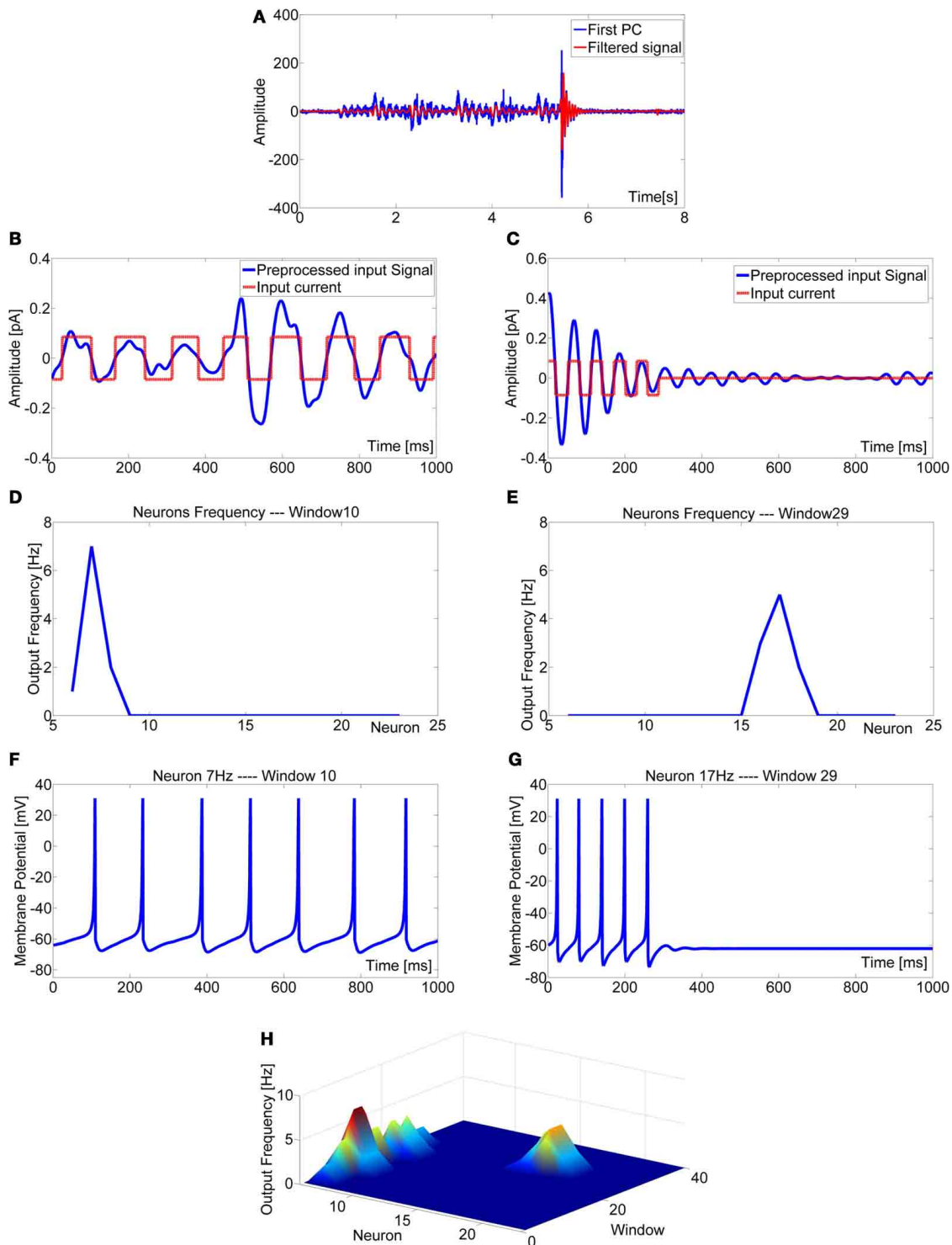


**FIGURE 10 | Experiment performed with the robot exploring a flat terrain at low speed. (A)** Principal component extracted from the acceleration data and filtered signal (after low-pass-filtering with a cut-off frequency of 30 Hz). Behavior of the network in absence of contact events: **(B)** normalized signal in the interval [2, 3] s (window 10); **(D)** spike rate of the sensory array of resonate neurons: the 7 Hz neuron is active because the robot is in motion; **(F)** membrane potential of the 7 Hz neuron. Behavior of the network in presence of a contact

event: **(C)** pre-processed input signal and corresponding input current in the interval [5.8, 6.8] s (window 29): a damped oscillation is recorded after a tactile contact; **(E)** spike rate of the sensory array of resonate neurons: the 17 Hz neuron it is active because the antenna touched an obstacle, the contact distance can be calculated using a non-linear mapping function (here  $d = 19$  cm from the base of the antenna); **(G)** membrane potential of the 17 Hz neuron in window 29. **(H)** Frequency map obtained for the entire experiment.

event. Compared to earlier work on artificial active tactile sensors, our method differs with respect to the sensorization of the beam. For example Kaneko et al. (1998), Lewinger et al. (2005), Solomon and Hartmann (2006), and Pearson et al. (2011) used sensors at the base of the beam, whereas we use a sensor on the tip. Despite the difference in sensor placement, our method bears some similarities with that proposed by Ueno et al. (1998), who also inferred the contact location along the beam by analysing its resonant behavior, though with a basal sensor. Technically, a major difference between basal and distal sensor placement is the number of oscillation cycles that can be measured during a single contact event. In the approach by Ueno et al. (1998), the fundamental frequency during the contact period needs to be inferred from half a cycle period, whereas in our method, several cycle periods can be analysed. Analysis of signals containing several complete cycles of oscillation arguably allows for more reliable computation of the frequency composition. Another advantage of our method might be its applicability for material classification in addition to tactile localization. This was not tested by Ueno et al. (1998). On the other hand, approaches with basal bending- and/or torque-sensors have been shown to be very efficient in tactile shape reconstruction (e.g., Solomon and Hartmann, 2006). As our sensing method relies on the analysis of discrete events rather than of a continuous stream of sensor readings, it may be more appropriate for local, discontinuous analysis of object features rather than for complete and continuous mapping tasks.

The present system uses PCA-based pre-processing of the sensory input that reduces the number of input channels from two to one. This reduction is not necessary as the signals could be also processed separately, with the overhead of doubling the processing structure. An advantage of parallel processing of both channels might be that the direction of motion relative to the surface contacted could be determined. Future experiments will need to address this issue.

The major advantage of the feed-forward ANN module concerns the robustness of accurate localization in the face of noise, and the applicability of fast and simple learning rules for any particular tactile classification task of choice. Both of these aspects are of relevance to the engineering of autonomous active tactile sensing systems. Concerning the resource-performance trade-off, the reduction of input dimensionality used in this study was based on NMF, yielding a relatively small set of basis vectors for efficient description of the sensor signal. Owing to its non-negativity constraint, NMF results in a set of basis vectors that can be interpreted as non-linear band-pass filters. In principle, similar results might have been obtained by an even-spaced set of band-pass filters with equal frequency bandwidth. In fact, the analysis of distance estimation revealed that simple down-sampling of the input by using every 10th value, still produced satisfying results. Potential disadvantages of such “simpler” choices of sensory filters could arise due to arbitrary heuristics, e.g., when choosing the bandwidth of band-pass filters. In contrast, application of NMF ensured purely data-driven optimization of filter properties. The result suggests that some 30 band-pass filters provide sufficient information for reliable classification of the eight materials tested, independent of contact location. Many sensory

systems are known to use a relatively small number of input channels with band-pass filter properties (e.g., see Olshausen and Field, 2004, on sparse coding in sensory systems). Thus, reducing the number of input dimensions by use of a set of band-pass filters is not only resource-efficient in technical terms, but also follows a common principle in natural sensory information processing.

Our active tactile sensor system is inspired by the stick insect antenna, albeit with strong simplification of the biomechanical features (Dirks and Dürr, 2011) and number of sensors (Monteforti et al., 2002). Stick insects of the species *Carausius morosus* continuously move their antennae during locomotion, thus actively exploring the ambient space (Dürr et al., 2001). They use mechanoreceptive information from their antennae for tactually mediated re-targeting of leg movements in a reach-to-grasp paradigm (Schütz and Dürr, 2011) though the source of this mechanoreceptive information is not known yet. At least two kinds of antennal mechanoreceptors could contribute to the encoding of fast rhythmic deformation of the long and thin flagellum: (i) campaniform sensilla, i.e., bending-sensitive sensilla that are embedded within the cuticle of different parts of the antenna; (ii) Johnston’s organ, a prominent chordotonal organ in the second segment of the antenna, near the base. Johnston’s organ is present in all higher insects. It is a proprioceptor known to measure antennal vibration in many insects, including mosquitoes, flies, and honeybees (reviewed by Staudacher et al., 2005). In stick insects, descending neurons of the antennal mechanosensory system have been shown to be vibration-sensitive (Westmark and Dürr, 2009), and the sensory structures that supply this information must have been located on the proximal part of the antenna, although their identity remains obscure. In a chordotonal organ of the stick insect leg, the sense of vibration has been analysed to considerable detail (Stein and Sauer, 1999), showing that the sense of vibration is of importance in these animals. In summary, the choice of a single distal acceleration sensor on our bionic antenna does not model any particular antennal mechanoreceptor. Rather it abstracts the property of antennal vibration-sensitivity, highlighting both advantages and disadvantages of vibration-sensitivity on an active sensor, and furthering our understanding of what kind of behavioral tasks vibration-sensitive proprioceptors potentially could contribute to.

In addition to their rich sensory infrastructure, real insect antennae have very complex mechanical properties. In many species, the antenna is sufficiently stiff for maintaining its shape during self-motion, even in very long and thin structures (e.g., 100:1 length-to-diameter ratio in the stick insect *Carausius morosus*). At the same time, antennae are compliant and readily bend when in contact with obstacles. Moreover, damping appears to be functionally important, and is known to vary along the length of the antenna (Dirks and Dürr, 2011). Near the base of the stick insect antenna, damping is over-critical, preventing long-lasting oscillation of the structure, while supporting fast return to the natural shape after release of contact. Closer to the tip of the antenna, damping is weaker and oscillation of the flagellum has been shown (Dirks and Dürr, 2011). The bionic tactile sensor used in this study does not model a proximal-to-distal gradient of damping properties. Taken together, the

sensing principle based on a distal vibration sensor monitoring damped harmonic oscillations is a simplification based on the observation that antennal contacts cause deflections of the flagellum which lead to fast return movements inducing oscillation of the tip.

### STATE-DEPENDENT SENSORY GATING BY MEANS OF A FORWARD MODEL

Mechanoreceptors are particularly susceptible to self-stimulation during motion, mainly because movement may directly interfere with their adequate stimuli, e.g., the deflection of a hair or passive movement of a joint. As a consequence, active sensing, i.e., involving self-motion into the sensing process, is likely to generate self-stimulation that potentially could confound sensory readout. On the other hand, active mechanoreception may also have advantages in fidelity over passive mechanoreception, as shown by Kim and Möller (2006). Here we use a bio-inspired neural network approach for state-dependent modulation of sensory input. It is inspired by central modulation of sensory processing in insects (e.g., Poulet and Hedwig, 2007), and bears many parallels to gating properties described in the central nervous system of walking crickets (Staudacher and Schildberger, 1998).

Bio-inspired solutions can be applied in robots for finding alternative ways to deal with classical problems of obstacle detection in roving platforms. With the proposed spiking-network architecture we provide an alternative method for the frequency analysis of the input data originally performed through the FFT. The spiking-network is based on resonate-and-fire neurons for processing sensory information coming from mechanoreceptors on the antenna. Apart from resonance-based frequency decomposition of the input signal, we modulate a key parameter of the resonate-and-fire neurons for state-dependent modulation of their sensitivity. This allows for state-dependent cancellation of self-induced sensor readings.

Resonance in neural circuits is considered an essential ingredient for giving rise to self-sustained activity (i.e., in the absence of external stimuli), suggesting a primary role in higher cognitive processes such as working memory, decision-making, and goal directed behavior (Wang, 2003). On the other hand, dynamical system theory traditionally exploits resonance for detecting the essential dynamical characteristics of the system under consideration, emphasizing the role of enhancing specific input patterns locked around the system's resonance frequency. Joined together, these two concepts led to the design of neural models which were both able to exhibit self-sustained oscillations (Muresan and Savin, 2007), and to show the emergence of oscillations only if stimulated by input signals possessing specific frequency contents (Izhikevich, 2001). Complex strategies of selective communications were hypothesized using networks endowed with such models (Izhikevich et al., 2003). One of the first applications of resonators was in the field of sound detection, localization and clustering from sensory data (Arena et al., 2005). A similar principle has been applied by Webb et al. (2007), investigating the ability of bushcrickets to respond to different song patterns. The implementation through spiking networks, as proposed here, can be a first step toward a bio-inspired formalization of the structure,

allowing its transfer and application to modeling higher brain functions of insects as well, for example functions that involve the mushroom bodies or the central complex (Arena et al., 2010). Future work will consider the introduction of local excitatory and global inhibitory connections among the resonate neurons to create a winner-takes-all topology to improve the filtering capabilities and the detection performance. Moreover the proposed architecture allows embedded solutions by using either networks of microcontrollers or FPGA-based boards (Arena et al., 2007, 2008).

In nature, mechanisms for self-motion detection are frequently met. For example, flies readily estimate their self-motion from the acquired optic flow field (Krapp, 2009). Forward models are used for predicting and compensating specific effects of own body motions, recorded from exteroceptive sensors: there is a large body of literature suggesting that biological systems use efference copy and internal models to filter out disturbances in a fast, robust, and adaptive way (Franz et al., 2004; Webb, 2004). Applications in the area of biorobotics include prediction and compensation of self-induced disturbances on sensor readings in a biped robot (Manoonpong and Woergoetter, 2009), using a recurrent neural network. The particular implementation of forward models through spiking neural networks is an interesting topic as discussed by Russo et al. (2005). Their modeling work on multimodal integration in crickets allowed them to deal with conflicting effects of auditory and visual orientation reflexes (phonotaxis and optomotor turning response). For this, they suppressed self-induced visual input activity during voluntary turning movements and phonotaxis-induced turning. In this case, a simple non-linear feed-forward compensator was designed as part of a bio-inspired spiking neural network to model sensorimotor integration and control on a roving robot. The proposed architecture included a forward model for ego-motion compensation that was based on a sensory gating strategy for an efficient and robust solution, requiring neither time prediction nor compensation mechanisms. The present model could be extended to include a reward-based learning method, allowing the robot to learn the appropriate threshold values. A potential candidate structure for implementing such a learning method is a Motor Map (Ritter et al., 1992). In a Motor Map, a lattice of neurons can be specialized to find the best threshold value for different robot speed. Moreover, it could be extended easily to include further inputs, including inputs that classify different types of environments. The reward signal could be generated by a teacher that indicated to the robot whether a detected contact event was a true or false positive. Instead of a teacher, other sensors, such as sonar or infrared distance sensors, could provide the signals necessary validation of true positives.

The control architecture used in the present robot system can be improved further by introducing a behaviour association network as proposed in Arena et al. (2009). The robot could then try different basic behaviors on the detected objects, for instance avoidance, climbing, or pushing, while monitoring the consequences of its own actions. By using a simple associative learning method, the robot could choose the most suitable action for each object, depending on information about dimension and type of

material that can be acquired from the bionic antennae. It is important to underline that the spiking-network structure can be considered as a functional module that can be integrated with other modules for a more detailed control strategy.

In summary, our active tactile sensing system successfully applies a simple feed-forward ANN module for robust and reliable tactile localization and material classification. Moreover, we exploit the resonant behavior of a spiking-network for implementing a mechanism of state-dependent modulation or gating. This allows suppression of self-induced mechanoreceptive inputs from the antenna as it occurs during self-motion. Thus, it is applicable to active tactile sensors mounted to mobile platforms.

## REFERENCES

- Arena, P., Berg, C., Patanè, L., Strauss, R., and Termini, P. S. (2010). "An insect brain computational model inspired by *Drosophila melanogaster*: architecture description," in *WCCI (2010), World Congress on Computational Intelligence* (CCIB, Barcelona, Spain), 831–837.
- Arena, P., De Fiore, S., Fortuna, L., Frasca, M., Patanè, L., and Vagliasindi, G. (2008). Reactive navigation through multiscroll systems: from theory to real-time implementation. *Anton. Rob.* 25, 123–146.
- Arena, P., De Fiore, S., Patanè, L., Pollino, M., and Ventura, C. (2009). "STDP-based behaviour learning on the tribot robot," in *Proceedings of Microtechnologies for the New Millennium (SPIE 09)*, (Prague, Czech Republic), 1–12.
- Arena, P., Fortuna, E., Frasca, M., Patanè, L., and Sala, C. (2007). "Integrating high-level sensor features via STDP for bio-inspired navigation," in *International Symposium on Circuits and Systems*, (New Orleans, LA, USA), 1–4.
- Arena, P., Fortuna, L., Frasca, M., Ganci, G., and Patanè, L. (2005). "A bio-inspired auditory perception model for amplitude-frequency clustering," in *Proceedings of the SPIE 05 Europe International Symposium on Microtechnologies for the New Millennium* (Sevilla, Spain), 9–11 May.
- Arena, P., and Patanè, L. (2012). "A spiking network for object and ego-motion detection in roving robots," in *International Joint Conference on Neural Networks (IJCNN 2012)*, Brisbane, Australia June 10–15.
- Braddick, O., Campbell, F. W., and Atkinson, J. (1978). "Channels in vision: basic aspects," in *Handbook of Sensory Physiology VIII: Perception*, eds R. Held, H. W. Leibowitz, and H.-L. Teuber, (Berlin, Heidelberg: Springer), 3–38.
- Cowan, N. J., Ma, E. J., Cutkosky, M., and Full, R. J. (2003). "A biologically inspired passive antenna for steering control of a running robot," in *Robotics Research. The Eleventh International Symposium*, eds P. Dario and R. Chatila (Wien: Springer), 541–550.
- Crapse, T. B., and Sommer, M. A. (2008). Corollary discharge across the animal kingdom. *Nat. Rev. Neurosci.* 9, 587–600.
- Demir, A., Samson, E. W., and Cowan, N. J. (2010). "A tunable physical model of arthropod antennae," in *IEEE International Conference on Robotics and Automation*, (Anchorage, Alaska, USA, 03.-08.05.2010), 3793–3798.
- Diamond, M. E., Heimendahl, M. V., Knutsen, P. M., Kleinfeld, D., and Ahissar, E. (2008). 'Where' and 'what' in the whisker sensorimotor system. *Nat. Rev. Neurosci.* 9, 601–612.
- Dirks, J.-H., and Dürr, V. (2011). Biomechanics of the stick insect antenna: damping properties and structural correlates of the cuticle. *J. Mech. Behav. Biomed. Mat.* 4, 2031–2042.
- Dürr, V., König, Y., and Kittmann, R. (2001). The antennal motor system of the stick insect *Carausius morosus*: anatomy and antennal movement pattern during walking. *J. Comp. Physiol. A* 187, 131–144.
- Dürr, V., Krause, A. F., Neitzel, M., Lange, O., and Reimann, B. (2007). "Bionic tactile sensor for near-range search, localisation and material classification," in *Autonome Mobile Systeme*, 2007, 20. Fachgespräch Kaiserslautern, 18./19. Oktober 2007 eds K., Berns and T., Luksch (Heidelberg: Springer), 240–246.
- Franz, M., Chahl, J., and Krapp, H. G. (2004). Insect-inspired estimation of egomotion. *Neural Comput.* 16, 2245–2260.
- Gebhardt, M., and Honegger, H.-W. (2001). Physiological characterisation of antennal mechanosensory descending interneurons in an insect (*Gryllus bimaculatus*, *Gryllus campestris*) brain. *J. Exp. Biol.* 204, 2265–2275.
- Hellbach, S., Krause, A. F., and Dürr, V. (2010). "Feel like an insect: a bio-inspired tactile sensor system," in *Proceedings of the International Conference in Neural Information Processing*, ICONIP, (Sydney, Australia).
- Hellbach, S., Otto, M., and Dürr, V. (2011). *Helping a Bio-Inspired Tactile Sensor System to Focus on the Essential*. Berlin, Heidelberg: Springer-Verlag.
- Izhikevich, E. M. (2001). Resonate-and-fire neurons. *Neural Netw.* 14, 883–894.
- Izhikevich, E. M. (2003). Simple model of spiking neurons. *IEEE Trans. Neural Netw.* 14, 1569–1572.
- Izhikevich, E. M., Desai, N. S., Walcott, E. C., and Hoppensteadt, F. C. (2003). Bursts as a unit of neural information: selective communication via resonance. *TINS* 26, 161–167.
- Kaneko, M., Kanayama, N., and Tsuji, T. (1998). Active antenna for contact sensing. *IEEE Trans. Robot. Autom.* 14, 278–291.
- Karniel, A. (2002). Three creatures named 'forward model'. *Neural Netw.* 15, 305–307.
- Kim, D., and Möller, R. (2006). "Passive sensing and active sensing of a biomimetic whisker," in *International Conference on the Simulation and Synthesis of Living Systems*, (Indianapolis, IN: MIT Press), 282–288.
- Krapp, H. G. (2009). Sensory integration: neuronal adaptations for robust visual self-motion estimation. *Curr. Biol.* 19, R413–R416.
- Lamperski, A., Loh, O., Kutscher, B., and Cowan, N. J., (2005). "Dynamical wall-following for a wheeled robot using a passive tactile sensor," in *IEEE International Conference in Robotics and Automation*, ICRA'05, (Barcelona, Spain).
- Lange, O., and Reimann, B. (2005). Vorrichtung und Verfahren zur Erfassung von Hindernissen. German Patent No 102005005230, Germany.
- Lange, O., Reimann, B., Saenz, J., Dürr, V., and Elkmann, N., (2005). "Insectoid obstacle detection based on an active tactile approach," in *Proceedings of the 3rd International Symposium on Adaptive Motion in Animals and Machines*, ed H. Witte (AMAM2005, Ilmenau, Germany), September 25–30.
- Lee, D. D., and Seung, H. S. (1999). Learning the parts of objects by non-negative matrix factorization. *Nature* 401, 788–791.
- Lee, J., Sponberg, S. N., Loh, O. Y., Lamperski, A. G., Full, R. J., and Cowan, N. J. (2008). Templates and anchors for antenna-based wall following in cockroaches and robots. *IEEE Trans. Robot.* 24, 130–143.
- Lewinger, W. A., Harley, C. M., Ritzmann, R. E., Branicky, M. S., and Quinn, R. D., (2005). "Insect-like antennal sensing for climbing and tunneling behavior in a biologically-inspired mobile robot," in *Proceedings of the IEEE International Conference on Robotics and Automation (ICRA'05)*, (Barcelona), April 18–22.
- Manoonpong, P., and Woergetter, F. (2009). Efference copies in neural control of dynamic biped walking. *Robot. Auton. Syst.* 57, 1140–1153.
- Mehta, B., and Schaal, S. (2002). Forward models in visuomotor control. *J. Neurophysiol.* 88, 942–953.
- Miall, R. C., and Wolpert, D. M. (1996). Forward models for physiological

- motor control. *Neural Netw.* 9, 1265–1279.
- Mitchinson, B., Grant, R. A., Arkley, K., Rankov, V., Perkon, I., and Prescott, T. J. (2011). Active vibrissal sensing in rodents and marsupials. *Philos. Trans. R. Soc. Lond. B Biol. Sci.* 366, 3037–3048.
- Monteforti, G., Angeli, S., Petacchi, R., and Minnocci, A. (2002). Ultrastructural characterization of antennal sensilla and immunocytochemical localization of a chemosensory protein in *Carausius morosus* Brunner (Phasmida: Phasmatidae). *Arthropod Struct. Dev.* 30, 195–205.
- Muresan, R. C., and Savin, C. (2007). Resonance or integration? Self-sustained dynamics and excitability of neural microcircuits. *J. Neurophysiol.* 97, 1911–1930.
- Olshausen, B. A., and Field, D. J. (2004). Sparse coding of sensory inputs. *Curr. Opin. Neurobiol.* 14, 481–487.
- Pearson, M. J., Mitchinson, B., Sullivan, J. C., Pipe, A. G., and Prescott, T. J. (2011). Biomimetic vibrissal sensing for robots. *Philos. Trans. R. Soc. Lond. B Biol. Sci.* 366, 3085–3096.
- Pearson, M. J., Pipe, A., Melhuish, C., Mitchinson, B., and Prescott, T. (2007). Whiskerbot: a robotic active touch system modeled on the rat whisker sensory system. *J. Adapt. Behav.* 15, 223–240.
- Poulet, J. F. A., and Hedwig, B. (2002). A corollary discharge maintains auditory sensitivity during sound production. *Nature* 418, 872–876.
- Poulet, J. F. A., and Hedwig, B. (2007). New insights into corollary discharges mediated by identified neural pathways. *Trends Neurosci.* 30, 14–21.
- Prescott, T. J., Diamond, M. E., and Wing, A. M. (2011). Active touch sensing. *Philos. Trans. R. Soc. Lond. B Biol. Sci.* 366, 2989–2995.
- Ritter, H., Martinez, T., and Schulten, K. (1992). *Neural Computation and Self-organizing Maps: An Introduction*. New York, NY: Addison-Wesley.
- Russo, P., Webb, B., Reeve, R., Arena, P., and Patanè, L. (2005). “A cricket-inspired neural network for feedforward compensation and multisensory integration,” in *IEEE Conference on Decision and Control and European Control Conference*, (Seville, Spain).
- Schröder-Schetelig, J., Manoonpong, P., and Wörgötter, F. (2010). Using efference copy and a forward internal model for adaptive biped walking. *Auton. Rob.* 29, 357–366.
- Schütz, C., and Dürr, V. (2011). Active tactile exploration for adaptive locomotion in the stick insect. *Philos. Trans. R. Soc. Lond. B Biol. Sci.* 366, 2996–3005.
- Schwartz, W. R., Kembhavi, A., Harwood, D., and Davis, L. S. (2009). “Human detection using partial least squares analysis,” in *IEEE 12th International Conference on Computer Vision* (Los Alamitos, CA: ICCV), 24–31.
- Solomon, J. H., and Hartmann, M. J. Z. (2006). Robotic whiskers used to sense features. *Nature* 443, 525.
- Staudacher, E., Gebhardt, M. J., and Dürr, V. (2005). Antennal movements and mechanoreception: neurobiology of active tactile sensors. *Adv. Insect Physiol.* 32, 49–205.
- Staudacher, E., and Schildberger, K. (1998). Gating of sensory responses of descending brain neurons during walking in crickets. *J. Exp. Biol.* 201, 559–572.
- Stein, W., and Sauer, A. E. (1999). Physiology of vibration-sensitive afferents in the femoral chordotonal organ of the stick insect. *J. Comp. Physiol. A* 184, 253–263.
- Tsujimura, T., and Yabuta, T. (1992). A tactile sensing method employing force/torque information through insensitive probes. *Proc. IEEE Int. Conf. Robot. Autom.* 1992, 1315–1320.
- Ueno, N., Svinin, M. M., and Kaneko, M. (1998). Dynamic contact sensing by flexible beam. *IEEE-ASME Trans. Mechatronics* 3, 254–264.
- Wang, X. (2003). Persistent neural activity: experiments and theory. *Cereb. Cortex* 13, 1123.
- Webb, B. (2004). Neural mechanisms for prediction: do insects have forward models? *Trends Neurosci.* 27, 278–282.
- Webb, B., Wessnitzer, J., Bush, S., Schul, J., Buchli, J., and Ijspeert, A. J. (2007). Resonant neurons and bushcricket behaviour. *J. Comp. Physiol. A* 193, 285–288.
- Westmark, S., and Dürr, V. (2009). “Functional grouping of descending interneurons that mediate antennal mechanosensory information to motor networks,” in *Proceedings of Göttingen Neurobiological Conference*, (Göttingen, Germany), T20-1C Abstract.

**Conflict of Interest Statement:** The authors declare that the research was conducted in the absence of any commercial or financial relationships that could be construed as a potential conflict of interest.

Received: 13 March 2012; paper pending published: 11 April 2012; accepted: 18 July 2012; published online: 02 August 2012.

Citation: Patanè L, Hellbach S, Krause AF, Arena P and Dürr V (2012) An insect-inspired bionic sensor for tactile localization and material classification with state-dependent modulation. *Front. Neurobot.* 6:8. doi: 10.3389/fnbot.2012.00008

Copyright © 2012 Patanè, Hellbach, Krause, Arena and Dürr. This is an open-access article distributed under the terms of the Creative Commons Attribution License, which permits use, distribution and reproduction in other forums, provided the original authors and source are credited and subject to any copyright notices concerning any third-party graphics etc.



# Active tactile sampling by an insect in a step-climbing paradigm

André F. Krause<sup>1</sup> and Volker Dürr<sup>1,2\*</sup>

<sup>1</sup> Cognitive Interaction Technology – Centre of Excellence, Universität Bielefeld, Bielefeld, Germany

<sup>2</sup> Fakultät für Biologie, Lehrstuhl für Biologische Kybernetik, Universität Bielefeld, Bielefeld, Germany

## Edited by:

Pavel M. Itskov, Champalimaud Foundation, Portugal

## Reviewed by:

Jeremy E. Niven, University of Sussex, UK

Jiro Okada, Nagasaki University, Japan

## \*Correspondence:

Volker Dürr, Fakultät für Biologie, Lehrstuhl für Biologische Kybernetik, Bielefeld University, Universitätsstr. 25, Bielefeld 33615, Germany.  
e-mail: volker.duerr@uni-bielefeld.de

Many insects actively explore their near-range environment with their antennae. Stick insects (*Carausius morosus*) rhythmically move their antennae during walking and respond to antennal touch by repetitive tactile sampling of the object. Despite its relevance for spatial orientation, neither the spatial sampling patterns nor the kinematics of antennation behavior in insects are understood. Here we investigate unrestrained bilateral sampling movements during climbing of steps. The main objectives are: (1) How does the antennal contact pattern relate to particular object features? (2) How are the antennal joints coordinated during bilateral tactile sampling? We conducted motion capture experiments on freely climbing insects, using steps of different height. Tactile sampling was analyzed at the level of antennal joint angles. Moreover, we analyzed contact patterns on the surfaces of both the obstacle and the antenna itself. Before the first contact, both antennae move in a broad, mostly elliptical exploratory pattern. After touching the obstacle, the pattern switches to a narrower and faster movement, caused by higher cycle frequencies and lower cycle amplitudes in all joints. Contact events were divided into wall- and edge-contacts. Wall contacts occurred mostly with the distal third of the flagellum, which is flexible, whereas edge contacts often occurred proximally, where the flagellum is stiff. The movement of both antennae was found to be coordinated, exhibiting bilateral coupling of functionally analogous joints [e.g., left head-scape (HS) joint with right scape-pedicel (SP) joint] throughout tactile sampling. In comparison, bilateral coupling between homologous joints (e.g., both HS joints) was significantly weaker. Moreover, inter-joint coupling was significantly weaker during the contact episode than before. In summary, stick insects show contact-induced changes in frequency, amplitude and inter-joint coordination during tactile sampling of climbed obstacles.

**Keywords:** insect antenna, tactile sense, climbing, inter-joint coordination, active touch, stick insect, *Carausius*

## INTRODUCTION

The tactile sense provides important sensory cues about the near-range environment, with detailed information about shape, location, and surface properties of touched objects, not all of which is easily accessible to other senses, including surface texture and stiffness. Especially animals that operate under difficult lighting conditions, for example nocturnal or aquatic animals, use their tactile sense to acquire vital information about the surrounding environment. Harbor seals use their whiskers to detect subtle currents of water flow, collecting hydrodynamic information about other aquatic animals (prey, predators, or conspecifics; Dehnhardt et al., 1998; Miersch et al., 2011). Shrews use their vibrissae to catch prey in demanding environments, for example hunting insects in complete darkness or underwater. Their tactile sensors allow them to detect the “gestalt” of objects in a scale- and motion-invariant manner (Anjum et al., 2006; Brecht, 2007). Rats explore their environment by rapidly sweeping their long facial whiskers back and forth. This behavior, called “whisking,” is actively controlled relative to the environment and the movement of the animal (e.g., Mitchinson et al.,

2011). By means of whisking, rats can tactually localise objects (Ahissar and Knutsen, 2008) and discriminate fine-scale surface textures (Diamond et al., 2008; Morita et al., 2011).

Elaborate forms of active touch sensing are also found in arthropods (Staudacher et al., 2005). Unlike the mammals mentioned above, arthropods do not sample their environment with patches of specialized hairs, but with a pair of antennae (feelers). Antennae are limbs of the head that, during evolution, have become dedicated sensory organs involved in behavioral functions as diverse as course control, pattern recognition, and tactile localization. For example, lobsters use their antennae for navigation and obstacle avoidance on the ocean floor. They are able to discriminate antennal deflections due to water currents from deflections caused by obstacle contacts (Barnes et al., 2001). Flying insects, for example locusts, sense the airflow by measuring the deflection of their antennae (Gewecke and Heinzl, 1980; Heinzl and Gewecke, 1987). Cockroaches use the passive deflection of their long feelers for behaviors like fast wall tracking (Camhi and Johnson, 1999). During tactile near-range exploration, object localization and pattern recognition are frequently

observed. Active antennal sensing increases the likelihood of detecting obstacles (Krause and Dürr, 2004). Active sensing is a common strategy among animals for improving information gain (Prescott et al., 2011). Honeybees, for example, are able to discriminate the microtexture of flower petals in the range of few tens of microns (Kevan and Lane, 1985) or artificial gratings (ca. 150  $\mu\text{m}$ ) (Erber et al., 1998) by tactile scanning of surfaces with their antennal tip. Bees can also discriminate patterns visually, but on considerably larger scale (Srinivasan, 2010). Cockroaches can distinguish between predators and conspecifics by means of antennation, i.e., repetitive antennal touching (Comer et al., 2003) and show tactually induced turning toward- and climbing of objects (Okada and Toh, 2000, 2006). Stick insects continuously move their antennae during walking and sample the space ahead of the walking direction. Because stick insect antennae are approximately the same length as the front legs, touched obstacles are within reach of the front legs. A re-targeting of ongoing leg swing movements to antennal contact position was described by Schütz and Dürr (2011) and shows that the antennae provide short-latency information for adaptive locomotion. Removing the antennae lowers the animal's climbing performance on square obstacles (Dürr et al., 2003). These examples show the relevance of antennal information for pattern and shape recognition, but also for context-dependent adaptation of motor behaviors. Despite its relevance, neither the spatial sampling patterns nor the kinematics of antennal tactile sampling movements of arthropods are well understood. In particular, studies on shape-dependent differences and touch-induced changes in the movement pattern of antennae are very few. Whereas it is clear that insects use antennal tactile cues for decisions about motor acts dependent on location and distance of touched objects (Bläsing and Cruse, 2004a; Harley et al., 2009), almost nothing is known about timing and coupling of antennal joints during tactile sampling, nor about which part of the antennal flagellum is used for sampling the obstacles in order to acquire the information used for decision-making.

In several stick insect species, the location and orientation of both antennal joint axes are known (Dürr et al., 2001; Mujagic et al., 2007), allowing for inverse kinematic calculation of antennal joint angles in walking and climbing insects (Krause and Dürr, 2004). As in all higher insect orders, the antenna of the stick insect *Carausius morosus* consists of three functional segments: two short, proximal segments called scape and pedicel, and a long flagellum (Figure 1D). The antenna is articulated by two revolute joints: the head-scape joint (HS joint) and the scape-pedicel joint (SP joint) (Dürr et al., 2001; Staudacher et al., 2005). The long flagellum is almost straight and sufficiently stiff not to bend during self-motion. This simplifies the computation of contact points with obstacles, e.g., by application of intersection algorithms from computer graphics. So far, detailed analysis of antennal inter-joint coordination exist for active tactile exploration during locomotion (Krause et al., 2012) and for antennal sampling of simple objects (Schütz and Dürr, 2011). The latter studies focussed on unilateral antennal movements and on the sampling of a nearly one-dimensional object (vertical rod). Here, we investigate unrestrained bilateral antennal tactile sampling movements in a step-climbing paradigm,

involving repeated antennal contacts of both antennae. First, we show the influence of object features on antennal contact patterns and the distribution of contacts along antennal parts, revealing a functional regionalization. Second, we show changes in bilateral antennal coordination, antennal working-range, and cycle frequency prior to and during tactile sampling of the climbed obstacle.

## MATERIALS AND METHODS

### ANIMAL PREPARATION

All experiments were carried out on adult female stick insects of the species *Carausius morosus* (de Sinéty, 1901) that were bred in a laboratory culture at Bielefeld University. Five animals were prepared for kinematic analysis by means of marker-based motion-capture. For this, animals were labelled with four custom-made retro-reflective foil markers (Scotchlight M3SS-28 8850, 3M Corp., St. Paul/MN, USA). Markers were placed near the caudal margin of the mesonotum, on the head between the eyes, and on the left and right flagellum of the antenna. The antennal markers were placed on the first third of the flagellum, where the antenna is sufficiently stiff to avoid bending due to the mass of the marker. Markers were fixed to the insect cuticle with a drop of translucent nail polish, except for the antennal markers. The latter were attached by a knot around the flagellum. Markers were approximately 1 mm in diameter. The neck joint and the joint between the pro- and mesothorax were fixed with hot beeswax, keeping the body axis straight during locomotion and, thus, increasing the accuracy of marker tracking. Fixation of these joints did not impair climbing ability of the animals. It did, however, reduce the turning tendency such that animals were less likely to turn although they were still able to do so.

### MOTION CAPTURE

Animals walked along a 40 mm wide footbridge while being filmed from above, and via a slanted mirror from the side. Within the field of view of the camera, the footbridge was blocked by a step of 19, 32, 47, or 66 mm height (Figure 1). Step heights were randomized. Walking trials of five animals were recorded, with at least five trials per animal and step height. Videos were recorded using an infrared-sensitive digital video camera (Basler A602f, Ahrensburg, Germany) equipped with a 70 mm zoom lens, operated at 100 frames per second. Camera exposure was synchronized with a custom-built infrared flash light. The setup was painted in black and surrounded by black drapery. The room was darkened except for a red light, just bright enough for handling of the insects. The camera was calibrated with the "Caltech Camera Calibration Toolbox for Matlab" (Bouguet, 2005), using Matlab (MathWorks Inc., Natick/MA, USA). Videos were captured via fire-wire (IEEE 1394) by use of custom-written frame grabber software (Christoph Schütz, Bielefeld University) and stored on a standard personal computer. All videos were saved as avi-files and cut using the software VirtualDub ([www.VirtualDub.org](http://www.VirtualDub.org)). Video analysis was implemented in Matlab (VideoTrack M, written by Christoph Schütz, Bielefeld University), based on software as described by Zakotnik et al. (2004). In a first step, potential marker coordinates were detected using a standard image processing sequence (thresholding, dilating, and eroding with

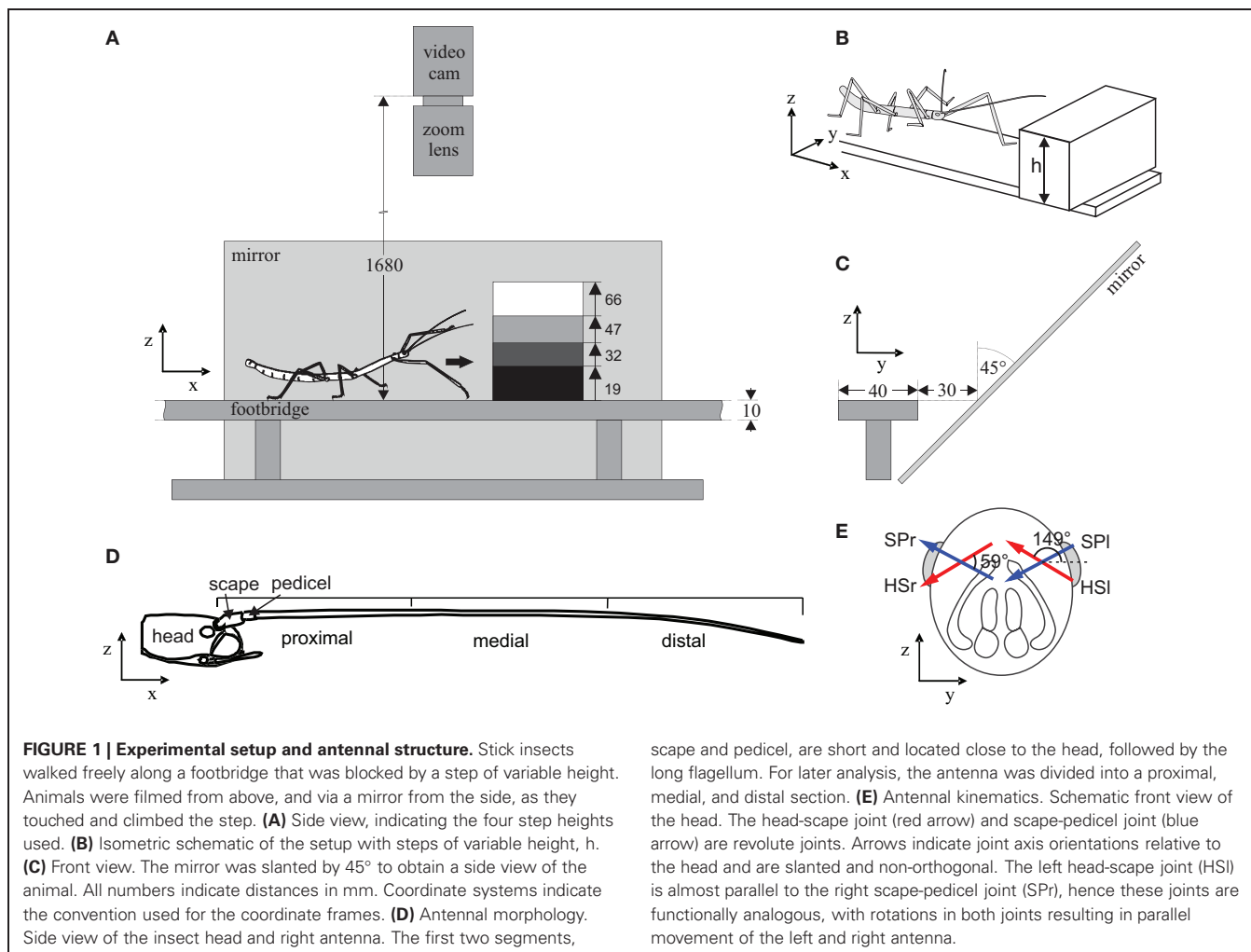


**FIGURE 1 | Experimental setup and antennal structure.** Stick insects walked freely along a footbridge that was blocked by a step of variable height. Animals were filmed from above, and via a mirror from the side, as they touched and climbed the step. **(A)** Side view, indicating the four step heights used. **(B)** Isometric schematic of the setup with steps of variable height,  $h$ . **(C)** Front view. The mirror was slanted by  $45^\circ$  to obtain a side view of the animal. All numbers indicate distances in mm. Coordinate systems indicate the convention used for the coordinate frames. **(D)** Antennal morphology. Side view of the insect head and right antenna. The first two segments,

scape and pedicel, are short and located close to the head, followed by the long flagellum. For later analysis, the antenna was divided into a proximal, medial, and distal section. **(E)** Antennal kinematics. Schematic front view of the head. The head-scape joint (red arrow) and scape-pedicel joint (blue arrow) are revolute joints. Arrows indicate joint axis orientations relative to the head and are slanted and non-orthogonal. The left head-scape joint (HSI) is almost parallel to the right scape-pedicel joint (SPr), hence these joints are functionally analogous, with rotations in both joints resulting in parallel movement of the left and right antenna.

subsequent clustering). Then the root marker of the body model (see below) was marked manually in the first frame and tracked by a nearest-neighbor algorithm.

### KINEMATIC ANALYSIS

Body posture, i.e., segment orientations and antennal joint angles were determined from marker coordinates frame by frame, using a model-based optimization algorithm (Zakotnik et al., 2004) implemented in Matlab (VideoTrack M). Time sequences of coordinates and joint angles were calculated using a Hidden Markov Chain algorithm based on 100 independent optimization runs per frame (Zakotnik and Dürr, 2005). Body models for kinematic analysis were established individually per animal. For this, segment lengths and marker locations along the segments were measured by use of a calliper, achieving an accuracy of at least 0.1 mm. Body models consisted of a kinematic chain including the “body axis” (mesothorax marker to head marker) and an antenna, consisting of the segments scape and pedicel-flagellum. Two such kinematic chains were used for each animal, one for the left and another for the right antenna. As both body models contain the body axis, a discrepancy of the calculated body axis orientation could arise due to independent optimization

procedures. A comparison of the pitch and yaw angles of the body axis of each solution served as a measure for the robustness of our motion capture algorithm. Ideally, the differences between the solutions should be zero. Indeed, deviations were always small and the median differences of pitch and yaw angles were well below  $1^\circ$  (pitch: median  $-0.15^\circ$ , range  $-0.7$  to  $0.6^\circ$ ; yaw: median:  $0.65^\circ$ , range  $-1.4$  to  $2.3^\circ$ ).

The body models contained 6 degree of freedom of rotation per animal and frame: azimuth and elevation of body axis orientation and two joint angles per antenna. Movements of the antennal joints were expressed such that positive angles denote levation above the horizontal plane and negative angles denote depression. Note that the antennal joint axes of stick insects are slanted (Mujagic et al., 2007), such that levation always has a sideward component. Following the notation of Dürr et al. (2001), oblique levation of the SP joint is caused by adductor muscles of the scape and, thus, is a mediad adduction of the pedicel. Similarly, levation of the HS joint is accompanied by a lateral abduction of the scape. Here, antennal joint axes were defined as described in Krause and Dürr (2004). Owing to the mirror symmetry of the head and the slanted antennal joint axes, homologous antennal joints on both sides of the head do not move the antenna

in the same direction. Rather, it turns out that the left HS joint affects pointing-direction of the left antenna in almost the same way as the right SP joint affects pointing-direction of the right antenna. To emphasize their parallel action, we call bilateral pairs of HS and SP joints “functionally analogous.”

Assuming that the flagellum remained almost straight between the antennal joints and the marker, antennal contacts with the obstacle were computed with a ray-box intersection algorithm (Woo, 1990). Note that this procedure neglects curvature of the flagellum in contact with the obstacle and may lead to the situation that an elongate contact zone between the flagellum and an obstacle surface gets reduced to a single point (see Results section on object contacts for further considerations). To compensate for small motion tracking errors, the intersection box was expanded by 1.5 mm. This guaranteed that almost all contacts were identified, as verified by inspection. Contacts with an obstacle, i.e., the step, were distinguished into wall, edge and top contacts, where wall and top contacts correspond to the two surfaces that could be touched. Edge contacts were classified as such, if they were inside a cylindrical bounding region with radius 3 mm around the edge.

#### DATA ANALYSIS

Based on the distinction of antennal contact types, time courses or measured variables were divided into four episodes: an episode *before* antennal contacts, a *wall* contact episode beginning with the first wall contact and ending with the first edge contact, an *edge* contact episode beginning with the first and ending with the last edge contact, and an *after*-episode beginning with the end of the last edge contact. If both left and right antenna made wall or edge contacts, the average of those contact times was used to delimit the *wall* and *edge* episodes. Episodes with less than 25 frames (250 ms) duration were excluded from further analysis, because a minimum amount of data was required to reliably measure cycle frequency and working-range per episode.

Working-ranges of antennal joints in the four episodes were measured as the 5–95% quantile ranges of the joint angle distribution. The baseline of a working-range was defined as the 50% quantile, equivalent to the median joint angle. Cycle frequencies were estimated using FFT, by calculating the weighted average over the amplitude spectrum in the range from 0 to 10 Hz. Patterns of coordination between antennal joints were analyzed in two ways: by cross-correlation of time courses or by a cycle-to-cycle phase analysis. Antennal coordination was calculated for six pairs of joints, divided into three groups: ipsilateral (e.g., left HS joint with left SP joint), contralateral (e.g., left HS joint with right HS joint), and functionally analogous joints (e.g., left HS joint with right SP joint). For cycle-to-cycle analysis of phase relationships between antennal joints, we used the Matlab toolkit “Peakfinder” to extract local maxima in the time courses (by Nate Yoder, <http://www.mathworks.com/matlabcentral/fileexchange/25500-peakfinder>). Peakfinder extracts local peaks from noisy data using a threshold,  $p$ , to determine whether a peak is significantly larger or smaller than the surrounding data. An optimal parameter ( $p = 8$ ) was obtained with the goal to minimize the spread between peak distances. This was based on the assumption

of regular periodic antennal movements with almost constant frequency per episode. Only local maxima were extracted, and cycle periods thus concern intervals between two local peak joint angles.

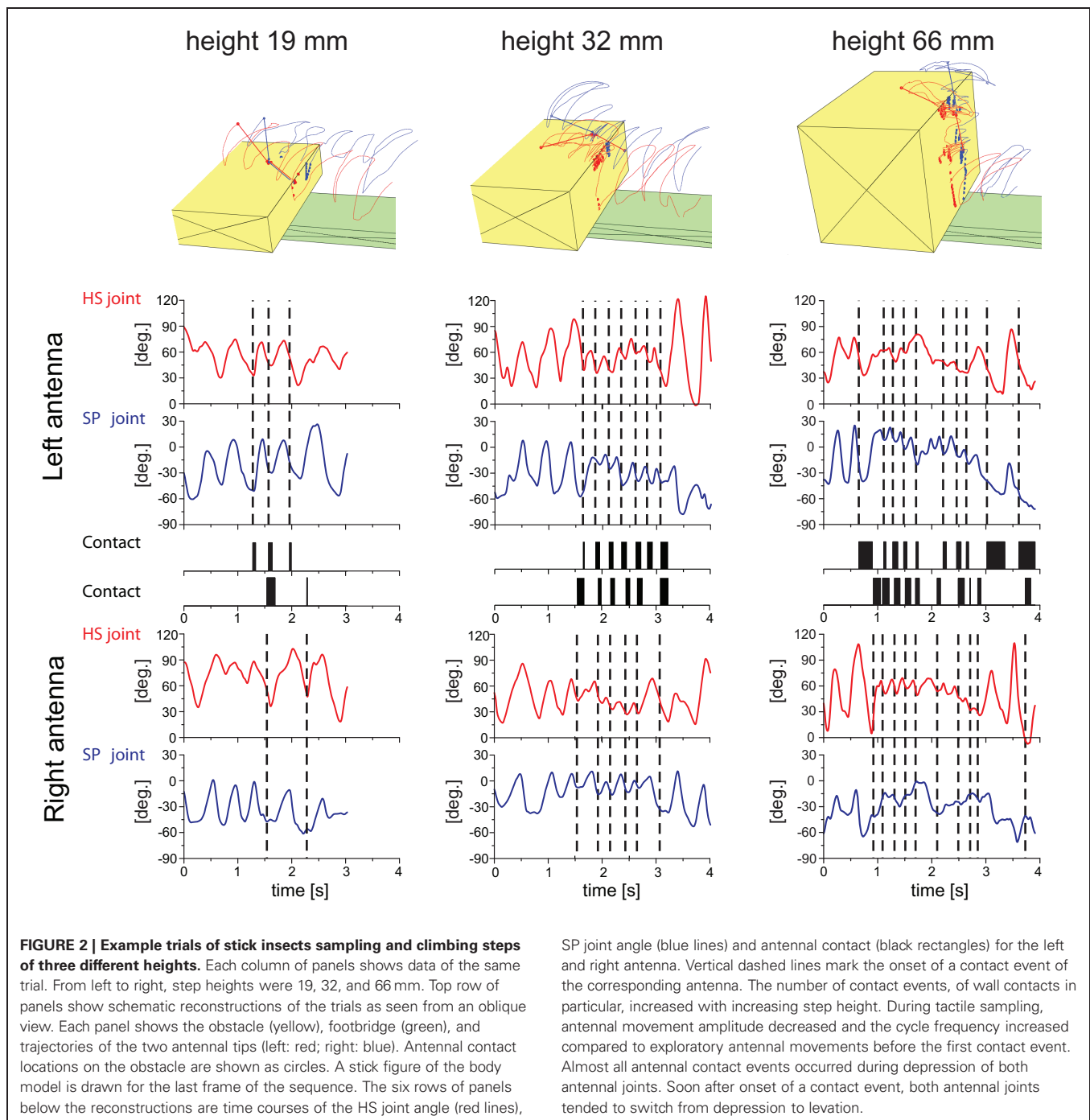
Statistics were calculated with the statistics toolbox of Matlab, and a significance level of 5% was used throughout this study. Data from  $n = 5$  animals were used for statistical tests, by averaging extracted parameters, for example antennal working-range, over the five trials per animal. Throughout the text, the following episode pairs were compared for significant differences between kinematic parameters: *before* vs. *wall*, *wall* vs. *edge* and *edge* vs. *after*. In case of multiple comparisons of medians, e.g., in the form of multiple Wilcoxon tests, the significance threshold was Bonferroni-corrected by dividing 0.05 by the number of comparisons (e.g., 0.016 for three comparisons).

## RESULTS

### OVERALL OBSERVATIONS

Stick insects readily walked along the footbridge and climbed the obstacles. As reported in earlier studies (Dür et al., 2001), all animals showed active tactile exploration behavior by continuously and rhythmically moving both of their antennae during locomotion. Climbing was always accompanied by repeated, bilateral antennation of the obstacle, i.e., tactile sampling with both antennae. Here we report how climbing insects sample the obstacle climbed, and how the antennal movement pattern changes during tactile sampling.

Video-recordings of climbing sequences lasted 2–6 s, mainly depending on the height of the obstacle climbed. Four trial conditions were compared, differing in the height of the obstacle, only. The data-set reported in this study comprises a total of 100 trials, with five trials from five animals per condition. All animals used both antennae for tactile sampling with no evidence for a side preference in any of them. Obstacles were sampled on the vertical wall and at the upper edge of the step. **Figure 2** shows three representative trials, giving an overall impression of the antennal contact patterns on the obstacle surface, spatial trajectories of both antennal tips, and joint angle time courses of all four antennal joints. In the three trials shown, climbing was accompanied by antennation involving 5, 13, and 20 antennal contacts with the low, middle, and high obstacle, respectively. During tactile contact sequences, the joint angle time courses often revealed marked changes in amplitude and cycle frequency. In the trials shown in **Figure 2**, these changes are very subtle in the case of the lowest obstacle but obvious in the other two cases, where antennal movement amplitude decreased and cycle frequency increased during tactile sampling. Antennal contacts often occurred during downward antennal movement, i.e., during depression of both antennal joints. In the examples shown in **Figure 2**, this can be seen by the dashed vertical lines that mark the onset of contact events. In nearly all cases, the antennal joint angle was decreasing when the contact occurred, indicating depression of both scape and pedicel. Note that, in most of the contact events shown, both antennal joint angles reach a local minimum soon after onset of contact, indicating that all antennal joints tended to switch to levation upon tactile contact. This is similar to the situation in unilateral sampling of vertical objects as reported by



Schütz and Dür (2011). In 67% of all trials, we found an intriguing similarity of joint angle time courses between the HS joint on one side with that of the contralateral SP joint during the wall contact episode (criterion: maximum cross-correlation coefficient  $>0.5$  within  $\pm 0.25$  s time-lag; see **Figure 9**). An example for this can be seen in the right trial shown in **Figure 2**, where the overall structure of the SP joint angle time courses bear less similarity with the joint angle time course of the ipsilateral HS joint than with that of the contralateral HS joint. As the joint axes of

contralateral pairs of HS and SP joints are almost parallel, they are essentially functionally analogous joints. Synchronous movement of functionally analogous joints maintains parallel pointing directions of both antennae.

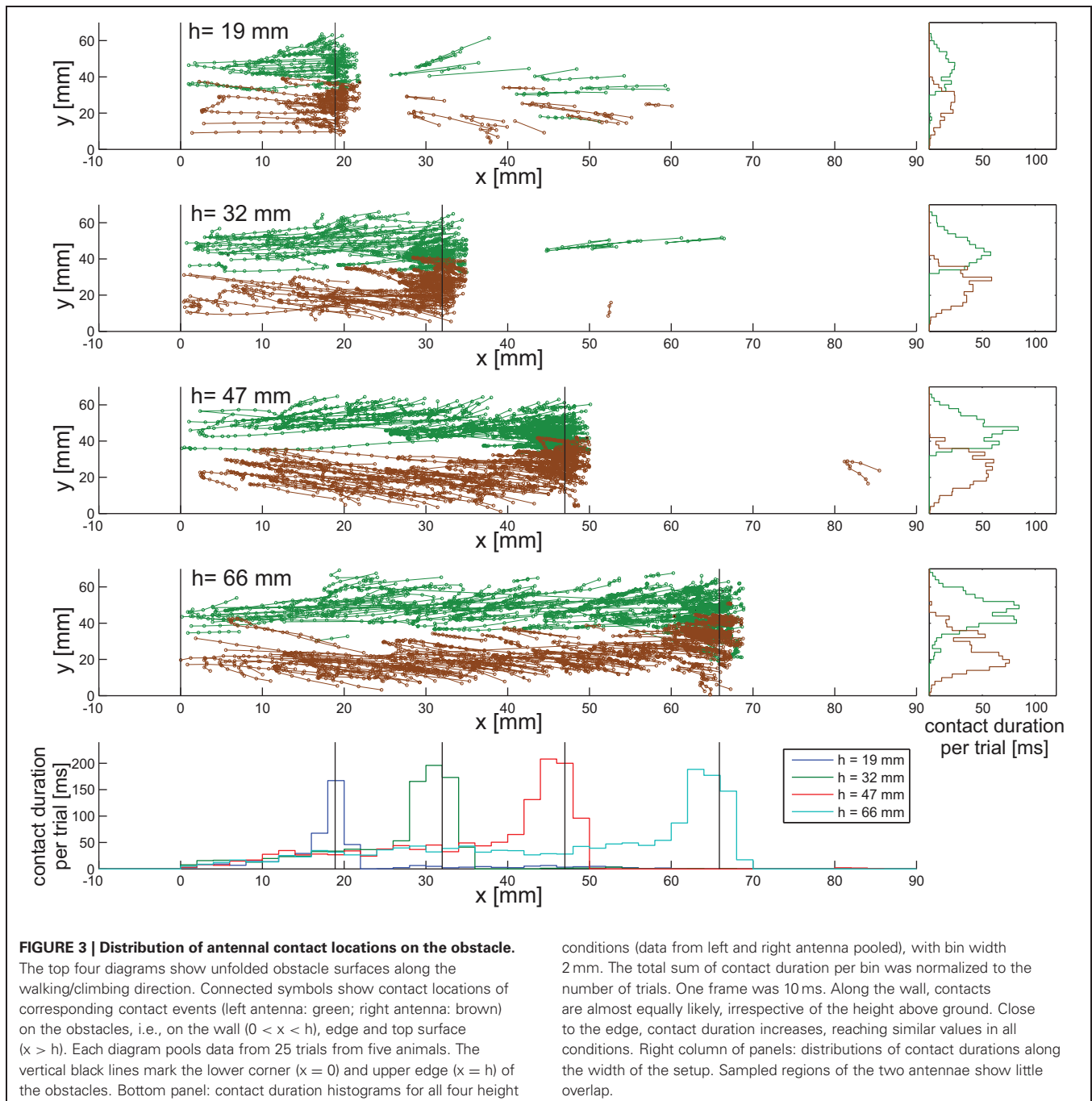
In the following, we analyse these general observations in more detail, beginning with the spatial pattern of contact locations, followed by the changes in amplitude and cycle frequency and by quantification of inter-joint coupling before, during and after tactile sampling.

### CONTACT PATTERNS ON OBSTACLES

To understand how and where stick insects touched the obstacle during climbing, we estimated antennal contact locations by calculating the intersection point of the vector describing the antennal pointing-direction with the obstacle. If the distance of this intersection point from the antennal base was shorter than the length of the antenna, we assumed that a contact event had occurred. This procedure neglects bending of the antennal flagellum and, as a result, introduces a bias of the estimated location toward the direction of movement. This is because antennal

movement will always “drag” the true contact point behind the tangent to the curvature at the antennal base.

**Figure 3** shows the distribution of antennal contacts on the surface of the four obstacles used. Individual antennal contact events with a step lasted several frames of the video recording, forming streak-like patterns on the vertical wall of the obstacle. The prevalent direction of the streaks is upward and slightly lateral, i.e., toward the margin of the obstacle. This indicates that the antennae were levated during wall contacts. The lateral component coincides with the movement direction caused by HS



joint levation. In all four conditions, density of contacts increased near the edge of the step, suggesting that the edge was an “interesting feature” to the animal. This is mirrored by the contact duration histograms in **Figure 3**. All four of these histograms have a broad peak near the edge and a broad, shallow tail at lower contact heights on the wall. The tails indicate that wall contacts are almost equally likely irrespective of height above ground. Close to the edge, contact duration increased to approximately 200 ms per trial, equivalent to 20 video frames. The apparent lack of contact events on the top surface is partly due to sampling bias, as not all trials had a distinctly long post-contact episode. Contact histograms along the width of the obstacles, i.e., the *y*-direction, show that both antennae sample different regions with very little overlap. In fact, the contact patterns reveal a region in the middle of the wall that is almost devoid of antennal contacts. This suggests that the overlap of the histograms is mainly caused by edge contacts. Means and standard deviations of the distributions are given in **Table 1**. Mean locations of left and right

antennal contacts were more than two standard deviations apart. More overlap may be expected for animals without fixed neck and prothorax-mesothorax joints.

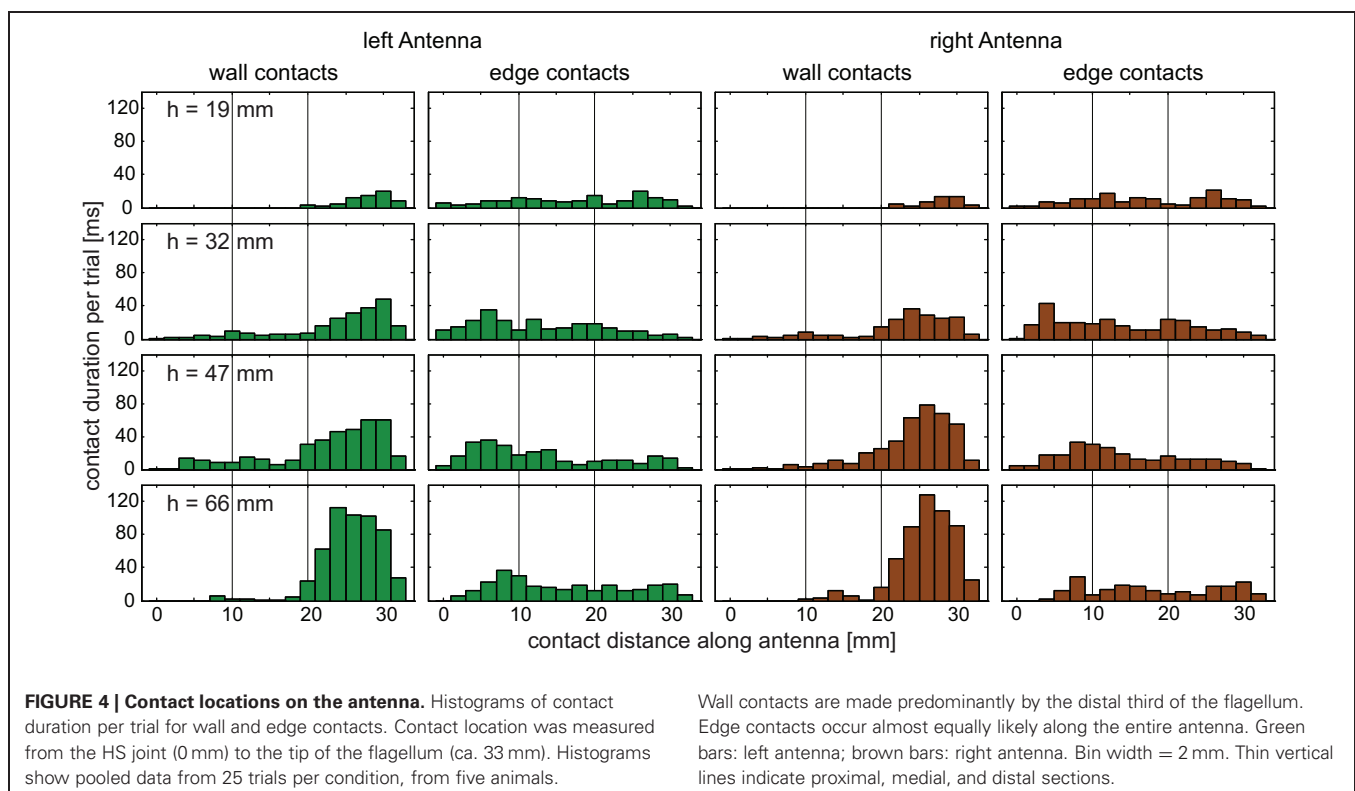
### CONTACT LOCATIONS ON THE ANTENNA REVEAL FUNCTIONAL REGIONALIZATION

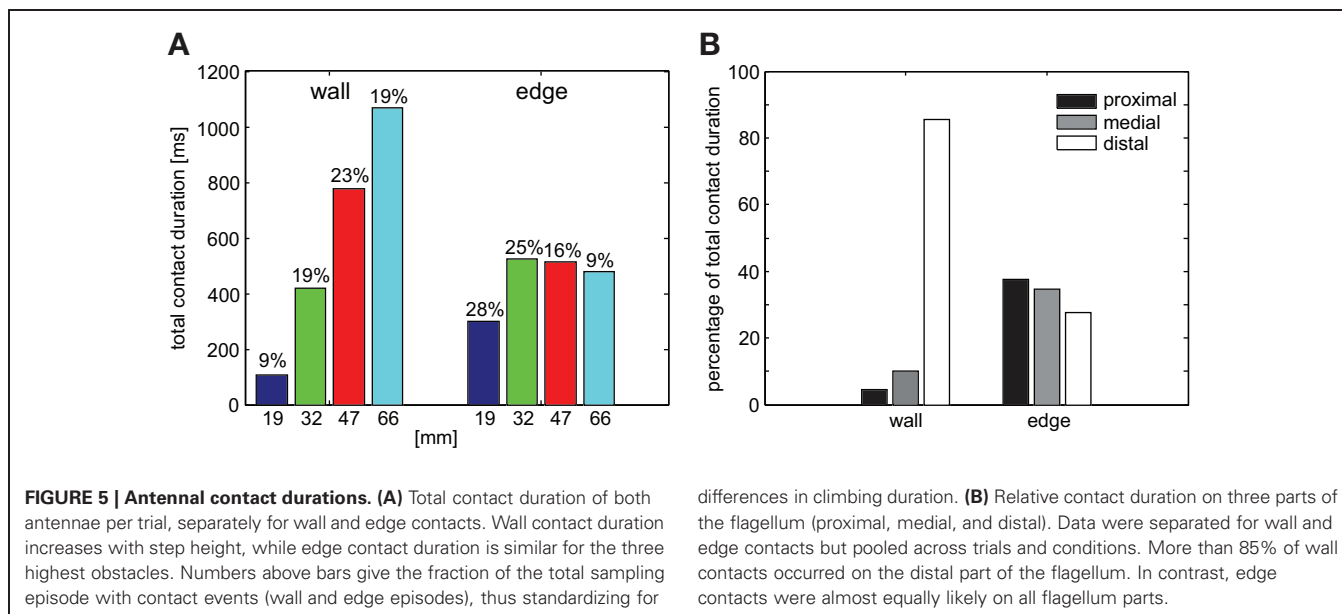
For determining which sensillae were potentially involved in detecting contact events, we were interested to map the distribution of antennal contacts along the antenna. There was a clear difference between the distributions of wall contacts and edge contacts, but also among the wall contact distributions on the four obstacles (**Figure 4**). Whereas for wall contacts, the distal third of the flagellum spent much more time in contact with the obstacle than the proximal two-thirds, contact durations of edge contacts were nearly equal at all locations along the flagellum (**Figure 5B**). More than 85% of wall contact duration involved the distal third of the antenna.

The total duration of wall contacts per trial increased with step height, while the total duration of edge contacts was nearly the same for the three highest obstacles (**Figure 5A**). Edge contact duration dominated wall contact duration for the two lowest obstacle heights (19 mm and 32 mm). Considering that higher obstacles take longer to be climbed than lower obstacles, we also determined the fraction of the entire tactile sampling episode spent in wall or edge contacts (numbers in **Figure 5A**). In case of the three highest obstacles, this fraction was 19–23% for wall contacts, suggesting that the increase in total contact duration was proportional to the increase in duration of the sampling episode (time from onset of first wall contact to end of last edge contact). In case of edge contacts, the fraction decreased with the

**Table 1 | Mean and standard deviation of contact locations along the *y*-axis in mm.**

Step	Left antenna		Right antenna	
	Mean	SD	Mean	SD
19	44.1	8.0	24.3	7.1
32	45.1	6.9	24.6	7.5
47	46.1	6.8	24.2	7.9
66	46.4	8.3	24.2	8.9





height of the obstacle, as expected if the edge contact episode was equally long but the total sampling episode became longer with obstacle height. Individual contact event durations did not differ significantly between wall and edge episodes, although wall contacts tended to be slightly longer (wall:  $134 \pm 82$  ms; edge:  $115 \pm 84$  ms, Wilcoxon's rank sum test on mean values per animal,  $n = 5$ ,  $p = 0.31$ ).

#### ANTENNAL WORKING-RANGE AND CYCLE FREQUENCY CHANGE DURING TACTILE SAMPLING

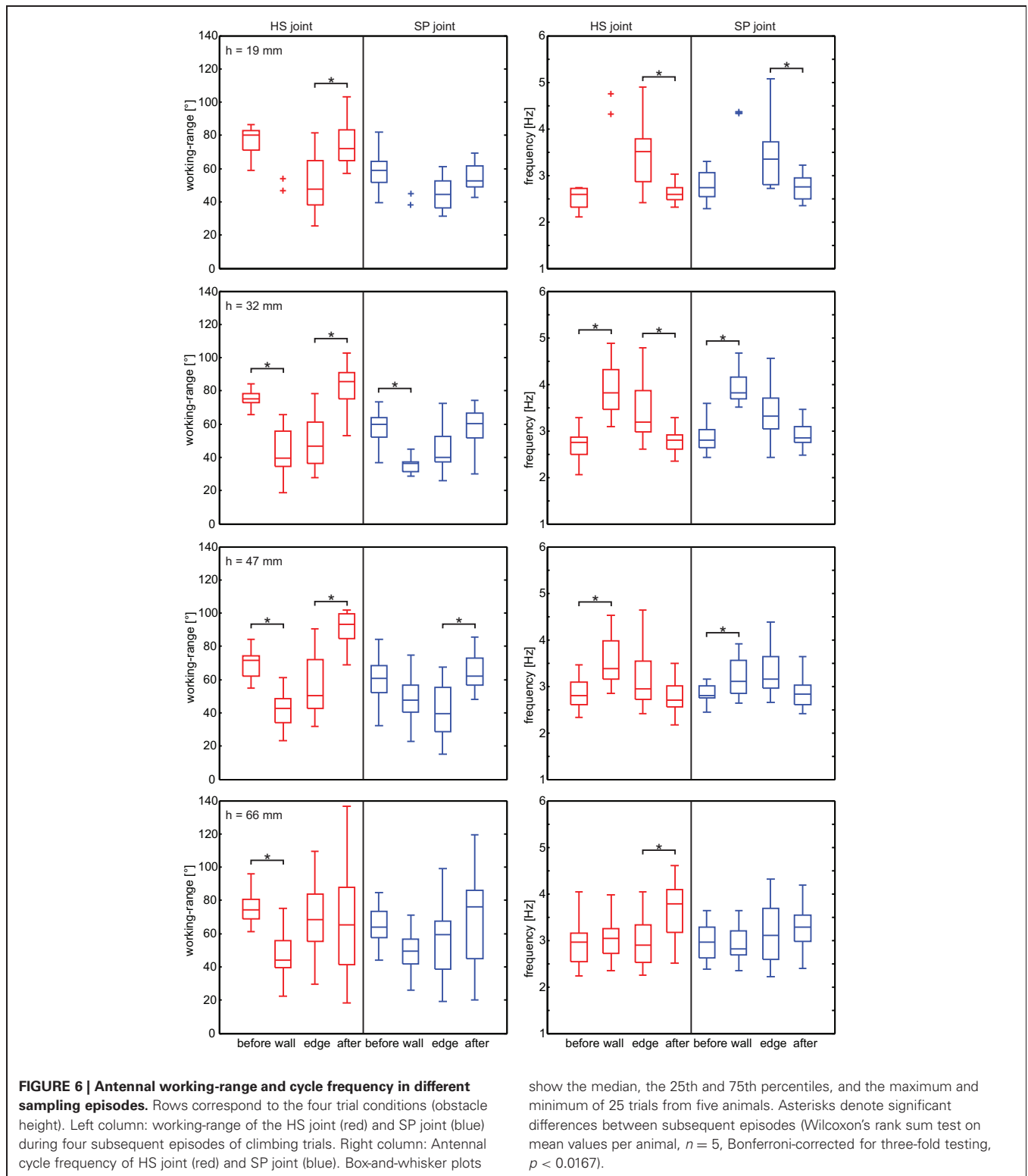
Next, we tested how the overall kinematics of the antennal movement pattern changed during tactile sampling of the obstacle. To account for potential differences between wall contacts and edge contacts, we determined the antennal working-range and cycle frequency of both antennal joints during four subsequent trial episodes. These were: (1) before first antennal contact, (2) during the wall contact episode, (3) during the edge contact episode, and (4) after the edge contact episode (Figure 6). Note that antennal wall contacts for the lowest 19 mm obstacle were rare. Only two trials from two animals had wall contacts. While sampling the obstacle wall, the working-range of the HS joint decreased significantly for obstacle heights 32, 47, and 66 mm (Wilcoxon's rank sum test on mean values per animal,  $n = 5$ , Bonferroni-corrected:  $p < 0.0167$ ). A significantly reduced working-range was also found in the SP joint for the 32 mm obstacle. After the last edge contact, the working-range of the HS joint increased significantly for climbing all but the highest obstacle. In the SP joint, the same effect was statistically significant only for height 47 mm. Additionally, the entire working-range of the antennal joints shifted during climbing, revealing a significant dorsal shift during the wall contact episode in both joints (Figure 8; Wilcoxon's rank sum test on mean values per animal,  $n = 5$ ; HS:  $10^\circ$ ,  $p = 0.016$ ; SP:  $12^\circ$ ,  $p = 0.0079$ ).

As antennal working-range decreased, cycle frequency tended to increase in both joints, though this effect was statistically

significant only for obstacle heights 32 and 47 mm. Similarly, cycle frequency tended to decrease after the last edge contact, with median values close to those of the pre-contact episode. This effect was statistically significant when climbing low obstacles (HS joint: 19 and 32 mm; SP joint: 19 mm). When climbing the highest obstacle, animals on average did not increase cycle frequency, although an increase was evident in some trials (see Figure 2). A possible reason might be that, due to the strong inclination of the body axis, the vertical obstacle wall essentially gets treated like a horizontal surface relative to the animal's body coordinate system. In Figure 6, data from left and right antenna were pooled because no systematic directional bias could be observed. Differences between left and right antennal working-range, base line, and frequency were tested and none of them were significant (Wilcoxon's rank sum test on mean values per animal,  $n = 5$ ,  $p > 0.33$ ).

If animals climb obstacles, changes in heading and body axis elevation must be expected. Indeed, apart from changes of the antennal movement pattern, significant changes in body axis orientation were observed (Figure 7). As the neck joint was immobilized in these experiments, body axis orientation was equal to the head orientation and, thus, affected the resting posture of the antennae. The body axis orientation was expressed as yaw and pitch angles, equivalent to polar coordinates (azimuth and elevation, respectively). As expected, the body pitch angle continuously decreased during climbing, and the magnitude of this decrease depended on the height of the obstacle. Significant changes in body pitch angle were found for all obstacle heights but not between all episode pairs (see Figure 7). As the body axis became increasingly inclined, the body yaw angle became more variable: Whereas low steps were climbed with little or no change in yaw angle, its range of variation strongly increased for higher obstacles (height 47 and 66 mm in Figure 7).

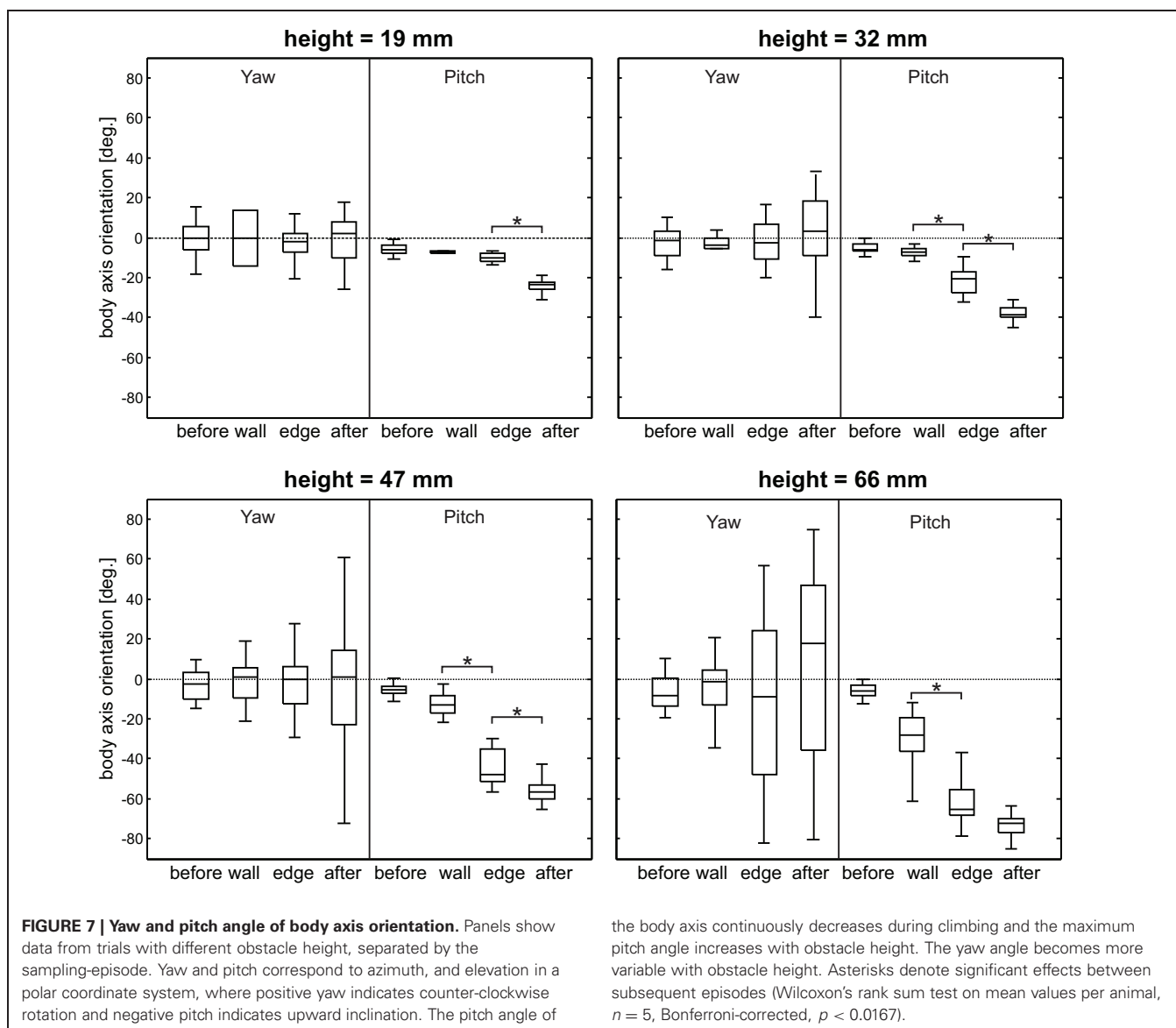
Taken together, the kinematic changes of antennae and body axis are summarized in Figure 8, pooling across all animals



and obstacle heights. During tactile sampling, the joint angle working-ranges significantly shifted upward and decreased in width. At the same time, the cycle frequencies of both joints increased.

**ANTENNAL INTER-JOINT COUPLING CHANGES DURING TACTILE SAMPLING**

Finally, we wanted to know whether and how the coordination between antennal joints changed during tactile sampling. For this,

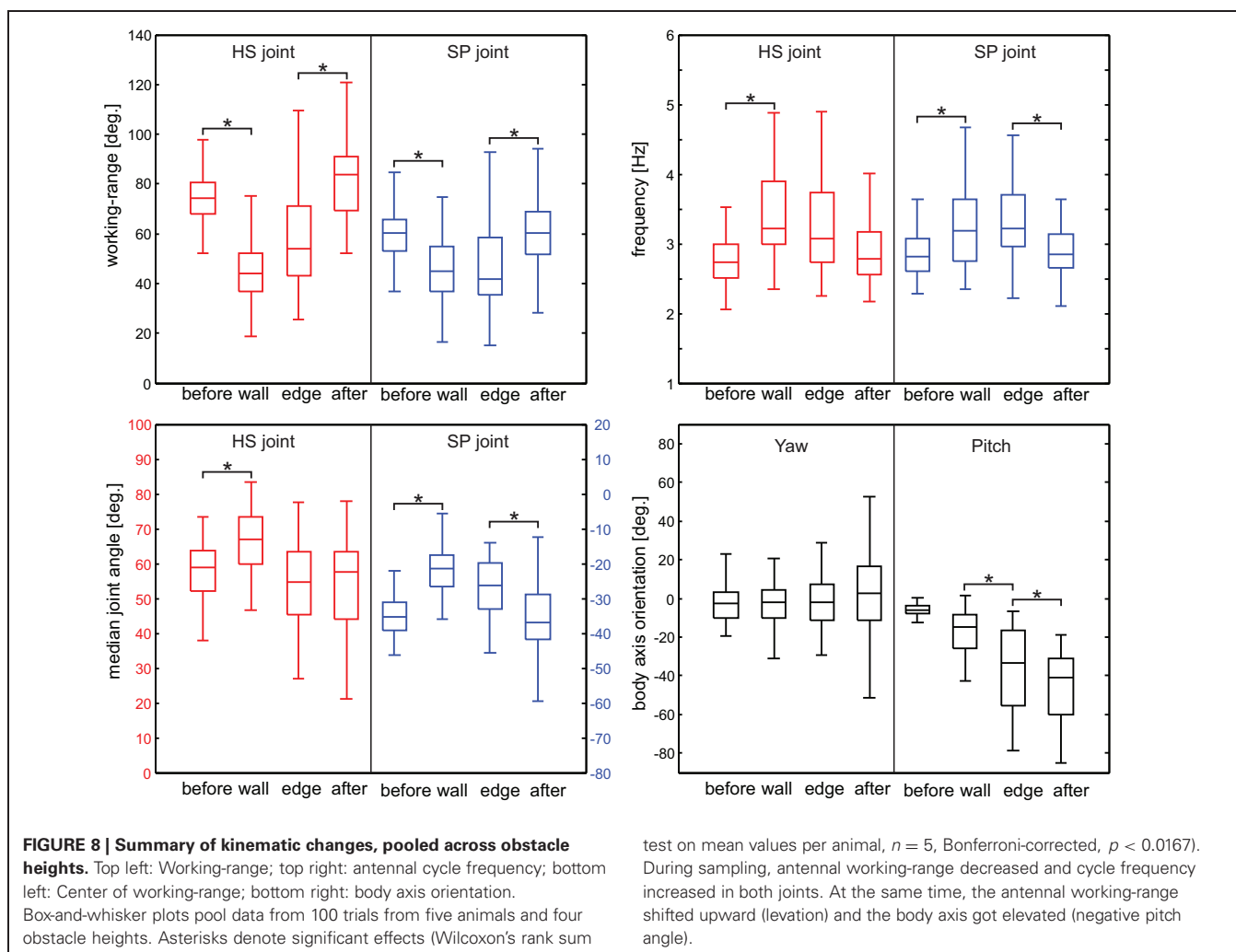


we considered both ipsilateral and contralateral inter-joint coupling, and pairs of antennal joints were grouped into three types: ipsilateral joints (HS-L:SP-L, HS-R:SP-R), contralateral homologous joints (HS-L:HS-R, SP-L:SP-R), and contralateral, functionally analogous joints (HS-L:SP-R, HS-R:SP-L). Functionally analogous joints are joints with nearly parallel joint axes, such that rotation about their joint axis results in nearly the same antennal movement. For example, the left HS joint in *C. morosus* is almost parallel to the right SP joint (Dürr et al., 2001; Mujagic et al., 2007).

Inter-joint coupling was measured in two ways. The first measure quantified the overall correlation of two joint angle time courses during a certain trial episode. The other measure analysed the cycle-to-cycle phase relationship between the two antennal joints, quantifying the timing of local extrema of their joint angle time courses. **Figure 9** shows the distribution of correlation coefficients for the four trial episodes, pooling across all

obstacle heights. During the before-contact episode, all types of joint pairs showed correlation coefficients significantly different from zero (Wilcoxon's rank sum test on mean values per animal,  $n = 5$ ,  $p = 0.0079$ ). During the two sampling episodes with wall and edge contacts, the coordination changed and the median correlation coefficients were close to zero, except for those of contralateral, functionally analogous joints (Wilcoxon's rank sum test on mean values per animal,  $n = 5$ ,  $p = 0.0079$ ). This suggested that functionally analogous joints on both sides of the body midline stay coordinated during tactile sampling.

Whether correlation coefficients close to zero were due to the lack of a fixed coordination pattern or rather due to a  $90^\circ$  phase shift could not be distinguished without considering non-zero phase lag between the joints. Therefore, **Figure 9B** shows sliding-window cross-correlograms of a representative trial. For ipsilateral coordination of antennal joints, the correlogram showed a horizontal white band at small negative lag



values. This is typical for non-contact episodes of tactile exploration (Krause et al., 2012). This indicated that the alternating movement pattern of the SP joint lead that of the ipsilateral HS joint. During the wall contact episode, the phase between HS and SP joint was less stable, revealing a phase shift compared to the before-contact episode (Figure 9 with a gray to black band where previously was a white band). For contralateral homologous joints the correlogram shows a drifting phase relationship. For contralateral, functionally analogous joints, the initial white band persists well into the tactile sampling episodes, indicating that their coupling changes only little in response to contact events.

The quantitative analysis of cycle-to-cycle inter-joint coupling (Figure 10) revealed similar results as the simple correlation analysis in Figure 9A for contralateral joints (both homologous and functionally analogous joints), and emphasized the role of a systematic phase shift during tactile sampling in case of ipsilateral joints. The phase relationship between peaks revealed consistent and strong coupling between all joint pairs before antennal contact (Rayleigh test,  $p < 0.0001$ ) with a phase lag between  $338^\circ$  and  $361^\circ$  (Figure 10, Table 1). During tactile sampling, cycle-to-cycle phase lag was more variable,

but was still significant for ipsilateral joints (in both tactile sampling episodes, Rayleigh test,  $p < 0.01$ ) and contralateral, functionally analogous joints (wall contact episode, Rayleigh test,  $p < 0.01$ ). In case of contralateral homologous joints, no consistent phase lag could be observed. After the last edge contact, phase relationships tended to return to the values before antennal contact values and showed a significant phase lag in all cases ( $p < 0.01$ ).

If a phase lag in Figure 10 was found to be statistically significant (Table 2), we tested whether the preferred phase lag changed between subsequent episodes. In the coupling of ipsilateral antennal joints, the phase lag did not change significantly from the before-contact episode ( $\phi = 338.4^\circ$ ) to the wall contact episode ( $\phi = 337.6^\circ$ , Watson-Williams test,  $p = 0.9427$ ), but did change significantly from wall to edge contact episode ( $\phi = 375.6^\circ$ ,  $p = 0.0082$ ) and again after the last edge contact ( $\phi = 324.9^\circ$ , Watson-Williams test,  $p < 0.0001$ ). For contralateral joint pairs, the phase lag after antennal contact was not significantly different from that before antennal contact in case of homologous HS joints (Watson-Williams test,  $p = 0.0535$ ) and functionally analogous joints ( $p = 0.1328$ ), but was weakly significant for homologous SP joints (Watson-Williams test,  $p = 0.0270$ ).

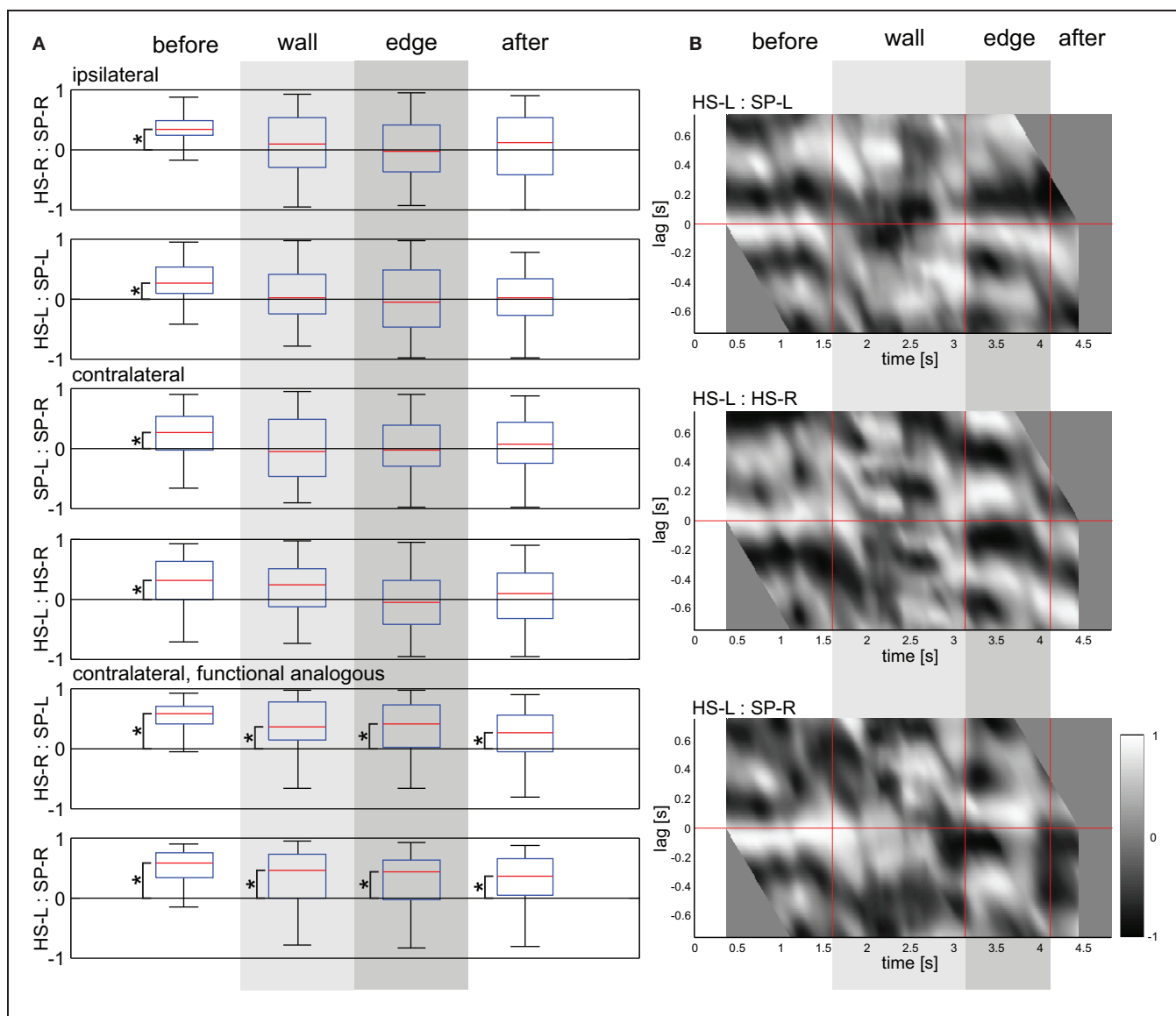


**FIGURE 9 | Correlations between ipsilateral and contralateral antennal joints. (A)** Box-whisker plots show correlation coefficients between the pair of joint angle time courses indicated (HS: head scape joint; SP: scape pedicel joint; -L: left; -R: right), for the four subsequent trial episodes (before, wall, edge, and after). Data from all four obstacle heights were pooled ( $n = 100$ ). Coefficients were calculated for the duration of whole trial episodes. Asterisks denote significant difference from zero (Wilcoxon's rank sum test on mean values per animal,  $n = 5$ , Bonferroni-corrected to

$p < 0.0167$ ). **(B)** Sliding cross-correlograms of a representative trial. The ordinate shows the lead/lag of the joints SP-L (top), HS-R (middle), and SP-R (bottom) relative to the joint HS-L. Gray levels code the correlation coefficient from  $-1$  (black) to  $1$  (white), centred on the middle of a sliding window of  $0.75$  s width. Vertical red lines mark the start of the wall contact episode, edge contact episode, and after-contact episode. Wall and edge contact episodes are marked by light and dark gray shading, respectively.

Taken together, antennal inter-joint coupling clearly changed during tactile sampling, though to different degree between different pairs of joints. During active exploration movements without contact events, as in the “before-contact” episode of climbing trials, all antennal joint pairs revealed mutual coupling. Contralateral, homologous joints had an inter-joint coupling with nearly zero phase lag (between  $-12$  and  $1^\circ$ ), while phase lag between contralateral, functionally analogous joints was very similar to ipsilateral joints ( $9$ – $20^\circ$ ). During tactile sampling, inter-joint coupling generally got weaker (as revealed by lower resultant

vector lengths in **Table 2**) but was still statistically significant between pairs of SP joints and HS joints, though with different phase lag in at least one tactile sampling episode, compared to the episode before contact.

## DISCUSSION

Stick insects use their antennae for near-range exploration (Dürr et al., 2001; Krause et al., 2012) and active tactile sampling of obstacles (Dürr et al., 2003; Schütz and Dürr, 2011). Building on these previous studies on non-contact exploration and unilateral

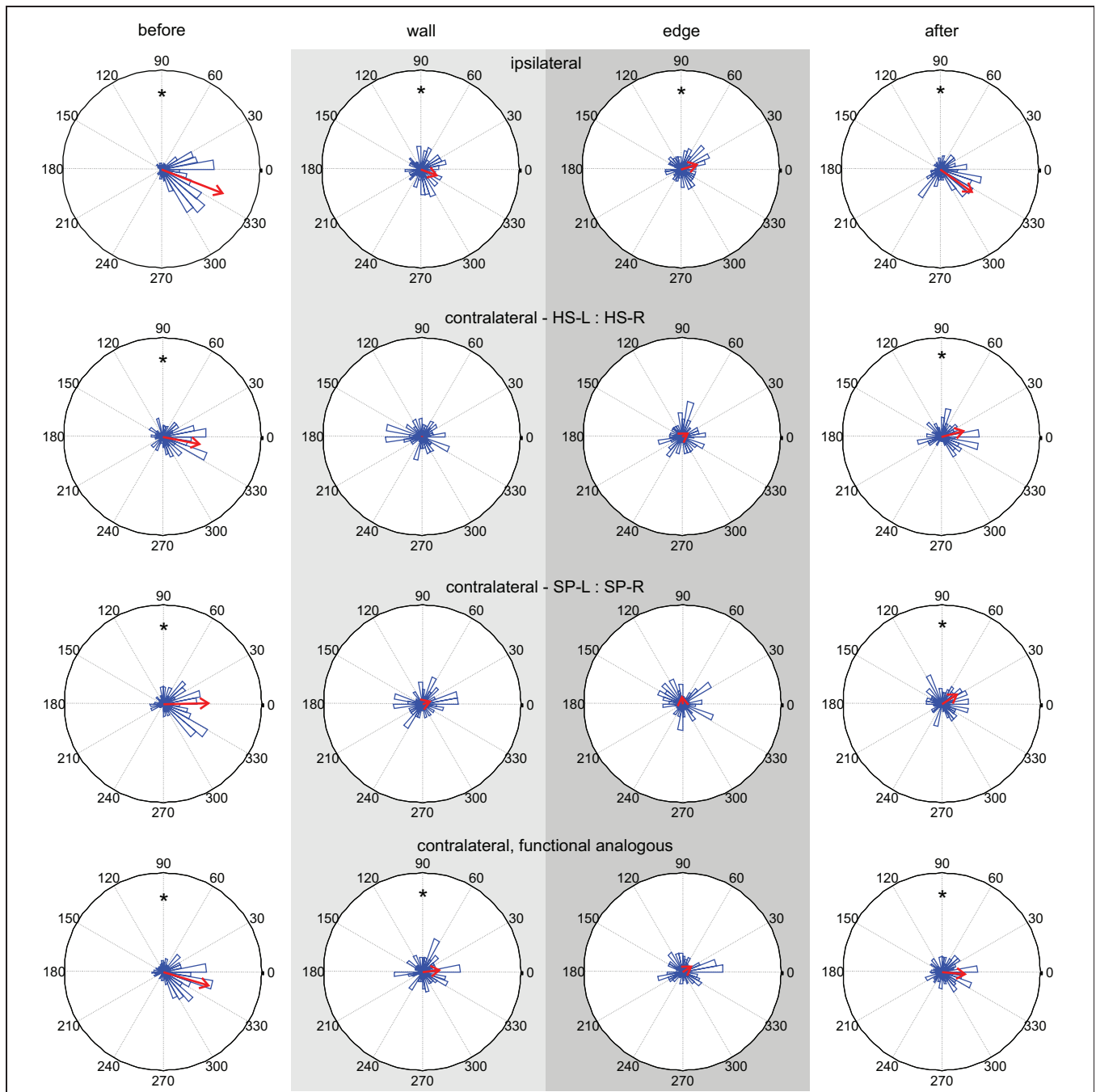


**FIGURE 10 | Inter-joint coupling of ipsilateral and contralateral antennal joints.** Columns show phase histograms of four types of inter-joint coupling (ipsilateral HS and SP joints; contralateral homologous HS or SP joints; contralateral functionally analogous HS and SP joints). The four plots of each column correspond to the same trial episode (before, wall, edge, and after contact). Wall and edge contact episodes are marked by light

and dark gray shading, respectively. Red arrows indicate the mean phase lag. Asterisks indicate statistically significant preferred phase lag (Rayleigh test). Before and after antennal contact, all pairs of antennal joints show significant cycle-to-cycle coupling. During the sampling episodes, contralateral homologous joints are not coupled.

tactile sampling, here we contribute first insights on kinematics and coordination of unrestrained bilateral tactile sampling in a climbing paradigm (Figures 1, 2). We show (1) that the distribution of antennal contact locations differs for distinct object features such as a wall or an edge (Figures 3, 4); (2) that

the distribution of contacts along the antenna depends on the contact type, revealing a functional regionalization of the antenna: wall contacts are sampled with the distal part of the flagellum, edge contacts are sampled with the whole flagellum (Figure 4); (3) that antennal working-range and cycle frequency

**Table 2 | Parameters of the phase histograms.**

	$\phi$	$R$	$P$
<b>IPSILATERAL</b>			
Before	338.36	0.6774	0.0000*
Wall	337.60	0.1932	0.0070*
Edge	375.57	0.1779	0.0064*
After	324.90	0.4137	0.0000*
<b>CONTRALATERAL: HS</b>			
Before	348.58	0.3977	0.0000*
Wall	433.72	0.0105	0.9911
Edge	387.38	0.0801	0.5847
After	373.68	0.2486	0.0016*
<b>CONTRALATERAL: SP</b>			
Before	361.09	0.4693	0.0000*
Wall	377.70	0.0896	0.5766
Edge	454.70	0.0814	0.6096
After	390.28	0.1935	0.0084*
<b>CONTRALATERAL: FUNCTIONALLY ANALOGOUS</b>			
Before	342.47	0.4932	0.0000*
Wall	366.33	0.1859	0.0072*
Edge	392.31	0.1152	0.1227
After	355.07	0.2501	0.0000*

$\phi$ , mean phase;  $R$ , resultant vector length;  $P$ , p-values of a Rayleigh test. Asterisks mark rows with p-values below 0.05. Same data as in **Figure 10**.

is significantly different before, during and after obstacle sampling (**Figures 6, 8**); (4) that body axis inclination and turning tendency increases with step height (**Figures 7, 8**); (5) that correlations and phase relationships between ipsilateral, contralateral homologous, and contralateral functionally analogous joints differ between the four trial episodes, revealing a strong coupling between all antennal joints during the pre-contact phase and a weaker coupling of ipsilateral and functionally analogous joints (left HS joint with right SP joint and *vice versa*) during sampling of the obstacle (**Figures 9, 10**). Coupling strength of contralateral homologous joints (left and right HS joint, left and right SP joint) reduces during antennation of objects.

Some assumptions were made to simplify the experimental procedure and data analysis. First, possible roll angles around the rostro-caudal body axis were neglected, because it is known that stick insects stabilise their roll angle, keeping it below 10° even on highly inclined surfaces up to 60° (Diederich et al., 2002). Second, the stick insect antennae were assumed to be a straight beam for contact point calculation. This neglects the bending of the antennal flagellum during obstacle contacts especially in the highly flexible, distal part of the flagellum. When deflected, the site of maximum curvature of the stick insect flagellum shifts with the contact site (Dürr and Dirks, 2006). This fits well to the finding that the flagellar cuticle gets thicker toward the base (Dirks and Dürr, 2011), suggesting that it is getting stiffer towards the base as well. Thus, edge contacts made with the medial or proximal part of the antenna should cause little antennal deflection. Bending of the flagellum particularly concerns the wall contact events. Owing to the bending, the calculated contact locations on the flagellum

must be considered an estimate of the most proximal contact site. The precise location and also the length of the flagellum part that is in contact with the obstacle could not be determined by this study, but it is likely that the contacting region of the flagellum may be several millimetres long, beginning distally from the contact site calculated. As for the contact location on the obstacle, the upward movement of the calculated contact site suggests that the true contact location of the bent distal flagellum is located below, owing to the contacting part being dragged upwards along the contacted wall. As a result, computed wall contact points tend to deviate from the real contact position. Nonetheless, we assume that calculated contact durations are not influenced by antennal bending, because the antenna rapidly returns to its straight posture after object contact (Dirks and Dürr, 2011). Future studies will need to employ a model of antennal bending biomechanics in order to determine contact locations both on the flagellum and on the obstacle with higher precision. Third, prothorax and head movements were suppressed by fixating them with hot bee's wax. This simplified the calculation of the body axis orientation by removing four degrees of freedom from the body model used for marker based motion tracking. These were yaw and pitch rotation of the mesothorax-prothorax joint and of the neck joint. The fixation did not affect locomotion other than making the walking direction more straight. Animals readily climbed obstacles of all heights. Nevertheless, observed body axis elevation values might be different compared to animals with full flexibility in prothorax and head joints.

When walking stick insects encounter an obstacle in their path, they show a strong tendency to climb that obstacle after initial antennal contact (Dürr et al., 2003; Schütz and Dürr, 2011). Antennation continues until the obstacle is climbed, resulting in numerous contacts. Climbing small obstacles caused little change in heading and animals kept almost straight during climbing. In contrast, high obstacles increased the variability of body axis yaw rotation up to 80°. Contact induced change in heading was also reported for cockroaches (Camhi and Johnson, 1999; Okada and Toh, 2000, 2006) and crayfish (Sandeman and Varju, 1988).

Antennal contact information plays an important role for initiation of climbing (Dürr et al., 2003) and body axis inclination increases already after a single antennal contact event (Schütz and Dürr, 2011). During wall- and edge-sampling, animals inclined their body axis, with higher obstacles inducing a more pronounced body axis elevation up to 72° for the 66 mm step. Similar results were reported for other insect species. Colorado potato beetles for example raise their body axis proportional to obstacle height after antennal contact to reach the top of the obstacle with the prothoracic leg (Pelletier and McLeod, 1994). Stick insects with cut antennae are less efficient in climbing obstacles (Dürr et al., 2003) or in crossing large gaps (Bläsing and Cruse, 2004b) underlining the importance of tactile information for obstacle negotiation. Cockroaches alter their body posture by first tilting the front of the body upwards and then elevating the center of mass to the height of the step (Watson et al., 2002; Harley et al., 2009). Changes in body posture after wall contacts are also observed in rats. Rats tilt their head upwards as a "contact maximizing" strategy for exploring walls (Grant et al., 2009).

## WHERE DO CONTACT EVENTS OCCUR?

We show that contact point distribution along the stick insect flagellum differs for contacts on vertical walls and horizontal edges. Stick insects may use the contact distance along the flagellum for behavior adaptation. For example, distal antennal contacts are more likely to occur with a large obstacle (such as a wall) with uncertain height, whereas proximal contacts are more likely to occur with the top edge of an object. While both objects may require climbing, proximal edge contacts contain information about the height to be climbed, whereas distal contacts may require additional sampling for acquiring this information. Comparable results show that cockroaches can maintain a constant distance to a vertical wall using the bend position and contact point along the flagellum in wall-following behavior (Camhi and Johnson, 1999). In their interpretation, flagellar information constitutes a one dimensional sensory map, enabling the control of wall-distance. This interpretation matches the observation of a somatotopic organization of antennal afferents in the deutocerebrum and subesophageal ganglion of the cockroach (Nishino et al., 2005) as well as antennal mechanosensory afferents entering the deutocerebrum of crickets in parallel bands, suggesting a somatotopic map (Staudacher and Schildberger, 1999). We show that left and right antenna of stick insects sample separate “regions of interest” with very little overlap. Mean locations of left and right antennal contacts along the width of the obstacles (y-direction) are more than two standard deviations apart. Broader overlap may be expected for animals without fixed neck and prothorax-mesothorax joints because active head movements may add variability. Separate “regions of interest” per antenna might increase tactile sampling efficacy in terms of overall energy consumption, as was suggested in a previous simulation study (Krause and Dürr, 2004). Assuming dominant viscoelastic friction in joints and muscles, separate regions of interest reduce overall angular velocity necessary to cover the combined sampling area of left and right antenna and thus reduce energy loss due to velocity dependent friction. Average horizontal edge contact durations (115 ms) are close to reported contact durations of unilateral sampling of a vertical beam (90 ms) (Schütz and Dürr, 2011). Mean contact durations seem to be independent of predominant edge or surface orientation of sampled objects, but future studies will need to clarify the relationship between object properties and contact durations in stick insects.

## TACTUALLY INDUCED CHANGES IN KINEMATICS AND INTER-JOINT COUPLING

While sampling the wall of an obstacle, stick insects show significantly higher antennal cycle frequencies in both the HS and SP joint. In combination with a significantly reduced working-range in both joints a contextual switch after first antennal contact from a broad, exploratory search pattern to a fine-grained object sampling pattern was observed. Schütz and Dürr (2011) reported a four-fold increase in antennal cycle frequency after first contact with a vertical beam. In this study, cycle frequency increase is not as pronounced. Reasons can be the different behavioural context (step with vertical face and horizontal edge vs. vertical beam) and different analysis methods. Here, cycle frequency was estimated from a weighted average of the FFT

spectrum in contrast to frequency estimation by counting the number of local minima and maxima in Schütz and Dürr (2011). Context-modulated changes in antennal behavior were reported in Okada and Toh (2006) for cockroaches, where contact frequency positively correlates with the animals turn angle toward a wooden rod placed at a lateral position relative to the animal. Rats show a very similar behavior: in “exploratory whisking,” they sweep their whiskers in large amplitudes with a frequency in a range of 5–15 Hz. If presented an object, rats thrust their whiskers forward and palpate the object with low-amplitude and high frequency (15–25 Hz) movements called “foveal whisking” (Berg and Kleinfeld, 2003). Additionally, rats reduce the “spread” between individual whiskers to maximize surface contacts while sampling vertical walls (Grant et al., 2009). Other small mammals also show contact induced changes in whisking patterns (Brecht et al., 2011; Mitchinson et al., 2011). An interesting question is the role of antennal proprioceptors for the control of active tactile sampling. Okada and Toh (2000) have shown the importance of HS joint hair plates for orientation toward touched objects in cockroaches. Krause et al. (2012) have shown the influence of antennal hair fields on antennal working-range during exploratory, non-contact antennal movements in stick insects. Future studies will need to investigate the effect of antennal proprioceptor ablation on antennal coordination, kinematic parameters, and contact patterns in the stick insect.

Little is known about the temporal coordination of antennal movements on the level of individual joints in insects. Okada and Toh (2004) found that bilateral antennal coordination depends on the animal’s behavioral state and is significantly stronger in walking than in resting. Schütz and Dürr (2011) reported a distinct switch in ipsilateral antennal coordination while unilateral sampling of vertical rods. Ipsilateral antennal joint coordination in stick insects was reported to be strong in non-contact situations and was not affected by ablation of proprioceptive hair fields close to the antennal joints (Krause et al., 2012). Apart than that, a simulation study suggested that an elliptical sampling pattern with a fixed phase relationship in ipsilateral antennal joints increases the likelihood to detect obstacles (Krause and Dürr, 2004). In this study we show that antennal inter-joint coordination changes upon obstacle contact. In the pre-contact episode, we observe a strong cycle-to-cycle coupling among ipsilateral, contralateral and functionally analogous joints. After antennal contact, ipsilateral cycle-to-cycle coordination is weaker, but still significant with a distinct change in mean phase while edge-sampling, indicating a contact-triggered switch in sampling behaviour (**Figure 10, Table 2**). Bilateral antennal coordination changes upon obstacle contact. Correlation values in **Figure 9** indicate a clear difference between contralateral homologous and contralateral functionally analogous joints. Functionally analogous joints keep a weak but significant cycle-to-cycle coupling during wall sampling (**Figure 10**), resulting in concerted parallel movements of both antennae. This might be a special characteristic of stick insect antennae or could be an efficient bilateral obstacle sampling strategy. Homologous joints in contrast show no consistent phase lag anymore during contact episodes.

During obstacle sampling, both antennae now seem to operate more contact-feedback driven and independent from each other. After tactual contacts (post-contact episode), bilateral phase coupling tends to return to pre-contact values. Post-contact episodes in this set of experiments were rather short, because high speed recording time was limited to RAM size. A full recovery to pre-contact coordination and phase relationships after an obstacle was completely climbed is predicted. Contact driven feedback control is discussed by Mitchinson et al. (2007) for rats. They found that whisker movements are under active, contact induced feedback control to increase the likelihood of environmental contacts.

## REFERENCES

- Ahissar, E., and Knutsen, P. M. (2008). Object localization with whiskers. *Biol. Cybern.* 98, 449–458.
- Anjum, F., Turni, H., Mulder, P. G., van der Burg, J., and Brecht, M. (2006). Tactile guidance of prey capture in Etruscan shrews. *Proc. Natl. Acad. Sci. U.S.A.* 103, 16544–16549.
- Barnes, T. G., Truong, T. Q., Adams, G. G., and McGruer, N. E. (2001). Large deflection analysis of a biomimetic lobster antenna due to contact and flow. *ASME J. Appl. Mech.* 68, 948–951.
- Berg, R. W., and Kleinfeld, D. (2003). Rhythmic whisking by rat: retraction as well as protraction of the vibrissae is under active muscular control. *J. Neurophysiol.* 89, 104–117.
- Bläsing, B., and Cruse, H. (2004a). Mechanisms of stick insect locomotion in a gap crossing paradigm. *J. Comp. Physiol. A Neuroethol. Sens. Neural Behav. Physiol.* 190, 173–183.
- Bläsing, B., and Cruse, H. (2004b). Stick insect locomotion in a complex environment: climbing over large gaps. *J. Exp. Biol.* 207, 1273–1286.
- Bouquet, J. Y. (2005). Complete camera calibration toolbox for Matlab. Available online at: <http://www.vision.caltech.edu/bouquetj/calib-doc>
- Brecht, M. (2007). Barrel cortex and whisker-mediated behaviors. *Curr. Opin. Neurobiol.* 17, 408–416.
- Brecht, M., Naumann, R., Anjum, F., Wolfe, J., Munz, M., Mende, C., and Roth-Alpermann, C. (2011). The neurobiology of Etruscan shrew active touch. *Philos. Trans. R. Soc. Lond. B Biol. Sci.* 366, 3026–3036.
- Camhi, J. M., and Johnson, E. N. (1999). High-frequency steering maneuvers mediated by tactile cues: antennal wall-following in the cockroach. *J. Exp. Biol.* 202, 631–643.
- Comer, C. M., Parks, L., Halvorsen, M. B., and Breese-Terteling, A. (2003). The antennal system and cockroach evasive behavior. II. Stimulus identification and localization are separable antennal functions. *J. Comp. Physiol. A Neuroethol. Sens. Neural Behav. Physiol.* 189, 97–103.
- de Sinéty, R. (1901). “Recherches sur la biologie et l’anatomie des Phasmes,” *La Cellule XIX* (J. van In and Cie, Liège), 118–278.
- Dehnhardt, G., Mauck, B., and Bleckmann, H. (1998). Seal whiskers detect water movements. *Nature* 394, 235–236.
- Diamond, M. E., von Heimendahl, M., and Arabzadeh, E. (2008). Whisker-mediated texture discrimination. *PLoS Biol.* 6:e220. doi: 10.1371/journal.pbio.0060220
- Diederich, B., Schumm, M., and Cruse, H. (2002). Stick insects walking along inclined surfaces. *Integr. Comp. Biol.* 42, 165–173.
- Dirks, J. H., and Dürr, V. (2011). Biomechanics of the stick insect antenna: damping properties and structural correlates of the cuticle. *J. Mech. Behav. Biomed. Mater.* 4, 2031–2042.
- Dürr, V., and Dirks, J. H. (2006). “Biomechanics of active tactile sensing with an insect antenna,” in *Proceedings of the 99th Annual Meeting of the German Zoological Society*, (Münster, Germany), 59.
- Dürr, V., Krause, A. F., Schmitz, J., and Cruse, H. (2003). Neuroethological concepts and their transfer to walking machines. *Int. J. Robotics. Res.* 22, 151–167.
- Dürr, V., König, Y., and Kittmann, R. (2001). The antennal motor system of the stick insect *Carausius morosus*: anatomy and antennal movement pattern during walking. *J. Comp. Physiol. A* 187, 131–144.
- Erber, J., Kierzek, S., Sander, E., and Grandy, K. (1998). Tactile learning in the honeybee. *J. Comp. Physiol. A* 183, 737–744.
- Gewecke, M., and Heinzel, H.-G. (1980). Aerodynamic and mechanical properties of the antennae as air-current sense-organs in *Locusta migratoria*. I. Static characteristics. *J. Comp. Physiol. A* 139, 357–366.
- Grant, R. A., Mitchinson, B., Fox, C. W., and Prescott, T. J. (2009). Active touch sensing in the rat: anticipatory and regulatory control of whisker movements during surface exploration. *J. Neurophysiol.* 101, 862–874.
- Harley, C. M., English, B. A., and Ritzmann, R. E. (2009). Characterization of obstacle negotiation behaviors in the cockroach, *Blaberus discoidalis*. *J. Exp. Biol.* 212, 1463–1476.
- Heinzel, H.-G., and Gewecke, M. (1987). Aerodynamic and mechanical properties of the antennae as air-current sense-organs in *Locusta migratoria*. II. Dynamic characteristics. *J. Comp. Physiol. A* 161, 671–680.
- Kevan, P. G., and Lane, M. A. (1985). Flower petal microtexture is a tactile cue for bees. *Proc. Natl. Acad. Sci. U.S.A.* 82, 4750–4752.
- Krause, A. F., and Dürr, V. (2004). Tactile efficiency of insect antennae with two hinge joints. *Biol. Cybern.* 91, 168–181.
- Krause, A. F., Winkler, A., and Dürr, V. (2012). Central drive and proprioceptive control of antennal movements in the walking stick insect. *J. Physiol. Paris* (in press).
- Miersch, L., Hanke, W., Wieskotten, S., Hanke, F. D., Oeffner, J., Leder, A., Brede, M., Witte, M., and Dehnhardt, G. (2011). Flow sensing by pinniped whiskers. *Philos. Trans. R. Soc. Lond. B Biol. Sci.* 366, 3077–3084.
- Mitchinson, B., Grant, R. A., Arkley, K., Rankov, V., Perkon, I., and Prescott, T. J. (2011). Active vibrissal sensing in rodents and marsupials. *Philos. Trans. R. Soc. Lond. B Biol. Sci.* 366, 3037–3048.
- Mitchinson, B., Martin, C. J., Grant, R. A., and Prescott, T. J. (2007). Feedback control in active sensing: rat exploratory whisking is modulated by environmental contact. *Proc. R. Soc. B Biol. Sci.* 274, 1035–1041.
- Morita, T., Kang, H., Wolfe, J., Jadhav, S. P., and Feldman, D. E. (2011). Psychometric curve and behavioral strategies for whisker-based texture discrimination in rats. *PLoS ONE* 6:e20437. doi: 10.1371/journal.pone.0020437
- Mujagic, S., Krause, A. F., and Dürr, V. (2007). Slanted joint axes of the stick insect antenna: an adaptation to tactile acuity. *Naturwissenschaften* 94, 313–318.
- Nishino, H., Nishikawa, M., Yokohari, F., and Mizunami, M. (2005). Dual, multilayered somatosensory maps formed by antennal tactile and contact chemosensory afferents in an insect brain. *J. Comp. Neurol.* 493, 291–308.
- Okada, J., and Toh, Y. (2000). The role of antennal hair plates in object-guided tactile orientation of the cockroach (*Periplaneta americana*). *J. Comp. Physiol. A* 186, 849–857.
- Okada, J., and Toh, Y. (2004). Spatio-temporal patterns of antennal movements in the searching cockroach. *J. Exp. Biol.* 207, 3693–3706.
- Okada, J., and Toh, Y. (2006). Active tactile sensing for localization of objects by the cockroach antenna. *J. Comp. Physiol. A Neuroethol. Sens. Neural Behav. Physiol.* 192, 715–726.
- Pelletier, Y., and McLeod, C. D. (1994). Obstacle perception by insect antennae during terrestrial locomotion. *Physiol. Entomol.* 19, 360–362.
- Prescott, T. J., Diamond, M. E., and Wing, A. M. (2011). Active touch sensing. *Philos. Trans. R. Soc. Lond. B Biol. Sci.* 366, 2989–2995.
- Sandeman, D. C., and Varju, D. (1988). A behavioral study of tactile localization in the crayfish *Cherax destructor*. *J. Comp. Physiol. A* 163, 525–536.

- Schütz, C., and Dür, V. (2011). Active tactile exploration for adaptive locomotion in the stick insect. *Philos. Trans. R. Soc. Lond. B Biol. Sci.* 366, 2996–3005.
- Srinivasan, M. V. (2010). Honey bees as a model for vision, perception, and cognition. *Annu. Rev. Entomol.* 55, 267–284.
- Staudacher, E., Gebhardt, M. J., and Dür, V. (2005). Antennal movements and mechanoreception: neurobiology of active tactile sensors. *Adv. Insect Physiol.* 32, 49–205.
- Staudacher, E., and Schildberger, K. (1999). A newly described neuropile in the deutocerebrum of the cricket: antennal afferents and descending interneurons. *J. Zool.* 102, 212–226.
- Watson, J. T., Ritzmann, R. E., Zill, S. N., and Pollack, A. J. (2002). Control of obstacle climbing in the cockroach, *Blaberus discoidalis*. I. Kinematics. *J. Comp. Physiol. A Neuroethol. Sens. Neural Behav. Physiol.* 188, 39–53.
- Woo, A. (1990). “Fast ray-box intersection,” in *Graphics Gems*, ed A. S. Glassner (San Diego, CA: Academic Press Professional, Inc.), 395.
- Zakotnik, J., and Dür, V. (2005). “Motion analysis using stochastic optimisation and posture disambiguation,” in *Proceedings of the 3rd International Symposium on Adaptive Motion in Animals and Machines*, ed H. Witte (Ilmenau, Germany: AMAM2005).
- Zakotnik, J., Matheson, T., and Dür, V. (2004). A posture optimisation algorithm for model-based motion capture of movement sequences. *J. Neurosci. Methods* 135, 43–54.
- Conflict of Interest Statement:** The authors declare that the research was conducted in the absence of any commercial or financial relationships that could be construed as a potential conflict of interest.
- Received: 28 March 2012; accepted: 01 June 2012; published online: 28 June 2012.
- Citation: Krause AF and Dür V (2012) Active tactile sampling by an insect in a step-climbing paradigm. *Front. Behav. Neurosci.* 6:30. doi: 10.3389/fnbeh.2012.00030
- Copyright © 2012 Krause and Dür. This is an open-access article distributed under the terms of the Creative Commons Attribution Non Commercial License, which permits non-commercial use, distribution, and reproduction in other forums, provided the original authors and source are credited.